PARTRAC

Arklow Bank Wind Park Morphodynamic Study
Interpretative Report
LF100034-MIP-GT-REP-0001

February 2022



DOCUMENT CONTROL

Version History					
Version	Date	Prepared by	Reviewed by	Approved by	Approved as
V01	29/10/2021	J. Poleykett L. Huynh M. Wright J. Hernon W. Cooper K. Black M. Gasmalseed	J. Poleykett J. Hernon W. Cooper K. Black M. Wright	K. Black	Draft
V02	14/01/2022	J. Poleykett M. Gasmalseed L. Huynh	J. Hernon W. Cooper K. Black	K. Black	Draft
V03	15/02/2022	J. Poleykett	K. Black	K. Black	Final

Changes from the Previous Version	
n/a	Original version.
V02	Updated in response to client comments.
V03	Updated in response to client comments

Recipient	Distribution Method		
	Paper (copies)	PDF	Online
John Davidson (SSE Renewables)		x	
Holders of controlled copies will automatically be provided with subsequent approved versions of this document when they become available.			

This document is of UK origin and is copyright © 2022 Partrac Ltd. It contains proprietary information which is disclosed for the purposes of evaluation only. The contents of the document shall not in whole or in part: (i) be used for any other purpose; (ii) be disclosed to any member of the recipient's organisation not having a need to know such information nor to any third party, individual, organisation or government; (iii) be stored in any retrieval system nor be reproduced or transmitted in any form by photocopying or any optical, electronic, mechanical or other means without the prior written permission from a Director of Partrac Ltd.

The following commission has been delivered by Partrac Ltd, MetOceanWorks Ltd and Cooper Marine Advisors Ltd

Glossary

The following list describes common metocean and sediment dynamics terms used throughout this report, and where appropriate presents the abbreviation.

T_0	Bed Shear Stress
T_{crit}	Critical Bed Shear Stress
ABMS	Arklow Bank Modelling Suite
ABWP	Arklow Bank Wind Park
AGDS	Acoustic Ground Discrimination Systems
Amphidromic point	A location where the tidal range is effectively nil but increases with distance from this point in a rotary manner due to the Coriolis effect.
Bedload transport	Transport of sediment grains by means of rolling, sliding, and/or saltating (hopping).
BGS	British Geological Survey
BPZ	Bedload parting zone. The region where the sediment transport pathways (mostly under bedload transport) diverge.
CD	Chart Datum
CSM	Conceptual Sediment Model: a synthesis of available evidence which brings together all the component parts of the analysis for different timescales and spatial scales to develop an overall understanding of system behaviour.
Current speed	Magnitude of local current flow.
d_{50}	Grain size representing the 50th percentile grain size in the distribution from a sample
Diamict	A terrigenous sediment (a sediment resulting from dry-land erosion) that is unsorted to poorly sorted and contains particles ranging in size from clay to boulders, suspended in a matrix of mud or sand, most commonly applied to

	unsorted glacial deposits
EIA	Environmental Impact Assessment
ES	Environmental Statement
Fetch	The uninterrupted distance of open water over which the wind blows without significant change in direction
FNU	Formazin Nephelometric Unit
GIS	Geographical Information System
Global Scour	Erosion of seabed material at a group of foundations as the flow speeds increase around it, causing complex vortex patterns
Graben	An elongated block of the earth's crust lying between two faults and displaced downwards relative to the blocks on either side, as in a rift valley
GSI	Geological Survey of Ireland
HAT	Highest Astronomical Tide. The maximum level of sea surface due to tidal forcing alone
HD	Hydrodynamic
H_{max}	Maximum Wave Height
H_s	Significant wave height. Approximately the average height of the highest one third of the waves in a defined period, estimated from the wave spectrum as $4\sqrt{m_0}$.
LAT	Lowest Astronomical Tide. The minimum level of sea surface due to tidal forcing alone
Local Scour	Erosion of seabed material at a single foundation as the flow speeds up around it, causing complex vortex patterns
Local-scale	Near-field spatial scale considers sandwave features, individual foundations and cable routes

Long-term	Temporal scale considers over years and decades (compatible with project lifetime) and climate change influences
MBES	Multibeam echosounder
Medium-term	Temporal scale considers over months to years in response to the periodic lunar tidal cycles and episodic seasonal wave variations
Meso-scale	Intermediate-field spatial scale considers sandbank features, coastlines and array scale issues
MHW	Mean High Water. Mean of all high-water levels
MHWN	Mean High Water Neap. Mean high water level during neap phase of tidal cycle
MHWS	Mean High Water Spring. Mean high water level during spring phase of tidal cycle
MLW	Mean Low Water. Mean of all low water levels
MLWN	Mean Low Water Neap. Mean low water level during neap phase of tidal cycle
MLWS	Mean Low Water Spring. Mean low water level during spring phase of tidal cycle
Morphodynamics	The interaction and adjustment of the seafloor topography and fluid hydrodynamic processes, seafloor geomorphologies and sequences of change dynamics involving the motion of sediment
MSL	Mean Sea Level. Mean sea surface elevation over a prolonged period of time
NTU	Nephelometric Turbidity Units
Porosity	The proportion of sediment to voids in a sample of sediment
PSA	Particle Size Analysis
Regional-scale	Far-field spatial scale considers exposure conditions or site and wider linkages between macro bedforms (e.g. sediment pathways, sources and stores)
Relative density	The density of the grains of sediment relative to water

Residual level	Difference between the tidal level estimated by harmonic analysis/prediction and the actual level. Includes any errors due to failure to adequately resolve the tidal signal. Includes meteorologically induced storm surge
Short-term	Temporal scale considers individual tidal cycle, individual extreme events
SPM	Suspended Particulate Material
Still water level	Instantaneous water level in the absence of waves but including water level variations due to tide and meteorologically induced forcing
Surge current	Current driven by processes excluding astronomical forcing and wave induced motions
Suspended load transport	Sediment uplifted by the fluid's flow in the process of sediment transportation. It is kept suspended by the fluid's turbulence
Tidal current	Current driven by astronomical forcing
Tidal level	Still water level relative to a defined datum due to astronomical forcing. Tidal elevations exclude all meteorologically induced forcing
Total current	Combination of tidal and surge current
T_p	The spectral peak period. The period at which most energy is present in the wave spectrum.
T_z	The mean zero-crossing wave period. Estimated from the wave spectrum as $\sqrt{m_0/m_2}$.
WTG	Wind Turbine Generator
Basal till	Material carried in the base of the glacier and commonly laid down under the feature
BP	Before Present
EMODnet	The European Marine Observation and Data Network

Glacial moraine	Accumulation of unconsolidated rocky debris produced by a glacier
Holocene	The most recent geological epoch from around 11,700 BP to the present day which is defined by the time since the end of the last glacial period (Pleistocene)
ka	Thousand years
Isobath	A contour line connecting all points of equal depth below the surface of a body of water
Marine transgression	A geologic event during which sea level rises relative to the land and the shoreline moves toward higher ground, resulting in coastal inundation and the possibility for sediment to be eroded
Moribund	A sandbank feature formed during periods of lower sea level that are no longer actively maintained by contemporary sediment transport processes (stranded in locations where currents become weaker) and thus have become relict features. Moribund is a term first introduced by Kenyon et al. (1981)
Pleistocene	Geological epoch that lasted from about 2,580,000 to 11,700 BP, spanning the world's most recent period of repeated glaciations. The end of the Pleistocene corresponds with the end of the last glacial period
Tunnel valley	Elongated and over-deepened depression formed by glacial meltwater flowing under an ice sheet at high-pressure leading to erosion of the channel bed

Units and Conventions

The following list describes the units and conventions used in this report. Unless stated otherwise, units have been expressed using the SI convention.

- Wave direction is expressed in compass points or degrees, relative to true North [°T], and describes the direction from which the waves are propagating.
- Wave heights are expressed in metres [m].
- Wave periods are expressed in seconds [s].
- Current direction is expressed in compass points or degrees, relative to true North [°T], and describes the direction towards which the currents are flowing.
- Current speeds are expressed in metres per second [m/s].
- Water levels are expressed in metres [m].
- Positions are quoted relative to WGS 84 except where stated.
- All times are quoted in Coordinated Universal Time [UTC].
- Vertical levels are quoted relative to Lowest Astronomical Tide (LAT).
- The friction at the seabed expressed in terms of a bed shear stress (units N/m^2); the associated drag coefficient (Manning's n) is non-dimensional and expressed as a drag coefficient applicable to depth-averaged flow.
- The threshold for incipient sediment motion is expressed in terms of bed shear stress [N/m^2] derived using the Shields parameter. The Shields parameter, which is a dimensionless threshold, is converted to a dimensional threshold velocity, which once exceeded the sediment starts to move. The threshold for movement of sediments is expressed in metres per second [m/s].
- Volume concentrations of sediment are expressed in kilograms per cubic metre [kg/m^3].
- Suspended load and bedload transport rate are expressed as volume of grains moving per unit times per unit width of bed (if applicable) [m^3/s or m^2/s].

Defining Key Terms

The following list describes the units and conventions used in this report. Unless stated otherwise, units have been expressed using the SI convention.

Key definitions are as follows:

- *Seabed mobility:* In many offshore locations the seabed is mobile due to the action of currents and/or waves. The criteria for mobility (sediment transport) is that the shear stress imparted by the currents and/or waves exceeds the resisting forces holding the sediment in place (Draper *et al.*, 2018). Note: a mobile seabed does not necessarily drive a vertical change in seabed level if the sediment supply is equal to the sediment loss from the area, the net change in seabed level will be negligible.
- *Vertical seabed level change:* Spatio-temporal changes to the form, and profile, of the seabed. Bathymetric (or topographic) changes which are not influenced by the presence of a structure (as opposed to scour). The difference in seabed level at any given point in time, or space. is calculated by subtracting one bathymetry $(\mathbf{t_x})$ from the other $(\mathbf{t_0})$ $(\mathbf{t_x - t_0})$.
- *Morphodynamics:* The process by which morphology affects hydrodynamics in such a way as to influence the further evolution of the morphology itself (Friedrichs, 2011).
- *Scour:* When a temporary or permanent structure is placed onto the seabed, its presence disturbs the natural flows in a way that can result in spatial variations in sediment transport close to the structure. This can result in net erosion (i.e., scour) or accumulation (i.e., sedimentation) of sediment in the vicinity of the structure (Draper *et al.*, 2018).
    - *Local scour:* scour around an individual structure, for example around a single monopile or around one leg of a jacket structure.
    - *Global scour:* scour within and closely around a group of foundations as the flow speeds increase around the array, causing complex vortex patterns and potentially significant erosion.
    - *Edge scour:* scour occurring outside the scour protection caused by the interaction of the flow with the structure and protection.
- *Live bed scenario*: Where $T_0 > T_{crit}$ almost constantly, resulting in mobilsed sediments being in a state of flux during all periods of the tide except during slack water.
- *Sandbank*: bedforms consisting of cohesive or non-cohesive sediments in estuaries and continental shelf areas.
- *Sandwaves:* flow-transverse marine subaqueous dunes, often with superimposed megaripples. These features have a typical length of 100 to 800 m and crest heights (i.e. amplitude, crest to trough) of several metres (e.g. van Dijk and Kleinhans, 2005).
- *Megaripples:* flow-transverse bed forms with a typical length of 5 to 20 m and crest heights of 0.2 to 1.5 m (e.g. Tobias, 1989; Ashley, 1990).

- *Bank Crest*: The point at which mobile sediments moving in opposing directions on either side of a sandbank converge at the crestline. The bank crest on Arklow Bank, in an analogous fashion to sandwave migration, is postulated to move in the direction of the lee slope.
- *Flanks of the bank*: The area of the bank that sits between the shallowest regions of the bank, the bank crest and the seafloor surrounding the bank feature. The flanks of a sandbank are typically characterised by steep slopes. Review of the bathymetric datasets collected in 2016, and 2019, shows on Arklow Bank, the flanks of the bank can be considered to extend from approximately the -10 m LAT contour to the -30 m LAT contour.
- *Bank head*: The area of the bank which is nourished by the dominant regional sediment supply. At Arklow Bank this is coincident with the northern end of the bank.
- *Bank tail*: The opposite end of the bank to the head of the bank, typically characterised by a net loss of sediment from the sediment cell. At Arklow Bank this is coincident with the southern end of the bank.

Executive Summary

Arklow Bank is a narrow linear sandbank formed across a glacial moraine. The bank is situated in the Irish Sea to the east of Arklow, County Wicklow. Arklow Bank forms part of a series of coast-parallel, north-south trending, offshore banks. SSE Renewables is currently in the development phase of the Arklow Bank Wind Park (ABWP). The company holds a lease to develop up to 200 Wind Turbine Generators (WTG) on a rectangular area of seabed aligned with Arklow Bank, which also includes two consented routes for grid connection cables from the wind farm site to shore. Presently, there are seven, 3.6MW WTG, operating within the pre-existing Phase 1 lease area on the central crest area of Arklow Bank.

When offshore wind farms are located on, or adjacent to, shallow sandbanks high levels of seabed mobility are likely to occur which increases the need to understand potential seabed level variability, and account for the variability during design. The consortium was commissioned to undertake a comprehensive morphodynamic assessment for the ABWP development area. The overarching aim of the project was to predict the magnitude of likely bed level change which may occur across the lease area, and along the export cable route, over the lifetime of the development. The approach to the work involved a combination of qualitative/quantitative assessments of site data, empirical evaluation, detailed site modelling and application of professional judgement. This report provides a description of the sediment and morphodynamic regimes and includes the following:

- A review of the area of investigation including the regional and local setting, formation of the sandbanks on the eastern Irish coastline and their contemporary form;
- The distribution of water depths and associated sediment cover across the development area;
- The nature and influence, of the tidal and wave regimes across the development area;
- A suite of complementary data-led analysis including a shear stress assessment, detailed analysis of mobile bedforms and quantification of historic morphological change including seabed level elevation, bank shape, and profile, through time;
- A synthesis of the sediment transport regime, including the development of a regional, and local scale, Conceptual Site Models (CSM); and,
- An integrated, systems-based approach, determining future seabed levels and the potential envelope of seabed level variation which may occur across the area, over the lifetime of the development.

Observed and predicted changes to seabed levels through time, on occasion, exceed circa. 15 to 20 m, which illustrates the significant risks to windfarm infrastructure associated with seabed dynamics across the development area. The seabed region is complex and has the potential to follow multiple response pathways over the project lifetime and thus display multiple, distinct, system states. Throughout the assessment, our understanding of the hydro-sedimentary

processes which underpin the prevailing sediment transport regime across the lease area, and proposed export cable routes, has evolved. This understanding has informed the development, configuration, and application of the coupled hydrodynamic, wave and sediment transport model to provide outputs suitable to inform decision-making during design. An integrated approach was established which combined modelling efforts (focussed solely on supporting the assessment of the lateral (east-west) movement of the sandbank crestline and the subsequent effects on the shape and profile of the bank), with available measured datasets and complementary forms of analysis. In total, 31 seabed levels derived from measured (bathymetry) datasets, complementary analysis, and numerical model simulations were utilised to predict the highest and lowest potential system states likely to occur over the lifetime of the development. Appropriate confidence limits were applied, though no additional safety margins, beyond those described in this report were used.

At the conclusion of the current stage of the morphodynamic study for the Arklow Bank Offshore Wind Farm it is judicious to identify possible next steps which would potentially improve confidence in the predictions made regarding the estimated variation in future seabed levels across the lease area, to support the subsequent design process. Two options exist:

1. Further, data collection, specified, reviewed, and interpreted within the framework of conceptual understanding developed to date; and
2. Research and development type studies to explore potential further numerical modelling options or remote sensing opportunities for long term monitoring of the form, and profile, of the shallowest regions of the bank.

Where the potential exists for existing datasets to be bolstered by additional data/analyses to provide further lines of evidence from which to draw conclusions, these opportunities should be explored. In addition to further data collection, it has been postulated that research and development type projects may also benefit the study and wider project. To investigate these concepts further, small-scale research and development type pilot studies would be proposed, the overarching aim of which would be to assess the potential application and value of these options.

Contents

Glossary 3

Units and Conventions 8

Defining Key Terms 9

Executive Summary 11

1 Project Appreciation 43

2 Study Scope and Approach 45

2.1 Report Structure 47

3 Data Availability 49

3.1 Historic Bathymetric Data 49

3.2 Metocean Measurement Campaign 52

3.3 Outstanding Data 60

4 Modelling Tools and Applications 61

5 Project Considerations 64

5.1 Defining Spatial-Temporal Scales 65

5.2 Determination of the Nearshore Boundary 67

5.3 Coordinate Reference System 69

5.4 Wind Farm Infrastructure 69

5.5 Climate Change Effects 69

6 Geology and the Origin of the Sand Banks on the Eastern Irish Seaboard 72

6.1 Modern Day Setting: Historic Chart Analysis 75

6.2 Classification of Arklow Bank 78

7 Regimes at the Regional Scale 80

7.1 Hydrodynamic Regime 80

7.2 Wave Regime 84

7.3 Sediment Regime 86

7.4 Conceptual Understanding of Prevailing Regimes at the Regional Scale 94

8 Prevailing Regimes at the Local Scale 97

8.1 Anatomy of Arklow Bank 97
8.2 Seven Fathom Bank 98
8.3 Local Bathymetry and Slope 99
8.4 Hydrodynamic Regime 102
8.5 Wave Regime 123
8.6 Sediment Regime 133
8.7 Observed Bed Level Change 172
8.8 Bedform Analysis 188
8.9 Repositioning of the Crestline and Changes to the Shape and Profile of the Bank 210
8.10 Conceptual Understanding of Processes Occurring at the Local Scale 280
9 Predicting Future Seabed Levels 287
9.1 Model Development 290
9.2 Model Setup: Morphological Reduction Technique 293
9.3 Model Performance During Validation 295
9.4 Application of the Model 310
9.5 Model Simulations Performed 311
9.6 Confidence Limits Applied to Future Seabed Levels 315
9.7 Combining Data Driven Analysis, Numerical Modelling Outputs and Confidence Limits 320
10 Predicted Seabed Levels 322
10.1 LSBL vs. the Depth of the Mobile Layer 333
11 Implications for Foundations and Cabling 334
11.1 Layout Optimisation and Seabed / Structure Interaction 334
11.2 Cable Exposure, Burial or Re-burial 336
12 Concluding Remarks 342
12.1 Possible Next Steps 346
13 References 348
14 Appendix A: Data Available to the Commission 362
Appendix B: Determining the Depth of Closure 387

Appendix C: The Formation of Sand Banks on the Eastern Irish Seaboard 388

Appendix D: Threshold Current Speed (U_{cr}) 404

Appendix E: Flow Through the Water Column 405

Appendix F: Sandwave Analysis 408

Appendix G: Merging Bathymetry Datasets 443

Appendix H: Arklow Bank Modelling Suite (ABMS) 459

Appendix I: Local Scour Potential 471

FIGURES

Figure 1. ABWP Lease Area: and consented cable routes overlain the local and regional bathymetry (source: EMODnet and INFOMAR Bathymetry). Note bathymetry at the regional scale is relative to MSL. 43

Figure 2. Schematic showing the spatial and temporal scales associated with morphological response of the seabed. Image reproduced from Whitehouse (1997). 47

Figure 3. The spatial layout of available historic bathymetry data. 51

Figure 4. A schematic detailing the modelling tools and their application within the study of site morphodynamics at the ABWP. 63

Figure 5. The boundary extents for 'regional' and 'meso' spatial scales overlain on the bathymetry (m MSL) of the Irish Sea (source: EMODnet Bathymetry). 66

Figure 6. Estimated depth of closure following the equations presented by Hallermeir,1981 and 1983. The 'outer' closure depth denotes the projects nearshore boundary. 68

Figure 7. The three emission scenarios presented in the form of a time series of time-mean sea level change. Plot reproduced from UKCP 18 (2018). 71

Figure 8. Location of the various sandbanks, which form the local bathymetry along the eastern seaboard of Ireland1. (Source: INFOMAR Bathymetry). 73

Figure 9. The -10 m contour analysis from the 1978 and 2018 edition of Chart no 1787 and the MBES data acquired in 2016 and 2019. 77

Figure 10. The -20 m contour analysis from the 1978 and 2018 edition of Chart no 1787 and the MBES data acquired in 2016 and 2019. 78

Figure 11. Classification of tidal and non-tidal sandbanks. Image reproduced from Kenyon and Cooper (2005) and including the classification of Dyer and Huntley, (1999). 79

Figure 12. tidal range during a mean spring tide. The location of Arklow Bank within each plot is marked as a bounded area as a white line. Source: ABMS. 81

Figure 13. maximum depth-averaged current velocities. The location of Arklow Bank within each plot is marked as a bounded area as a white line. Source: ABMS. 82

Figure 14. 50-year return period storm surge elevations in cm (figure reproduced from Flather, 1987). 83

Figure 15. 50-year return period storm surge currents in m/s (figure reproduced from Flather, 1987). 84

Figure 16. Map of indicative values of 50-year return period significant wave height (m). Figure reproduced from Carter (1993). 86

Figure 17. Surficial Sediment Distribution in the Irish Sea at the regional scale. Source: BGS (2019): digital map SBS250. Note for sediment classification, the standard Folk triangle was used, based on the percentage of gravel and the sand: mud ratio. 87

Figure 18. Regional sediment transport directions and bedload parting zones. The Arklow regional scale is indicated by the bounded area coloured magenta. The BPZ is adapted from Holmes and Tappin, (2005). Image reproduced from Mellet et al. (2015). 89

Figure 19. The regional bedload transport pathways (left) and a zoomed in image of the bedload parting zone to the north of Arklow Bank. Image reproduced from Van Landeghem et al. (2009). (Arklow Bank is bounded in red area). 90

Figure 20. Average net sandwave migration rates per year from repeated MBES data. Image reproduced from Van Landeghem et al., (2012). 91

Figure 21. Spatial plots showing the tracks from particles, released on peak flood (left and peak ebb (right) from a location next to the mouth of the Avoca River and at the coast, south of Wicklow Head. Note: the particles released at the mouth of the Avoca River did not move in the 30-day simulation. 93

Figure 22. Visualisation of the conceptual understanding of processes occurring at the regional scale. 96

Figure 23. A schematic diagram showing the anatomy of the bank and delimiting the five primary process environments across Arklow Bank. 98

Figure 24. Bathymetric plot of Arklow Bank. The dashed line shows the distinction between the north, central and south sections of the bank. Data sources: INFOMAR (2016) and EMODNET. 100

Figure 25. Slope derived from the 2019 bathymetric dataset. 101

Figure 26. The predicted relative influence of surges on water levels (top panel), and current speed (lower panel) at the north of the site, for the year 2010 derived from comparison of modelled hindcast data and data derived from a harmonic tidal analysis. 104

Figure 27. The water level data, and depth-averaged current speed, measured at frame location 'A' presented in the form of a time series. 107

Figure 28. The water level data, and depth-averaged current speed, measured at frame location 'B' presented in the form of a time series. 107

Figure 29. The water level data, and depth-averaged current speed, measured at frame location 'C' presented in the form of a time series. 108

Figure 30. The water level data, and depth-averaged current speed, measured at frame location 'D' presented in the form of a time series. 108

Figure 31. The water level data, and depth-averaged current speed, measured at frame location 'E' presented in the form of a time series. 109

Figure 32. Current speed presented as a function of direction in the form of a current rose. The data presented were measured at frame location 'A'. 109

Figure 33. Current speed presented as a function of direction in the form of a current rose. The data presented were measured at frame location 'B'. 110

Figure 34. Current speed presented as a function of direction in the form of a current rose. The data presented were measured at frame location 'C'. 110

Figure 35. Current speed presented as a function of direction in the form of a current rose. The data presented were measured at frame location 'D'. 111

Figure 36. Current speed presented as a function of direction in the form of a current rose. The data presented were measured at frame location 'E'. 111

Figure 37. Joint probability distribution showing current speed and direction. The data were retrieved from the instruments deployed at location 'A". 112

Figure 38. Joint probability distribution showing current speed and direction. The data were retrieved from the instruments deployed at location 'B". 112

Figure 39. Joint probability distribution showing current speed and direction. The data were retrieved from the instruments deployed at location 'C". 113

Figure 40. Joint probability distribution showing current speed and direction. The data were retrieved from the instruments deployed at location 'D". 113

Figure 41. Joint probability distribution showing current speed and direction. The data were retrieved from the instruments deployed at location 'E". 114

Figure 42. Water surface elevation and flow vectors during peak ebb. 117

Figure 43. Water surface elevation and flow vectors during peak flood. 118

Figure 44. The head difference derived from the water level data acquired from frame location 'B' and 'D', The values are derived by subtracting values for water levels from frame location 'D' from water levels at frame location 'B', thus negative values shows that the measured water level at frame location 'B' is less than at frame location 'D' indicating a bias towards the east of the bank and vice versa. Note: the variation in the water level data presented suggests some artificial artefacts persist within the data record. 119

Figure 45. Water surface elevation during flood (right) and ebb (left) tides showing head difference between east and west of bank. 119

Figure 46. Residual flow vectors (left panel), and residual total load transport (right panel) across the local model domain, over the lunar cycle. 120

Figure 47. Residual flow vectors (left panel), and residual total load transport (right panel) over the lunar cycle. Zoomed in to the south of the bank. 121

Figure 48. Residual flow vectors (left panel), and residual total load transport (right panel) over the lunar cycle. Zoomed in to the north of the bank. 122

Figure 49. Time series showing H_s, T_p and T_z from data retrieved from instruments deployed at location 'A'. 125

Figure 50. Time series showing H_s, T_p and T_z from data retrieved from instruments deployed at location 'B'. 125

Figure 51. Time series showing H_s, T_p and T_z from data retrieved from instruments deployed at location 'C'. 125

Figure 52. Time series showing H_s, T_p and T_z from data retrieved from instruments deployed at location 'D'. 125

Figure 53. Time series showing H_s, T_p and T_z from data retrieved from instruments deployed at location 'E'. 125

Figure 54. H_s, T_z and T_p presented as a function of direction in the form of a wave rose for each measurement frame location. 128

Figure 55. Scatter plot showing H_s vs T_z (left panel) and H_s vs T_p (right panel). 131

Figure 56. Coincident conditions occurring at frame location A during the largest wave event observed at this frame location during the measurement campaign. 132

Figure 57. Coincident conditions occurring at frame location B during the largest wave event observed at this frame location during the measurement campaign. 132

Figure 58. Coincident conditions occurring at frame location C during the largest wave event observed at this frame location during the measurement campaign. 132

Figure 59. Coincident conditions occurring at frame location D during the largest wave event observed at this frame location during the measurement campaign. 133

Figure 60. Coincident conditions occurring at frame location E during the largest wave event observed at this frame location during the measurement campaign. 133

Figure 61. The sediment volume analysis derived from the 2016 and 2019 bathymetric datasets. Plot 1, and Plot 2, shows the area of deposition, and erosion, in the form of spatial plots, respectively. Plot 3 presents these data empirically to determine the net effect of the deposition/erosion pattern observed between 2016 and 2019. 135

Figure 62. The location of the seabed grab samples (ASU, 2010 & 2011) and the borehole locations across Arklow Bank (Fugro, 2000). 137

Figure 63. The interpretation of the distribution of seabed sediments across the lease and export cable routes (GDG, 2020). 145

Figure 64. The spatial variation in the thickness of Unit 0A and Unit I (the potentially mobile layers) derived from the interpretation of seismic data. Gaps in the data coincident with the shallowest regions of the bank are evident. Shapefile provided by GDG (2020). 148

Figure 65. The spatial variation in the thickness of Unit 2 (the interpreted non-erodible level) derived from the interpretation of seismic data. Gaps in the data coincident with the shallowest regions of the bank are evident. Shapefile provided by GDG (2020). 149

Figure 66. Overview of borehole logs obtained during the Phase 1 campaign. Figure reproduced from GDG, 2020. 151

Figure 67. Hydrodynamic model outputs. Maximum bed shear stress on spring tide only (without wave action). 153

Figure 68. Time series showing the water level and current speed at frame location A. The coincident stress due to currents is also plotted. 155

Figure 69. Time series showing the water level and current speed at frame location B. The coincident stress due to currents is also plotted. 155

Figure 70. Time series showing the water level and current speed at frame location C. The coincident stress due to currents is also plotted. 156

Figure 71. Time series showing the water level and current speed at frame location D. The coincident stress due to currents is also plotted. 156

Figure 72. Time series showing the water level and current speed at frame location E. The coincident stress due to currents is also plotted. 157

Figure 73. Maximum wave orbital velocity at the seabed during typical 'p50' wave conditions. 159

Figure 74. Maximum wave orbital velocity at the seabed during the 1 in 50 years wave conditions. 161

Figure 75. Time series showing water level, H_s and current velocity and coincident turbidity data (collected using the OBS and ABS instrument) across the entire measurement campaign (top) and during a period of enhanced wave action (bottom). Data retrieved from frame location A. 163

Figure 76. Time series showing water level, H_s and current velocity and coincident turbidity data (collected using the OBS and ABS instrument) across the entire measurement campaign (top) and during a period of enhanced wave action (bottom). Data retrieved from frame location B. 164

Figure 77. Time series showing water level, H_s and current velocity and coincident turbidity data (collected using the OBS and ABS instrument) across the entire measurement campaign (top) and during a period of enhanced wave action (bottom). Data retrieved from frame location C. 165

Figure 78. Time series showing water level, H_s and current velocity and coincident turbidity data (collected using the OBS and ABS instrument) across the entire measurement campaign (top) and during a period of enhanced wave action (bottom). Data retrieved from frame location D. 166

Figure 79. Time series showing water level, H_s and current velocity and coincident turbidity data (collected using the OBS and ABS instrument) across the entire measurement campaign (top) and during a period of enhanced wave action (bottom). Data retrieved from frame location E. 167

Figure 80. Model extraction locations along the crestline. 168

Figure 81. Sediment transport normal to the bank for eight positions along the bank crest (top to bottom, north to south). 169

Figure 82. 30 day running mean sediment transport normal to the bank for eight positions along the bank crest (top to bottom, north to south). 170

Figure 83. 30 day running mean sediment transport normal to the bank for eight positions along the bank crest (top to bottom, north to south), 2000 bathymetry. 171

Figure 84. 30 day running mean sediment transport normal to the bank for eight positions along the bank crest (top to bottom, north to south), 2019 bathymetry. 172

Figure 85. Observed bed level change across the lease area. The plot is developed by comparing the single beam data acquired in 2000 with MBES data acquired in 2016. The red shading indicates accretion, and the blue shading indicates erosion. 176

Figure 86. Observed bed level change across the lease area. The plot is developed by comparing the singlebeam data acquired in 2000 with the MBES data acquired in 2019. The red shading indicates accretion, and the blue shading indicates erosion. 177

Figure 87. Observed bed level change between 2000 and 2016 (left panel) and 2000 and 2019 (right panel) presented as a nominal 'rate of change' plot. The red shading indicates accretion, and the blue shading indicates erosion. 178

Figure 88. Spatial plots showing the observed bed level change between 2016 and 2019. The red shading indicates accretion, and the blue shading indicates erosion. For reference, the -10 m contours derived from data collected in 2000 and the 2016 and 2019 datasets are included for reference. 179

Figure 89. Spatial plots showing the observed bed level change observed between 2011 and 2019. The red shading indicates accretion, and the blue shading indicates erosion. Note: the southernmost cable route has since been dropped but the data is presented as it provides useful data to consider the bed level change across the region to the west of Arklow Bank. 180

Figure 90. Various comparisons of the data acquired in IA 1 during the 2020 survey campaign. The plots presented show the bed level change through time and on occasion, pertinent profiles extracted from the data. 181

Figure 91. Various comparisons of the data acquired in IA 2 during the 2020 survey campaign. The plots presented show the bed level change through time and on occasion, pertinent profiles extracted from the data. 182

Figure 92. Various comparisons of the data acquired in IA 3 during the 2020 survey campaign. The plots presented show the bed level change through time and on occasion, pertinent profiles extracted from the data. 183

Figure 93. A comparison of the data acquired from a transect across the crestline in IA 3 during the 2020 survey campaign between the period 13.07.2020 and 07.08.2020. The plots presented are postulated to show wave influence at the crestline with a flattened profile evident, following which the reform of megaripples along the transect is clear. 184

Figure 94. Various comparisons of the data acquired in IA 4 during the 2020 survey campaign. 187

Figure 95. Schematic diagram of the three dominant processes in sandwave formation, bed load transport (net flux towards the crest, causing sandwave growth), slope induced transport (causing sandwave decay), and suspended load transport (causing sandwave decay). Reproduced from Borsje et al., 2014). 189

Figure 96. Transect analysis at a location to the SE of the bank (sandwaves crests to the left indicating southward sediment movement) (left panel). Transect analysis at a location to the SW of the Bank (sandwaves crests to the right indicating northward sediment movement) (right panel). The image at the top shows a red line which depicts the length and orientation of the profile presented below where the blue line shows the data from 2011 and the red line shows the data from 2016. 191

Figure 97. Transect analysis at a location to the mid-west of the central part of the bank (sandwaves crests to the right indicating northwardsediment movement) (left panel). Transect analysis at a location to the mid-east of the central part of the bank (sandwaves crests to the left indicating southward sediment movement) (right panel). The image at the top shows a red line which depicts the length and orientation of the profile presented below where the blue line shows the data from 2011 and the red line shows the data from 2016. 192

Figure 98. Transect analysis at a location to the NW of the bank (sandwaves crests to the right indicating: northward sediment movement). Transect analysis at a location to the NE of the bank (sandwaves crests to the left indicating southward sediment movement). Note: 2011 data is not available. 193

Figure 99. The analysis of sandwaves at the southern tail, and southeast region, of the bank derived from the bathymetry data collected in 2016 and 2019. The red arrows in the top image depicts the length and orientation of the profile presented below where the blue line shows the data from 2016 and the red line shows the data from 2019. 194

Figure 100. The analysis of sandwaves at the southwest and southeast region, of the bank derived from the bathymetry data collected in 2016 and 2019. The red arrows in the top image depicts the length and orientation of the profile presented below where the blue line shows the data from 2016 and the red line shows the data from 2019. 195

Figure 101. The analysis of sandwaves at the central west and central east region, of the bank derived from the bathymetry data collected in 2016 and 2019. The red arrows in the top image depicts the length and orientation of the profile presented below where the blue line shows the data from 2016 and the red line shows the data from 2019. 196

Figure 102. The analysis of sandwaves at the central east region, of the bank derived from the bathymetry data collected in 2016 and 2019. The red arrows in the top image depicts the length and orientation of the profile presented below where the blue line shows the data from 2016 and the red line shows the data from 2019. 197

Figure 103. The 'minimum' RSBL determined from the 2019 bathymetry dataset using the TPI method. Note: the maximum RSBL has also been determined and is provided as part of the complementary data package provided alongside this report. 199

Figure 104. The comparison of the RSBL to areas of sandwaves identified in the 2019 bathymetry survey. Within the profile plots the RSBL is represented by the black line whereas the 2019 bathymetry profile is represented by the red line. 200

Figure 105. The potential vertical change predicted to occur through time due to the migration of sandwave features. The bed change is quantified by comparing the RSBL determined from the 2019 data, compared to the corresponding bathymetry. 201

Figure 106. The potential vertical change predicted to occur through time due to the migration of sandwave features. The bed change is quantified by comparing the RSBL determined from the 2016 data, compared to the corresponding bathymetry.....202

Figure 107. An example of the Fourier transform analysis. This method was applied to all transects across the lease area for the data acquired in 2016 and in 2019.....204

Figure 108. The mean, 95th percentile and maximum sandwave height derived from the Fourier transform method applied to the 2016 bathymetry data (left panel) and the 2019 bathymetry data (centre panel). The right panel shows the respective difference plot. 205

Figure 109. Sandwave migration rates determined from comparison of the data acquired in 2016 and 2019.....206

Figure 110. The profiles extracted from IA1. 211

Figure 111. The profiles extracted from IA2. 212

Figure 112. The profiles extracted from IA3.....212

Figure 113. The profiles extracted from IA5.....213

Figure 114. The profile extracted along the transect surveyed in IA1 on 21.07.20. The full profile (top left panel), the zoomed in profile above the -10 m contour (top right panel), the west (bottom left panel) and east (bottom right panel) face of the bank in areas deeper than the -10 m contour are presented. 215

Figure 115. The profile extracted along the transect surveyed in IA2 on 21.07.20. The full profile (top left panel), the zoomed in profile above the -10 m contour (top right panel), the west (bottom left panel) and east (bottom right panel) face of the bank in areas deeper than the -10 m contour are presented. 215

Figure 116. The profile extracted along the transect surveyed in IA2 on 11.08.20. The full profile (top left panel), the zoomed in profile above the -10 m contour (top right panel), the west (bottom left panel) and east (bottom right panel) face of the bank in areas deeper than the -10 m contour are presented. 216

Figure 117. The profile extracted along the transect surveyed in IA5 on 07.08.20. The full profile (top left panel), the zoomed in profile above the -10 m contour (top right panel), the west (bottom left panel) and east (bottom right panel) face of the bank in areas deeper than the -10 m contour are presented. 216

Figure 118. The profile extracted along the transect surveyed in IA5 on 28.07.20. The full profile (top left panel), the zoomed in profile above the -10 m contour (top right panel), the west (bottom left panel) and east (bottom right panel) face of the bank in areas deeper than the -10 m contour are presented. 217

Figure 119. The profile extracted along the transect surveyed in IA1 over the period between 06.08.20 and 07.08.20. The full profile (top left panel), the zoomed in profile above the -10 m contour (top right panel), the west (bottom left panel) and east (bottom right panel) face of the bank in areas deeper than the -10 m contour are presented. 219

Figure 120. The profile extracted along the transect surveyed in IA2 over the period between 20.07.20 and 21.07.21. The full profile (top left panel), the zoomed in profile above the -10 m contour (top right panel), the west (bottom left panel) and east (bottom right panel) face of the bank in areas deeper than the -10 m contour are presented. 219

Figure 121. The profile extracted along the transect surveyed in IA2 over the period between 06.08.20 and 07.08.20 on 28.07.20. The full profile (top left panel), the zoomed in profile above the -10 m contour (top right panel), the west (bottom left panel) and east (bottom right panel) face of the bank in areas deeper than the -10 m contour are presented. 220

Figure 122. The profile extracted along the transect surveyed in IA3 over the period between 06.08.20 and 07.08.20. The full profile (top left panel), the zoomed in profile above the -10 m contour (top right panel), the west (bottom left panel) and east (bottom right panel) face of the bank in areas deeper than the -10 m contour are presented. 220

Figure 123. The profile extracted along the transect surveyed in IA5 over the period between 28.07.20 and 29.07.20. The full profile (top left panel), the zoomed in profile above the -10 m contour (top right panel), the west (bottom left panel) and east (bottom right panel) face of the bank in areas deeper than the -10 m contour are presented. 221

Figure 124. The profile extracted along the transect surveyed in IA1 over the period between 15.07.20 and 20.07.20. The full profile (top left panel), the zoomed in profile above the -10 m contour (top right panel), the west (bottom left panel) and east (bottom right panel) face of the bank in areas deeper than the -10 m contour are presented. 223

Figure 125. The profile extracted along the transect surveyed in IA2 over the period between 15.07.20 and 21.07.20. The full profile (top left panel), the zoomed in profile above the -10 m contour (top right panel), the west (bottom left panel) and east (bottom right panel) face of the bank in areas deeper than the -10 m contour are presented. 223

Figure 126. The profile extracted along the transect surveyed in IA2 over the period between 21.07.20 and 26.07.20. The full profile (top left panel), the zoomed in profile above the -10 m contour (top right panel), the west (bottom left panel) and east (bottom right panel) face of the bank in areas deeper than the -10 m contour are presented. 224

Figure 127. The profile extracted along the transect surveyed in IA2 over the period between 26.07.20 and 06.08.20. The full profile (top left panel), the zoomed in profile above the -10 m contour (top right panel), the west (bottom left panel) and east (bottom right panel) face of the bank in areas deeper than the -10 m contour are presented. 224

Figure 128. The profile extracted along the transect surveyed in IA2 over the period between 06.08.20 and 11.08.20. The full profile (top left panel), the zoomed in profile above the -10 m contour (top right panel), the west (bottom left panel) and east (bottom right panel) face of the bank in areas deeper than the -10 m contour are presented. 225

Figure 129. The profile extracted along the transect surveyed in IA5 over the period between 15.07.20 and 21.07.20. The full profile (top left panel), the zoomed in profile above the -10 m contour (top right panel), the west (bottom left panel) and east (bottom right panel) face of the bank in areas deeper than the -10 m contour are presented. 225

Figure 130. The profile extracted along the transect surveyed in IA5 over the period between 21.07.20 and 28.07.20. The full profile (top left panel), the zoomed in profile above the -10 m contour (top right panel), the west (bottom left panel) and east (bottom right panel) face of the bank in areas deeper than the -10 m contour are presented. 226

Figure 131. The profile extracted along the transect surveyed in IA5 over the period between 28.07.20 and 06.08.20. The full profile (top left panel), the zoomed in profile above the -10 m contour (top right panel), the west (bottom left panel) and east (bottom right panel) face of the bank in areas deeper than the -10 m contour are presented.....226

Figure 132. The profile extracted along the transect surveyed in IA1 over the period between 11.07.20 and 25.07.20. The full profile (top left panel), the zoomed in profile above the -10 m contour (top right panel), the west (bottom left panel) and east (bottom right panel) face of the bank in areas deeper than the -10 m contour are presented.....229

Figure 133. The profile extracted along the transect surveyed in IA1 over the period between 25.07.20 and 09.08.20. The full profile (top left panel), the zoomed in profile above the -10 m contour (top right panel), the west (bottom left panel) and east (bottom right panel) face of the bank in areas deeper than the -10 m contour are presented.....229

Figure 134. The profile extracted along the transect surveyed in IA1 over the period between 11.07.20 and 25.07.20. The full profile (top left panel), the zoomed in profile above the -10 m contour (top right panel), the west (bottom left panel) and east (bottom right panel) face of the bank in areas deeper than the -10 m contour are presented.....230

Figure 135. The profile extracted along the transect surveyed in IA1 over the period between 25.07.20 and 09.08.20. The full profile (top left panel), the zoomed in profile above the -10 m contour (top right panel), the west (bottom left panel) and east (bottom right panel) face of the bank in areas deeper than the -10 m contour are presented.....230

Figure 136. The profile extracted along the transect surveyed in IA1 over the period between 21.07.20 and 06.08.20. The full profile (top left panel), the zoomed in profile above the -10 m contour (top right panel), the west (bottom left panel) and east (bottom right panel) face of the bank in areas deeper than the -10 m contour are presented.....231

Figure 137. The profile extracted along the transect surveyed in IA1 over the period between 11.07.20 and 25.07.20. The full profile (top left panel), the zoomed in profile above the -10 m contour (top right panel), the west (bottom left panel) and east (bottom right panel) face of the bank in areas deeper than the -10 m contour are presented.....231

Figure 138. The profile extracted along the transect surveyed in IA1 over the period between 25.07.20 and 09.08.20. The full profile (top left panel), the zoomed in profile above the -10 m contour (top right panel), the west (bottom left panel) and east (bottom right panel) face of the bank in areas deeper than the -10 m contour are presented.....232

Figure 139. The profile extracted along the transect surveyed in IA1 over the period between 11.07.20 and 25.07.20. The full profile (top left panel), the zoomed in profile above the -10 m contour (top right panel), the west (bottom left panel) and east (bottom right panel) face of the bank in areas deeper than the -10 m contour are presented.....232

Figure 140. The profile extracted along the transect surveyed in IA1 over the period between 25.07.20 and 09.08.20. The full profile (top left panel), the zoomed in profile above the -10 m contour (top right panel), the west (bottom left panel) and east (bottom right panel) face of the bank in areas deeper than the -10 m contour are presented.....233

Figure 141. The profile extracted along the transect surveyed in IA1 over the period between 11.07.20 and 25.07.20. The full profile (top left panel), the zoomed in profile above the -10 m contour (top right panel), the west (bottom left panel) and east (bottom right panel) face of the bank in areas deeper than the -10 m contour are presented.....233

Figure 142. The profile extracted along the transect surveyed in IA1 over the period between 25.07.20 and 09.08.20. The full profile (top left panel), the zoomed in profile above the -10 m contour (top right panel), the west (bottom left panel) and east (bottom right panel) face of the bank in areas deeper than the -10 m contour are presented.....234

Figure 143. The profile extracted along the transect surveyed in IA2 over the period between 14.07.20 and 29.07.20. The full profile (top left panel), the zoomed in profile above the -10 m contour (top right panel), the west (bottom left panel) and east (bottom right panel) face of the bank in areas deeper than the -10 m contour are presented.....234

Figure 144. The profile extracted along the transect surveyed in IA2 over the period between 29.07.20 and 11.08.20. The full profile (top left panel), the zoomed in profile above the -10 m contour (top right panel), the west (bottom left panel) and east (bottom right panel) face of the bank in areas deeper than the -10 m contour are presented.....235

Figure 145. The profile extracted along the transect surveyed in IA2 over the period between 14.07.20 and 29.07.20. The full profile (top left panel), the zoomed in profile above the -10 m contour (top right panel), the west (bottom left panel) and east (bottom right panel) face of the bank in areas deeper than the -10 m contour are presented.....235

Figure 146. The profile extracted along the transect surveyed in IA2 over the period between 29.07.20 and 11.08.20. The full profile (top left panel), the zoomed in profile above the -10 m contour (top right panel), the west (bottom left panel) and east (bottom right panel) face of the bank in areas deeper than the -10 m contour are presented.....236

Figure 147. The profile extracted along the transect surveyed in IA2 over the period between 15.07.20 and 26.07.20. The full profile (top left panel), the zoomed in profile above the -10 m contour (top right panel), the west (bottom left panel) and east (bottom right panel) face of the bank in areas deeper than the -10 m contour are presented.....236

Figure 148. The profile extracted along the transect surveyed in IA2 over the period between 26.07.20 and 11.08.20. The full profile (top left panel), the zoomed in profile above the -10 m contour (top right panel), the west (bottom left panel) and east (bottom right panel) face of the bank in areas deeper than the -10 m contour are presented.....237

Figure 149. The profile extracted along the transect surveyed in IA2 over the period between 14.07.20 and 29.07.20. The full profile (top left panel), the zoomed in profile above the -10 m contour (top right panel), the west (bottom left panel) and east (bottom right panel) face of the bank in areas deeper than the -10 m contour are presented.....237

Figure 150. The profile extracted along the transect surveyed in IA2 over the period between 29.07.20 and 11.08.20. The full profile (top left panel), the zoomed in profile above the -10 m contour (top right panel), the west (bottom left panel) and east (bottom right panel) face of the bank in areas deeper than the -10 m contour are presented.....238

Figure 151. The profile extracted along the transect surveyed in IA2 over the period between 14.07.20 and 29.07.20. The full profile (top left panel), the zoomed in profile above the -10 m contour (top right panel), the west (bottom left panel) and east (bottom right panel) face of the bank in areas deeper than the -10 m contour are presented.....238

Figure 152. The profile extracted along the transect surveyed in IA2 over the period between 29.07.20 and 11.08.20. The full profile (top left panel), the zoomed in profile above the -10 m contour (top right panel), the west (bottom left panel) and east (bottom right panel) face of the bank in areas deeper than the -10 m contour are presented.....239

Figure 153. The profile extracted along the transect surveyed in IA2 over the period between 14.07.20 and 29.07.20. The full profile (top left panel), the zoomed in profile above the -10 m contour (top right panel), the west (bottom left panel) and east (bottom right panel) face of the bank in areas deeper than the -10 m contour are presented. 239

Figure 154. The profile extracted along the transect surveyed in IA2 over the period between 29.07.20 and 11.08.20. The full profile (top left panel), the zoomed in profile above the -10 m contour (top right panel), the west (bottom left panel) and east (bottom right panel) face of the bank in areas deeper than the -10 m contour are presented. 240

Figure 155. The profile extracted along the transect surveyed in IA3 over the period between 12.07.20 and 28.07.20. The full profile (top left panel), the zoomed in profile above the -10 m contour (top right panel), the west (bottom left panel) and east (bottom right panel) face of the bank in areas deeper than the -10 m contour are presented. 240

Figure 156. The profile extracted along the transect surveyed in IA3 over the period between 28.07.20 and 12.08.20. The full profile (top left panel), the zoomed in profile above the -10 m contour (top right panel), the west (bottom left panel) and east (bottom right panel) face of the bank in areas deeper than the -10 m contour are presented. 241

Figure 157. The profile extracted along the transect surveyed in IA3 over the period between 12.07.20 and 28.07.20. The full profile (top left panel), the zoomed in profile above the -10 m contour (top right panel), the west (bottom left panel) and east (bottom right panel) face of the bank in areas deeper than the -10 m contour are presented. 241

Figure 158. The profile extracted along the transect surveyed in IA3 over the period between 28.07.20 and 12.08.20. The full profile (top left panel), the zoomed in profile above the -10 m contour (top right panel), the west (bottom left panel) and east (bottom right panel) face of the bank in areas deeper than the -10 m contour are presented. 242

Figure 159. The profile extracted along the transect surveyed in IA3 over the period between 12.07.20 and 28.07.20. The full profile (top left panel), the zoomed in profile above the -10 m contour (top right panel), the west (bottom left panel) and east (bottom right panel) face of the bank in areas deeper than the -10 m contour are presented. 242

Figure 160. The profile extracted along the transect surveyed in IA3 over the period between 28.07.20 and 12.08.20. The full profile (top left panel), the zoomed in profile above the -10 m contour (top right panel), the west (bottom left panel) and east (bottom right panel) face of the bank in areas deeper than the -10 m contour are presented. 243

Figure 161. The profile extracted along the transect surveyed in IA3 over the period between 12.07.20 and 28.07.20. The full profile (top left panel), the zoomed in profile above the -10 m contour (top right panel), the west (bottom left panel) and east (bottom right panel) face of the bank in areas deeper than the -10 m contour are presented. 243

Figure 162. The profile extracted along the transect surveyed in IA3 over the period between 28.07.20 and 12.08.20. The full profile (top left panel), the zoomed in profile above the -10 m contour (top right panel), the west (bottom left panel) and east (bottom right panel) face of the bank in areas deeper than the -10 m contour are presented. 244

Figure 163. The profile extracted along the transect surveyed in IA3 over the period between 12.07.20 and 28.07.20. The full profile (top left panel), the zoomed in profile above the -10 m contour (top right panel), the west (bottom left panel) and east (bottom right panel) face of the bank in areas deeper than the -10 m contour are presented. 244

Figure 164. The profile extracted along the transect surveyed in IA5 over the period between 28.07.20 and 12.08.20. The full profile (top left panel), the zoomed in profile above the -10 m contour (top right panel), the west (bottom left panel) and east (bottom right panel) face of the bank in areas deeper than the -10 m contour are presented.....245

Figure 165. The profile extracted along the transect surveyed in IA5 over the period between 15.07.20 and 28.07.20. The full profile (top left panel), the zoomed in profile above the -10 m contour (top right panel), the west (bottom left panel) and east (bottom right panel) face of the bank in areas deeper than the -10 m contour are presented.....245

Figure 166. The profile extracted along the transect surveyed in IA1 over the period between 11.07.20 and 09.08.20. The full profile (top left panel), the zoomed in profile above the -10 m contour (top right panel), the west (bottom left panel) and east (bottom right panel) face of the bank in areas deeper than the -10 m contour are presented.....247

Figure 167. The profile extracted along the transect surveyed in IA1 over the period between 11.07.20 and 09.08.20. The full profile (top left panel), the zoomed in profile above the -10 m contour (top right panel), the west (bottom left panel) and east (bottom right panel) face of the bank in areas deeper than the -10 m contour are presented.....247

Figure 168. The profile extracted along the transect surveyed in IA1 over the period between 15.07.20 and 07.08.20. The full profile (top left panel), the zoomed in profile above the -10 m contour (top right panel), the west (bottom left panel) and east (bottom right panel) face of the bank in areas deeper than the -10 m contour are presented.....248

Figure 169. The profile extracted along the transect surveyed in IA1 over the period between 11.07.20 and 09.08.20. The full profile (top left panel), the zoomed in profile above the -10 m contour (top right panel), the west (bottom left panel) and east (bottom right panel) face of the bank in areas deeper than the -10 m contour are presented.....248

Figure 170. The profile extracted along the transect surveyed in IA5 over the period between 11.07.20 and 09.08.20. The full profile (top left panel), the zoomed in profile above the -10 m contour (top right panel), the west (bottom left panel) and east (bottom right panel) face of the bank in areas deeper than the -10 m contour are presented.....249

Figure 171. The profile extracted along the transect surveyed in IA5 over the period between 11.07.20 and 09.08.20. The full profile (top left panel), the zoomed in profile above the -10 m contour (top right panel), the west (bottom left panel) and east (bottom right panel) face of the bank in areas deeper than the -10 m contour are presented.....249

Figure 172. The profile extracted along the transect surveyed in IA2 over the period between 14.07.20 and 11.08.20. The full profile (top left panel), the zoomed in profile above the -10 m contour (top right panel), the west (bottom left panel) and east (bottom right panel) face of the bank in areas deeper than the -10 m contour are presented.....250

Figure 173. The profile extracted along the transect surveyed in IA2 over the period between 14.07.20 and 11.08.20. The full profile (top left panel), the zoomed in profile above the -10 m contour (top right panel), the west (bottom left panel) and east (bottom right panel) face of the bank in areas deeper than the -10 m contour are presented.....250

Figure 174. The profile extracted along the transect surveyed in IA2 over the period between 15.07.20 and 11.08.20. The full profile (top left panel), the zoomed in profile above the -10 m contour (top right panel), the west (bottom left panel) and east (bottom right panel) face of the bank in areas deeper than the -10 m contour are presented.....251

Figure 175. The profile extracted along the transect surveyed in IA2 over the period between 14.07.20 and 11.08.20. The full profile (top left panel), the zoomed in profile above the -10 m contour (top right panel), the west (bottom left panel) and east (bottom right panel) face of the bank in areas deeper than the -10 m contour are presented. 251

Figure 176. The profile extracted along the transect surveyed in IA2 over the period between 14.07.20 and 11.08.20. The full profile (top left panel), the zoomed in profile above the -10 m contour (top right panel), the west (bottom left panel) and east (bottom right panel) face of the bank in areas deeper than the -10 m contour are presented. 252

Figure 177. The profile extracted along the transect surveyed in IA2 over the period between 14.07.20 and 11.08.20. The full profile (top left panel), the zoomed in profile above the -10 m contour (top right panel), the west (bottom left panel) and east (bottom right panel) face of the bank in areas deeper than the -10 m contour are presented. 252

Figure 178. The profile extracted along the transect surveyed in IA3 over the period between 12.07.20 and 12.08.20. The full profile (top left panel), the zoomed in profile above the -10 m contour (top right panel), the west (bottom left panel) and east (bottom right panel) face of the bank in areas deeper than the -10 m contour are presented. 253

Figure 179. The profile extracted along the transect surveyed in IA3 over the period between 13.07.20 and 07.08.20. The full profile (top left panel), the zoomed in profile above the -10 m contour (top right panel), the west (bottom left panel) and east (bottom right panel) face of the bank in areas deeper than the -10 m contour are presented. 253

Figure 180. The profile extracted along the transect surveyed in IA3 over the period between 12.07.20 and 12.08.20. The full profile (top left panel), the zoomed in profile above the -10 m contour (top right panel), the west (bottom left panel) and east (bottom right panel) face of the bank in areas deeper than the -10 m contour are presented. 254

Figure 181. The profile extracted along the transect surveyed in IA3 over the period between 12.07.20 and 12.08.20. The full profile (top left panel), the zoomed in profile above the -10 m contour (top right panel), the west (bottom left panel) and east (bottom right panel) face of the bank in areas deeper than the -10 m contour are presented. 254

Figure 182. The profile extracted along the transect surveyed in IA3 over the period between 12.07.20 and 12.08.20. The full profile (top left panel), the zoomed in profile above the -10 m contour (top right panel), the west (bottom left panel) and east (bottom right panel) face of the bank in areas deeper than the -10 m contour are presented. 255

Figure 183. The profile extracted along the transect surveyed in IA3 over the period between 12.07.20 and 12.08.20. The full profile (top left panel), the zoomed in profile above the -10 m contour (top right panel), the west (bottom left panel) and east (bottom right panel) face of the bank in areas deeper than the -10 m contour are presented. 255

Figure 184. The profile extracted along the transect surveyed in IA5 over the period between 15.07.20 and 06.08.20. The full profile (top left panel), the zoomed in profile above the -10 m contour (top right panel), the west (bottom left panel) and east (bottom right panel) face of the bank in areas deeper than the -10 m contour are presented. 256

Figure 185. The profiles extracted from the survey data collected at the Phase 1 turbine locations between 2005 and 2016. 258

Figure 186. The 12 profiles extracted from the Phase 1 surveys over the period October 2005 and June 2006. 259

Figure 187. The 12 profiles extracted from the Phase 1 surveys over the period June 2006 to April 2007. 260

Figure 188. The 12 profiles extracted from the Phase 1 surveys over the period April 2007 to May 2008. 261
Figure 189. The 12 profiles extracted from the Phase 1 surveys over the period May 2008 to April 2009. 262
Figure 190. The 12 profiles extracted from the Phase 1 surveys over the period April 2009 and July 2011. 263
Figure 191. The 12 profiles extracted from the Phase 1 surveys over the period July 2011 and April 2015. 264
Figure 192. The 12 profiles extracted from the Phase 1 surveys over the period April 2015 and June 2016. 265
Figure 193. The profiles extracted coincident with IA1. 266
Figure 194. The profiles extracted coincident with IA2. 267
Figure 195. The profiles extracted coincident with IA3. 267
Figure 196. The three profiles extracted from areas of the bank coincident from IA1. The profiles compare data surveyed in 2000 and 2016 (top panel), 2016 and 2019 (centre panel) and 2019 and 2020 (bottom panel. 268
Figure 197. The two profiles extracted from areas of the bank coincident from IA2. The profiles compare data surveyed in 2000 and 2016 (top panel), 2016 and 2019 (centre panel) and 2019 and 2020 (bottom panel). 269
Figure 198. The two profiles extracted from areas of the bank coincident from IA2. The profiles compare data surveyed in 2000 and 2016 (top panel), 2016 and 2019 (centre panel) and 2019 and 2020 (bottom panel. 270
Figure 199. Profiles extracted along the length of Arklow Bank to consider movement of the bank over the period 2000 to 2019. 271
Figure 200. The profiles extracted along the length of the bank, comparing the data acquired in 2000 with those acquired in 2016 (left panel) and those acquired in 2016 and 2019 (right panel). 272
Figure 201. The -10 mLAT contour plotted from the 2000, 2016 and 2019 datasets. 275
Figure 202. The – 15 mLAT contour plotted from the 2000, 2016 and 2019 datasets. 276
Figure 203. The -20 mLAT contour plotted on the 2000, 2016 and 2019 datasets. 277
Figure 204. The observed bed level change over Seven Fathom Bank along the export cable route. The location of the profiles presented in Figure 204, is overlain. 278
Figure 205. Data acquired in 2011 and 2019 along the export cable route in areas coincident with Seven Fathom Bank, presented in the form of cross section profiles. 279
Figure 206. The conceptual site model at the local scale. 286
Figure 207. Flow chart showing approach adopted for determining future seabed levels for the different process environments across the development area. 289
Figure 208. 5.3 year running mean sediment transport normal to the bank for eight positions along the bank crest (top to bottom, north to south). 294
Figure 209. 60 day running mean sediment transport normal to the bank for eight positions along the bank crest (top to bottom, north to south). 295

Figure 210. The observed (measured) and predicted (modelled) bed level change across the lease area and export cable routes over the validation period 2016 to 2019. 301

Figure 211 Cross section, west to east profiles of Arklow Bank. The profiles present the data from the 2016 and 2019 model input bathymetry and the model output following the 2016 to 2019 validation run. 302

Figure 212. A scatter plot showing the discrepancy between observations (measured) and predictions (modelled) of vertical bed level change from 2016 to 2019 split by bank region. The quantiles and a regression line are also presented, along with a 1:1 reference line. 303

Figure 213. The observed (measured) and predicted (modelled) bed level change across the lease area and export cable routes over the validation period 2000 to 2016 304

Figure 214. Cross section, west to east profiles of Arklow Bank. The profiles present the data from the 2016 and 2019 model input bathymetry and the model output following the 2016 to 2019 validation run. 305

Figure 215. A scatter plot showing the discrepancy between observations (measured) and predictions (modelled) of vertical bed level change from 2000 to 2016 split by bank region. The quantiles and a regression line are also presented, along with a 1:1 reference line. 306

Figure 216. The observed (measured) and predicted (modelled) bed level change along the export cable routes over the validation period 2011 to 2019. 307

Figure 217. A scatter plot showing the discrepancy between observations (measured) and predictions (modelled) of vertical bed level change from 2011 to 2019 along the export cable route. The route is split by bank region. The quantiles and a regression line are also presented, along with a 1:1 reference line. 308

Figure 218. Four east – west cross section profiles of Seven Fathom Bank. The image to the left shows where the profiles were extracted from and the image to the right shows the bathymetry data as implemented in the model. 309

Figure 219. Periods selected for the simulations. Maximum durations indicated by coloured boxes, and maximum amplitudes indicated by coloured sections of the time series. Sediment transport biased westward is shown in red, and sediment transport biased eastwards shown in green. 312

Figure 220. A map showing the spatial variation in error derived from the comparison of predictions vs observations of seabed level change over the period, 2000 to 2016, 2016 to 2019 and 2011 to 2019. It should be noted this is an error derived solely from the model output over the period assessed during validations. 316

Figure 221. A map showing the spatial variation in error which has been moderated. 317

Figure 222. Cross section profiles showing the spatially varying average error (blue line) and the moderated error. 318

Figure 223. Growth potential of sandwaves to the east, west, north, and south of the bank. 319

Figure 224. Cross section profiles along the length of Arklow Bank demonstrating how the 'maximum' RSBL has been raised to account for the growth potential of sandwaves in this area. 320

Figure 225. Predicted highest system state for Arklow Bank. The data are extracted from the 24 model simulations for locations along the length of Arklow Bank, presented in the form of cross-section profiles. The HSBL is traced and highlighted in red. 323

Figure 226. Surfaces derived from model outputs, complementary analysis (i.e. derived RSBL's), and existing bathymetries including for relevant contribution to applied confidence limits presented in the form of cross-section profiles along the length of Arklow Bank. The resulting, composite, HSBL is traced. 324

Figure 227. Predicted lowest system state for Arklow Bank. The data are extracted from the 24 model simulations for locations along the length of Arklow Bank, presented in the form of cross-section profiles. The LSBL is traced and highlighted in red. 325

Figure 228. Surfaces derived from model outputs, complementary analysis (i.e. derived RSBL's), and existing bathymetries including for relevant contribution to applied confidence limits presented in the form of cross-section profiles along the length of Arklow Bank. The resulting, composite, LSBL is traced. 326

Figure 229. HSBL compared to the 2019 bathymetry showing the potential magnitude of raising of the seabed level predicted to occur across the lifetime of the development. The absolute difference between the two datasets is presented, however as this is the LSBL these differences reflect potential raising of the seabed level. 327

Figure 230. LSBL compared to the 2019 bathymetry showing the potential magnitude of lowering of the seabed level predicted to occur across the lifetime of the development. The absolute difference between the two datasets is presented, however as this is the LSBL these differences reflect potential lowering of the seabed level. 328

Figure 231. Cross-section profiles showing the potential envelope of seabed level variation which may occur across the lifetime of the development. The 2019 bathymetry is shown for reference. 329

Figure 232. Comparison of the predicted LSBL against the depth of the interpreted non-mobile layer (seabed unit 2, GDG 2020). The regions coloured in red, shows where the seabed was predicted to lower beyond the level coincident with the interpreted non-erodible layer. 333

Figure 233. The points across the lease area and export cable from which time series data of bed level change have been extracted. These data are presented in the form of time series in Figure 233. 337

Figure 234. Predictions of seabed level change over a period of months, derived from a pertinent model simulation. 338

Figure 235. Schematic diagram presenting the implications for cabling across different process environments across the ABWP. 341

Figure 236. Maximum extent of ice sheet, circa 23 ka BP, after Clark, Hughes, Greenwood, Jordan, & Sejrup (2012). Blue arrows indicate glacial movement. 388

Figure 237. Predicted components of sea level change (i. contribution from distant ice sheets, ii. contribution from local ice sheet, iii. net predicted sea level change) (adapted from Lambeck & Purcell, 2001) with indication of mean sea level at 11,000 BP. 390

Figure 238. Indicative alignment of the former coastline at commencement of Holocene (circa 11,000 BP).....391

Figure 239. Variation of contemporary surficial sediment types along with inferred sediment transport pathways circa 11,000 BP.....393

Figure 240. Predicted components of sea level change (i. contribution from distant ice sheets, ii. contribution from local ice sheet, iii. net predicted sea level change) (adapted from Lambeck & Purcell, 2001) with indication of mean sea level at 8,500 BP.....394

Figure 241. Indicative alignment of the former coastline on reconstructed landscape and seascape during Holocene (circa 8,500 BP).....395

Figure 242. Predicted components of sea level change (i. contribution from distant ice sheets, ii. contribution from local ice sheet, iii. net predicted sea level change) (adapted from Lambeck & Purcell, 2001) with indication of mean sea level at 7,500 BP.....397

Figure 243. Indicative alignment of the former coastline on reconstructed landscape and seascape during Holocene (circa 7,500 BP).....398

Figure 244. Predicted components of sea level change (i. contribution from distant ice sheets, ii. contribution from local ice sheet, iii. net predicted sea level change) (adapted from Lambeck & Purcell, 2001) with indication of mean sea level at 6,000 BP.....400

Figure 245. Indicative alignment of the former coastline on reconstructed landscape and seascape during Holocene (circa 6,000 BP).....401

Figure 246. Vertical profiles showing current speed through the water column measured at frame location 'A' across a representative ebb / flood phase during a period of negligible wave action.....406

Figure 247. Transects from which profiles were extracted to assess sandwave migration rates.....408

Figure 248. Observed sandwave migration between 2016 and 2019 on profile 1, transect 1. The maximum observed sandwave migration rate, and direction of migration, is detailed at the top of the plot.....408

Figure 249. Observed sandwave migration between 2016 and 2019 on profile 1, transect 2. The maximum observed sandwave migration rate, and direction of migration, is detailed at the top of the plot.....409

Figure 250. Observed sandwave migration between 2016 and 2019 on profile 1, transect 3. The maximum observed sandwave migration rate, and direction of migration, is detailed at the top of the plot.....409

Figure 251. Observed sandwave migration between 2016 and 2019 on profile 1, transect 4. The maximum observed sandwave migration rate, and direction of migration, is detailed at the top of the plot.....409

Figure 252. Observed sandwave migration between 2016 and 2019 on profile 1, transect 5. The maximum observed sandwave migration rate, and direction of migration, is detailed at the top of the plot.....410

Figure 253. Observed sandwave migration between 2016 and 2019 on profile 1, transect 6. The maximum observed sandwave migration rate, and direction of migration, is detailed at the top of the plot.....410

Figure 254. Observed sandwave migration between 2016 and 2019 on profile 1, transect 7. The maximum observed sandwave migration rate, and direction of migration, is detailed at the top of the plot. 410

Figure 255. Observed sandwave migration between 2016 and 2019 on profile 1, transect 8. The maximum observed sandwave migration rate, and direction of migration, is detailed at the top of the plot. 411

Figure 256. Observed sandwave migration between 2016 and 2019 on profile 1, transect 9. The maximum observed sandwave migration rate, and direction of migration, is detailed at the top of the plot. 411

Figure 257. Observed sandwave migration between 2016 and 2019 on profile 1, transect 10. The maximum observed sandwave migration rate, and direction of migration, is detailed at the top of the plot. 411

Figure 258. Observed sandwave migration between 2016 and 2019 on profile 1, transect 11. The maximum observed sandwave migration rate, and direction of migration, is detailed at the top of the plot. 412

Figure 259. Observed sandwave migration between 2016 and 2019 on profile 1, transect 12. The maximum observed sandwave migration rate, and direction of migration, is detailed at the top of the plot. 412

Figure 260. Observed sandwave migration between 2016 and 2019 on profile 1, transect 13. The maximum observed sandwave migration rate, and direction of migration, is detailed at the top of the plot. 412

Figure 261. Observed sandwave migration between 2016 and 2019 on profile 1, transect 14. The maximum observed sandwave migration rate, and direction of migration, is detailed at the top of the plot. 413

Figure 262. Observed sandwave migration between 2016 and 2019 on profile 6, transect 1. The maximum observed sandwave migration rate, and direction of migration, is detailed at the top of the plot. 413

Figure 263. Observed sandwave migration between 2016 and 2019 on profile 6, transect 2. The maximum observed sandwave migration rate, and direction of migration, is detailed at the top of the plot. 413

Figure 264. Observed sandwave migration between 2016 and 2019 on profile 6, transect 3. The maximum observed sandwave migration rate, and direction of migration, is detailed at the top of the plot. 414

Figure 265. Observed sandwave migration between 2016 and 2019 on profile 6, transect 4. The maximum observed sandwave migration rate, and direction of migration, is detailed at the top of the plot. 414

Figure 266. Observed sandwave migration between 2016 and 2019 on profile 6, transect 5. The maximum observed sandwave migration rate, and direction of migration, is detailed at the top of the plot. 414

Figure 267. Observed sandwave migration between 2016 and 2019 on profile 6, transect 6. The maximum observed sandwave migration rate, and direction of migration, is detailed at the top of the plot. 415

Figure 268. Observed sandwave migration between 2016 and 2019 on profile 6, transect 7. The maximum observed sandwave migration rate, and direction of migration, is detailed at the top of the plot. 415

Figure 269. Observed sandwave migration between 2016 and 2019 on profile 6, transect 8. The maximum observed sandwave migration rate, and direction of migration, is detailed at the top of the plot. 415

Figure 270. Observed sandwave migration between 2016 and 2019 on profile 6, transect 9. The maximum observed sandwave migration rate, and direction of migration, is detailed at the top of the plot. 416

Figure 271. Observed sandwave migration between 2016 and 2019 on profile 6, transect 10. The maximum observed sandwave migration rate, and direction of migration, is detailed at the top of the plot. 416

Figure 272. Observed sandwave migration between 2016 and 2019 on profile 6, transect 11. The maximum observed sandwave migration rate, and direction of migration, is detailed at the top of the plot. 416

Figure 273. Observed sandwave migration between 2016 and 2019 on profile 6, transect 12. The maximum observed sandwave migration rate, and direction of migration, is detailed at the top of the plot. 417

Figure 274. Observed sandwave migration between 2016 and 2019 on profile 6, transect 13. The maximum observed sandwave migration rate, and direction of migration, is detailed at the top of the plot. 417

Figure 275. Observed sandwave migration between 2016 and 2019 on profile 6, transect 14. The maximum observed sandwave migration rate, and direction of migration, is detailed at the top of the plot. 417

Figure 276. Observed sandwave migration between 2016 and 2019 on profile 11, transect 1. The maximum observed sandwave migration rate, and direction of migration, is detailed at the top of the plot. 418

Figure 277. Observed sandwave migration between 2016 and 2019 on profile 11, transect 2. The maximum observed sandwave migration rate, and direction of migration, is detailed at the top of the plot. 418

Figure 278. Observed sandwave migration between 2016 and 2019 on profile 11, transect 3. The maximum observed sandwave migration rate, and direction of migration, is detailed at the top of the plot. 418

Figure 279. Observed sandwave migration between 2016 and 2019 on profile 11, transect 4. The maximum observed sandwave migration rate, and direction of migration, is detailed at the top of the plot. 419

Figure 280. Observed sandwave migration between 2016 and 2019 on profile 11, transect 5. The maximum observed sandwave migration rate, and direction of migration, is detailed at the top of the plot. 419

Figure 281. Observed sandwave migration between 2016 and 2019 on profile 11, transect 6. The maximum observed sandwave migration rate, and direction of migration, is detailed at the top of the plot. 419

Figure 282. Observed sandwave migration between 2016 and 2019 on profile 11, transect 7. The maximum observed sandwave migration rate, and direction of migration, is detailed at the top of the plot. 420

Figure 283. Observed sandwave migration between 2016 and 2019 on profile 11, transect 8. The maximum observed sandwave migration rate, and direction of migration, is detailed at the top of the plot. 420

Figure 284. Observed sandwave migration between 2016 and 2019 on profile 11, transect 9. The maximum observed sandwave migration rate, and direction of migration, is detailed at the top of the plot. 420

Figure 285. Observed sandwave migration between 2016 and 2019 on profile 11, transect 10. The maximum observed sandwave migration rate, and direction of migration, is detailed at the top of the plot. 421

Figure 286. Observed sandwave migration between 2016 and 2019 on profile 11, transect 11. The maximum observed sandwave migration rate, and direction of migration, is detailed at the top of the plot. 421

Figure 287. Observed sandwave migration between 2016 and 2019 on profile 11, transect 12. The maximum observed sandwave migration rate, and direction of migration, is detailed at the top of the plot. 421

Figure 288. Observed sandwave migration between 2016 and 2019 on profile 11, transect 13. The maximum observed sandwave migration rate, and direction of migration, is detailed at the top of the plot. 422

Figure 289. Observed sandwave migration between 2016 and 2019 on profile 11, transect 14. The maximum observed sandwave migration rate, and direction of migration, is detailed at the top of the plot. 422

Figure 290. Observed sandwave migration between 2016 and 2019 on profile 16, transect 1. The maximum observed sandwave migration rate, and direction of migration, is detailed at the top of the plot. 422

Figure 291. Observed sandwave migration between 2016 and 2019 on profile 16, transect 5. The maximum observed sandwave migration rate, and direction of migration, is detailed at the top of the plot. 423

Figure 292. Observed sandwave migration between 2016 and 2019 on profile 16, transect 6. The maximum observed sandwave migration rate, and direction of migration, is detailed at the top of the plot. 423

Figure 293. Observed sandwave migration between 2016 and 2019 on profile 16, transect 7. The maximum observed sandwave migration rate, and direction of migration, is detailed at the top of the plot. 423

Figure 294. Observed sandwave migration between 2016 and 2019 on profile 16, transect 8. The maximum observed sandwave migration rate, and direction of migration, is detailed at the top of the plot. 424

Figure 295. Observed sandwave migration between 2016 and 2019 on profile 16, transect 9. The maximum observed sandwave migration rate, and direction of migration, is detailed at the top of the plot. 424

Figure 296. Observed sandwave migration between 2016 and 2019 on profile 16, transect 10. The maximum observed sandwave migration rate, and direction of migration, is detailed at the top of the plot. 424

Figure 297. Observed sandwave migration between 2016 and 2019 on profile 16, transect 11. The maximum observed sandwave migration rate, and direction of migration, is detailed at the top of the plot. 425

Figure 298. Observed sandwave migration between 2016 and 2019 on profile 16, transect 12. The maximum observed sandwave migration rate, and direction of migration, is detailed at the top of the plot. 425

Figure 299. Observed sandwave migration between 2016 and 2019 on profile 16, transect 13. The maximum observed sandwave migration rate, and direction of migration, is detailed at the top of the plot. 425

Figure 300. Observed sandwave migration between 2016 and 2019 on profile 16, transect 14. The maximum observed sandwave migration rate, and direction of migration, is detailed at the top of the plot. 426

Figure 301. Observed sandwave migration between 2016 and 2019 on profile 21, transect 1. The maximum observed sandwave migration rate, and direction of migration, is detailed at the top of the plot. 426

Figure 302. Observed sandwave migration between 2016 and 2019 on profile 21, transect 8. The maximum observed sandwave migration rate, and direction of migration, is detailed at the top of the plot. 426

Figure 303. Observed sandwave migration between 2016 and 2019 on profile 21, transect 9. The maximum observed sandwave migration rate, and direction of migration, is detailed at the top of the plot. 427

Figure 304. Observed sandwave migration between 2016 and 2019 on profile 21, transect 14. The maximum observed sandwave migration rate, and direction of migration, is detailed at the top of the plot. 427

Figure 305. Observed sandwave migration between 2016 and 2019 on profile 26, transect 1. The maximum observed sandwave migration rate, and direction of migration, is detailed at the top of the plot. 427

Figure 306. Observed sandwave migration between 2016 and 2019 on profile 26, transect 14. The maximum observed sandwave migration rate, and direction of migration, is detailed at the top of the plot. 428

Figure 307. Observed sandwave migration between 2016 and 2019 on profile 31, transect 1. The maximum observed sandwave migration rate, and direction of migration, is detailed at the top of the plot. 428

Figure 308. Observed sandwave migration between 2016 and 2019 on profile 31, transect 2. The maximum observed sandwave migration rate, and direction of migration, is detailed at the top of the plot. 428

Figure 309. Observed sandwave migration between 2016 and 2019 on profile 31, transect 3. The maximum observed sandwave migration rate, and direction of migration, is detailed at the top of the plot. 429

Figure 310. Observed sandwave migration between 2016 and 2019 on profile 31, transect 4. The maximum observed sandwave migration rate, and direction of migration, is detailed at the top of the plot. 429

Figure 311. Observed sandwave migration between 2016 and 2019 on profile 31, transect 14. The maximum observed sandwave migration rate, and direction of migration, is detailed at the top of the plot. 429

Figure 312. Observed sandwave migration between 2016 and 2019 on profile 36, transect 1. The maximum observed sandwave migration rate, and direction of migration, is detailed at the top of the plot. 430

Figure 313. Observed sandwave migration between 2016 and 2019 on profile 36, transect 2. The maximum observed sandwave migration rate, and direction of migration, is detailed at the top of the plot. 430

Figure 314. Observed sandwave migration between 2016 and 2019 on profile 36, transect 3. The maximum observed sandwave migration rate, and direction of migration, is detailed at the top of the plot. 430

Figure 315. Observed sandwave migration between 2016 and 2019 on profile 36, transect 4. The maximum observed sandwave migration rate, and direction of migration, is detailed at the top of the plot. 431

Figure 316. Observed sandwave migration between 2016 and 2019 on profile 36, transect 7. The maximum observed sandwave migration rate, and direction of migration, is detailed at the top of the plot. 431

Figure 317. Observed sandwave migration between 2016 and 2019 on profile 36, transect 10. The maximum observed sandwave migration rate, and direction of migration, is detailed at the top of the plot. 431

Figure 318. Observed sandwave migration between 2016 and 2019 on profile 36, transect 11. The maximum observed sandwave migration rate, and direction of migration, is detailed at the top of the plot. 432
Figure 319. Observed sandwave migration between 2016 and 2019 on profile 36, transect 12. The maximum observed sandwave migration rate, and direction of migration, is detailed at the top of the plot. 432
Figure 320. Observed sandwave migration between 2016 and 2019 on profile 36, transect 13. The maximum observed sandwave migration rate, and direction of migration, is detailed at the top of the plot. 432
Figure 321. Observed sandwave migration between 2016 and 2019 on profile 36, transect 14. The maximum observed sandwave migration rate, and direction of migration, is detailed at the top of the plot. 433
Figure 322. Observed sandwave migration between 2016 and 2019 on profile 41, transect 1. The maximum observed sandwave migration rate, and direction of migration, is detailed at the top of the plot. 433
Figure 323. Observed sandwave migration between 2016 and 2019 on profile 41, transect 2. The maximum observed sandwave migration rate, and direction of migration, is detailed at the top of the plot. 433
Figure 324. Observed sandwave migration between 2016 and 2019 on profile 41, transect 3. The maximum observed sandwave migration rate, and direction of migration, is detailed at the top of the plot. 434
Figure 325. Observed sandwave migration between 2016 and 2019 on profile 41, transect 4. The maximum observed sandwave migration rate, and direction of migration, is detailed at the top of the plot. 434
Figure 326. Observed sandwave migration between 2016 and 2019 on profile 41, transect 5. The maximum observed sandwave migration rate, and direction of migration, is detailed at the top of the plot. 434
Figure 327. Observed sandwave migration between 2016 and 2019 on profile 41, transect 6. The maximum observed sandwave migration rate, and direction of migration, is detailed at the top of the plot. 435
Figure 328. Observed sandwave migration between 2016 and 2019 on profile 41, transect 7. The maximum observed sandwave migration rate, and direction of migration, is detailed at the top of the plot. 435
Figure 329. Observed sandwave migration between 2016 and 2019 on profile 41, transect 8. The maximum observed sandwave migration rate, and direction of migration, is detailed at the top of the plot. 435
Figure 330. Observed sandwave migration between 2016 and 2019 on profile 41, transect 9. The maximum observed sandwave migration rate, and direction of migration, is detailed at the top of the plot. 436
Figure 331. Observed sandwave migration between 2016 and 2019 on profile 41, transect 10. The maximum observed sandwave migration rate, and direction of migration, is detailed at the top of the plot. 436
Figure 332. Observed sandwave migration between 2016 and 2019 on profile 41, transect 11. The maximum observed sandwave migration rate, and direction of migration, is detailed at the top of the plot. 436
Figure 333. Observed sandwave migration between 2016 and 2019 on profile 41, transect 12. The maximum observed sandwave migration rate, and direction of migration, is detailed at the top of the plot. 437

Figure 334. Observed sandwave migration between 2016 and 2019 on profile 41, transect 13. The maximum observed sandwave migration rate, and direction of migration, is detailed at the top of the plot. 437
Figure 335. Observed sandwave migration between 2016 and 2019 on profile 41, transect 14. The maximum observed sandwave migration rate, and direction of migration, is detailed at the top of the plot. 437
Figure 336. Observed sandwave migration between 2016 and 2019 on profile 46, transect 1. The maximum observed sandwave migration rate, and direction of migration, is detailed at the top of the plot. 438
Figure 337. Observed sandwave migration between 2016 and 2019 on profile 46, transect 2. The maximum observed sandwave migration rate, and direction of migration, is detailed at the top of the plot. 438
Figure 338. Observed sandwave migration between 2016 and 2019 on profile 46, transect 3. The maximum observed sandwave migration rate, and direction of migration, is detailed at the top of the plot. 438
Figure 339. Observed sandwave migration between 2016 and 2019 on profile 46, transect 4. The maximum observed sandwave migration rate, and direction of migration, is detailed at the top of the plot. 439
Figure 340. Observed sandwave migration between 2016 and 2019 on profile 46, transect 5. The maximum observed sandwave migration rate, and direction of migration, is detailed at the top of the plot. 439
Figure 341. Observed sandwave migration between 2016 and 2019 on profile 46, transect 6. The maximum observed sandwave migration rate, and direction of migration, is detailed at the top of the plot. 439
Figure 342. Observed sandwave migration between 2016 and 2019 on profile 46, transect 7. The maximum observed sandwave migration rate, and direction of migration, is detailed at the top of the plot. 440
Figure 343. Observed sandwave migration between 2016 and 2019 on profile 46, transect 8. The maximum observed sandwave migration rate, and direction of migration, is detailed at the top of the plot. 440
Figure 344. Observed sandwave migration between 2016 and 2019 on profile 46, transect 9. The maximum observed sandwave migration rate, and direction of migration, is detailed at the top of the plot. 440
Figure 345. Observed sandwave migration between 2016 and 2019 on profile 46, transect 10. The maximum observed sandwave migration rate, and direction of migration, is detailed at the top of the plot. 441
Figure 346. Observed sandwave migration between 2016 and 2019 on profile 46, transect 11. The maximum observed sandwave migration rate, and direction of migration, is detailed at the top of the plot. 441
Figure 347. Observed sandwave migration between 2016 and 2019 on profile 46, transect 12. The maximum observed sandwave migration rate, and direction of migration, is detailed at the top of the plot. 441
Figure 348. Observed sandwave migration between 2016 and 2019 on profile 46, transect 13. The maximum observed sandwave migration rate, and direction of migration, is detailed at the top of the plot. 442
Figure 349. Observed sandwave migration between 2016 and 2019 on profile 46, transect 14. The maximum observed sandwave migration rate, and direction of migration, is detailed at the top of the plot. 442
Figure 350. All available bathymetry data (relative to MSL). 443

Figure 351. Difference between 2016 bathymetry survey data and Oceanwise data, with 1 km buffer zone overlaid. 444
Figure 352. Bathymetry merge 2016 to Oceanwise – diagnostic plot – overview. 446
Figure 353. Bathymetry merge 2016 to Oceanwise – diagnostic plot – southeast corner. 447
Figure 354. Bathymetry merge 2016 to Oceanwise – transect diagnostic plot – southeast corner. 448
Figure 355. Bathymetry merge 2016 to Oceanwise – diagnostic plot – northwest of bank. 449
Figure 356. Bathymetry merge 2016 to Oceanwise – diagnostic plot – northwest of bank. 450
Figure 357. Difference between 2019 and 2016 bathymetry survey data, with 250 m buffer zone overlaid 451
Figure 358. Bathymetry merge 2019 to 2016 – diagnostic plot – overview. 453
Figure 359. Bathymetry merge 2019 to 2016 – diagnostic plot – southwest corner. 454
Figure 360. Bathymetry merge 2019 to 2016 – transect diagnostic plot – southwest corner. 455
Figure 361. Bathymetry merge 2019 to 2016 – diagnostic plot – southeast corner. 456
Figure 362. Bathymetry merge 2019 to 2016 – transect diagnostic plot – southeast corner 457
Figure 363. Domain of the local-scale model used in sediment transport modelling. 462
Figure 364. Time-series comparison of measured and modelled water level difference between east and west of the bank. 463
Figure 365. Validation scatter plot of difference in water level head difference between east and west of the bank, selected data. 464
Figure 366. INFOMAR spatial distribution of sediments and the 5 class Folk classification applied. 465
Figure 367. Map of sediment grain size used in sediment transport modelling. 466
Figure 368. Map showing the depth of the mobile layer as implemented across the local model domain. 468
Figure 369. Effect of storm waves on bed levels as derived from sensitivity runs. 470
Figure 370. Time series of model outputs during the first 2 months of the simulation (left panel). The spatial plot of scour for WTG 74, calculated using the Fredsoe method, is also presented as an example (right panel). 473
Figure 371. Scour hole in close vicinity to wreck id 2002 observed in the bathymetry data acquired in 2016 (top panel) and 2019 (middle panel). 476
Figure 372. Scour hole in close vicinity to wreck id 2039 observed in the bathymetry data acquired in 2016 (ltop panel). Note the scour hole was not evident at this location in the data acquired in 2019. 477

TABLES

Table 1. Description of seabed frame locations. 53

Table 2. The parameters measured at each bedframe location. 56

Table 3. The predicted rise in water level for the 'low', 'medium' and 'high' emissions scenario. Note: the central estimate of the medium emission scenario is to be utilised as part of the model simulations. 71

Table 4. Key Statistics related to water levels in Arklow Harbour (Source: Admiralty Tide Figure, 2001-2018). 102

Table 5. The key statistics regarding current speed, water depth and water level from each measurement frame. 105

Table 6. The key statistics in regard to wave height and period from each measurement frame. 124

Table 7. Particle Size Distribution (PSD) data and textural classification of surface sediments collected as part of the benthic sampling campaign. Source: ASU, 2010 & 2011. The highlighted rows show sample locations positioned on the bank. 138

Table 8. Grain size data obtained from borehole locations as part of the Phase 1 campaign. Data source: Fugro (2000). 141

Table 9. Seismic interpretation (reproduced from GDG, 2020). Depths are presented as metres below seafloor (mBSF). 146

Table 10. Grain size information and shear stress thresholds applied as part of the stress exceedance analysis. Note: when comparing relative mobility between sites this is principally a function of water depth. 157

Table 11. Estimated omni-directional extreme wave parameters. 160

Table 12. Bathymetry data available at tidal timescales. 213

Table 13. Bathymetry data available at daily timescales. 218

Table 14. Bathymetry data available at weekly timescales. 222

Table 15. Bathymetry data available at bi-weekly timescales. 227

Table 16. Bathymetry data available at monthly timescales. 246

Table 17. Bathymetry data available at yearly timescales. 257

Table 18. The framework for development of the sediment transport model. 291

Table 19. The key statistics derived from the direct comparison of predicted vs measured bed level change across the validation periods 2000, 2016 and 2016 and 2019 across the development area. 310

Table 20. Details of morphological simulations performed. 313

Table 21. A summary of the predicted magnitude of lowering or raising of the seabed level which may occur across the lifetime of the development, split by region. 330

Table 22. The bathymetry data available to the assessment of site morphodynamics. The utility of these data to the study of site morphodynamics and the assessment of processes occurring at various spatio-temporal scales is described. 362

Table 23. The data sources utilised as part of the study of site morphodynamics. 380

Table 24. The key statistics regarding the influence of water depth and the bottom roughness length on tidal currents and shear stress impacting the seabed. 407

Table 25. Scenarios of sediment transport calculated. 460

Table 26. Sediment description and grain size assigned to the sediment transport map. 466

Table 27. Input parameters applied to the MIKE21 Scour Calculator Toolbox. 472

Table 28. Wrecks of significance within the ABWP lease area. 474

1 Project Appreciation

SSE is currently in the development phase of the Arklow Bank Wind Park (ABWP); SSE holds a lease to develop up to 200 Wind Turbine Generators (WTG) (which will provide a minimum total installed capacity of 520MW) on a rectangular area of seabed aligned with the Arklow sandbank which is located 8-12 km off the east coast of Ireland. The current lease area, which also includes two consented routes for grid connection cables from the wind farm site to shore, is presented in Figure 1. Presently, there are 7, 3.6MW WTG, operating within the Phase 1 lease area, referred to as *Arklow Bank Phase 1*.

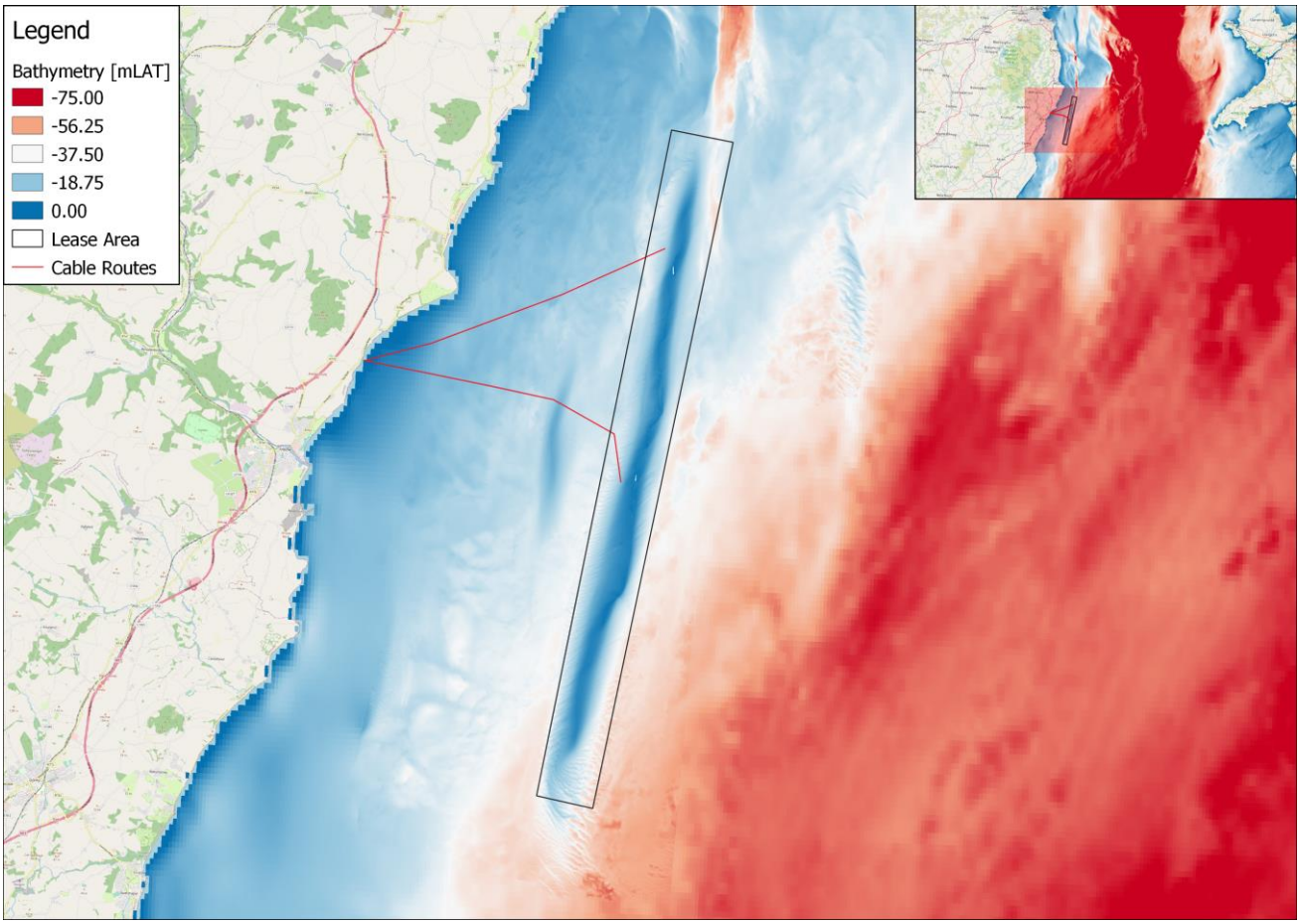


Figure 1. ABWP Lease Area: and consented cable routes overlain the local and regional bathymetry (source: EMODnet and INFOMAR Bathymetry). Note bathymetry at the regional scale is relative to MSL.

When offshore wind farms are located on, or adjacent to, sandbanks then further engineering considerations may apply over and above an equivalent project situated in open water on a (more) stable seabed. Higher levels of seabed mobility are likely to occur which increases the need to understand issues such as local scour and potential seabed level variability. To inform engineering design, SSE has commissioned Partrac, MetOceanWorks and Cooper Marine Advisors to conduct a morphodynamic assessment of Arklow Bank and the surrounding area (including the export cable routes). The purpose of this study is to investigate the physical processes and associated morphological

response of Arklow Bank to, as best as possible, predict the envelope of seabed level variation likely to occur over the lifetime of the ABWP.

2 Study Scope and Approach

The overarching aim of the study is to provide a robust understanding of morphological processes across the region, and locally, to assess, with an appropriate degree of confidence, the implications of these processes for the offshore wind farm, both now and across the operational lifetime of the development. To do this, a systems-based approach was adopted, reliant on a data led analysis complemented by numerical modelling. This approach was applied to assess the magnitude of predicted bed level change likely to occur across the lease area and along the proposed export cable routes over the lifetime of the development.

The primary objective of the morphodynamic study is to quantify the extents, magnitude and timelines associated with the morphological processes occurring across the Arklow Bank and surrounding area. To ensure that the study is of suitable quality and content to allow detailed design decisions to be undertaken, future seabed levels were estimated to determine, and predict changes through time, to:

- The estimated Lowest SeaBed Level (LSBL), and,
- The estimated Highest SeaBed Level (HSBL).

A staged approach was adopted specifically designed to incrementally increase the confidence in the assessment and project outputs, and to ensure numerical modelling tools were judiciously applied to support the prediction of future seabed levels. This interpretative report compiles the works completed to date as part of the assessment of site morphodynamics at the ABWP. The assessment can be summarised via the description of the two staged approach:

Stage 1: The first stage, conducted upstream of the programme of site- specific surveys scheduled at the ABWP, drew upon a combination of qualitative and quantitative assessments of presently available site data; empirical evaluation; initial site modelling; and the application of professional judgement. A review of the relevant literature and data sources was conducted to develop a regional and local appreciation of the prevailing hydrodynamic, wave and sediment transport regimes. To support this, a coupled hydrodynamic / wave / sediment transport model was developed to predict antecedent conditions influencing the morphology of the site over the last forty years.

Stage 2: The second stage utilised survey data to refine and improve the models developed in Stage 1 and further develop our technical understanding of sediment dynamics on Arklow Bank. Relying upon the outputs of bed-updating, sediment transport simulations and complementary data-led analysis, estimates of future seabed levels were made. This supported the assessment of the potential range of seabed level variability likely to occur across the lifetime of the development site.

Achieving a detailed understanding of the sediment transport processes and the geomorphological response of Arklow Bank through time relies on the consideration of a range of information as well as a combination of suitable methods of analysis. Numerical modelling is a useful tool to aid and extend our understanding and thus formed an integral part of our overall approach. Modelling was used to support our expert analysis by testing various hypotheses. The outputs of the model simulations enable us to quantify the geomorphological response of the study area to key process drivers. The application and interpretation of model outputs is supported by other complementary industry-standard methods of assessment, such as quantitative analyses of bedforms, and expert morphological assessment. Study outputs were interpreted within the framework of the local scale Conceptual Site Model (CSM) and considered in tandem with the independent assessment of measured data. This integrated approach avoided placing complete dependency on any one method of analysis and allows multiple viewpoints to be integrated into an overall understanding.

Recognising, and moderating for, the limitations of numerical modelling in accurately forecasting morphological change into the future is crucial and requires the intelligent application of numerical modelling tools grounded within a robust understanding of the process drivers of sediment transport at the regional, and local scale. Restrictions exist when performing long-term morphological predictions principally due to the many underlying assumptions which may lead to results diverging from a realistic or true answer (a problem commonly referred to as *'compound error'*). As experienced users of sediment transport models for predicting geomorphological behaviour in and around wind farms, we are keenly aware of the need to use such tools intelligently, and in combination with an already developed understanding of sediment transport behaviours and rates. We understand the caution that must be employed when undertaking geomorphological upscaling from a period of ebb and flood tides to spring-neap cycles, through to annual and decadal changes. Sediment transport models are also limited in that they can only infer the influences of smaller scale (i.e. sub-grid) features, such as sandwaves through roughness coefficients, and are unable to fully resolve near-field turbulence induced scour forces around small structures. As such an independent, quantitative assessment of bedform features and local scour processes/effects was performed, informed by the modelling.

To predict large scale morphodynamic behaviour, a systems level approach is adopted which relies on a framework which integrates conceptual models, meso-scale coastal area models and data driven analysis (van Maanen *et al.*, 2015)[1]. This approach requires a detailed appreciation of the interactions that occur between the coast and the shallow seabed through time, across space (Figure 2).

1 The methodology utilised within this study builds upon the framework established by van Maanen *et al.* (2015). It also follows methodologies applied within recent morphodynamic assessments conducted by Deltares for offshore wind farm developments in Dutch waters (e.g. Deltares, 2015, 2016 and 2019) who advocate for a 'data led' assessment. Though no specific guidance exists for predicting future morphological response of the seabed at offshore wind farm sites, useful guidance for the use of numerical modelling techniques exists (e.g. Lambkin *et al.*, 2009 and Pye *et al.*, 2017) and this has also been considered.

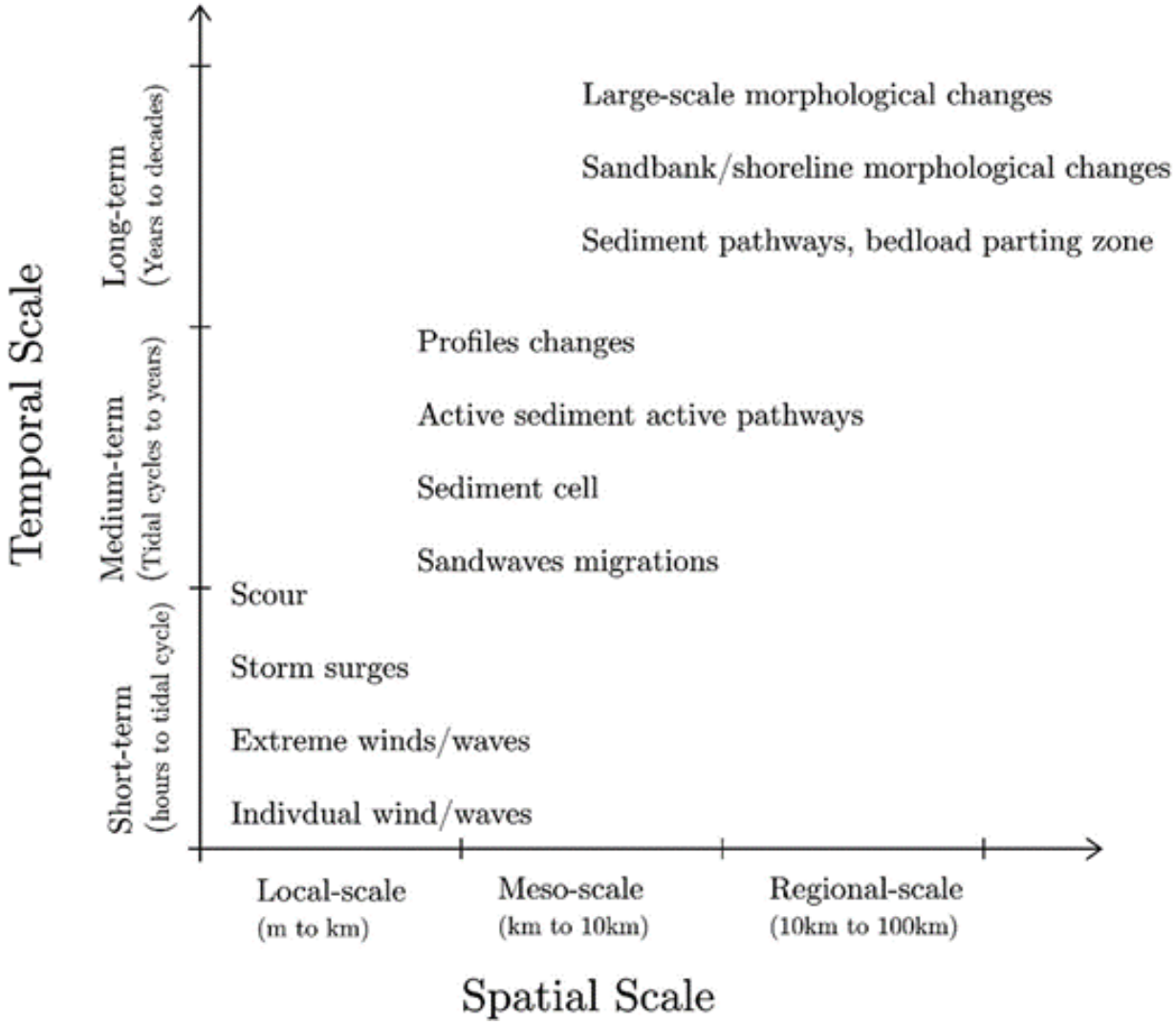


Figure 2. Schematic showing the spatial and temporal scales associated with morphological response of the seabed. Image reproduced from Whitehouse (1997).

2.1 Report Structure

This interpretative report, which supersedes all previous reports, provides a description of the following relating to the development site, including:

- The definitions of the various temporal and spatial scales considered as part of this assessment and key project considerations;
- A review of the relevant literature and assessment of the data and information gaps which exist;
- A synthesis of the regional and local setting, including:
    - The general nature and form of the seabed
    - The distribution of water depths (bathymetry)
    - The nature of the prevailing tidal flow and wave regimes

  - The sediment cover and a conceptual understanding of the associated local sediment regime
  - An assessment of seabed mobility within the development site
- A data led assessment including:
  - Detailed bedform analysis
  - Assessment of historic trends and observed bed level change
- Application of numerical modelling to determine the range of potential seabed level variability likely to occur across the development site, over the lifetime of the development;
- Consideration of confidence limits associated with the predictions; and,
- To support consideration of the potential seabed level variability through time, a preliminary assessment of scour potential around foundations, and global scour effects at the site associated with both foundations and existing wrecks, is described.

3 Data Availability

The ability to deliver a detailed understanding of these processes with a high confidence level is closely linked to the availability of good quality primary evidence, for example:

- Repeated high-resolution multibeam surveys of strategic areas of the sandbank,
- Long-term wave and tidal measurements; and,
- Geophysical and geotechnical surveys to identify depths and types of mobile sediment.

To date, a wide variety of data sources have been collated to inform this assessment. Site-specific geophysical, geotechnical and metocean datasets available for regional and local scales have been used, and these have been supported through inclusion of regional and site-specific data and information garnered from publicly available data sources and data archive centres. Further information was also provided by SSE; these included data from previous bathymetric surveys of the site and various geotechnical / geophysical and environmental data and reports.

All data and information were critically assessed in regard to their utility / quality to the assessment of site morphodynamics based on their issue dates, their origin and the data resolution. For example, a measured dataset is considered superior to an equivalent modelled one; a high-resolution dataset superior to a low-resolution one; an up-to-date dataset superior to an out-of-date one, etc. Appendix A summarises the datasets utilised, and the various technical reports and journal articles consulted. Due to their significance to the study of site morphodynamics, the quality, spatial and temporal coverage, and overall utility to the study, the historic MBES datasets and metocean measurement campaign are described in detail in Section 3.1 and Section 3.2. Outstanding datasets are also discussed in Section 3.3.

3.1 Historic Bathymetric Data

An extensive suite of bathymetric data exists of varying resolution, quality, and coverage.
Table 22 in Appendix A and Figure 3 summarises the bathymetry datasets available to the assessment. High resolution swath bathymetry data were collected during a survey of the lease area (including the consented export cable routes) conducted in 2019 (Alpha Marine, 2019). The 2019 bathymetry is the primary (most up to date and of greatest resolution) bathymetric dataset, and thus has been implemented within the model for the purposes of validation of the hydrodynamic and wave models. Comparisons between datasets are performed cautiously due to differences between the quality, coverage, resolution and vertical datum of historic datasets (see quality review of 2000 data [Cooper Marine Advisors, 2020]). In addition, due to the high rate of seabed mobility of certain bedform features across the bank system, composite bathymetries derived from survey operations which span periods of weeks to months (and which may have been delayed due to adverse sea conditions) do not represent an instantaneous view of

the seabed but are likely to comprise various system states. An appreciation of these issues is required when interpreting apparent changes with comparable data of this type.

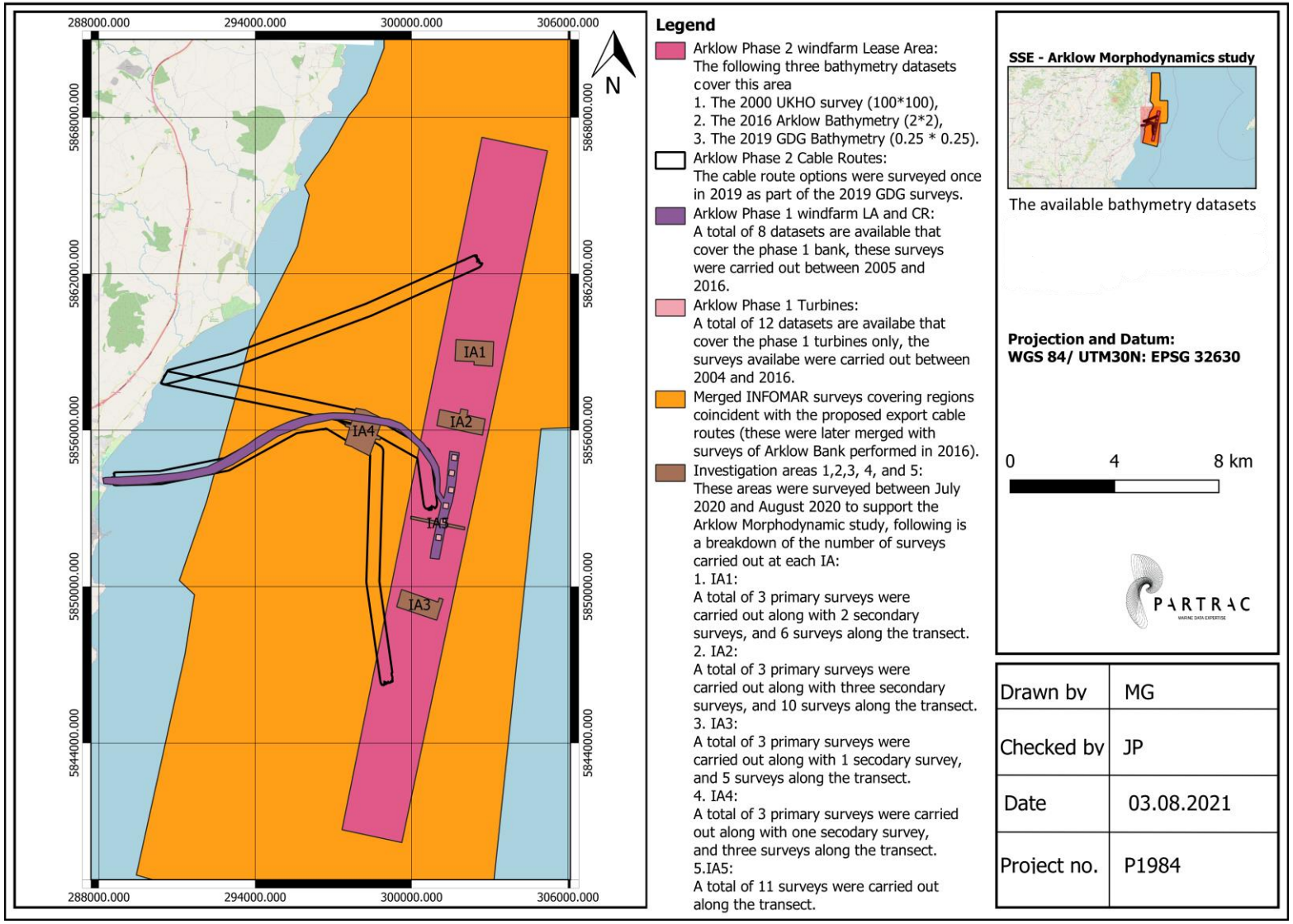


Figure 3. The spatial layout of available historic bathymetry data.

3.2 Metocean Measurement Campaign

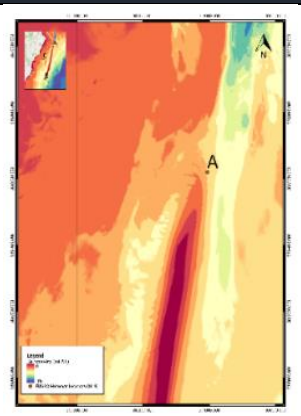
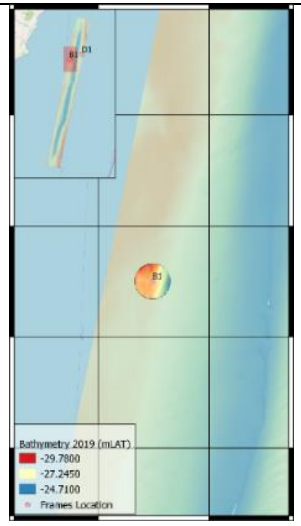
A 12-month metocean measurement campaign was conducted at the ABWP Lease Area variously between November 2019 and March 2021 (Fugro, 2021). In total, five seabed frames, configured with various instrumentation to measure currents, waves and suspended particulate material, were deployed at locations denoted 'A', 'B', 'C', 'D' and 'E'[2].

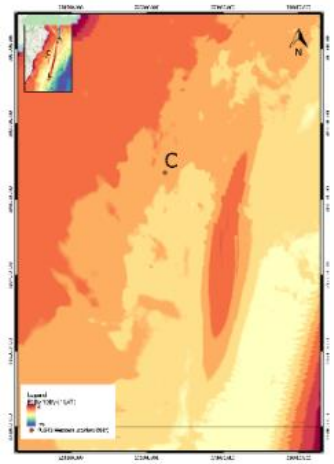
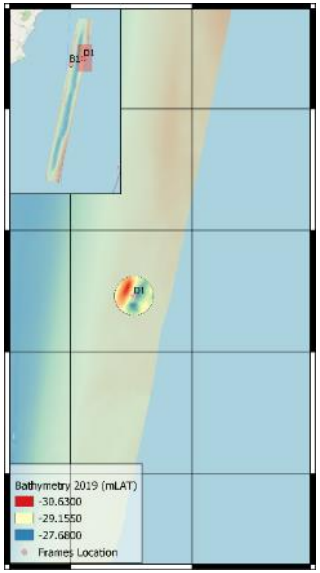
The frame locations are described in detail in Table 1 along with the purpose of the deployment. Further detail regarding the configuration of the seabed frames is presented in Table 2 (note; instrument setup, sampling frequency and data return statistics for the measurement campaign are presented in Fugro, 2021). The frame locations were micro-sited so as to optimise their locations to provide suitable data for local model validation, and to improve understanding of the hydro–sedimentary regime at the local scale (e.g. to investigate the postulated flood-ebb dominance on either side of Arklow Bank and investigate wave attenuation as waves transit across/along the bank).

These data informed the data led analysis (i.e. the assessment of the driving processes of sediment transport and relative sediment mobility) and were utilised to calibrate–validate the driving models of sediment transport (i.e. the hydrodynamic and wave models described in Section 4 and Appendix G,). The performance of these models during validation is described in detail by MetOceanWorks Ltd (2021).

2 At the interim six-month service visit, the frames deployed at location 'B' and 'D' were not recoverable, as such new measurement frames were re-deployed at locations determined to be 'less mobile' to facilitate recovery operations.

Table 1. Description of seabed frame locations.

Frame Location	Local Bathymetry	Site Description
'A''		The frame was positioned at the northern end of Arklow Bank in a mean water depth of circa 28 m. Based on the latest bathymetry, the frame appears to be deployed on a gentle sloping seabed, with water depths increasing to the north/north-north-east of the frame location. Water depths shallow over the bank immediately to the south/southwest of the frame. Several large sandwaves are positioned just to the west/southwest which appear to continue to migrate northwards from the shallower regions of the bank. Prior to deployment the frame location was moved slightly to the east to provide an unimpeded (or less impeded) ebb / flood signal to support validation of the hydrodynamic and wave models. The primary purposes for deploying the frame at this location was to assess the attenuation of wave energy across the bank from south to north.
'B'		The frame's position was amended following burial of the initial deployment. Inspection of the bathymetry indicates that the frame was positioned on the northwest flank of the bank at a location characterised by an average water depth of circa 27 m. The latest bathymetry (acquired in 2019) indicates the frame was deployed on a sloping seabed, with water depths shallowing to the east and deepening to the west. Megaripples, characterised by a wave height of circa 0.1 m are evident in close proximity (circa 100 m) to the east of the frame deployment location. The primary purposes for deploying the frame at this location was to assess asymmetry in tidal flows either side of the bank and to compare these data to those collected at frame location 'D'.

Frame Location	Local Bathymetry	Site Description
'C'		Inspection of the local bathymetry shows the frame is positioned along the proposed export cable route inshore of Arklow Bank and Seven Fathom Bank, on a relatively flat plain between Seven Fathom Bank and the coast. At the frame location a mean water depth of circa 26 m was observed. At this location, the seabed appears to be broadly devoid of large-scale bedforms. The primary purpose for deploying the frame at this location was to investigate processes occurring between the lease area and the nearshore, along the proposed export cable route(s).
'D'		The frame's position was amended following burial of the measurement frame initially deployed. Inspection of the bathymetry indicates that the frame was located towards the northeast of the bank. The frame was positioned in an area of the seabed characterised by average water depths of circa 28 m. Water depths increase gradually to the North of the frame. A small depression is observed immediately south of the frame location. West of the frame (towards the crest of the bank), water depths shallow gradually. No bedform features were observed in the immediate vicinity of the frame's location. The primary purposes for deploying the frame at this location was to assess asymmetry in tidal flows either side of the bank and to compare these data to those collected at frame location 'B'.

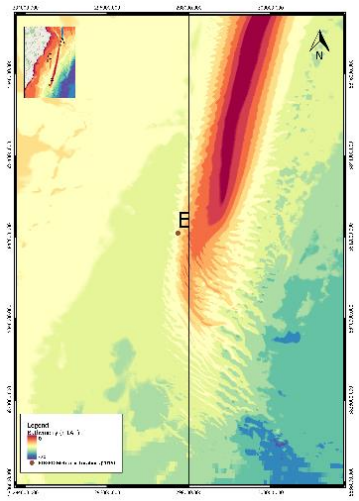
Frame Location	Local Bathymetry	Site Description
'E'		Inspection of the local bathymetry shows the frame was positioned at the southern end of Arklow Bank in a mean water depth of circa 38 m. Water depths shallow over the bank immediately to the northeast. The local bathymetry reveals a significant sandwave field, particularly to the southwest of the bank. Prior to deployment the frame location was moved slightly to the west to provide an unimpeded (or less impeded) ebb / flood signal for model validation. The purpose for deploying the frame at this location was to measure waves approaching the bank from the southerly directions.

Table 2. The parameters measured at each bedframe location.

Frame Location *Table*	Latitude (WGS 84)	Longitude (WGS 84)	Instruments Deployed	Parameters Measured	Start Date	End Date
'A'	52° 54.577' N	005° 54.943' W	Nortek AWAC 600 kHz Aqualogger 210 TYT Starmon Mini SeaGuard SW/ Seabird SBE 37-SM Valeport Fast CTD NISKIN bottle	Current profiles Water level Waves Seabed water temperature Turbidity (ABS) Seabed water temperature Turbidity (OBS) Surface water temperature Seabed water temperature Conductivity Salinity Density Turbidity Suspended Particulate Matter	06/11/2019 01/08/2020 05/01/2020	18/05/2020 16/10/2020 07/03/2021
'B'	52° 51.025' N	005° 56.764' W	Nortek AWAC 600 kHz Aqualogger 210 TYT Valeport Fast CTD NISKIN bottle	Waves Water Level Current Profiles Seabed Water Temperature	02/08/2020 07/11/2020	15/10/2020 07/03/2021

Frame Location *Table*	Latitude (WGS 84)	Longitude (WGS 84)	Instruments Deployed	Parameters Measured	Start Date	End Date
				Turbidity (ABS) Seabed Water Temperature Turbidity (OBS) Conductivity Depth Temperature Conductivity Salinity Density Turbidity Suspended Particulate Matter		
'C'	52° 49.306' N	006° 01.237' W	Nortek AWAC 600 kHz Aqualogger 210 TYT Starmon Mini Valeport Fast CTD NISKIN bottle	Waves Water Level Current Profiles Seabed Water Temperature Turbidity (ABS) Seabed Water Temperature Turbidity (OBS) Surface Water Temperature Conductivity	24/11/2019	19/05/2020

Frame Location *Table*	Latitude (WGS 84)	Longitude (WGS 84)	Instruments Deployed	Parameters Measured	Start Date	End Date
				Depth Temperature Conductivity Salinity Density Turbidity Suspended Particulate Matter		
'D'	52° 51.570' N	005° 55.035' W	Nortek AWAC 600 kHz Aqualogger 210 TYT Valeport Fast CTD NISKIN bottle	Waves Water Level Current Profiles Seabed Water Temperature Turbidity (ABS) Seabed Water Temperature Turbidity (OBS) Conductivity Depth Temperature Conductivity Salinity Density	01/08/2020 07/11/2020"	16/10/2020 07/03/2021"

Frame Location *Table*	Latitude (WGS 84)	Longitude (WGS 84)	Instruments Deployed	Parameters Measured	Start Date	End Date
				Turbidity Suspended Particulate Matter		
'E'	52° 41.462' N	005° 59.581' W	Nortek AWAC 600 kHz Aqualogger 210 TYT Starmon Mini SeaGuard SW/ Seabird SBE 37-SM Valeport Fast CTD NISKIN bottle	Waves Water Level Current Profiles Seabed Water Temperature Turbidity (ABS) Seabed Water Temperature Turbidity (OBS) Surface Water Temperature Seabed Water Temperature Conductivity Depth Temperature Conductivity Salinity Density Turbidity Suspended Particulate Matter	"24/11/2019 02/08/2020 22/11/2020"	"19/05/2020 15/10/2020 08/03/2021"

3.3 Outstanding Data

The present study will inform several aspects of the project (e.g. scheme layout and foundation design, de-risking operations and maintenance activities, cable routing etc.). Our ability to inform each aspect of the study, with a high confidence level, is closely linked to the availability of primary evidence.

At the time of publication, data from the Ground Investigation (GI) campaign remain outstanding. As such only limited site-specific geotechnical survey data, and unverified interpretation of geophysical data is available to assist in the identification of depths and physical characteristics of mobile sediment. The ground-truthed, estimated, thickness of the sand mobile (erodible) layer (i.e. the sand deposit) across the lease area and along the proposed export cable routes is required to verify predictions of future seabed levels. Particle size data for all surficial (< 1 m below the seabed) sediment samples collected from seabed grab samples, vibracore or borehole locations are critical input data for the sediment transport model.

At this stage, the presently available data is deemed sufficient to progress the morphodynamic assessment. To do this, informed assessments, grounded in the available data and relying on professional judgement, are applied to obviate for existing data gaps. We tacitly acknowledge that the data acquired from the ongoing/programmed site-specific survey work will further strengthen our understanding of (and thus our ability to predict) morphodynamic processes occurring on the bank. The outstanding ground-truthed geophysical interpretation and the geotechnical data will be reviewed and implemented within the study at which time they become available to the commission.

4 Modelling Tools and Applications

Obtaining a detailed spatio-temporal understanding of seabed level change relies upon the consideration of a range of information as well as a combination of suitable methods of analysis. Numerical modelling is a useful tool to aid and extend our understanding, particularly for forecasting change (e.g. Zanuttigh, 2007; and Brown and Davies, 2009). The analysis and interpretation of outputs from model simulations enables the quantification of the geomorphological response (i.e. the bed level change) of the study area to key process drivers (e.g. tides, storms) throughout the project lifetime (28 years after installation). The focus of the modelling exercise was to, as best as possible, predict (and quantify) how the profile and form of the seabed (i.e. the seabed level) is likely to behave and evolve through time, and across space. Seabed behaviour is the result of many processes and mechanisms which act and interact on a variety of space and time scales. Coastal area morphodynamic models are used to predict short-term (days to months) bathymetric changes to address specific engineering challenges (Nicholson, et al 1997). Typically, schemes focus on two-dimensional, depth-averaged approaches (e.g. Wang et al., 1992; Sato et al., 1995; Price et al., 1995), which provide a strong basis for performing detailed simulations of morphological evolution (i.e. seabed level change) and have been proven to provide good results during application over shorter time scales (e.g. Broker et al. 2007, Dronen and Deigaard, 2007). Approaches typically rely on standard models focused on the constituent physical processes (waves, currents, sediment transport), which rely on a feedback loop where the updated bed topography is applied into the hydrodynamic and sediment transport computations. One of the key considerations in usefully using such models for predictive purposes is that good quality datasets are available within any analysis; these tools should not generally be used, and perform poorly, when used with disparate or sparse datasets. This study has a suitable volume of quality, relevant data for use in the following modelling exercise.

To support the assessment a coupled hydrodynamic / wave / sediment transport model was developed. The coupled model is referred to as the Arklow Bank Modelling Suite (ABMS) and is presented in the form of a schematic diagram in Figure 4. The setup and validation of the hydrodynamic and wave models is described in Appendix G and in greater detail in MetOceanWorks Ltd (2021)[3]. The setup, concept testing and validation of the sediment transport model is described in detail in Section 9 and Appendix G. An assessment of the performance of the sediment transport model in representing the key driving processes of sediment transport across the development site is detailed in Section 9.3. A discussion of the confidence limits which should be considered with the predictions of future seabed levels is presented in Section 9.6. Finally, in addition to scenarios targeted at the morphological response of the bank, simulations were run using the MIKE21 Particle Tracking (PT) module to assess the Lagrangian transport pathways on and around the bank (e.g. interactions with the coast, etc.) via particle releases at strategic positions within the model

3 The hydrodynamic and wave models (termed the *driving models*) are the same base model as that which has been applied to develop metocean design criteria statistics.

domain. Particles were ascribed the characteristics of local sediments to the release locations, and the releases were simulated in conjunction with different tidal phases including periods of greatest cross bank flows, which have been identified by the metocean climate assessment and sediment transport modelling as being key drivers of bank change. These simulations aim to improve our understanding of the potential interaction between Arklow Bank and the coastline and provide an improved appreciation of the sediment transport pathways occurring within the area of interest.

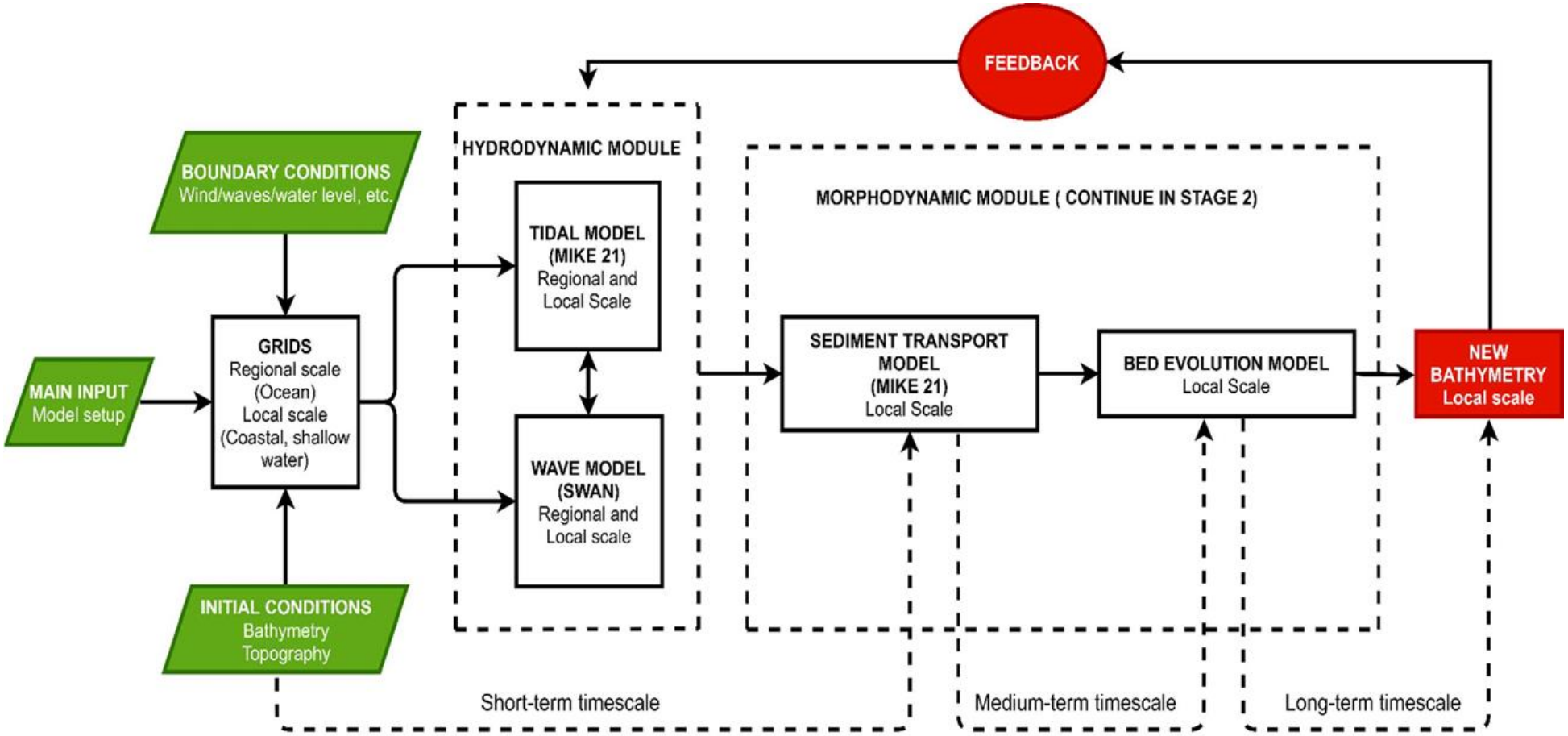


Figure 4. A schematic detailing the modelling tools and their application within the study of site morphodynamics at the ABWP.

5 Project Considerations

Working individually, or in combination, several processes have the potential to influence net sediment transport (i.e. cause seabed levels to raise or lower through time) within the lease area, and along the export cable routes, during the lifetime of the wind farm. This includes a combination of periodic and episodic processes:

- Asymmetry[4] in local tidal flows (and local effects on flows or water levels) which drives net sediment transport.
- Influence of waves, and high energy, storm events.
- Influence of negative and positive surge events (i.e. surge induced flows).
- The influence on flows of local bathymetric features and seabed infrastructure.

Factors which may influence these processes include:

- *Sediment Type*: The horizontal, and vertical, variability of sediment types and composition across the lease area, export cable route and wider region of interest which controls the rate(s) of sediment mobility and erosion/scour.
- *Seabed Infrastructure*: Local, and global, effects on the sediment regime during, and post, construction of seabed infrastructure (e.g. the installation of a monopile, or an array of monopiles).
- *Climate Change Effects:* quantifying the potential effects of the predicted rise in sea level over the lifetime of the development on the hydrodynamic, metocean and sediment regimes (local and regional) and judging their impact in terms of the response of the bank.

Such processes can drive the following morphological response at the seabed.

- *Episodic, periodic, or progressive changes to seabed levels*: changes through time and across space, due to local erosional/depositional regimes driven by tidal flows, water level, waves, and storms,
- *The migration and evolution of morphological features (i.e. sandwaves and megaripples)*; the transient influence of the migration of mobile features on seabed levels.
- *The evolution of the shape and relative position of the bank*: temporal, or episodic, changes to the relative position of the bank through time and changes to the cross-sectional shape and profile of the bank along its length.
- *Local scour processes*; quantifying the potential impact on local seabed levels due to the presence of WTG foundations. Note: analysis presented in this document does not consider scour protection.

Section 5.1 to Section 5.5 detail the key project considerations.

4 Net transport can either be a result of temporal asymmetry (i.e. flows go in one direction for a greater period of time during the flood / ebb phase) and / or asymmetry in the amplitude of the prevailing flow (i.e. flow velocity is greater in one direction during the flood / ebb phase); these imbalances in the flow regime control net transport.

5.1 Defining Spatial-Temporal Scales

This project presents information across a broad range of spatial and temporal scales. Well-defined spatial and temporal scales are important to establish how the formation and evolution of Arklow Bank is linked with larger-scale influences and processes from the far-field (e.g. tidal and wave processes and sediment sources) (Whitehouse, 1997). The relevant spatial and temporal scales for this project are defined as follows:

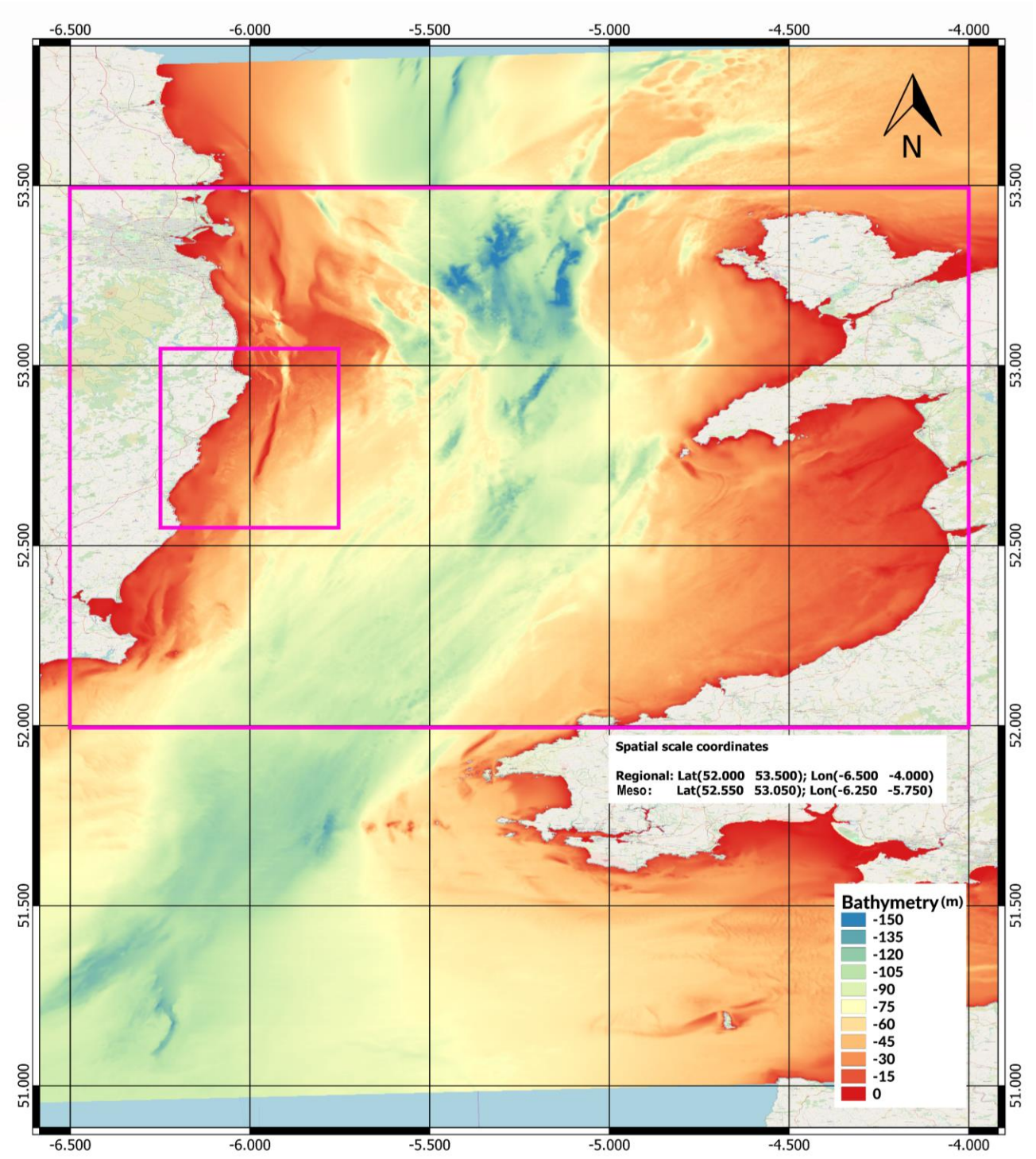
Spatial Scales:

- *Local scale*: morphological features including bedforms existing within the lease area and along the proposed export cable routes.
- *Meso-scale*: sandbank features and coastline. The meso-scale, which is associated with the CSM at the local scale, is defined as that 'from the north of Arklow Bank (in the south of the bed load parting zone) at 53.050 N' and extending to 52.550 N''; this includes the area inshore of the bank to the coastline and captures the main sediment pathways from the north of the bank; and,
- *Regional scale*: Irish Sea, establishes exposure conditions for the site and wider linkages between macro bedforms (e.g. sediment pathways, sources, and stores). The regional scale is defined as that 'between Ireland and Wales and 52.00 N 'and 53.50 N'. This definition encompasses the St George's Channel Bedload Parting Zone (BPZ) to the north of Arklow Bank, which is relevant to the assessment of sediment supply to the bank and the assessment of regional sediment transport pathways.

Temporal Scales:

- Short-term processes: bedform and sandbank response to individual tidal cycles and individual (high energy) events;
- Medium-term processes: assess variations in the bank profile over months to years in response to the periodic lunar tidal cycles and episodic seasonal wave variations; and;
- Long-term processes: long-term changes in the bank geometry and position over years and decades (compatible with the lifetime of the development) including for climate change influences.

Figure 5 shows on a map of the Irish Sea, the extents of the *regional* and *meso* scales, as defined above.



PARTRAC
MARINE DATA EXPERTISE

Coordinate System: WGS84/ UTM Zone 29N
Projection: Transverse Mercator
Datum: WGS 1984
False Easting: 500,000.0000
False Northing: 0.0000
Central Meridian: -9.0000
Lattitude of Origin: 0.0000
Scale: 1:450,000

0 10 20 30 40 km

Spatial Scale Definition	
Drawn by	LH
Checked by	KB
Date	10.08.2019

Figure 5. The boundary extents for 'regional' and 'meso' spatial scales overlain on the bathymetry (m MSL) of the Irish Sea (source: EMODnet Bathymetry).

5.2 Determination of the Nearshore Boundary

This assessment provides quantitative predictions for seabed level change for the export cable route from the lease area to the nearshore. The study does not provide an assessment of the cable landfall and thus will not consider sediment transport regimes inshore of the estimated depth of closure. For this purpose, the depth of closure for a given or characteristic time interval is defined as *"the most landward depth seaward of which there is no significant change in bottom elevation and no significant net sediment exchange between the nearshore and the offshore" (Kraus, 1983).* Furthermore, activities performed as part of the construction, operation and decommissioning of the proposed development have the potential to bring about changes to the local, and far-field, hydrodynamic, metocean and sedimentary regimes. This report does not consider such effects. Predictions of future seabed levels along the export cable route do not consider effects associated with wind farm infrastructure being present, as part of this development, or at other locations in the region. Figure 6 shows the estimated depth of closure, following the equations of Hallermeir (1981) and Hallermeir (1983). The depth of closure is estimated as being between the 5.5 m and 7.0 m contour. The outer closure depth of 7.0 m defines the nearshore boundary. See Appendix B for further detail.

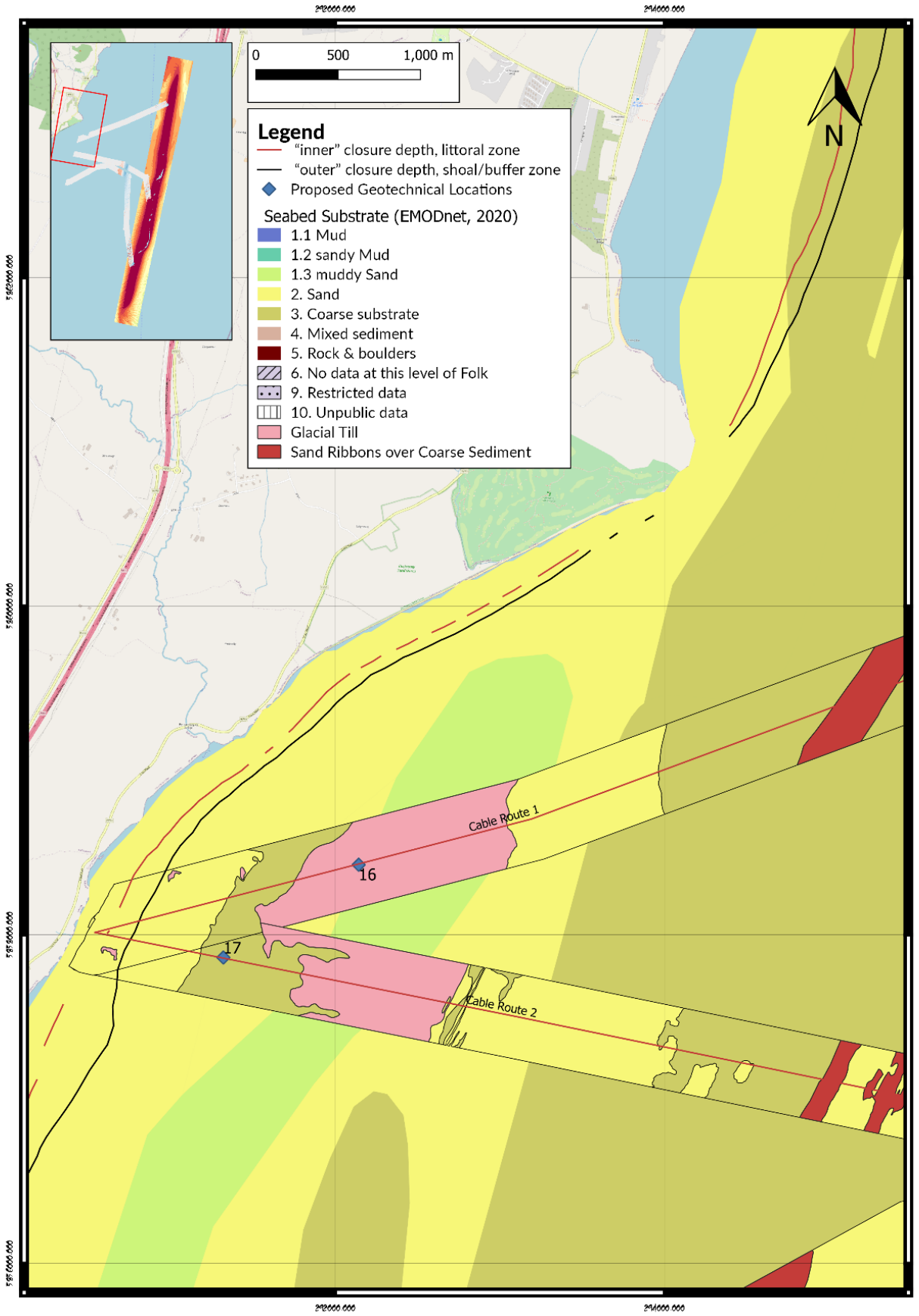


Figure 6. Estimated depth of closure following the equations presented by Hallermeir,1981 and 1983. The 'outer' closure depth denotes the projects nearshore boundary.

5.3 Coordinate Reference System

The data available to the study displayed various geodetic horizontal and vertical datum. All datasets were standardised to a single coordinate reference system being WGS 84 / UTM zone 30°N. Though some data is presented in the report using the vertical datum of MSL, for all primary study outputs, the vertical datum of LAT was applied.

5.4 Wind Farm Infrastructure

The impact of constructing a wind farm, regardless of layout or foundation design, will likely have a negligible impact upon bank scale morphology. However, the construction of WTG structures on the bank will display a local impact on the tidal flows and local sediment regime which is typically manifested local to the structure as scour, referred to as local scour. The potential also exists for cumulative flow disturbances (which is a complex function of flow vortices, localised turbulence, flow acceleration and de-acceleration around structures) having a cumulative effect (i.e. wake to wake interaction) on certain areas of the bank. This is entirely dependent on scheme layout, but a preliminary assessment and discussion of scour potential and cumulative flow disturbances is presented in Appendix H to inform future decision making.

Predictions of future seabed levels do not consider effects associated with wind farm infrastructure being present, as part of this development, or at other sites in the region.

The key project dates considered as part of this assessment were as follows:

- Design life – currently assuming 28 years for WTGs (also to consider 40 years for OSPs and export cables)
- WTG foundation installation date (Q1 2025/ Q1 2026)
- OSP foundation installation date (Q2 2025/ Q3 2025)
- Array cables installation date (Q4 2025/ Q3 2026)
- Offshore export cables installation date (Q1 2026/ Q2 2026)

5.5 Climate Change Effects

Estimated future seabed levels assume the metocean, hydrodynamic and sedimentary regimes within the Irish Sea will broadly remain similar through the lifetime of the wind farm. Climate change issues warrant consideration. The goal here is to understand, assess, and if required, account for, such effects on the prevailing regimes.

Due to impacts upon the prevailing hydrodynamic and metocean conditions (i.e. the drivers of sediment transport), changes to observed water levels have the potential to modify local and regional sediment regimes. Climate change gives rise to global effects which are anticipated to be manifested at regional scales by rising mean sea levels. The

effects of a changing climate, and the relative significance of such effects, on the sediment regime in the Irish Sea, and at the development site, are difficult to predict with accuracy. However, within the literature there is general agreement that water levels will rise during the lifetime of the development[5]. This change is widely accepted to include contributions from global eustatic (water volume) changes in mean sea level and regionally varying vertical (isostatic) adjustments of the land / seabed.

Information on the rate and magnitude of anticipated relative sea level change during the 21st Century is available from the United Kingdom Climate Projections (UKCP18, 2018) whose models include the Irish Sea and coastline. It is predicted that the Wicklow coast will be impacted in a similar manner to the north coast of Wales for which quantitative projection data can been obtained. The projected sea-level changes are associated with three different forcing scenarios, being RCP 2.6, 4.5 and 8.5 which are presented in Figure 7. Current estimates are that over the next century the Irish Sea (Wicklow coast) will experience a rise in sea level of between 0.1 – 0.5 m (Table 3). Sea levels are predicted to rise at a greater rate during the second half of this century. Though it is recognised that current estimates extend beyond the lease period, it is reasonable, though conservative, to utilise the central estimate of the medium emissions scenario as part of targeted model simulations designed to assess climate change effects on bank morphology.

5 A significant body of work exists regarding the postulated increase in storminess due to climate change effects (e.g. Beniston *et al.*, 2007; Feser *et al.* 2015). The impact of storminess can be considered as the result of several interlinked factors being storm intensity, storm frequency and storm track. Changes in any, or all, of these parameters may have implications for sediment transport (and thus morphological adjustment at the seabed) within the region. At present, within the scientific community it is widely agreed that contradictory evidence exists regarding the potential for climate change effects to increase relative storminess. Due to this climate change effects implanted within the model will only include for sea level rise.

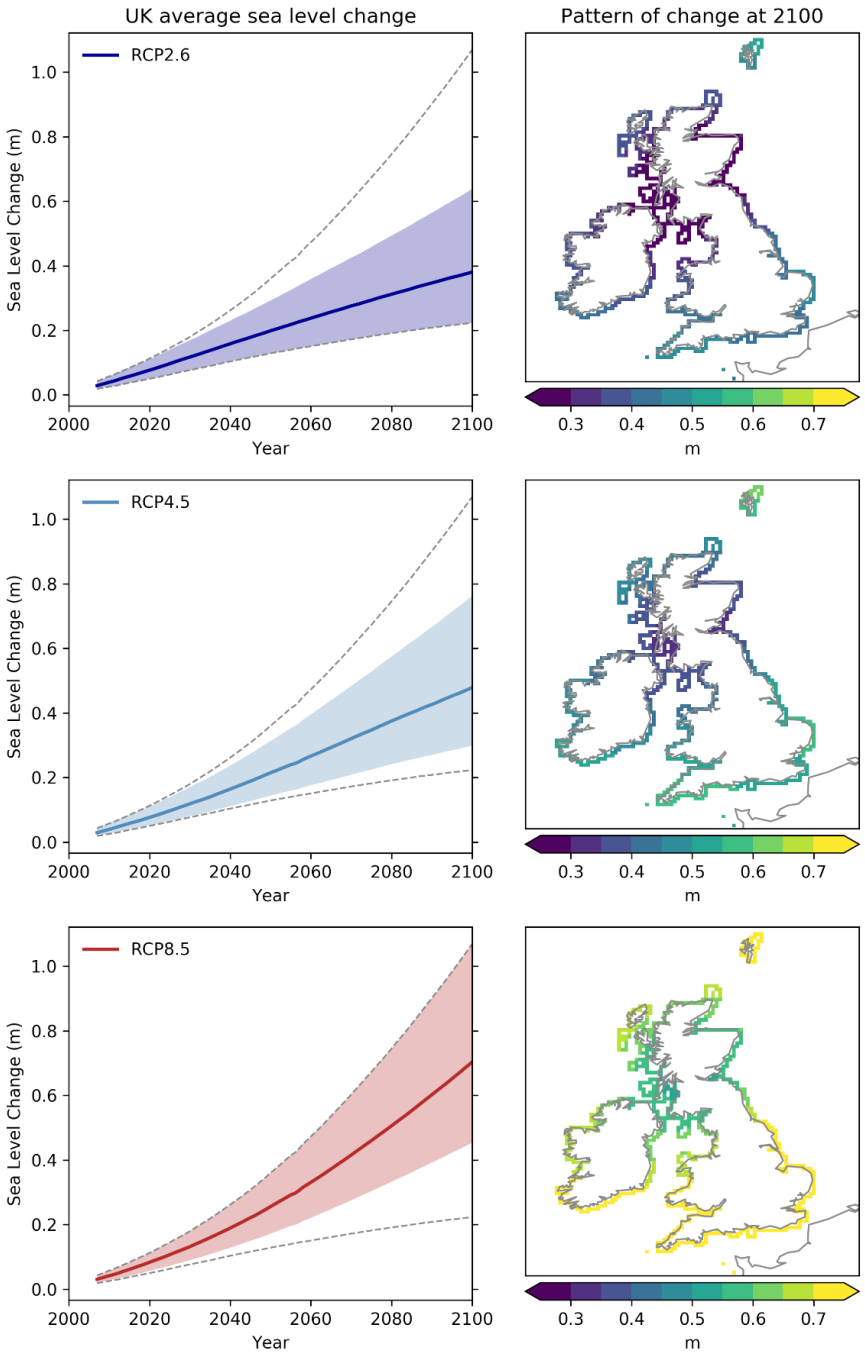


Figure 7. The three emission scenarios presented in the form of a time series of time-mean sea level change. Plot reproduced from UKCP 18 (2018).

Table 3. The predicted rise in water level for the 'low', 'medium' and 'high' emissions scenario. Note: the central estimate of the medium emission scenario is to be utilised as part of the model simulations.

Scenario	5th	50th	95th
RCP2.6	0.14	0.23	0.35
RCP4.5	0.17	*0.26*	0.39
RCP8.5	0.21	0.32	0.46

6 Geology and the Origin of the Sand Banks on the Eastern Irish Seaboard

The geological history of the Irish Sea dates to pre-Cambrian times, however, for present purposes it can most usefully be traced from the Devonian, Carboniferous and Permian periods in the late Palaeozoic. The details of the formation of the Irish Sea basin through geological times is beyond the scope of this commission, however the reader is referred to Ziegler (1982) who reconstructs the palaeogeography of the Irish Sea throughout these periods. Further aspects of the geological background are found in Belderson (1964); Cathie Associates Ltd (2018); Holmes and Tappin (2005) and Mellett *et al* (2015). The Irish Sea basin is thought to contain rocks from several geological systems, ranging from Precambrian schists and gneisses to Cretaceous chalk and Palaeogene basalts. These rock formations exist, or sub-crop, beneath a locally thick cover of Quaternary (<2.6 million years old) sediments. The properties of Quaternary sediment are highly variable laterally, and with depth, due to repeated fluctuations of ice sheet margins during the last glacial period.

Arklow Bank is a narrow linear sandbank formed across a glacial moraine (Clark *et al*, 2012). The bank is situated in the Irish Sea to the east of Arklow, County Wicklow. Arklow Bank does not exist in isolation but rather forms part of a series of coast-parallel, north-south trending, offshore banks. These banks are generally about 10 km offshore, typically stand in 20 to 40 m of water and rise to within a few metres of the water surface. The banks form a punctuated line along the eastern Irish coast, and from north to south include Bennet, Kish, Frazer, Bray, Codling, India, Arklow, Glassgorman, Rusk, Blackwater/Moneyweights, Lucifer, Long and Holdens banks (in which Bennet, Kish, Arklow, Blackwater/Moneyweights banks are considered to be similar in terms of their characteristics to Arklow Bank). The location of the various banks along the eastern Irish coast are detailed in Figure 8.

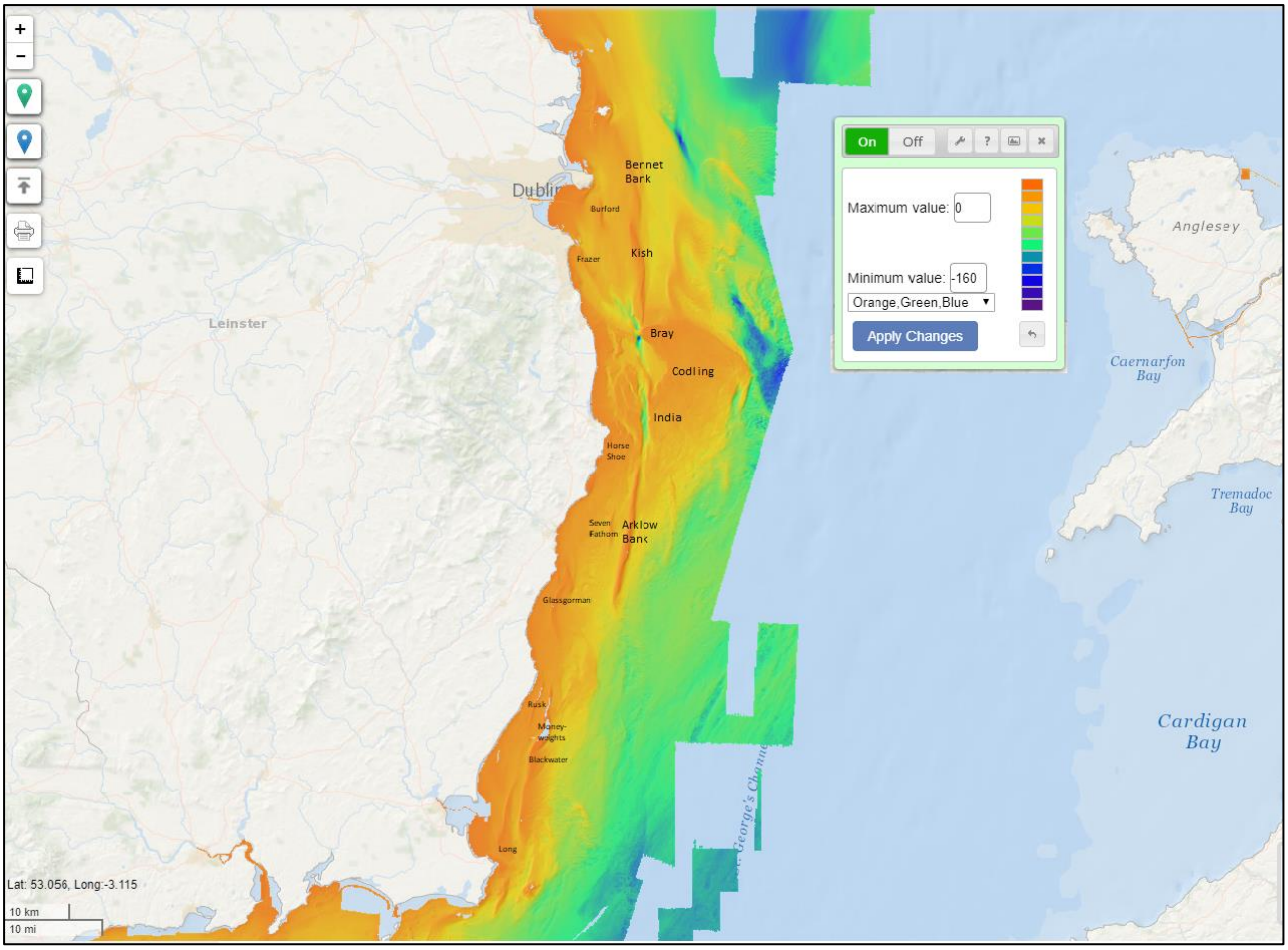


Figure 8. Location of the various sandbanks, which form the local bathymetry along the eastern seaboard of Ireland1. (Source: INFOMAR Bathymetry).

The location of sandbanks on continental shelves depends on the presence of tidal (or other) currents capable of moving sand, and the availability, or supply, of sand. Dyer and Huntley (2001) state that most sandbanks on the European continental shelf (and elsewhere) appear to have been created during the post-glacial rise in sea-level; they are features resulting from glacial action and retreat.

Seismic profile and seismo-stratigraphic analysis of the Kish, Burford, Bray and Fraser banks to the north of Arklow reveal a typically homogeneous upper unit devoid of internal structures or 'hard' cores, suggesting that these banks are comprised of sand/gravel and are *not* founded on a glacial morainic core (i.e. they do not have a geological genesis) (Wheeler *et al.*, 2001). These banks are of Holocene age, and the source of the bank material is from erosion and re-working of local fluvio-glacial and glacial deposits during the marine transgression during the last ice retreat. Wheeler *et al* (2001) estimates stranding of the banks by rising sea-levels around 5,000 BP (Before Present) and bathymetric comparisons published by Wheeler *et al* (2001) suggest that these banks are quasi-stable over time, broadly maintaining their position due to the interaction of the prevailing regimes. In contrast, Fahy *et al* (2002), Keary (cited in Wheeler *et al* (2001)) and Warren and Keary (1989) indicate that both Arklow Bank and Codling Bank are

stable formations which consist of glacial outwash sand and gravel moraine sediments deposited during the last ice-age, an inference also supported by Cathie Associates Ltd (2018). In the vicinity of Arklow, this is likely a result of the development of Wicklow Trough which creates focused tidal flows sediment transport from the north. Such formations have been described elsewhere on the European continental shelf; for example, Smith, (1988) has suggested that the Sandettie and South Falls banks were formed with their southern ends attached to a gravel ridge in the Dover Straits.

Appendix D details the key stages of geological development on the eastern Irish Seaboard from the Pleistocene through to the Holocene, as presented by Cooper Marine Advisors Ltd (2020). The main points of the assessment can be summarised as follows:

- The origin of Arklow Bank occurred during a period of marine transgression which was driven by a rapid rate of sea level rise through the early part of the Holocene, creating a recessional coastline and high levels of sediment supply from newly inundated areas of land.
- The change in orientation of the (former) coastline to the north against a flat coastal plain created a tidal circulation which helped spawn a succession of headland associated recessional sandbanks (Type 3(B)) on a seabed formed of glacial moraine.
- As sea levels continued to rise, the coastline further receded and the combination of coastal processes then favoured new banks forming further to the west and in shallower water, leaving former banks to the east in deeper water with a much-reduced sediment supply. These easterly banks eventually became moribund due to loss of sediment supply and weaker near-bed flows.
- By around 8,500 BP sea level rise opened Wicklow Trough to tidal exchange, providing the conditions to form a new bank at the southern confluence of this feature. By 7,500 BP the coastal plain became submerged altering the local flow regime leaving a headland to influence the formation of Arklow Bank as a Type 3(B) sandbank.
- By 6,000 BP sea levels submerged the coastal plain to such an extent that the former headland was submerged and that flows became more rectilinear. At this time, Arklow Bank developed as a Type 1: Open shelf linear sandbank. The association of the northern end of the bank with Wicklow Trough supported bank development by offering enhanced "channeled" ebb flows and thus additional sediment supply from the coastal plain to the north (a location which is now associated with a bedload parting area).
- The slowing of sea level rise from this time against a generally steeper coastline reduced the sediment supply (and thus concluded the period of marine transgression) which then slowed down further bank development to form a present-day equilibrium condition.

The future long-term development of Arklow Bank remains linked to changes in mean sea level (and associated effects on tidal propagation), coastal recession, sediment supply and flow interactions with Wicklow Trough. It is postulated, that over the next millennium, sea level rise may begin to move the bank into a moribund state, local sediments may

be eroded (i.e. the sediment budget will move into deficit) and transported away from the bank resulting in a reduction in the bank profile

6.1 Modern Day Setting: Historic Chart Analysis

In the modern era, Admiralty Chart No. 1787 (United Kingdom Hydrographic Office [UKHO]) covers the area from Wicklow Head to Kilmichael Point, and thus includes for Arklow Bank. An assessment of the -10 mLAT, and -20 mLAT contours derived from the 1978 version (surveyed in 1914) and 2018 version (surveyed in 2000) of the Admiralty Chart and the bathymetric data collected in 2000, and 2019, has been conducted to assess the relative position, form, and profile of the bank over the last century. Due to the uncertainty associated with the development of historic charts, analyses are treated with caution and no assessment of morphological trends is offered[6]. These data indicate:

- The position of the bank, relative to the coastline, has largely remained the same over the period between surveys (86 years). Comparison of contours derived from the historic bathymetry chart indicate that parts of the bank appeared to have moved to the east and west and the northern and southern tails of the bank have extended through time to the north and south, respectively.
- Through time, Seven Fathom Bank appears to have expanded in size and become elongated to the north.

Figure 9 and

6 Only low to medium confidence is placed on this analysis due to the age and resolution of the chart data, scale of reproduction and the method of contouring applied to the data.

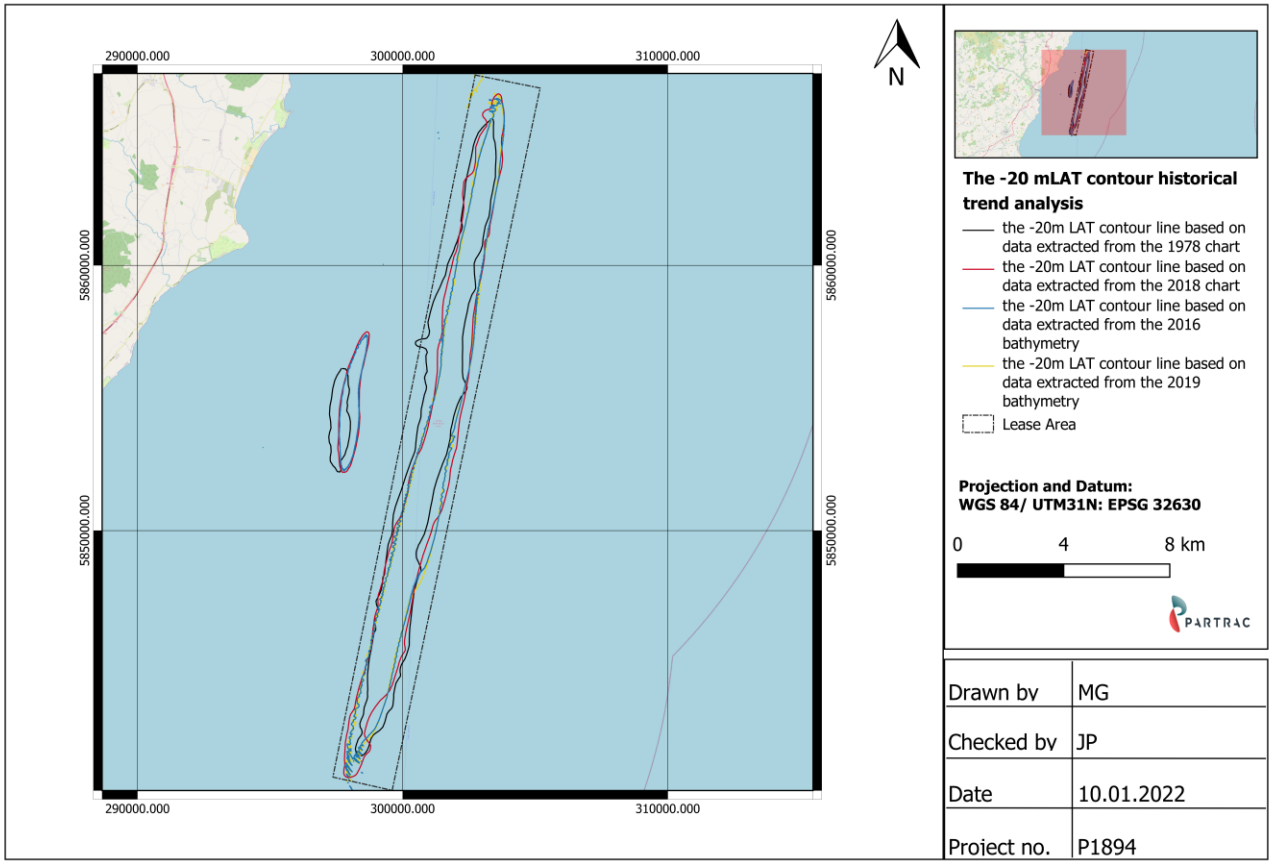


Figure 10 presents the -10 mLAT and – 20 mLAT contour derived from the 1978 (surveyed in 1914) and 2018 (surveyed in 2000) editions of the local Admiralty Chart; the MBES data collected in 2016, and 2019, is also included for reference.

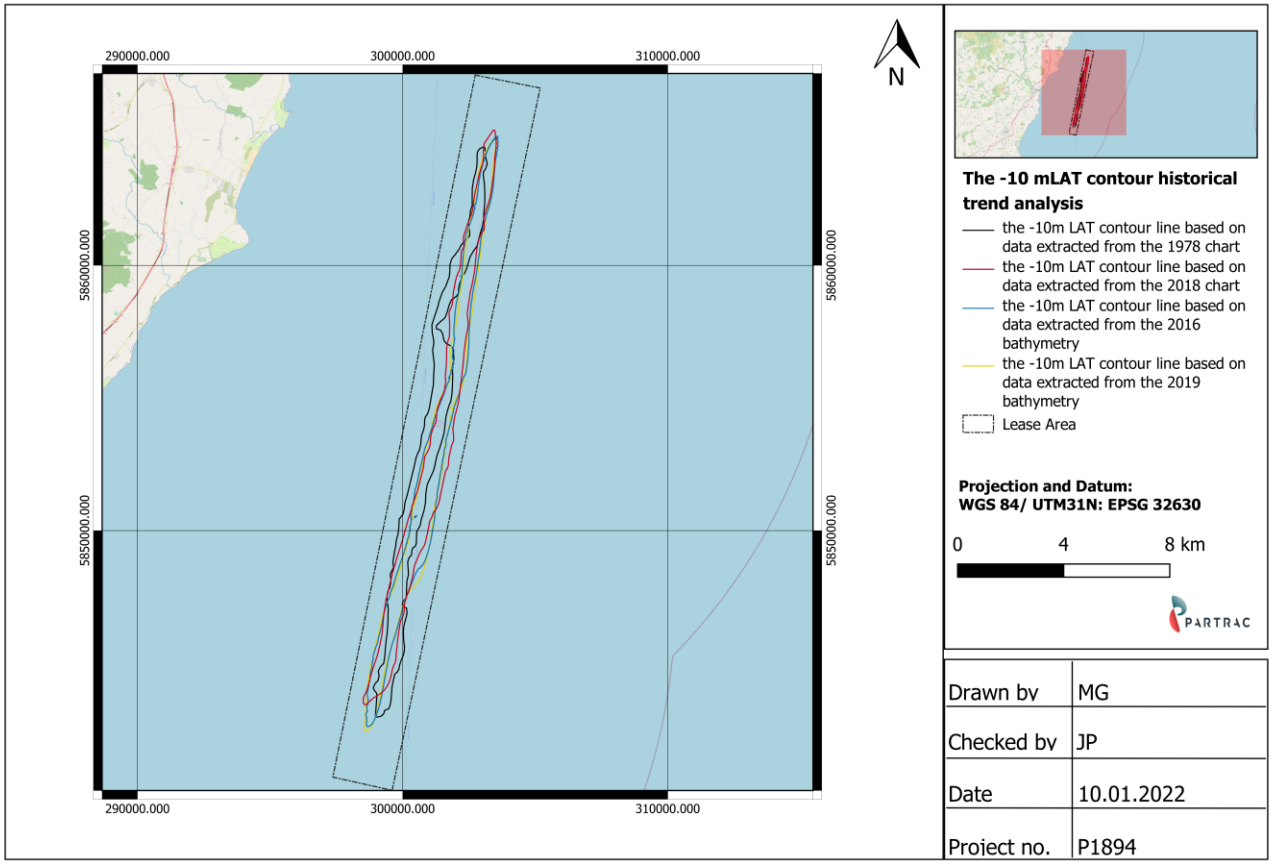


Figure 9. The -10 m contour analysis from the 1978 and 2018 edition of Chart no 1787 and the MBES data acquired in 2016 and 2019.

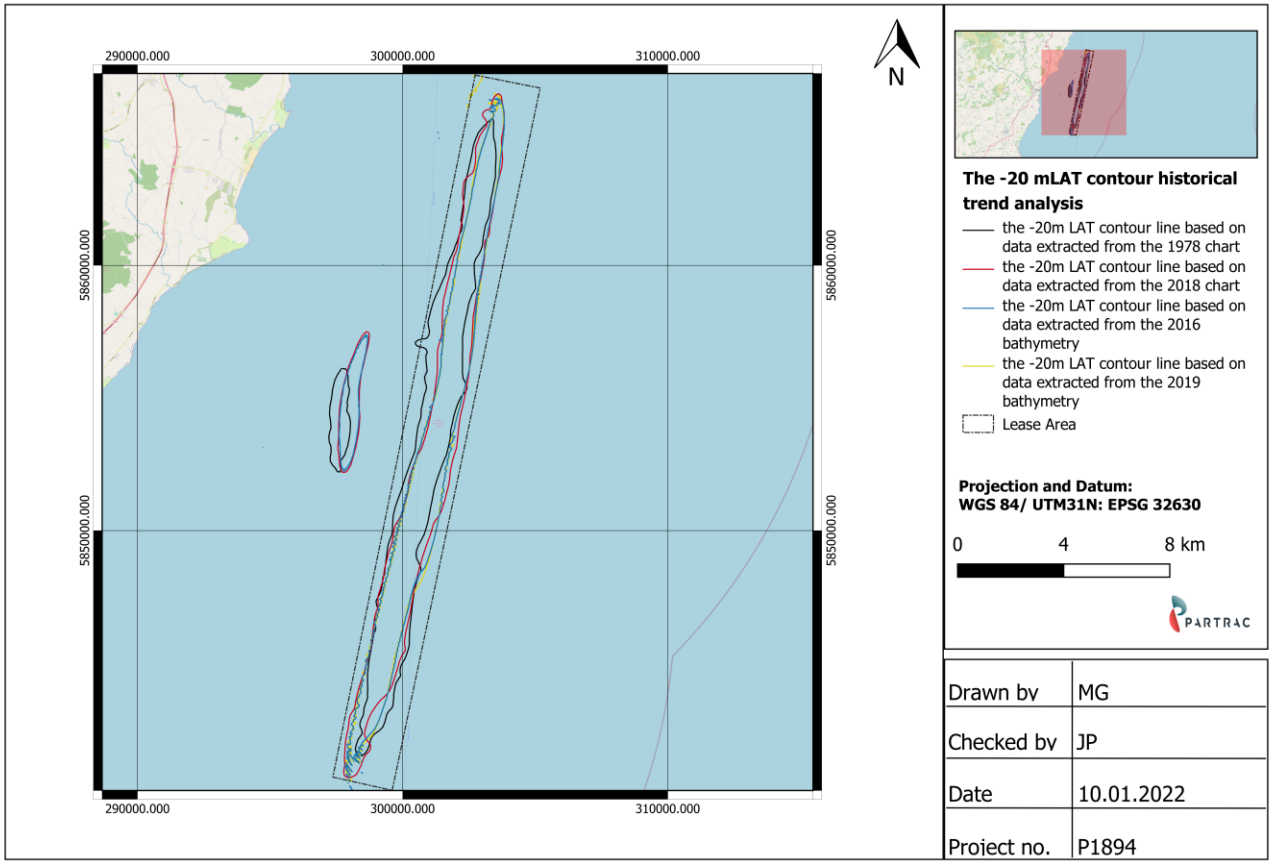


Figure 10. The -20 m contour analysis from the 1978 and 2018 edition of Chart no 1787 and the MBES data acquired in 2016 and 2019.

6.2 Classification of Arklow Bank

As described in Section 6, the contemporary form of Arklow Bank has been classified as a Type 1: Open Shelf Linear Sandbank based on the classification described by Dyer and Huntley (1999), however, the bank is believed to have formed as a Type 3(B) 'banner bank' when a former headland receded. For reference, the various bank types, as classified by Kenyon and Cooper (2005), are presented in Figure 11.

Type 1 sandbanks are maintained by the convergence of sediment towards the crest from opposite sides of the bank; on Arklow Bank sediment is also transported across the bank. The rotary residual sediment transport typically observed on an open shelf linear sandbank is driven by two vorticity forces that increase toward the bank crest due to the increase of bottom friction in shallower water over the crest. Due to the orientation of the bank relative to the axis of the peak tidal flow, the Coriolis effect enhances the friction-driven circulation (Hulscher *et al.*, 1993; Reynaud and Dalrymple, 2012; Roos and Hulscher, 2002).

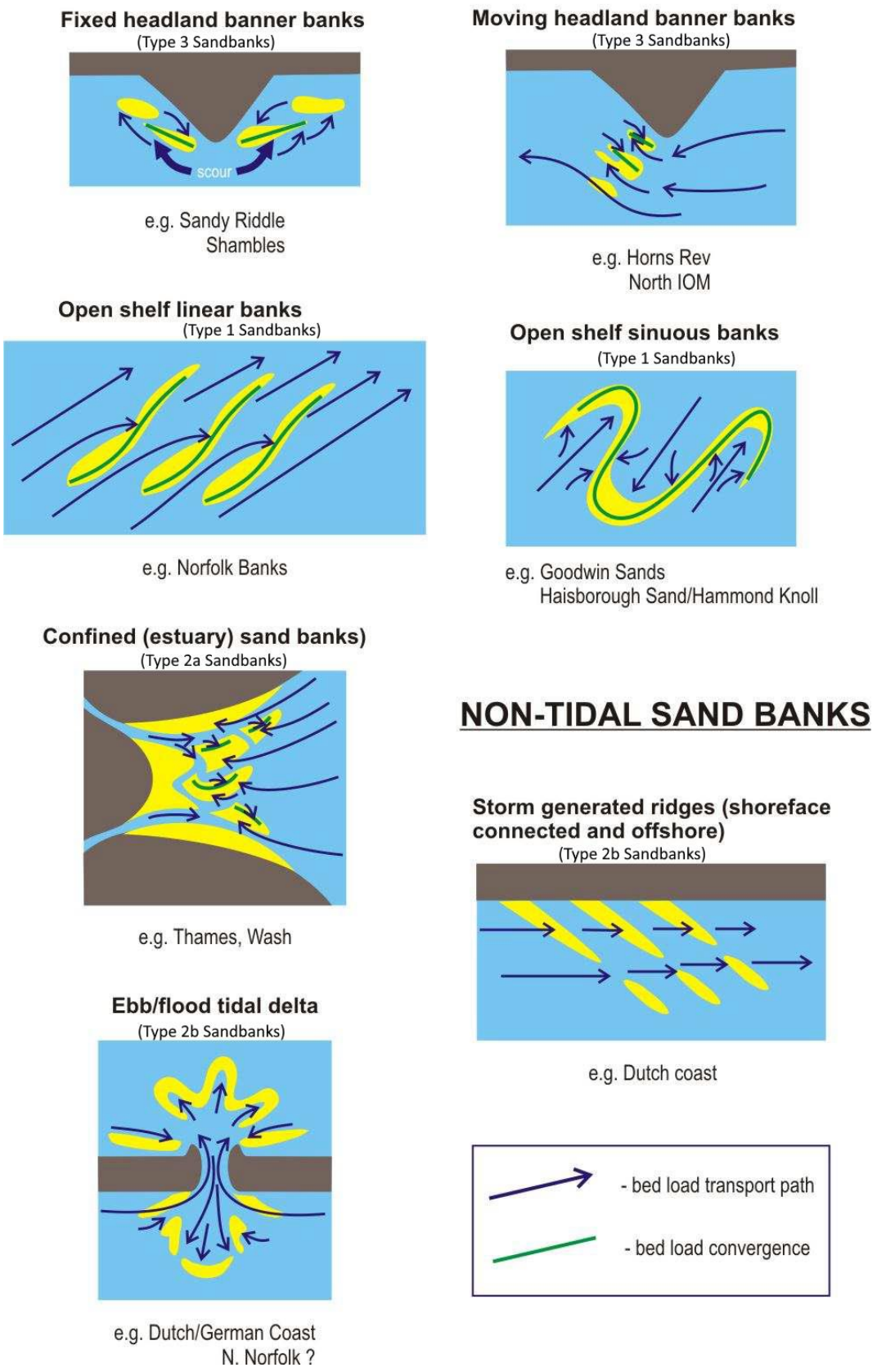


Figure 11. Classification of tidal and non-tidal sandbanks. Image reproduced from Kenyon and Cooper (2005) and including the classification of Dyer and Huntley, (1999).

7 Regimes at the Regional Scale

Our understanding of the hydro–sedimentary processes at the regional scale has been developed first following a review of the available literature and data. The region of interest falls within the Irish Sea, a semi-enclosed body of water bounded by Ireland, southern Scotland, north-west England and Wales. The sea has restricted outlets to the Atlantic Ocean through the North Channel to the north, and via the St. George's Channel to the south. The following describes the hydrodynamic, wave and sediment regimes at the regional scale.

7.1 Hydrodynamic Regime

The oceanic tidal wave propagates into the Irish Sea basin from the Atlantic Ocean through both the North Channel and the St. George's Channel. The tidal regime is characterised by a standing wave, which is a function of the proximity of the amphidromic point and the interaction of the tidal waves propagating into the Irish Sea from the north and the south[7]. The tidal regime in the vicinity of Arklow Bank is complex due to the location of the amphidromic point at Courtown to the south of Arklow. The amphidrome during spring tides is degenerate, being located inland, but at neap tides the position moves into the Irish Sea. This movement is due to proportionally more energy being absorbed from spring than from neap tides (Pugh, 1981). The eastern continental seaboard of southeast Ireland is rather unusual in that it is an area of comparatively fast flows characterised by a small tidal range. The tidal range progressively increases with distance from the amphidromic point, varying from a micro-tidal range in the south of the region to a meso-tidal range to the north of the region; across the Irish Sea ranges of tidal elevation vary from <1 m to up to 9 m (Figure 12). The tidal cycle is semi-diurnal in the Irish Sea and is dominated by the M2 and S2 tidal constituents (Pingree and Griffiths, 1978), with a common period of 12.4 hours. Due to the complexity of the tidal regime the tidal range exhibits significant variations (e.g. during the spring – neap phase through to the lunar nodal cycle [18.6 years]).

7 A standing wave is classically defined by the timing of peak flows coinciding with high and low water rather than mid ebb/flood which is defined as a progressive wave.

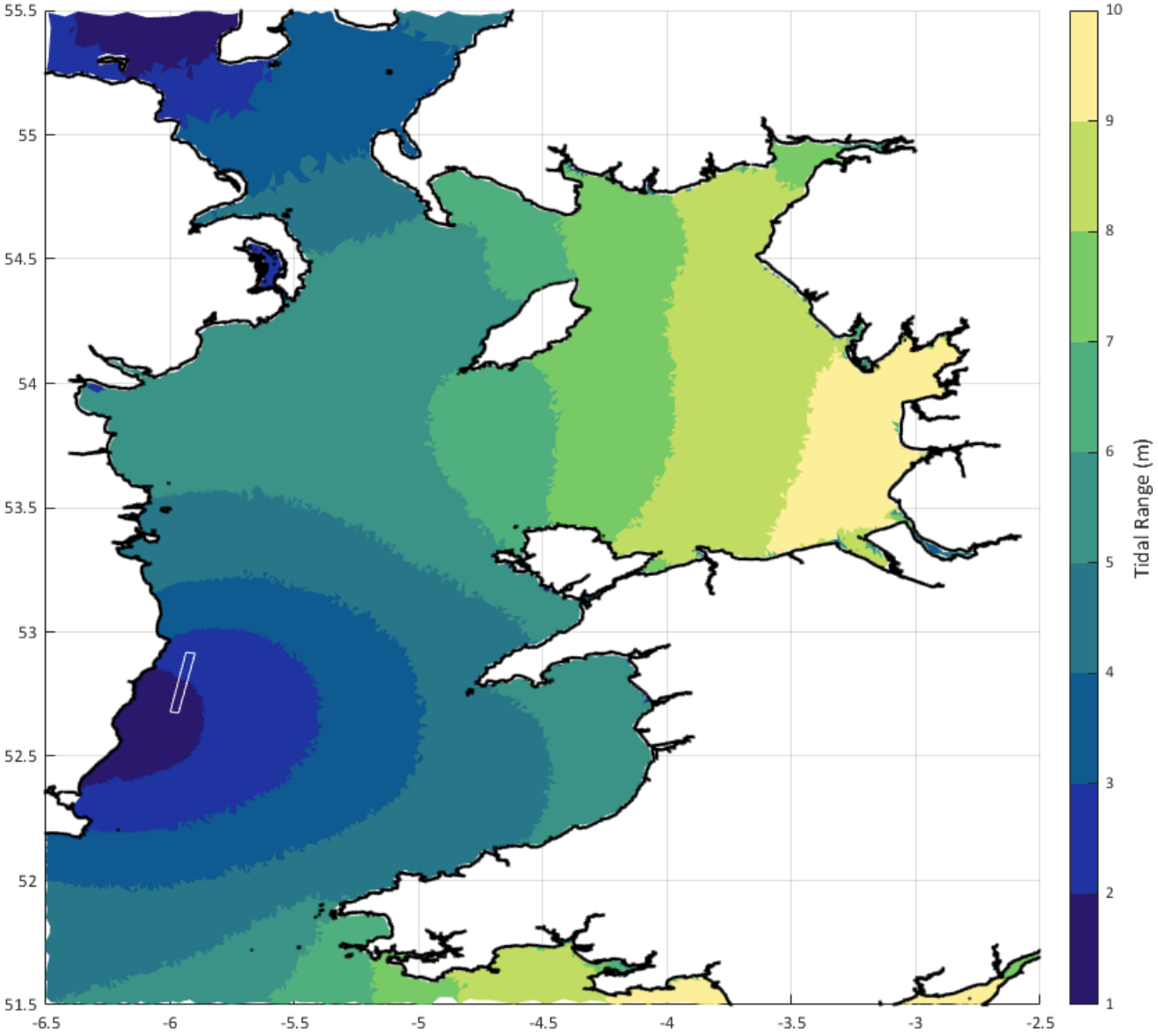


Figure 12. tidal range during a mean spring tide. The location of Arklow Bank within each plot is marked as a bounded area as a white line. Source: ABMS.

Flow velocities vary significantly within the region, though typically depth-averaged flows exceed 1 m/s during the spring tidal phase (Howarth, 2005). Peak flow velocities observed range from 0.5 m/s to > 1.5 m/s, which is a function of the broader tidal regime with local differences in flow velocity observed due to local bathymetry variations (Figure 13).

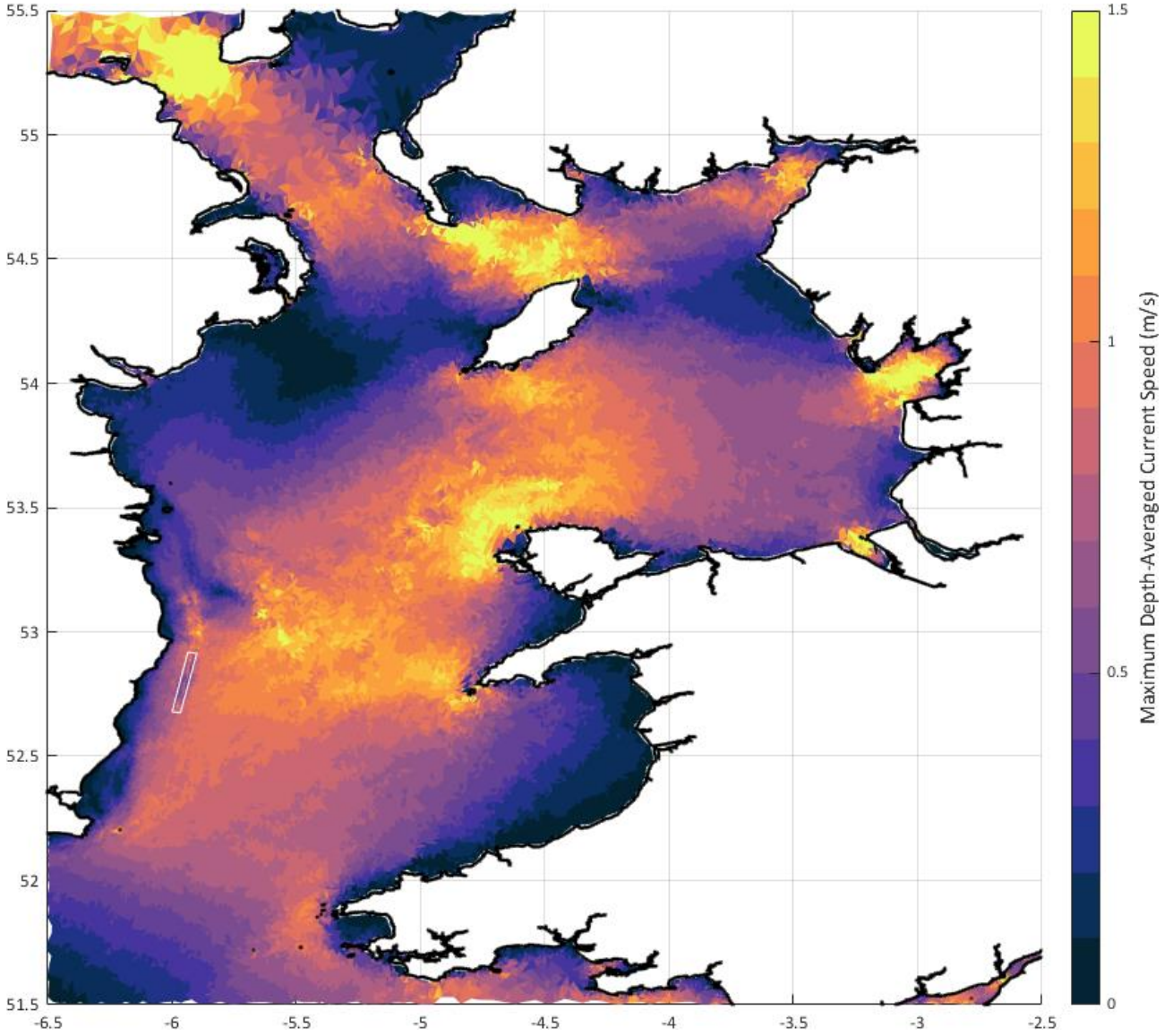


Figure 13. maximum depth-averaged current velocities. The location of Arklow Bank within each plot is marked as a bounded area as a white line. Source: ABMS.

The tidal regime is, on occasion, also affected by surges[8]. The largest positive surges occur in the eastern Irish Sea, with maximum 50-year return period surge levels, predicted to be < 2 m for the Lancashire and Cumbrian coasts and up to 1.25 m on the Irish coast and across the St. George's Channel (Howarth, 2005). Despite the increase in water level from positive surges, surge currents in the Irish Sea are typically weak, predicted to increase (or on some occasions decrease) flow velocity away from the coast by up to 0.4 m/s (Flather, 1987). The complicated non-linear interactions between surge and tide may potentially yield a significant impact on the local sediment transport regime via an increase in local flow velocities and, during negative surges, an increased transmission of wave energy to shallow areas of seabed.

8 Surges are generated by storms, both locally through the action of wind stress on the sea surface and on the scale of the depression, through the action of atmospheric pressure (high pressure depresses the sea surface and low pressure raises it).

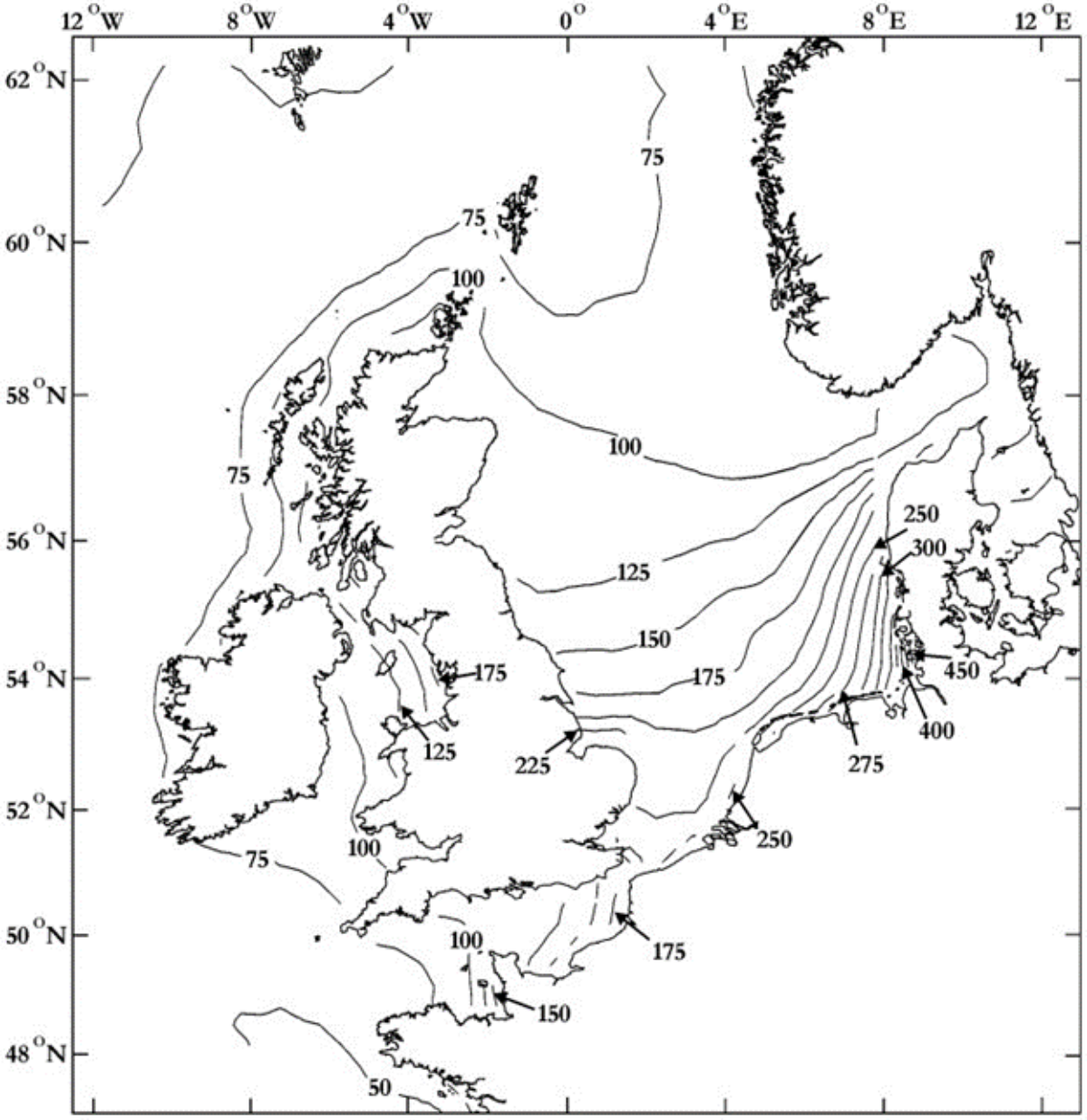


Figure 14. 50-year return period storm surge elevations in cm (figure reproduced from Flather, 1987).

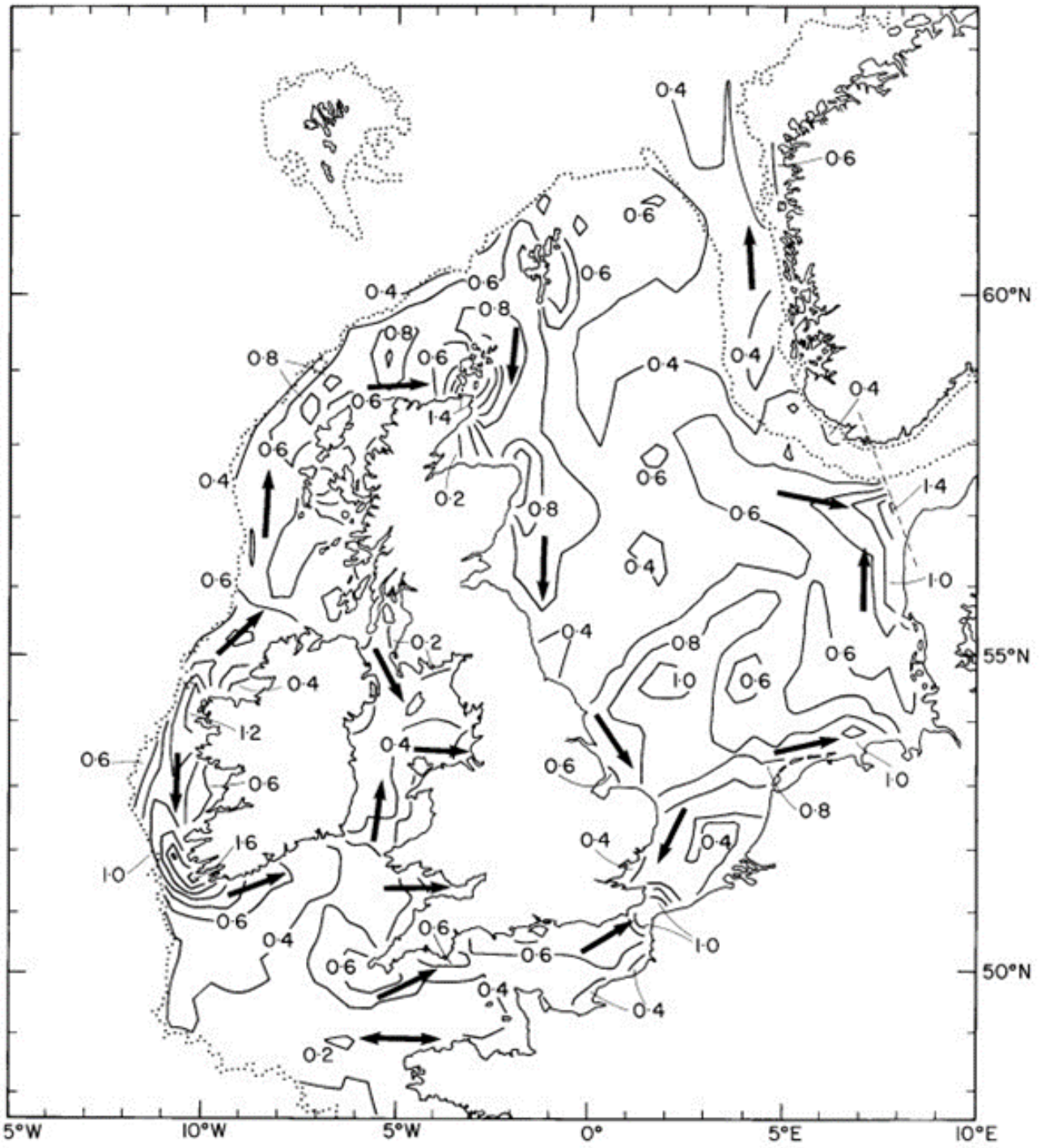


Figure 15. 50-year return period storm surge currents in m/s (figure reproduced from Flather, 1987).

7.2 Wave Regime

Waves result from the transfer of wind energy to create sea states and the propagation of such energy across the water surface by wave motion. The amount of wind energy transfer and wind-wave development is a function of the available fetch distance across which the wind blows; wind speed; wind duration; and the original sea state. The greater the fetch distance, the greater the potential there is for the wind to interact with the water surface and generate waves. Swell waves are a

series of mechanical (sometimes referred to as surface gravity) waves generated by distant weather systems that propagate thousands of miles across oceans and seas. Wind waves are generated by local winds and thus are characterised by lower wave periods. Since wind generated waves originate from meteorological forcing the wave regime is highly episodic and exhibits strong seasonal variability. The Irish Sea is a semi-enclosed body of water, swell propagation is limited and thus, locally generated, wind waves dominate. The magnitude of locally generated wind and swell waves depends on the duration and fetch of the wind. Wave energy propagation into the Irish Sea from Atlantic Storms is generally curtailed by headlands such as Carnsnore Point which acts to shelter the western side of the Irish Sea. Only two relatively narrow 'fetch windows' exist along the axes of the St. George's and North Channel. As such, bigger, swell waves (i.e. T_p > 8 s), which are more powerful drivers of sediment transport at the seabed, are generally observed near the entrances to the Irish Sea, at the southern end of the St. George's Channel (although these longer period waves can propagate as far up the southern Irish Sea basin as the Lleyn Peninsula in North Wales) and to the northern end of the North Channel (Howarth, 2005). As water depths shallow, energy is lost due to bed friction as waves propagate up the southern Irish Sea, this equates to peak wave heights of circa 8 m for a fifty-year return period (Figure 16). As the fetch is limited, generally waves in the Irish Sea are locally wind-generated, and of fairly short period (i.e. T_p < 8 s). Dependent on the associated wave height, waves characterised with periods of 8 s possess only a moderate capacity to influence sediment transport, which is typically limited to water depths less than 30 m (noting that depths across Arklow Bank are typically less than 30 m).

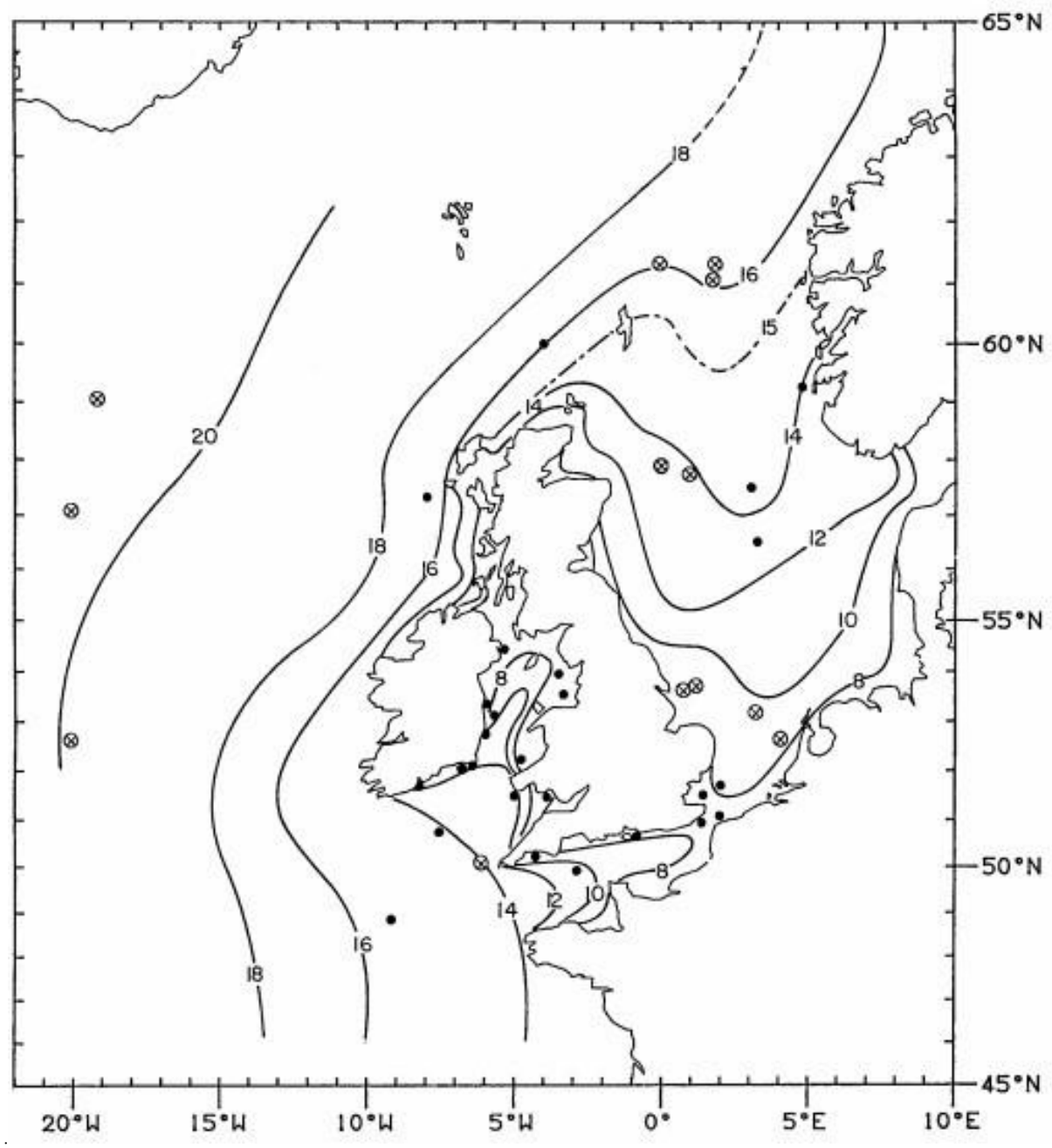


Figure 16. Map of indicative values of 50-year return period significant wave height (m). Figure reproduced from Carter (1993).

7.3 Sediment Regime

Seabed sediment data are available from several projects, including HabMap (Robinson *et al.*, 2008), and the Southwest Irish Sea Survey [SWISS} (Wilson *et al.*, 2001). The surficial sediments of the Irish Sea have also been mapped by British Geological Survey [BGS] (Figure 17), and a seabed mobility index developed by Coughlan *et al.*, (2021).

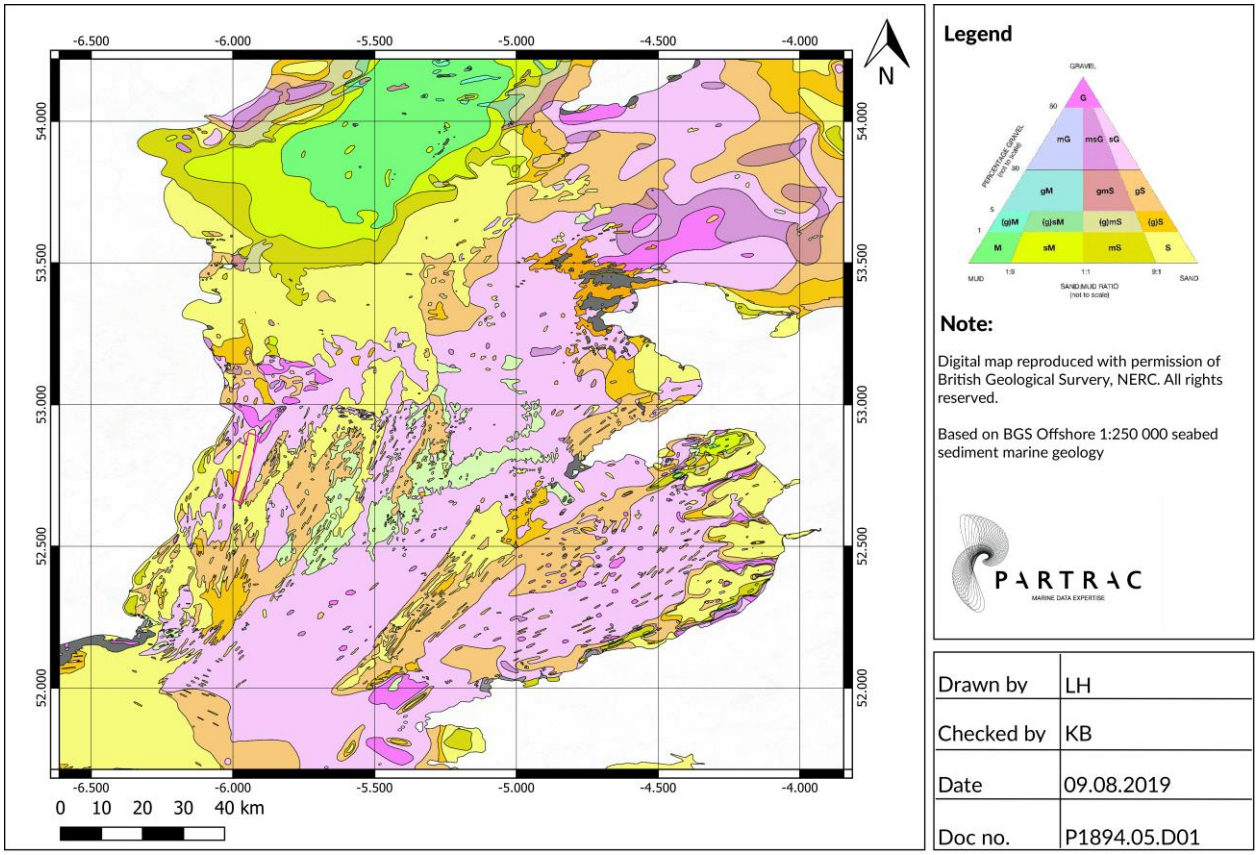


Figure 17. Surficial Sediment Distribution in the Irish Sea at the regional scale. Source: BGS (2019): digital map SBS250. Note for sediment classification, the standard Folk triangle was used, based on the percentage of gravel and the sand: mud ratio.

Across the Irish Sea, the most common sediment type is sandy gravel (Figure 17). Pantin and Evans (1984) hypothesised that these sediments form a gravelly lag deposit which blankets the entire area except in places of exposed (underlying) relict Quaternary sediment or bare rock. Areas of gravel are also found to the north of Anglesey, offshore of St. David's Head, and to the north and west of Arklow Bank. These coarse deposits exist due to continuous reworking of the seabed sediments by tidal flows which acts to winnow away finer sediments. On top of these gravel areas, particularly on the shallower platforms, irregular patches of nominally mobile gravelly sands, sandy gravels and sands are found. These are commonly < 0.3 m in thickness except in areas where they have coalesced into more extensive deposits and formed into bedforms. Finally, a large area of sand containing flow transverse sandwaves is observed; from this area fine material has been winnowed away and transported north into the Western Irish Sea mud-belt which is found within the depositional environments offshore of Dublin/Dublin Bay where flow velocities are reduced. It is noteworthy that much of the surrounding seabed is described or classified as coarse sediment which is considered to be significantly less erodible than the sandy environment forming Arklow Bank.

Tides exert a time varying bed stress on sediments associated with daily tidal and lunar spring – neap variability. Within the Irish Sea, tidal flows interact, and on occasion mobilise, unconsolidated seabed sediments which are then transported as long as the threshold for transportation is maintained (i.e. $\tau_0 > \tau_{0crit}$), and it ceases when the threshold

for transportation is lost (i.e. $\tau_0 > \tau_{0crit}$). Where a flat seabed persists, comprised of (potentially) mobile sediments, and impacted by flows which exceed the threshold of motion, the seabed may deform generating various types of bedforms, ranging in size from small ripples up to major sandbanks (depending on the composition of the seabed and supply of mobile sediment). In the Irish Sea many bedforms are observed (Mellet *et al*, 2015), and generally, areas of the seabed not comprised of gravel lag deposits, can be considered highly dynamic in terms of sediment transport. The various types of bedforms which exist, their typical migration speeds and the broader seabed morphology are indicative of complex interactions between tidal flows, seabed sediments and seabed features across the region (McCarron *et al*., 2019, Van Landeghem *et al* 2009, 2012).

It is important to understand sediment transport pathways at the regional scale to characterise the rate and magnitude of sediment supply to the development site. The regional sediment transport regime is broadly controlled by the area of divergence in the sediment transport pathway at the so-called St George's Channel BPZ to the north of the bank which extends eastwards across the Irish Sea between approximately south of Dublin on the eastern Irish Coast and Anglesey in North Wales. Divergent zones are found at several locations around the British and Irish coast, where complex tidal interactions give rise to an area of enhanced bed shear stress (see Harris *et al*., 1995). In terms of judging regional sediment transport pathways, consideration must be given to the presence of the BPZ. Typically, BPZ's are regions of the seabed, discernible through both their sediment, and hydrodynamic, features but which are often quite heterogeneous in character. Due to the enhanced shear stress, through time, localised scouring occurs, and opposing sediment transport directions are observed either side of the scour feature which is a function of both seabed topography and tidal asymmetry (i.e. a flood and ebb dominance exists either side of the feature). Predominant regional sediment transport pathways and the approximate location of these BPZ's are reported by several authors (e.g. Holmes and Tappin (2005), Kenyon and Cooper (2005); Van Landeghem *et al*. (2012, 2009) and presented in Figure 18.

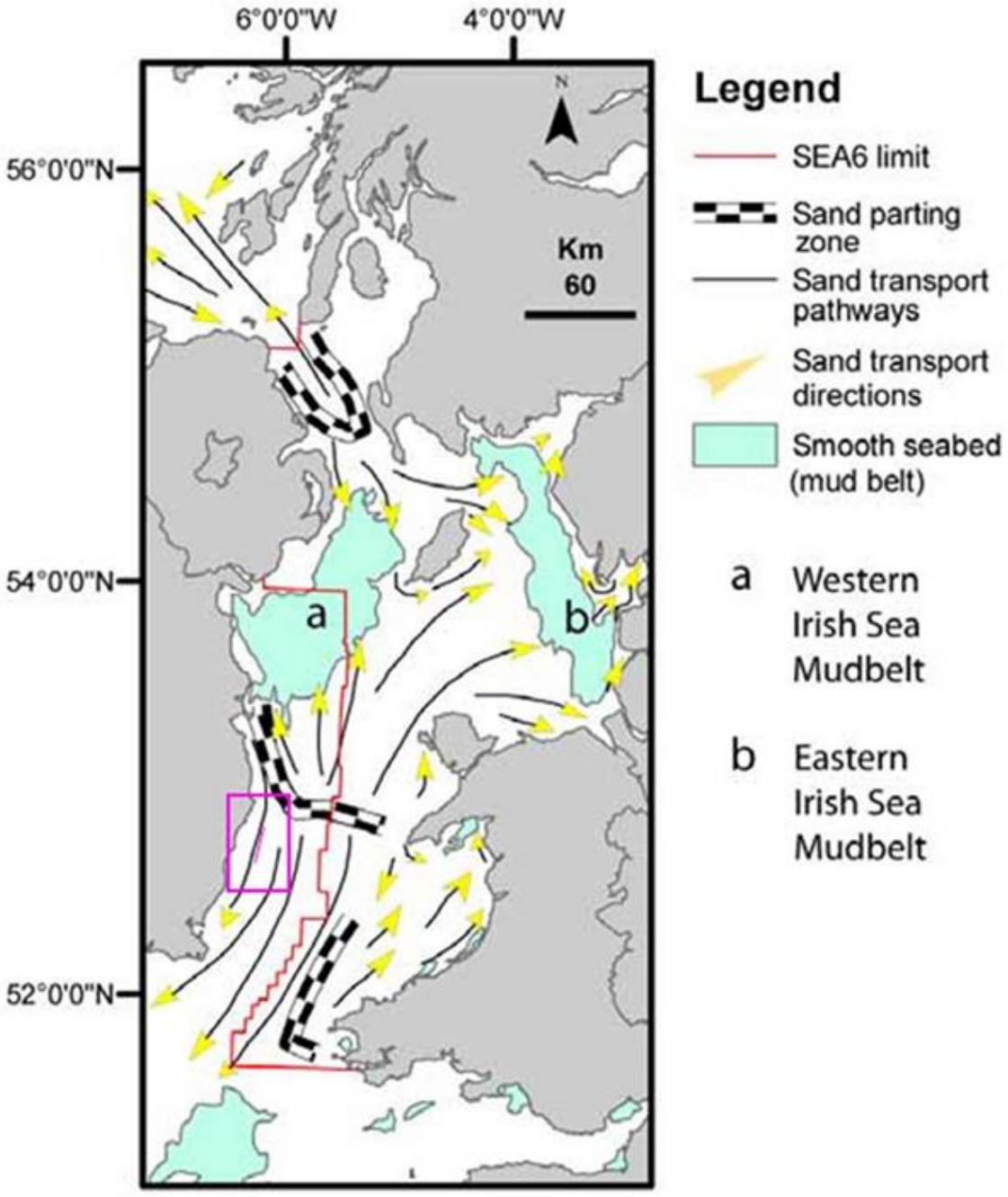


Figure 18. Regional sediment transport directions and bedload parting zones. The Arklow regional scale is indicated by the bounded area coloured magenta. The BPZ is adapted from Holmes and Tappin, (2005). Image reproduced from Mellet et al. (2015).

The BPZ to the north of Arklow Bank was first reported by Stride (1963), however, the exact location of the BPZ remains an area of contention with several authors proposing slightly different locations (e.g. Holmes and Tappin (2005); Kenyon and Cooper (2005); Van Landeghem *et al.* (2009)), depending on the data used to inform their interpretation. The latest interpretation in Van Landeghem *et al.* (2009, 2012) employed both detailed numerical modelling and high resolution MBES data. Regardless, the BPZ to the north is coincident with dominantly sandy gravel sediments (Figure 17), with sediments transported northwards from the BPZ towards the Western Irish Sea mud belt and southwards towards Arklow Bank (Holmes and Tappin, 2005; Mellett *et al.*, 2015; Van Landeghem *et*

al., 2009 & 2012). The sediment transport pathways in the region of Arklow Bank were considered in greater detail by Van Landeghem *et al*., (2009 & 2012) who confirmed a net southward transport of sand sized sediments and defined areas of convergence which persist within the area (Figure 19). Southwards transport from the BPZ through Wicklow Trough is hypothesised to be the primary pathway from the BPZ towards Arklow Bank.

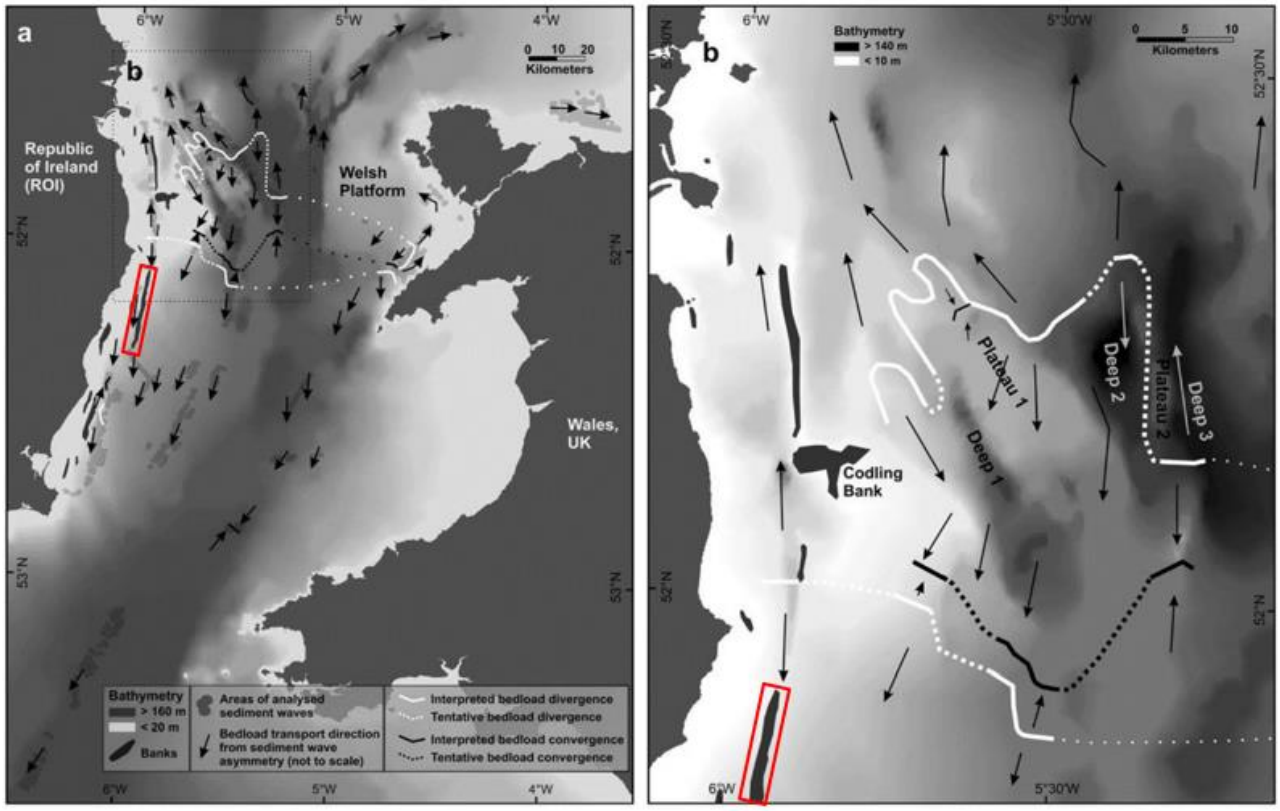


Figure 19. The regional bedload transport pathways (left) and a zoomed in image of the bedload parting zone to the north of Arklow Bank. Image reproduced from Van Landeghem et al. (2009). (Arklow Bank is bounded in red area).

Across the region, bedforms show a high degree of variability in regard to their size, shape, and groupings on the seabed. The rate of migration of these bedforms (which usefully can be considered a proxy rate of bedload sand supply to the region local to Arklow Bank) is complex to determine over extended spatial scales, being a function of the local flow regime, water depth and seabed sediment characteristics. Van Landeghem *et al*., (2012) reports rates of up to 30 m per year (note; the maximum rate of migration was observed in the enclosed area in the vicinity of Codling Deep to the west of India Bank and on the shallow seabed to the west of Arklow Bank), with a mean rate of migration of circa 6 m per year occurring across the region (Mellett *et al*., 2015). This suggests that post glacial features such as the narrow basin and the fault between Codling Deep and Wicklow Trough (the southern extent which aligns with Arklow Bank), act to enhance flow velocity and thus enhance the rate of sediment transport. Interestingly, it was revealed migration rates were relatively consistent, suggesting bedforms, on a regional scale, migrate broadly in one direction and at a fairly constant rate, however, inspection of the migration pathways of individual or grouped bedforms at the regional scale reveals some irregular patterns with either a higher rate of migration observed or a

reversal in the direction of migration. A summary of the migration rates of macro bedform features is presented in Figure 20.

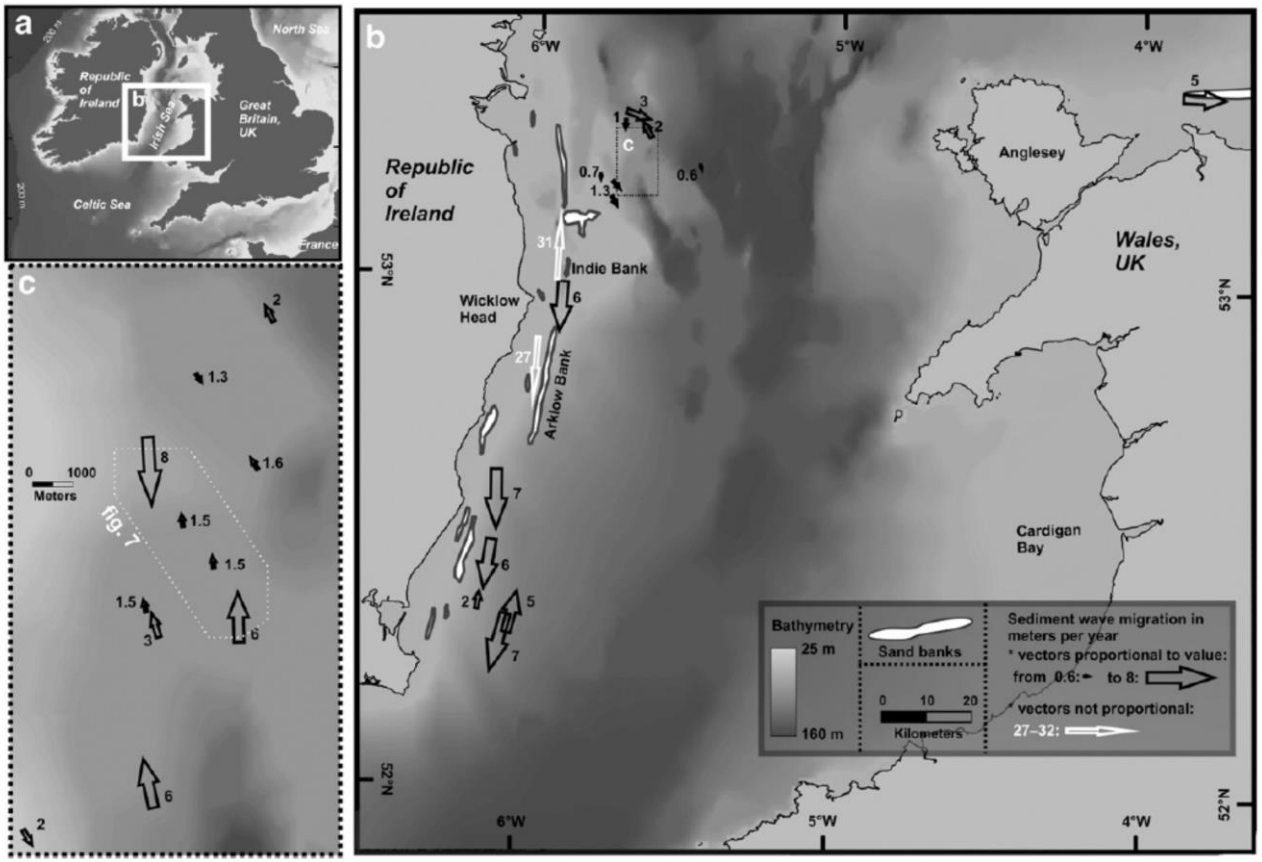


Figure 20. Average net sandwave migration rates per year from repeated MBES data. Image reproduced from Van Landeghem et al., (2012).

7.3.1 Sediment Supply from the Coast

Prior to 2005, when hard defence structures were constructed in Arklow, the coastline was in a phase of retreat (ARUP, 2018). Analysis of historic and contemporary survey data conducted by Byrne Looby Consulting Engineers in 2017. Indicated a continued and persistent, but low magnitude, loss of material from the beach face and nearshore region in front of the coastal defence infrastructure. These data, considered in the context of the origin and maintenance hypotheses for linear sandbanks suggested by Dyer and Huntley (1999), would indicate that the contemporary supply of sediment from the coastline across the development area, and toward Arklow Bank, is broadly limited.

To bolster the evidence pool regarding contemporary sediment sources to the bank, targeted particle tracking simulations were performed. To do this, the MIKE21 particle tracking module was coupled with the validated hydrodynamic model to perform simulations. Undertaking these simulations enabled estimation of the transport trajectory (transport pathways) and residence time of coarse-grained particles (sand and gravel) using a Lagrangian

approach[9]. These particles are created within the model at the discharge location(s) and assigned[10] basic forms of behaviour such as grain size, settling velocities and critical erosion thresholds. Simulations were run over the lunar cycle with releases timed at peak ebb, and peak flood, during the spring tidal phase. Two release locations were simulated, including:

1. Offshore of Brittas Bay, a stretch of beach between Arklow and Wicklow Head, backed by dunes and with limited coastal protection measures. This location was chosen to assess connectivity between Arklow Bank and the coastline south of Wicklow Head.
2. The mouth of the Avoca River[11] to assess connectivity between fluvial sediment sources and Arklow Bank.

The particle tracks from these two release locations are presented in Figure 21. Interestingly, particles released offshore of Brittas Bay appear to reach, and remain, on Arklow Bank, suggesting some partial retention of sediments within the bank system. Though the simulation does indicate potential connectivity between the bank and the coast to the north of Arklow, it is not possible to discern from these simulations how active this source might be as a contemporary supply for the bank. Considering the other available evidence, it is postulated that the supply from the coastline, though likely a source of sediment to the area, is generally limited in terms of direct supply to the bank. That the particles, regardless of release times, moved southwards, is consistent with the BPZ located to the north of the bank.

7.3.2 Sediment Supply from Rivers

Previous investigations described by Arup Ltd (2018), concluded that the flow from the Avoca River is typically low and thus it is unlikely that the buoyant freshwater plume has sufficient momentum to drive sediments offshore. This is supported by the grain size data available from the bank which does not show any fine sediment content, similar to that anticipated to be discharged from a fluvial source. The outputs of the particle tracking simulations presented in Figure 21, provide corroborating evidence that there is limited connectivity between sand sized sediments released at the mouth of the Avoca River and Arklow bank.

9 Particle tracking models are limited in that they do not account for bedload transport processes, consolidation at the seabed and the physics controlling the formation, and migration, of mobile bedforms. Despite particles being assigned coarse grain sizes (based on the quantitative evidence from borehole locations across the bank), the model simply suspends those materials at which point the critical erosion threshold is exceeded and deposits these particles at which point the shear stress acting on the seabed reduces below the critical erosion threshold. As such, excursion distances are often enhanced when compared to reality and outputs must be considered within the context of the limitations of the approach. Note also these simulations remain unvalidated against real-word data.

10 Grain size was ascribed based on available data at the bank, and professional judgement. The settling velocities and critical erosion thresholds were determined empirically using coefficients presented by Soulsby, 1997.

11 Releases were made from the mouth of the Avoca River however flow conditions within the model do not include for freshwater discharges.

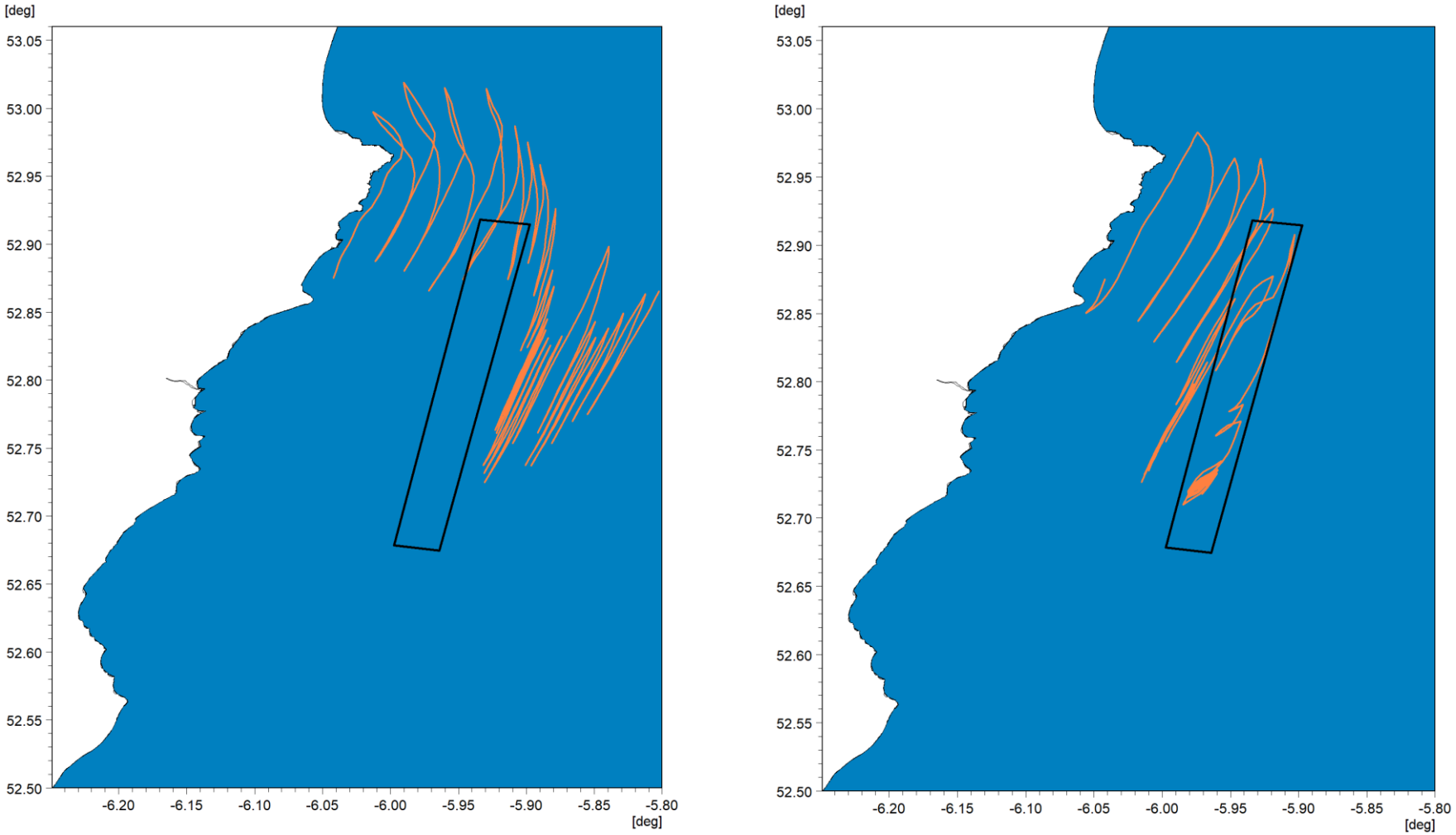


Figure 21. Spatial plots showing the tracks from particles, released on peak flood (left and peak ebb (right) from a location next to the mouth of the Avoca River and at the coast, south of Wicklow Head. Note: the particles released at the mouth of the Avoca River did not move in the 30-day simulation.

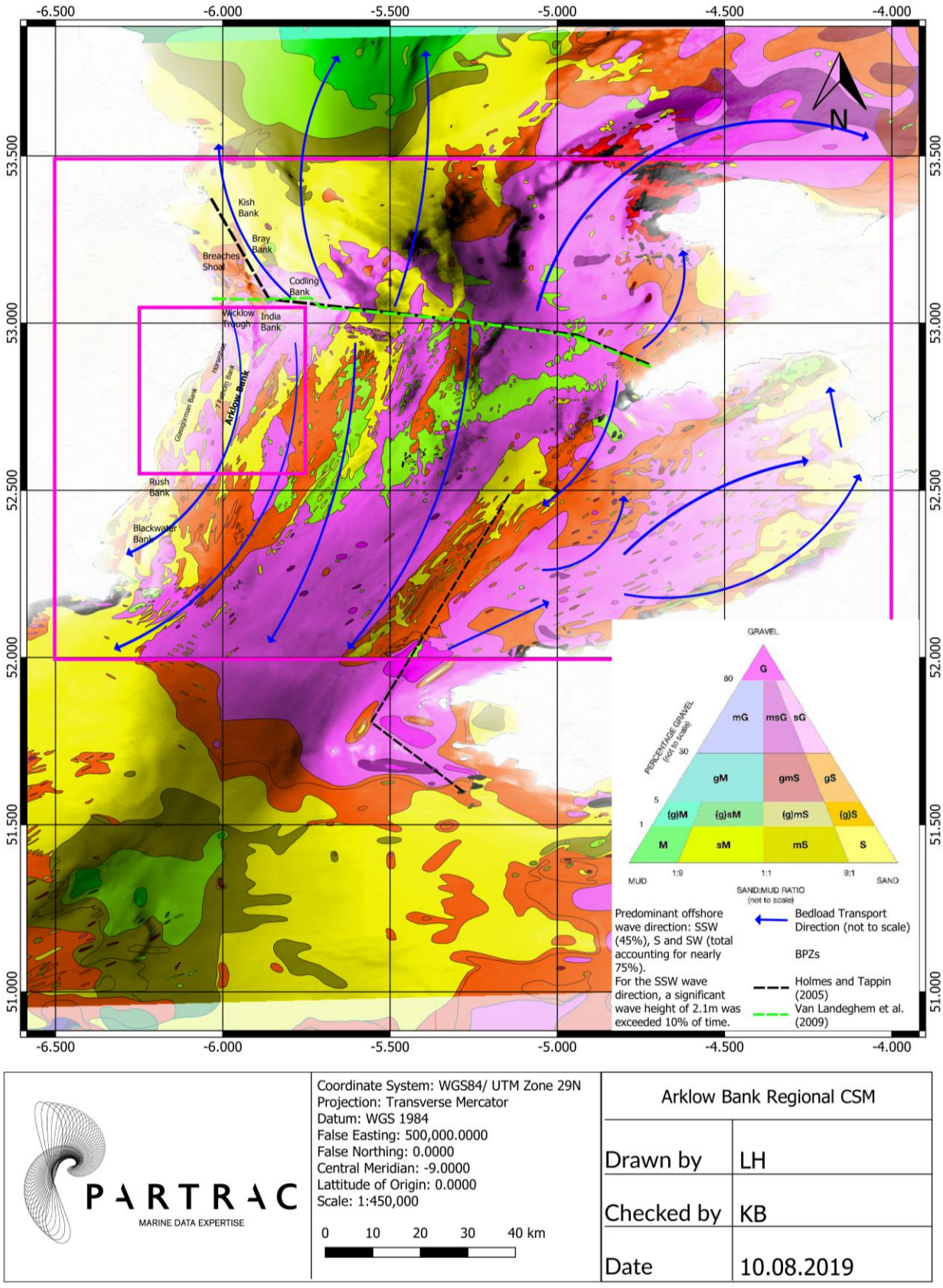
7.4 Conceptual Understanding of Prevailing Regimes at the Regional Scale

From the review of relevant literature, a regional scale Conceptual Site Model (CSM) has been developed; this has been visualised in Figure 22. The pertinent points regarding the hydrodynamic, wave and sediment regimes of the region are as follows:

- Arklow Bank formed across glacial moraine and thus the base of the bank comprises glacial sediments (compacted till, coarse gravels etc). This base of less mobile sediments acts to maintain the relative position of the sandbank, but the highly mobile veneer of sand which overlies these sediments (and is maintained in dynamic equilibrium with the local, and regional, hydrodynamic, wave and sediment regimes), indicates potential for significant vertical bed level change associated with mobile bedforms (e.g. sandwaves and megaripples) and changes to the form and profile of the bank itself.
- The tidal regime in the vicinity of Arklow Bank is complex due to the occasionally degenerate amphidromic point at Courtown to the south of Arklow and the interaction of the two tidal waves, propagating from the North Channel and St Georges' Channel. This leads to a tidal range which progressively increases in a northward direction, varying from a micro-tidal range in the south to a meso-tidal range to the north of the region.
- Peak flow velocities which range from 0.5 m/s to > 2.0 m/s are sufficient to mobilise unconsolidated sediments.
- Overall, the distribution patterns of coarser sediments reflect the variation in flow velocities with deposits of coarser sediments observed in areas of higher flow velocities.
- Generally, waves are locally wind-generated and of fairly short period (T_p < 8 s). Waves with periods up to 8 s possess only a moderate capacity to influence the local sediment transport regime; their influence is depth limited (i.e. typically to water depths < 30 m). It is noteworthy, that, on occasion, particularly at the coast, such low period waves are constructive rather than destructive.
- The predominant sediment transport pathways observed within the region and the (approximate) area of the BPZ in the central Irish Sea has been defined from the literature (i.e. the location of the BPZ is based upon the findings of Van Landeghem *et al.*, 2009 & 2012). Despite some contention in the exact location of the BPZ, there is no contention regarding the dominant transport pathway from the BPZ with net transport southwards observed (broadly in the direction of Arklow Bank).
- Migration rates of sandwaves within Wicklow Trough positioned to the north of Arklow Bank indicate the trough enhances local flow velocities and thus increases sediment transport. It is postulated that the funnelling effect of the trough provides an important pathway for sediment transported south from the BPZ towards Arklow Bank.
- Though sediment supply from the BPZ (and potentially from erosion of the coastline), through Wicklow

Trough nourishes Arklow Bank, it is anticipated that supply is limited and thus it has been concluded Arklow Bank does not appear to have a significant contemporary supply of sediment nourishing the bank. Sediment supply to Arklow Bank is controlled by the bedload parting zone (to the north of the bank) in the central Irish Sea (first described by Stride *et al* 1982 and further described by Van Landeghem *et al*., 2009 & 2012) which is characterised by net transport southwards (broadly in the direction of Arklow Bank). Limited contributions are predicted to occur from alternative sources (e.g. the southern Irish Sea, the local coastline, or local fluvial sources). Thus, Arklow Bank can be considered *a semi-closed sediment cell*.

The knowledge garnered from the assessment of the sedimentological, hydrodynamic and wave regimes at the regional scale was applied to both the assessment of local scale processes and to the setup of the coupled hydrodynamic / wave / sediment transport model.



PARTRAC
MARINE DATA EXPERTISE

Coordinate System: WGS84/ UTM Zone 29N
Projection: Transverse Mercator
Datum: WGS 1984
False Easting: 500,000.0000
False Northing: 0.0000
Central Meridian: -9.0000
Lattitude of Origin: 0.0000
Scale: 1:450,000

0 10 20 30 40 km

Arklow Bank Regional CSM	
Drawn by	LH
Checked by	KB
Date	10.08.2019

Figure 22. Visualisation of the conceptual understanding of processes occurring at the regional scale.

8 Prevailing Regimes at the Local Scale

Moving from a broader view of the prevailing regimes at the regional scale the following chapter describes the more detailed local view of the development area. The following sections describe the analyses performed to understand, and conceptualise, the prevailing hydrodynamic, wave and sediment regimes occurring across the ABWP lease area and export cable routes.

8.1 Anatomy of Arklow Bank

To provide a framework, within which the following analysis of the prevailing regimes at the local scale, can be considered and interpreted, the anatomy of Arklow Bank is presented below. Arklow Bank exists as a dynamic equilibrium. The Bank can be split into five main process environments, which amplify different influences on morphology and collectively form the overall bank processes. The five process environments are summarised below:

Head of bank: this process environment is linked to Wicklow Trough with enhanced flows and possible sediment supply from a bedload parting zone to the north of bank. In this area of the bank there is sediment exchange between east and west flanks but due to the deeper water, the influence of head difference is almost negligible. The relative position of the head of the bank is linked with Wicklow Trough.

Tail of bank: an unconstrained area "tailing off" into deeper water. The tail of the bank is open to greatest wave influence from prevailing southerly waves. Again, sediment exchange occurs between the east and west flanks though due to the water depths the influence of head difference is almost negligible.

East flank: this process environment is ebb dominant with the seabed characterised by significant sand wave features displaying net migration southwards. Due to the water depth wave influence is limited. Cross bank flows driven by a tidal head difference drive repositioning of the crestline through time with weiring effects enhancing transport in the shallowest regions of the bank. Transport of sediment from the flanks to the crest via ripple and megaripple migration and enhanced by Coriolis acts to maintain the crestline. The east flank is potentially more wave exposed than the west flank due to the angle of wave approach.

West flank: this process environment is flood dominant with the seabed characterised by significant sand wave features displaying net migration northwards. Due to the water depth wave influence is limited. Cross bank flows driven by a tidal head difference drive repositioning of the crestline through time with weiring effects enhancing transport in the shallowest regions of the bank. Transport of sediment from the flanks to the crest via ripple and megaripple migration and enhanced by Coriolis acts to maintain the crestline. The west flank is potentially less exposed to wave action due to the angle of wave approach.

Crest of bank: the bank crest (i.e. water level of < -10 mLAT) is prone to sediment transfer between the east and west flank driven by a tidal head difference and Coriolis pathways. Due to the shallow water depths wave influence is significant, particularly to the south and southeast. Wave action smooths the crest free of bedforms and enhances sediment transport.

Figure 23 delimits the process environments summarised above.

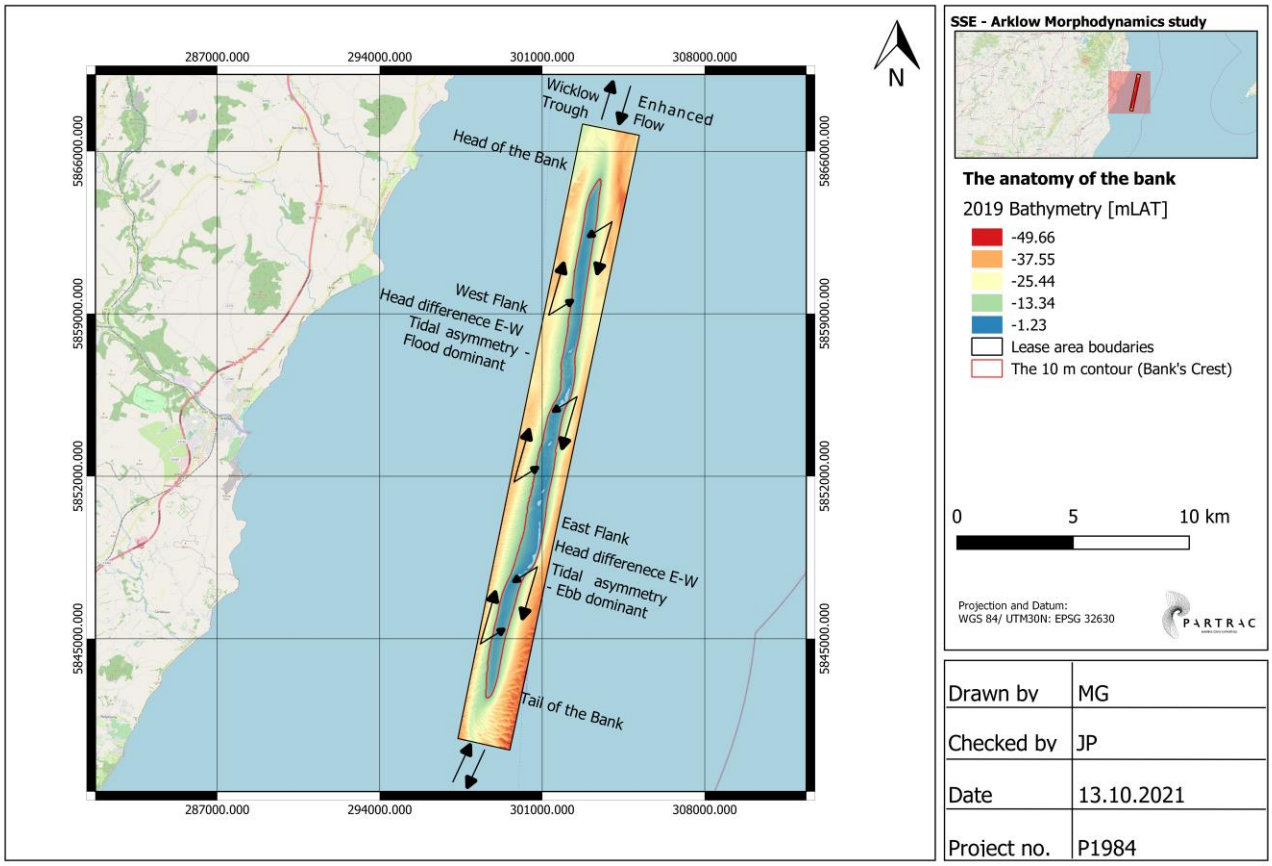


Figure 23. A schematic diagram showing the anatomy of the bank and delimiting the five primary process environments across Arklow Bank.

8.2 Seven Fathom Bank

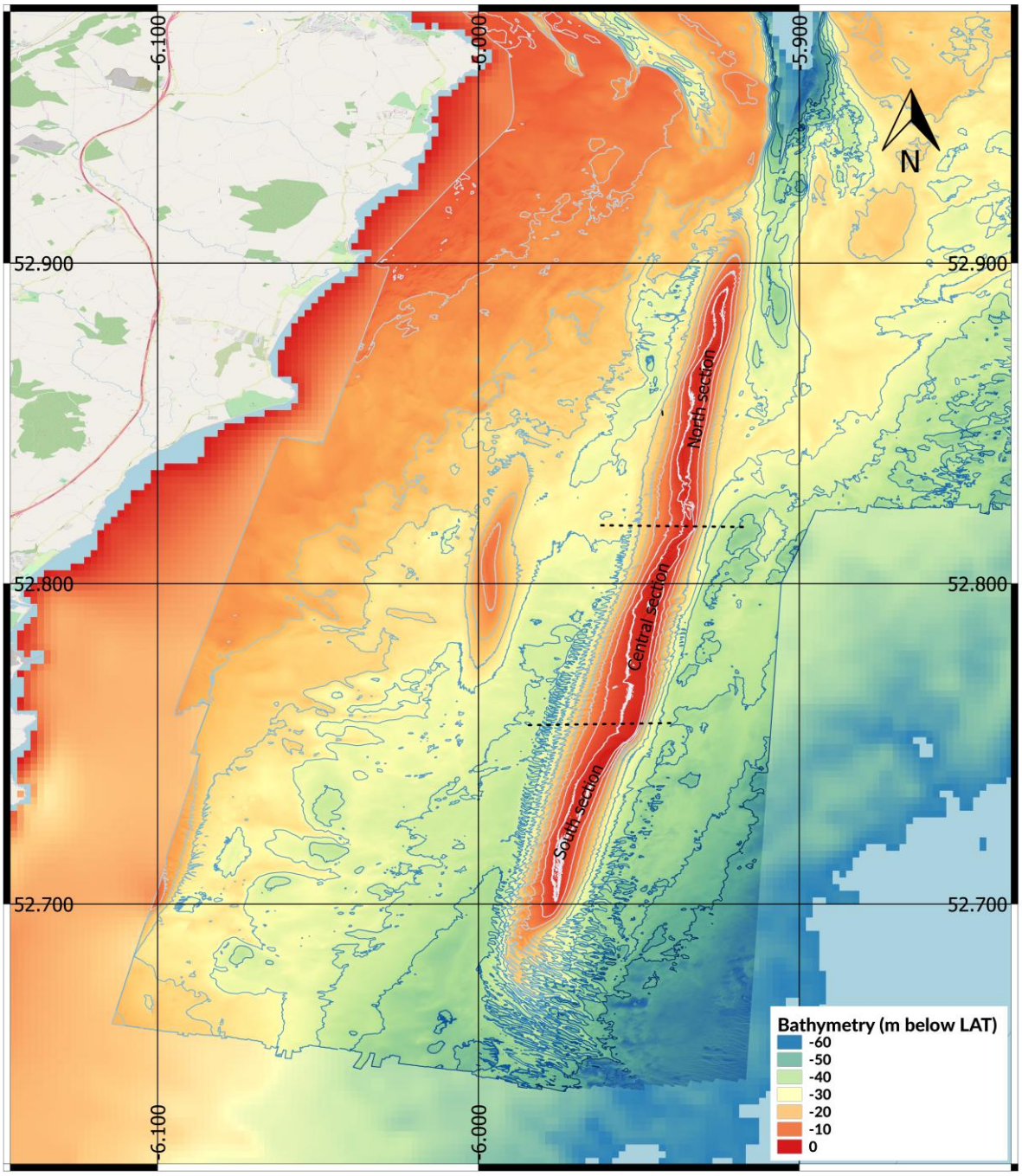
Seven Fathom Bank forms a satellite bank to Arklow Bank which is located approximately 1.5 km to the west of Arklow bank. Seven Fathom Bank has a similar orientation to that of Arklow Bank but is smaller being circa 5.5 km in length along the north – south axis. In comparison with Arklow Bank, Seven Fathom bank has received limited scientific attention. However, it is reasonable to postulate that due to its relative location, shape, profile and orientation, analogous processes to that which occur across Arklow Bank, occur across Seven Fathom Bank. However, several key differences are evident between Arklow Bank and Seven Fathom Bank which reduce the magnitude of sediment transport on Seven Fathom Bank, these include:

- Across Seven Fathom Bank water depths shallow gradually reducing to circa -15 mLAT in the centre of the bank. Within the boundaries of the survey the bathymetric data shows seabed levels range from *circa* -50 mLAT shallowing to a minimum water depth of *circa* -1 mLAT along the ridge feature which traverses the bank and forms the bank crest (Figure 24). Thus, Seven Fathom Bank is significantly deeper than Arklow Bank across the bank crest.
- Due to the depth of the crestline, cross bank flows, though do exist, do not develop in the same manner as Arklow Bank.
- Due to sheltering effects from Arklow Bank, waves likely have only a limited role in the sediment transport regime.
- Limited data is available to support the assessment of sandwave features which exist, on or close to, Seven Fathom bank but it is postulated that sandwaves are less prominent than observed on Arklow Bank.

8.3 Local Bathymetry and Slope

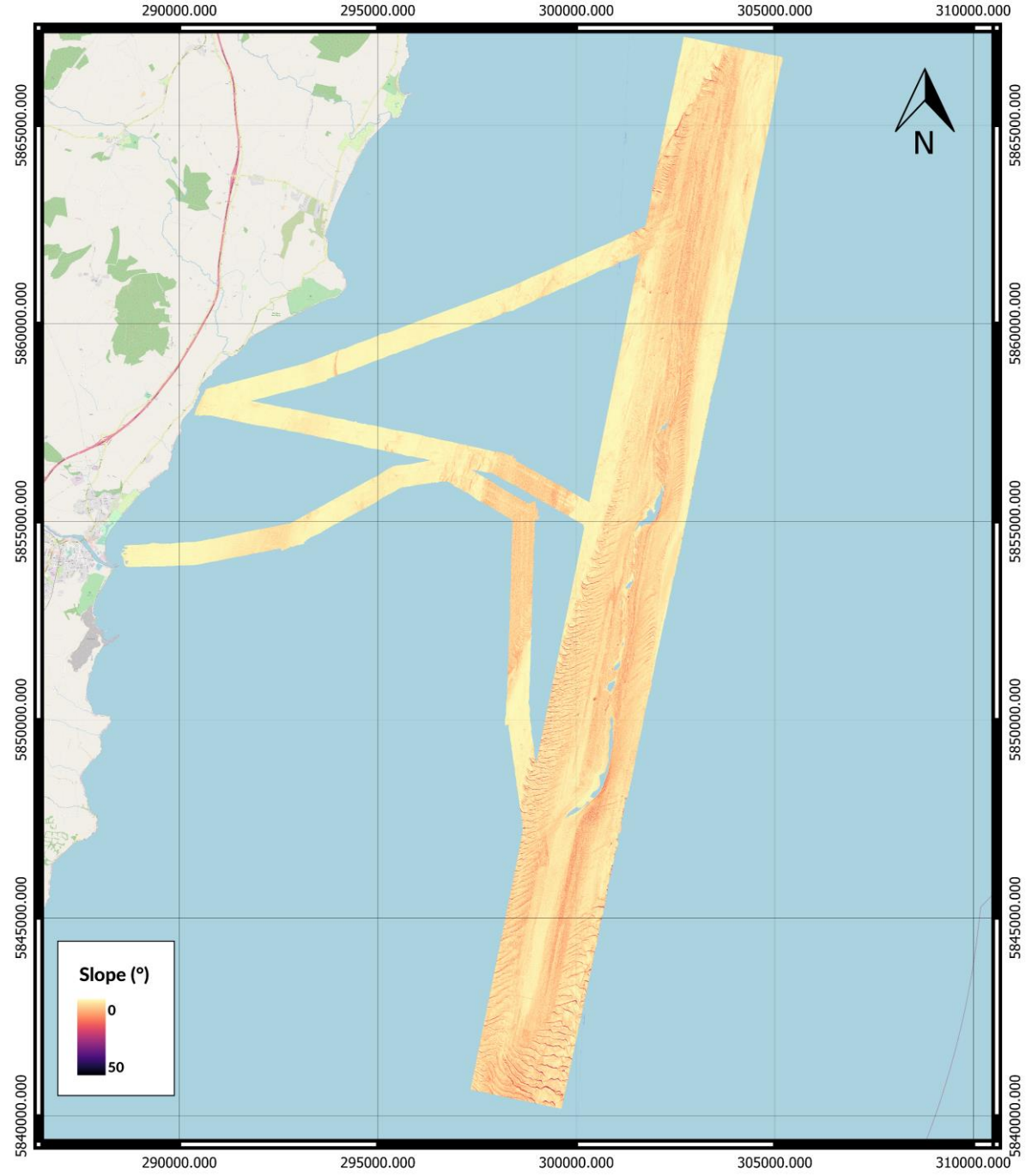
Figure 24 shows the local bathymetry derived from INFOMAR (2016) and EMODnet datasets. Arklow Bank is located approximately 6.5 km from the east coast of Ireland. From the coast the bathymetry shows a shallow gradient to around 18 km offshore, after which the gradient of the seabed steepens to a depth of circa 38 m. Significant sandwaves are evident along the flanks of the bank, and at the northern head and southern tail, with a highly active and expansive sandwave field observed at the southern end of the bank.

Figure 25 presents slope across the lease area, derived using the project GIS from the 2019 bathymetric dataset (Alpha Marine, 2019). The stability of cohesionless grains on a slope is related to the angle of repose (φ). The top layer of grains on a slope is stable if the top surface has a slope less than the angle of maximum stability (φ_{max}). When the slope angle is > φ_{max}, the grains begin to move, and an *avalanche* of grains occurs (referred to as slope failure). Typical values for φ , for cohesionless grains are 30^0 (+/- 3^0) and 35^0 (+/- 3^0) for sands and gravels, respectively (van Rijn, 2018; Barabasi *et al*. 1999). Slopes exceeding 30^0 within the lease area are rare (i.e. occurring in areas covering 0.02% and 0.04% of the cable route and bank, respectively), with the greatest slope angles occurring in deeper waters (i.e. below -20 mLAT). It should be noted here that the snapshot provided by MBES data shows slopes post-failure, and slope induced transport, where gravity favours downslope transport is considered likely to occur variously across the lease area, across space and through time.



PARTRAC MARINE DATA EXPERTISE	Coordinate System: WGS84/ EPSG:4326 Source: INFOMAR Bathymetry (2011, 2016) EMODnet (unknown time) Scale: 1:50,000 0	Arklow Bank Area Bathymetry Data
		Drawn by: LH
		Checked by: KB
		Date: 20.06.2019

Figure 24. Bathymetric plot of Arklow Bank. The dashed line shows the distinction between the north, central and south sections of the bank. Data sources: INFOMAR (2016) and EMODNET.



PARTRAC MARINE DATA EXPERTISE	Sources: SSE Bathymetry 0.25m resolution (2019) Coordinate System: WGS84/ UTM Zone 30N Projection: Transverse Mercator Horizontal Datum: WGS 1984 Vertical Datum: LAT Scale: 1:90,000 0 1 2 3 4 5 km	Arklow Bank Seabed Slope (2019) Drawn by: LH Checked by: KB Date: 20.07.2020

Figure 25. Slope derived from the 2019 bathymetric dataset.

8.4 Hydrodynamic Regime

The hydrodynamic regime is defined here as the behaviour of bulk water movements driven by the action of tides and non-tidal influences (e.g. meteorological conditions; winds, atmospheric events and storm surges). The following analyses focuses on depth averaged currents; flow through the water column is discussed in Appendix E.

The mean tidal range during the spring and neap phases at Arklow Harbour are 0.8 m and 0.3 m, respectively, which classify Arklow Harbour as having a micro-tidal range[12] (Table 4). Thus, in the region local to Arklow Harbour (e.g. along the export cable route towards the nearshore, at proposed cable landfall or HDD pop out locations), water levels do not vary greatly through the tidal cycle. A phenomenon termed 'double high water' is observed in Arklow Harbour which influences the tidal flow regime and tidal phase dominance. This phenomenon is characterised with a "young flood stand" during the ebb tidal phase where the shortened duration of the ebb tide generates a sudden change in forcing, resulting in a greater flow velocity which occurs transiently. Due to this phasing, the nearshore region (i.e. the shallow water area between Arklow Bank and the coastline) is flood-dominant due to the shortened duration of the ebb tidal phase.

As there is not a significant difference in the tidal range in an E-W direction, the offshore tidal range (near Arklow Bank) is thought to broadly reflect that of Arklow Harbour. However, due to the length of the bank differences persist along the N – S axis, due to the location of the amphidromic point to the south of the bank at Courtown. These differences in the phase of the tidal constituents, water levels and the timing of high water is observed across the length of Arklow Bank (e.g. water levels increase towards the north within the lease area). Despite the limited tidal range, the observed peak and mean tidal flow velocities across the development site are relatively high. This was first confirmed by historic field measurements conducted at two locations to the east of the bank and at the head and tail of the bank, over a lunar cycle between August and September 1999. The data obtained revealed that the general direction of flow offshore from Arklow Bank is toward the NNE during a flooding tide and toward the SSW during an ebbing tide (Panigrahi *et al.*, 2009). At both measurement locations, the observed peak flow velocities ranged between 1.0 – 1.5 m/s through the neap-spring tidal cycle.

Table 4. Key Statistics related to water levels in Arklow Harbour (Source: Admiralty Tide Figure, 2001-2018).

Tidal Phase	Water Level relevant to Chart Datum (m)	Tidal Range (m)
Mean High Water Springs (MHWS)	1.4	Mean Spring: 0.8
Mean Low Water Springs (MLWS)	0.6	

12 A micro tidal range is defined as being an observed tidal range of less than 2 m (Masselink and Short, 1993).

Tidal Phase	Water Level relevant to Chart Datum (m)	Tidal Range (m)
High Water Neaps (MHWN)	1.2	Mean Neap: 0.3
Mean Low Water Neaps (MLWN)	0.9	
Lowest Astronomical Tide (LAT)	0.0	-

Figure 26 shows the predicted influence of surges on water levels and the flow velocities at a location at the northern end of the bank from modelled hindcast data from the year 2010[13]. These predictions indicate that surges have the potential to increase current speed by up to 40% in some extreme cases. In addition, water levels can vary (dependent on whether a positive or negative surge occurs) between +0.5 m to -0.4 m. Table 5 presents the key statistics from the metocean measurement campaign detailed in Section 3.2.

13 Figure 26 is derived from modelled hindcast data and data derived from a harmonic tidal analysis performed using the hindcast data. Surge effects on water levels and current speed is determined by comparing the difference between the model predictions and the harmonic data.

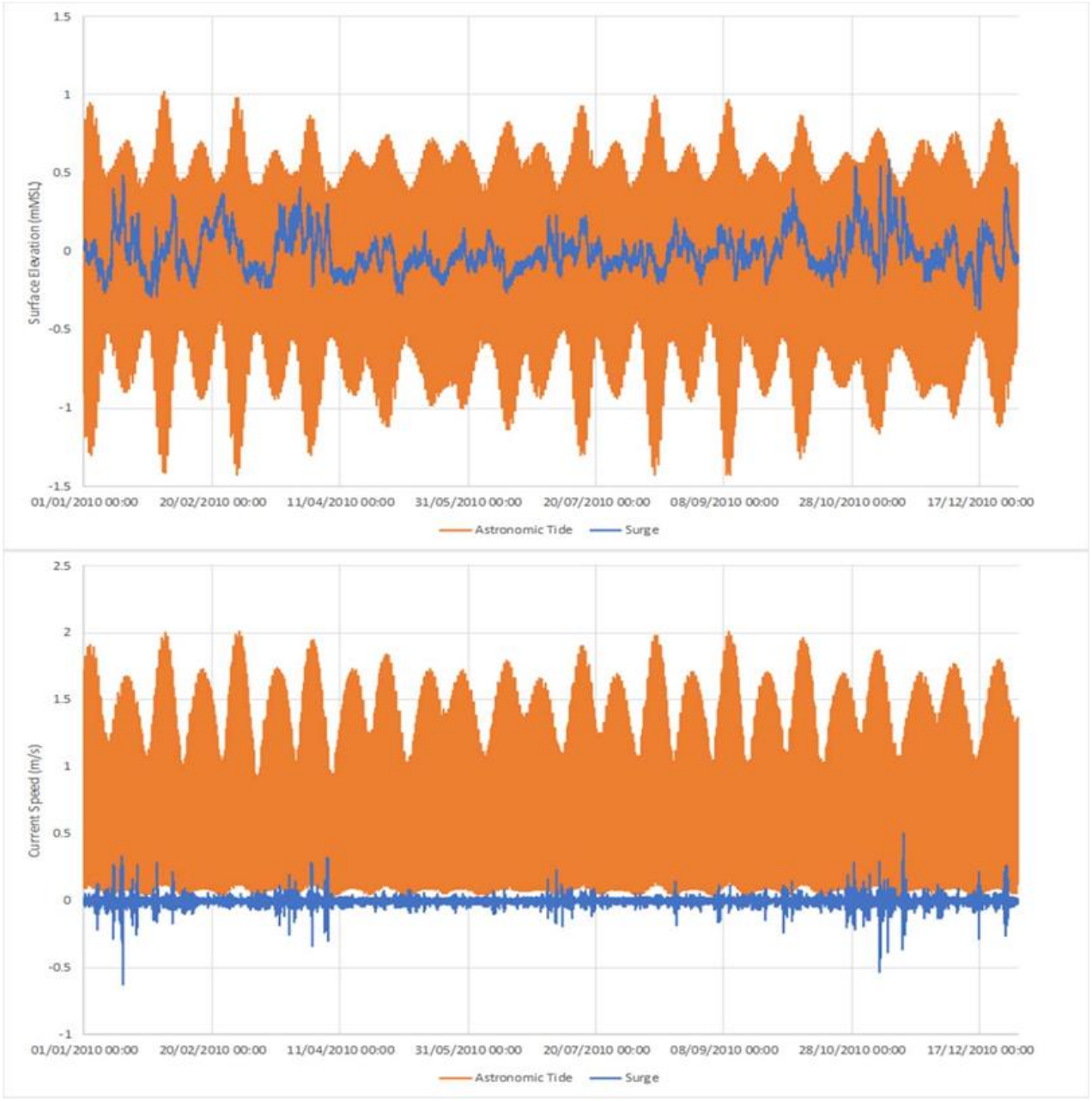


Figure 26. The predicted relative influence of surges on water levels (top panel), and current speed (lower panel) at the north of the site, for the year 2010 derived from comparison of modelled hindcast data and data derived from a harmonic tidal analysis.

Table 5. The key statistics regarding current speed, water depth and water level from each measurement frame.

Frame Location	Parameters	Minimum	Maximum	Mean	P_{50} (%)	P_{90} (%)	P_{99} (%)
'A'	Depth-averaged current [m/s]	0.02	2.36	0.91	0.92	1.51	1.92
	Water Depth [m]	26.58	29.02	27.94	27.99	28.49	28.76
	Water Level [mLAT]	-0.12	2.32	1.25	1.30	1.80	2.07
'B'	Depth-averaged current [m/s]	0.01	1.80	0.71	0.73	1.23	1.55
	Water depth [m]	29.01	31.43	30.21	30.25	30.70	31.03
	Water level [mLAT]	-0.10	2.33	1.11	1.15	1.60	1.93
'C'	Depth-averaged current [m/s]	0.01	1.47	0.62	0.64	1.04	1.26
	Water Depth [m]	24.50	26.51	25.68	25.72	26.07	26.32
	Water Level [mLAT]	-0.17	1.84	1.01	1.05	1.41	1.65
'D'	Depth-averaged current [m/s]	0.01	2.11	0.78	0.78	1.35	1.70
	Water depth [m]	29.31	31.66	30.51	30.54	30.99	31.26
	Water level [mLAT]	-0.09	2.26	1.11	1.14	1.59	1.86
'E'	Depth-averaged current [m/s]	0.01	1.52	0.55	0.53	1.00	1.31
	Water Depth [m]	37.22	39.30	38.30	38.29	38.63	39.00
	Water Level [mLAT]	-0.26	1.83	0.82	0.82	1.16	1.52

At each frame location a semi-diurnal tidal regime is observed, with each data record exhibiting a distinct spring-neap phasing with both water levels and flow velocities enhanced during the spring phase. Tidal flows, except for brief periods at slack water, are observed with a flow velocity of > 0.5 m/s, increasing to > 2.0 m/s during the spring tidal phase. Maximum and mean current velocities are enhanced at frame location 'A', 'B' and 'D' (i.e. frames located towards the head of the bank to the north) compared to other frame locations, which is postulated to be a function of the local bathymetry (e.g. the influence of Wicklow Trough to the north channelling flows to the south towards Arklow Bank). The variation in tidal range across the bank described previously is observed within the data record with the mean spring range and Highest Astronomical Tide (HAT) values at frame location 'A' (to the north of the bank) greater than at frame location 'E' due to its position relative to the local degenerate amphidromic point. Indeed, the 'double high water' effects become more apparent the closer the frame location is to the amphidromic point (i.e. at frame location 'C' and 'E').

Figure 27 to Figure 31 present time series showing the water level, tidal current velocity and direction data recorded at frame location 'A', 'B', 'C', 'D' and 'E', respectively. Superimposed upon the regular tidal behaviour, various random non-tidal effects may be present. Many of these non-tidal effects originate from meteorological influences (e.g. positive, or negative surge). The maximum water level (2.33 m above LAT) was recorded at frame location 'B' during a surge event during the month of August 2020. Figure 32 to Figure 36 display the observed current speed as a function of direction in the form of current roses, which provide a visually simple appreciation of the predominant tidal axis at each of the measurement frame locations. Strong rectilinearity is observed at all frame locations broadly along the axis north northeast to south southwest, though at all frame locations there is a component flow tending further towards the northern or southern quadrants which may be due to the direction of tidal flows shifting locally relative to the seabed topography. Note: as these plots are depth averaged, flow variation through the water column during different phase of the tide is not represented.

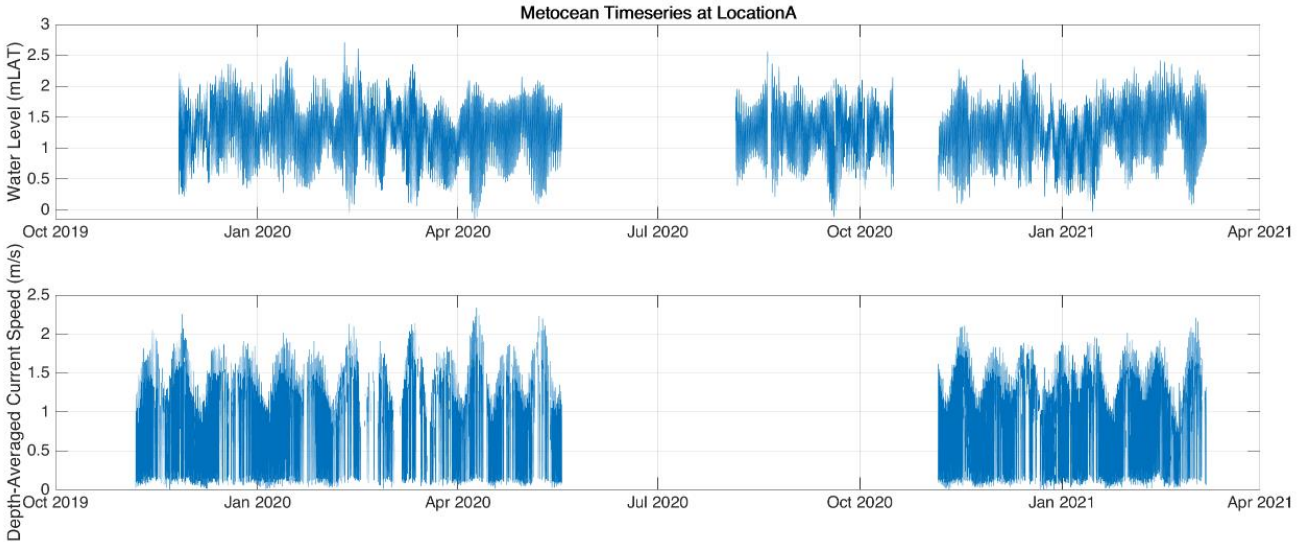


Figure 27. The water level data, and depth-averaged current speed, measured at frame location 'A' presented in the form of a time series.

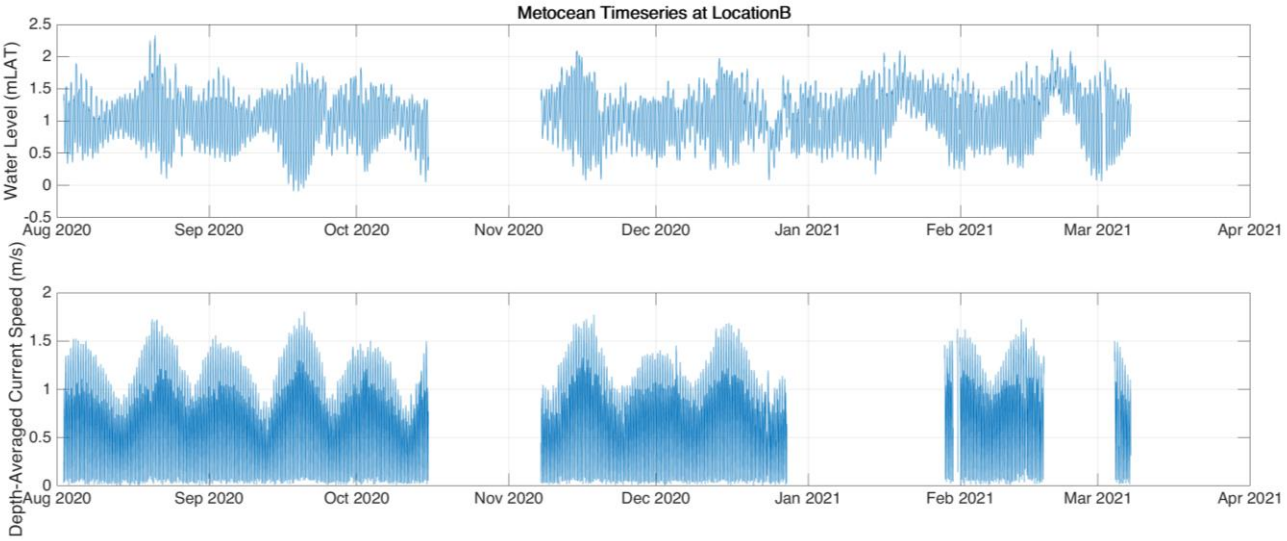


Figure 28. The water level data, and depth-averaged current speed, measured at frame location 'B' presented in the form of a time series.

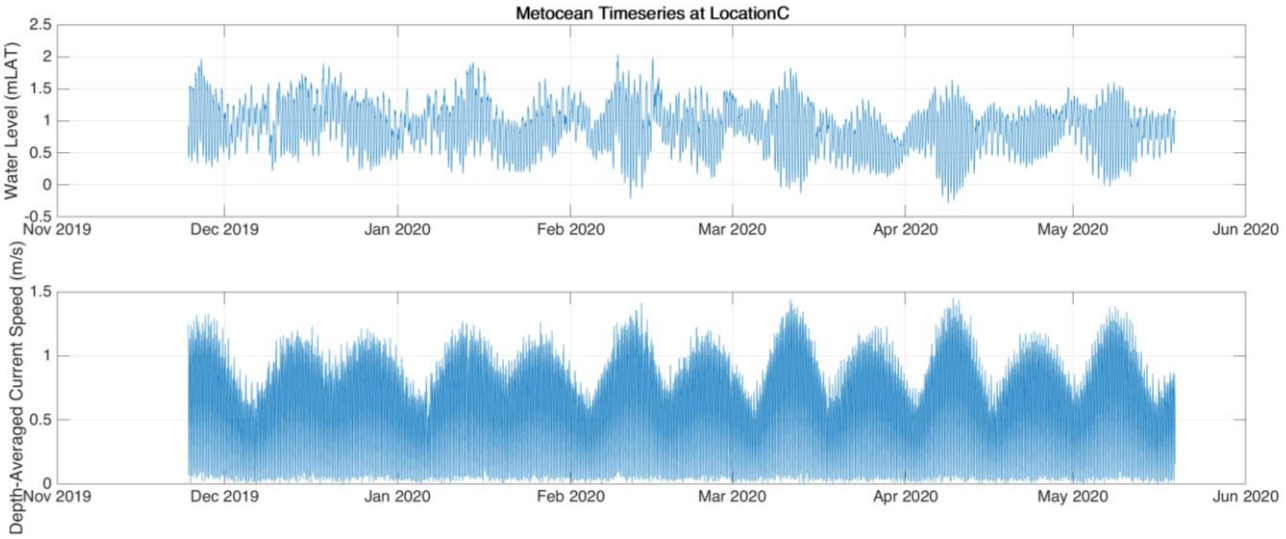


Figure 29. The water level data, and depth-averaged current speed, measured at frame location 'C' presented in the form of a time series.

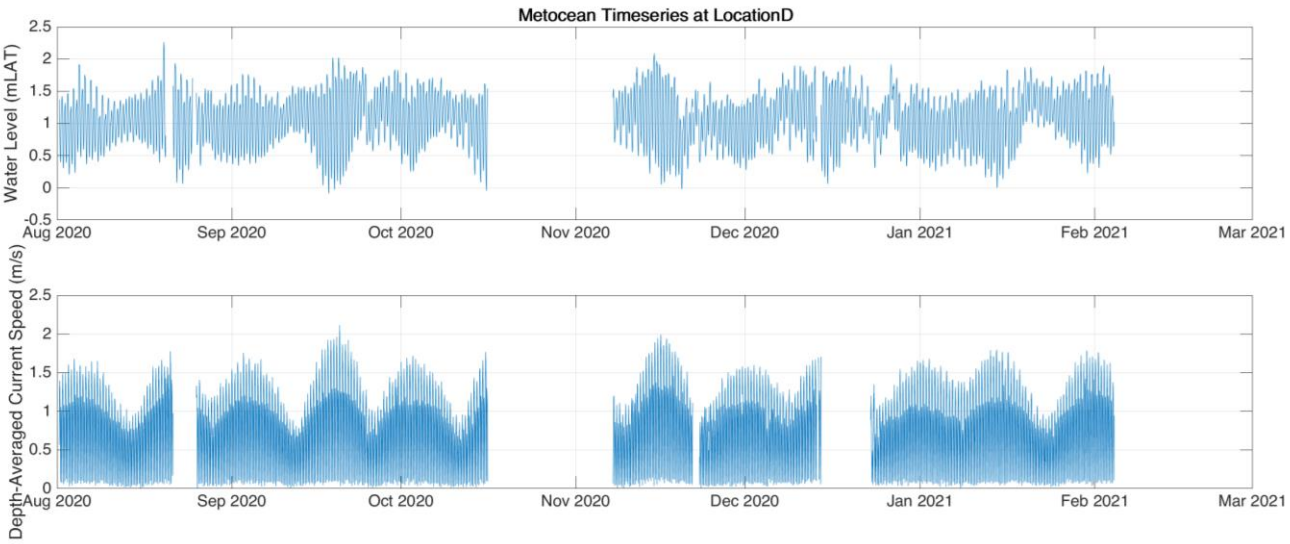


Figure 30. The water level data, and depth-averaged current speed, measured at frame location 'D' presented in the form of a time series.

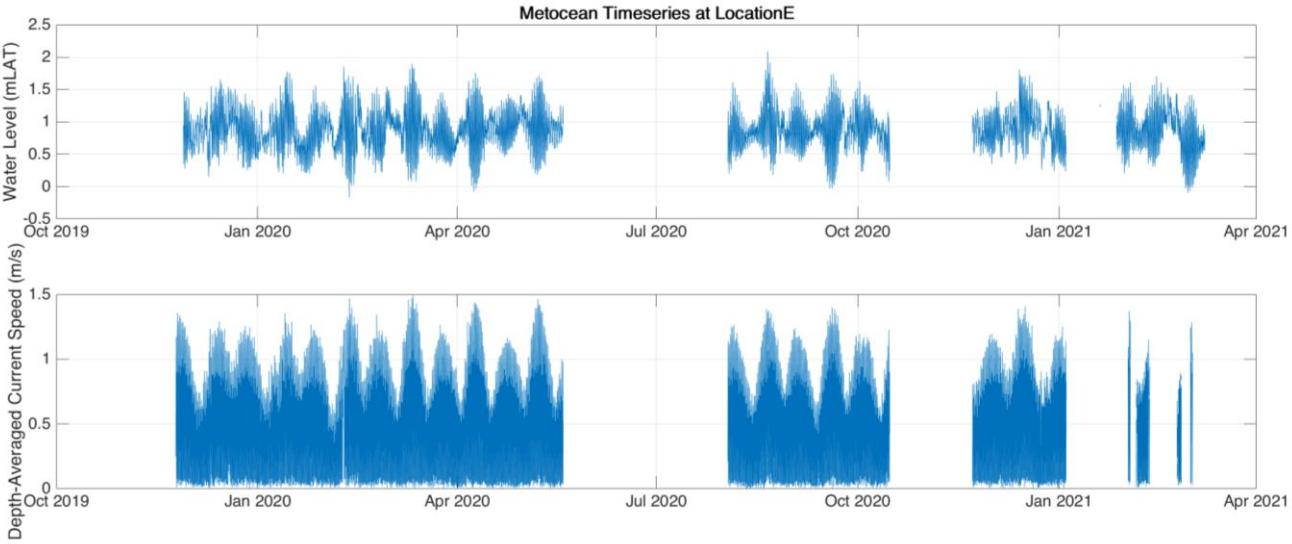


Figure 31. The water level data, and depth-averaged current speed, measured at frame location 'E' presented in the form of a time series.

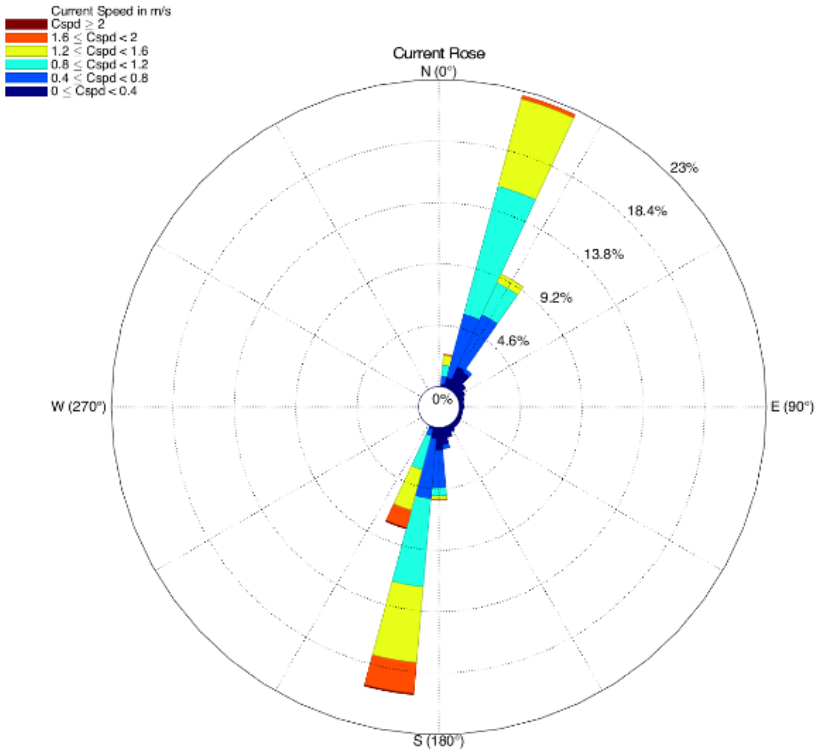


Figure 32. Current speed presented as a function of direction in the form of a current rose. The data presented were measured at frame location 'A'.

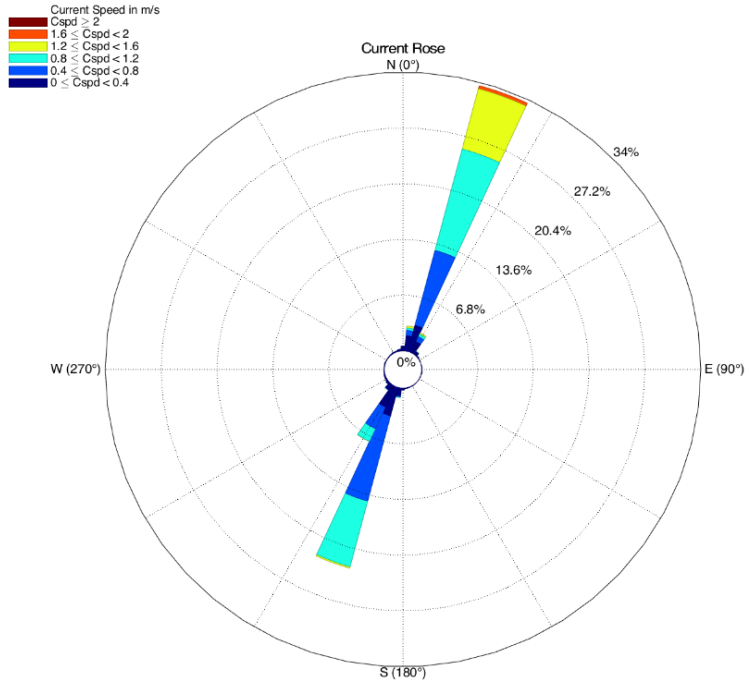


Figure 33. Current speed presented as a function of direction in the form of a current rose. The data presented were measured at frame location 'B'.

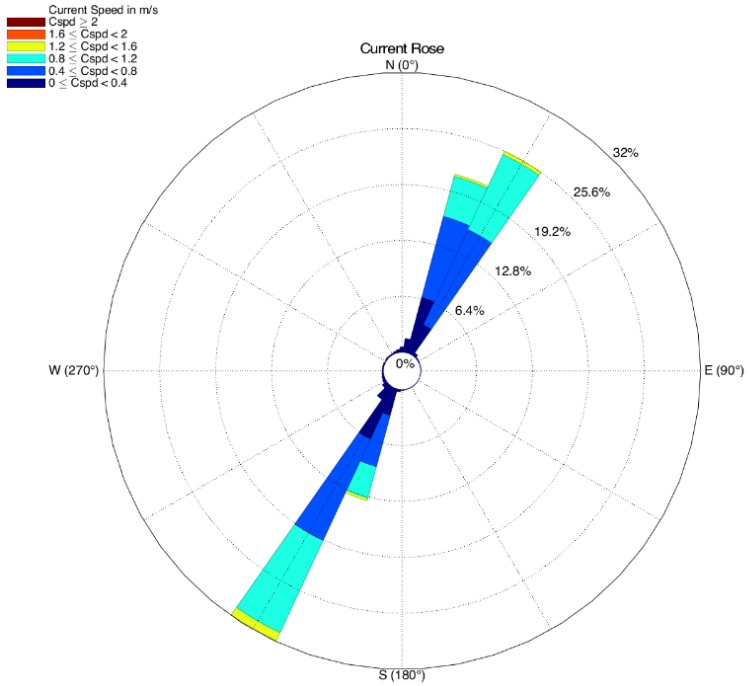


Figure 34. Current speed presented as a function of direction in the form of a current rose. The data presented were measured at frame location 'C'.

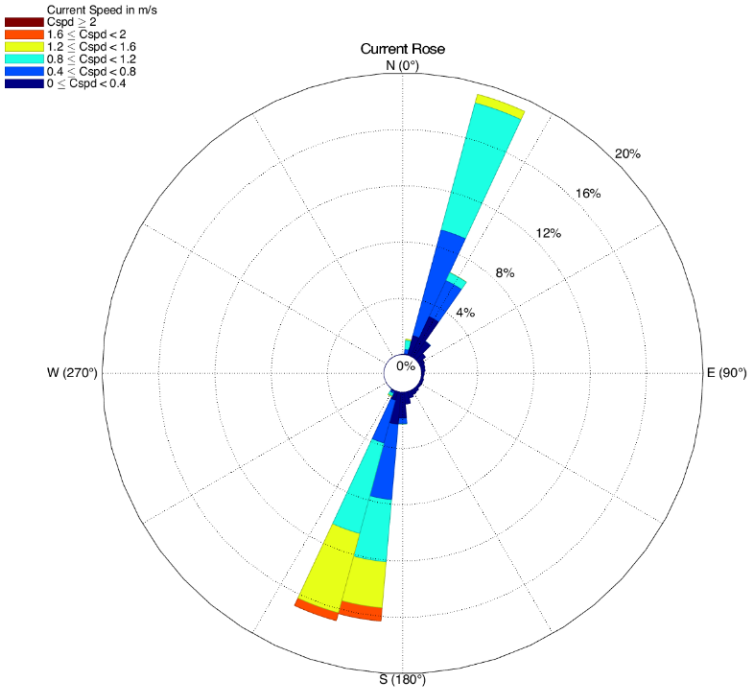


Figure 35. Current speed presented as a function of direction in the form of a current rose. The data presented were measured at frame location 'D'.

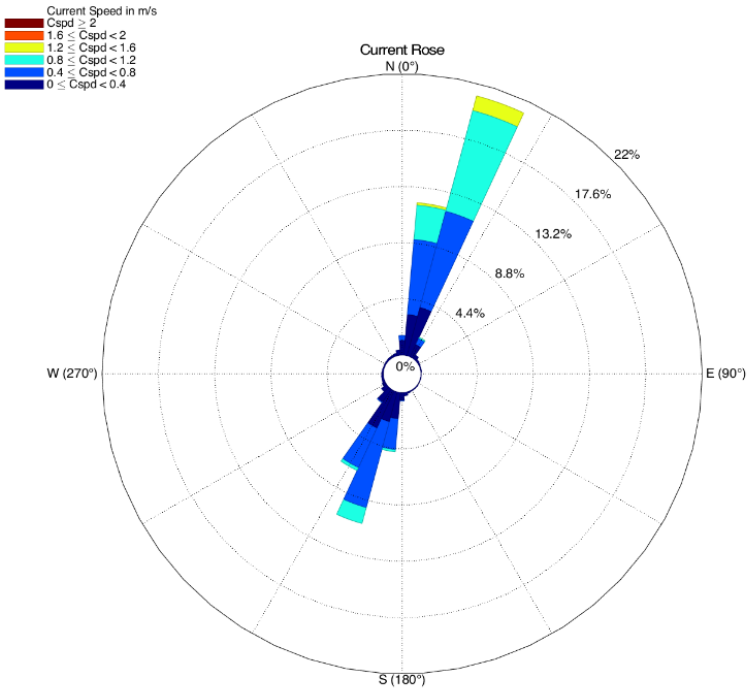


Figure 36. Current speed presented as a function of direction in the form of a current rose. The data presented were measured at frame location 'E'.

Further assessment of the frequency magnitude of occurrence of hydrodynamic conditions at each frame location is shown in Figure 37 to Figure 41, which presents joint probability distributions with respect to current velocity magnitude and direction. Presentation of the data in this manner further reveals the rectilinearity of tidal flows in the region, where current speeds between 0.5 to 1.5 m/s flowing in a north northeast direction and south, south southwest direction.

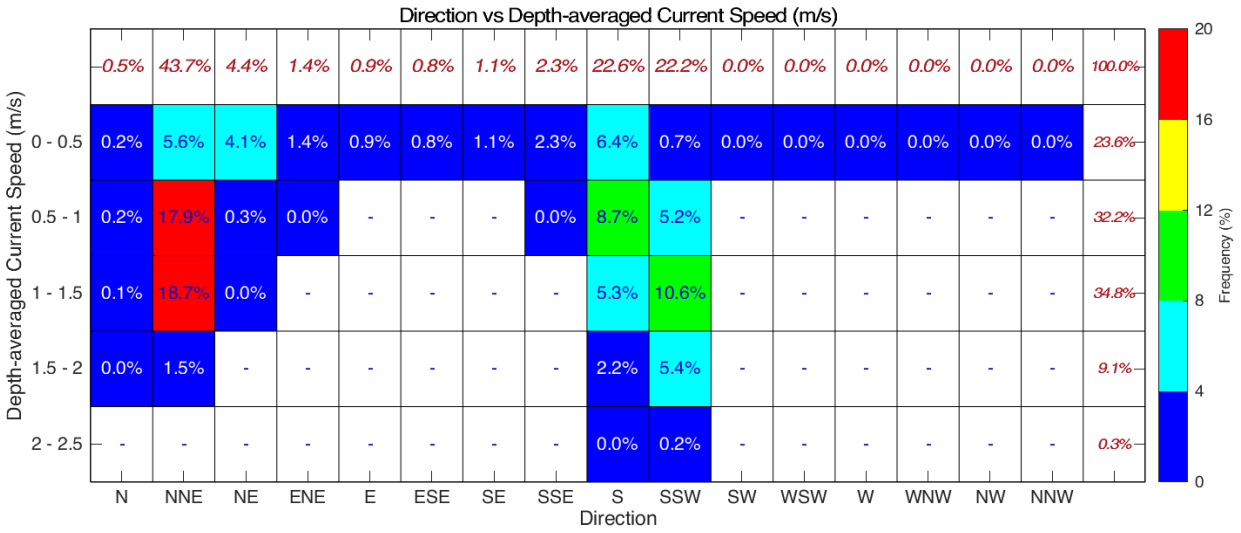


Figure 37. Joint probability distribution showing current speed and direction. The data were retrieved from the instruments deployed at location 'A".

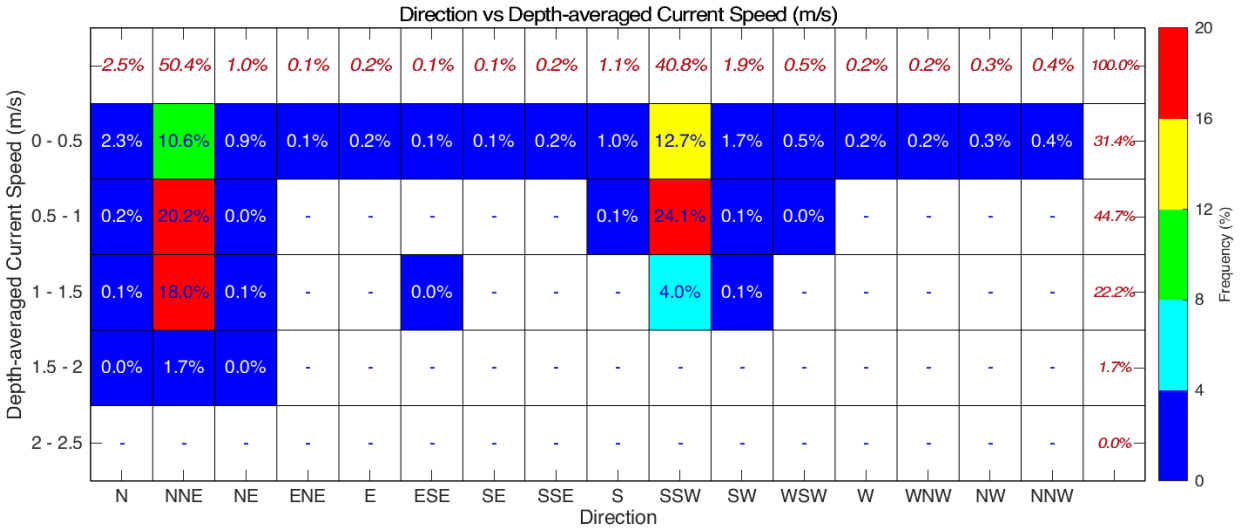


Figure 38. Joint probability distribution showing current speed and direction. The data were retrieved from the instruments deployed at location 'B".

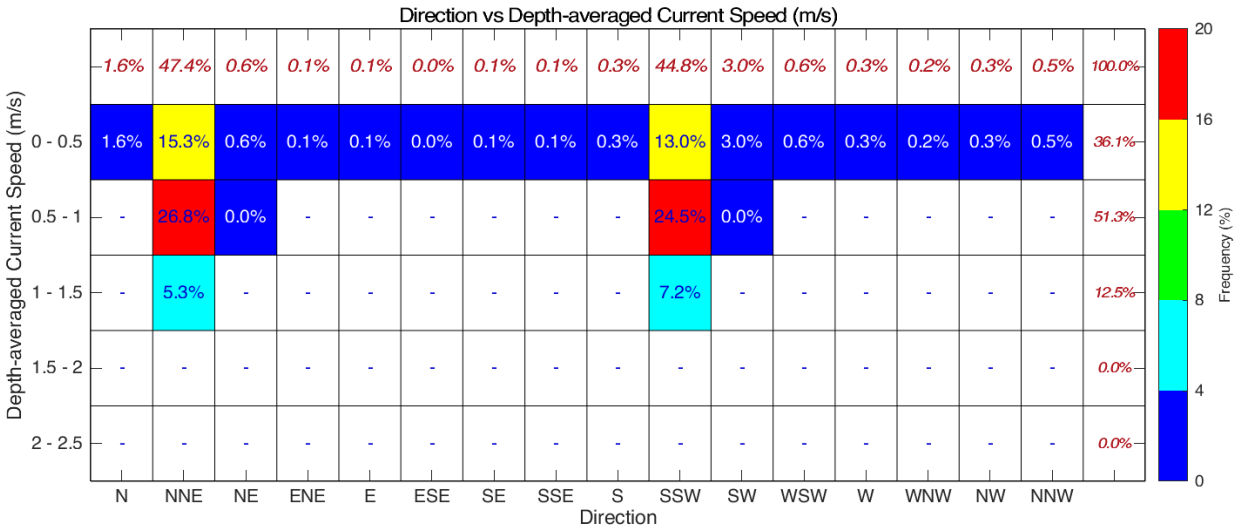


Figure 39. Joint probability distribution showing current speed and direction. The data were retrieved from the instruments deployed at location 'C".

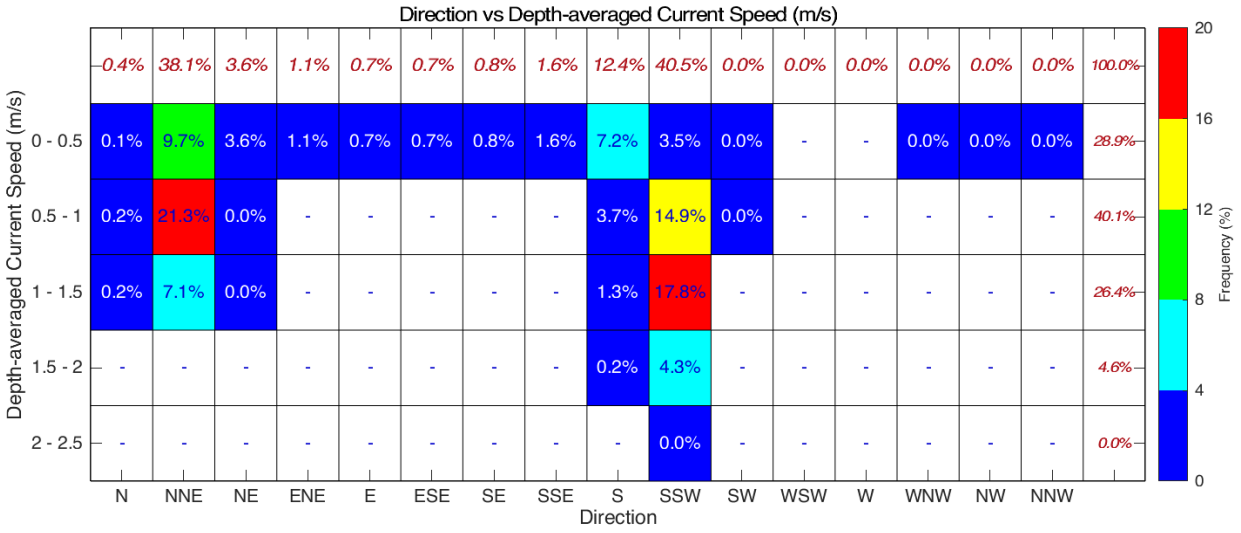


Figure 40. Joint probability distribution showing current speed and direction. The data were retrieved from the instruments deployed at location 'D".

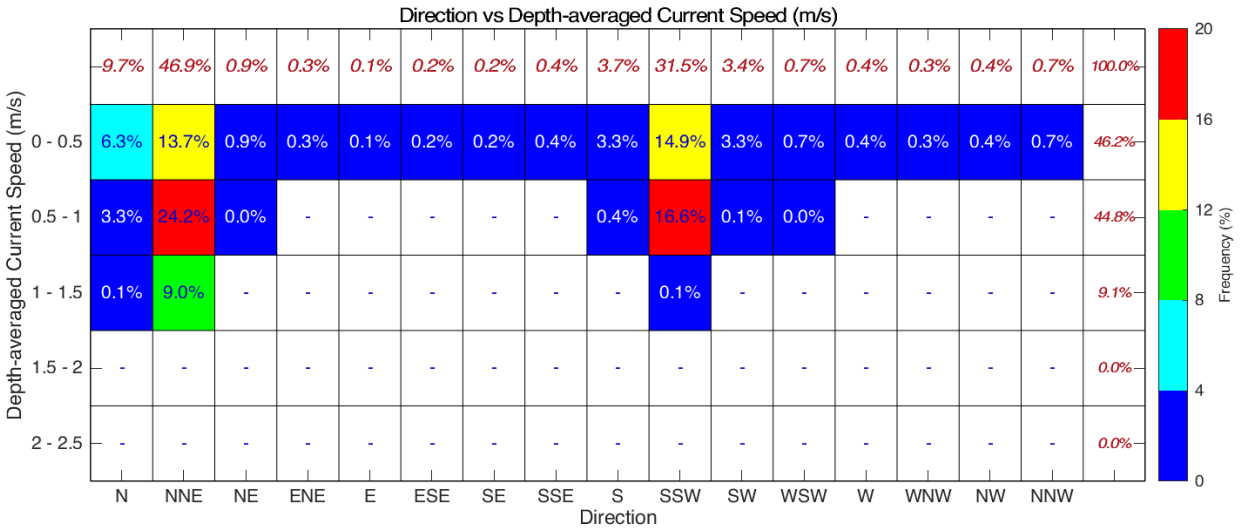


Figure 41. Joint probability distribution showing current speed and direction. The data were retrieved from the instruments deployed at location 'E".

Around the bank there is a pronounced tidal asymmetry with ebb dominant (i.e. southward) flows observed to the east of the bank and flood dominant (i.e. northward) flows observed to the west of the bank. As tidal flows are the primary physical mechanism driving sediment transport at the site the tidal asymmetry drives a residual (i.e. net[14]) sediment transport in a clockwise rotary circulation around the bank, which is a function of the bank topography; the orientation of the bank to the tidal axis; and Coriolis. Frame locations 'B' and 'D' positioned either side of the bank targeted these phenomena and the asymmetry (in terms of duration, and magnitude) is clearly observed in these datasets (see Figure 33, Figure 35, Figure 38 and Figure 40). Such asymmetry drives residual transport for both bedload and suspended sediments, particularly during spring tides, which are periods of greatest flow magnitude developing the highest rates of transport. Tidal asymmetry is less obvious in the data retrieved from frame 'C' located nearer shore along the proposed export cable route (Figure 34 and Figure 39).

14 Net sediment transport is created by an imbalance in flow velocity magnitude, direction and/or phase and duration of these effects.

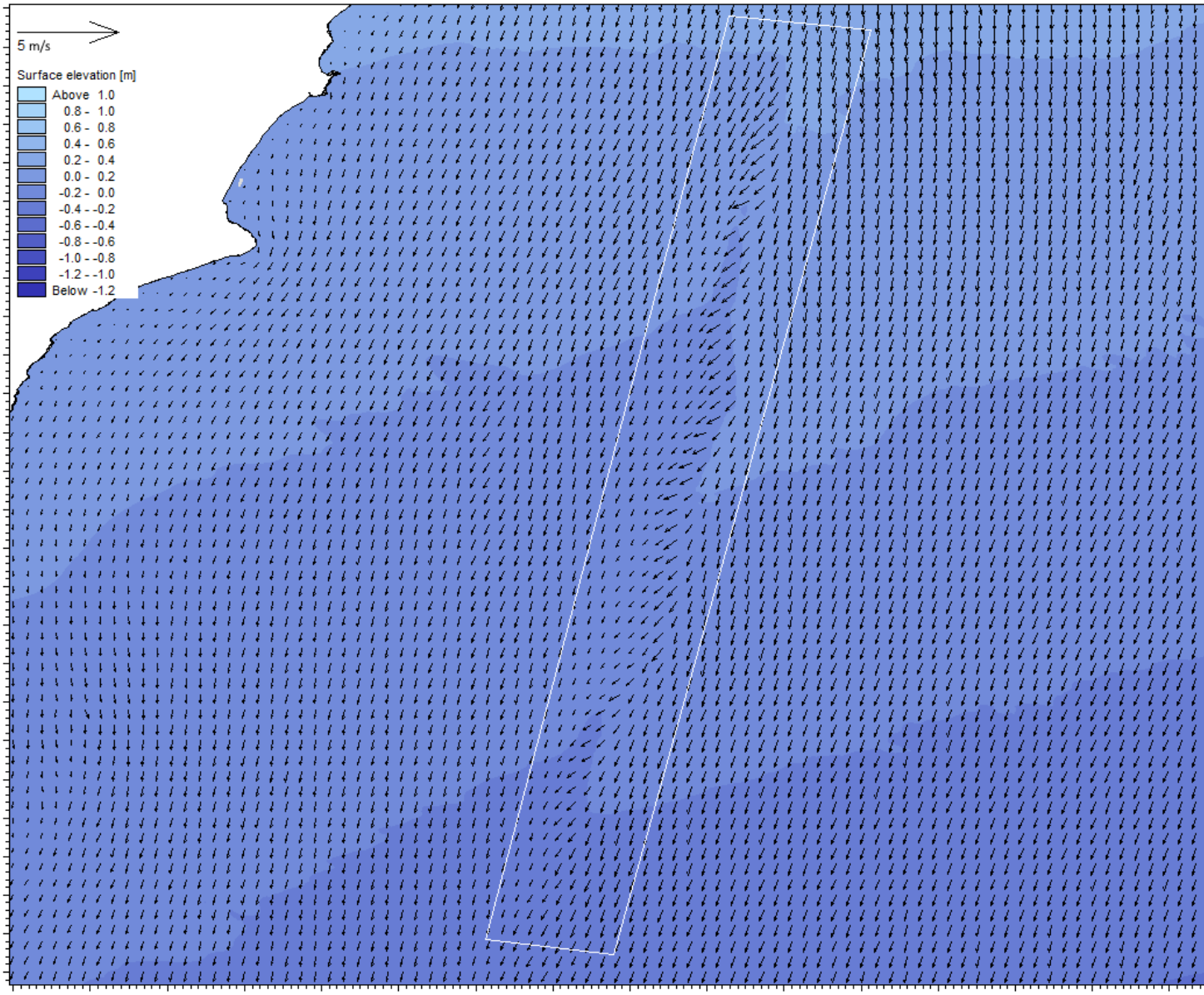


Figure 42 and Figure 43 presents spatial vector plots showing the cross-bank flows which occur during the ebb, and flood, phases of the tide respectively which develop due to a head difference between the east and west of the bank. The tidal wave arrives at, and departs from, the bank locality at a slightly oblique angle, relative to the orientation of the bank. This gives rise to a difference in water levels between the east and west of the bank, normal to its primary axis. This effect is illustrated in Figure 42, Figure 43, Figure 44 and Figure 45. In Figure 42 and Figure 43, the isolines of water surface are not normal to the orientation of the primary axis of the bank, hence normal to the bank the water levels vary between the east and west of the bank. This difference in water levels gives rise to a period of strong flows over the crest of the bank, eastward on the flooding tide, and westward on the ebbing tide (which is more pronounced in central regions of the bank where water depths are at their shallowest). In these areas, due to the shallow crest, the bank serves to act as a weir, holding up the difference in water levels between east and west, which leads to strong cross-bank flows on both phases of the tide. Figure 44 shows the head difference measured at frame locations B1 and D1 on the north-western and north-eastern flanks of the bank, respectively. To derive the head difference simultaneous

water level data from the two frame locations were extracted and the instantaneous difference in water level was calculated by subtracting the water level at frame location D1 from the water level at frame location B1. The measured signal appears to jump abruptly, suggesting issues in either instrument stability or data processing. However, there is a brief period of two weeks toward the beginning of the measurements where the data appear stable. Negative values shows that the measured water level at frame location 'B' is less than at frame location 'D' indicating a bias towards the east of the bank and vice versa. The implications for sediment transport at the crestline associated with the bias in head difference is explored in Section 8.6.4.

Residual flows, and residual sediment transport, across the local region, and lease area, over the period coincident with the lunar cycle are presented in Figure 46, including zoomed in images of the south and north of the bank are presented in Figure 47 and Figure 48, respectively. Residual flows, and thus net sediment transport, are directed southward and northward on the west and east of the bank, respectively. These figures also reveal a net cross-bank flow in an easterly direction over the central portion of the bank. The net bias in the direction of flow, and thus sediment transport at the crest, varies over the short to medium and long- term. As most linear sandbanks show a residual circulation of sediments around the bank, these characteristics make Arklow Bank atypical. The wider pattern across the model domain also reveals the link between Wicklow Head and the northern head of the bank, this contrasts with the southern tail of the bank which does not have any similar association (Figure 23).

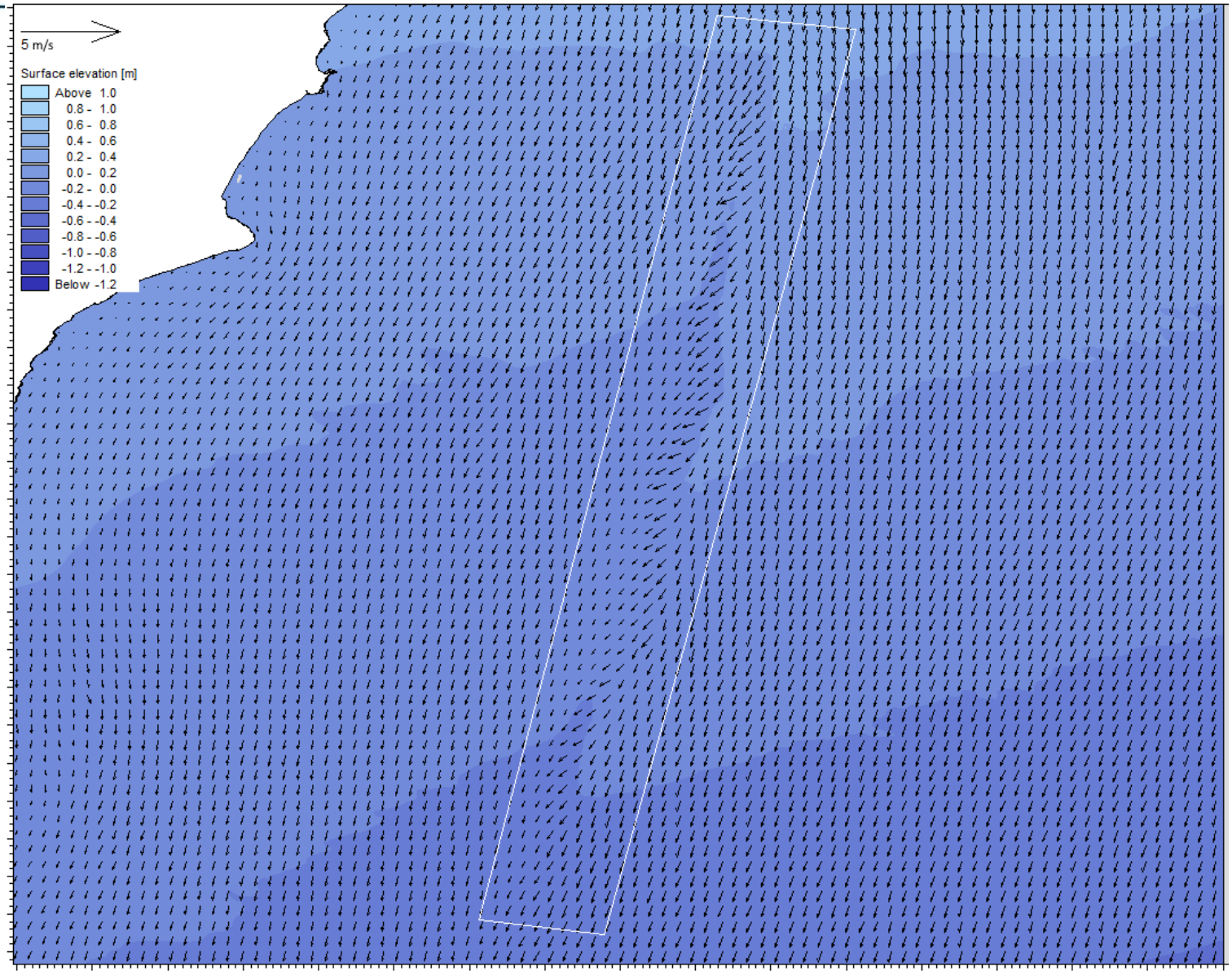


Figure 42. Water surface elevation and flow vectors during peak ebb.

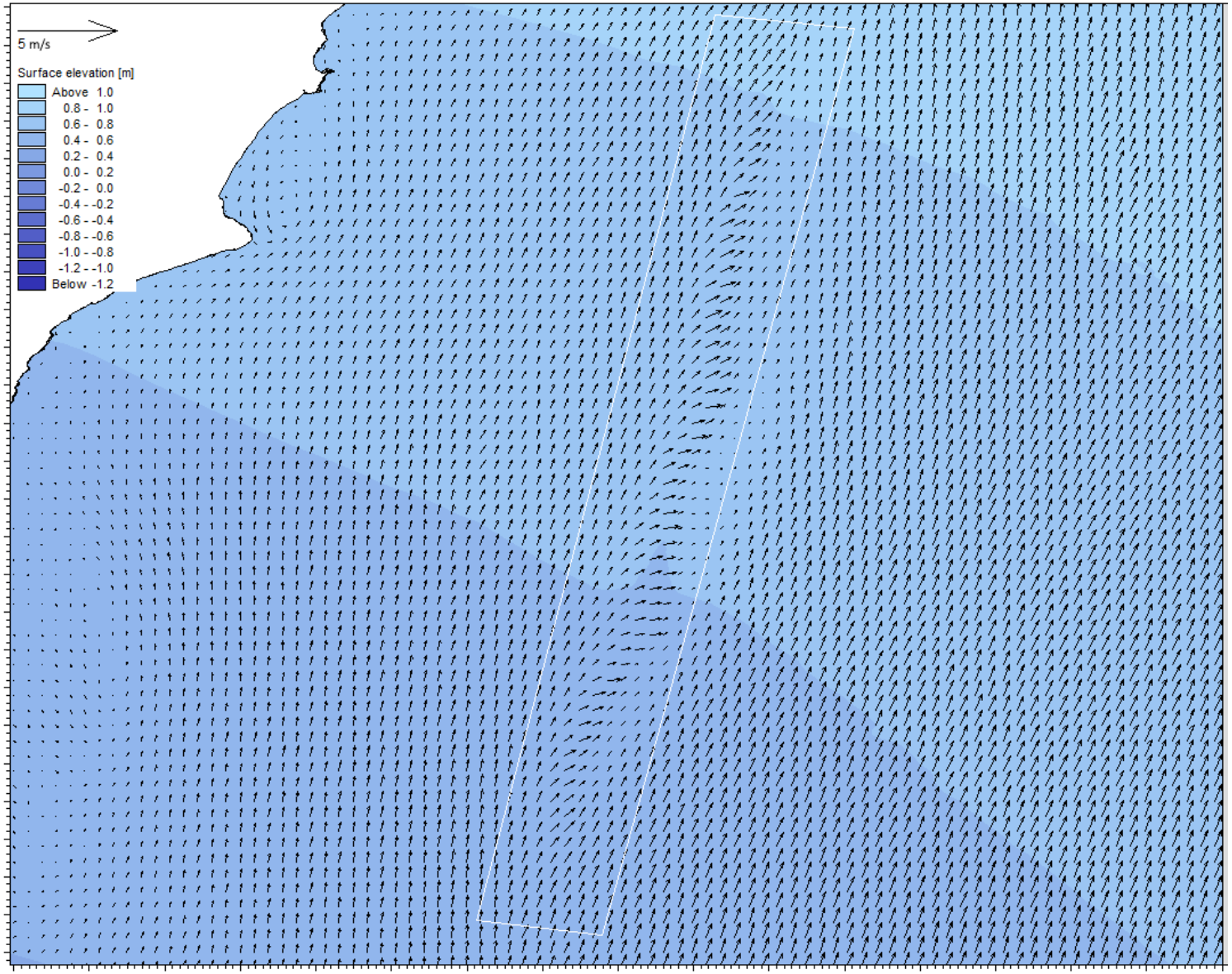


Figure 43. Water surface elevation and flow vectors during peak flood.

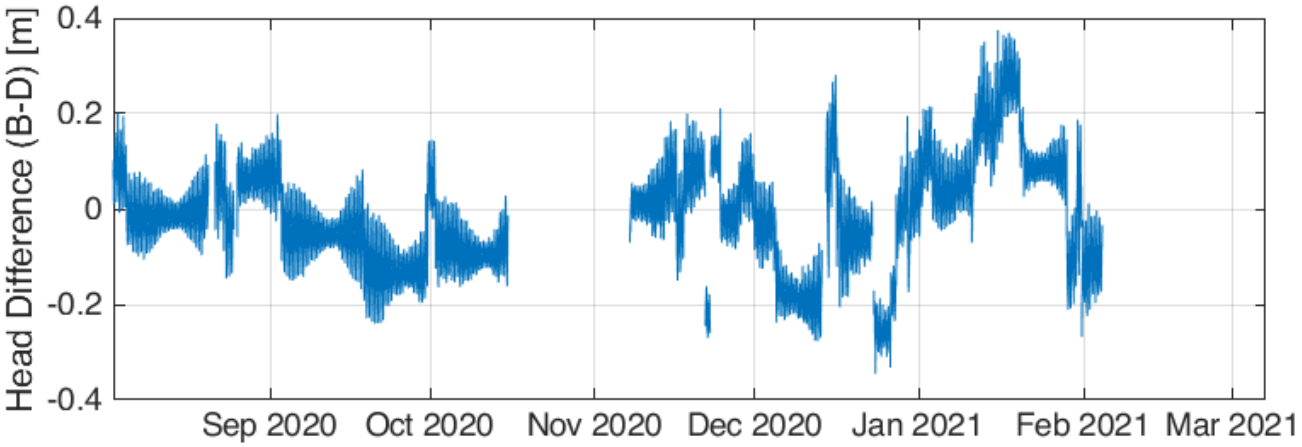


Figure 44. The head difference derived from the water level data acquired from frame location 'B' and 'D', The values are derived by subtracting values for water levels from frame location 'D' from water levels at frame location 'B', thus negative values shows that the measured water level at frame location 'B' is less than at frame location 'D' indicating a bias towards the east of the bank and vice versa. Note: the variation in the water level data presented suggests some artificial artefacts persist within the data record.

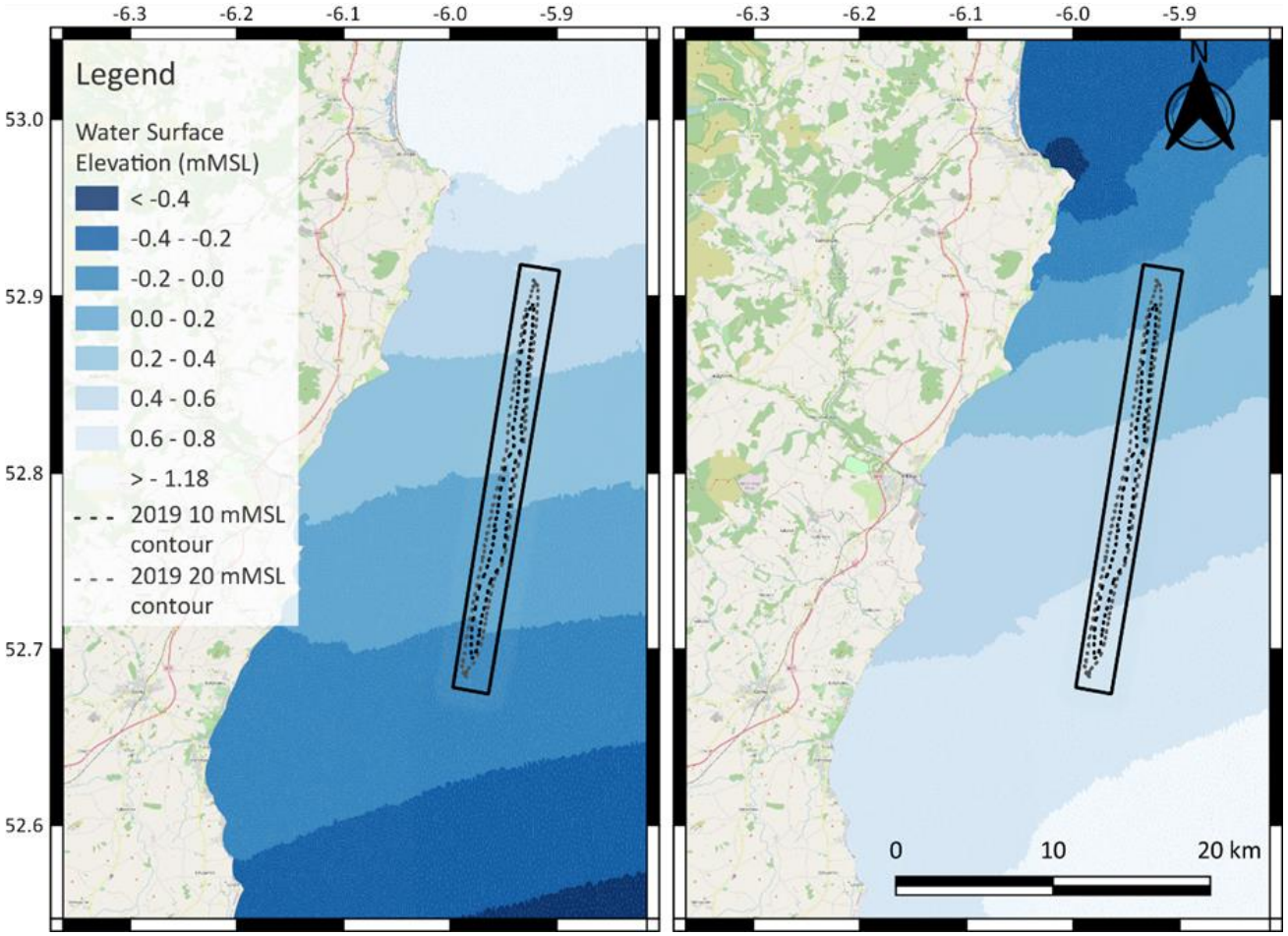


Figure 45. Water surface elevation during flood (right) and ebb (left) tides showing head difference between east and west of bank.

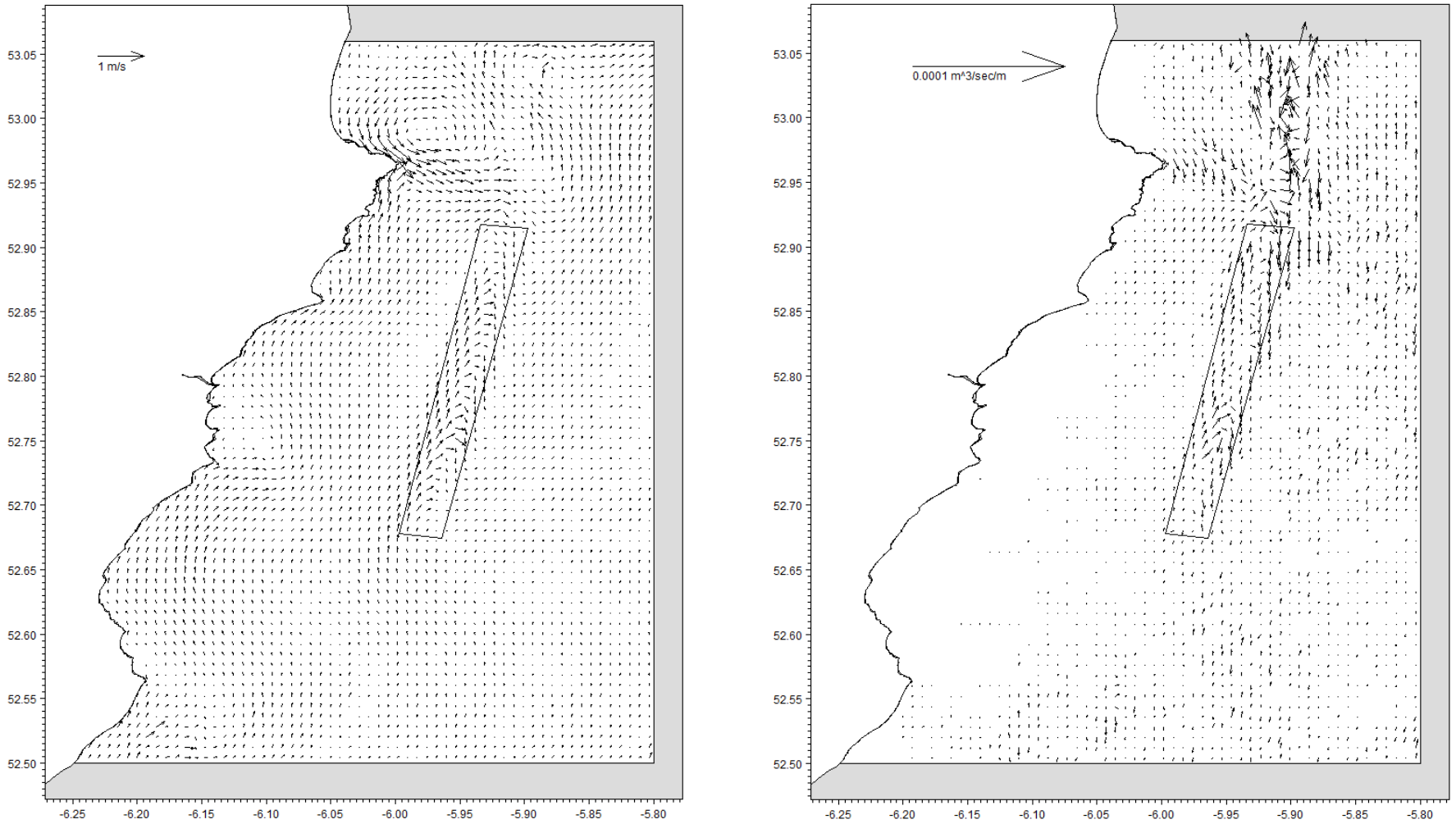


Figure 46. Residual flow vectors (left panel), and residual total load transport (right panel) across the local model domain, over the lunar cycle.

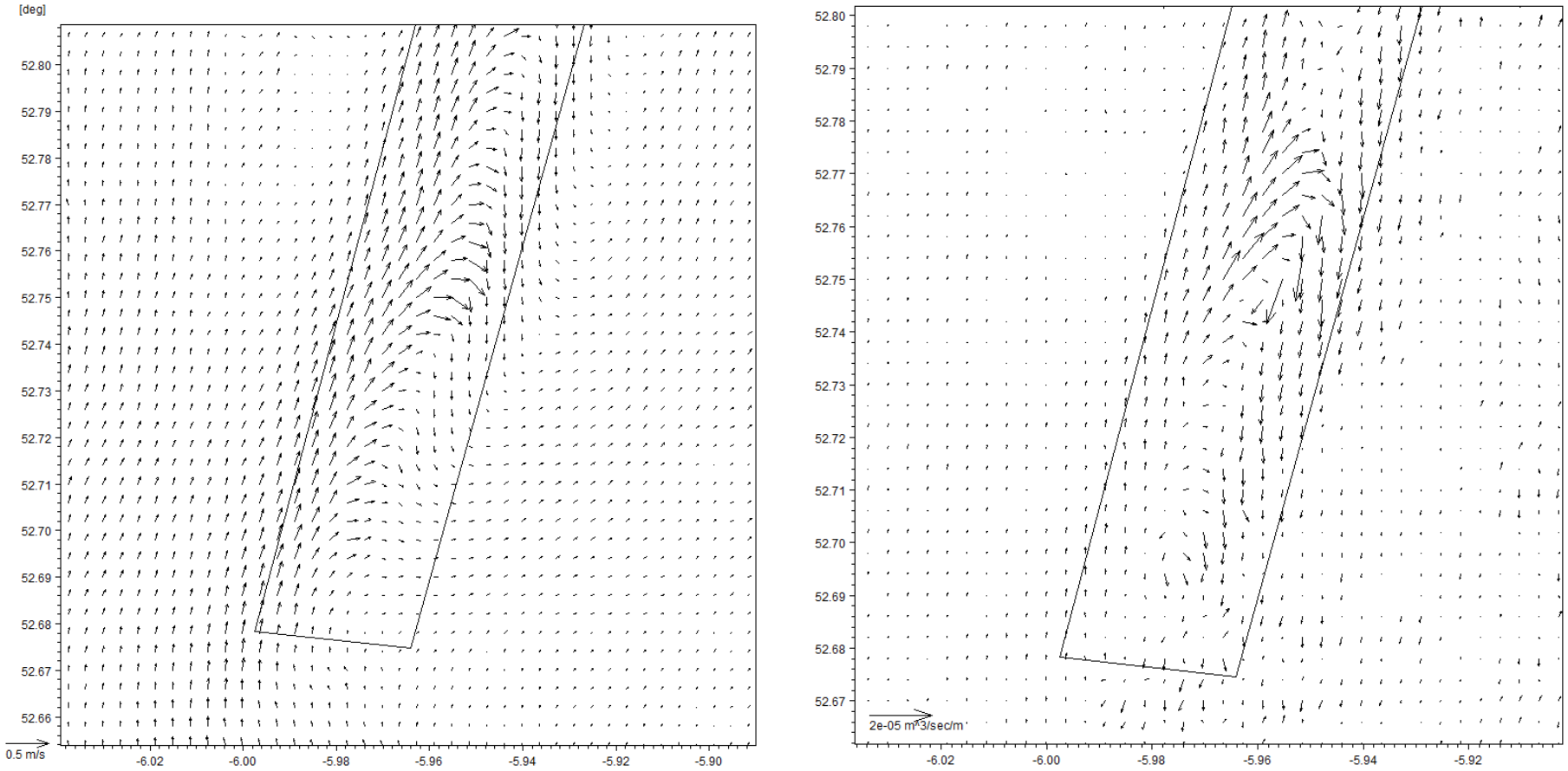


Figure 47. Residual flow vectors (left panel), and residual total load transport (right panel) over the lunar cycle. Zoomed in to the south of the bank.

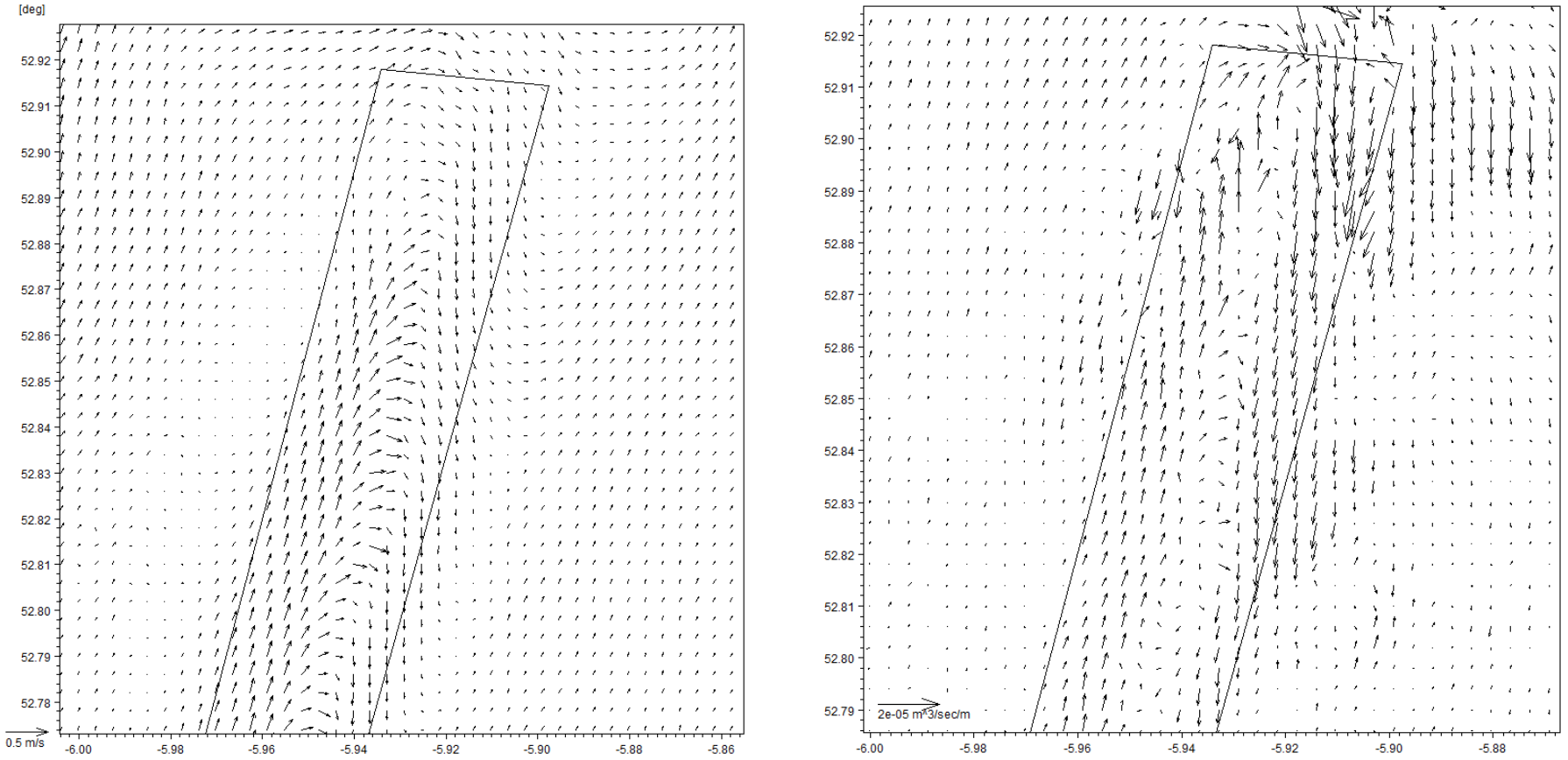


Figure 48. Residual flow vectors (left panel), and residual total load transport (right panel) over the lunar cycle. Zoomed in to the north of the bank.

8.5 Wave Regime

Arklow Bank is exposed to potentially severe (i.e. high energy) wave conditions generated within the Irish Sea, however, typically wind driven waves characterised by low wave heights and low wave periods dominate. The key statistics regarding wave height and wave period from the measurement campaign are detailed in Table 6. Figure 49 to Figure 53 present time series showing H_s, T_z and T_p. The direction of wave approach is visualised in Figure 54 which presents wave rose plots showing H_s, T_z and T_p as a function of wave approach (compass quadrants).

Due to the broadly limited fetch of the Irish Sea, the largest waves (with the greatest coincident wave period) originate from the southern quadrant which is coincident with the longest fetch. Waves from the north-northwest or north are generally smaller due to shorter fetches. This is corroborated by the observations which revealed that the most persistent and largest waves arrive at Arklow Bank from the south and south-southwest, and thus the southern section of the bank can be considered to be the most wave exposed. The wave climate to the east and west of the bank is similar to that observed at the south, albeit slightly less energetic, and with a slightly higher proportion of waves arriving from the north-northeast and south-southeast (Figure 54). However, the positions to the west and north of the bank exhibit a slightly moderated wave climate, in that they are less exposed to waves from the south due to local sheltering effects of the bank. Maximum wave heights observed during the measurement campaign at the south of the bank exceeded 4.6 m, comparatively, wave heights at the north of the bank did not exceed 3.8 m (Table 6). A complementary assessment of the frequency-magnitude of the wave climate measured at each frame location is presented in Figure 55 which show scatter plots showing the relationship between H_s , T_p and T_z. The most frequently observed wave conditions in the data record were H_s of < 2 m, with an associated T_p of 4 - 6 s and an associated T_z of 3 – 4 s, approaching the site from the south. Not surprisingly considering the episodic nature of wave events and the rarity (in a statistical sense) of storms or higher energy events, local wind generated seas (defined as waves with a mean period [T_z] of < 8 s) dominate the local wave climate with mean values of T_p and T_z at all frame locations being < 8 s[15]

15 The spectral representation of the local sea state may result in a large variety of shapes, from unimodal (one peak; see Pierson & Moskowitz, 1964) to bimodal or even multimodal (two or more non-artefact peaks; see Guedes Soares, 1984) which is a function of the joint occurrence of remotely generated swells and a local wind sea.

Table 6. The key statistics in regard to wave height and period from each measurement frame.

Frame Location	Parameters	Minimum	Maximum	Mean	P_{50} (%)	P_{90} (%)	P_{99} (%)
'A'	Significant Wave Height H_s [m]	0.19	3.74	1.09	0.98	1.87	2.73
	Mean Wave Period T_p [s]	1.07	15.43	5.24	5.20	6.87	9.15
	Peak Wave Period T_z [s]	1.61	7.88	3.57	3.44	4.86	5.91
'B'	Significant Wave Height [m]	0.09	3.23	0.91	0.78	1.63	2.36
	Peak Wave Period [s]	1.38	14.23	5.11	5.07	6.81	8.66
	Zero-crossing Wave Period [s]	1.77	6.20	3.53	3.45	4.67	5.36
'C'	Significant Wave Height H_s [m]	0.15	3.24	0.95	0.85	1.66	2.50
	Mean Wave Period T_p [s]	1.47	18.21	5.69	5.49	7.98	11.55
	Peak Wave Period T_z [s]	1.75	6.42	3.69	3.67	4.73	5.50
'D'	Significant Wave Height [m]	0.17	3.67	0.96	0.79	1.77	2.77
	Peak Wave Period [s]	1.04	16.67	5.34	5.30	7.22	9.89
	Zero-crossing Wave Period [s]	1.68	7.18	3.73	3.63	4.95	6.15
'E'	Significant Wave Height H_s [m]	0.12	4.62	1.03	0.94	1.83	2.91
	Mean Wave Period T_p [s]	1.73	16.02	6.50	5.99	10.27	12.06
	Peak Wave Period T_z [s]	2.04	8.29	4.07	3.98	5.22	6.63

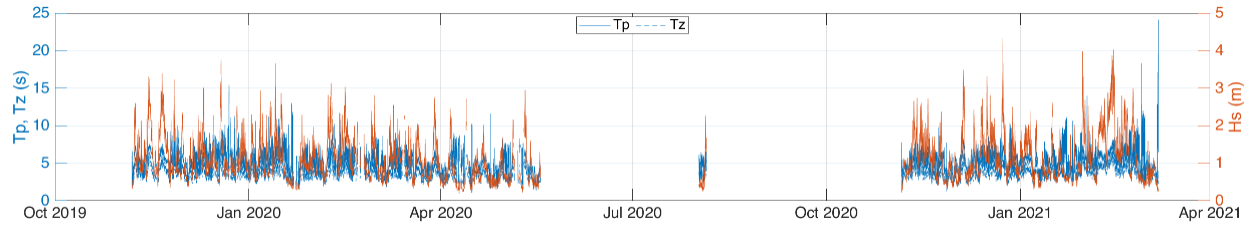


Figure 49. Time series showing H_s, T_p and T_z from data retrieved from instruments deployed at location 'A'.

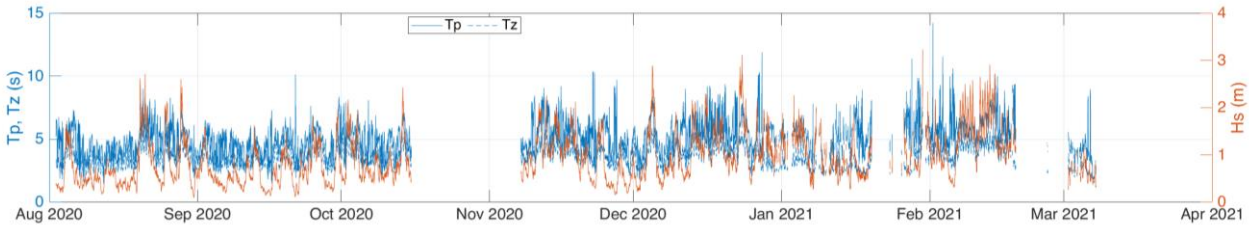


Figure 50. Time series showing H_s, T_p and T_z from data retrieved from instruments deployed at location 'B'.

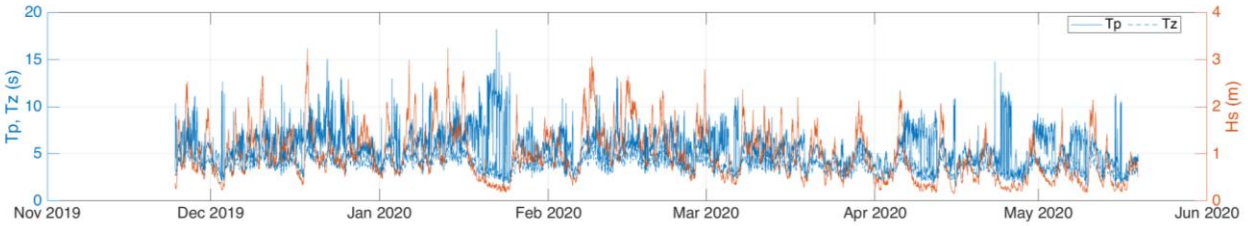


Figure 51. Time series showing H_s, T_p and T_z from data retrieved from instruments deployed at location 'C'.

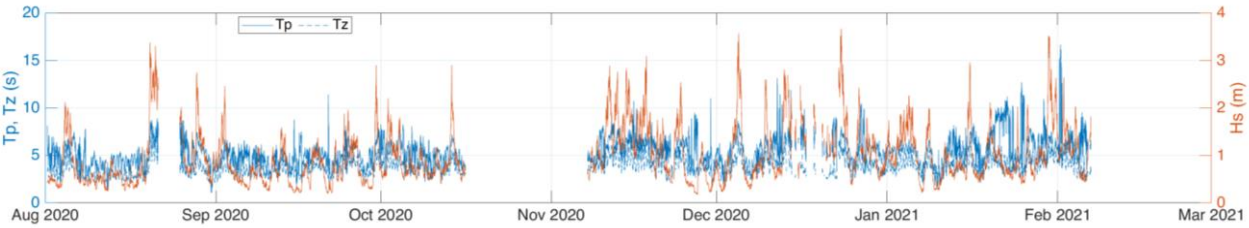


Figure 52. Time series showing H_s, T_p and T_z from data retrieved from instruments deployed at location 'D'.

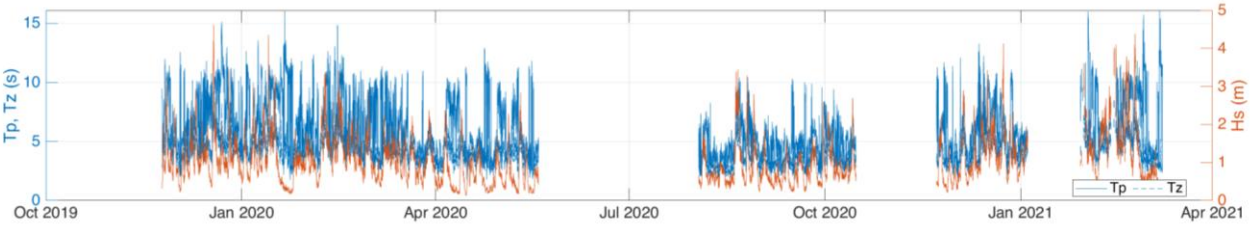
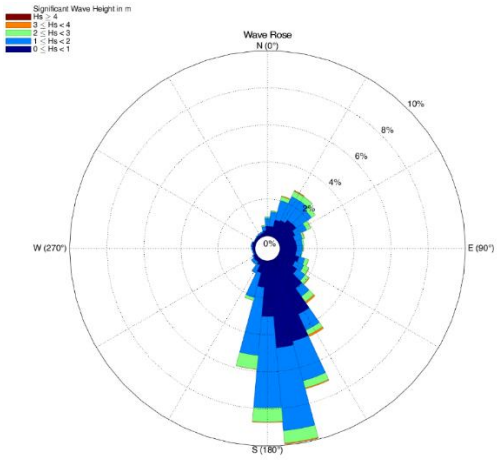
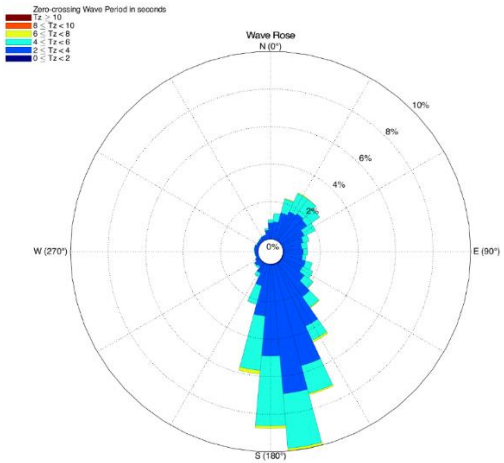


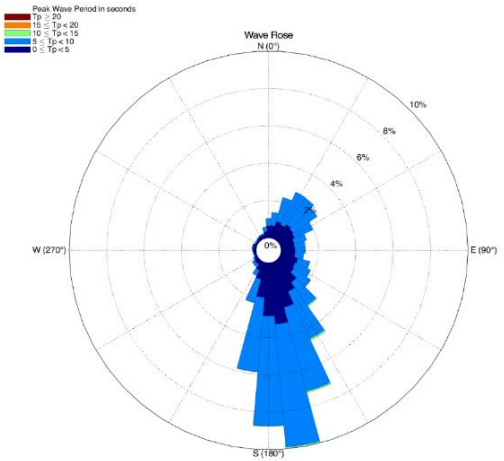
Figure 53. Time series showing H_s, T_p and T_z from data retrieved from instruments deployed at location 'E'.



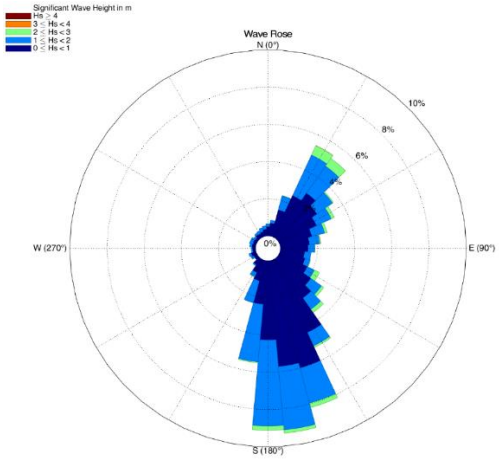
Location 'A' - H_s



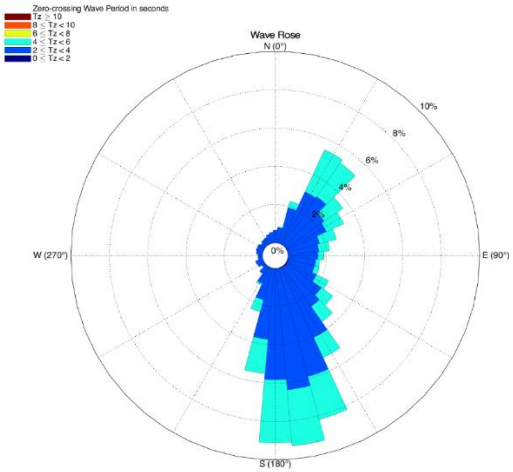
Location 'A' - T_z



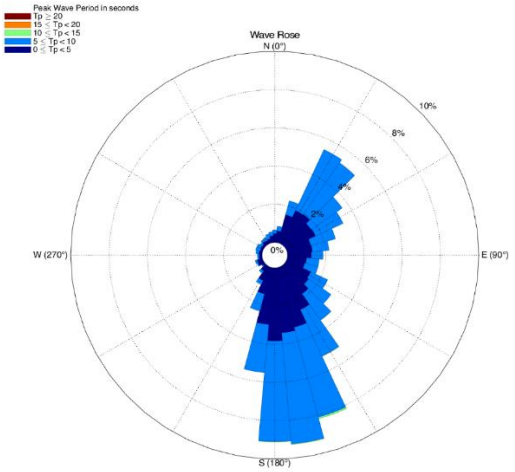
Location 'A' - T_p



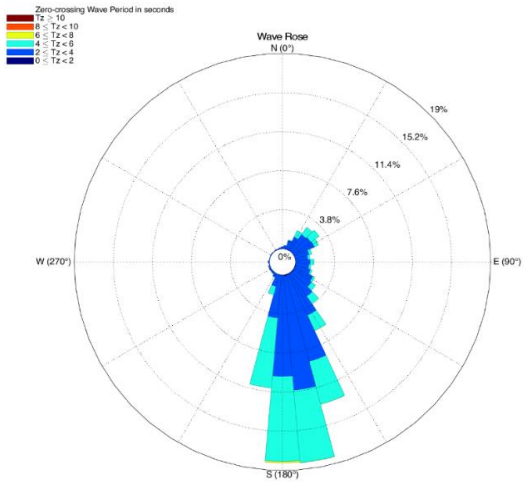
Location 'B' - H_s



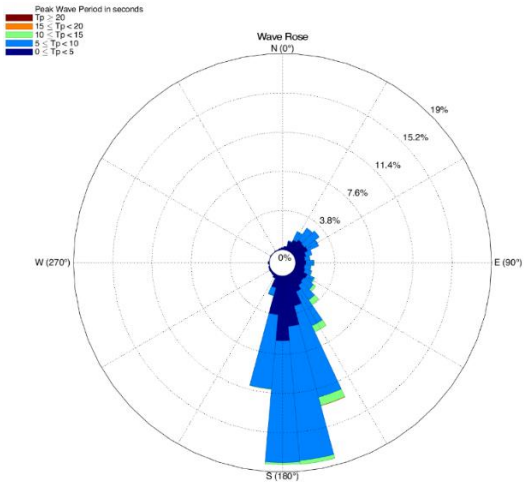
Location 'B' - T_z



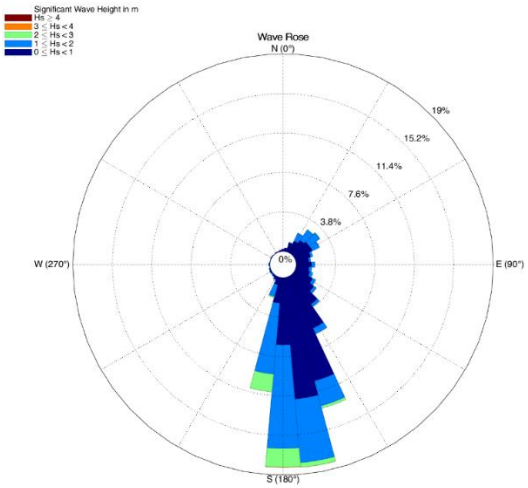
Location 'B' - T_p



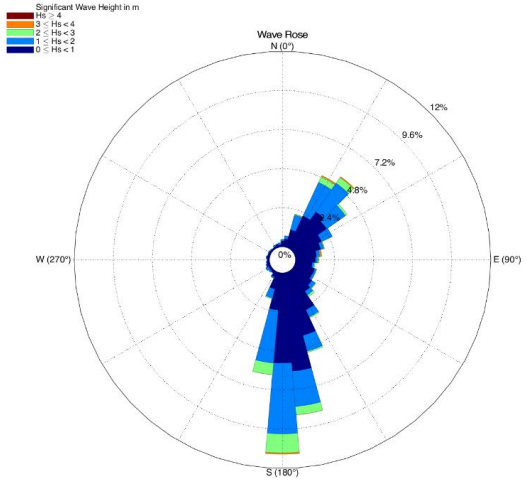
Location 'C' - H_s



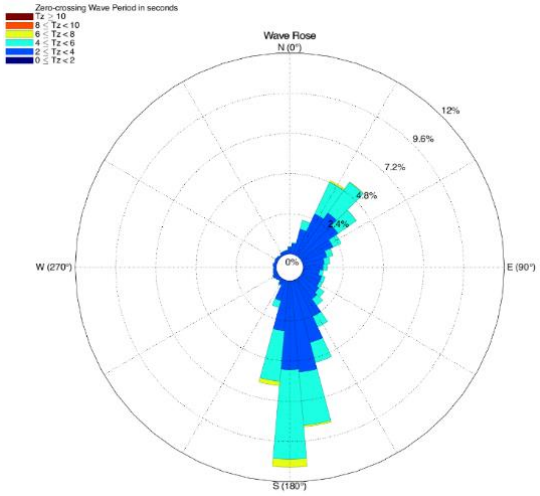
Location 'C' - T_z



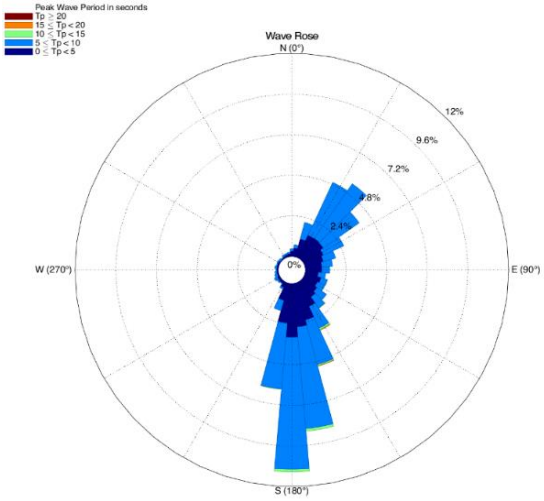
Location 'C' - T_p



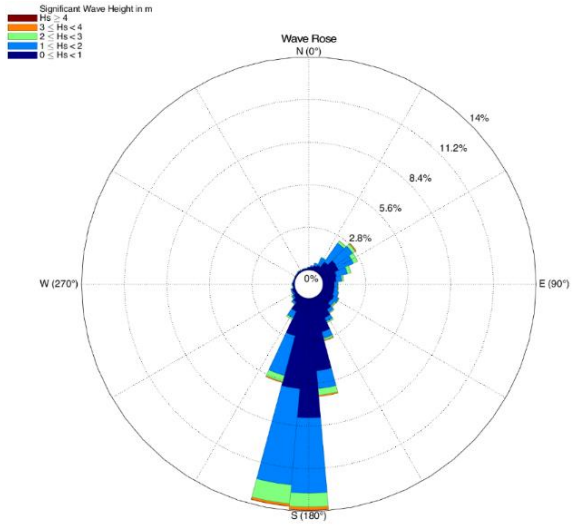
Location 'D' - H_s



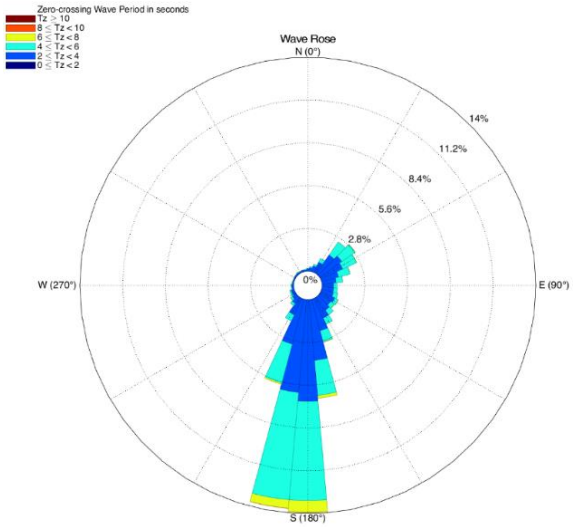
Location 'D' - T_z



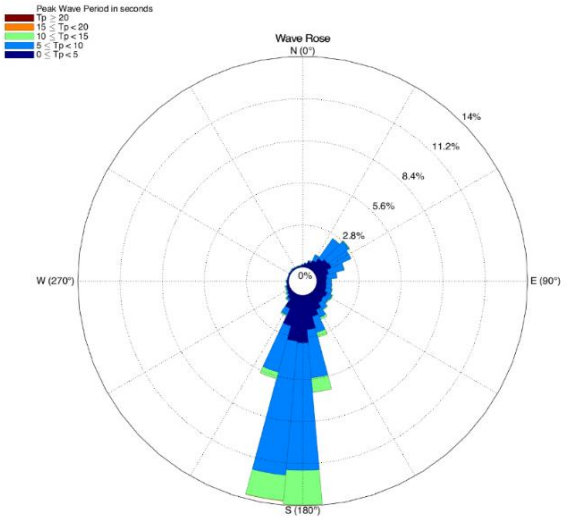
Location 'D' - T_p



Location 'E' - H_s

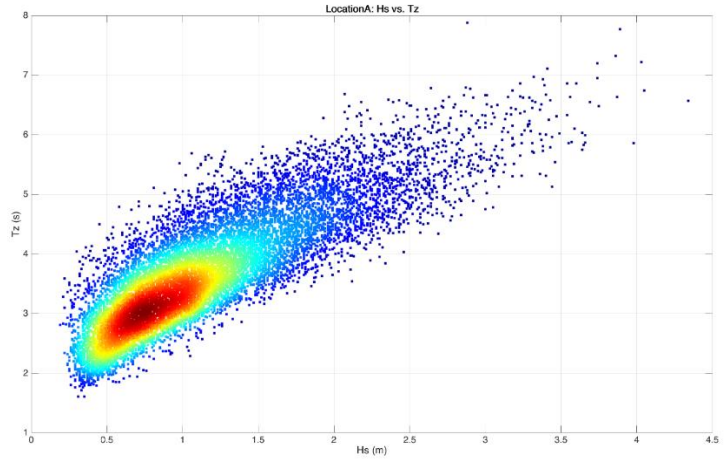


Location 'E' - T_z

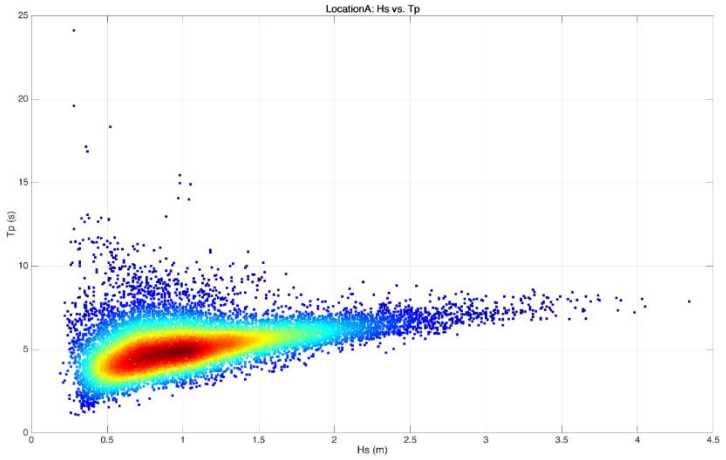


Location 'E' - T_p

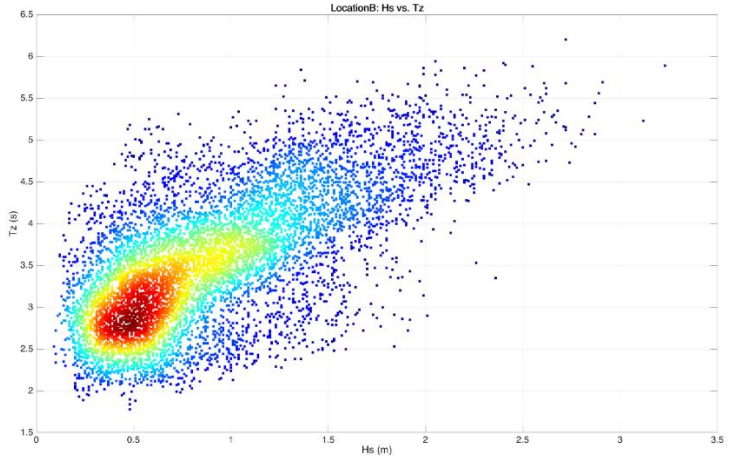
Figure 54. H_s, T_z and T_p presented as a function of direction in the form of a wave rose for each measurement frame location.



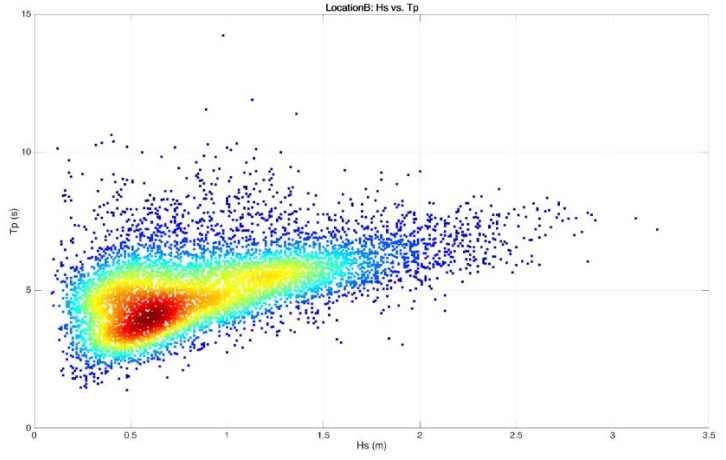
Location 'A' – H_s vs T_z



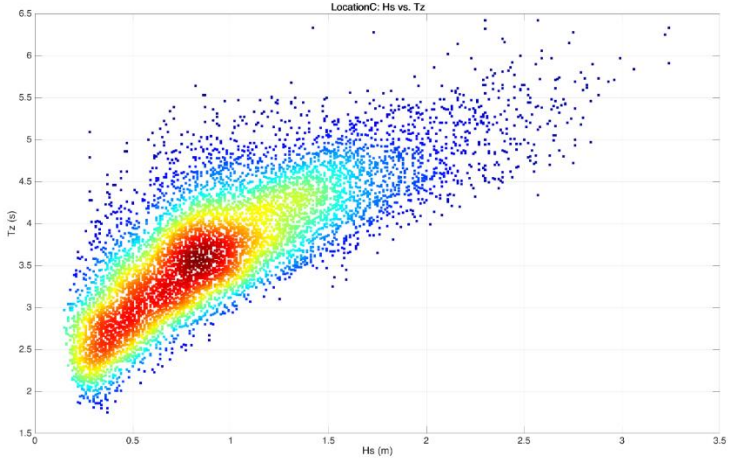
Location 'A' – H_s vs T_p



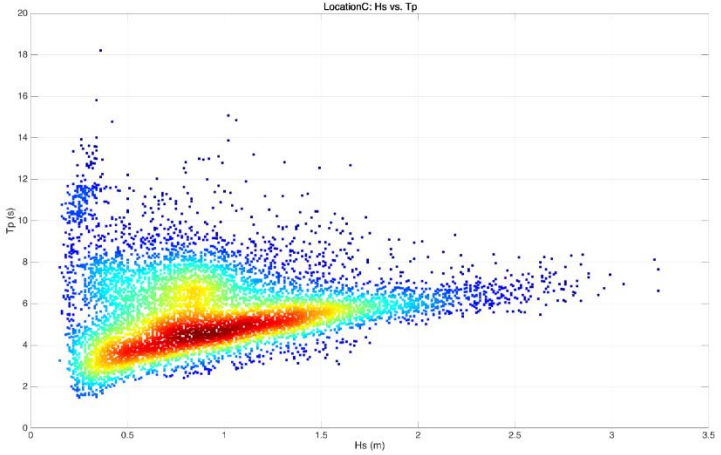
Location 'B' – H_s vs T_z



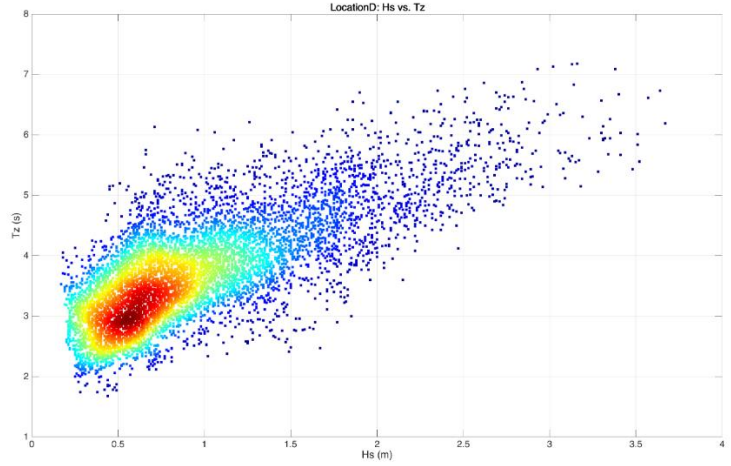
Location 'B' – H_s vs T_p



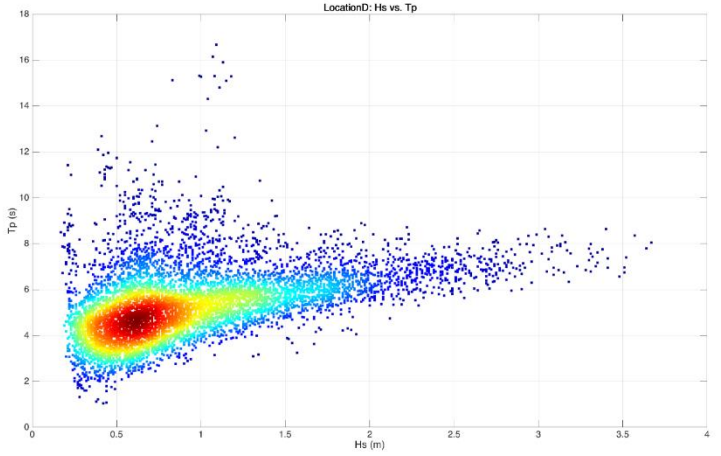
Location 'C' – H_s vs T_z



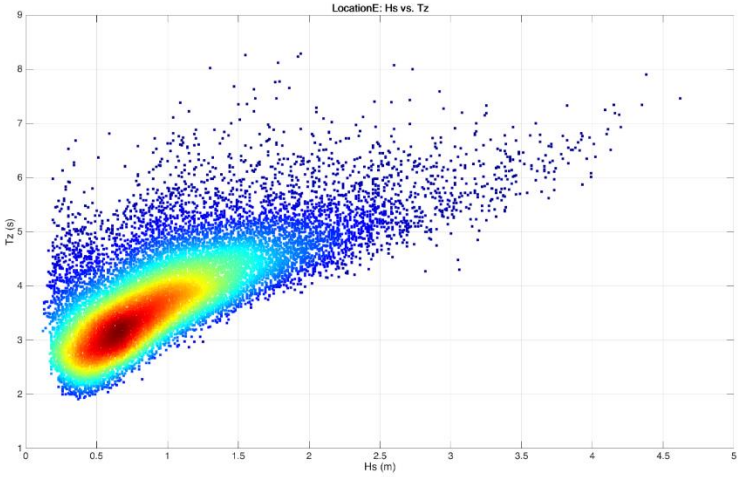
Location 'C' – H_s vs T_p



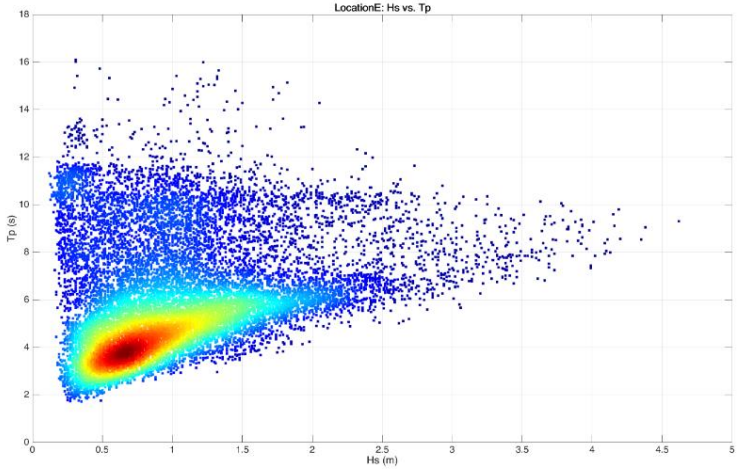
Location 'D' – H_s vs T_z



Location 'D' – H_s vs T_p



Location 'E' – H_s vs T_z



Location 'E' – H_s vs T_p

Figure 55. Scatter plot showing H_s vs T_z (left panel) and H_s vs T_p (right panel).

The highest waves (H_s = > 4 m) were recorded at Location 'E' on 18th December 2019. Figure 56 to Figure 60 presents time series showing the measured wave conditions occurring at each frame location, coincident with the highest energy event (measured at each frame location). As would be expected, variation in the wave conditions is observed between the frame locations, which is both a function of the frames' relative position (to Arklow Bank and to the approaching waves) and the local bathymetry at each frame location (Table 1). In deep water, waves will move across the sea surface without major modification, but as they move into shallower water the orbital motion of the wave through the water column eventually reaches the seabed, where upon frictional drag changes the shape of the wave. Refraction, shoaling (wave steepening) and eventually wave breaking will occur as the waves move progressively into shallower water.

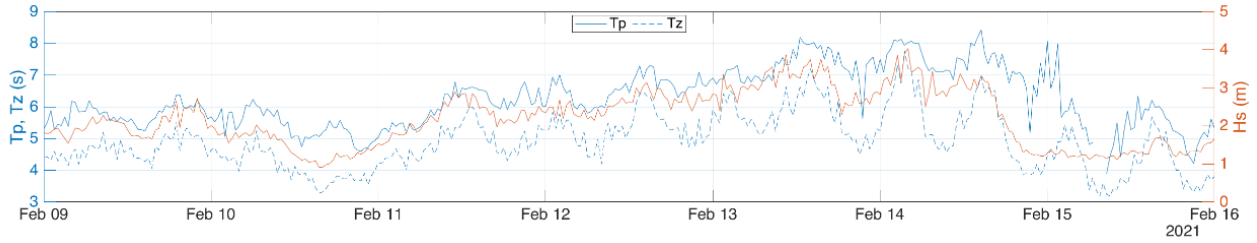


Figure 56. Coincident conditions occurring at frame location A during the largest wave event observed at this frame location during the measurement campaign.

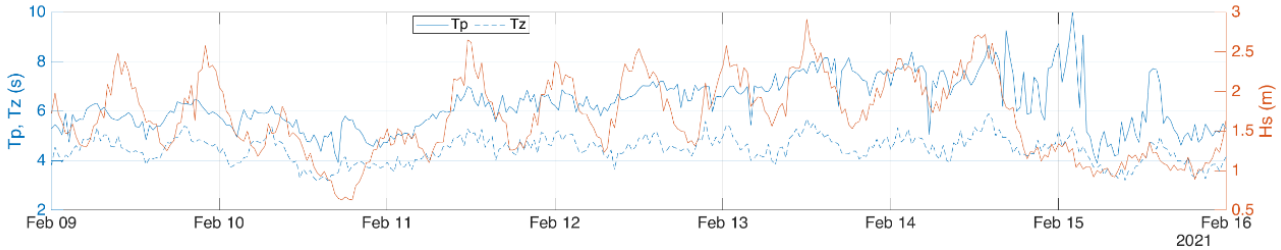


Figure 57. Coincident conditions occurring at frame location B during the largest wave event observed at this frame location during the measurement campaign.

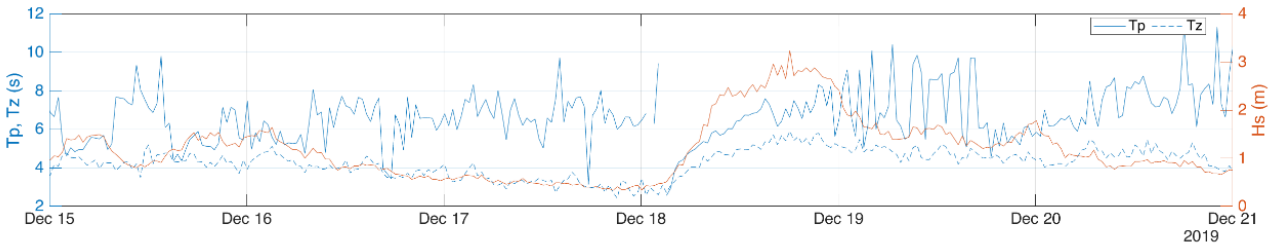


Figure 58. Coincident conditions occurring at frame location C during the largest wave event observed at this frame location during the measurement campaign.

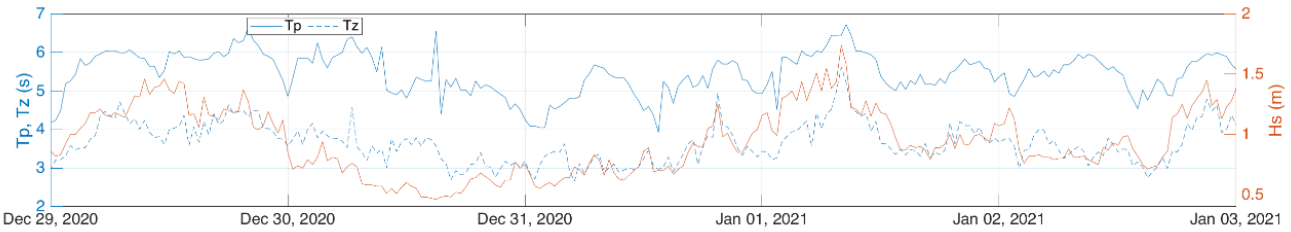


Figure 59. Coincident conditions occurring at frame location D during the largest wave event observed at this frame location during the measurement campaign.

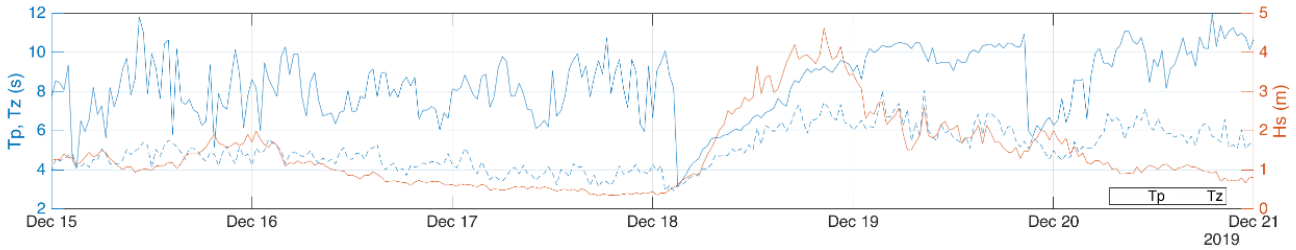


Figure 60. Coincident conditions occurring at frame location E during the largest wave event observed at this frame location during the measurement campaign.

In of itself, that the largest wave conditions occurring at frame location 'A' to the north of the bank, and frame location 'E' to the south of the bank differ through time is indicative of the attenuation, and spatial variation, of wave energy as waves pass along the bank. Consideration of the coincident data from frame location 'C' provides information on wave effects on the proposed cable route at locations inshore of Arklow and Seven Fathom Banks (Figure 58 and Figure 60). Comparing frame location 'E' (to the south of the bank) and frame Location 'C' (along the proposed cable route to the west of Arklow Bank). The maximum wave height recorded during the event was circa 1 m smaller at location 'C', indicating that the bank provided shelter from waves approaching from the E and SE to the adjacent areas nearshore and the coastline. Finally, site B displays distinct tidal modulation in wave height likely associated with a shallow water effect occurring across the bank.

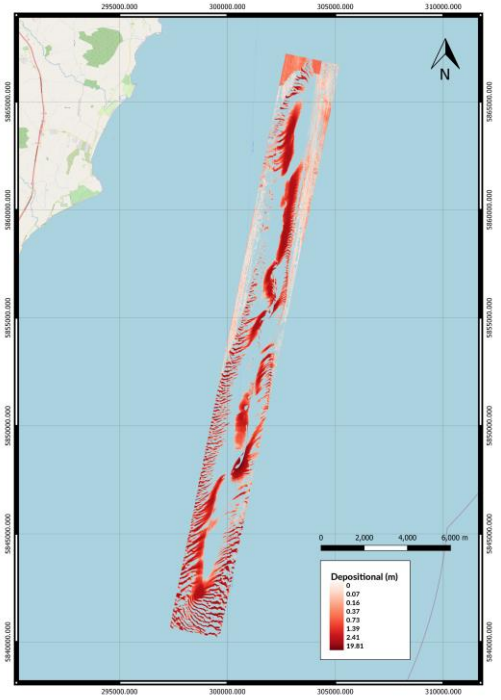
As evidenced by available satellite images, breaking waves occur across the shallowest regions of the bank, which due to the generally small tidal range remains shallow promoting wave influence across the crest. As the bank crest is very shallow in places, wave breaking must also be considered as a potential process for sediment mobilisation and seabed level adjustment. The influence of waves on the sediment transport regime and effects on bank morphology are discussed further in Section 8.6.3.

8.6 Sediment Regime

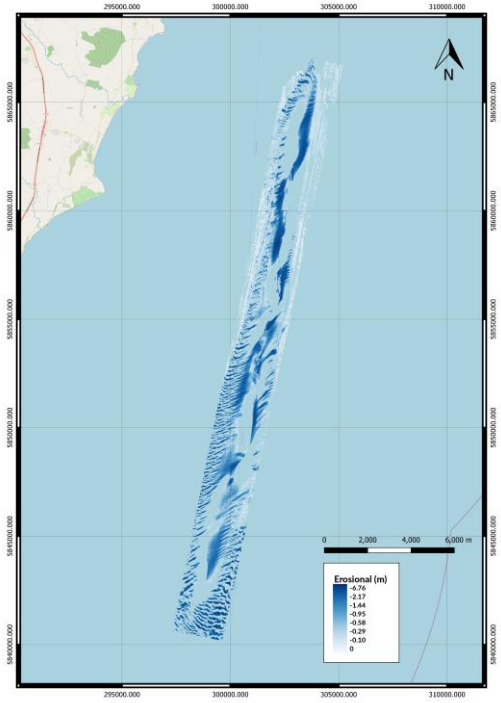
The following sections describe the sediment regime local to the ABWP development site.

8.6.1 Sediment Supply and Budget of the Bank System

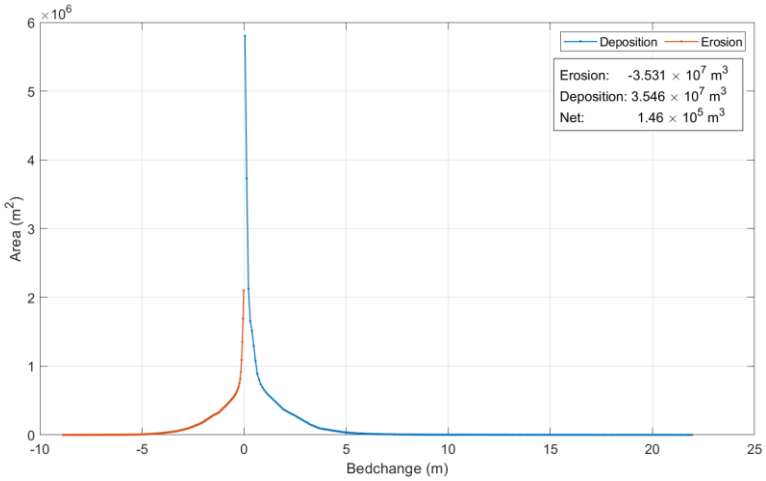
As described in Section 7.3, Arklow Bank does not appear to have a significant contemporary supply of sediment nourishing the bank. To understand this further, a sediment volume analysis was performed to assess potential sediment loss / gain from the bank system. The sediment volume analysis of Arklow Bank over the period 2016 to 2019 is presented in Figure 61 and indicates that the volume of material on the bank between 2016 and 2019 is comparable and thus, considering the regional context, this supports the hypothesis that Arklow Bank is a semi-closed sediment cell. This semi-closed sediment cell is postulated to be characterised by predominant, but limited, sediment supply at the head of the bank to the north with predominant, but limited, sediment loss occurring at the tail of the bank to the south. This relationship between sediment supply / loss from the bank system is in broad equilibrium as demonstrated from the sediment volume analysis (Figure 61).



1.



2.



3.

Figure 61. The sediment volume analysis derived from the 2016 and 2019 bathymetric datasets. Plot 1, and Plot 2, shows the area of deposition, and erosion, in the form of spatial plots, respectively. Plot 3 presents these data empirically to determine the net effect of the deposition/erosion pattern observed between 2016 and 2019.

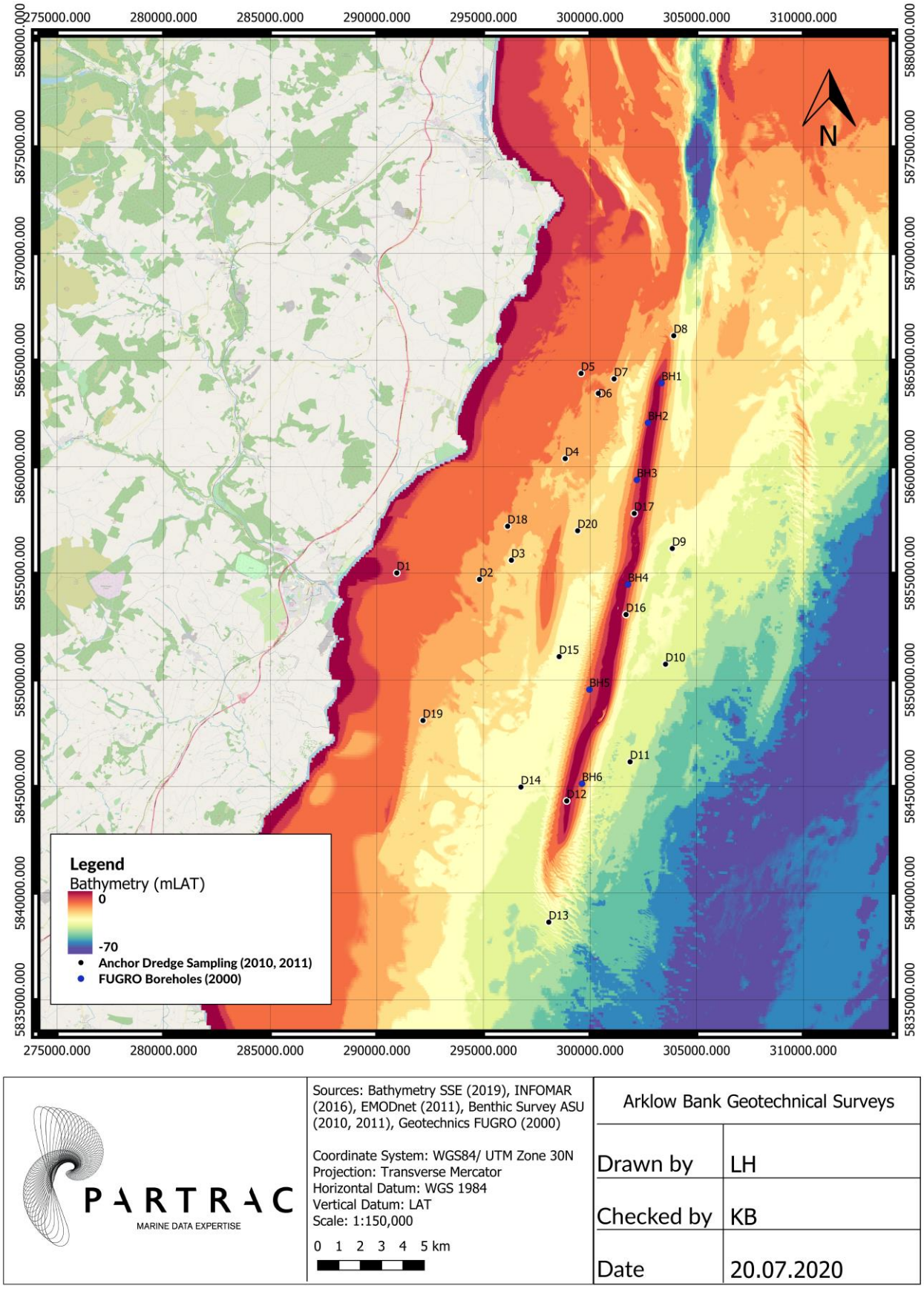
.

8.6.2 Surficial Sedimentology and Shallow Geology

To consider the sediment dynamics on Arklow Bank it is important to consider the properties of the mobile sediments (i.e. surficial, and potentially sub-surface sediment layers). To support Phase 1 of the Arklow Bank Wind Park, and as part of pre-consent activities for Phase 2 of the proposed development, several sediment sampling campaigns have been conducted to characterise the seabed across the lease area and the wider region. Sampling has been conducted as part of geotechnical borehole investigations (Fugro, 2000), geophysical (reported by GDG, 2020) and benthic seabed grab sampling (ASU, 2010 & 2011) surveys. The locations of these samples are plotted on a map in Figure 62. The grain size information derived from the benthic sampling campaign is presented in Table 7. Supporting surficial sediment classifications are available from the Integrated Mapping for the Sustainable Development of Ireland's Marine Resource (INFOMAR) and the British Geological Survey (BGS). The particle size data (classified following the methodology described by Folk, 1954) show the sediments across Arklow Bank are comprised of SAND, gravelly SAND, and sandy GRAVEL[16].

The information derived from site boreholes is presented in Table 8. The analyses revealed a seabed dominantly comprised of poorly sorted SAND and slightly gravelly SAND. A limited silt fraction is observed within the surficial sediments that is likely consistent with areas of near surface or outcropping, highly consolidated glacial till, or glacial clays. A coarser GRAVEL fraction was also observed in several samples, particularly towards the northwest of Arklow Bank. Borehole data collected across Arklow Bank as part of the site investigation for the Phase 1 WTGs provides some supporting evidence for a coarser core material (described in Section 6). Analysis of sediment samples at these locations showed that the surface sediment is primarily comprised of medium sand with sand fractions accounting for more than 80% and a d_{50} value ranging from 0.2 to 0.7 mm. However, at depths greater than 15 m in the three boreholes located towards the north of the bank, the sediment changes to gravelly sand with gravel fractions comprising up to 70% of the bulk sediment; though this is below the depth of the mobile layer, this is potentially further corroborating evidence of the existence of an immobile bank core.

16 Despite these surveys, data gaps persist which are being targeted as part of additional data collection planned as part of the wider GI campaign.



PARTRAC
MARINE DATA EXPERTISE

Sources: Bathymetry SSE (2019), INFOMAR (2016), EMODnet (2011), Benthic Survey ASU (2010, 2011), Geotechnics FUGRO (2000)

Coordinate System: WGS84/ UTM Zone 30N
Projection: Transverse Mercator
Horizontal Datum: WGS 1984
Vertical Datum: LAT
Scale: 1:150,000

0 1 2 3 4 5 km

Arklow Bank Geotechnical Surveys	
Drawn by	LH
Checked by	KB
Date	20.07.2020

Figure 62. The location of the seabed grab samples (ASU, 2010 & 2011) and the borehole locations across Arklow Bank (Fugro, 2000).

Table 7. Particle Size Distribution (PSD) data and textural classification of surface sediments collected as part of the benthic sampling campaign. Source: ASU, 2010 & 2011. The highlighted rows show sample locations positioned on the bank.

Sample	Easting (UTM 30N)	Northing (UTM 30N)	Grain Size (mm)			Buchanan Classification	Folk Classification (Folk, 1954)
			d_{10}	d_{50}	d_{90}		
Sampled June 2010							
D01	290934	5855016	0.125	0.204	2.571	Poorly sorted fine gravelly sand	Gravelly sand
D02	294812	5854715	< 0.063	0.272	> 4.000	Very poorly sorted gravelly muddy sand	Gravelly muddy sand
D03	296308	5855614	0.135	0.197	0.386	Well sorted slightly gravelly fine sand	slightly gravelly sand
D04	298832	5860379	0.152	0.307	0.468	Moderately Well Sorted Gravelly Medium Sand	Slightly Gravelly Sand
D05	299577	5864378	> 4.000	> 4.000	> 4.000	Gravel	Gravel
D06	300386	5863442	0.133	0.263	2.520	Poorly Sorted Gravelly Fine Sand	Gravelly Sand
D07	301126	5864119	> 4.000	> 4.000	> 4.000	Gravel	Gravel
D08	303923	5866145	0.252	0.407	1.200	Moderately Sorted Fine Gravelly Medium Sand	Slightly Gravelly Sand
D09	303854	5856165	0.278	0.923	> 4.000	Poorly Sorted Sandy Fine Gravel	Sandy Gravel
D10	303537	5850736	0.131	0.263	> 4.000	Very Poorly Sorted Fine Gravelly Fine Sand	Gravelly Sand
D11	301875	5846157	0.125	0.284	> 4.000	Very Poorly Sorted Fine Gravelly Fine Sand	Gravelly Sand
D12	298904	5844323	0.167	0.320	0.459	Well Sorted Medium Sand	Sand
D13	298062	5838636	0.198	0.347	0.504	Well Sorted Medium Sand	Sand
D14	296756	5844974	< 0.063	0.137	0.844	Very Poorly Sorted Gravelly Muddy Sand	Gravelly Muddy Sand
D15	298550	5851093	0.184	0.497	> 4.000	Poorly Sorted Sandy Fine Gravel	Sandy Gravel

Sample	Easting (UTM 30N)	Northing (UTM 30N)	Grain Size (mm)			Buchanan Classification	Folk Classification (Folk, 1954)
			d_{10}	d_{50}	d_{90}		
D16	301684	5853065	0.148	0.284	0.467	Moderately Well Sorted Gravelly Medium Sand	Slightly Gravelly Sand
D17	302071	5857808	0.175	0.390	> 4.000	Poorly Sorted Gravelly Medium Sand	Gravelly Sand
D18	296131	5857207	0.184	> 4.000	> 4.000	Very Poorly Sorted Sandy Fine Gravel	Sandy Gravel
D19	292161	5848095	0.160	0.332	0.871	Poorly Sorted Fine Gravelly Medium Sand	Gravelly Sand
D20	299415	5856997	0.182	0.351	1.212	Poorly Sorted Fine Gravelly Medium Sand	Gravelly Sand
Sampled June 2011							
D01	290934	5855016	0.127	0.209	> 4.000	Very Poorly Sorted Fine Gravelly Fine Sand	Gravelly Sand
D02	294812	5854715	0.141	0.289	~ 4.000	Poorly Sorted Very Fine Gravelly Fine Sand	Gravelly Sand
D03	296308	5855614	0.142	0.253	0.457	Moderately Well Sorted Slightly Very Fine Gravelly Fine Sand	Slightly Gravelly Sand
D04	298832	5860379	0.180	0.339	0.496	Moderately Well Sorted Slightly Very Fine Gravelly Medium Sand	Slightly Gravelly Sand
D05	299577	5864378	> 4.000	> 4.000	> 4.000	Gravel	Gravel
D06	300386	5863442	0.162	0.365	2.418	Poorly Sorted Very Fine Gravelly Medium Sand	Gravelly Sand
D07	301126	5864119	0.196	0.851	> 4.000	Poorly Sorted Sandy Fine Gravel	Sandy Gravel
D08	303923	5866145	0.262	0.457	1.563	Poorly Sorted Very Fine Gravelly Medium Sand	Gravelly Sand
D09	303854	5856165	0.158	0.347	1.050	Moderately Sorted Very Fine Gravelly Medium Sand	Gravelly Sand
D10	303537	5850736	0.147	0.559	> 4.000	Very Poorly Sorted Sandy Fine Gravel	Sandy Gravel
D11	301875	5846157	0.116	0.424	> 4.000	Very Poorly Sorted Coarse Silty Sandy Fine Gravel	Muddy Sandy Gravel
D12	298904	5844323	0.137	0.209	0.407	Moderately Well Sorted Moderately Well Sorted Fine Sand	Sand

Sample	Easting (UTM 30N)	Northing (UTM 30N)	Grain Size (mm)			Buchanan Classification	Folk Classification (Folk, 1954)
			d_{10}	d_{50}	d_{90}		
D13	298062	5838636	0.217	0.353	0.556	Well Sorted Slightly Very Fine Gravelly Medium Sand	Slightly Gravelly Sand
D14	296756	5844974	0.116	0.352	> 4.000	Very Poorly Sorted Fine Gravelly Fine Sand	Gravelly Sand
D15	298550	5851093	0.263	0.481	> 4.000	Poorly Sorted Fine Gravelly Medium Sand	Gravelly Sand
D16	301684	5853065	0.132	0.217	0.423	Moderately Well Sorted Moderately Well Sorted Fine Sand	Sand
D17	302071	5857808	0.245	1.276	> 4.000	Poorly Sorted Sandy Fine Gravel	Sandy Gravel
D18	296131	5857207	0.150	0.389	> 4.000	Poorly Sorted Very Fine Gravelly Fine Sand	Gravelly Sand
D19	292161	5848095	< 0.063	0.262	> 4.000	Very Poorly Sorted Fine Gravelly Very Coarse Silty Fine Sand	Gravelly Muddy Sand
D20	299415	5856997	0.200	0.654	> 4.000	Poorly Sorted Sandy Fine Gravel	Sandy Gravel

** The data was originally presented as the percentage passing through increasingly finer sieve sizes. These data have been analysed to determine grain size statistics (e.g. d_{10}, d_{50} and d_{90} values) via a tool managed and operated by British Geological Survey (BGS).*

Table 8. Grain size data obtained from borehole locations as part of the Phase 1 campaign. Data source: Fugro (2000).

Borehole Location	Easting (UTM 30N)	Northing (UTM 30N)	Penetration Depth	Grain Size (mm)			Soil Type (%)				
				d_{10}	d_{50}	d_{90}	Clay	Silt	Sand	Gravel	Cobbles
BH1	303348.7	5863925.76	0.0	0.32	0.70	3.10	0	1	81	18	0
			1.0	0.26	0.50	3.50	0	3	78	19	0
			3.0	0.25	0.41	0.56	0	2	98	0	0
			5.0	0.25	0.41	0.56	0	2	98	0	0
			7.0	0.24	0.43	0.58	0	1	99	0	0
			9.0	0.24	0.38	0.54	0	2	98	0	0
			12.0	0.22	0.43	0.58	0	2	98	0	0
			12.1	0.22	5.50	31.00	0	6	32	62	0
BH1 A	303362.79	5863940.91	11.0	0.10	0.36	0.55	0	8	92	0	0
			14.9	0.28	0.61	2.10	0	3	86	11	0
			20.5	0.23	0.36	0.55	0	1	97	2	0
			22.5	0.32	10.0	18.0	0	3	19	78	0
BH2	302714.17	5862058.04	2.0	0.2	0.32	0.55	0	2	97	1	0
			3.0	0.22	0.35	0.42	0	3	97	0	0
			6.0	0.10	0.35	0.50	0	9	91	0	0
			8.0	0.16	0.35	0.55	0	6	93	1	0
			11.0	0.22	0.30	0.42	0	1	99	0	0
			14.0	0.20	0.32	0.40	0	4	96	0	0
			16.0	0.35	5.90	22.00	0	5	22	73	0
			17.0	0.21	0.36	0.70	0	2	93	5	0
			17.2	0.26	5.10	25.00	0	2	34	64	0
			18.5	n/a	0.01	0.02	35	63	2	0	0
			18.7	0.02	0.02	0.09	2	83	15	0	0
BH3	302195.36	5859379.96	1.1	0.23	0.49	1.80	0	7	86	7	0
			3.0	0.24	0.36	0.78	0	2	96	2	0
			5.0	0.27	0.40	0.88	0	1	95	4	0
			7.0	0.25	0.71	6.90	0	4	67	29	0
			9.0	0.16	0.36	1.00	0	7	91	2	0
			11.0	0.25	0.91	6.20	0	3	69	28	0

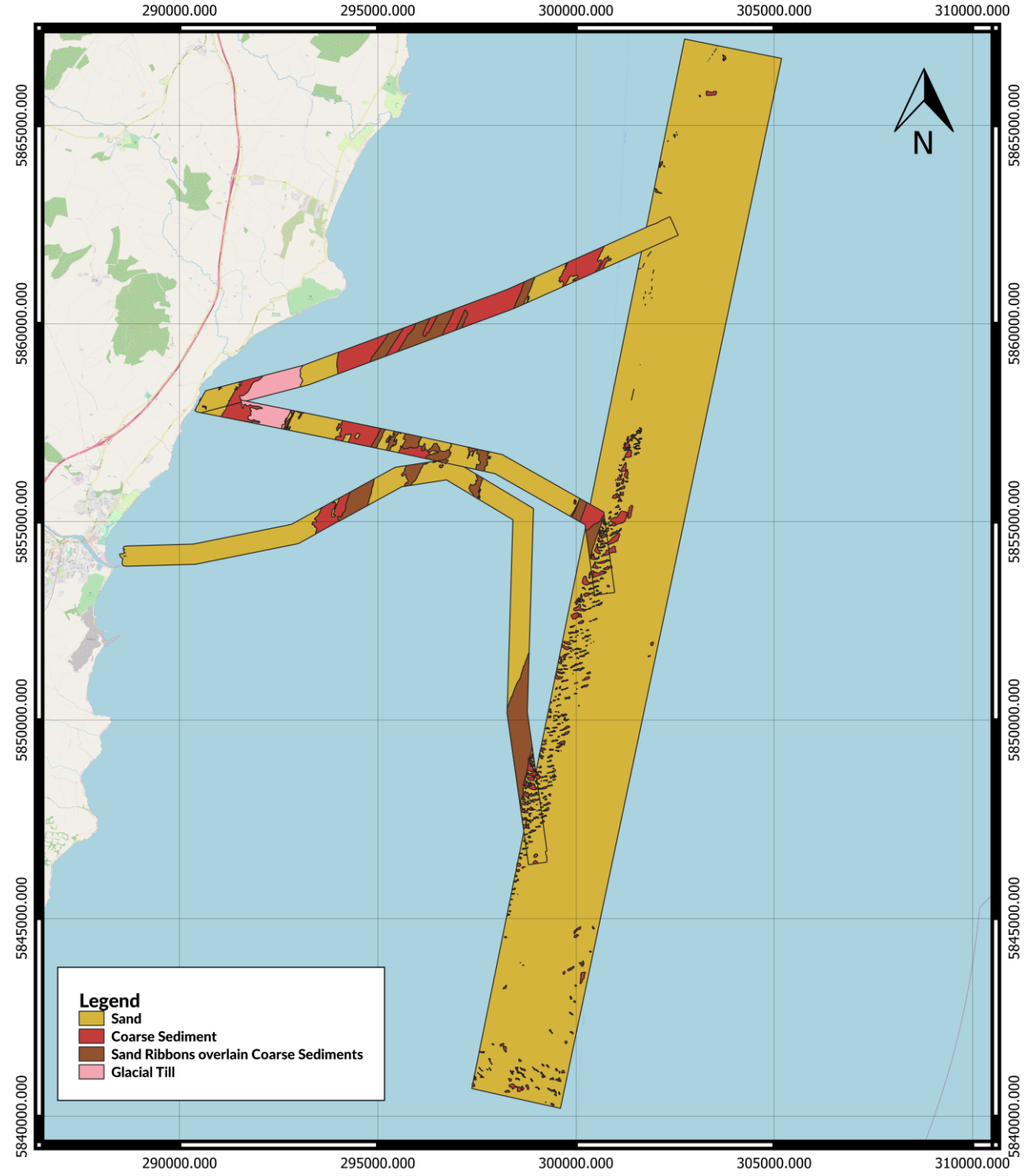
Borehole Location	Easting (UTM 30N)	Northing (UTM 30N)	Penetration Depth	Grain Size (mm)			Soil Type (%)				
				d_{10}	d_{50}	d_{90}	Clay	Silt	Sand	Gravel	Cobbles
			13.0	0.20	0.30	0.41	0	n/a	97	3	0
			15.0	0.20	0.35	1.00	0	6	90	4	0
			17.5	0.20	0.32	0.47	0	2	96	2	0
			19.5	0.25	1.40	17.00	0	6	54	40	0
			22.5	0.36	10.00	21.00	0	1	21	78	0
			24.0	0.20	0.45	0.81	0	3	97	0	0
BH4	301777.61	5854475.67	1.0	0.21	0.37	2.90	0	3	82	15	0
			2.0	0.25	0.70	4.00	0	4	73	23	0
			2.3	0.21	3.00	8.00	0	8	25	67	0
			4.0	0.18	0.25	0.35	0	4	96	0	0
			7.0	0.16	0.24	0.30	0	3	97	0	0
			8.0	0.17	0.25	0.39	0	8	88	4	0
			9.0	0.16	0.31	0.38	0	4	96	0	0
			11.0	0.16	0.25	0.40	0	2	97	1	0
			12.1	0.16	0.24	0.30	0	3	97	0	0
			13.0	0.18	0.30	0.80	0	3	88	9	0
			15.0	0.17	0.29	0.40	0	2	97	1	0
			17.0	0.17	0.32	2.20	0	2	86	12	0
			19.0	0.17	0.25	0.37	0	3	96	1	0
			20.5	0.16	0.30	2.90	0	3	85	12	0
			22.0	0.15	0.45	2.90	0	8	79	13	0
			25.0	0.16	0.28	0.41	0	2	98	0	0
BH5	299970.43	5849543.61	0.0	0.16	0.27	0.40	0	3	96	1	0
			2.5	0.20	0.27	0.45	0	1	96	3	0
			5.0	0.17	0.28	0.45	0	n/a	100	0	0
			7.0	0.20	0.32	0.60	0	2	97	1	0
			9.0	0.19	0.28	0.40	0	3	96	1	0
			11.0	0.18	0.26	0.37	0	1	99	0	0
BH6	299621.08	5845129.69	0.0	0.17	0.25	0.38	0	3	97	0	0
			2.0	0.16	0.26	0.39	0	3	97	0	0
			4.0	0.12	0.26	0.39	0	3	96	1	0
			6.0	0.17	0.24	0.29	0	3	97	0	0

Borehole Location	Easting (UTM 30N)	Northing (UTM 30N)	Penetration Depth	Grain Size (mm)			Soil Type (%)				
				d_{10}	d_{50}	d_{90}	Clay	Silt	Sand	Gravel	Cobbles
			8.0	0.08	0.22	0.29	0	7	93	0	0
			12.5	0.16	0.23	0.29	0	2	98	0	0
			15.5	0.16	0.23	0.29	0	2	98	0	0
			19.5	0.16	0.23	0.29	0	2	98	0	0
			22.0	0.10	0.27	0.40	0	9	91	0	0

In addition to direct sampling of the seabed, the recent geophysical survey has applied AGDS (based on side-scan sonar data) to provide a descriptive interpretation of the seabed into areas with different sediment textures, as follows:

- Sand.
- Sand ribbons overlain coarse sediment
- Coarse sediment.
- Glacial till.

At present, there has been no ground-truthing of the AGDS with grab samples to validate the interpretation of sediment type, however, the main transitions between different textures are likely to remain consistent. The interpreted seabed sediments map is presented in Figure 63 and shows a seabed type across Arklow Bank dominated by sand. Coarser sediments are prevalent along the proposed export cable routes, particularly the most northward route, and in highly localised areas across the bank surficial sediments are typically comprised of sand ribbons. Outcropping glacial till is observed on two of the three proposed cable routes, nearshore. In addition, where there is overlap in coverage from different survey lines (on different dates) there appears to be some conflict in the interpretation. This conflict may be due to an interpretation issue or a rapid seabed morphology that has changed in the intervening period. The present application of this information recognises the relative strengths and weaknesses in this dataset. Additional grab samples are planned to support ground-truthing of the AGDS to address the present weaknesses and improve confidence in this dataset. In particular, to inform a morphological assessment the definition of "sand" requires quantification as a sediment particle size distribution as well as how such values might vary spatially.



PARTRAC
MARINE DATA EXPERTISE

Sources: GDG Seabed Features Study (2019)

Coordinate System: WGS84/ UTM Zone 30N
Projection: Transverse Mercator
Horizontal Datum: WGS 1984
Vertical Datum: LAT
Scale: 1:90,000

0 1 2 3 4 5 km

Arklow Bank Seabed Sediment Features	
Drawn by	LH
Checked by	KB
Date	20.07.2020

Figure 63. The interpretation of the distribution of seabed sediments across the lease and export cable routes (GDG, 2020).

The Sub-Bottom Profile dataset[17] has been analysed and sub–seabed horizons related to several geological units have been identified (see Table 9). These units[18] have been plotted spatially allowing for an appreciation of their relative thickness (GDG, 2020). The thickness of the potentially mobile layers (considered to be Unit 0A and Unit 1) and the potentially non-erodible layer (Unit 2) are presented in Figure 64 and Figure 65, respectively. The thickness of the potentially mobile layer varies spatially, with a maximum interpreted thickness of up to 30 m at the northern end of the bank, reducing to < 15 m at the southern end of the bank. Typically, a thickness of *circa* 10 m is observed across the bank. In isolated areas within the lease area the thickness of this layer reduces to < 5 m (Figure 64). Note: the dark blue areas in the plot indicate areas where no sand exists (interpreted as areas of outcropping [non-erodible] glacial till). The depth of the non-erodible layer ranges between – 10 m to – 70 mLAT (Figure 65).

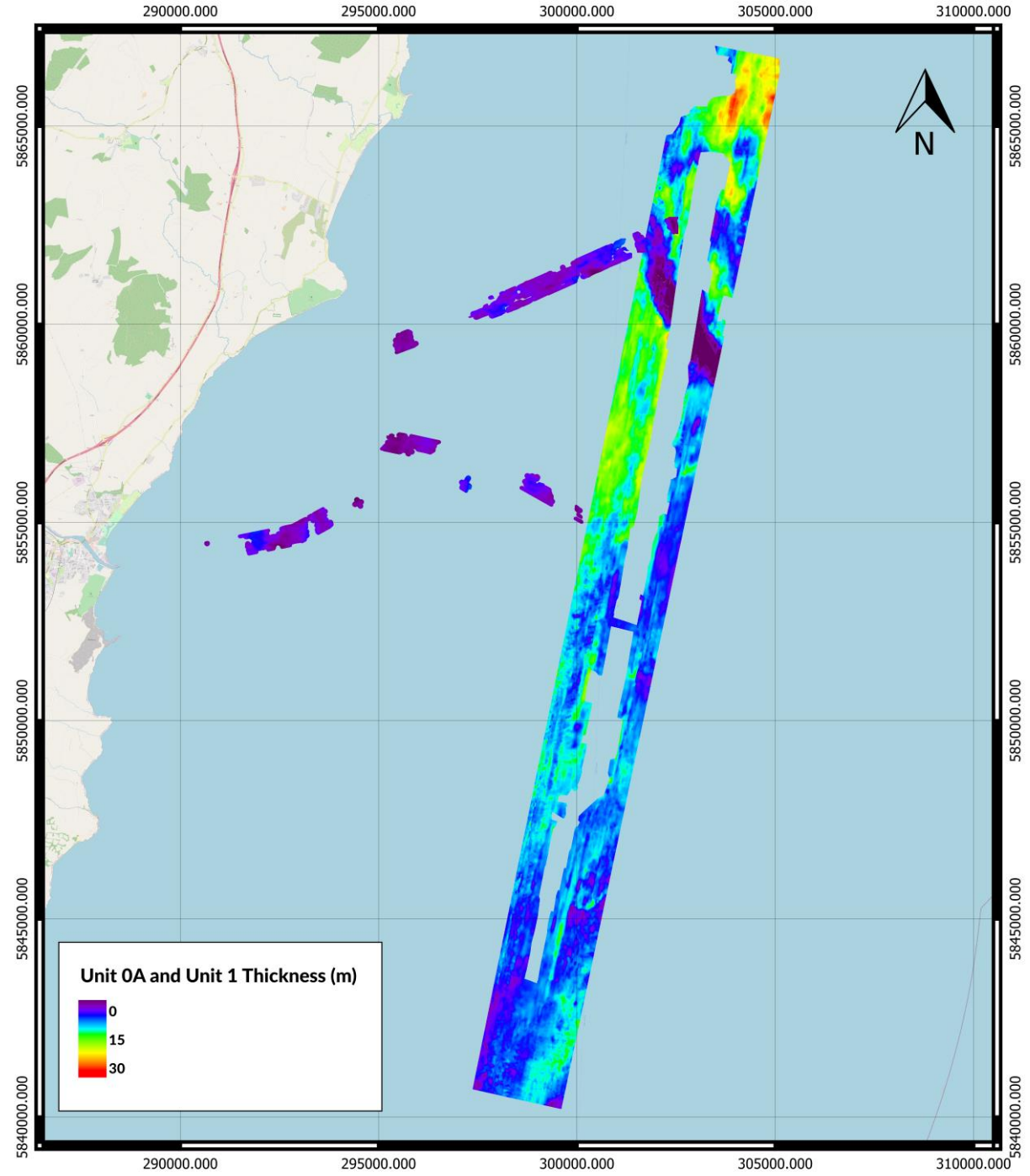
Table 9. Seismic interpretation (reproduced from GDG, 2020). Depths are presented as metres below seafloor (mBSF).

Seismic Units	Interpretation (reproduced from GDG, 2020)
Unit 0	This unit of surficial SAND that overlies Unit 1 is generally present as a veneer on the seabed but has accumulated in places into mobile sediment bedforms such as mega-ripples, sandwaves and sand banks which have been associated with the "Wave and Bank Facies". It has also been identified to fill depressions in the underlying sediment on occasion which have been associated with the "Seabed Depression Facies". In places, currents have shaped the sediment into thin ribbons overlying Unit 1. The unit is mostly acoustically transparent with little to no internal reflections. The unit is interpreted to be comprised of Holocene Sand.
Unit 0A	This unit comprises of channel infill found to the east of CR1, which overlays Unit 1. Top of the unit is marked by a mostly flat and continuous strong reflector. The unit is mostly acoustically transparent with little to no internal reflections. Sediment type is interpreted as Holocene SAND with some GRAVEL content.
Unit 1	It is interpreted that Unit 1 sediment is the product of reworking of the underlying Unit 2, glacial TILL, and is comprised of SAND and GRAVEL. This is observed on seismic data as faint internal reflections with high attenuation close to the seabed. It is likely that this unit is associated with the lag gravels. It is present very close to the seabed over much of the route and when it is close to the seabed it is generally covered by a veneer of Unit 0 sediments.
Unit 2	Unit 2 appears variable in its nature, chaotic in places and transparent in others. It is interpreted that this unit is glacial TILL and is associated with the "Upper Till Facies" of the Cardigan Bay Formation. The unit is suspected to comprise dense and compacted SAND and GRAVEL, with localised lenses of compacted sediment and/or clay, however, the composition of this unit varies across the site and in parts the unit is expected to be more fine-grained than others. It should therefore be noted that, conclusions regarding the composition of the unit are tentative at this stage, and this shall be confirmed as part of the future interim Geotechnical Site Investigation campaign.

17 The dataset is spatially limited with a large data gap coincident with the shallowest regions of the bank evident.

18 The Unit 0 raster file has not been provided to date.

Seismic Units	Interpretation (reproduced from GDG, 2020)
Unit 3	This unit, when resolved, denotes the acoustic basement of the dataset with no deeper reflectors detected, so no comment can be made on thickness. The top of Unit 3 ranges from 14.2 m to 63.8 m depth and no unit outcropping is observed across the Lease Area. Unit 3 is correlated with Unit 3 along the Export Cable Routes (as resolved using SBP Boomer data) and both units are correlated Palaeozoic Rock, which is present across most of the lease area according to BGS.



PARTRAC
MARINE DATA EXPERTISE

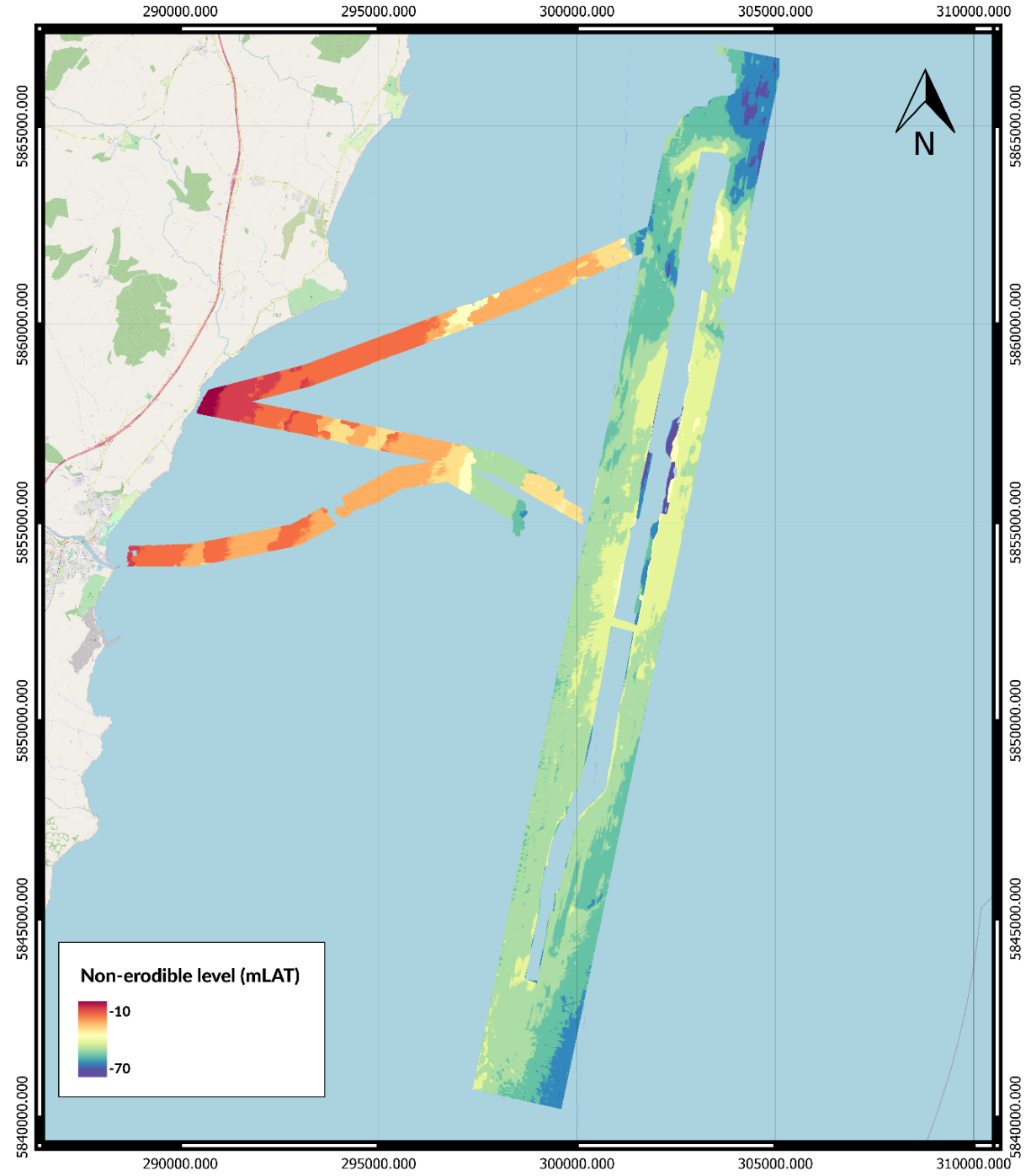
Sources: GDG Seabed Features Study (2019)

Coordinate System: WGS84/ UTM Zone 30N
Projection: Transverse Mercator
Horizontal Datum: WGS 1984
Vertical Datum: LAT
Scale: 1:90,000

0 1 2 3 4 5 km

Arklow Bank Sub-seabed Thickness	
Drawn by	LH
Checked by	KB
Date	20.07.2020

Figure 64. The spatial variation in the thickness of Unit 0A and Unit I (the potentially mobile layers) derived from the interpretation of seismic data. Gaps in the data coincident with the shallowest regions of the bank are evident. Shapefile provided by GDG (2020).



PARTRAC
MARINE DATA EXPERTISE

Sources: GDG Ground Survey (2019)

Coordinate System: WGS84/ UTM Zone 30N
Projection: Transverse Mercator
Horizontal Datum: WGS 1984
Vertical Datum: LAT
Scale: 1:90,000

0 1 2 3 4 5 km

Arklow Bank Non-erodible Level	
Drawn by	LH
Checked by	KB
Date	20.07.2020

Figure 65. The spatial variation in the thickness of Unit 2 (the interpreted non-erodible level) derived from the interpretation of seismic data. Gaps in the data coincident with the shallowest regions of the bank are evident. Shapefile provided by GDG (2020).

The upper unit boundaries have been ground-truthed against data retrieved from 6 boreholes (and six CPT's) obtained as part of the Phase 1 campaign (GDG, 2020; Fugro, 2000). An overview of the borehole logs is presented in Figure 66. A CLAY, SILT or Cobbly CLAY was sampled in borehole 1 and borehole 2 at depths below seafloor of -17 m thought to be glacial till (Figure 66). In borehole 1, borehole 2 and borehole 3 the presence of gravel sediments increases with depth (Table 8). The data derived from the interrogation of the sedimentological data and the interpretation of geophysical data corroborate the conclusion that an entirely immobile bank 'core' comprising glacial sediments (compacted till, coarse gravels etc) overlain bedrock, persists, at least partially, across the lease area (GDG, 2020). This immobile core likely anchors the bank to the seabed maintaining the position of the bank relative to the coastline.

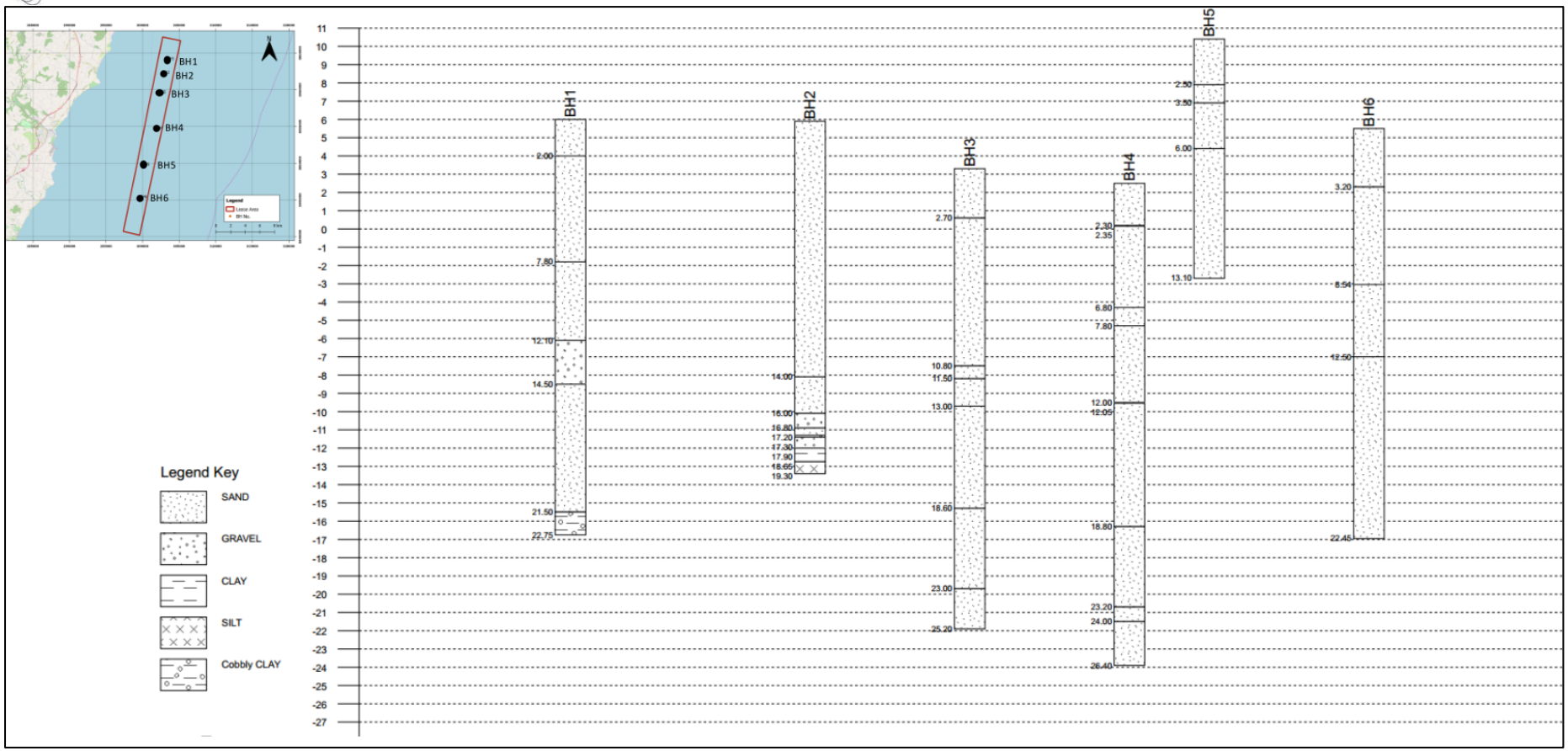


Figure 66. Overview of borehole logs obtained during the Phase 1 campaign. Figure reproduced from GDG, 2020.

8.6.3 Sediment Mobility

Seabed sediments are susceptible to entrainment and transport, either as bedload or suspended load (dependent on sediment grain size), by tidal currents. This occurs when the frictional drag (the 'bed stress'; τ) exerted by currents and waves, separately (e.g. during summer months when wave action is negligible), and in combination (e.g. during winter storms), exceeds the submerged weight of particles, which acts to retain particles on the bed. The stress at which sediment motion is first produced is called the 'critical bed stress', denoted τ_{crit}. When τ exceeds τ_{crit}. (i.e. $\tau > \tau_{crit}$) sediments are mobilised and transported in the direction of the prevailing flow. Through time, a mobile seabed often triggers a morphological response (i.e. an adjustment of the seabed level) which can be manifested as a positive topographical change through time (via the formation of bedforms) or give rise to a general seabed lowering; each are dependent on the sediment supply to the area. The term (τ - τ_{crit}) defines the 'excess bed stress'. Lower values of this metric may be regarded as indicative of relatively low rates of sediment transport, whereas larger values of this metric would drive greater rates of sediment transport, and thus, potentially greater adjustment at the seabed. To assess the likely response of the seabed through time it is critical to understand net sediment transport which is a function of asymmetry in the flow regime during periods of excess bed stress. The frictional drag at the seabed on flow motions (waves or tides, separately or in combination) is parameterised by the 'bed shear stress'. If the coincident components of flow are not known, consideration of bed stress provides no information, per se, on sediment transport direction (aside from gradients), however, insofar as it represents the local energy driving sediment movement it shows areas where it may be expected sediment transport is more / less intense, and (by extension) the magnitude, and rate, of bed level change may be expected to be higher / lower.

Figure 67[19] shows the spatial variation of maximum bed shear stress (i.e. the highest value of stress) impacting the seabed during spring tides. The maximum tide-only bed shear stress shows an axial gradient, generally increasing in magnitude along the crest of the bank from south to north (this is a function of the increased tidal range moving away from the amphidromic point located to the south of the bank); further, the region of greatest bed stress is broadly bounded by the 10 m contour, with lower values typically observed in deeper areas. Bed stress values can reach up to about 50 N/m^2 near the bank crest and toward the north of the bank; these are sufficiently powerful to entrain, and transport, sandy gravels / gravelly sands. It should be noted that, if the sediments which comprise the seabed are mobile under the prevailing regime, the high bed shear stress area near Wicklow Head agrees with the hypothesis of sediment supply source from the north of the bank. In the region around the bank, Figure 67 shows broadly lower bed stresses (except around the major headlands) but which are nevertheless capable of mobilising fine and medium sands. A pattern of spatial heterogeneity is recognisable, with areas to the north and northwest of the bank, and areas

19 To develop the plot, an entrainment threshold for surface sediments of 0.2 N/m^2 is applied within the model which represents a grain size of 0.35 mm (this value is within the range of d_{50} found in many boreholes along the bank, see Fugro 2000).

farther to the east of the bank, exhibiting slightly higher bed stresses. The distribution of bed stress supports the hypothesis of a northern source of sediments to the bank, and a generally less dynamic, less mobile body of sediments between the bank and the coast.

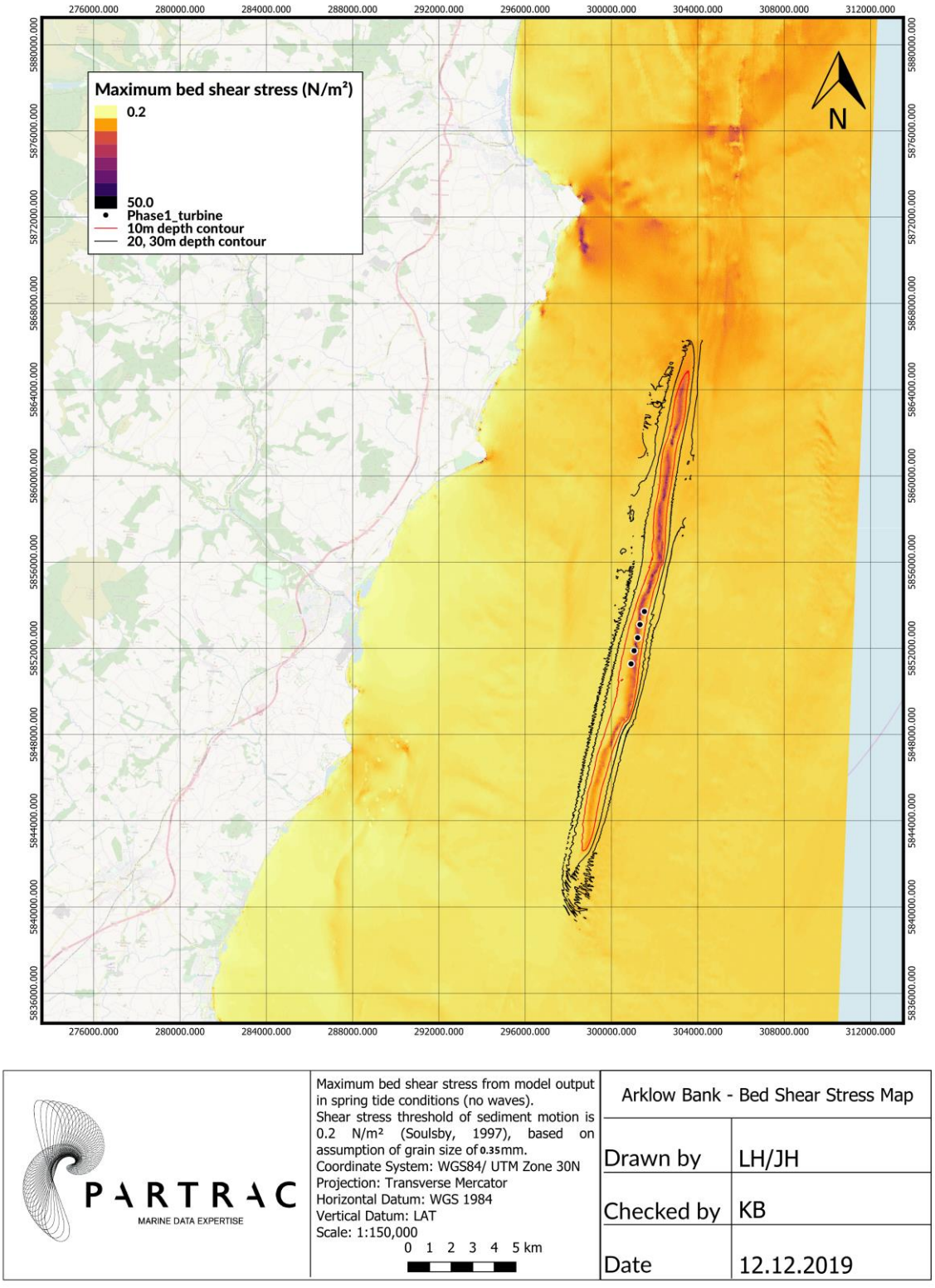


Figure 67. Hydrodynamic model outputs. Maximum bed shear stress on spring tide only (without wave action).

A review of previous efforts to characterise, and model, sediment transport on Arklow Bank indicates that where water depths are < -10 mLAT the sediment transport regime appears to be highly dynamic, particularly in the southern portion of the bank where net transport of sediment in an easterly direction was observed (Panigrahi *et al*. 2009). Comparatively, in the northern and central portion, the bank appeared to be slightly less dynamic with net transport towards the west, which is gradually reshaping the bank profile above the 5 to 10 m depth contour (Panigrahi *et a*l. 2009). It is noteworthy that it was concluded that bedforms were generally scarce along the crest of the bank[20], a conclusion which does not reflect the latest bathymetry from the site but does provide further corroborating evidence indicating that the top of the bank is within the wave-influenced region, and thus the sediments in this locale are routinely reworked by wave action (Panigrahi *et al*., 2009). Despite a dynamic sediment transport regime, previous morphological modelling efforts (e.g. Ramboll, 2002 and Panigrahi *et al*. 2009) indicate that, generally, the bank appears to be 'dynamically stable' with the northern, central, and southern parts of the bank characterised by average bed level changes on the order of ± 0.08 m per day[21].

To further assess the mobility potential[22] of seabed sediments, the critical threshold for sediment mobilisation due to currents (Ucr[23]) was determined utilising seabed composition data derived from grab samples collected near to each frame location. The critical threshold is compared to the observed current velocities and presented in the form of time series in Figure 68 to Figure 72. The percentage time where U_{cr} is exceeded is presented in Table 10. These data reveal sediments are routinely mobilised under the prevailing flow regime (Figure 68 to Figure 72). Through the measurement period, asymmetry is clear, which results in clockwise circulation of sediments around the bank. Either side of the bank, the duration of time the threshold for mobility was exceeded was greater during the ebb and flood phase on the east (frame location 'D') and west (frame location 'B') side of the bank, respectively (Table 10). Typically, shear stress is strongly dependent upon the water depth with the greatest stress observed coincident with the shallowest areas. (Note: within this analysis, only the stress acting on the bed at each frame location is determined). The analyses of the data acquired during the metocean measurement campaign presented in Figure 68 to Figure 72 reveal that the threshold for mobility of surficial sediments was exceeded, and thus surficial sediments are mobilised

20 This may be a function of data quality noting in 2009 high resolution MBES was not available.

21 Where non-linear processes influence seabed levels presentation of data in terms of a rate can be misleading and thus should be treated with caution, as though the rate of change may be low, the net effect may be severe.

22 These sediment size fractions (and the threshold mobility criteria, U_{cr}) do not accurately represent the sediment transport regime occurring across the lease area, rather the analysis provides an indication of the mobility potential of sediments across the site. These analyses do not account for processes occurring at the bed such as compaction and/or armouring of the bed which act to reduce the mobility potential of seabed sediments and the dominantly mixed seabed composition. However, this approach, enables a nominal but quantitative assessment of the mobility of various grain size fractions on the seabed under the forcing applied by local flow conditions. These data, considered with other available lines of evidence and within the context of its limitations, provides a useful tool by which to assess the mobility potential of an area of interest on the seabed.

23 U_{cr} was computed using the coefficients presented by Soulsby (1997) (see Appendix C).

on each tidal cycle[24]. This *'live bed'* scenario at these deep-water locales reveals a cyclic, tidally driven transport cycle. Limited asymmetry was observed at frame location 'C' located in the nearshore, between the bank and the coastline.

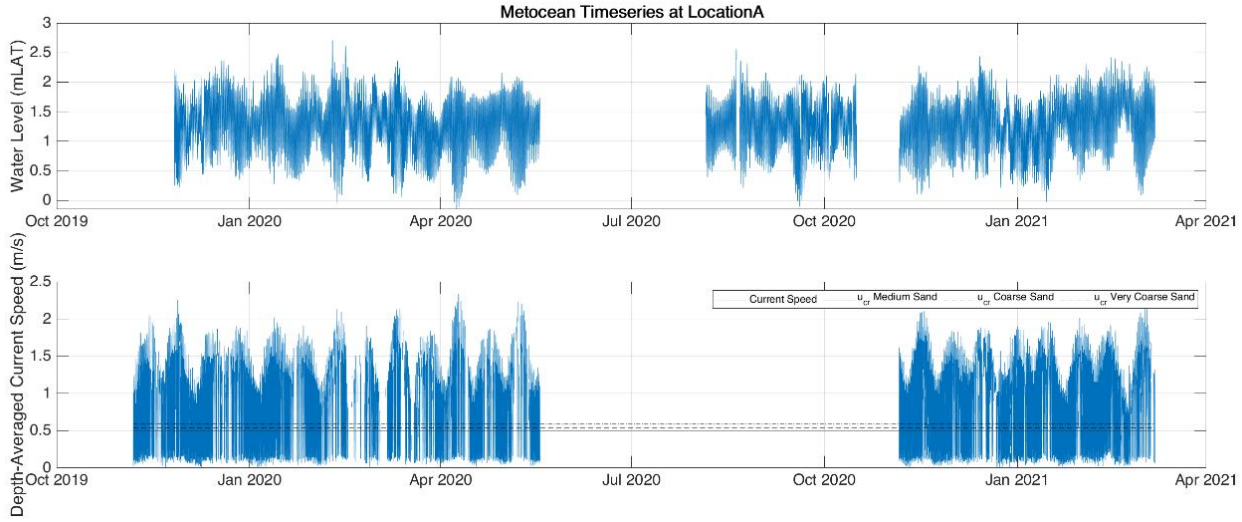


Figure 68. Time series showing the water level and current speed at frame location A. The coincident stress due to currents is also plotted.

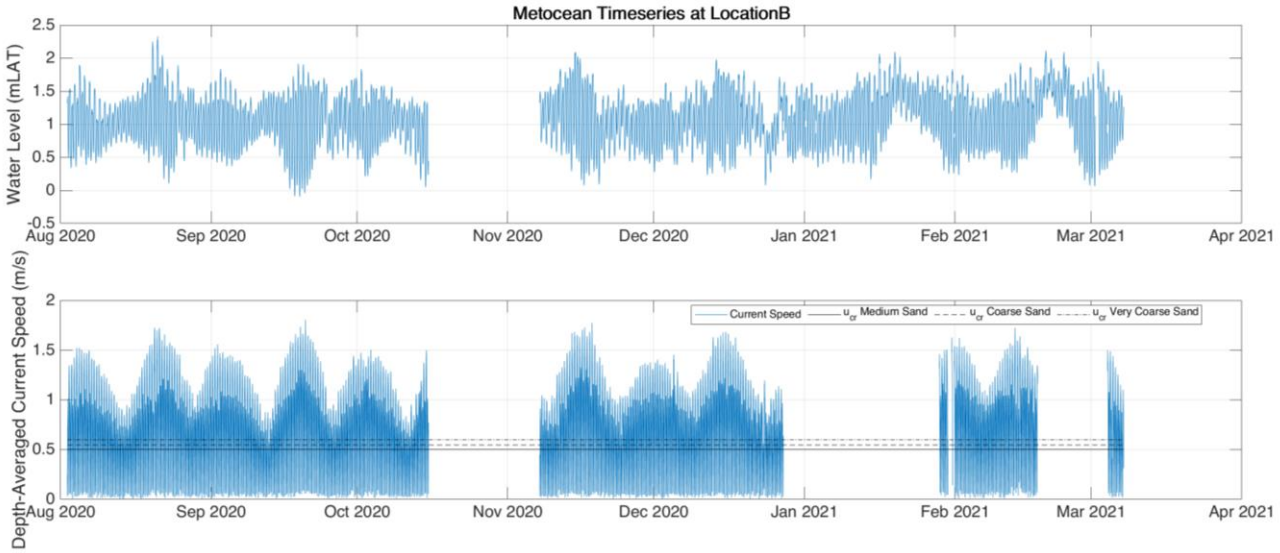


Figure 69. Time series showing the water level and current speed at frame location B. The coincident stress due to currents is also plotted.

24 The shear stress exceedance analysis only indicates the duration of the exceedance of the critical threshold for mobility; this is indicative of a flood or ebb dominance however net sediment transport is not simply a function of the duration of exceedance it is also a function of the flow velocity magnitude.

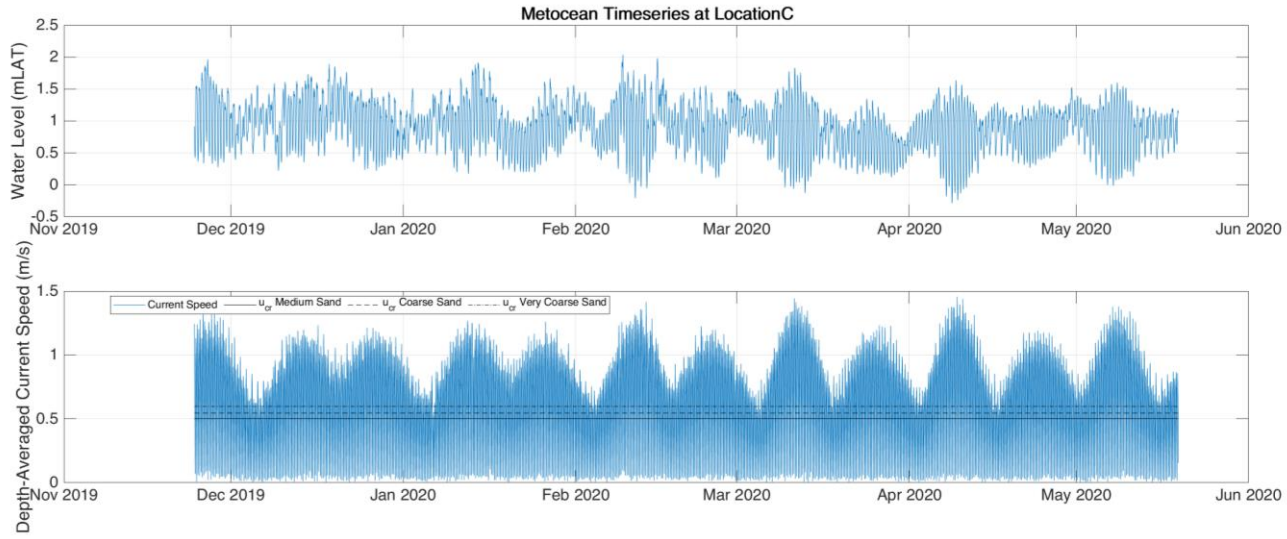


Figure 70. Time series showing the water level and current speed at frame location C. The coincident stress due to currents is also plotted.

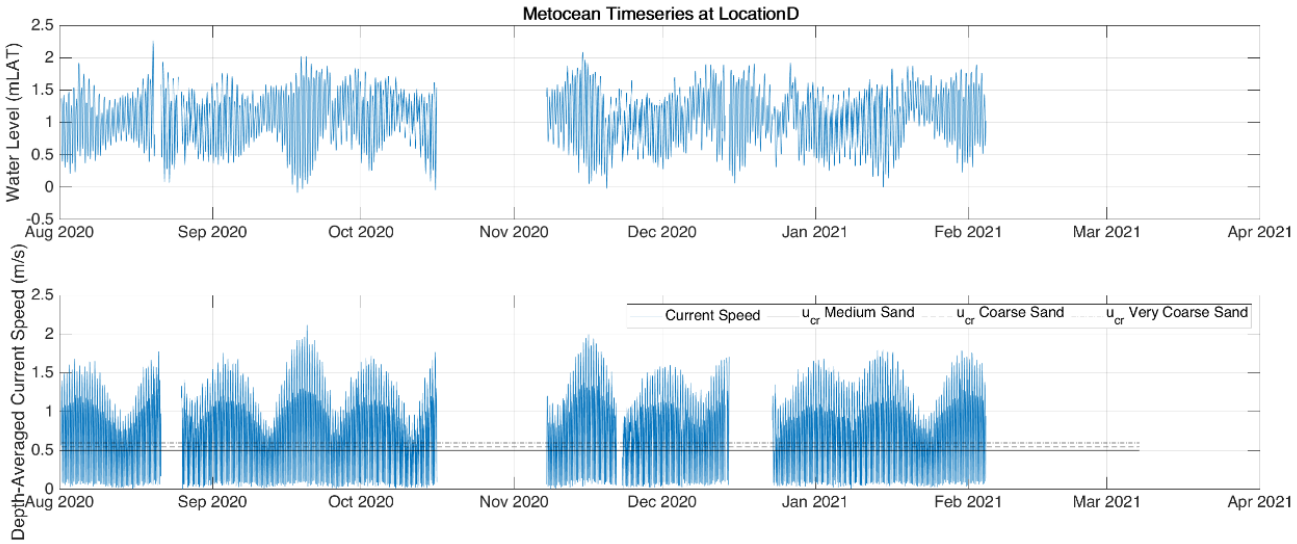


Figure 71. Time series showing the water level and current speed at frame location D. The coincident stress due to currents is also plotted.

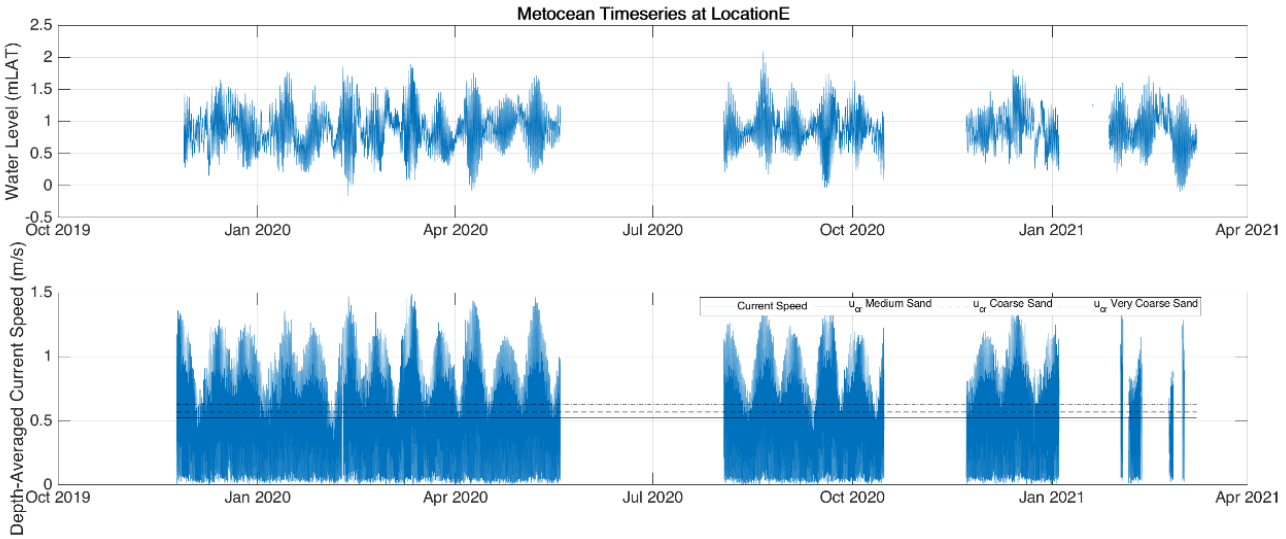


Figure 72. Time series showing the water level and current speed at frame location E. The coincident stress due to currents is also plotted.

Table 10. Grain size information and shear stress thresholds applied as part of the stress exceedance analysis. Note: when comparing relative mobility between sites this is principally a function of water depth.

Frame Location	Nearest Sediment Sample	Particle Size (mm)			Shear stress threshold (N m^{-2})			% time threshold exceeded (due to currents only)		
		d_{10}	d_{50}	d_{90}	$\tau_{cr,10}$	$\tau_{cr,50}$	$\tau_{cr,90}$	Flood Phase	Ebb Phase	Total
A	D8 & BH1	0.26	0.43	1.38	0.19	0.24	0.71	29.50	28.85	58.35
B	D17 & BH3	0.12	0.55	4.80	0.15	0.28	3.80	29.23	20.01	49.24
C	D3 & D18	0.14	0.20	0.39	0.16	0.18	0.23	32.46	32.17	64.64
D	D9	0.10	0.20	0.98	0.14	0.17	0.47	19.79	29.12	48.91
E	D12 & D13	0.18	0.31	0.48	0.17	0.21	0.26	22.50	9.97	32.47

Wave driven sediment transport processes are a function of the wave approach, wave height and (crucially) wave period. Whereas the energy of a wave is proportional to height, the period of the wave determines the depth of influence of wave energy, i.e. how deep the energy of the wave penetrates below the sea surface. Thus, over a large sediment body such as Arklow Bank, wave period is a primary consideration on the horizontal and vertical spatial extent over which waves may induce sediment mobilisation. Consequently, swell waves, associated with greater wave periods (defined here as > 8 s), are a more significant driver of sediment transport, capable of mobilising and resuspending (finer grade) sediments over greater range of water depths (noting here that the site is dominantly exposed to lower period wind waves). The influence of waves and storms on the local sediment transport regime and morphological response of the bank was originally hypothesised to be significant, especially in shallower parts of the bank along the crest. It was also postulated that the more regular lower energy events had the potential to be

constructive and the infrequent higher energy events would be destructive (i.e. these events serve to add or remove material from the sandbank, respectively), and those breaking waves may act to sweep material along the bank in a process analogous to longshore drift observed at the coast. To judge the effects of waves on the bank, and to help understand those areas of the bank expected to be more dynamic as a result of wave processes, several specified data visualisations were obtained from the ABMS. This included the spatial distribution of the maximum wave orbital velocity at the seabed, during *'Typical (P_{50}) conditions'*, determined from the hindcast data record as 0.7 m wave height with a 5.1 s period, approaching from the south. This spatial plot is presented in Figure 73[25]. There is high correlation between wave orbital velocity with the water depth. During typical conditions the wave 'active' area, or spatial extent over which wave energy capable of mobilising sediments on the bank, is bounded within the - 10 mLAT depth contour, suggesting that the waves under typical everyday conditions penetrate to such water depths. Note that over substantial areas of the seabed to the east, north and west of the bank (except in the shoreline zone) wave energy during typical conditions does not penetrate to the seabed since water depths are higher.

25 This analysis is based on linear wave and monochromatic wave assumption given in many theoretical simplified formulae (see Soulsby, 1997), and represents only orbital velocities above that required to represent suspension of 0.35mm sand (u_{orb}>0.1 m/s).

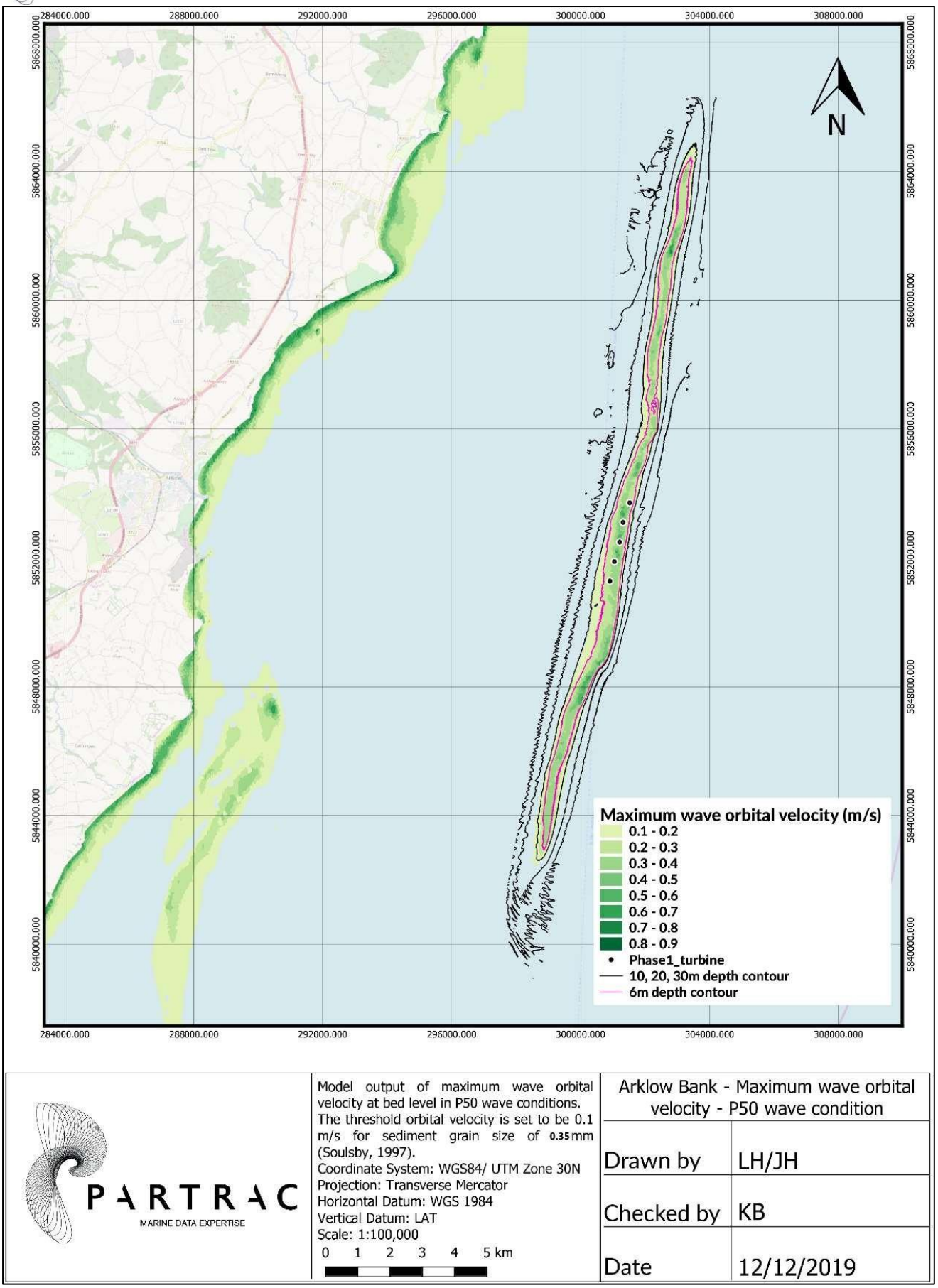


Figure 73. Maximum wave orbital velocity at the seabed during typical 'p50' wave conditions.

Despite high energy swell wave events being statistically rare, to investigate wave influence across the bank further, using established extreme value theories, wave heights were extrapolated from the model hindcast to investigate the possible range of wave heights that could be expected to occur at extreme return periods. The extrapolation was conducted for waves from all directions, and so the values presented are omni-directional despite the foregoing analysis confirming that larger wave heights are predominately associated with waves arriving from the south. Alongside the analysis of extreme wave heights, the associated wave periods were calculated by fitting a log-normal distribution to binned H_s data and calculating the mean and variance of the distribution to provide central estimates of wave periods associated with the extreme waves. The estimated extreme wave parameters to the north and south of the bank are presented in Table 11.

Table 11. Estimated omni-directional extreme wave parameters.

Return Period (Years)	North of Bank			South of Bank		
	H_s (m)	T_p (s)	T_z (s)	H_s (m)	T_p (s)	T_z (s)
1	3.8	9.2	6.8	4.6	10.0	7.0
10	4.8	10.2	7.7	5.8	10.9	7.8
50	5.5	10.8	8.4	6.7	11.5	8.3
100	5.7	11.0	8.6	7.1	11.7	8.5

Modelling of the 1:50 year event (noting that the lease period is 40 years) indicated that during storm events, wave energy penetrates to deeper areas on the bank, to around 30 m, slightly deeper in some areas (Figure 74). Cross-crest asymmetry in terms of wave influence is evident with higher values down the entire length of the crest on the seaward facing (eastern) side and down the eastern flank of the bank. Off the bank itself, the 1:50 year return event is sufficiently powerful to mobilise bottom sediments (0.35 mm sand fraction) almost everywhere, including across Seven Fathoms Bank and along the proposed export cable routes.

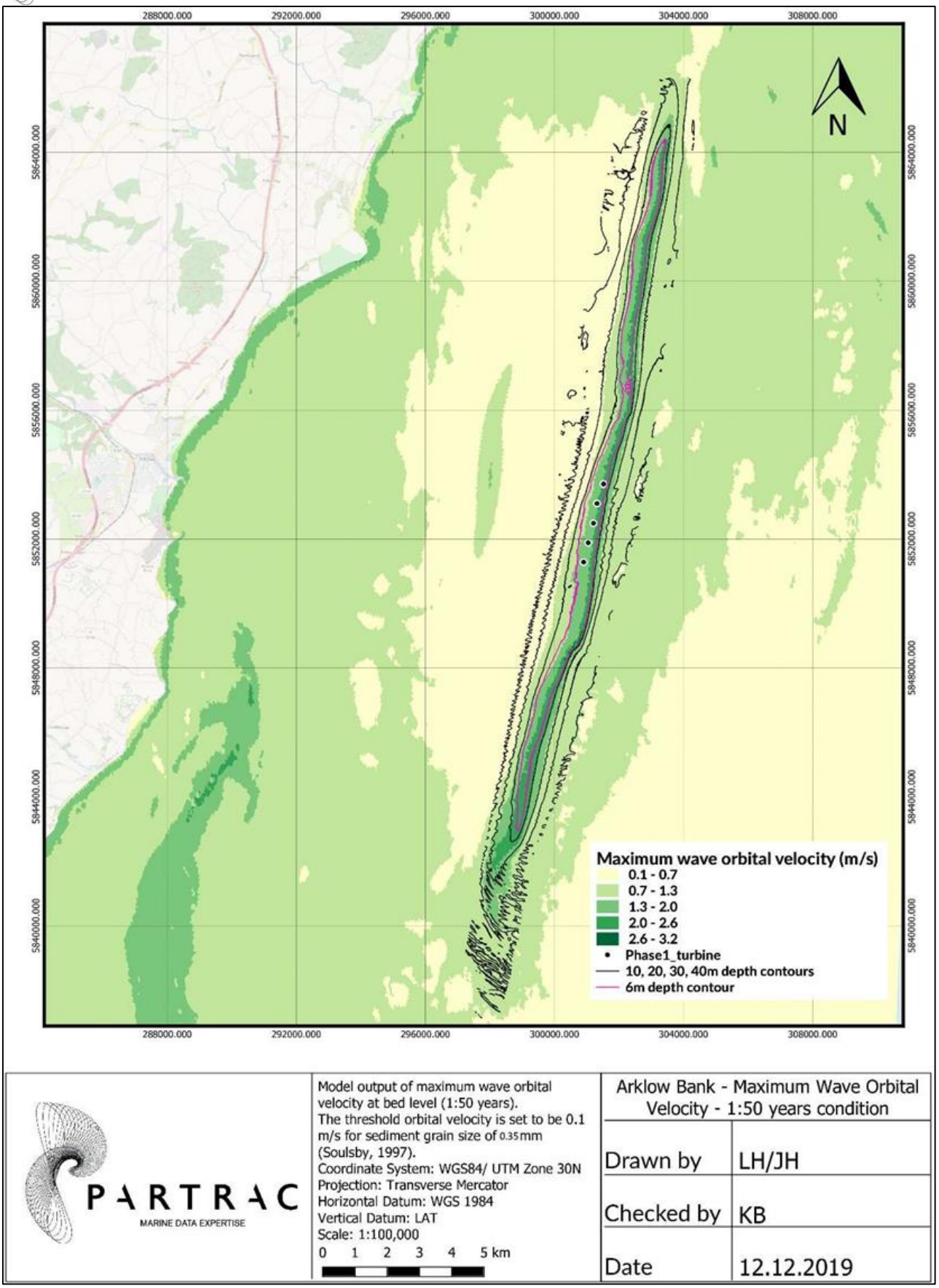


Figure 74. Maximum wave orbital velocity at the seabed during the 1 in 50 years wave conditions.

As the sediment transport regime is tidally dominant and characterised as a 'live bed scenario' and due to the episodic nature of wave events and spatial variation of wave influence, wave action likely plays a potentially limited role in the sediment transport regime occurring within the bank system. The evidence indicates that waves, only on occasion, possess sufficient energy to mobilise seabed sediments at water depths greater than the –10 mLAT contour and thus, conceptually, combining these data and observations, suggests that the -10 mLAT depth contour is an appropriate datum above which the bank can be considered to be highly dynamic and mobile on a regular basis, and then more so as waves impact the bank and storms track over the site.

These assertions are further corroborated by the analyses of the turbidity[26] data from the measurement campaign which was interrogated for signal response to driving processes (e.g. wave action). Turbidity data (nominally expressed as FTU[27]), is routinely used to estimate Total Suspended Solids (TSS) concentrations within the water column via a regression analysis of turbidity versus TSS concentration (in milligrams per litre[28]). Turbidity data over the full measurement period, and during periods of high wave action, are presented in the form of time series in Figure 75 to Figure 79. The following points are noteworthy:

- Generally, at each frame location, there is high correlation between observed turbidity and the tidal currents with no time lag observed.
- There is limited correlation between observed turbidity and wave action and thus these data indicate that waves have a limited role in mobilising and transporting sediments at each of the frame locations. Interestingly, on occasion waves do appear to trigger a re-suspension event with sensors at frame location 'B' postulated to have captured a pulse of wave generated suspended sediment swept off the shallower bank crest where wave influence is far greater.

This evidence corroborates the hypothesis that wave action has a limited, and transient, effect on the sediment transport regime and bank morphology at water levels deeper than the –10 mLAT contour; an important conclusion when considering the potential response of the bank into the future and the optimal approach for modelling such processes. The largest storms display a significant influence on the seabed, however, as these occur infrequently their relative contribution to bank morphology is highly limited.

26 The increased 'murkiness' of a water body due to either suspended particulates (both mineral and biological) in the water column, or discoloration of the water body which, acts to reduce the depth of light penetration through the water is referred to as turbidity.

27 Turbidity units have no intrinsic physical, chemical, or biological significance.

28 Caution is urged when considering the turbidity data as the conversion of data from NTU to mg/l was developed from generally sparse water samples and the regression fit was low (r^2 value of circa 0.7).

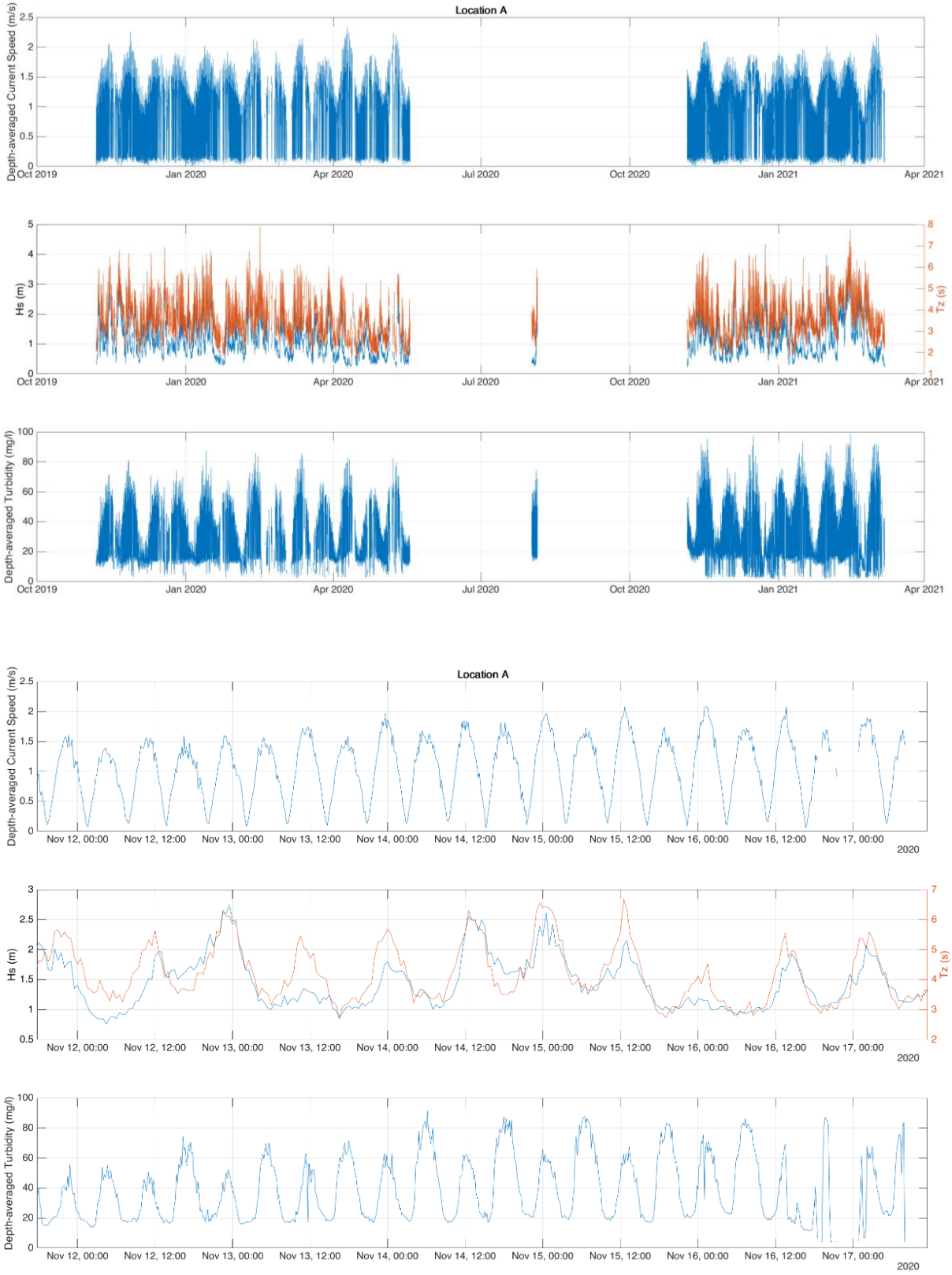


Figure 75. Time series showing water level, H_s and current velocity and coincident turbidity data (collected using the OBS and ABS instrument) across the entire measurement campaign (top) and during a period of enhanced wave action (bottom). Data retrieved from frame location A.



Figure 76. Time series showing water level, H_s and current velocity and coincident turbidity data (collected using the OBS and ABS instrument) across the entire measurement campaign (top) and during a period of enhanced wave action (bottom). Data retrieved from frame location B.

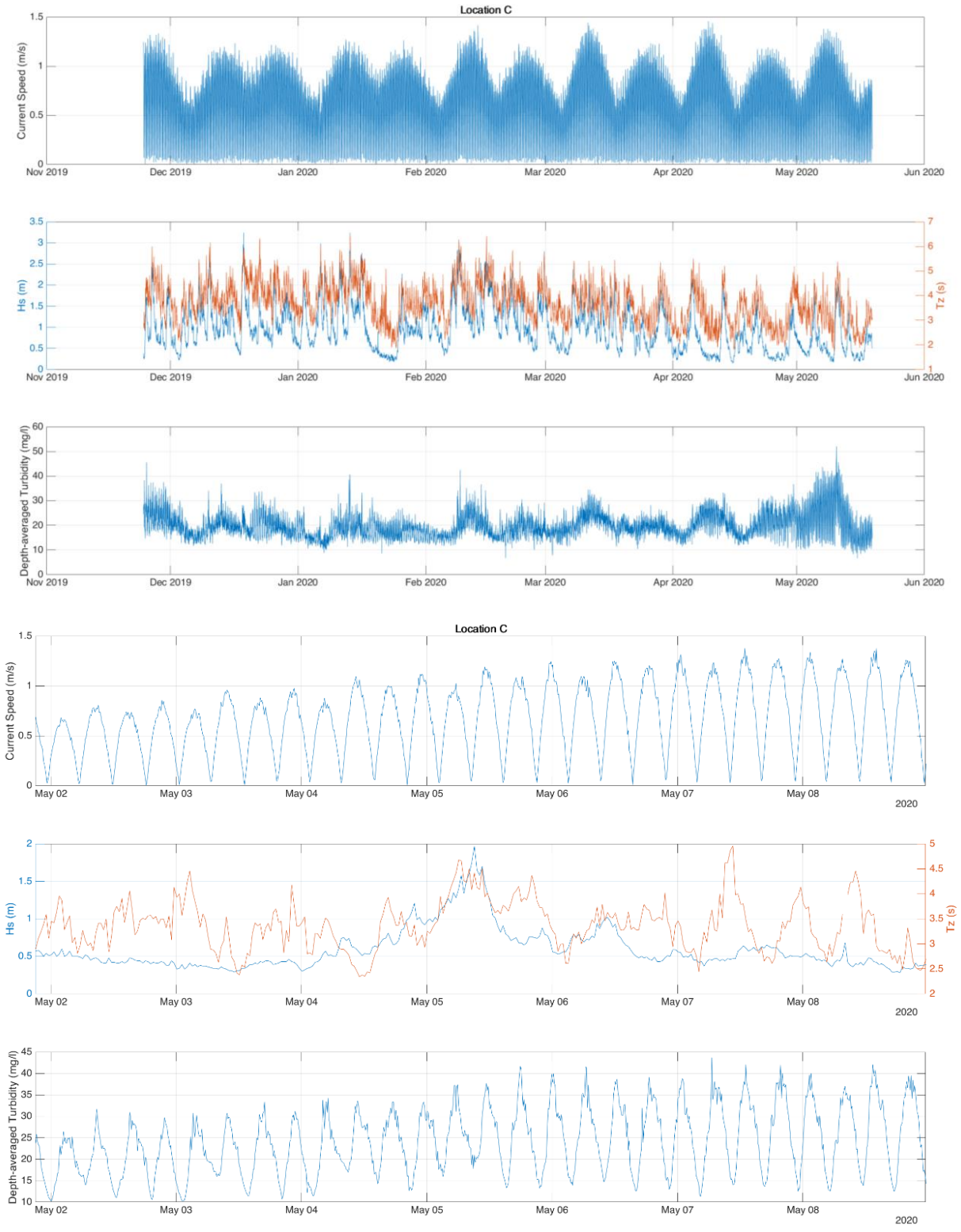


Figure 77. Time series showing water level, H_s and current velocity and coincident turbidity data (collected using the OBS and ABS instrument) across the entire measurement campaign (top) and during a period of enhanced wave action (bottom). Data retrieved from frame location C.



Figure 78. Time series showing water level, H_s and current velocity and coincident turbidity data (collected using the OBS and ABS instrument) across the entire measurement campaign (top) and during a period of enhanced wave action (bottom). Data retrieved from frame location D.



Figure 79. Time series showing water level, H_s and current velocity and coincident turbidity data (collected using the OBS and ABS instrument) across the entire measurement campaign (top) and during a period of enhanced wave action (bottom). Data retrieved from frame location E.

8.6.4 One Dimensional (1D) Sediment Transport Model

The cross-bank flows described in Section 8.4, serve as the primary mechanism for moving sediments eastward or westward over the crest, and hence they are also the primary driver of eastward or westward movement of the crestline itself. Whilst material is liberally transported east or west between the flood and ebb phases of the tide, the net effect is small over a single tidal cycle. Only when a bias eastward or westward occurs in the medium to long-term, do we see a modification in the cross-section profile of the bank. To investigate the form of these medium to long-term biases in transport over the crest, we employed a 39-year record of hindcasted current speed and direction at various locations along the bank crest, from the metocean hindcast model, along with a 1D sediment transport model. The 1D transport model is based on the work of Van Rijn (2015), and computes velocity profiles, sand concentration profiles, depth-integrated suspended sand transport and bed-load transport in response to tidal currents and waves. In total, eight 39-year time series of current velocity at 20-minute intervals were extracted from the metocean hindcast model. The directions of the velocities were then adjusted by 10° clockwise, such that the u velocity component was normal to the orientation of the primary axis of the bank. The u velocity component of flow was then used as the input to the sediment transport model. By these means, the input to the sediment transport model relates directly to the strength of flow over the crest. The equations of the sediment transport model were slightly modified so as to be able to accept a negative input flow speed (i.e., westward flow), and produce a corresponding negative output (i.e., westward sediment transport). Model extraction locations are presented in the form of a map in Figure 80. The full time series of sediment transport over the crest of the bank is shown in Figure 81.

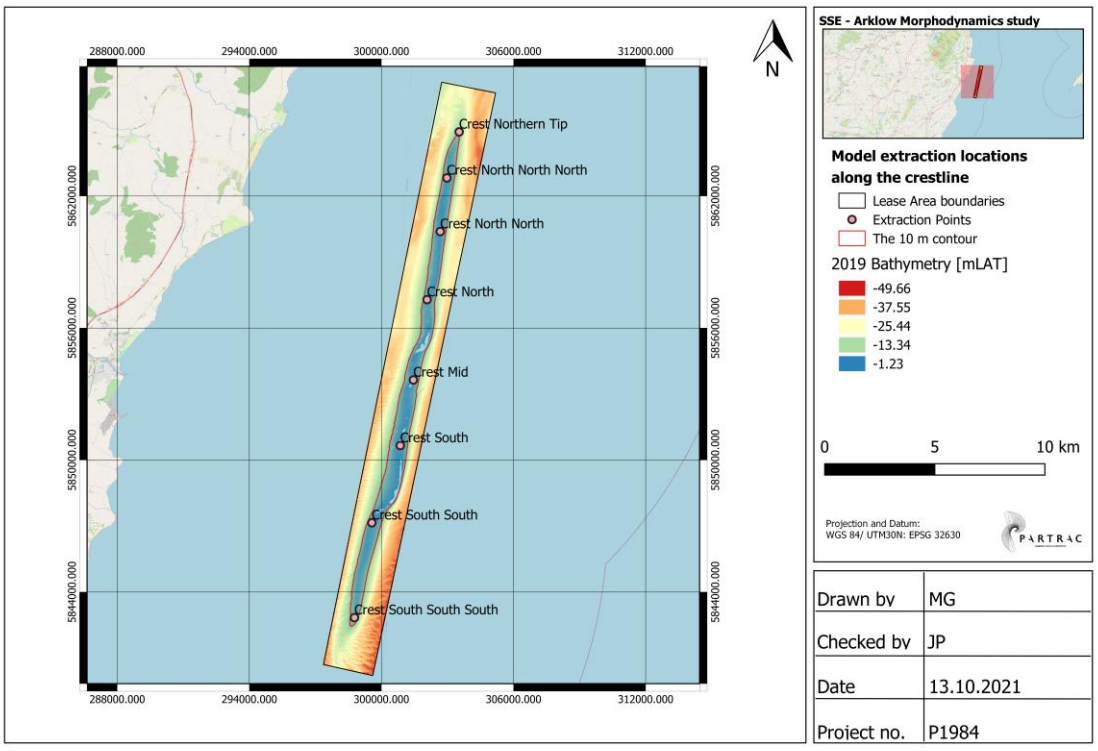


Figure 80. Model extraction locations along the crestline.

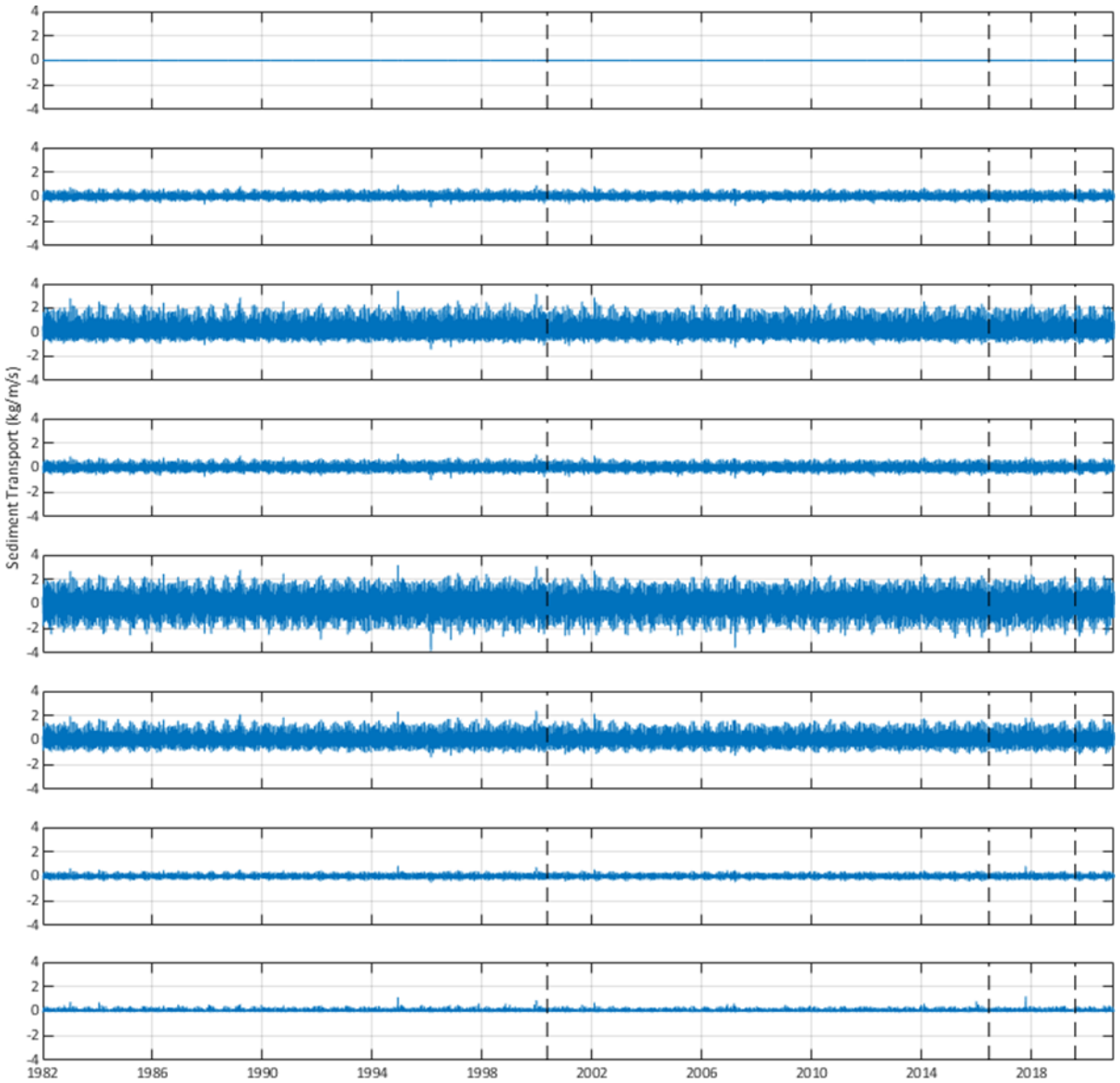


Figure 81. Sediment transport normal to the bank for eight positions along the bank crest (top to bottom, north to south).

The times of the three survey datasets are also shown as black dashed vertical lines. Because there is transport over the crest on every tide, it is hard to discern a signal when looking at the entire time-series. We undertook a Fast Fourier Transform of the data and found that strong regular signals in the data exist for periods less than 30 days, after which non-regular signals become more prominent. Figure 82 shows the same time-series data as Figure 81 except the data is plotted as a 30-day running mean.

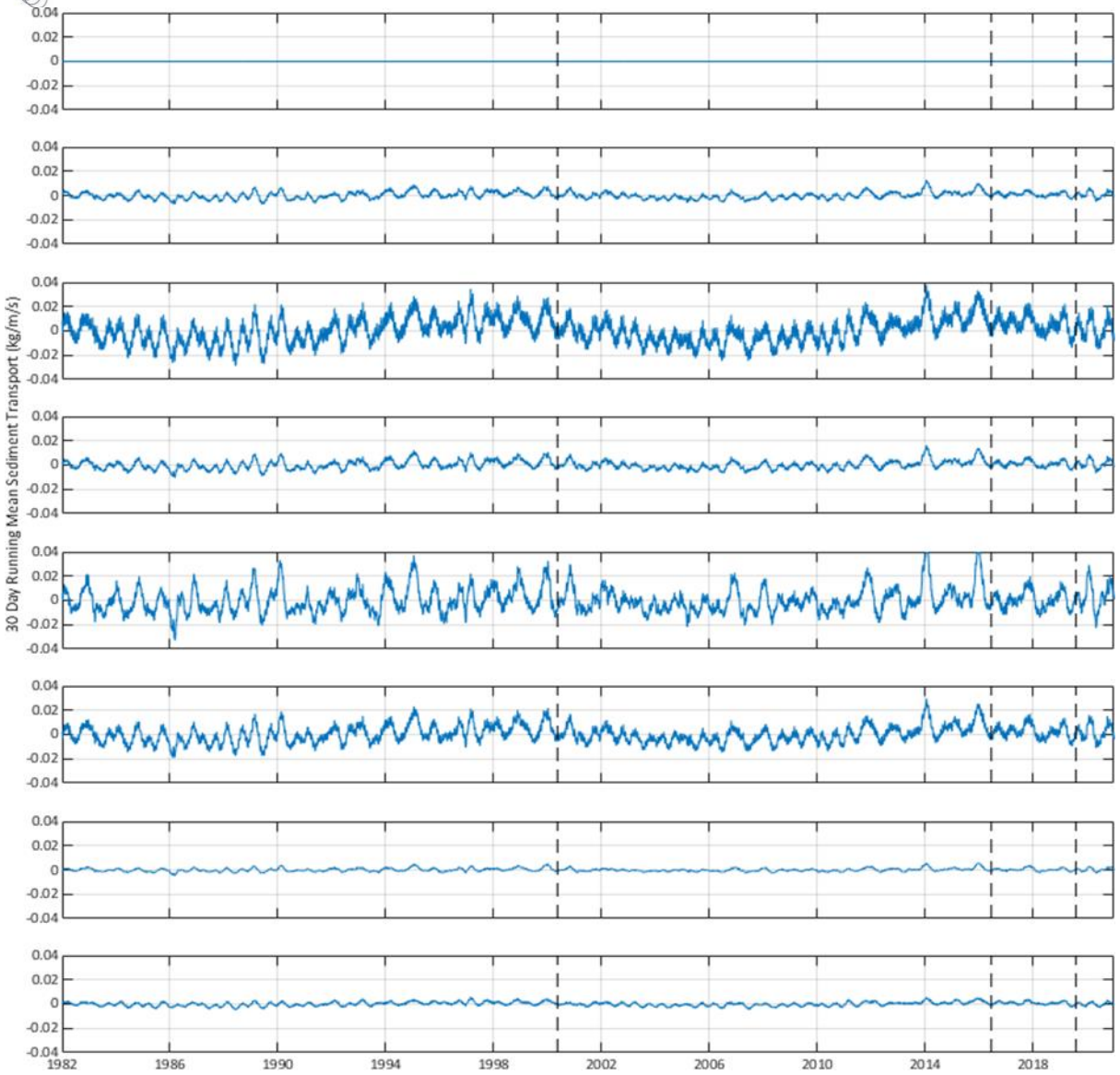


Figure 82. 30 day running mean sediment transport normal to the bank for eight positions along the bank crest (top to bottom, north to south).

Using a 30-day running mean, it becomes easier to discern any non-regular behaviour of the bank in terms of bias of transport over the crest to the east or to the west. In particular, we can relate the timings of the 2000, 2016 and 2019 surveys to any prior periods of eastward or westward bias in transport over the crest, to assist in understanding whether these surveys might represent more or less extreme easterly or westerly biased system states.

The metocean hindcast which forms the basis of information for Figure 81 and Figure 82 uses the 2019 bathymetry. To ascertain whether bathymetry has any effect on bias in sediment transport patterns, we carried out a shorter hindcast, covering the period February 2016 to December 2019, inclusive, using the 2000 bathymetry. Sediment transport normal to the crest of the bank was calculated, and the results are shown in

Figure 84. Figure 83 shows the same period, using the 2019 bathymetry, for comparison.

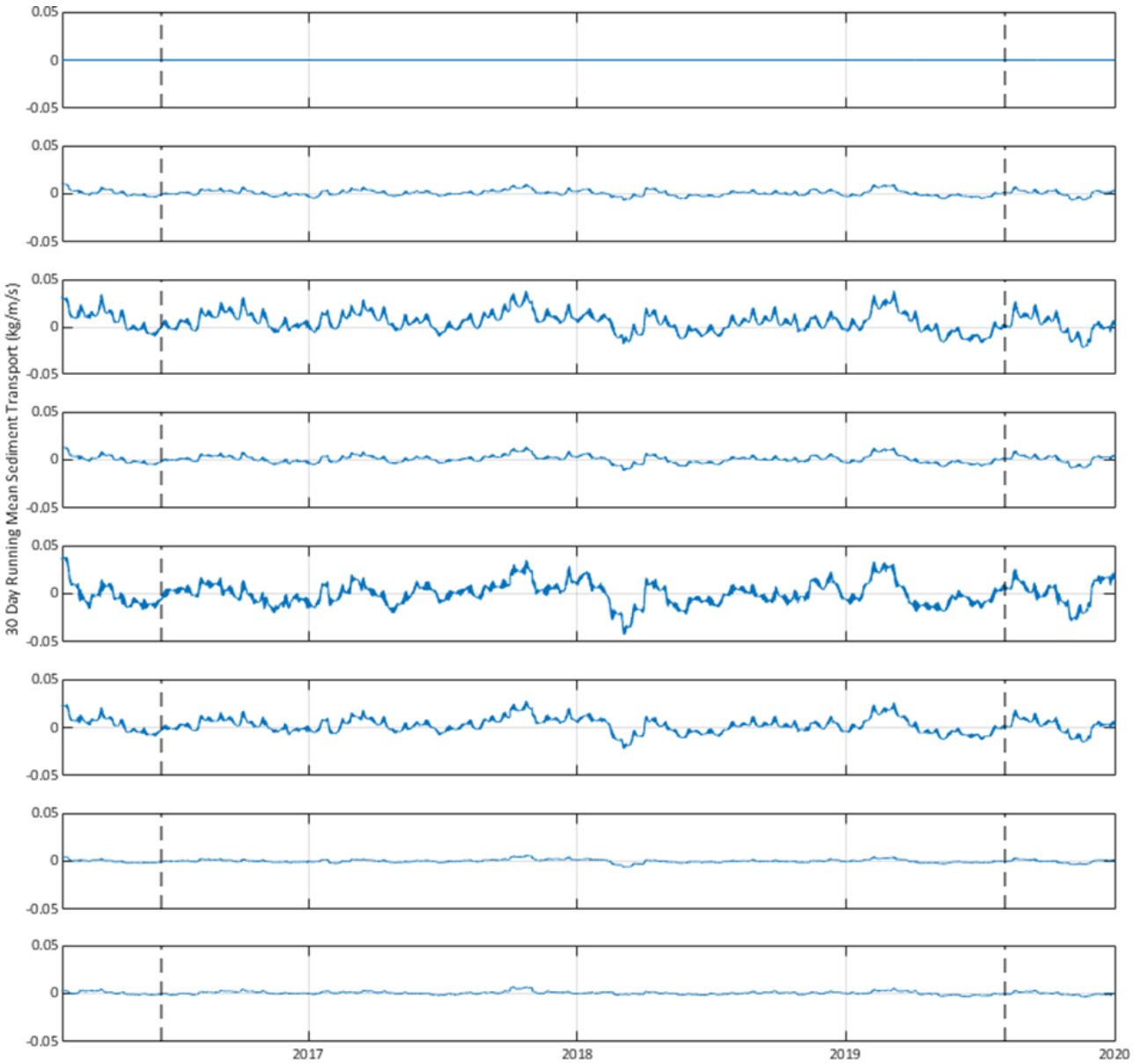


Figure 83. 30 day running mean sediment transport normal to the bank for eight positions along the bank crest (top to bottom, north to south), 2000 bathymetry.

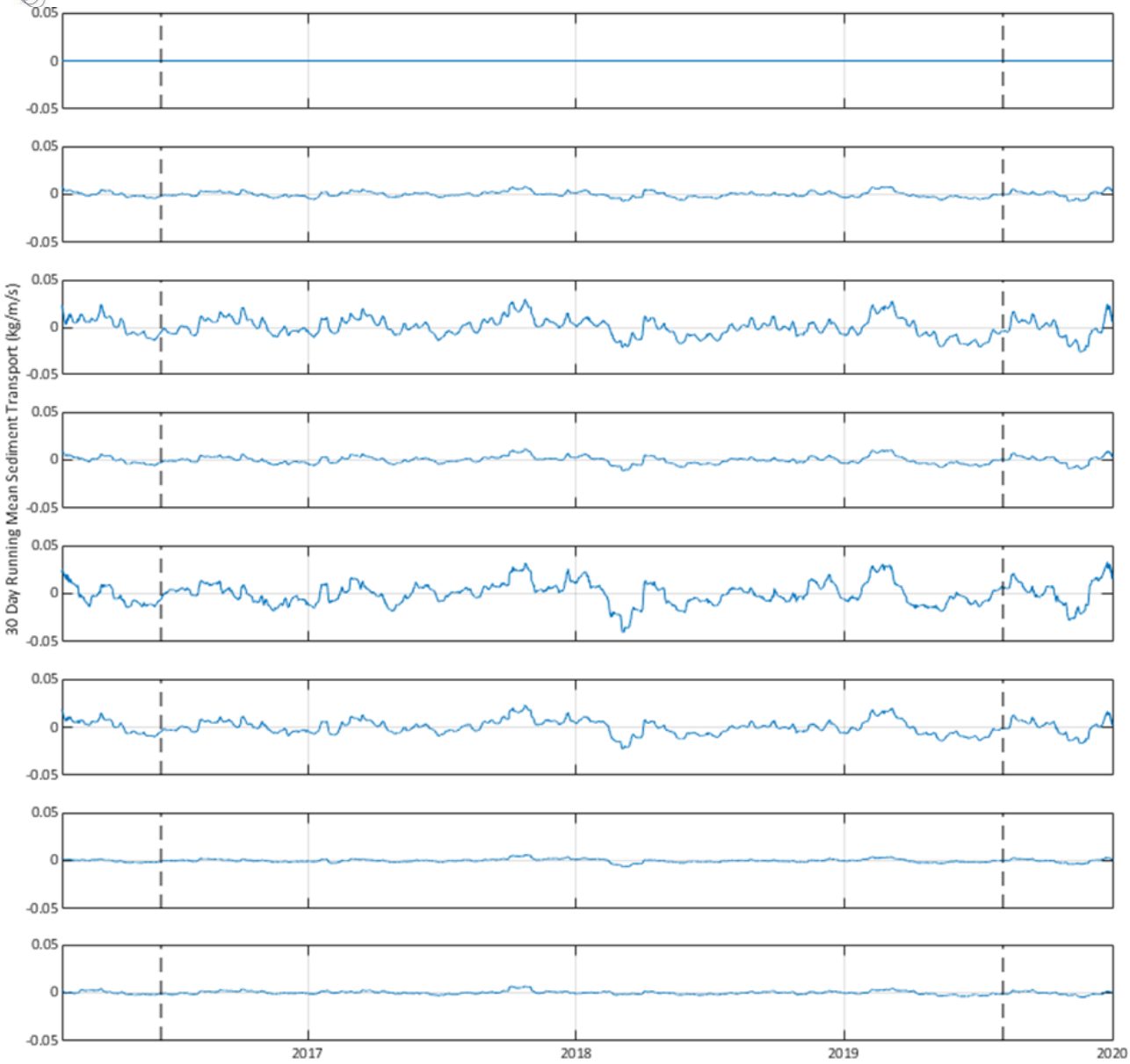


Figure 84. 30 day running mean sediment transport normal to the bank for eight positions along the bank crest (top to bottom, north to south), 2019 bathymetry.

Comparing Figure 84 and Figure 83, we can see that bathymetry of the bank has limited influence on the bias in sediment transport normal to the crest (small differences are likely accounted for by slight difference in depths at the model extraction locations), and thus we determine that the head difference is a response to environmental influences (i.e. tidal variation), acting over the bank rather than the bathymetry of the bank as observed within the data acquired in 2000, 2016 and 2019.

8.7 Observed Bed Level Change

The historic morphological response of the seabed across the lease area and along the export cable routes is accessible via inspection of bathymetric datasets acquired between 2000 and 2020 (see Figure 3). Across the lease area the

observed vertical change is significant (Figure 85 to Figure 93), along the proposed export cable routes the observed bed level change is relatively benign (Figure 89 and Figure 94). The greatest vertical change across the lease area occurs due to a repositioning of the crestline which alters the shape, and cross-sectional profile, of the bank. Second to this is the bed level change due to the movement of large-scale sandwave features which persist around the base of the bank to the east and west, and at the head of the bank to the north and at the tail of the bank to the south.

The response of the bank over the longer term can be summarised as follows:

- Review of the 2000 data against the 2016 and 2019 data provides the best available data from which to consider the historic morphological response of the bank over the longer term (see Figure 85 to Figure 87). Review of these data show that, during this period, significant bed level change occurred due to the repositioning of the crestline and changes to the form and profile of the bank, with seabed levels, at the extreme, lowering and rising by between 18 m and 25 m, respectively. The most significant vertical change was observed on the east flank (particularly the southeast flank) which is a function of the steep slopes on the east of the bank meaning a relatively small lateral shift of part of the bank results in significant vertical change down to, and beyond, the -20 m LAT contour. The slopes on the east flank resemble the lee slope of an asymmetrical sandwave which are often characterised by steep slope gradients (typically between 5 and 15 degrees) which, only in isolated locations, exceed the angle of repose (i.e. suffer slope failure).

The response of the bank over the medium-term (2016 to 2020) can be summarised as follows:

- Spatial plots of observed bed level change during the period 2016 to 2019, show significant, mobile, sandwaves persist on the western and eastern flanks and at the head of the bank to the north and the tail of the bank to the south.
- The net effect of tidal asymmetry observed either side of the bank results in net migration of sandwaves to the north on the west flank and the south on the east flank driven by the flood / ebb dominance observed on the west and east flanks, respectively.
- During this period, the magnitude of bed level change across the bank is broadly consistent. Away from the large-scale features which surround the bank, and the highly mobile, shallow regions associated with the crestline, vertical change ranges from a lowering (i.e. erosion) of the seabed of circa. 1 - 3m and a rising seabed level (i.e. accretion) of circa. 1 – 2 m. In the areas characterised by large scale sandwaves up to 6 m vertical change is observed. At isolated points towards the central regions of the bank significant accretion is observed associated with the repositioning of the crestline, and local wave-tide influence though this may also be associated with the comparison of two composite bathymetries (See Section 3.1).
- Comparing the high-resolution bathymetric datasets (i.e. data collected in 2016 and 2019) shows the crestline is mobile, repositioning parts of the top of the bank (Figure 88). The top of the bank, and the crestline, form

the shallowest regions of the bank and are characterised by the presence of megaripple and sandwave features. The top of the bank and the crestline is postulated to be an area of sediment convergence; highly influenced by shallow water processes which continually act to modify the shape of the crestline and the profile of the shallowest regions of the bank.

- The targeted, repeat bathymetry surveys conducted in 2020 (Figure 90 to Figure 93 and Figure 94), provided study-critical data at strategic sections of the bank with which to calibrate the sediment transport model over the short-term, in areas of the bank broadly devoid of large scale sandwaves. Across this period (up to 6 weeks in the summer of 2020), in the areas on the bank surveyed, the net vertical change ranges between a lowering of the seabed (i.e. erosion) of up to 1.6 m and a rising of the seabed (i.e. accretion) of up to 3.5 m. These data also:
    - Provided further corroborating evidence of the scale of vertical change due to the movement of the large-scale sandwave features around the flanks and periphery of the bank. Note: the scale of vertical change reflects the amplitude (trough to crest) of these features.
    - Improved our understanding of the processes occurring in the most mobile shallowest regions of the bank providing tangible evidence of wave and tidal influence across the lease area (i.e. wave action flattens the bank profile, whereas tidal processes nourish the crestline and the shallowest regions of the bank) (particularly evident in profile data presented in Figure 93).
- In addition, the data derived from the repeat surveys conducted over the short-term provide corroborating evidence for the following processes occurring across the lease area and within the area surveyed along the export cable corridor:
    - Tidal asymmetry with flood tides dominant on the western flank and ebb on the eastern flank which drives a net clockwise circulation of sediment transport around the bank, as evidence by the corresponding asymmetry of sandwaves on east and west flanks.
    - Cross-bank flows developed from a tidal head difference drives sediment transport towards the crest over the mid-section of the bank. Over the period during the survey transport of material from west to east as evidenced by the formation of megaripple features on the west flank which appear to be migrating eastward towards the crestline.
    - The formation and migration of sandwave/megaripple features above the -10 m LAT contour.
    - The influence of wave action on the mobile features located within the shallowest regions of the bank. During/following the largest storms the adjustment at the seabed due to wave action (manifested within the shallowest regions of the bank by a lowering or flattening of the bank profile) is quickly re-established.
    - The repositioning of the crestline under the prevailing tidal regime.
    - Corroborates the hypothesis that processes driving sediment transport across Seven Fathom Bank, though similar to that of Arklow Bank, are of lesser magnitude which is a function of the shape, profile and water depths across Seven Fathom Bank.

The historic morphological change along the proposed export cable routes was examined via a comparison of bathymetric data from 2011 and data collected in 2019 (see Figure 89). Interrogation of these data shows:

- The seabed along the proposed cable routes can be considered relatively stable when compared to the lease area. Along the routes, less erodible soils are observed on occasion and limited evidence of mobile bedform features exists.
- Where the proposed southern export cable route traverses Seven Fathom Bank, comparison of the two bathymetric datasets indicate an area of the bank has migrated westward resulting in the seabed rising / lowering by up to 5 m forming a potential risk to the southernmost export cable route. Interestingly, only limited vertical change (circa +/- 1 m), is evident in the bathymetry data collected over the summer of 2020 (see Figure 94).
- The observed bed level change across IA4, positioned along the export cable corridor, indicates Seven Fathom bank, during the period between surveys, was broadly stable.

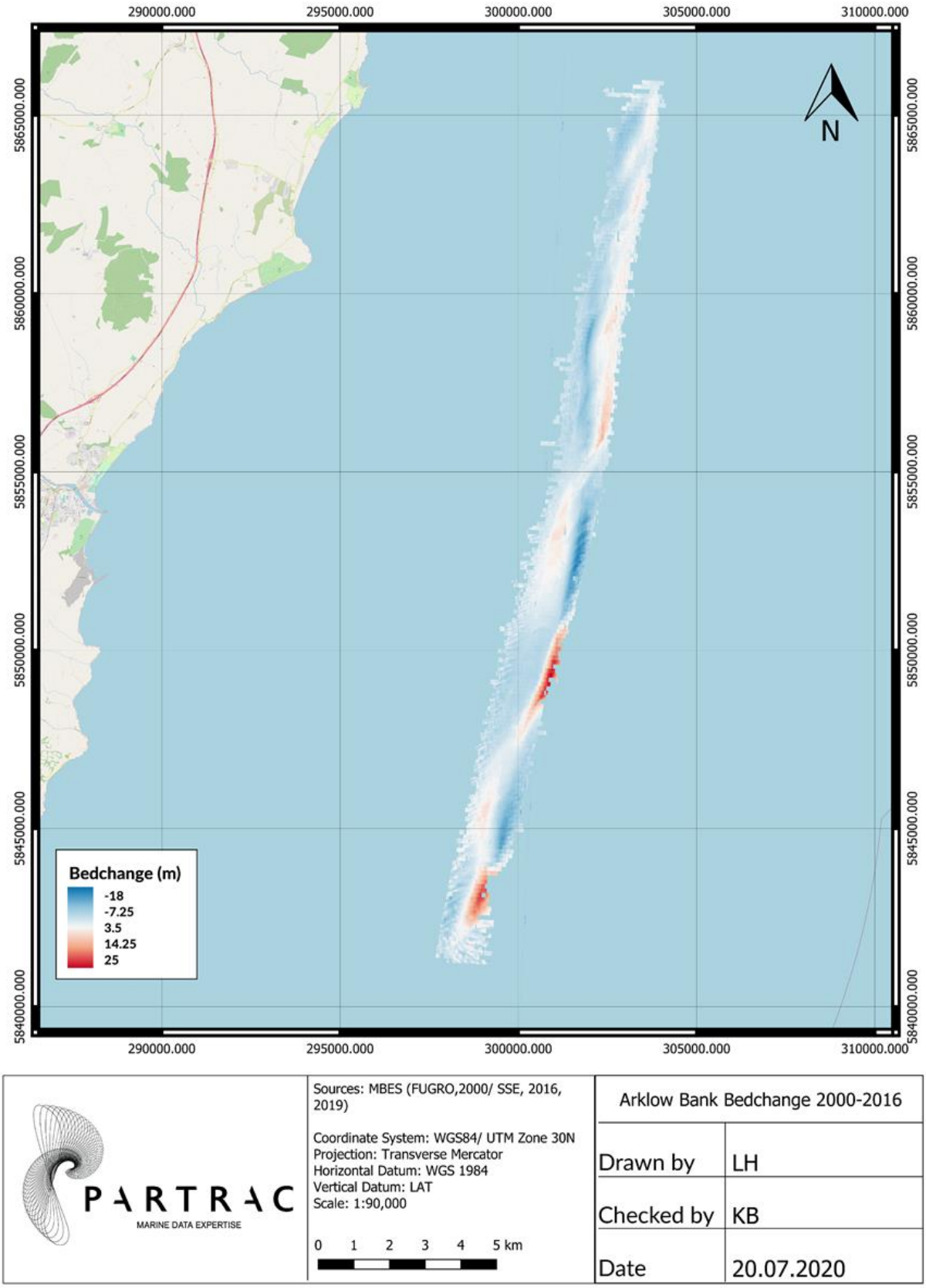


Figure 85. Observed bed level change across the lease area. The plot is developed by comparing the single beam data acquired in 2000 with MBES data acquired in 2016. The red shading indicates accretion, and the blue shading indicates erosion.

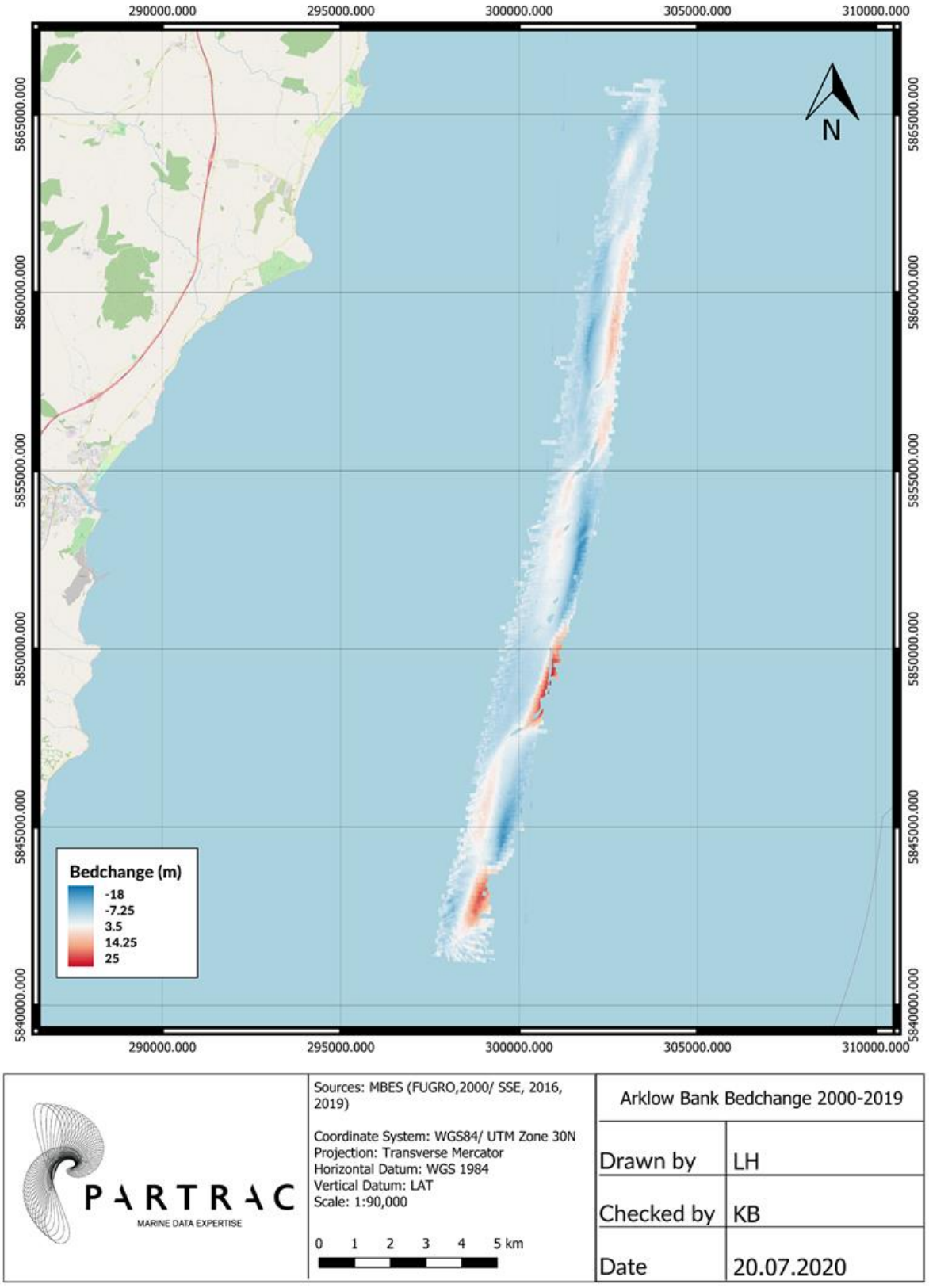
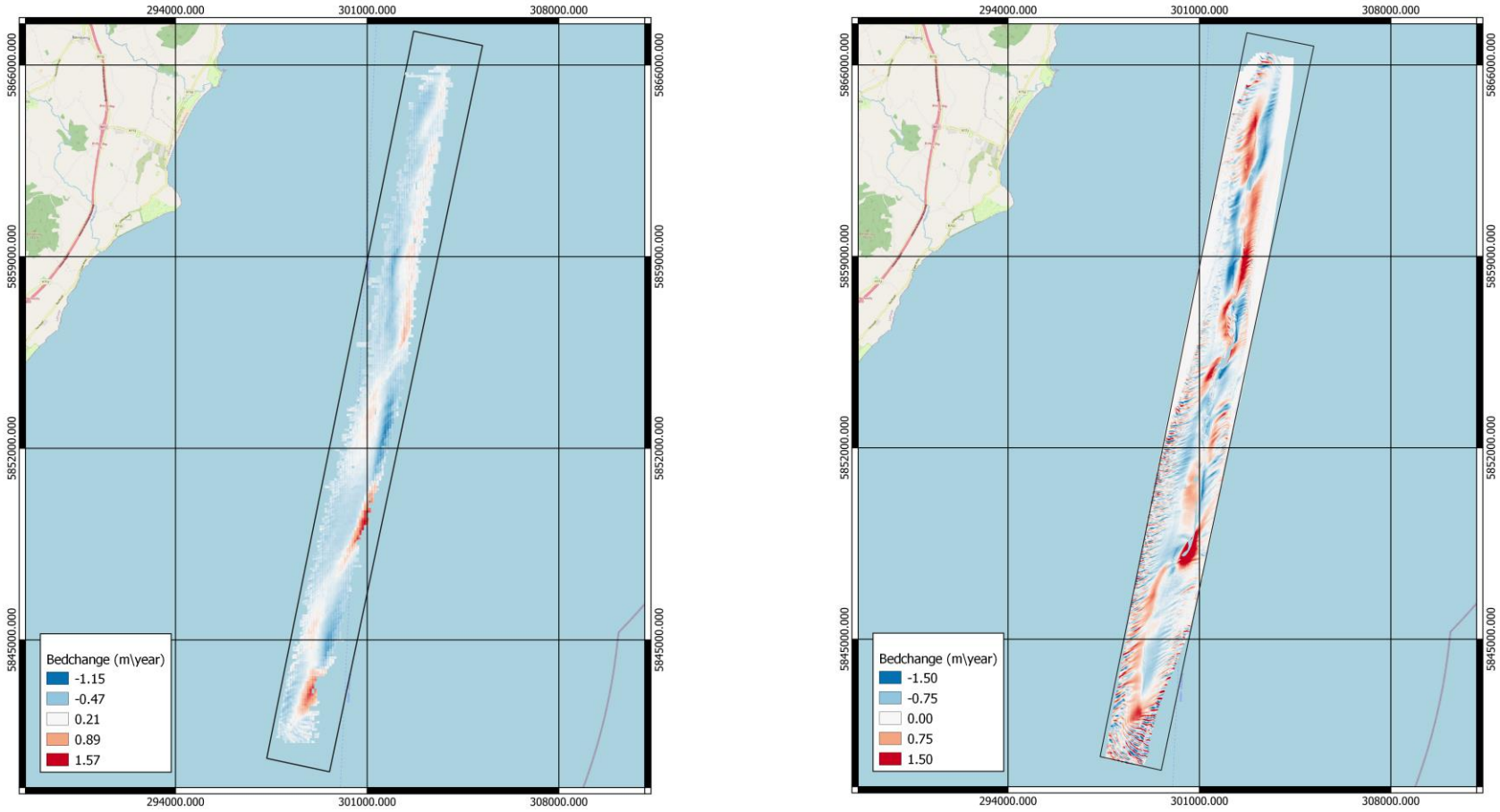


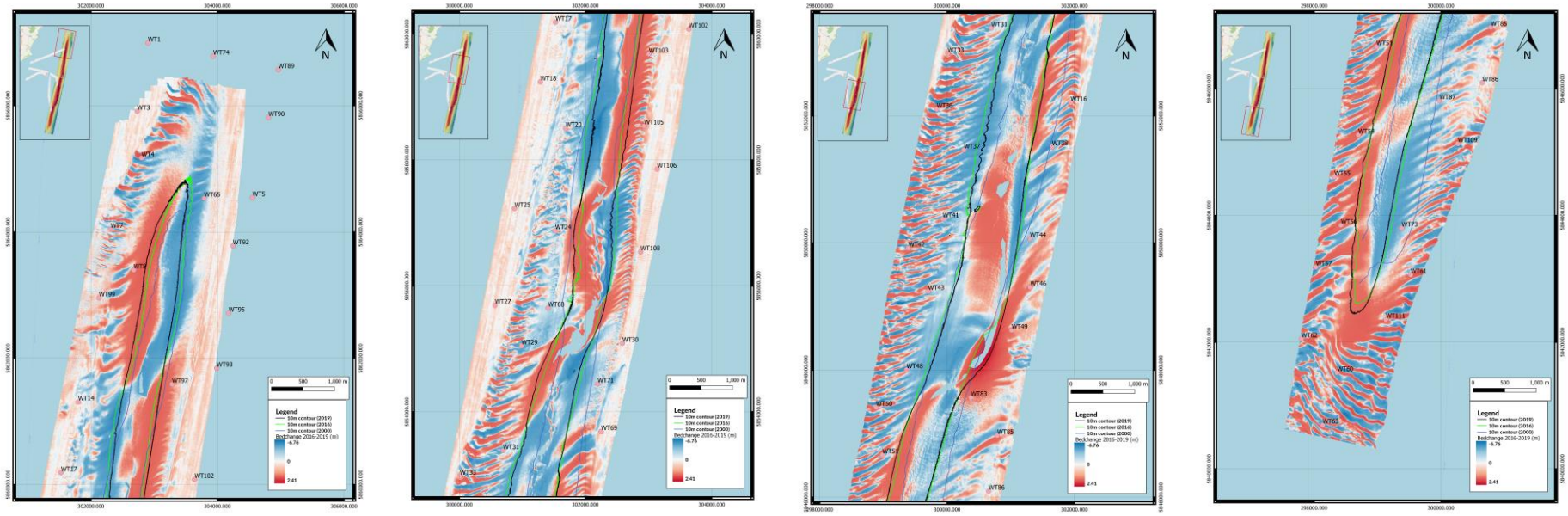
Figure 86. Observed bed level change across the lease area. The plot is developed by comparing the singlebeam data acquired in 2000 with the MBES data acquired in 2019. The red shading indicates accretion, and the blue shading indicates erosion.



2000 vs 2016

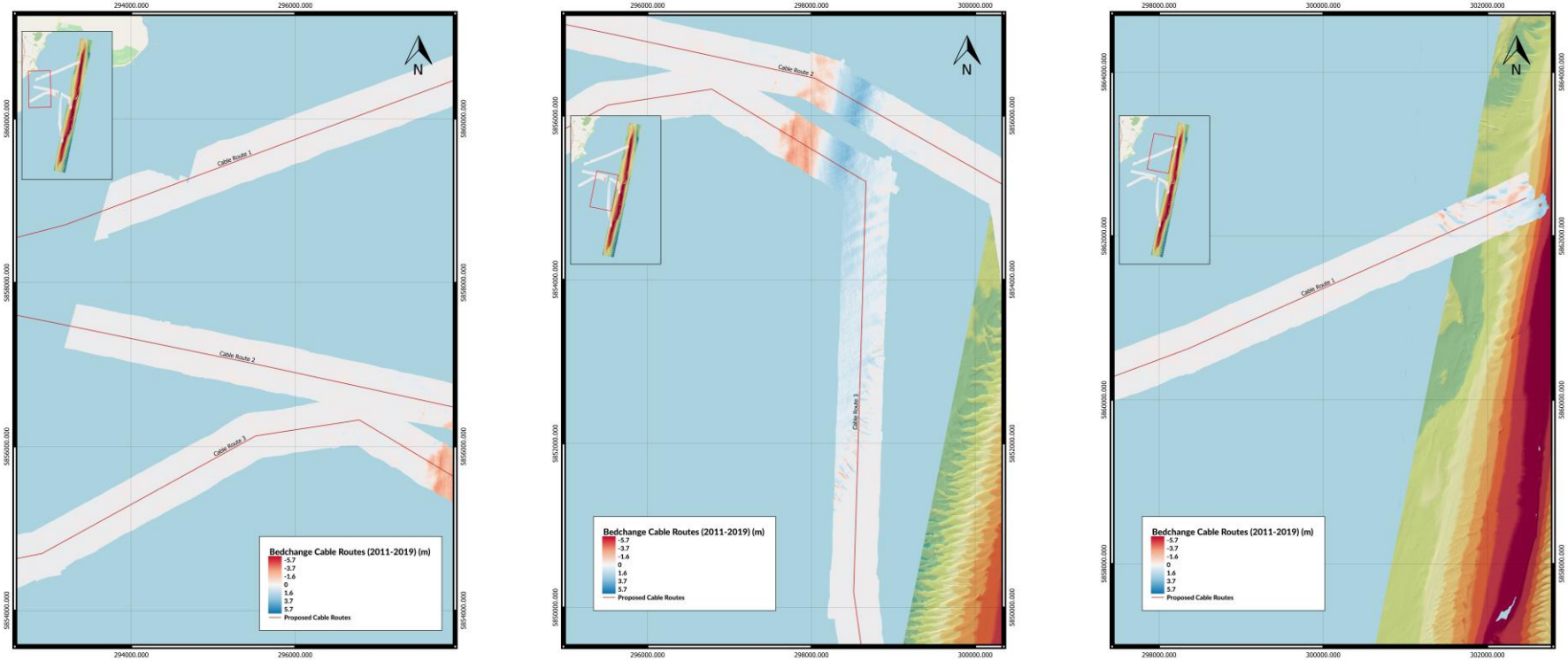
2016 vs 2019

Figure 87. Observed bed level change between 2000 and 2016 (left panel) and 2000 and 2019 (right panel) presented as a nominal 'rate of change' plot. The red shading indicates accretion, and the blue shading indicates erosion.



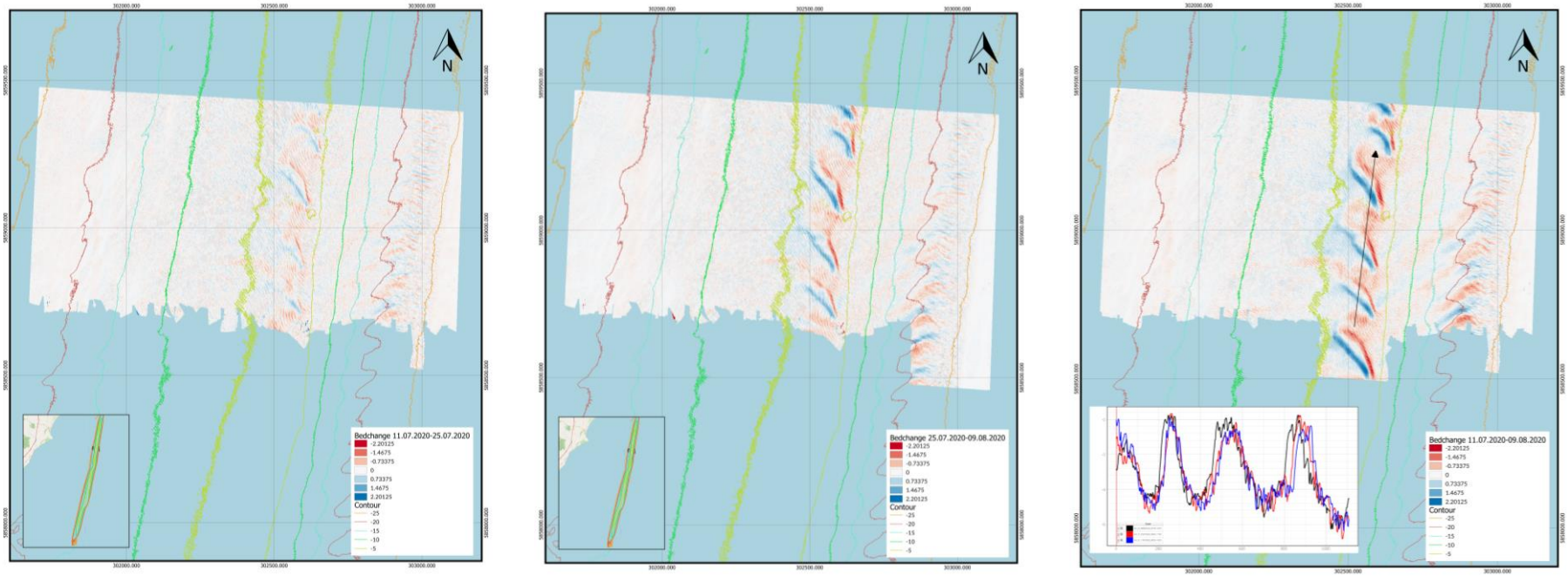
Northern Region (head of the bank) | Central North Region | Central South Region | Southern Region (tail of the bank)

Figure 88. Spatial plots showing the observed bed level change between 2016 and 2019. The red shading indicates accretion, and the blue shading indicates erosion. For reference, the -10 m contours derived from data collected in 2000 and the 2016 and 2019 datasets are included for reference.



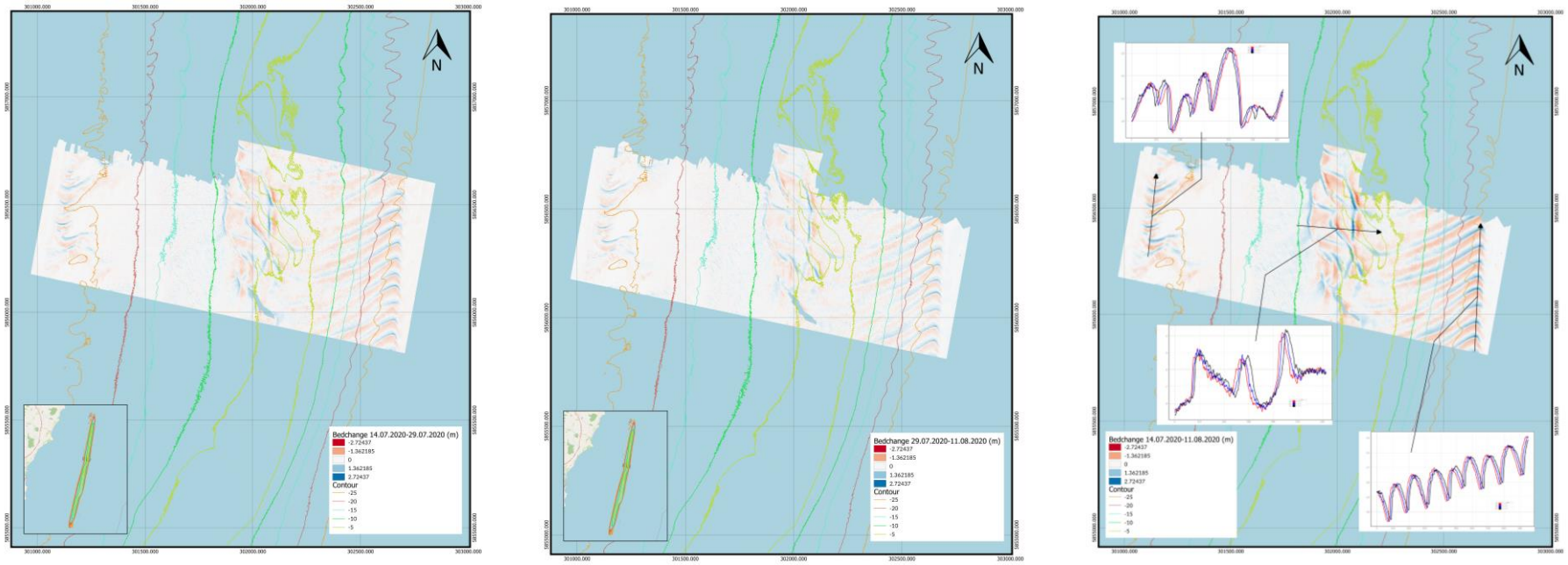
Towards the nearshore | Between the nearshore and the lease area | Towards the lease area

Figure 89. Spatial plots showing the observed bed level change observed between 2011 and 2019. The red shading indicates accretion, and the blue shading indicates erosion. Note: the southernmost cable route has since been dropped but the data is presented as it provides useful data to consider the bed level change across the region to the west of Arklow Bank.



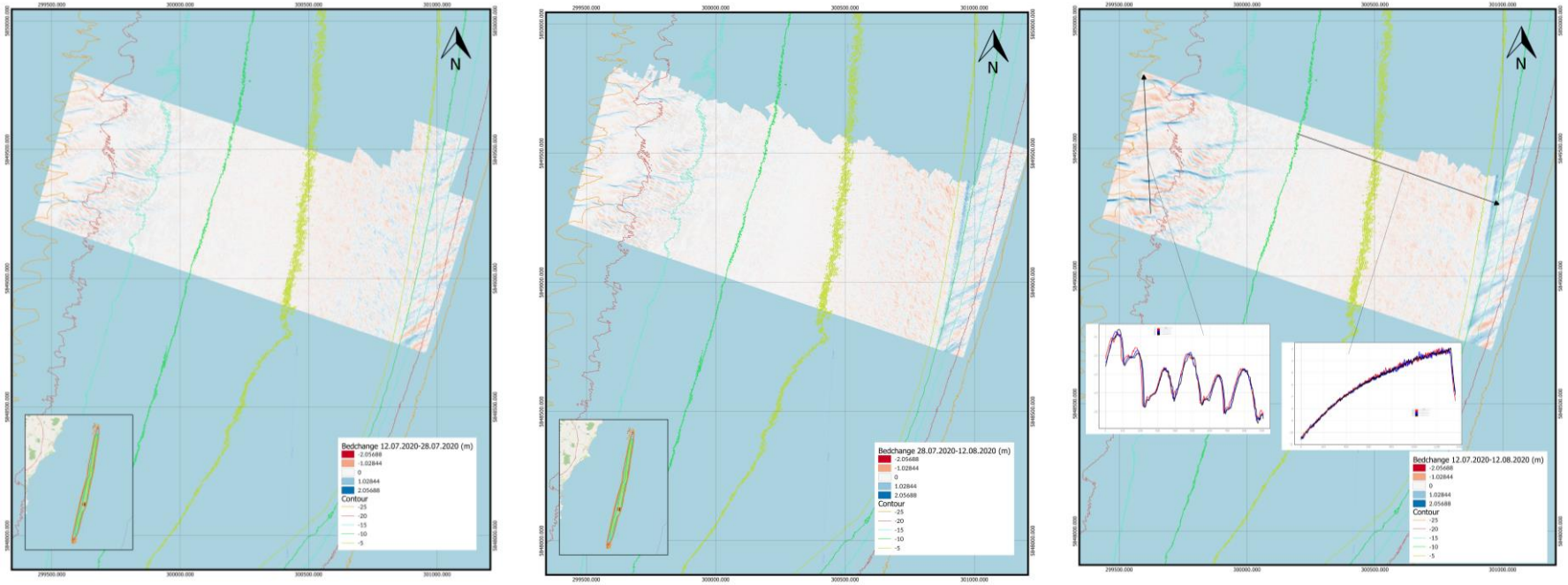
11.07.2020 vs. 25.07.2020 | 25.07.2020 vs. 09.08.2020 | 11.07.2020 vs. 09.08.2020

Figure 90. Various comparisons of the data acquired in IA 1 during the 2020 survey campaign. The plots presented show the bed level change through time and on occasion, pertinent profiles extracted from the data.



14.07.2020 vs. 29.07.2020 | 29.07.2020 vs. 11.08.2020 | 14.07.2020 vs. 11.08.2020

Figure 91. Various comparisons of the data acquired in IA 2 during the 2020 survey campaign. The plots presented show the bed level change through time and on occasion, pertinent profiles extracted from the data.



12.07.2020 vs. 28.07.2020 28.07.2020 vs. 12.08.2020 12.07.2020 vs. 12.08.2020

Figure 92. Various comparisons of the data acquired in IA 3 during the 2020 survey campaign. The plots presented show the bed level change through time and on occasion, pertinent profiles extracted from the data.

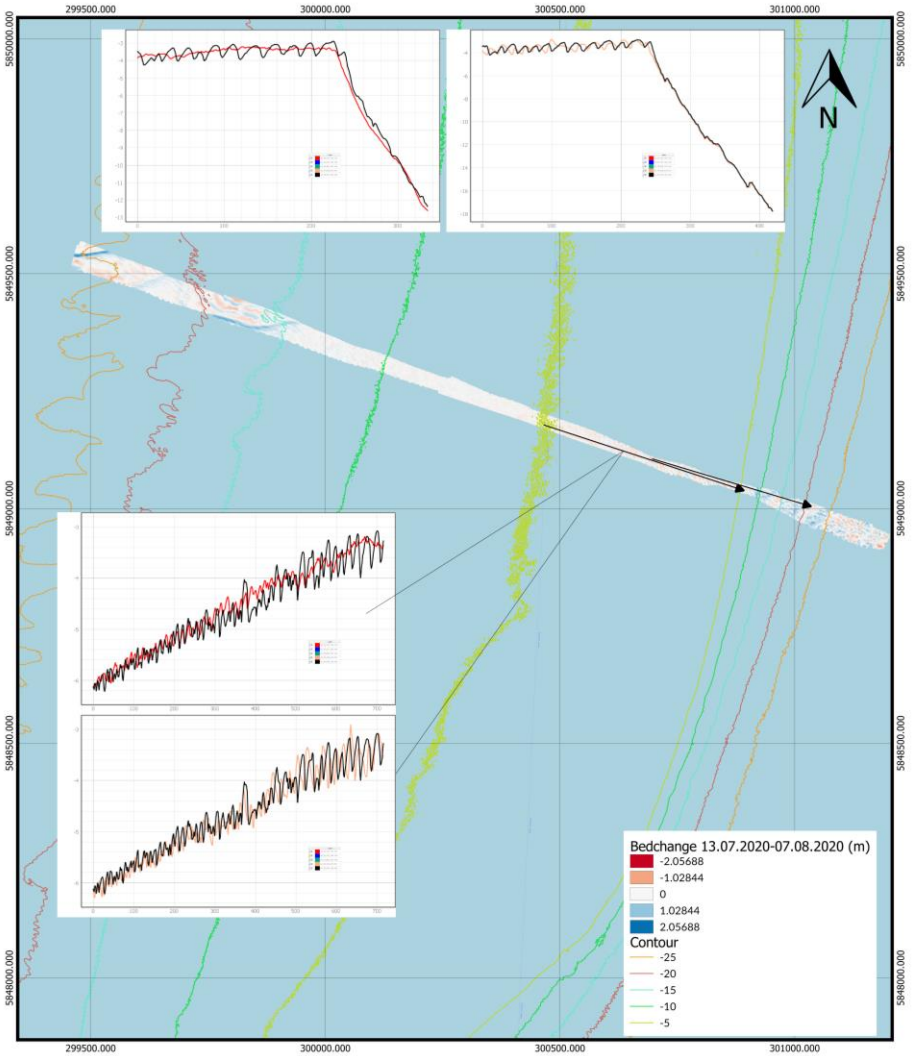
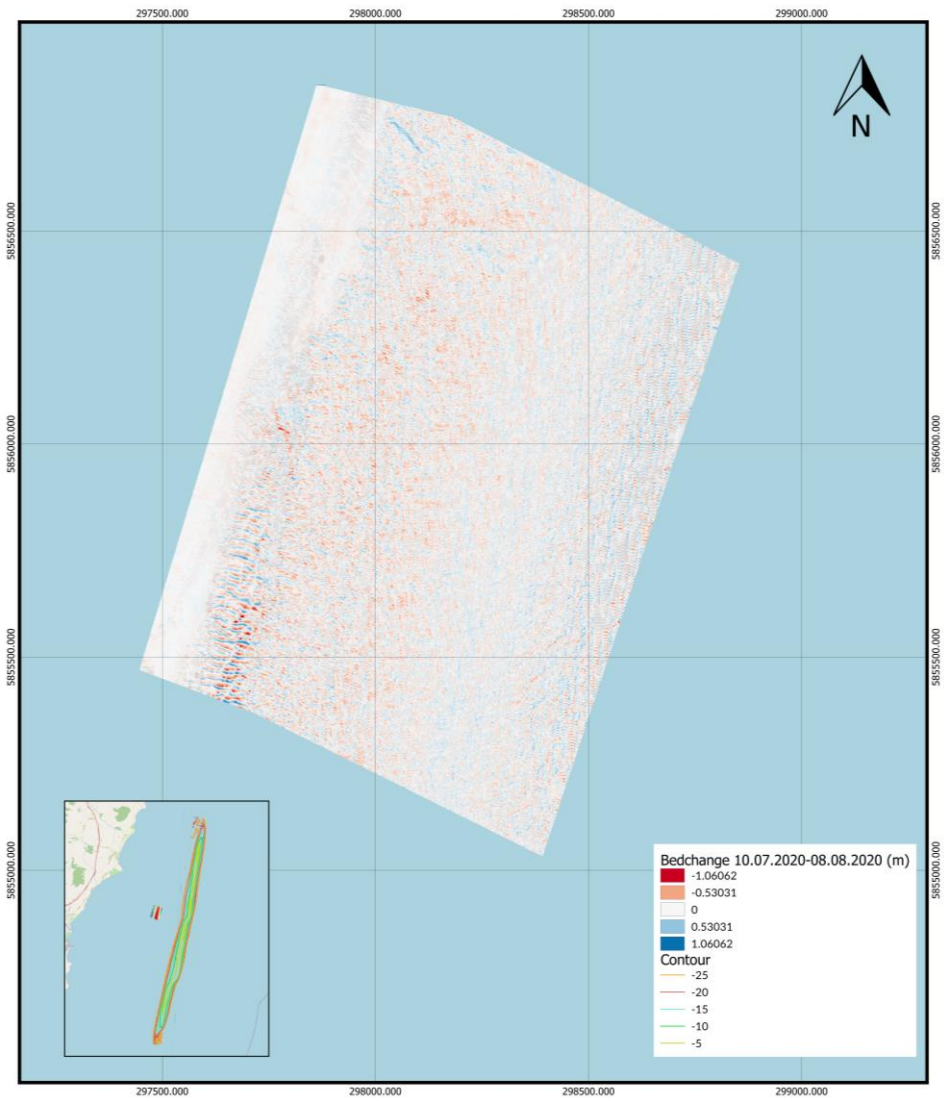
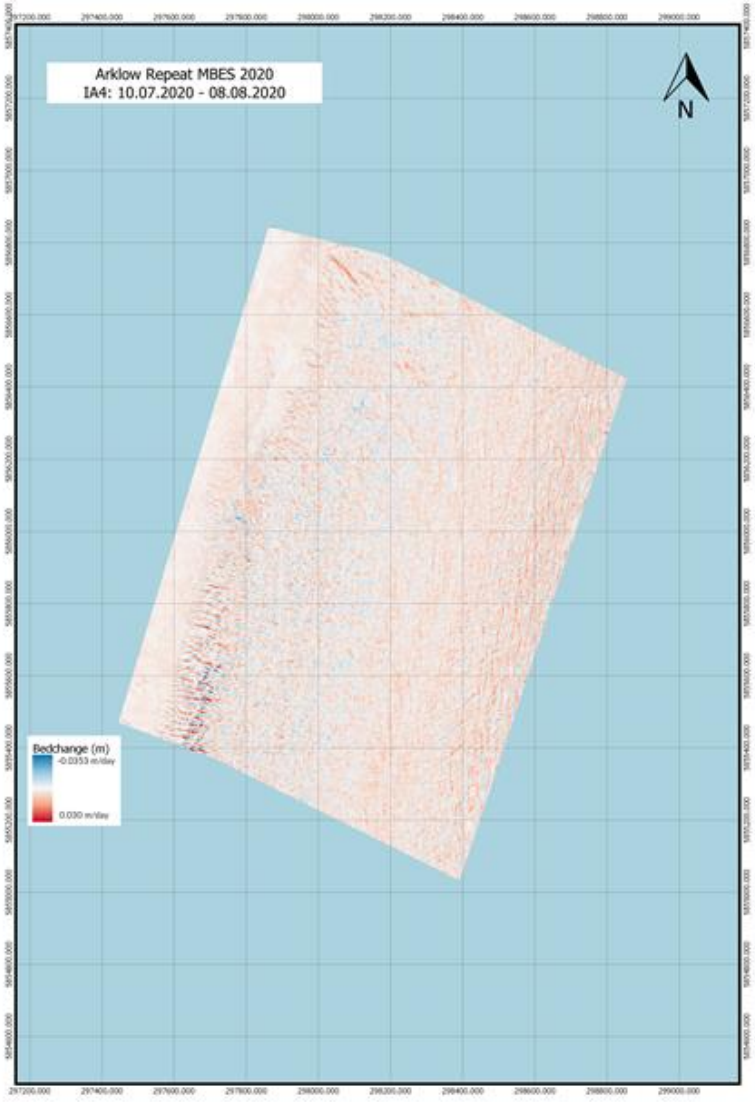


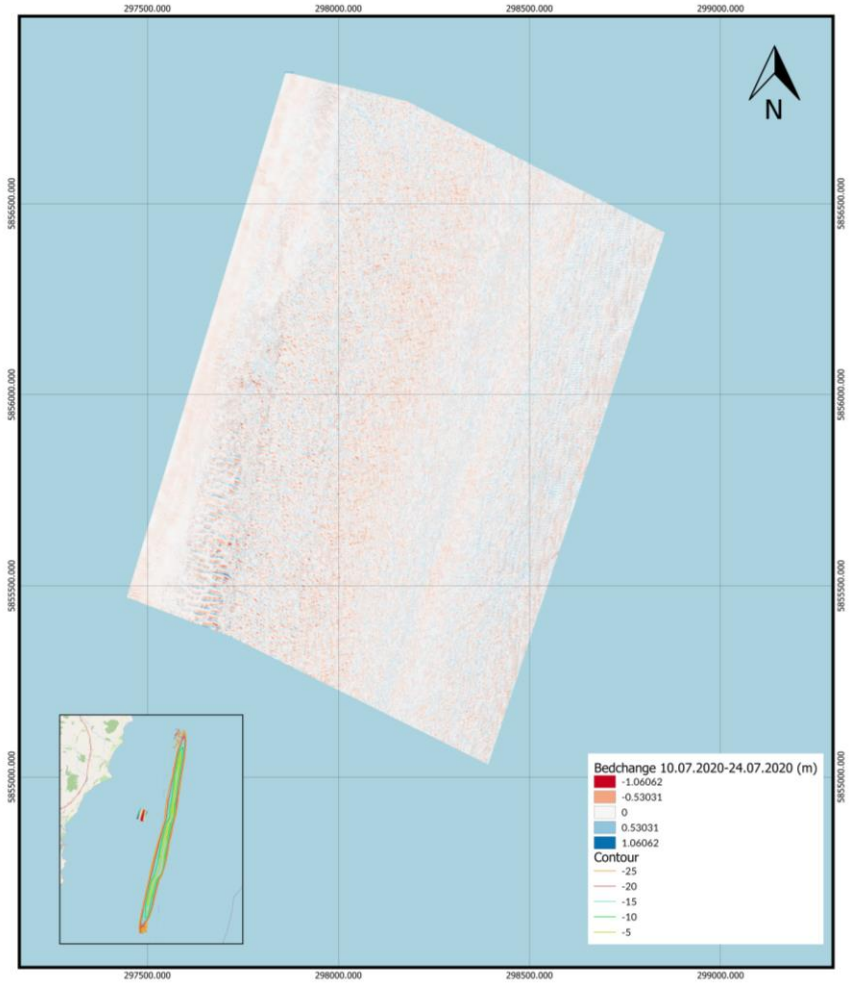
Figure 93. A comparison of the data acquired from a transect across the crestline in IA 3 during the 2020 survey campaign between the period 13.07.2020 and 07.08.2020. The plots presented are postulated to show wave influence at the crestline with a flattened profile evident, following which the reform of megaripples along the transect is clear.



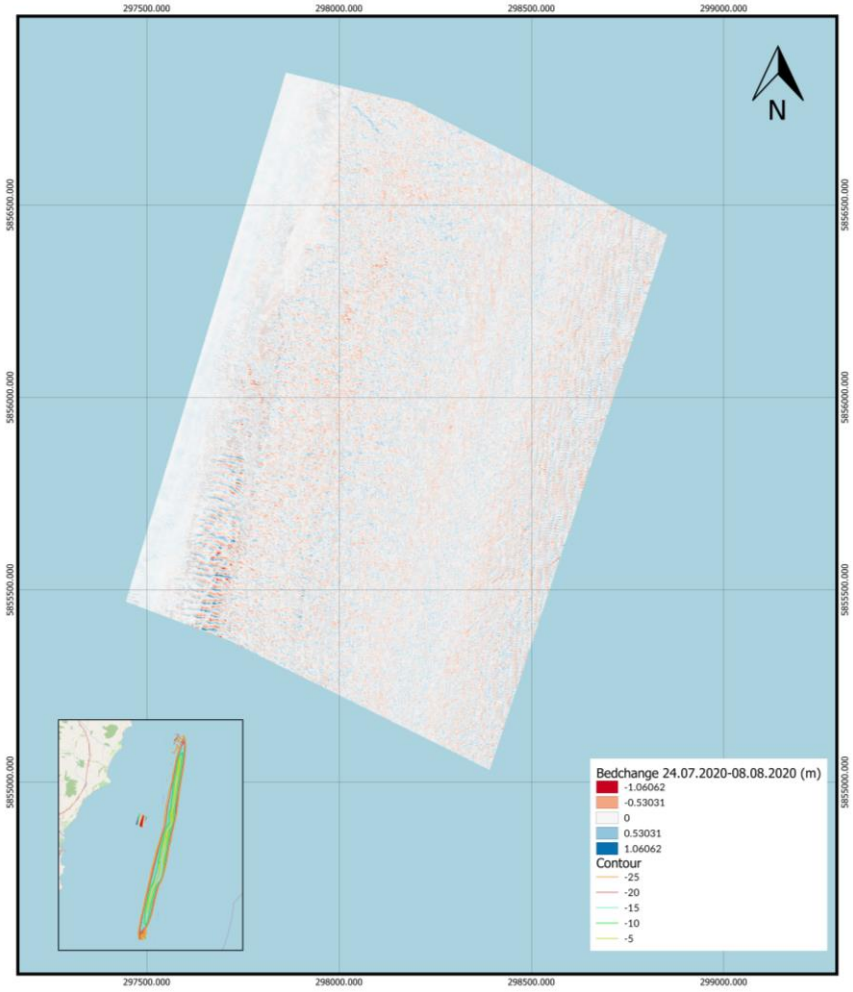
10.07.2020 vs. 08.08.2020



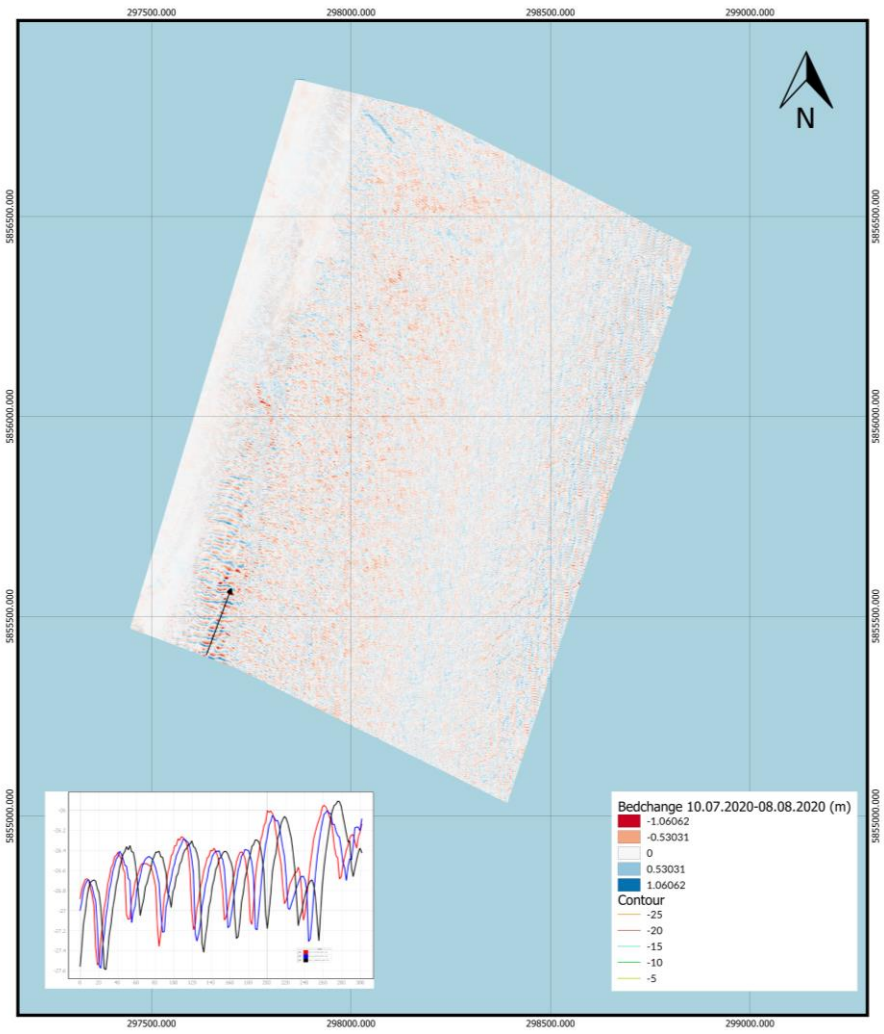
Nominal rate of bedchange 10.07.2020 vs. 08.08.2020



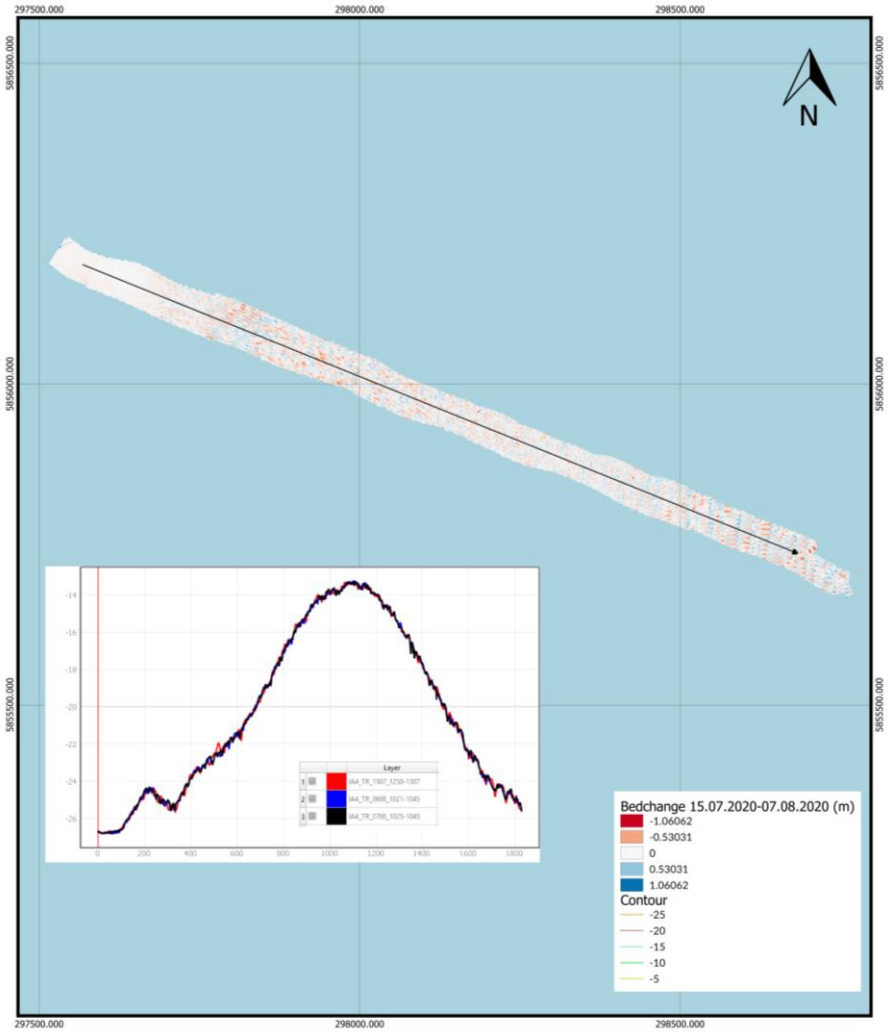
10.07.2020 vs. 24.07.2020



24.07.2020 vs. 08.08.2020



10.07.2020 vs. 08.08.2020



15.07.2020 vs. 07.08.2020

Figure 94. Various comparisons of the data acquired in IA 4 during the 2020 survey campaign.

8.8 Bedform Analysis

Tidal sandwaves pose a risk to offshore structures. Borsje *et al* (2014) found critical conditions for sandwave formation, which are a function of the dominant transport mode (Figure 95). As soon as suspended load is the dominant sediment transport mode, sandwave fields are absent. The lower limit of sandwave occurrence is found at a Rousse number of 1.9 (Rousse number is defined as the ratio between sediment settling velocity and shear velocity), which broadly reflects a situation in which the grain size is < 0.225 mm or the flow velocity amplitude is > 0.775 m/s (Deltares, 2021). Tidal sandwaves may grow up to 25% of the water depth (McCave, 1971), have wavelengths (defined as the distance between two successive crests) in the order of hundreds of metres (Van Dijk and Kleinhans, 2005), migrate at a speed of up to tens of metres per year (Dorst *et al*., 2009) and, if not moribund, fully regenerate after dredging in several years (Knaapen and Hulscher, 2002). Sandwaves are typically asymmetric with stoss and lee slope providing an indication of the direction of net migration (i.e. in the direction coincident with the steeper stoss slope), however they may also be symmetrical and reverse their asymmetry on tidal cycles in highly mobile regions and present as bifurcating features. Sandwaves may also be superimposed by megaripples, which have wavelengths of tens of metres and heights up to 1.5 m. These megaripples are flow-transverse bed patterns and migrate with a rate of circa 0.5 m per day (Ashley, 1990). Due to their limited size, and prevalence at the flanks and crest of the bank, the risk to wind farm infrastructure associated with megaripples is relatively low. The mobility potential of sandwaves, and the sandbank itself, pose far greater risk to infrastructure and thus require far greater consideration during the design phase. Sandwaves can migrate at rates sufficient to generate metres of seabed level variation across the lease area, however, at highly mobile sites (such as this one) the influence of sandwaves (i.e. the transient rise or fall of the seabed level at the foundation site as the wave passes) may be counteracted by local scour processes post WTG installation.

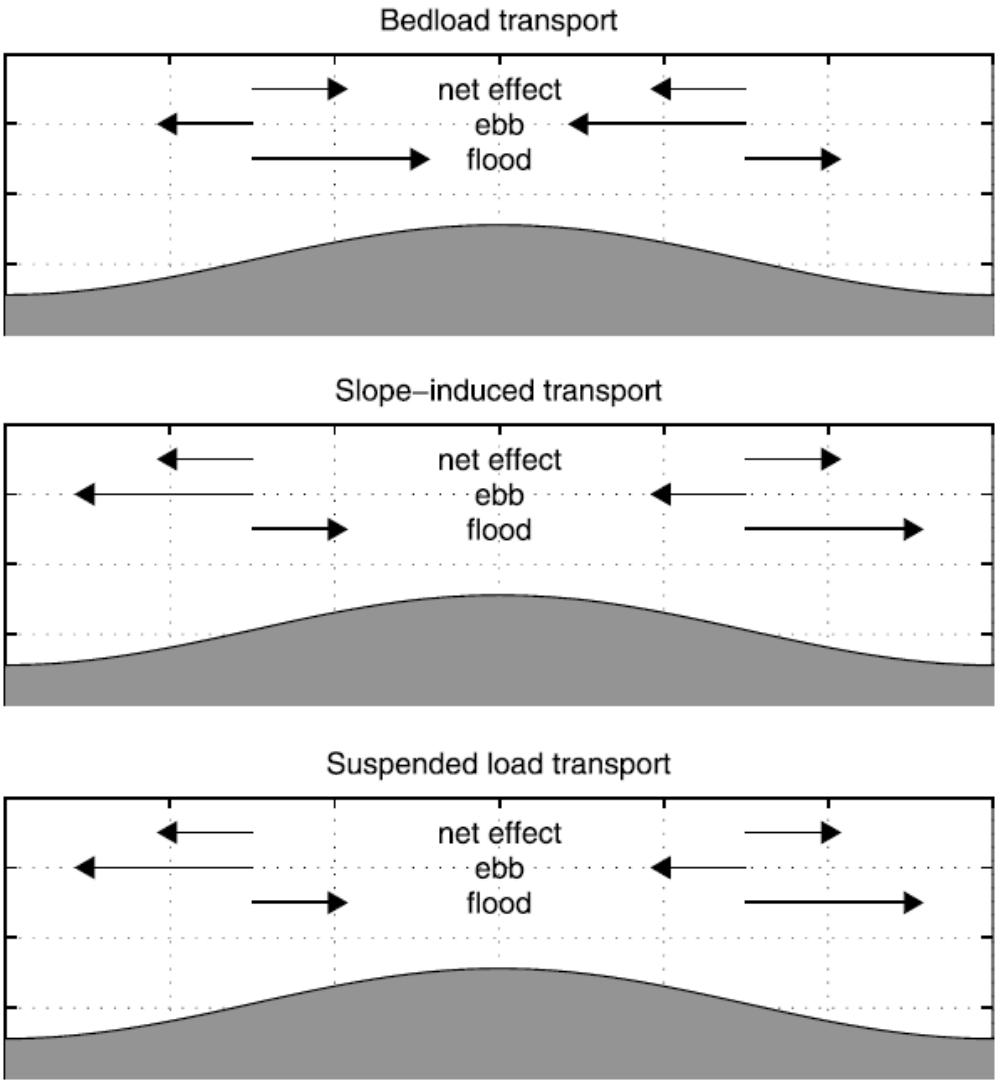


Figure 95. Schematic diagram of the three dominant processes in sandwave formation, bed load transport (net flux towards the crest, causing sandwave growth), slope induced transport (causing sandwave decay), and suspended load transport (causing sandwave decay). Reproduced from Borsje et al., 2014).

A significant feature of the sediment transport regime of Arklow Bank is the presence and migration of large bedforms. The tidal asymmetry (i.e. flood and ebb dominance) observed at the east and west flank of Arklow Bank drives sediment transport around the bank system; such asymmetry is clear in the shape and direction of travel of these mobile bedforms located along the flanks of the bank. The orientation of sandwave crests relative to the orientation of Arklow Bank varies (the alignment of the crest of sandwaves relative to the axis of the bank is approximately 38 degrees on the west flank and approximately 32 degrees on the east flank); providing further corroborating evidence that sediments are transported both along the base of the bank but also towards the crest of the bank.

Across the lifetime of the development, where sediment supply is maintained and the local hydrodynamic regime broadly remains the same, there is no evidence to suggest that observed bedforms will cease to exist or that the large-scale bathymetric patterns will significantly alter. Though, it is widely accepted that large-scale bathymetric patterns remain similar over decades, it is also recognised that the length, height, amplitude, and asymmetry of individual bedforms may be variable over the short-term (Sterlini *et al*., 2009; van Santen *et al*., 2011), influenced by seasonal variations (Buijsman and Ridderinkhof, 2008a, 2008b) and the frequency-magnitude of storm events (Houthuys *et al*., 1994, Sterlini *et al*., 2009 and 2012). Arklow Bank is also unique, in that changes to the bank profile and shape can influence bedforms at the base, and along the flanks, of the bank, though despite short-term changes these bedforms are anticipated to be re-established through time. A large body of scientific work exists (e.g. Passchier & Kleinhans (2005), Sterlini., Hulscher & Hanes (2009)) regarding the potential growth (increase in height), decay (decrease in height) and evolution of bedforms (i.e. changes to the shape, length and wavelength of these features over time). To facilitate assessment of bedforms which persist across the lease area (note; the proposed cable routes are broadly devoid of significant mobile bedforms) the following analysis was performed:

- Direct interrogation of available bathymetry datasets,
- Determination of a Reference SeaBed Level (RSBL) including derivation of the minimum RSBL (coincident with bedform troughs) and maximum RSBL (coincident with the crestal height of bedforms) to forecast potential, transient, seabed level change associated with mobile bedforms across the lease area; and,
- A Fourier transform analysis to quantify spatio-temporal changes to these features and support assessment of sandwave migration rates (which relies on manual interrogation of the data).

These analyses support the prediction of future seabed levels where sandwaves persist and thus is complementary to numerical modelling efforts. The crest alignment, and direction of asymmetry of sandwaves systems at the base of Arklow Bank, were determined from high-resolution MBES bathymetry data acquired in 2011, 2016 and 2019 and are presented in Figure 96 to Figure 102. For the purposes of this analyses several transects intersecting sandwave fields have been interrogated.

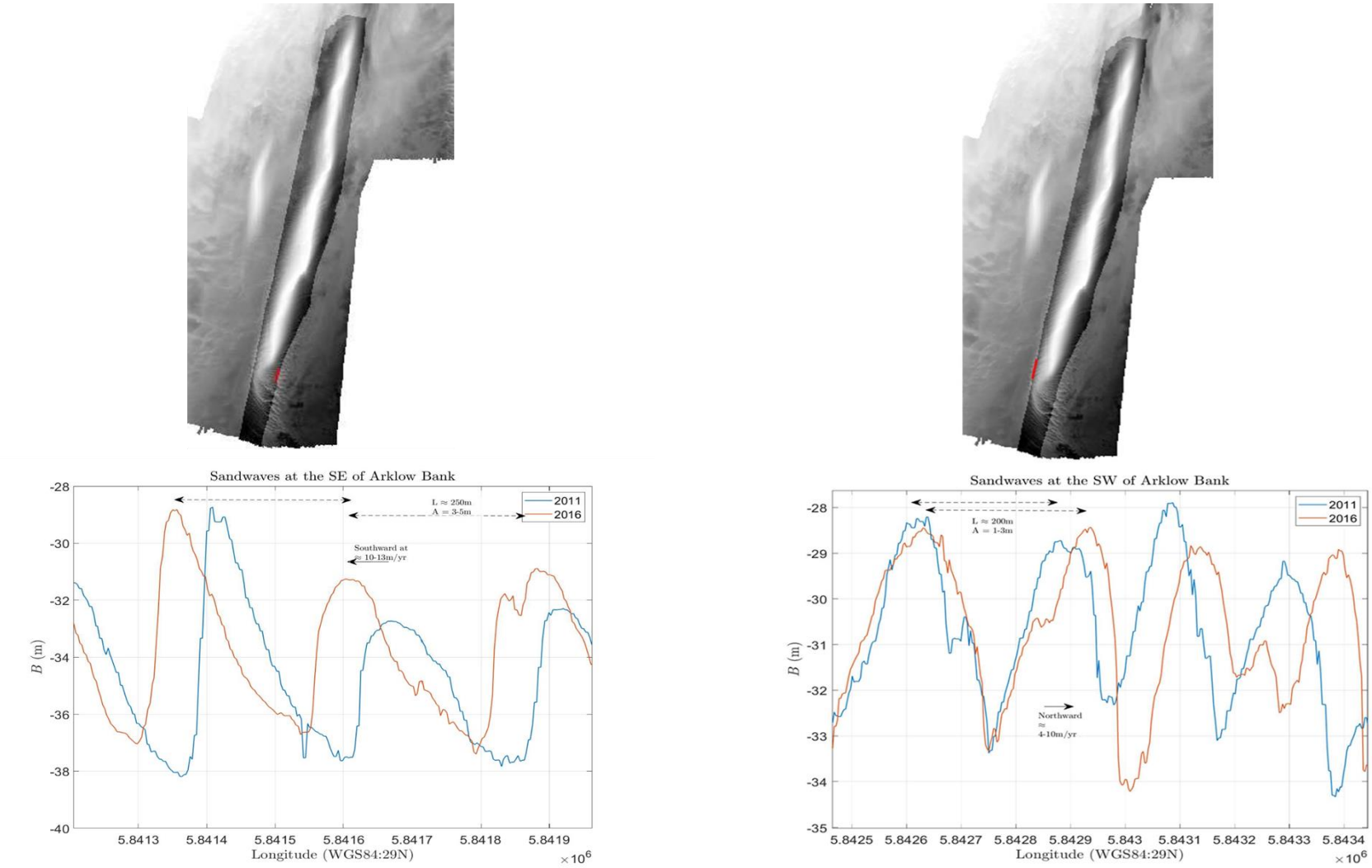


Figure 96. Transect analysis at a location to the SE of the bank (sandwaves crests to the left indicating southward sediment movement) (left panel). Transect analysis at a location to the SW of the Bank (sandwaves crests to the right indicating northward sediment movement) (right panel). The image at the top shows a red line which depicts the length and orientation of the profile presented below where the blue line shows the data from 2011 and the red line shows the data from 2016.

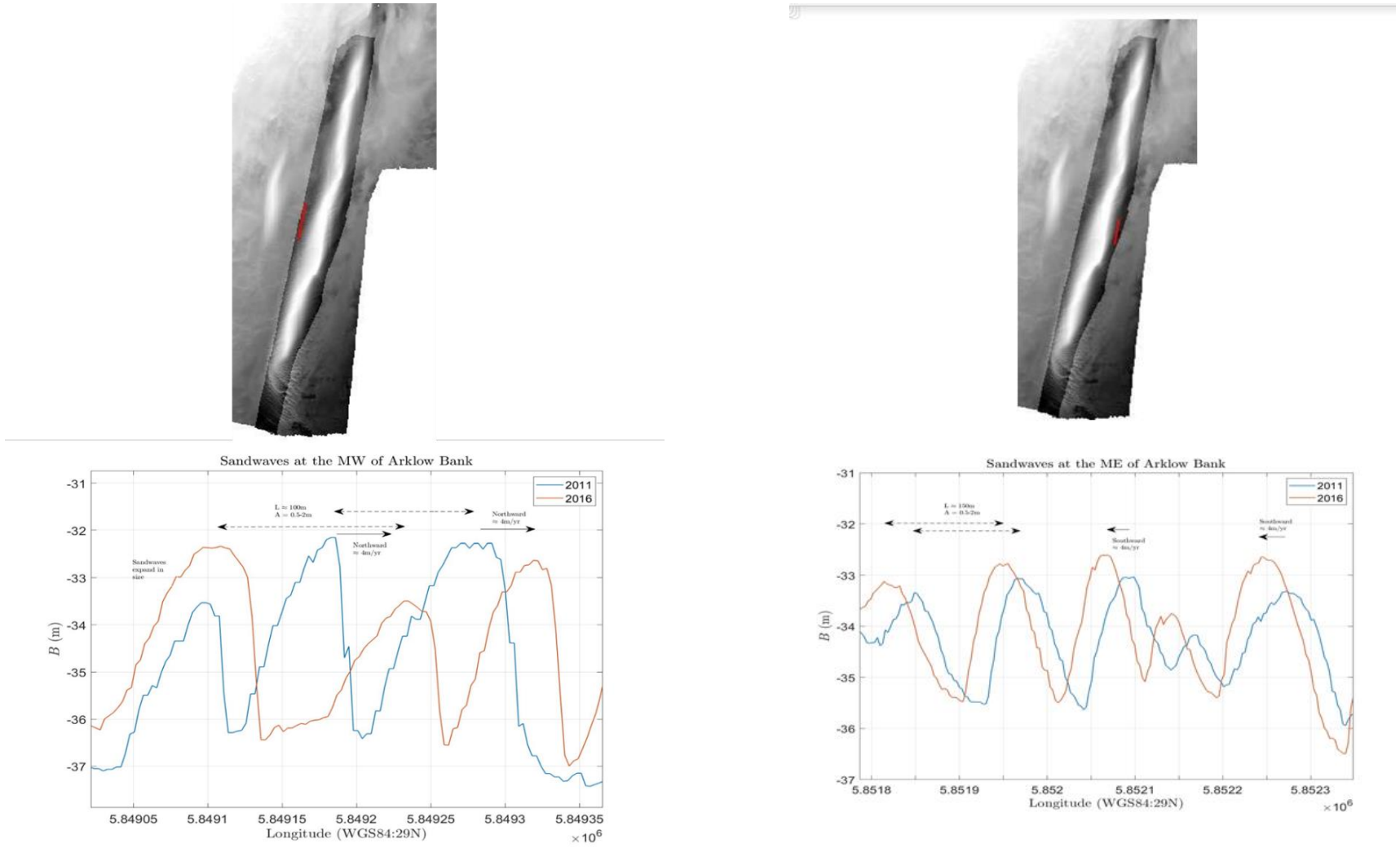


Figure 97. Transect analysis at a location to the mid-west of the central part of the bank (sandwaves crests to the right indicating northwardsediment movement) (left panel). Transect analysis at a location to the mid-east of the central part of the bank (sandwaves crests to the left indicating southward sediment movement) (right panel). The image at the top shows a red line which depicts the length and orientation of the profile presented below where the blue line shows the data from 2011 and the red line shows the data from 2016.

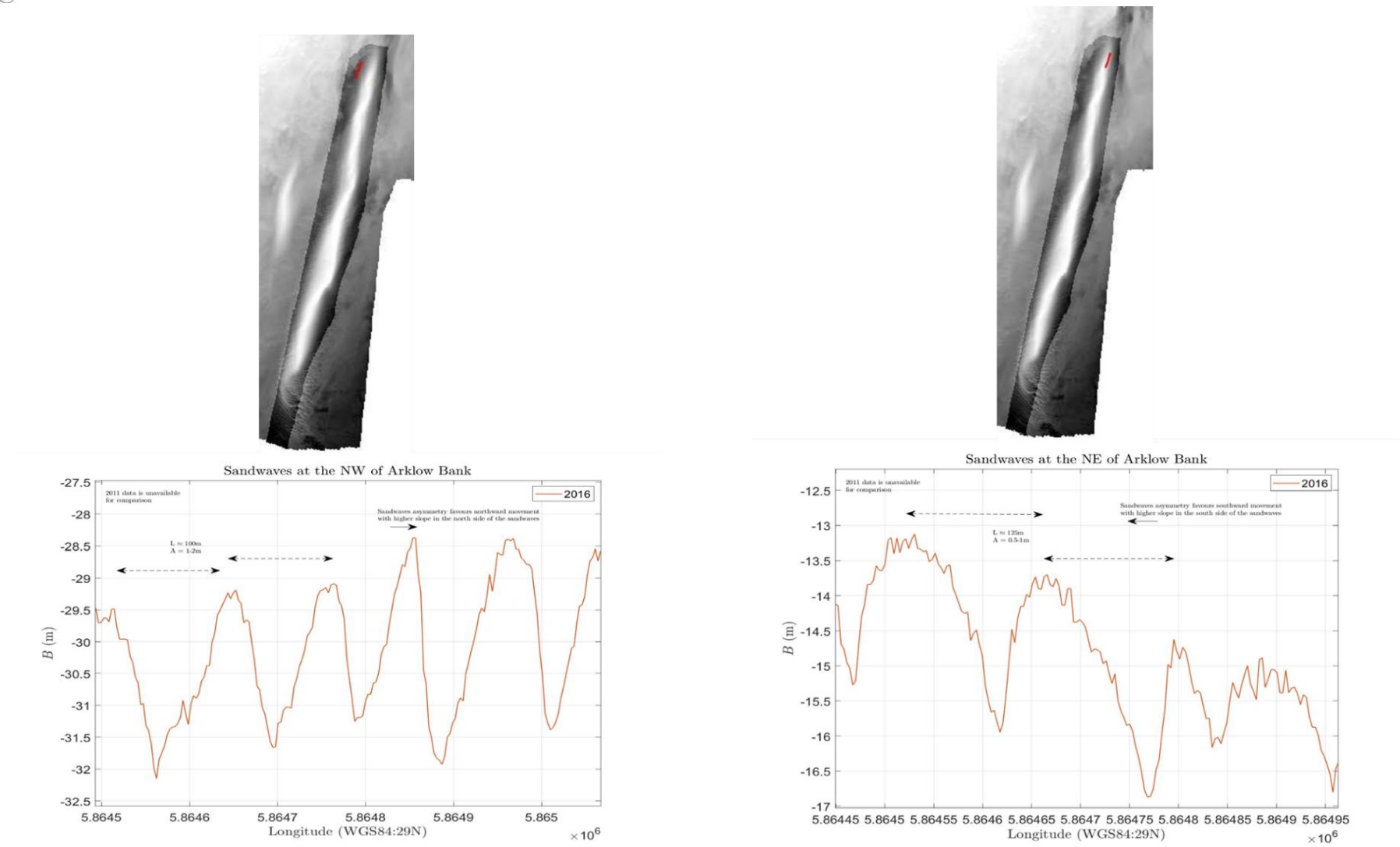


Figure 98. Transect analysis at a location to the NW of the bank (sandwaves crests to the right indicating: northward sediment movement). Transect analysis at a location to the NE of the bank (sandwaves crests to the left indicating southward sediment movement). Note: 2011 data is not available.

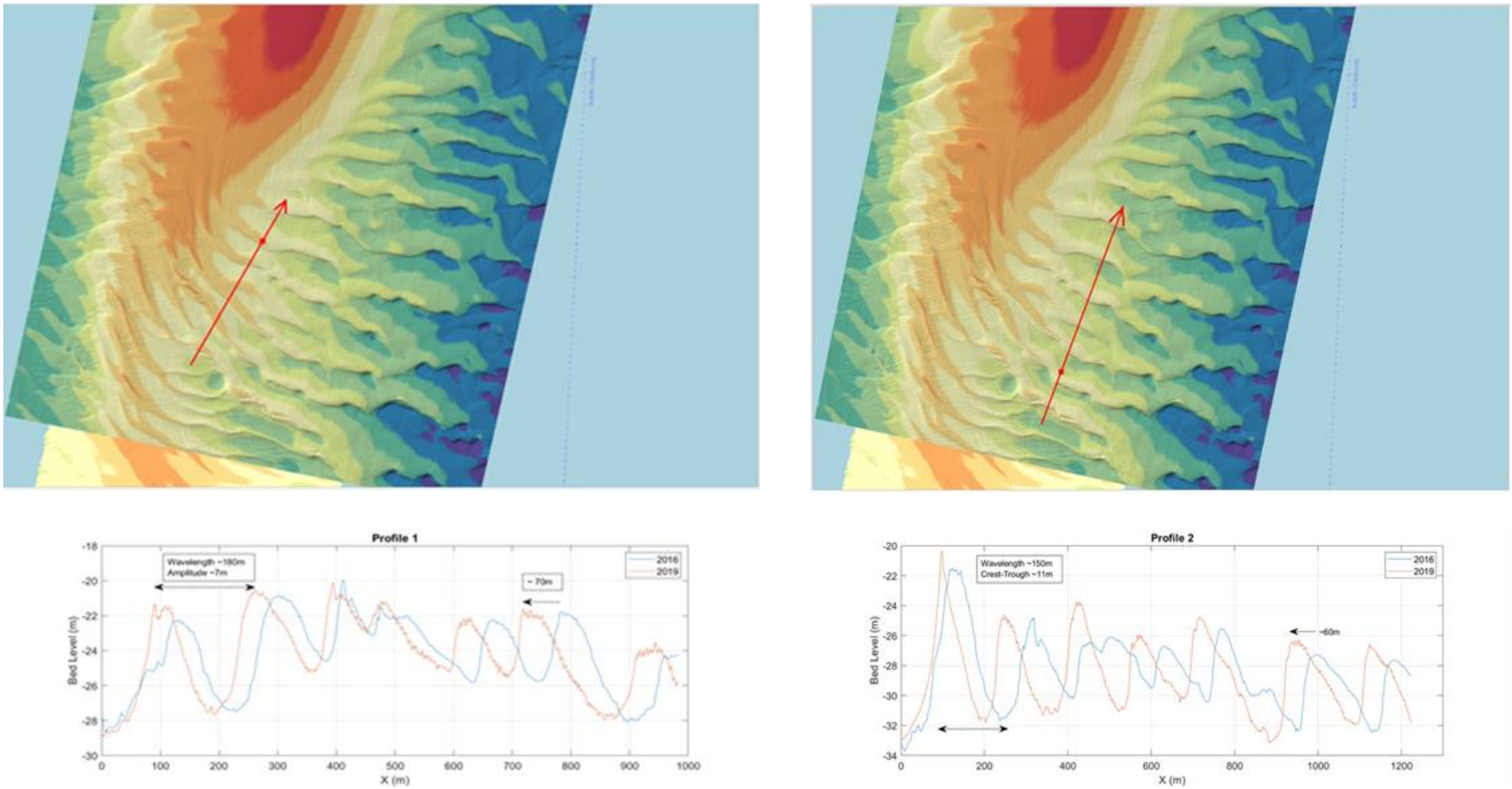


Figure 99. The analysis of sandwaves at the southern tail, and southeast region, of the bank derived from the bathymetry data collected in 2016 and 2019. The red arrows in the top image depicts the length and orientation of the profile presented below where the blue line shows the data from 2016 and the red line shows the data from 2019.

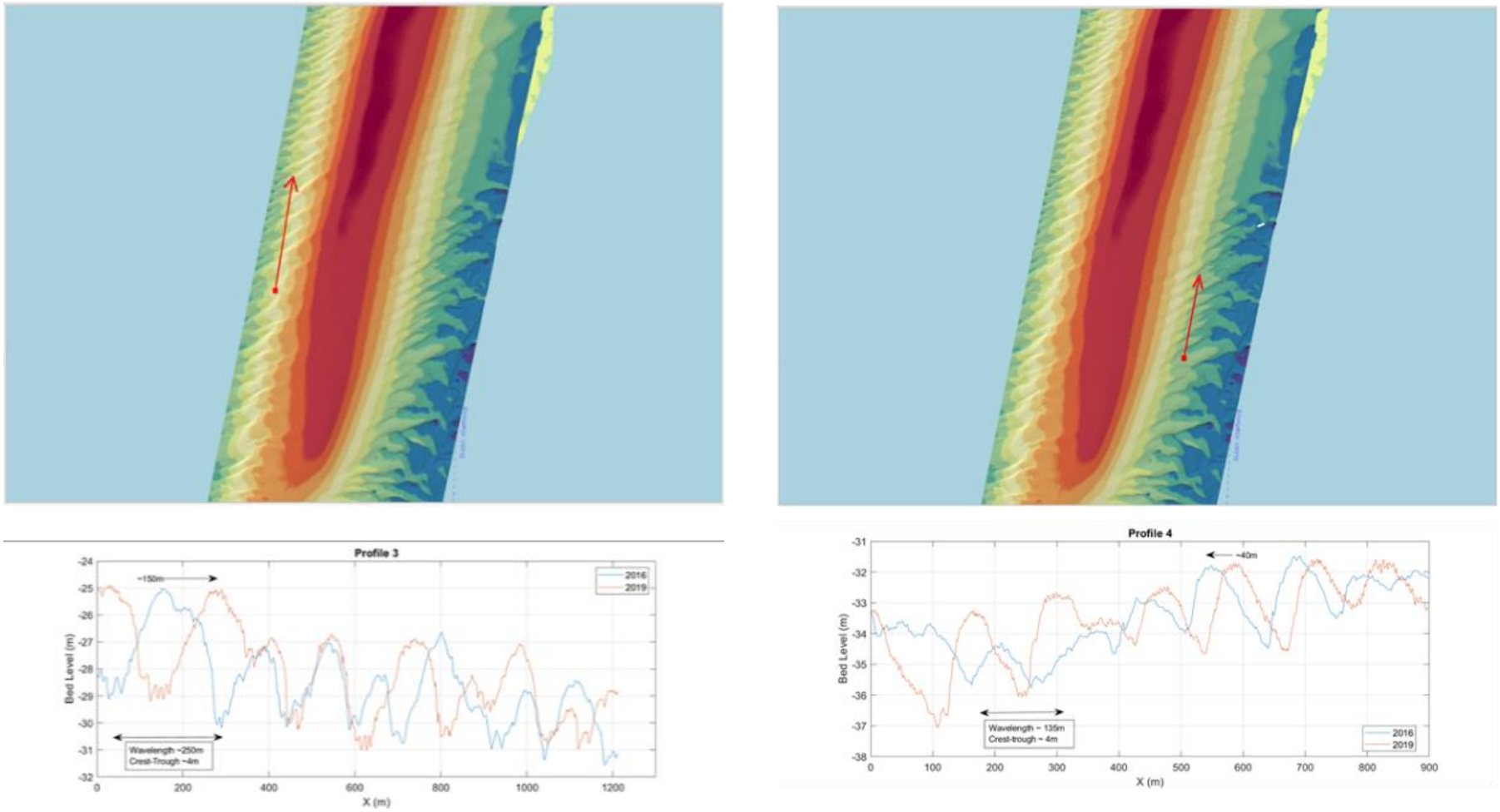


Figure 100. The analysis of sandwaves at the southwest and southeast region, of the bank derived from the bathymetry data collected in 2016 and 2019. The red arrows in the top image depicts the length and orientation of the profile presented below where the blue line shows the data from 2016 and the red line shows the data from 2019.

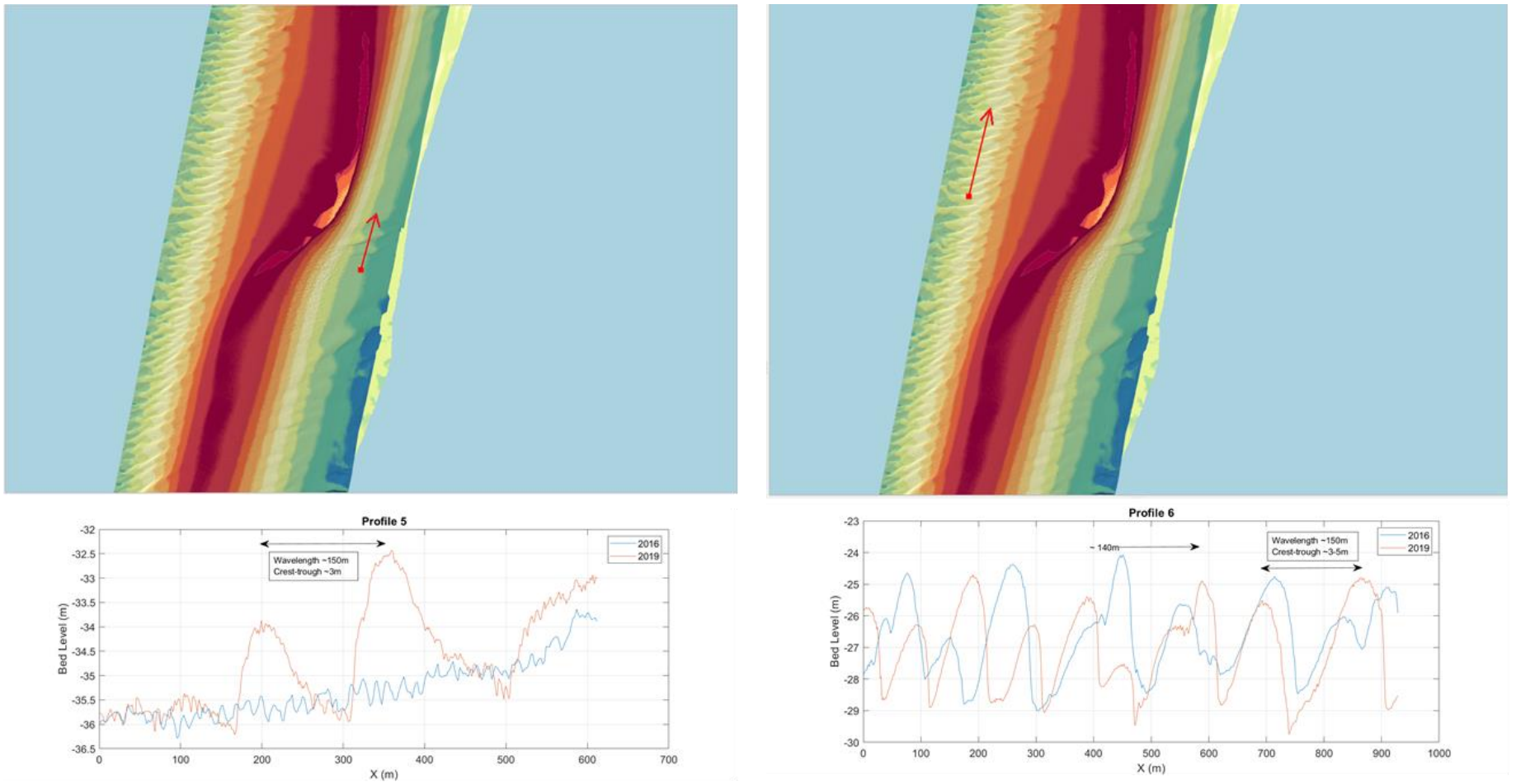


Figure 101. The analysis of sandwaves at the central west and central east region, of the bank derived from the bathymetry data collected in 2016 and 2019. The red arrows in the top image depicts the length and orientation of the profile presented below where the blue line shows the data from 2016 and the red line shows the data from 2019.

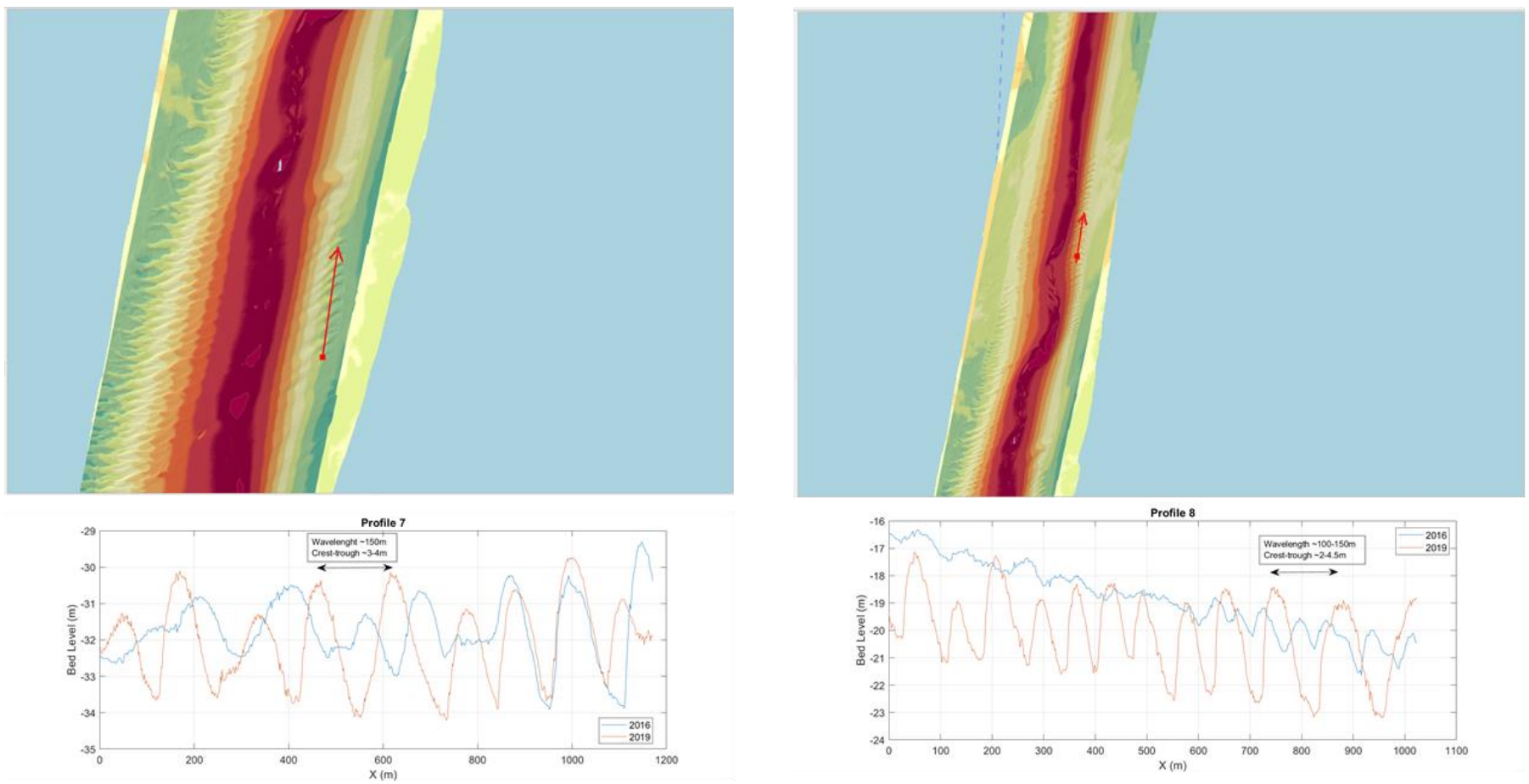


Figure 102. The analysis of sandwaves at the central east region, of the bank derived from the bathymetry data collected in 2016 and 2019. The red arrows in the top image depicts the length and orientation of the profile presented below where the blue line shows the data from 2016 and the red line shows the data from 2019.

Using the Topographic Position Index (TPI) method, as described by Weiss (2001) and Secomandi *et al* (2017), a 'minimum' and 'maximum[29]' RSBL was determined. The TPI compares the depth of each cell in the bathymetric dataset to the mean depth of a specified neighbourhood around that cell (Weiss, 2001). The bathymetric raster cells are then classified as either above or below average for the area (considering local ridges and troughs, respectively). A circular area was analysed, using a radius determined based on the bedform characteristics (e.g. 50m radius is used for sandwaves of wavelength < 100 m, and a radius of 125 m is used where wavelengths > 100 m). Through a process of filtering, the method isolates mobile seabed features; subtracting these isolated features from the bathymetric data (collected in 2016 and 2019) the RSBL or the 'static bathymetry' can be determined. The 'minimum' and 'maximum' RSBL were determined to support assessment of seabed level change associated with large scale mobile bedforms. Figure 103 shows the RSBL determined from the 2019 bathymetric dataset. Figure 104 presents, for reference, a comparison of the determined RSBL to bedforms captured in the 2019 bathymetry survey. Finally, Figure 105 and Figure 106 shows the potential vertical change predicted to occur through time due to the migration of mobile bedforms derived from the 2016, and 2019, bathymetry datasets, respectively. Note: the raising and lowering of the seabed level in areas dominantly comprised of mobile bedforms is considered to be transient in nature as the sandwave moves material along the seabed in the direction of net migration.

29 Where mobile bedforms persist, the 'minimum' RSBL determines the seabed level broadly coincident with the trough of those bedforms, whereas the 'maximum' RSBL determines the seabed level broadly coincident with the crest. The maximum RSBL has been issued as part of the complementary data package issued with this report. The determination of the RSBL forms useful data when considering engineering design for WTG substructures and particularly cable burial and routing. Consideration of the RSBL, in conjunction with the predicted LSBL forms a particularly powerful evidence base from which to optimise design. Determination of the RSBL does not account for the repositioning of any parts of the bank. The predicted LSBL and HSBL, output from model predictions, which does consider these processes, is critical to understand the implications of these processes on the seabed levels.

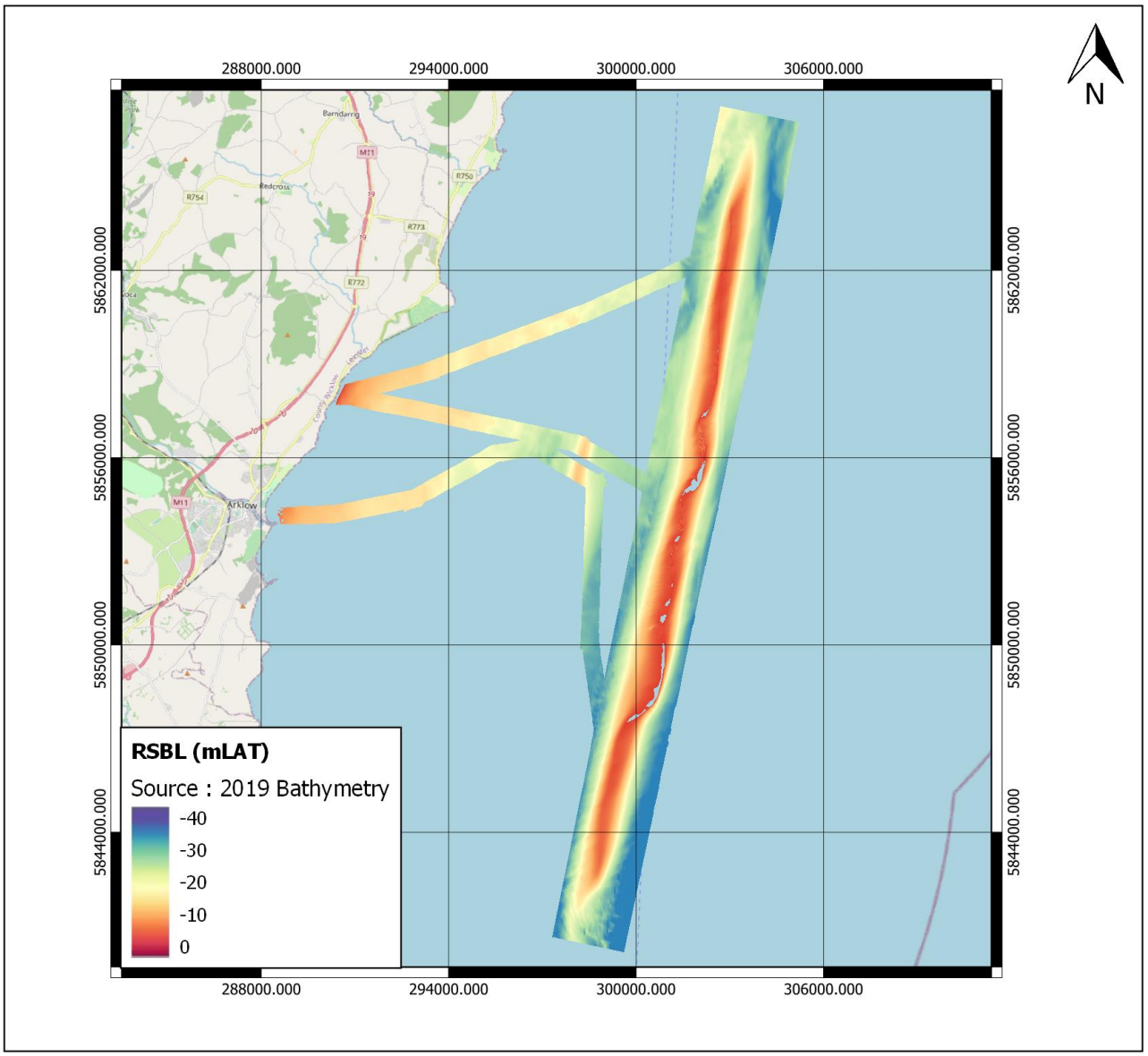


Figure 103. The 'minimum' RSBL determined from the 2019 bathymetry dataset using the TPI method. Note: the maximum RSBL has also been determined and is provided as part of the complementary data package provided alongside this report.

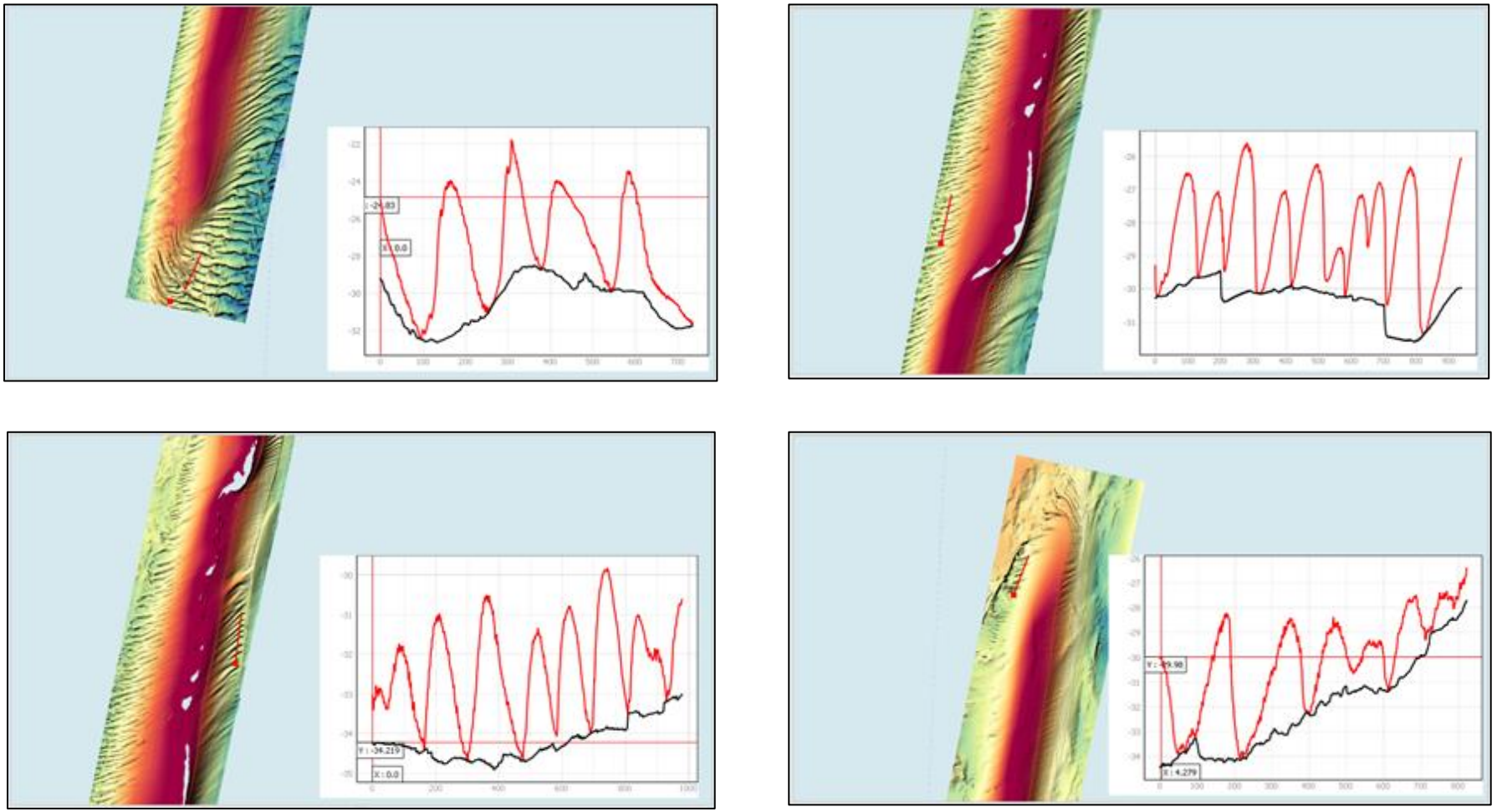
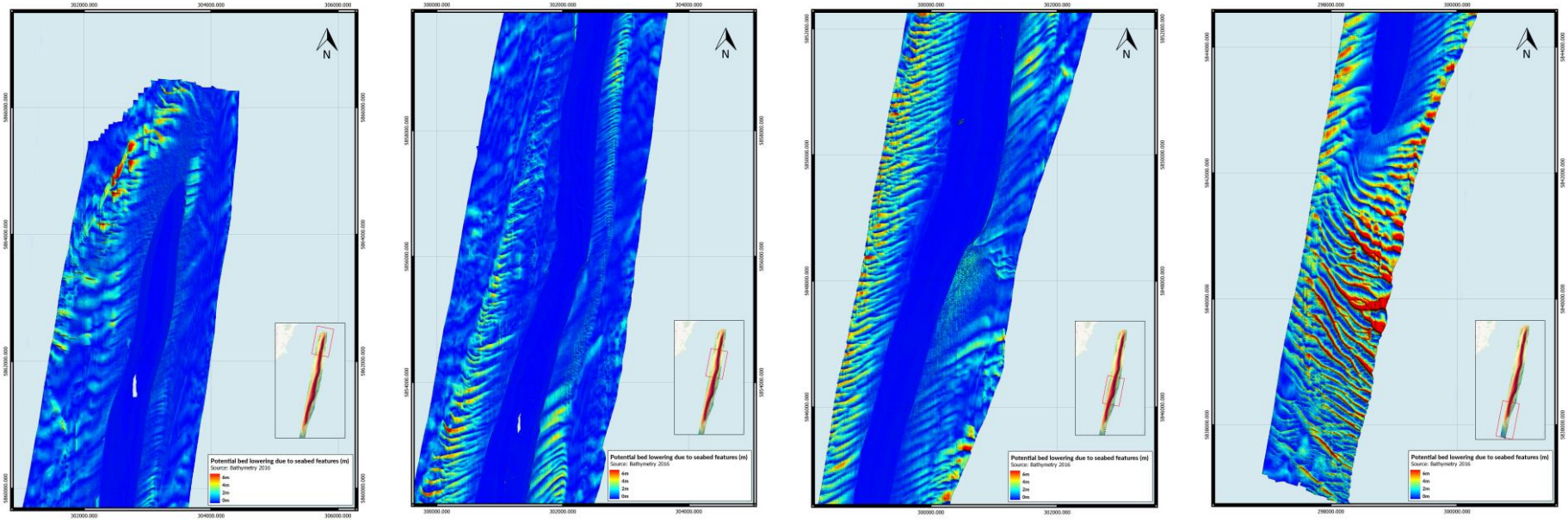
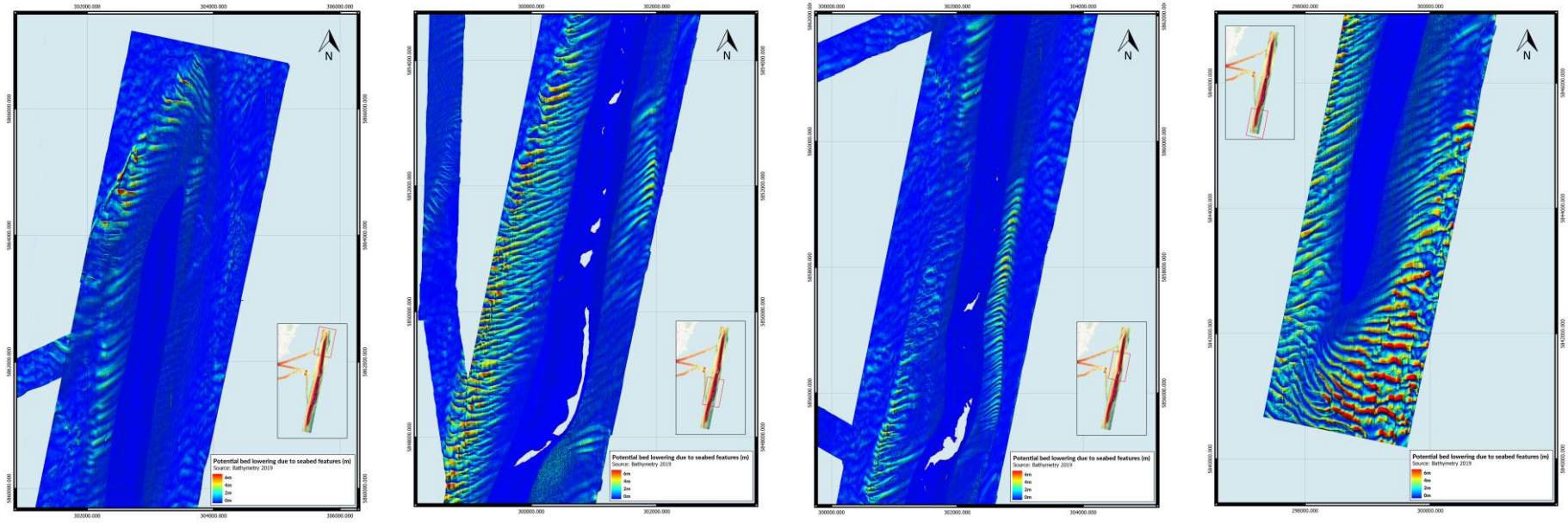


Figure 104. The comparison of the RSBL to areas of sandwaves identified in the 2019 bathymetry survey. Within the profile plots the RSBL is represented by the black line whereas the 2019 bathymetry profile is represented by the red line.



Northern region | Central North | Central South | Southern region

Figure 105. The potential vertical change predicted to occur through time due to the migration of sandwave features. The bed change is quantified by comparing the RSBL determined from the 2019 data, compared to the corresponding bathymetry.



Northern region | Central North | Central South | Southern region

Figure 106. The potential vertical change predicted to occur through time due to the migration of sandwave features. The bed change is quantified by comparing the RSBL determined from the 2016 data, compared to the corresponding bathymetry.

A Fourier transform method was applied to investigate changes to sandwaves through time across the lease area. The key benefit of a Fourier transform analysis is that it automates the process of assessing the crest / trough points of sandwaves enabling robust comparison of sandwave heights across the lease area; this is useful information for considering likely changes to sandwave characteristics over the short to medium term.

To perform this analysis the lease area was divided into profiles at 50 m intervals, which were then divided into equal transects of 200 m length (the length of these transects is chosen such that it at least covers a single sandwave. The orientation of these transects was along the axis NE – SW and thus the analysis only captures bedform oriented along this axis). For each transect, the analysis was performed. Based solely on wave height, sandwaves were classified as observed wave heights of > 1.5 m (Tobias, 1989). Figure 107 presents the results of the Fourier transform analysis for a single transect. The sandwave heights and lengths are deduced from the corresponding Fourier series. For each transect analysed, the results obtained from the Fourier analysis was plotted and the key statistics associated with sandwaves extracted at the centre of each transect. A difference plot was obtained for each locale by comparing the analysed data derived from the data acquired in 2016 and 2019 (Figure 108).

Sandwave migration rates were assessed manually via interrogation of profile data from bathymetry data acquired in 2016 and 2019 (see Figure 109, these profiles are presented in Figure 249 to Figure 349 in Appendix E). Migration rates determined from two bathymetry datasets should be treated with caution and the assessment would benefit from the collection of further bathymetry datasets.

.

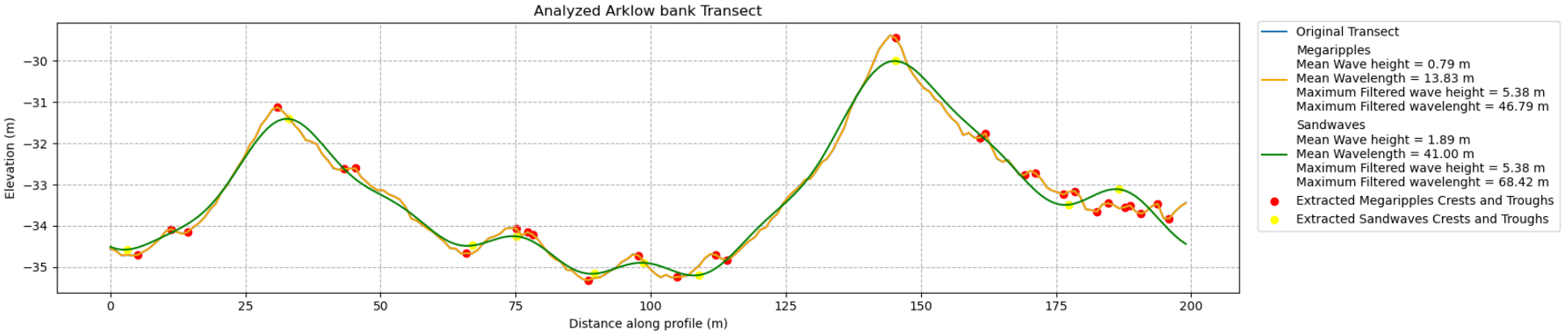
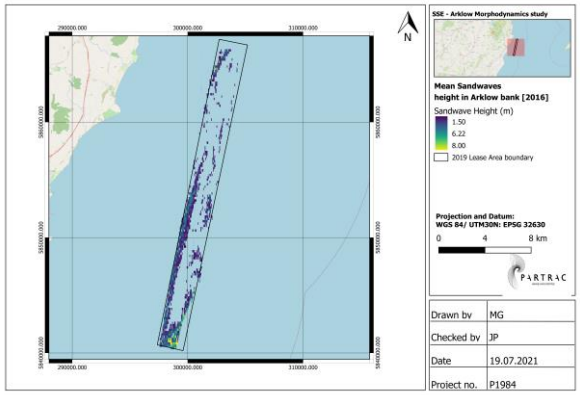
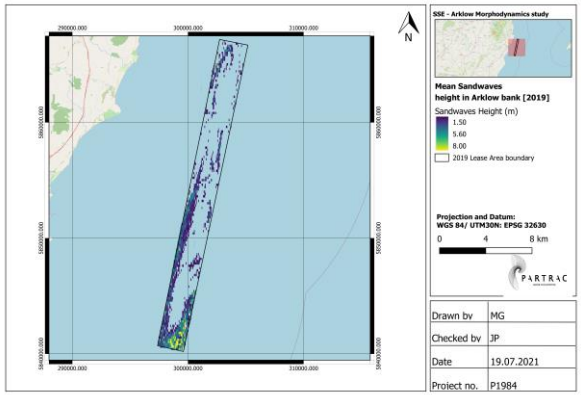
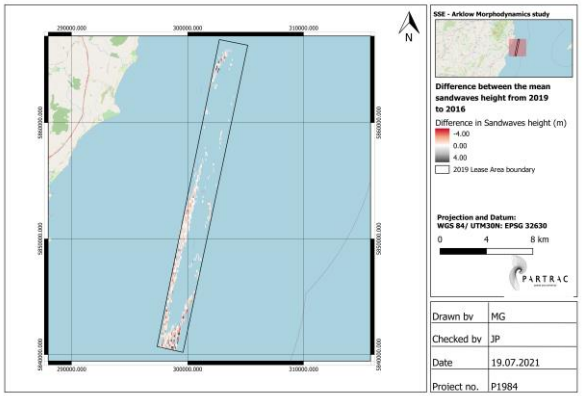


Figure 107. An example of the Fourier transform analysis. This method was applied to all transects across the lease area for the data acquired in 2016 and in 2019.







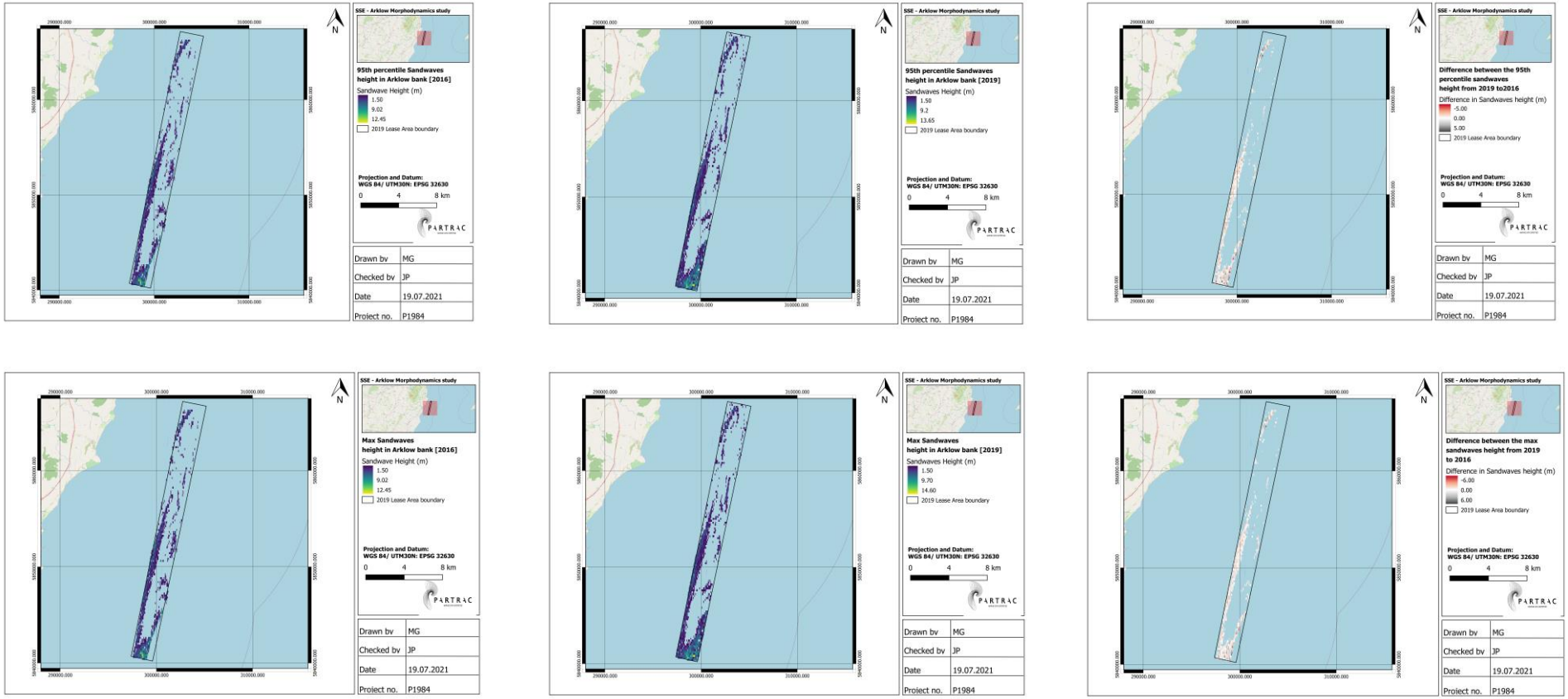


Figure 108. The mean, 95th percentile and maximum sandwave height derived from the Fourier transform method applied to the 2016 bathymetry data (left panel) and the 2019 bathymetry data (centre panel). The right panel shows the respective difference plot.

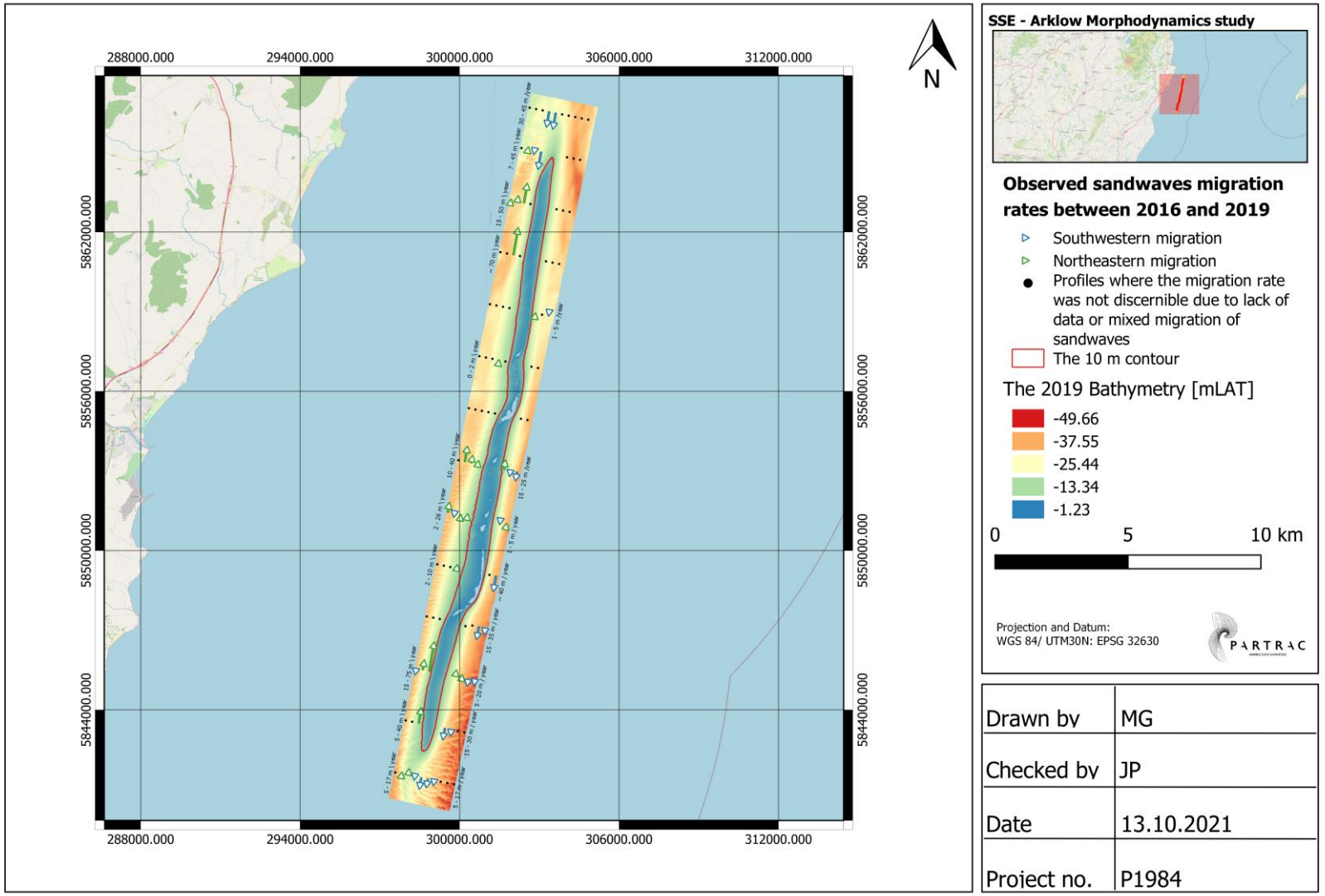


Figure 109. Sandwave migration rates determined from comparison of the data acquired in 2016 and 2019.

Direct interrogation of available bathymetry datasets has been performed. The analysis, which has been considered in the context of the process understanding presented in the foregoing analysis, was used to provide a detailed assessment of the bedforms observed across the lease area. Their dominant characteristics, influence on local seabed levels and their potential to migrate and evolve was assessed. The mobile bedforms observed across the lease area can be summarised as follows:

- Arklow Bank is tidally dominant, highly dynamic and with a sufficient supply of mobile, sand sized, sediments, to support the development of significant bedform features. Large scale sandwaves are prolific around the base of the bank, to the east and west and to the head of the bank to the north and the tail of the bank to the south (see Figure 96 to Figure 102). It is postulated that the bank shape and profile promote the formation of bedforms, and that these features act to nourish and sustain the bank over the longer term. Smaller scale megaripples persist across the east and west flanks of the bank and in the shallowest regions of the bank and at the crestline, where small sandwaves are also observed in the 2020 bathymetric datasets (see Figure 90 to Figure 92). The asymmetry of the sandwaves indicates consistency to the east and west sides of the bank, with sandwaves migrating northwards to the west of the bank and southwards to the east of the bank. At the base of the bank, the geophysical survey resolved sand over the main body of the sandwaves, and coarse sediment in parts of the trough, which indicates the trough may be limited by an immobile seabed layer and thus, the mobile sand is moving across this underlying coarser (potentially immobile) sediment.
- The largest sandwaves are observed to the south of the bank with wavelengths of 150-250 m and a typical amplitude (crest to trough) of between 3 – 5 m (Figure 96, Figure 99, Figure 100). The area is also prone to the greatest bed level change associated with the migration of these features which, on occasion, is up to circa ~11 m.
- Sandwaves with a wavelength of 150 to 250 m, and a typical amplitude of 3 – 5 m are observed at the base on both the east and west side of the bank (Figure 97, Figure 101 and Figure 102). Sandwaves at the base, to the west of the bank remain relatively consistent (i.e. amplitude and wavelength) through the period 2016 and 2019 with typical amplitudes of circa. 3-5m. The wavelength reduces from circa. 250 m in the south to circa. 150 m in the central region of the bank, as you move northward. The northward migration rate also appears to be consistent being circa. 50 m per year during the period 2016 to 2019.The sandwave system at the base of the bank, to the east of the bank is more complex. To the south, the sandwaves appear to be stable (in terms of their amplitude and wavelength) during the period 2016 to 2019, with features characterised by wavelengths of circa. 150 m and amplitudes of typically circa. 4 m. As you move north along the east flank of the bank into the central and northern regions of the bank, the amplitude, and wavelength, of the sandwaves in these areas increased over the period 2016 to 2019. These sandwaves continue to migrate southward but it is difficult to estimate their migration rate in these areas as there is limited correlation between the 2016 and 2019 profiles.

- Sandwave area at the northern region (head of the bank). This area is characterised by relatively large sandwaves positioned toward the northwest of Arklow Bank with a wavelength of circa. 150 m and a typical amplitude of 4 – 6 m (Figure 98).
- On the eastern and western flanks of the bank and above the -10 m contour megaripples are consistently observed, on occasion sandwaves are observed (see Figure 85 and Figure 86). These sandwaves are smaller than those observed around the base of the bank with typical amplitudes of < 2 m; this is a function of the shallow water depths and episodic wave influence across the shallowest regions of the bank (Figure 90, Figure 91 and Figure 92).

The determination of the minimum and maximum RSBL and the Fourier transform analysis indicated that

- The maximum potential seabed level lowering due to bedforms can be predicted by subtracting the RSBL from the original bathymetry of the area. The result shows that the crests of the sandwaves have the largest predicted lowering while the troughs have no predicted lowering (i.e. the predicted vertical change broadly reflects the amplitude of the sandwaves). The largest variations are predicted along the sandwaves crests at the southeast of the tail of the bank where the seabed is likely to lower (transiently), by up to circa 6 m. These findings are corroborated by the Fourier transform analysis which also indicated that the greatest change in sandwave height occurs at the southern tail of the bank. The magnitude of change ranges (i.e. raising or lowering of the seabed level) by up to 4 m when considering mean values, extending to up to 6 m when considering maximum values.
- The determination of the RSBL forms useful data when considering engineering design for WTG substructures and particularly cable burial and routing. Consideration of the RSBL, in conjunction with the predicted LSBL forms a particularly powerful evidence base on which to optimise design. However, determination of the RSBL does not account for the repositioning of any parts of the bank and thus *does not simply form the potential LSBL across the development site*.

The assessment of sandwave migration rates is summarised as follows:

- *Head of the bank (to the north)*: In this region observed migration rates range from 7 m per year to 45 m per year. Sandwave asymmetry indicates migration south westwards and north-eastwards, which is corroborating evidence of the changes to tidal asymmetry in this region of the bank which moves from the southeast to northeast either side of the head of the bank. Due to these changes in asymmetry, it is likely that bifurcating bedform features exist in this region.
- *East flank:* Along the east flank observed migration rates range from 1 m per year to 40 m per year. Sandwave migration rates are increased along the east flank to the south of the bank. Sandwave asymmetry indicates migration dominantly south westwards which corroborates our understanding of tidal asymmetry in the region. It is noteworthy that migration north-eastwards is also observed which indicates that sandwave asymmetry is, on occasion reversed, associated with the ebb / flood tidal phase.

- *West flank:* Along the west flank observed migration rates range from 2 m per year to 75 m per year. Sandwave migration rates decrease in the north central region but increase in southern regions of the bank and towards the head of the bank. Sandwave asymmetry indicates migration dominantly North westwards which corroborates our understanding of tidal asymmetry in the region. It is noteworthy that migration south-eastwards is also observed which indicates that sandwave asymmetry is, on occasion reversed, associated with the ebb / flood tidal phase.
- *Tail of the bank (to the south):* In this region observed migration rates range from 5 m per year to 17 m per year. Sandwave asymmetry indicates migration south westwards and north-eastwards, which is corroborating evidence of the changes to tidal asymmetry in this region of the bank which moves from the northeast to southwest either side of the tail of the bank. Due to these changes in asymmetry, it is likely that bifurcating bedform features exist in this region.

Looking forward across the lifetime of the development:

- Across the lifetime of the development, where sediment supply is maintained within the sediment cell and the local hydrodynamic regime broadly remains the same, there is no evidence to suggest that the observed sandwaves and megaripples will cease to exist or that the observed sandwave characteristics will significantly alter (beyond those alterations observed within the survey datasets). Large-scaled bathymetric patterns are highly likely to remain similar over decades, but it is also highly likely that temporary changes may occur to these bedforms i.e. changes in length, height, amplitude, and asymmetry of individual sandwaves. This conclusion is based upon the available evidence derived from interrogation of the 2016 and 2019 data. For example, a key question which requires consideration is, at the base of the bank, *how do bedform characteristics change as the profile of the bank, against which these features abut, changes through time?* It is evident from profile 5 and profile 8 presented in Figure 101 and Figure 102, respectively that in two locations towards the base, on the east flank of the bank, megaripples observed in 2016 have developed into sandwaves by 2019. This consistent bedform growth is evidence of consistent supply of sediment transported as bedload around the base of the bank. Considering this evidence, even where significant changes to the bank shape / profile occur, these changes are postulated to only likely cause temporary changes to the bedform patterns which persist around the base of the bank as the highly mobile tidal regime will quickly transport sediment to those areas, where bedforms will start to reform due to the dominant tidal regime.
- It is reasonable to assume that net changes over a period of decades (i.e. over the lifetime of the development) may be broadly negligible i.e. the maximum amplitude of sandwave features observed in the 2016 and 2019 datasets, broadly reflect the maximum predicted, bed level change within these locales. This is because wave influence across the lease area (even around the base of the bank where wave influence is infrequent) could, on occasion, have the capacity to temporarily reduce the height of the sandwaves which persist across the site. When considering the potential for significant sandwave growth across the lifetime of the development it is useful to consider that sandwave height is typically limited to 25 percent of observed

water depths (McCave, 1971). These uncertainties must be considered when predicting future seabed levels in regions of the seabed where large scale, highly mobile, sandwaves across the lease area. The collection of additional MBES data in areas characterised by the large scale sandwaves would improve confidence in the assessment of the evolution, and spatiotemporal changes, of such features.

8.9 Repositioning of the Crestline and Changes to the Shape and Profile of the Bank

To predict future seabed levels, it is critical to understand how those processes identified to occur across the bank drive changes through time to bank morphology over the short, medium, and longer term – particularly as it is postulated that the repositioning of the crestline and subsequent changes to bank shape and profile drive the most significant vertical change in seabed level, through time. This significantly slower process, drives change to the form and profile of the bank, may have a larger consequence for WTG structures, than the significant, but transient changes to the seabed level associated with sandwaves. The Interrogation of the historic bathymetry datasets provide the best opportunity to study such changes. It is recognised that the repositioning of parts of the bank driven by the movement of the crestline, and the associated effects on the form and profile of the bank, has the potential to induce significant bed level change across the lease area risking the stability of foundations and the integrity of inter-array and export cable assets. Tidal processes, enhanced during periods of wave activity, sweep the crest back and forth through time; asymmetry in cross bank flows govern the net migration of the crestline. The systems-based approach adopted relies on distinguishing between short-term changes and longer-term trends so as to predict future seabed levels. Indeed, several authors have postulated about whether the full bank feature is migrating in position over the longer-term. A comparison of bathymetric data collected in 2000 (Fugro, 2000) and 2002 (Seacore, 2002) was performed by Cathie Associates Ltd (2018). It was concluded that the analyses indicated that the bank migrated approximately 200 m in an eastward direction between the two survey dates (i.e. across the period of 2 years). This conclusion is deemed unlikely, as the distance migrated would exceed that expected of the overall movement of an open shelf linear sandbank, though as the original data is not available to this commission this inference cannot be confirmed. A holistic view of all available data leads the consortium to conclude that the bank (as a whole feature) is not migrating *per se* (i.e. there is no residual, long-term shift in location), with Wicklow Trough constraining the position of the north of the bank. Net sediment transport patterns derived from the model indicate that sediment transport from west to east, and east to west, over the crest of the bank. These residual transport patterns lead to erosion on the eastern or western flank of the bank and subsequent accretion on the opposite flank, and a progressive shift of the crestline in an easterly or westerly direction which drives a change in bank profile (i.e. forms a lower and extended profile on the eroded flank characterised by a gentler slope towards the crest, and a steeper slope on the opposite flank at the other side of the crestline). The behaviour of the bank is broadly analogous to the behaviour of a large tidal sandwave except that the relative position of the bank does not change significantly. This is a function of the following:

- The residual flow over the crest of the bank, which drives net changes in the position of the crestline, is subject to changes in direction across space, through time and thus the condition which drives repositioning of the crestline does not exist permanently resulting in bank movement to both the east or west, maintaining the relative position of the bank:
- Eastward or westward movement of the bank is eventually curtailed by the clockwise circulatory sediment transport around the base of the bank and slope induced transport down the steeper flank (noting that the relative steepness of the bank flank varies spatially) of the bank, and,
- The immobile core of the bank.

A detailed analysis of all bathymetric data available to the commission (see Section 3.1), is presented in Figure 114 to Figure 200. Multiple transects were specified to assess profile changes, and thus bank movement, along the E-W axis between coincident survey dates. For the periods coincident with survey data acquired in 2020 (i.e. timescales from individual tides to weeks and months) transects were extracted from each IA. The location of these transects is shown in a map of each IA in Figure 110 to Figure 113. To assess spatial differences, bank movement across different time scales was assessed in detail above the -10 mLAT contour, and below the -10 mLAT contour.

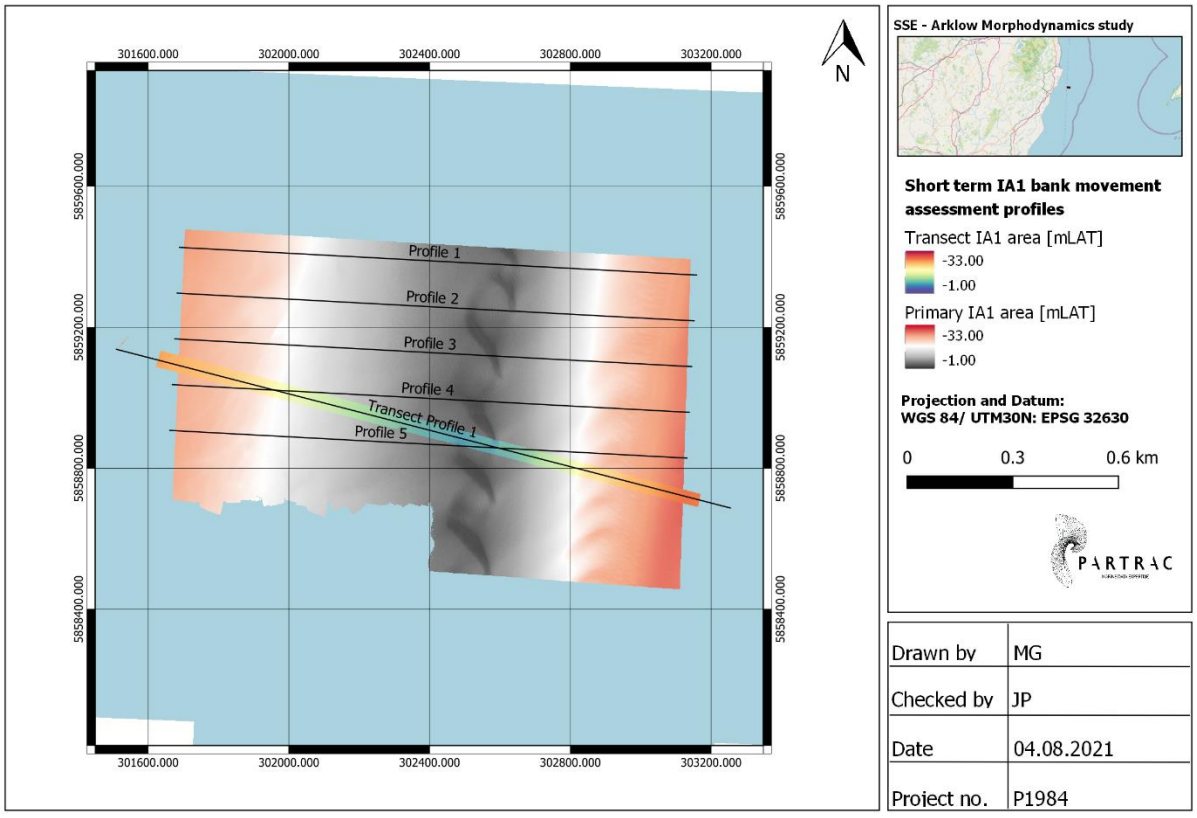


Figure 110. The profiles extracted from IA1.

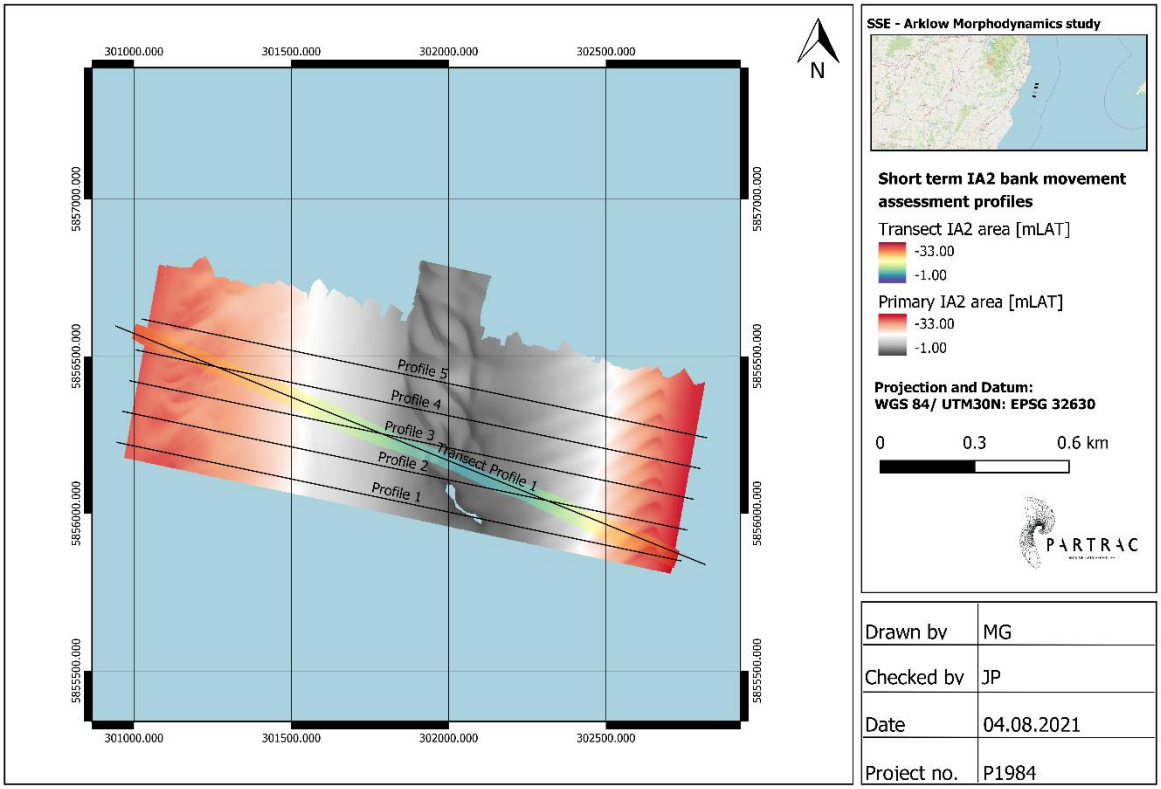


Figure 111. The profiles extracted from IA2.

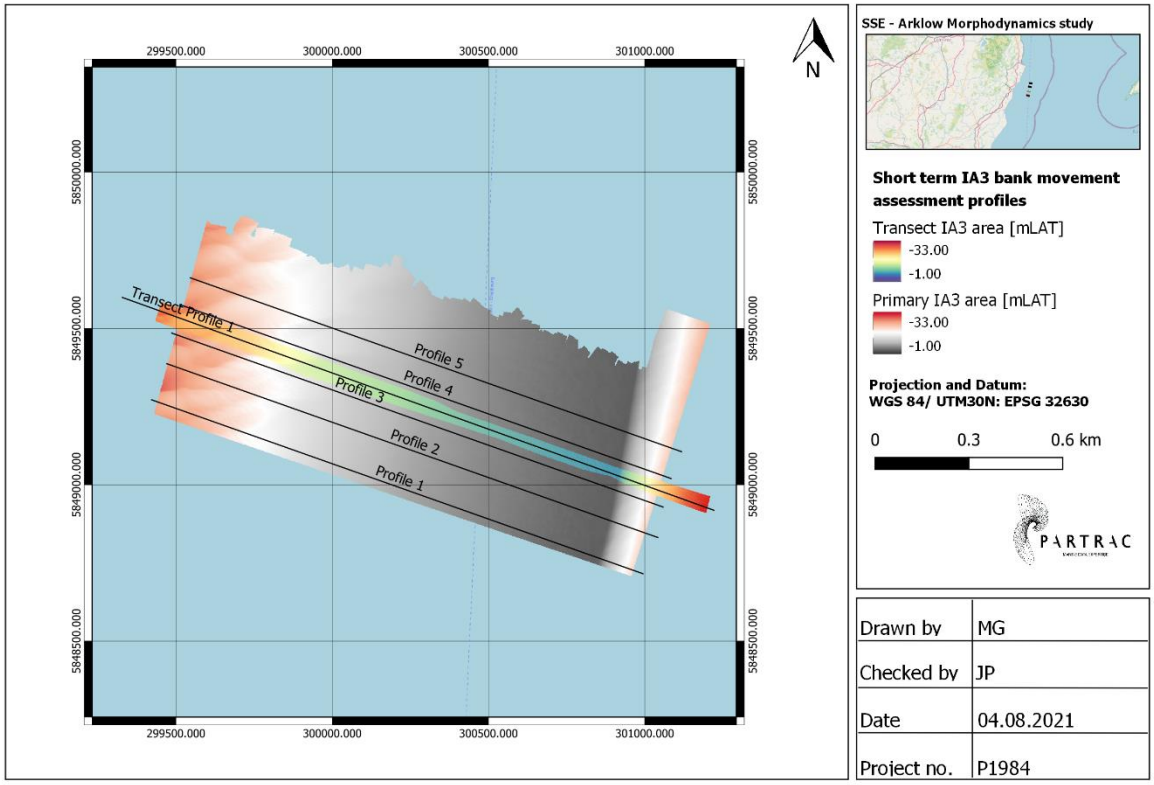


Figure 112. The profiles extracted from IA3.

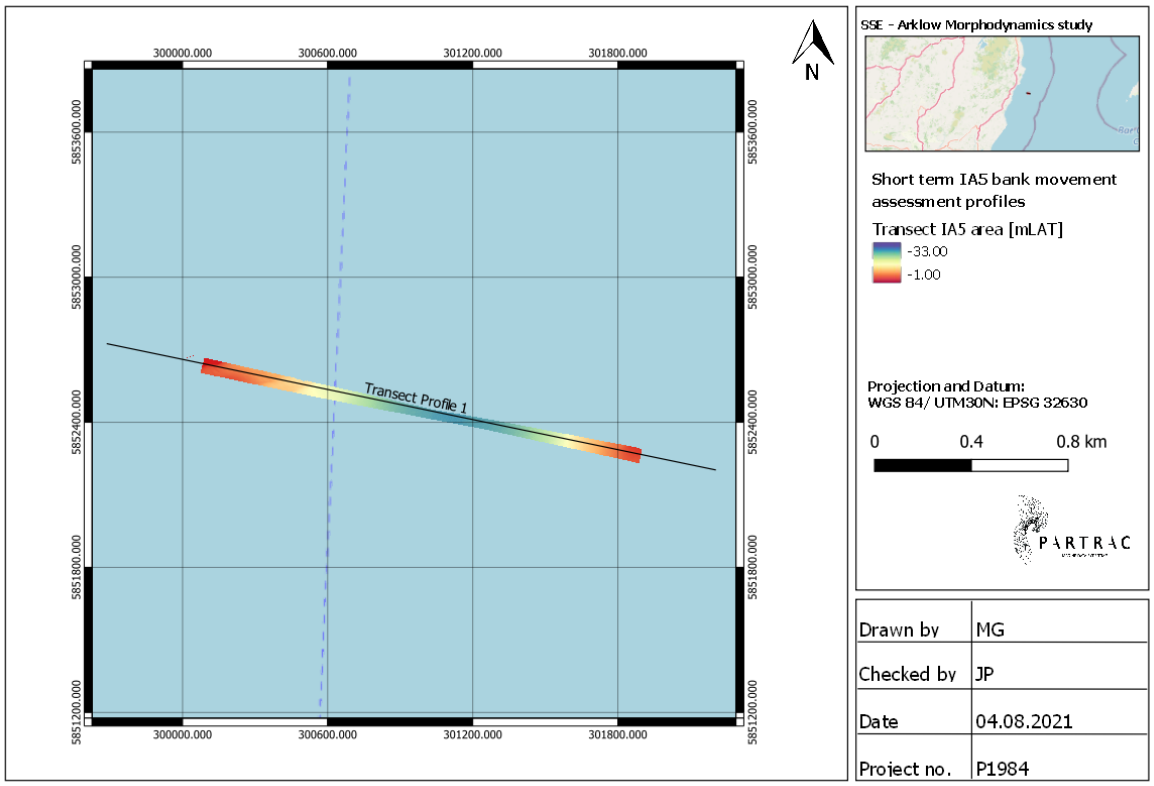


Figure 113. The profiles extracted from IA5.

To assess the response of the bank during tidal timescale (i.e. before and after the ebb / flood tidal phase), a series of transects were extracted and assessed from data acquired in the repeat surveys conducted in 2020 from IA1, IA2 and IA5. The bathymetry data available at tidal scales are detailed in Table 12. The profiles are presented in Figure 114 to Figure 118.

Table 12. Bathymetry data available at tidal timescales.

IA	Filename	Survey Date	Start Time	End Time
IA1	IA1_TR_203_1	21/07/2020	12:30	13:15
	IA1_TR_203_2	21/07/2020	16:10	16:40
IA2	IA2_TR_203_1	21/07/2020	10:45	11:20
	IA2_TR_203_2	21/07/2020	17:55	18:30
	IA2_TR_224_1	11/08/2020	09:31	09:57
	IA2_TR_224_2	11/08/2020	16:00	16:15
IA5	IA5_TR_210_1	28/07/2020	11:00	11:25
	IA5_TR_210_2	28/07/2020	17:15	17:40
	IA5_TR_220_1	07/08/2020	06:48	07:22
	IA5_TR_220_2	07/08/2020	13:01	13:25

Across the ebb/ flood tidal phase:

- Above the -10 m contour mobile bedforms (megaripples observed in IA1 and IA5 [see Figure 114, Figure 117 and Figure 118] and megaripples and small scale sandwaves observed in IA2 [see Figure 115 and Figure 116]) are observed moving in the direction of the tidal flow across the bank crest. Interrogation of these data indicated that these mobile bedforms moved laterally by up to 3 m along the transect in IA1, with up to 6 m of lateral movement observed along the transect in IA2 and IA5. These data indicate, that above the -10 mLAT contour the gross volume of sediments which are mobilised and transported during each tide is significant
- Where the seabed is deeper than the -10 m contour, along the east and west flanks of the bank, smaller scale megaripples (than those observed above the -10 mLAT contour) are evident, indicating transport of sediment toward, and over, the bank crest in the direction of the prevailing tidal flow. Though broadly negligible lateral movement of these bedforms, and changes to seabed level, is observed along the west and east flanks of the bank, over a single tide (Figure 114 to Figure 118).

  .

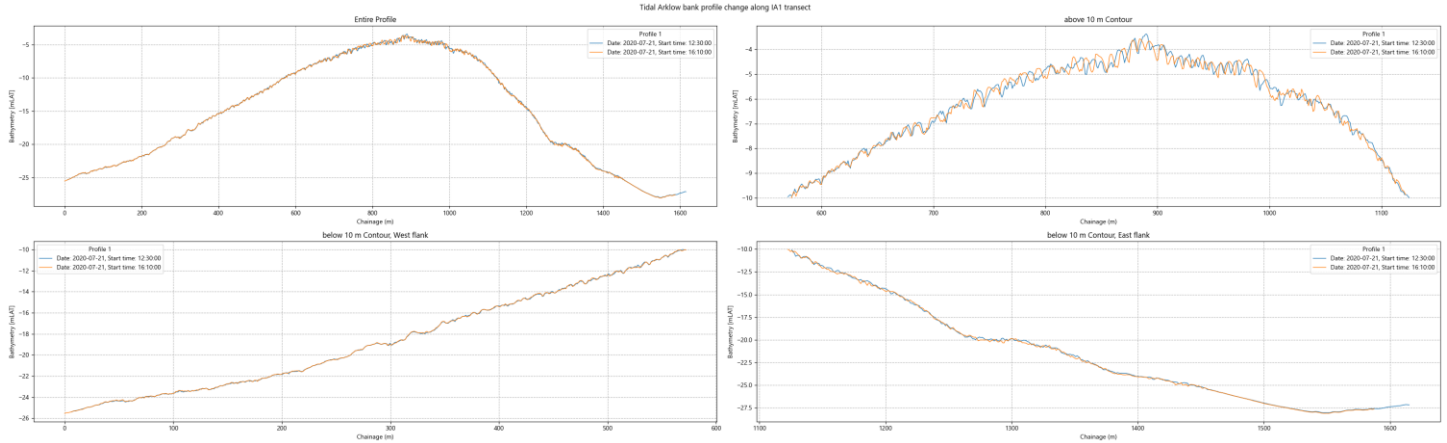


Figure 114. The profile extracted along the transect surveyed in IA1 on 21.07.20. The full profile (top left panel), the zoomed in profile above the -10 m contour (top right panel), the west (bottom left panel) and east (bottom right panel) face of the bank in areas deeper than the -10 m contour are presented.

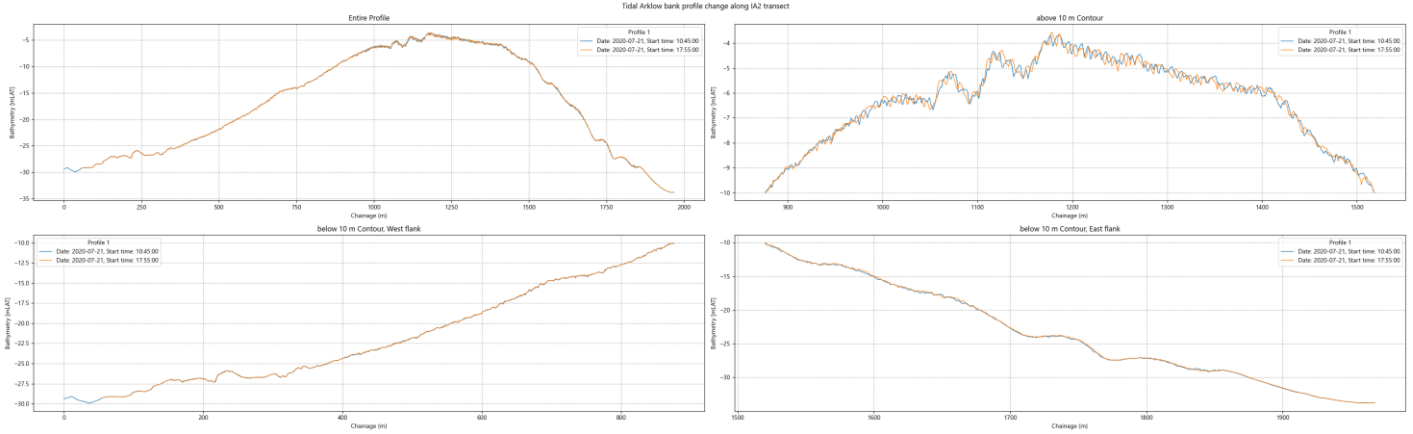


Figure 115. The profile extracted along the transect surveyed in IA2 on 21.07.20. The full profile (top left panel), the zoomed in profile above the -10 m contour (top right panel), the west (bottom left panel) and east (bottom right panel) face of the bank in areas deeper than the -10 m contour are presented.

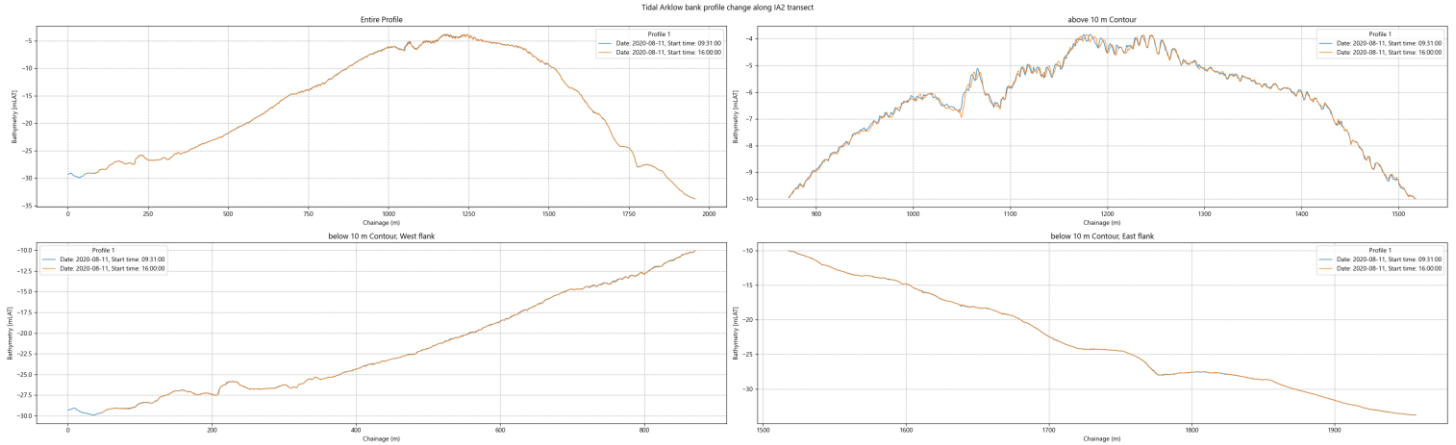


Figure 116. The profile extracted along the transect surveyed in IA2 on 11.08.20. The full profile (top left panel), the zoomed in profile above the -10 m contour (top right panel), the west (bottom left panel) and east (bottom right panel) face of the bank in areas deeper than the -10 m contour are presented.

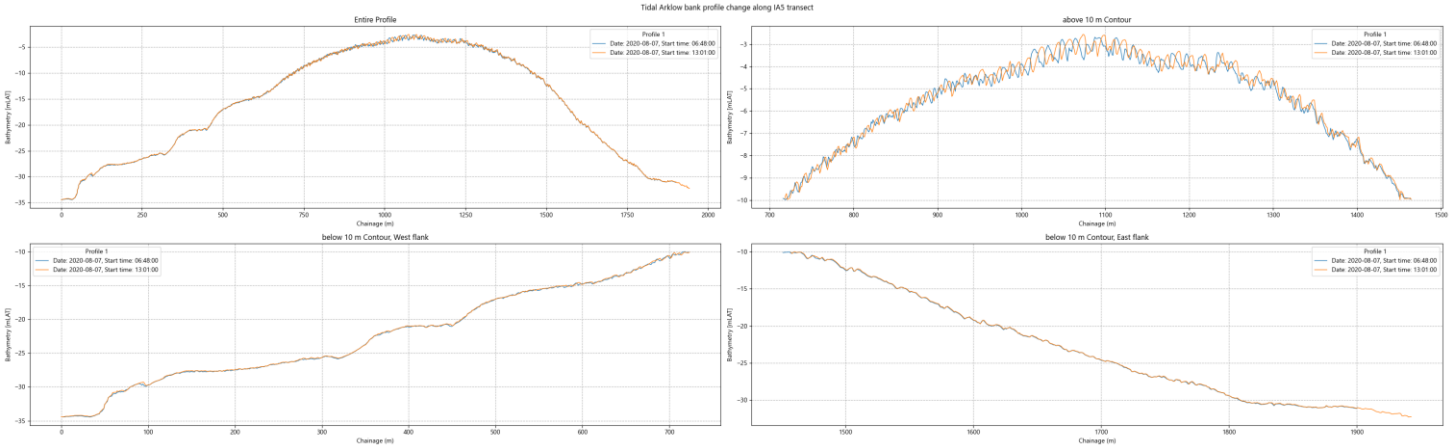


Figure 117. The profile extracted along the transect surveyed in IA5 on 07.08.20. The full profile (top left panel), the zoomed in profile above the -10 m contour (top right panel), the west (bottom left panel) and east (bottom right panel) face of the bank in areas deeper than the -10 m contour are presented.

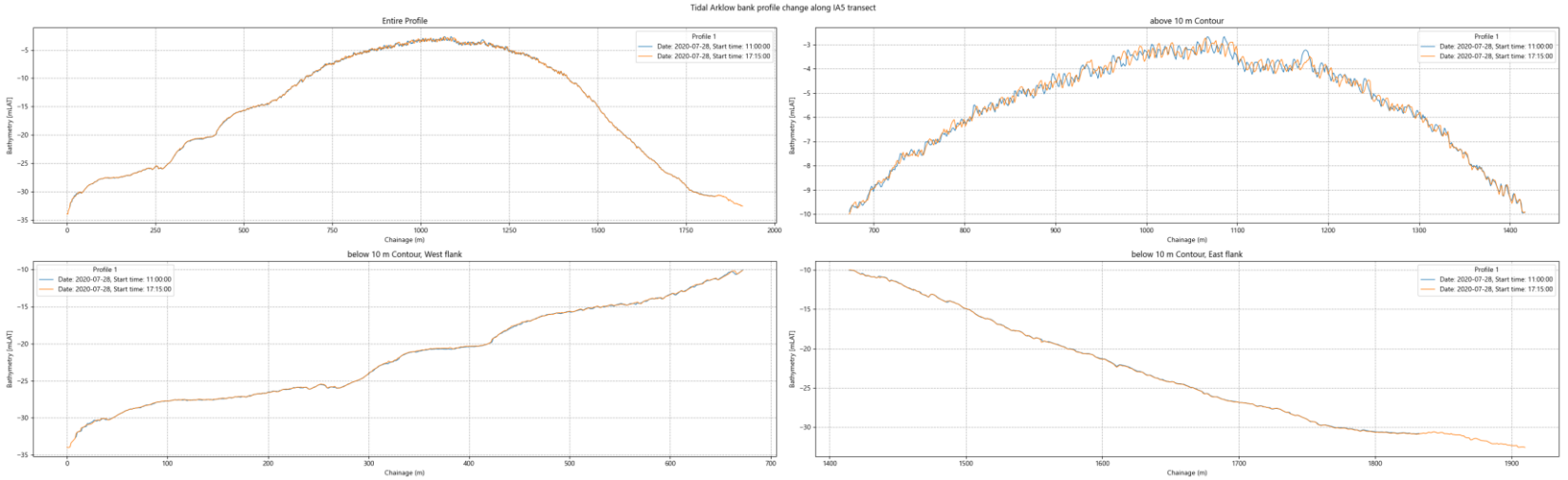


Figure 118. The profile extracted along the transect surveyed in IA5 on 28.07.20. The full profile (top left panel), the zoomed in profile above the -10 m contour (top right panel), the west (bottom left panel) and east (bottom right panel) face of the bank in areas deeper than the -10 m contour are presented.

To assess the response of the bank over daily timescales (i.e. observations made across circa 24-hour periods), a series of transects acquired from IA1, IA2, IA3, IA4 and IA5 were assessed. The bathymetry data available over this time are detailed in Table 13. The profiles are presented in Figure 119 to Figure 123.

Table 13. Bathymetry data available at daily timescales.

IA	Filename	Survey Date	Start Time	End Time
IA1	IA1_TR_219_1	06/08/2020	12:20	12:40
	IA1_TR_220_1	07/08/2020	08:30	10:15
IA2	IA2_TR_202_1	20/07/2020	11:20	11:50
	IA2_TR_203_1	21/07/2020	10:45	11:20
	IA2_TR_207_1	25/07/2020	07:45	08:20
	IA2_TR_208_1	26/07/2020	15:20	15:50
	IA2_TR_219_1	06/08/2020	14:24	14:43
	IA2_TR_220_1	07/08/2020	08:38	09:02
IA3	IA3_TR_219_1	06/08/2020	12:55	13:42
	IA3_TR_220_1	07/08/2020	07:35	07:57
IA4	IA4_TR_219_1	06/08/2020	10:21	10:45
	IA4_TR_220_1	07/08/2020	10:25	10:45
IA5	IA5_TR_210_2	28/07/2020	17:15	17:40
	IA5_TR_211_1	29/07/2020	11:50	12:43
	IA5_TR_219_1	06/08/2020	12:30	12:55
	IA5_TR_220_1	07/08/2020	06:48	07:22

Bank movement and observed seabed level change across a circa 24-hour period is summarised as follows:

- The net movement of mobile bedforms in regions shallower than the -10 mLAT contour is less than that observed across the ebb / flood phase, which would be anticipated as sediments are mobilised during both the ebb / flood phase. Review of the data acquired during the surveys conducted in 2020 from IA1 (Figure 119), and IA5 (Figure 123), indicated lateral movement of bedforms at the crestline of between circa 1 m, reducing in IA2 (Figure 121), and IA3 (Figure 122), to circa 0.5 m.
- Again, over the 24-hour period surveyed, the east and west flanks of the bank in areas deeper than the -10 mLAT contour, changes to the profile of the bank were broadly negligible which is likely due to the net effects of asymmetry being small over shorter time scales.

.

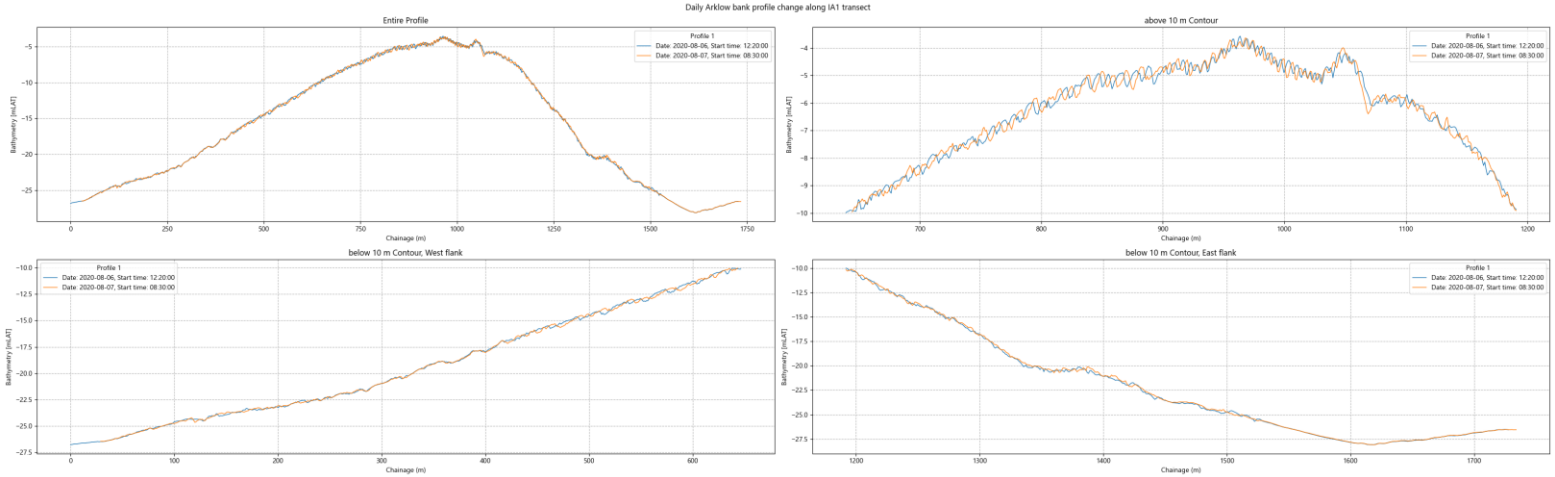


Figure 119. The profile extracted along the transect surveyed in IA1 over the period between 06.08.20 and 07.08.20. The full profile (top left panel), the zoomed in profile above the -10 m contour (top right panel), the west (bottom left panel) and east (bottom right panel) face of the bank in areas deeper than the -10 m contour are presented.

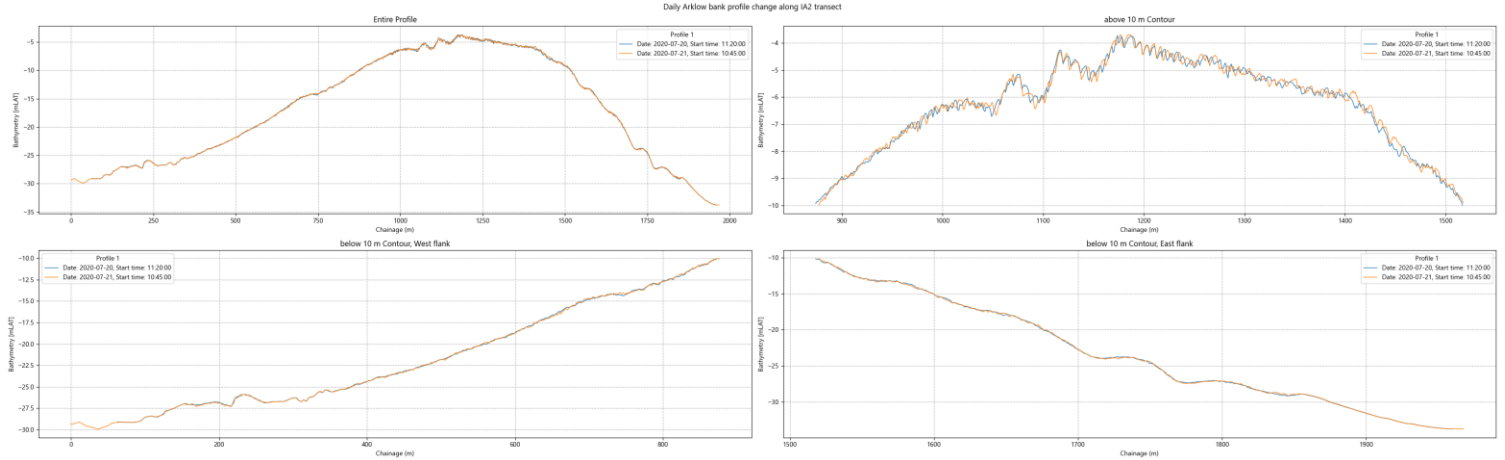


Figure 120. The profile extracted along the transect surveyed in IA2 over the period between 20.07.20 and 21.07.21. The full profile (top left panel), the zoomed in profile above the -10 m contour (top right panel), the west (bottom left panel) and east (bottom right panel) face of the bank in areas deeper than the -10 m contour are presented.

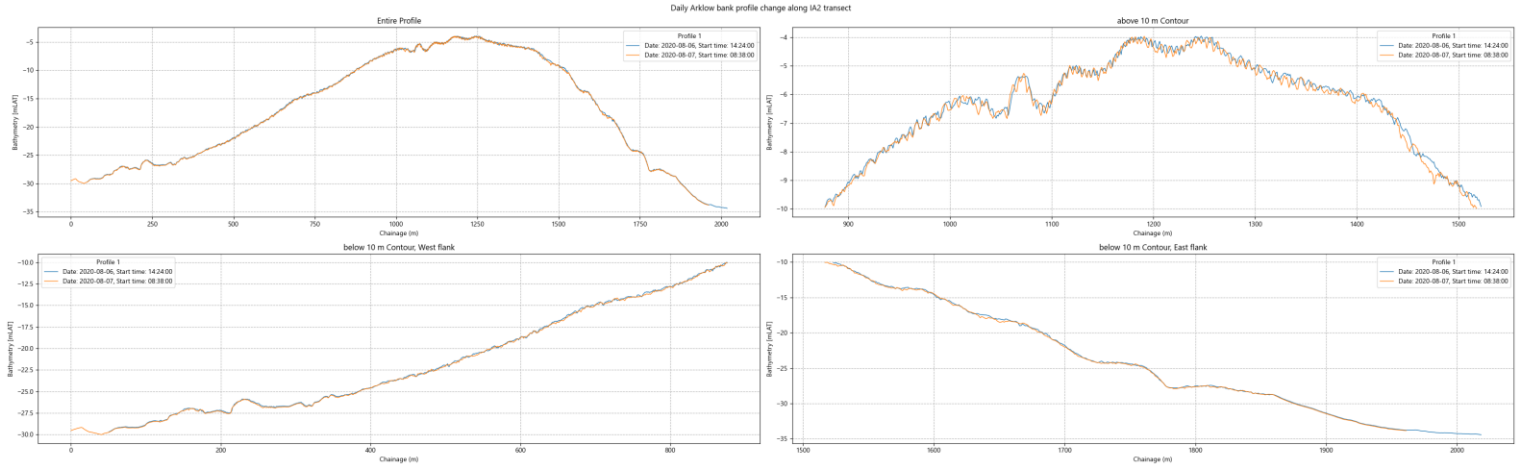


Figure 121. The profile extracted along the transect surveyed in IA2 over the period between 06.08.20 and 07.08.20 on 28.07.20. The full profile (top left panel), the zoomed in profile above the -10 m contour (top right panel), the west (bottom left panel) and east (bottom right panel) face of the bank in areas deeper than the -10 m contour are presented.

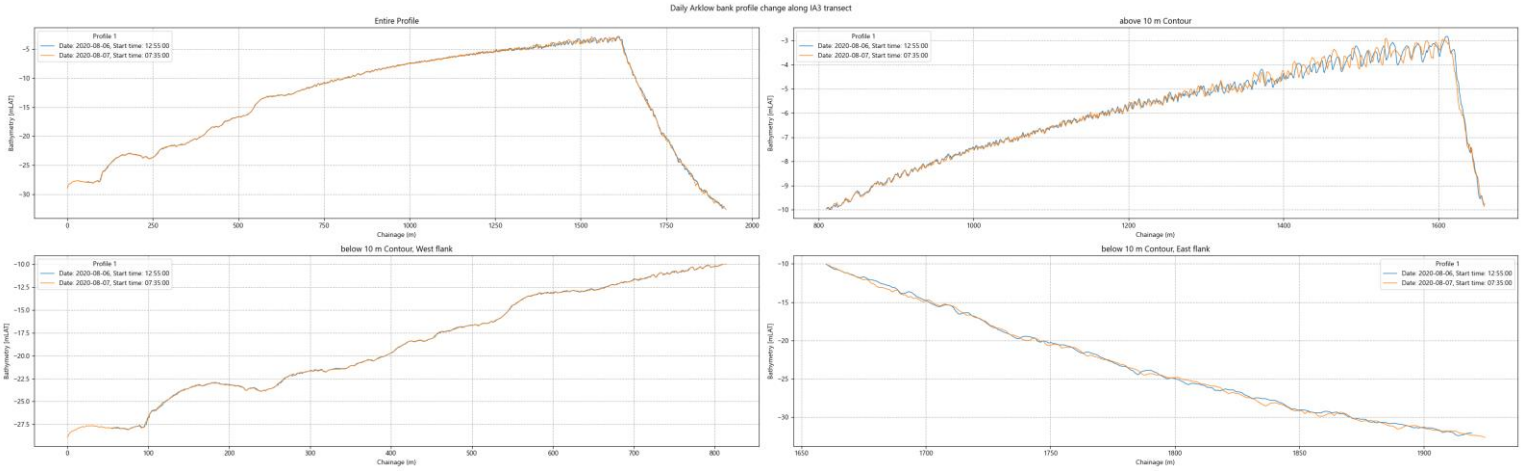


Figure 122. The profile extracted along the transect surveyed in IA3 over the period between 06.08.20 and 07.08.20. The full profile (top left panel), the zoomed in profile above the -10 m contour (top right panel), the west (bottom left panel) and east (bottom right panel) face of the bank in areas deeper than the -10 m contour are presented.

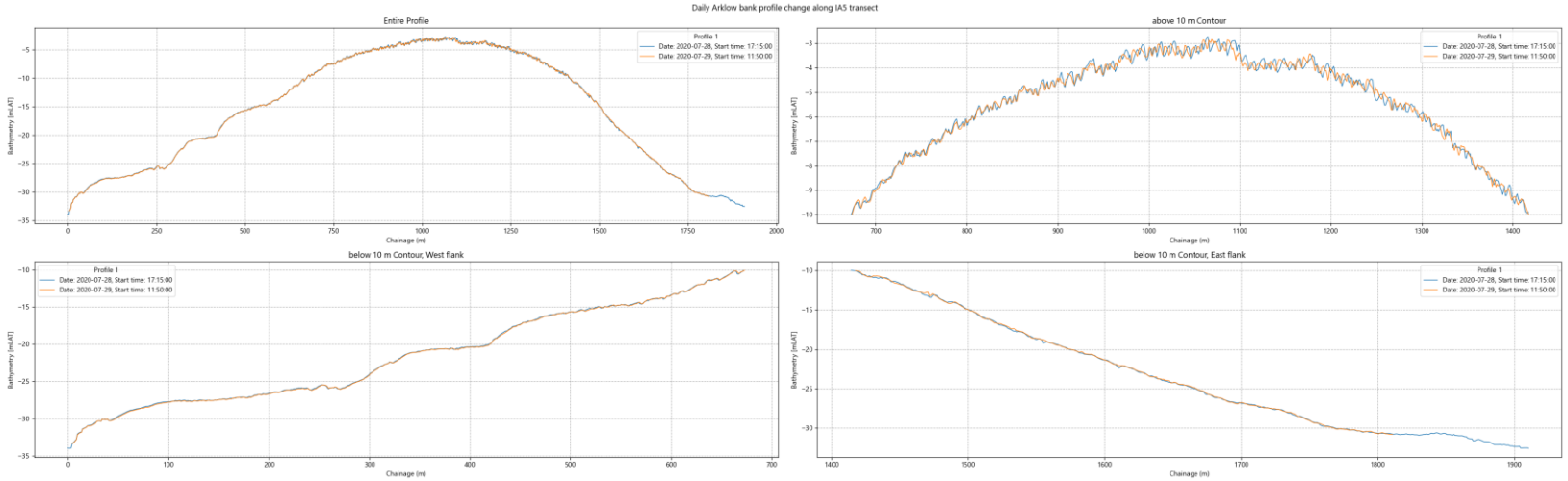


Figure 123. The profile extracted along the transect surveyed in IA5 over the period between 28.07.20 and 29.07.20. The full profile (top left panel), the zoomed in profile above the -10 m contour (top right panel), the west (bottom left panel) and east (bottom right panel) face of the bank in areas deeper than the -10 m contour are presented.

.

To assess the response of the bank over weekly timescales, a series of transects acquired from surveys conducted in the summer of 2020 from IA1, IA2, and IA5, were assessed. The bathymetry data available over this period are detailed in Table 14. The profiles are presented in Figure 124 to Figure 131.

Table 14. Bathymetry data available at weekly timescales.

IA	Sub-category	Filename	Survey Date	Start Time	End Time
IA1	Transect	IA1_TR_197_1	15/07/2020	09:17	09:50
		IA1_TR_202_1	20/07/2020	10:45	11:34
IA2	Transect	IA2_TR_197_1	15/07/2020	10:35	12:35
		IA2_TR_203_2	21/07/2020	17:55	18:30
		IA2_TR_208_1	26/07/2020	15:20	15:50
		IA2_TR_219_1	06/08/2020	14:24	14:43
		IA2_TR_224_2	11/08/2020	16:00	16:15
IA5	Transect	IA5_TR_197_1	15/07/2020	13:25	13:50
		IA5_TR_203_1	21/07/2020	11:30	12:10
		IA5_TR_210_1	28/07/2020	11:00	11:25
		IA5_TR_219_1	06/08/2020	12:30	12:55

On a weekly timescale:

- Above the -10 mLAT contour, lateral movement of mobile bedforms was observed in IA1, IA2 and along the IA5 transect. The magnitude of the lateral movement is similar to that observed on tidal time scales. Over the period of the survey, in IA1, limited lateral movement of bedforms was observed. However, in transects extracted from IA2, greater lateral movement is evident above the -10 mLAT contour, particularly to the west of this shallow region of the bank (Figure 126).
- Figure 115 does not appear to be a typical bank cross-section but one which potentially shows a post-slope failure profile with a volume of sediment dropping to the eastern flank and over sandwaves but still leaving evidence of a steep slope likely within the angle of repose.
- Between the 21st July and 6th August 2020, small changes to the east flank of the bank below the -10 mLAT contour is observed, evident by changes to the bank profile (Figure 127).
- Over this period, the IA5 transect shows bedforms above the -10 mLAT contour have grown in size through the period of observations which is indicative of a consistent supply of sediment to the shallowest regions of the bank.

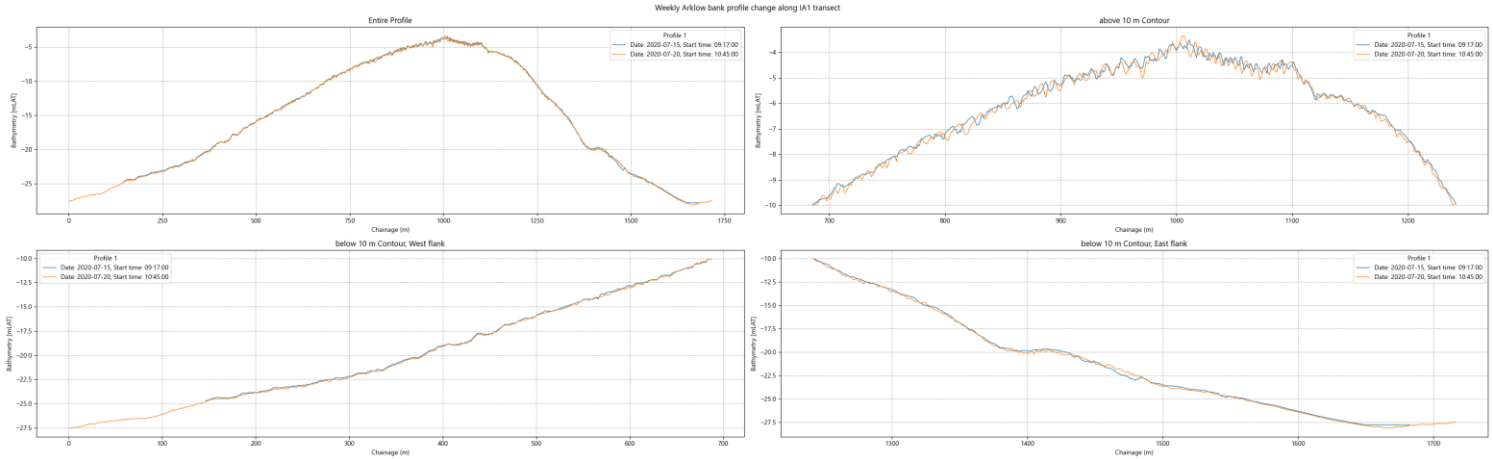


Figure 124. The profile extracted along the transect surveyed in IA1 over the period between 15.07.20 and 20.07.20. The full profile (top left panel), the zoomed in profile above the -10 m contour (top right panel), the west (bottom left panel) and east (bottom right panel) face of the bank in areas deeper than the -10 m contour are presented.

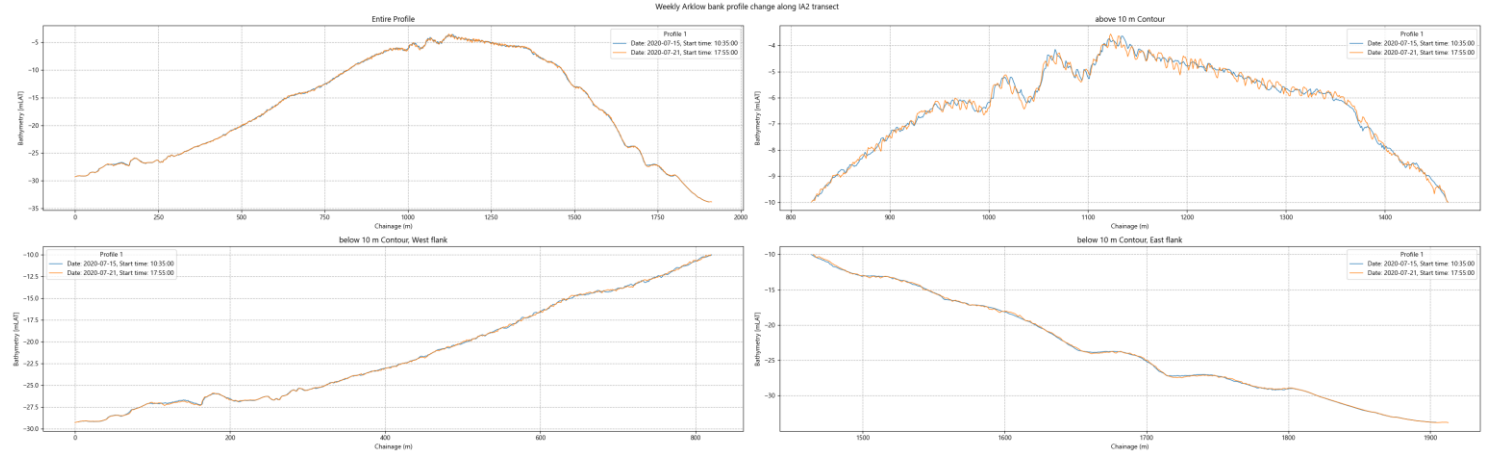


Figure 125. The profile extracted along the transect surveyed in IA2 over the period between 15.07.20 and 21.07.20. The full profile (top left panel), the zoomed in profile above the -10 m contour (top right panel), the west (bottom left panel) and east (bottom right panel) face of the bank in areas deeper than the -10 m contour are presented.

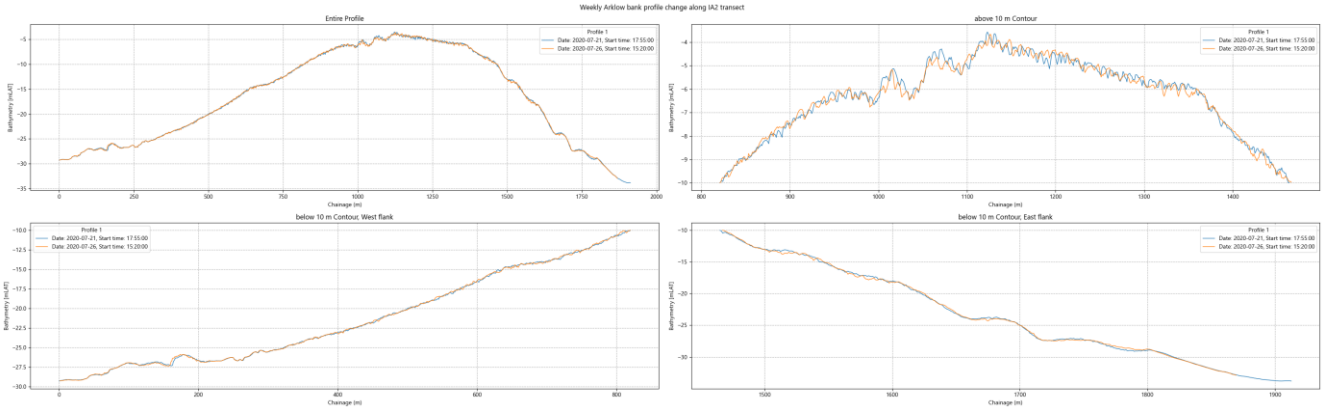


Figure 126. The profile extracted along the transect surveyed in IA2 over the period between 21.07.20 and 26.07.20. The full profile (top left panel), the zoomed in profile above the -10 m contour (top right panel), the west (bottom left panel) and east (bottom right panel) face of the bank in areas deeper than the -10 m contour are presented.

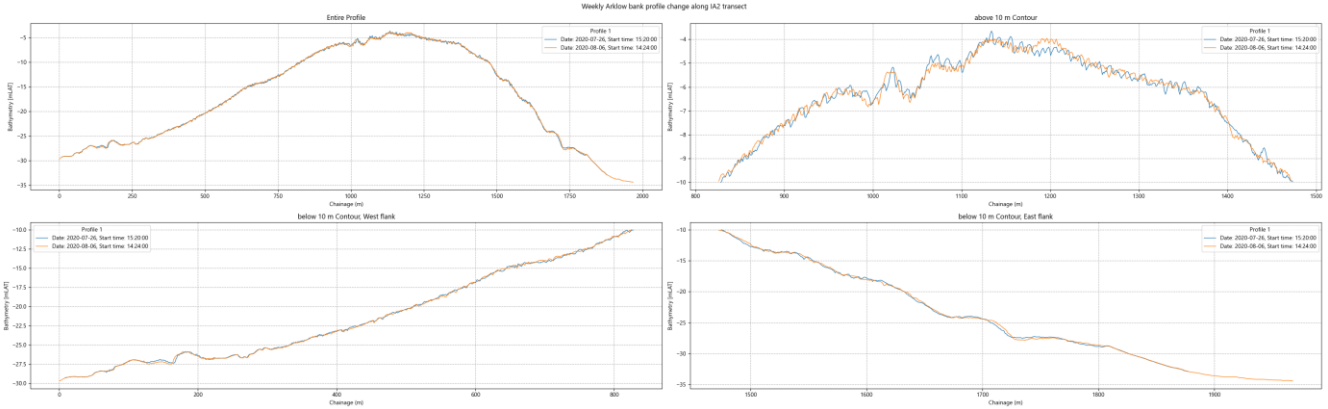


Figure 127. The profile extracted along the transect surveyed in IA2 over the period between 26.07.20 and 06.08.20. The full profile (top left panel), the zoomed in profile above the -10 m contour (top right panel), the west (bottom left panel) and east (bottom right panel) face of the bank in areas deeper than the -10 m contour are presented.

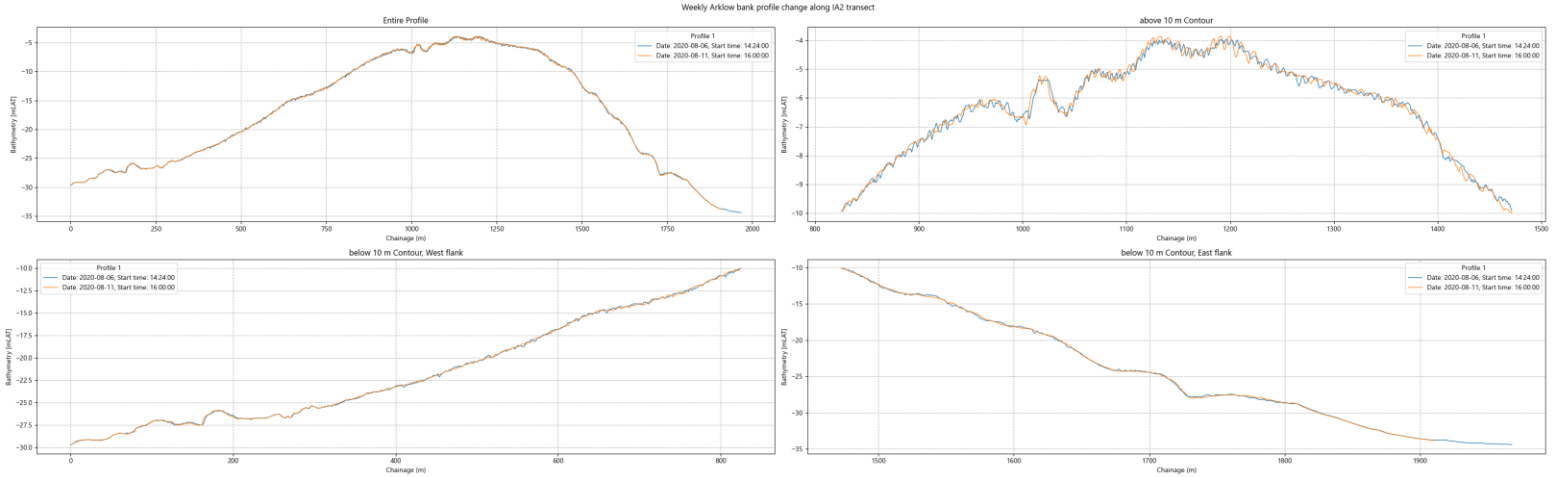


Figure 128. The profile extracted along the transect surveyed in IA2 over the period between 06.08.20 and 11.08.20. The full profile (top left panel), the zoomed in profile above the -10 m contour (top right panel), the west (bottom left panel) and east (bottom right panel) face of the bank in areas deeper than the -10 m contour are presented.

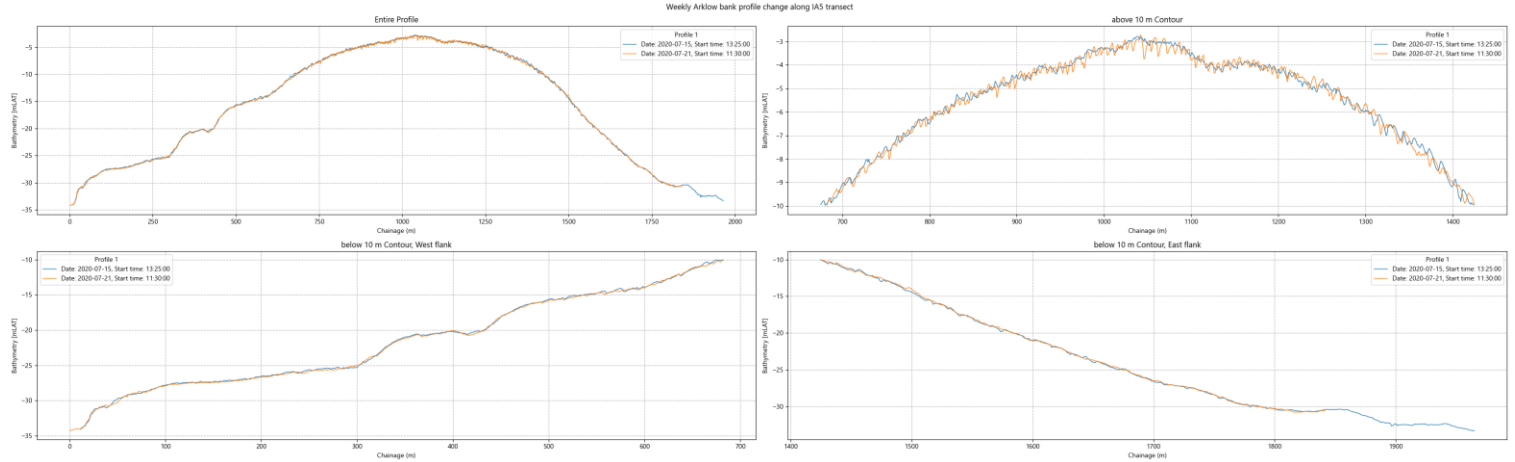


Figure 129. The profile extracted along the transect surveyed in IA5 over the period between 15.07.20 and 21.07.20. The full profile (top left panel), the zoomed in profile above the -10 m contour (top right panel), the west (bottom left panel) and east (bottom right panel) face of the bank in areas deeper than the -10 m contour are presented.

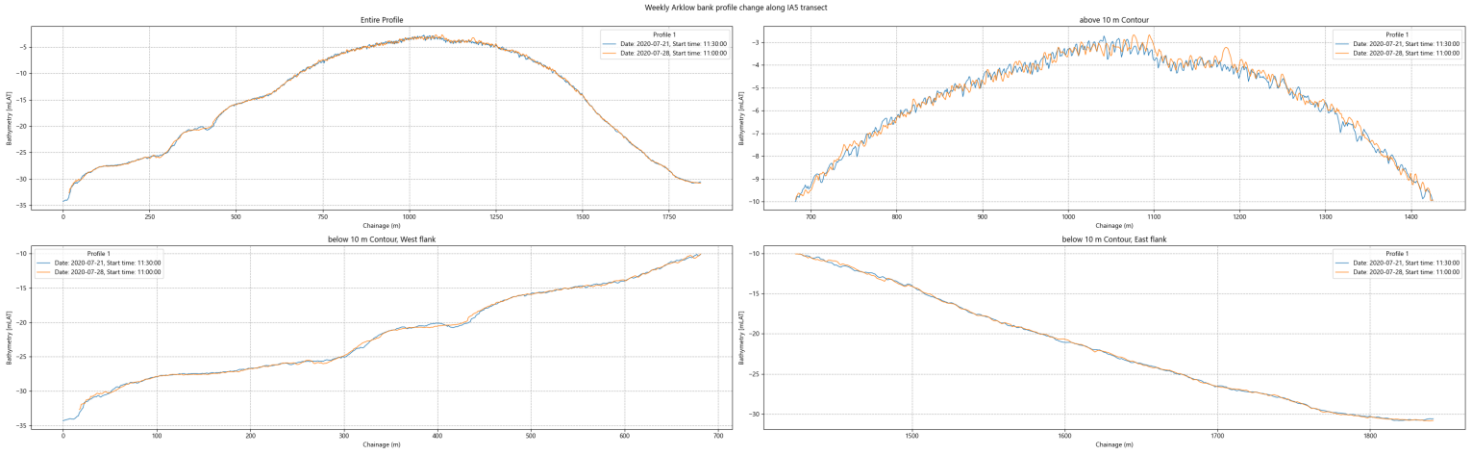


Figure 130. The profile extracted along the transect surveyed in IA5 over the period between 21.07.20 and 28.07.20. The full profile (top left panel), the zoomed in profile above the -10 m contour (top right panel), the west (bottom left panel) and east (bottom right panel) face of the bank in areas deeper than the -10 m contour are presented.

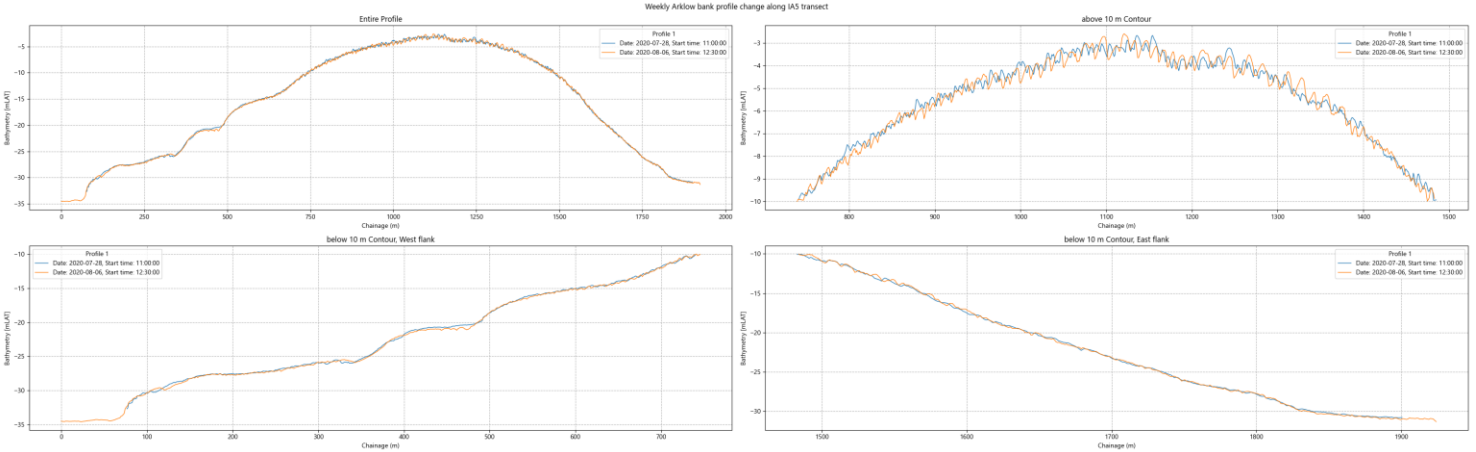


Figure 131. The profile extracted along the transect surveyed in IA5 over the period between 28.07.20 and 06.08.20. The full profile (top left panel), the zoomed in profile above the -10 m contour (top right panel), the west (bottom left panel) and east (bottom right panel) face of the bank in areas deeper than the -10 m contour are presented.

To assess the response of the bank over bi-weekly timescales, a series of transects acquired from IA1, IA2, IA3, IA4 and IA5 were assessed. The bathymetry data available over this period are detailed in Table 15. The profiles are presented in Figure 132 to Figure 165.

Table 15. Bathymetry data available at bi-weekly timescales.

IA	Sub-category	Filename	Survey Date	Start Time	End Time
IA1	Primary	IA1_P_PH01	11/07/2020	06:55	16:35
		IA1_P_PH02	25/07/2020	08:30	17:30
		IA1_P_PH03	09/08/2020	07:36	16:35
	Transect	IA1_TR_203_2	21/07/2020	16:10	16:40
		IA1_TR_219_1	06/08/2020	12:20	12:40
IA2	Primary	IA2_P_PH1	14/07/2020	07:50	16:15
		IA2_P_PH2	29/07/2020	08:00	11:40
		IA2_P_PH3	11/08/2020	06:56	09:23
	Transect	IA2_TR_197_1	15/07/2020	10:35	12:35
		IA2_TR_208_1	26/07/2020	15:20	15:50
		IA2_TR_224_1	11/08/2020	09:31	09:57
IA3	Primary	IA3_P_PH1	12/07/2020	06:55	16:35
		IA3_P_PH2	28/07/2020	11:40	16:50
		IA3_P_PH3	12/08/2020	06:47	13:28
IA4	Primary	IA4_P_PH1	10/07/2020	08:43	15:42
		IA4_P_PH2	24/07/2020	06:50	12:50
		IA4_P_S_PH3	08/08/2020	06:42	12:30
IA5	Transect	IA5_TR_197_1	15/07/2020	13:25	13:50
		IA5_TR_210_1	28/07/2020	11:00	11:25

On a bi-weekly timescale:

- Above the -10 mLAT contour, greater changes are observed which would be anticipated in this highly dynamic region of the bank; which is noticably enhanced during this period of observation within IA1 (Figure 132 to Figure 142). Bedforms above the -10 mLAT contour are mobile, and the data indicates variously growth / decay of these bedforms, through time and across space. Across this time period, significant migration of bedforms in IA1 starts to be observed, which is starting to drive changes to the shape of the bank above the -10 mLAT contour, and shows evidence of repositioning of the crestline to the west (Figure 137 and Figure 138).

- Over this period of observations areas of the bank below the -10 mLAT contour (i.e. the east and west flanks) remain broadly similar in terms of slope and profile and thus seabed level in IA2 and IA5. However, changes start to be observed to the seabed level along the west flank (Figure 155 to Figure 163).
- In IA2, it is noteworthy that bedforms above the -10 mLAT contour appear to be moving in eastward in profile 1, but westward in the other profiles. This is likely associated with the tidal phase (i.e. ebb / flood) during the survey period and is therefore evidence of short-term processes rather than the net movement of the crest on bi-weekly timescales and in this investigation can therefore be considered noise in the data (Figure 143 to Figure 154).
- Over these timescales, the crestline as observed in the profile, appears to show a sandwave which moves across the top of the bank. Where multiple sandwaves are observed the crestline comprises multiple crestlines associated with the crest of each distinct sandwave feature (see an example of this phenomenon in Figure 149)

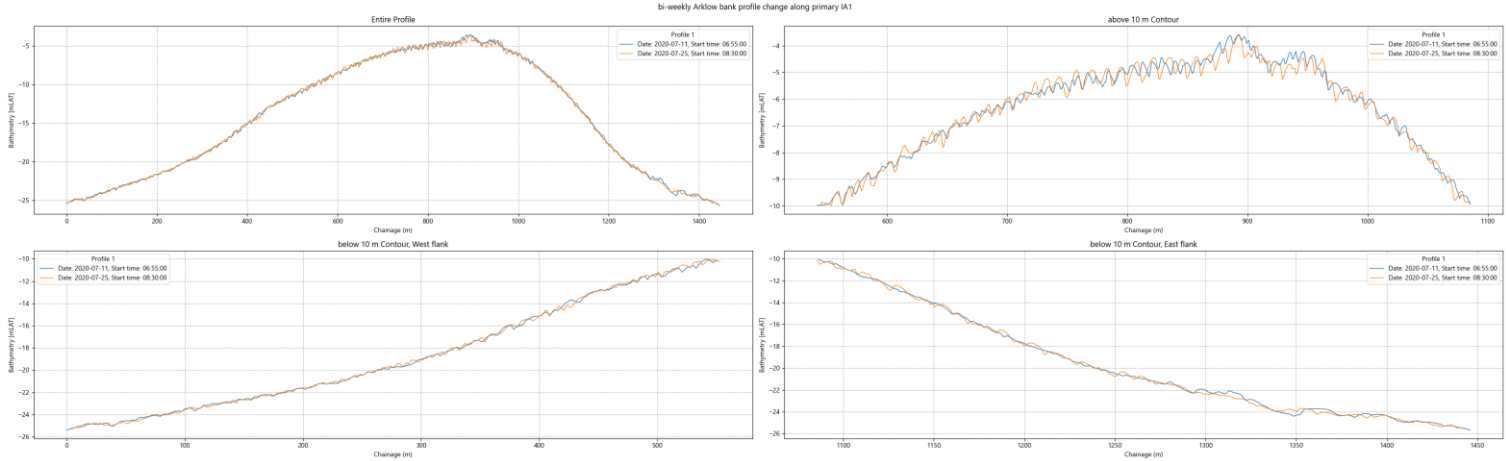


Figure 132. The profile extracted along the transect surveyed in IA1 over the period between 11.07.20 and 25.07.20. The full profile (top left panel), the zoomed in profile above the -10 m contour (top right panel), the west (bottom left panel) and east (bottom right panel) face of the bank in areas deeper than the -10 m contour are presented.

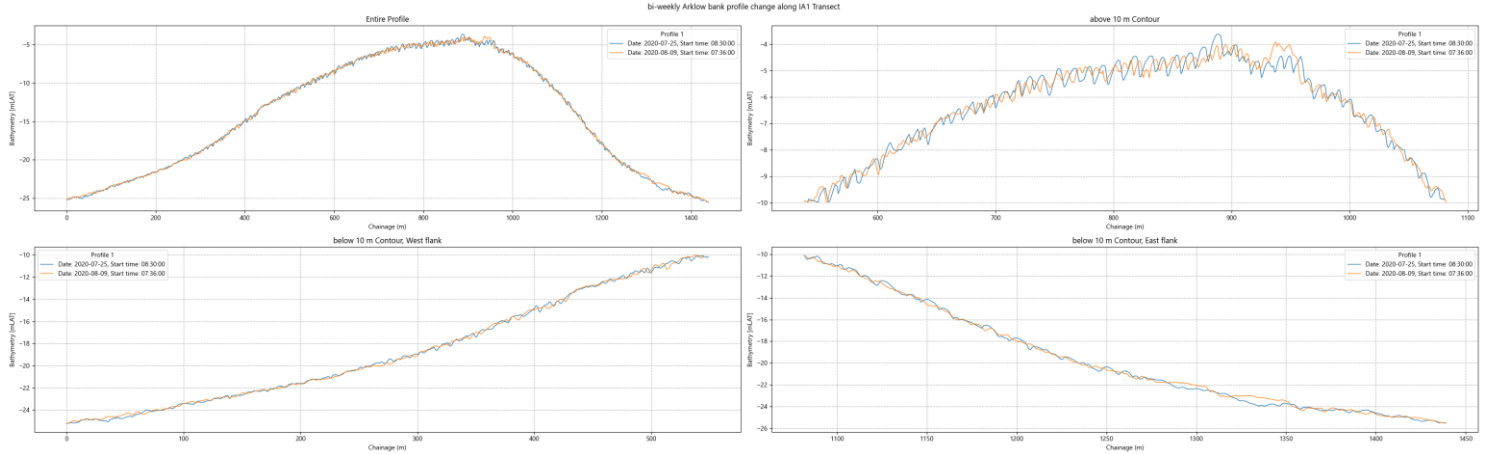


Figure 133. The profile extracted along the transect surveyed in IA1 over the period between 25.07.20 and 09.08.20. The full profile (top left panel), the zoomed in profile above the -10 m contour (top right panel), the west (bottom left panel) and east (bottom right panel) face of the bank in areas deeper than the -10 m contour are presented.

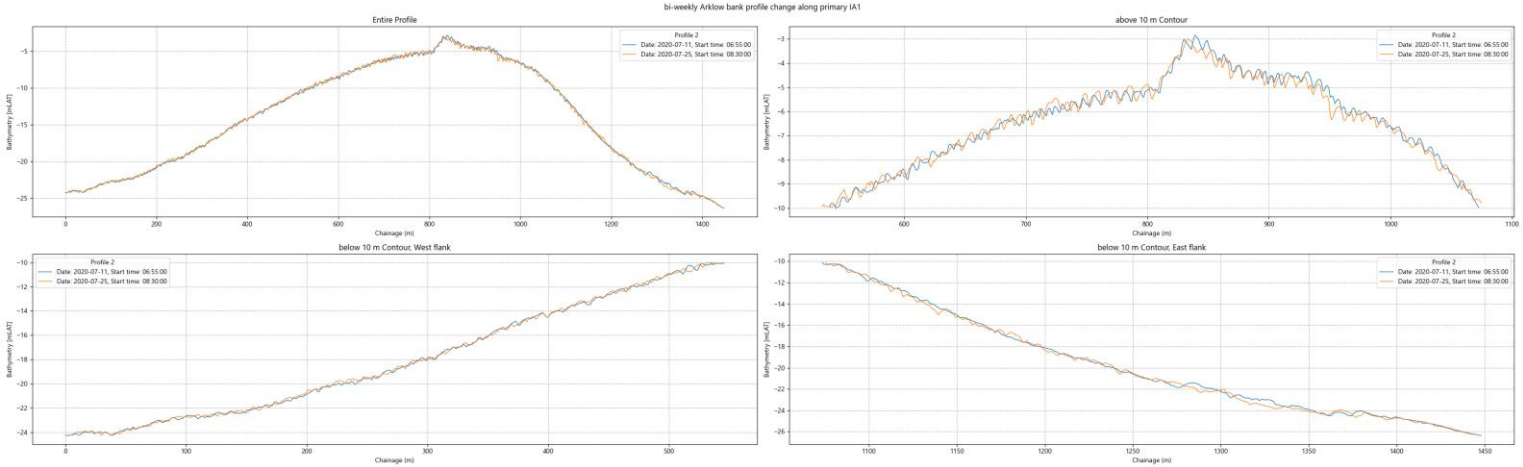


Figure 134. The profile extracted along the transect surveyed in IA1 over the period between 11.07.20 and 25.07.20. The full profile (top left panel), the zoomed in profile above the -10 m contour (top right panel), the west (bottom left panel) and east (bottom right panel) face of the bank in areas deeper than the -10 m contour are presented.

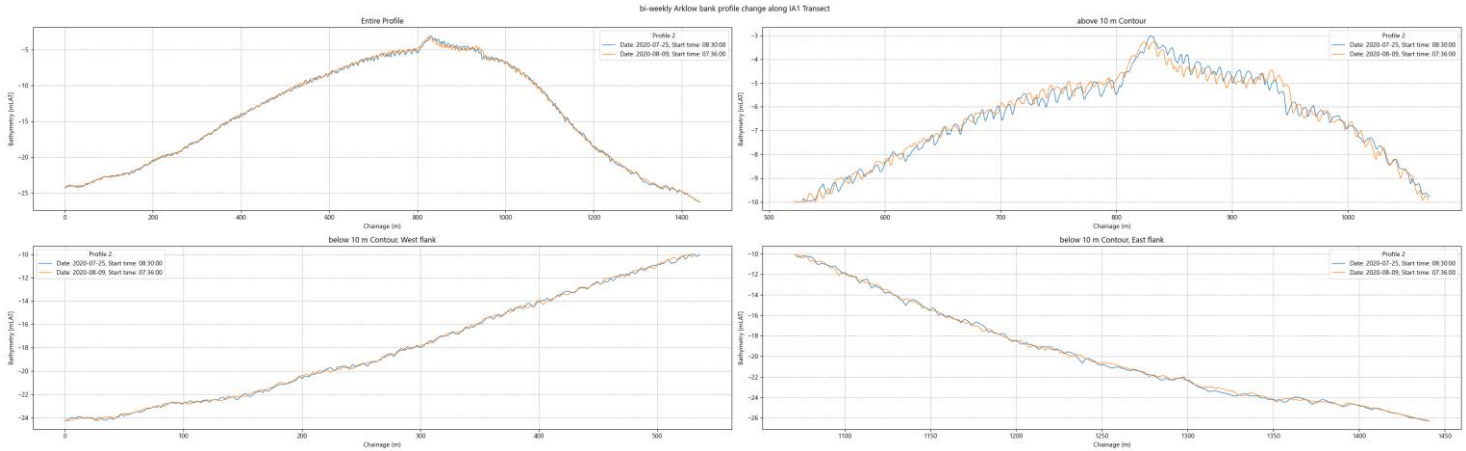


Figure 135. The profile extracted along the transect surveyed in IA1 over the period between 25.07.20 and 09.08.20. The full profile (top left panel), the zoomed in profile above the -10 m contour (top right panel), the west (bottom left panel) and east (bottom right panel) face of the bank in areas deeper than the -10 m contour are presented.

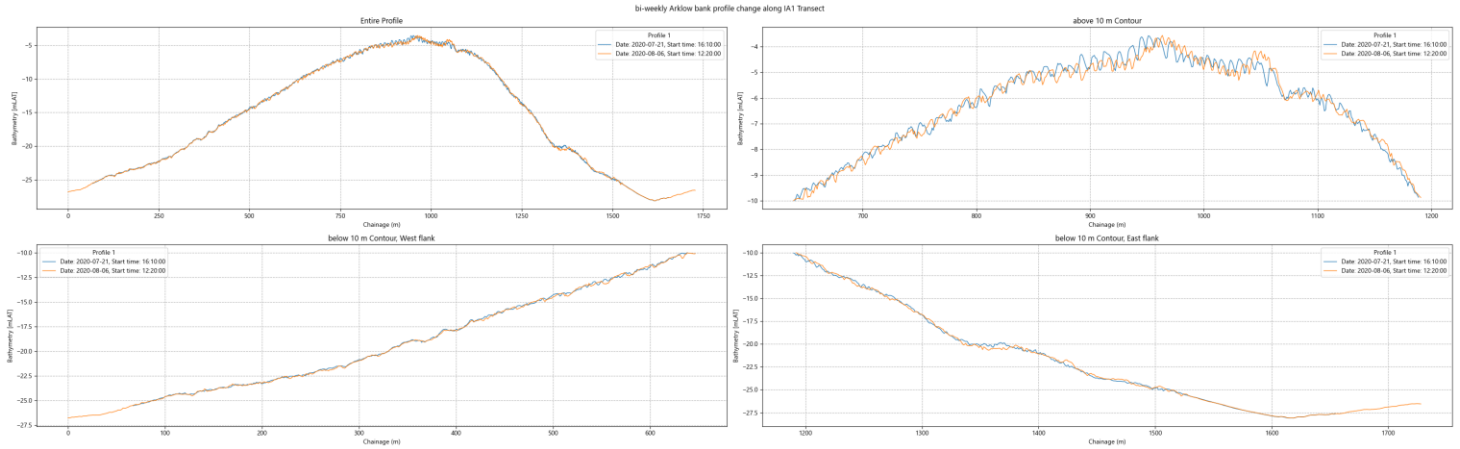


Figure 136. The profile extracted along the transect surveyed in IA1 over the period between 21.07.20 and 06.08.20. The full profile (top left panel), the zoomed in profile above the -10 m contour (top right panel), the west (bottom left panel) and east (bottom right panel) face of the bank in areas deeper than the -10 m contour are presented.

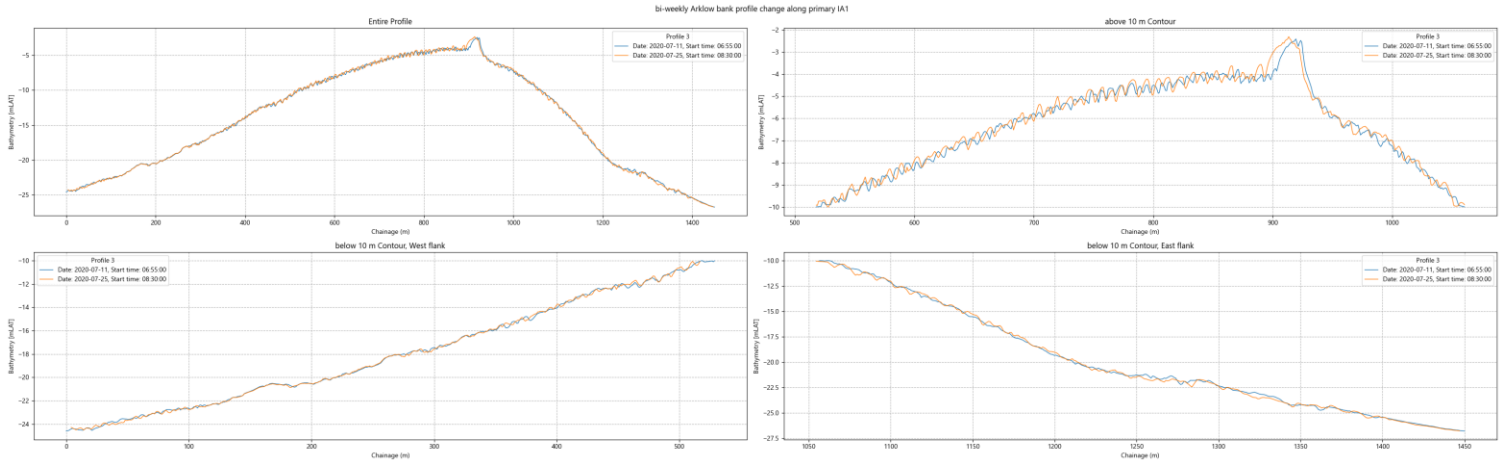


Figure 137. The profile extracted along the transect surveyed in IA1 over the period between 11.07.20 and 25.07.20. The full profile (top left panel), the zoomed in profile above the -10 m contour (top right panel), the west (bottom left panel) and east (bottom right panel) face of the bank in areas deeper than the -10 m contour are presented.

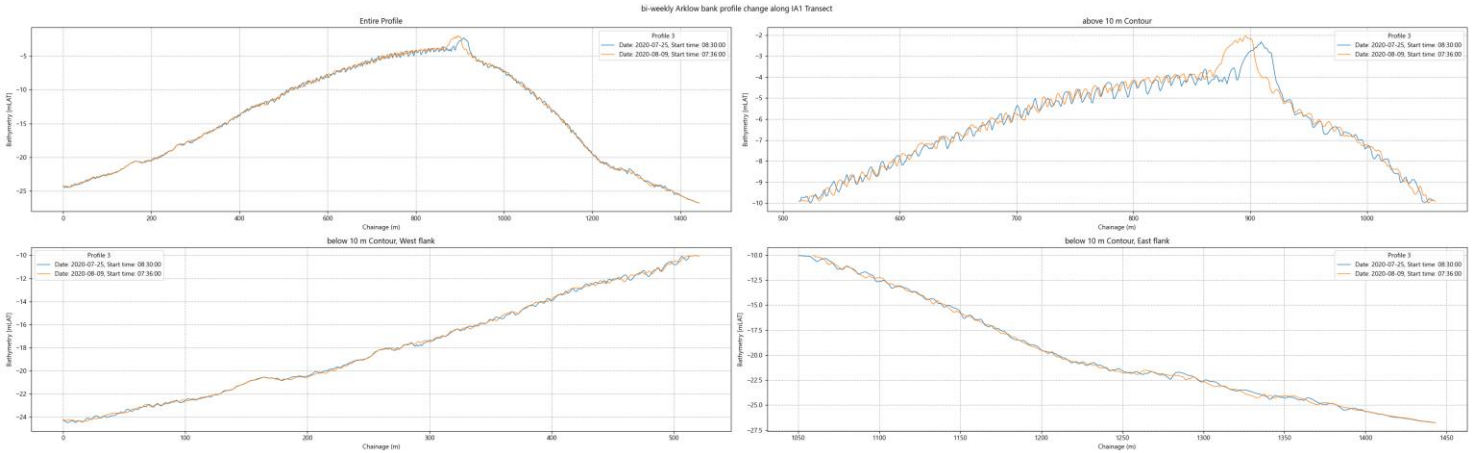


Figure 138. The profile extracted along the transect surveyed in IA1 over the period between 25.07.20 and 09.08.20. The full profile (top left panel), the zoomed in profile above the -10 m contour (top right panel), the west (bottom left panel) and east (bottom right panel) face of the bank in areas deeper than the -10 m contour are presented.

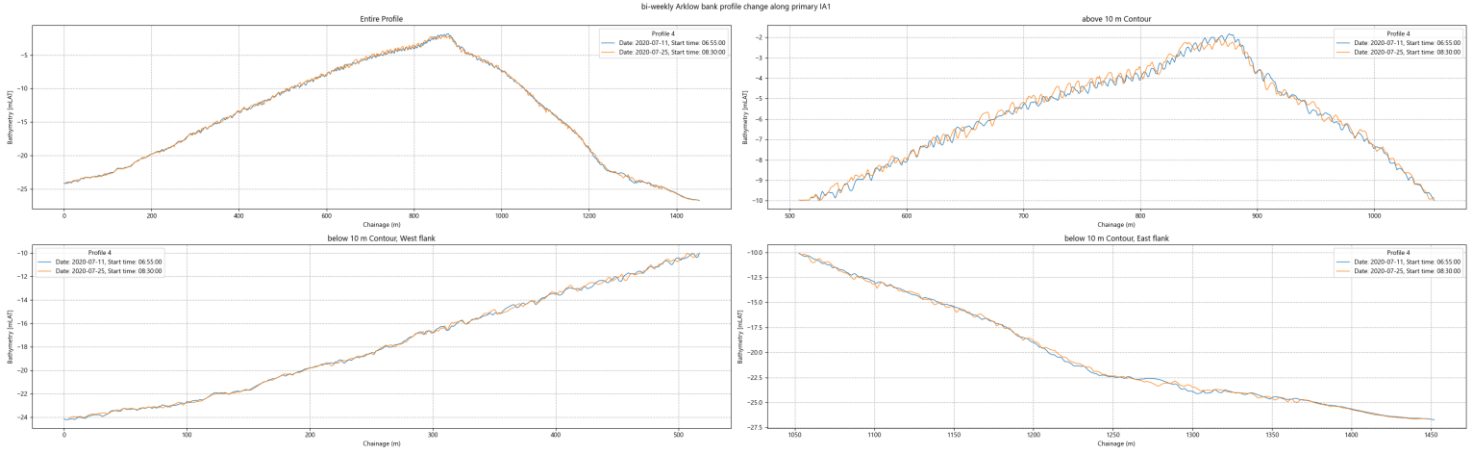


Figure 139. The profile extracted along the transect surveyed in IA1 over the period between 11.07.20 and 25.07.20. The full profile (top left panel), the zoomed in profile above the -10 m contour (top right panel), the west (bottom left panel) and east (bottom right panel) face of the bank in areas deeper than the -10 m contour are presented.

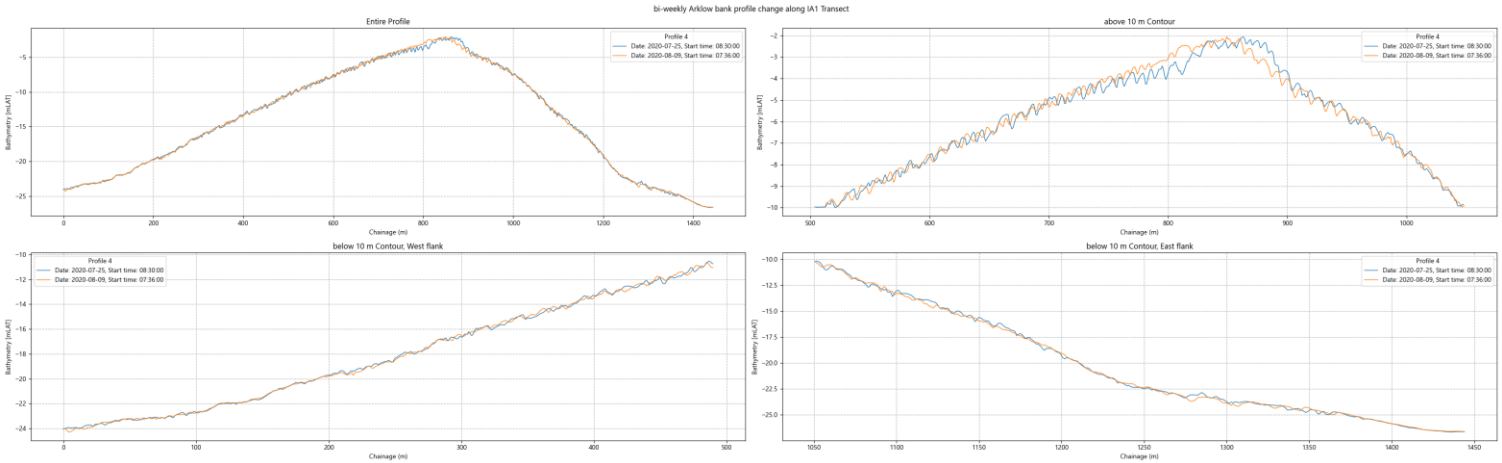


Figure 140. The profile extracted along the transect surveyed in IA1 over the period between 25.07.20 and 09.08.20. The full profile (top left panel), the zoomed in profile above the -10 m contour (top right panel), the west (bottom left panel) and east (bottom right panel) face of the bank in areas deeper than the -10 m contour are presented.

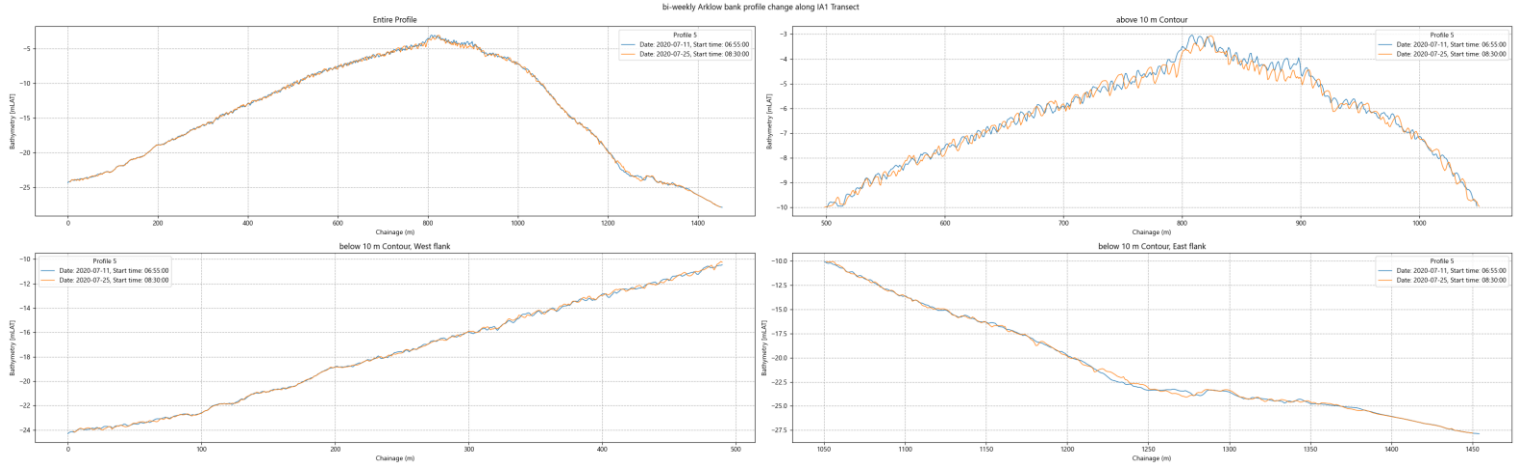


Figure 141. The profile extracted along the transect surveyed in IA1 over the period between 11.07.20 and 25.07.20. The full profile (top left panel), the zoomed in profile above the -10 m contour (top right panel), the west (bottom left panel) and east (bottom right panel) face of the bank in areas deeper than the -10 m contour are presented.

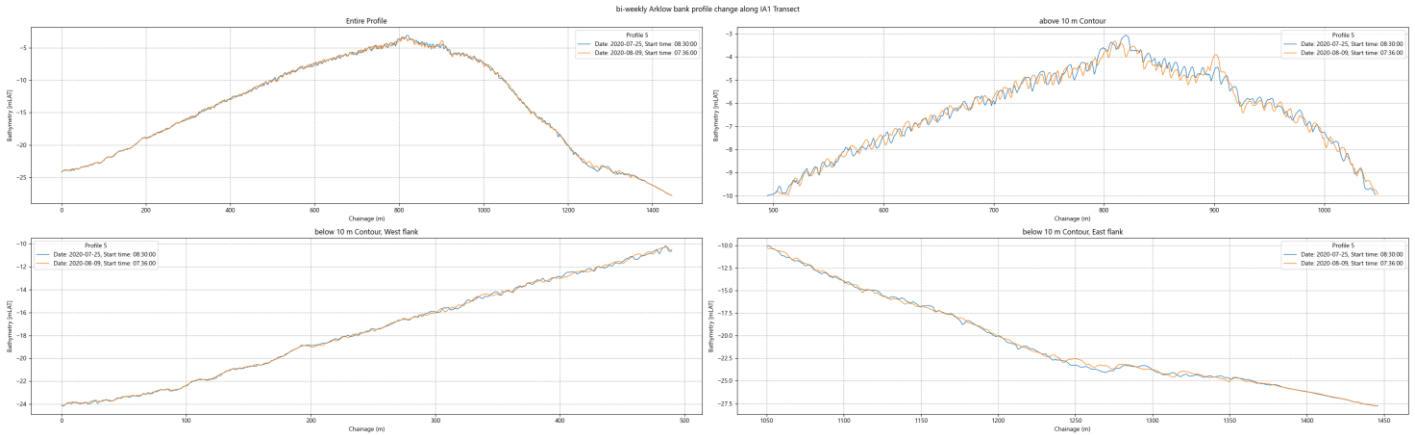


Figure 142. The profile extracted along the transect surveyed in IA1 over the period between 25.07.20 and 09.08.20. The full profile (top left panel), the zoomed in profile above the -10 m contour (top right panel), the west (bottom left panel) and east (bottom right panel) face of the bank in areas deeper than the -10 m contour are presented.

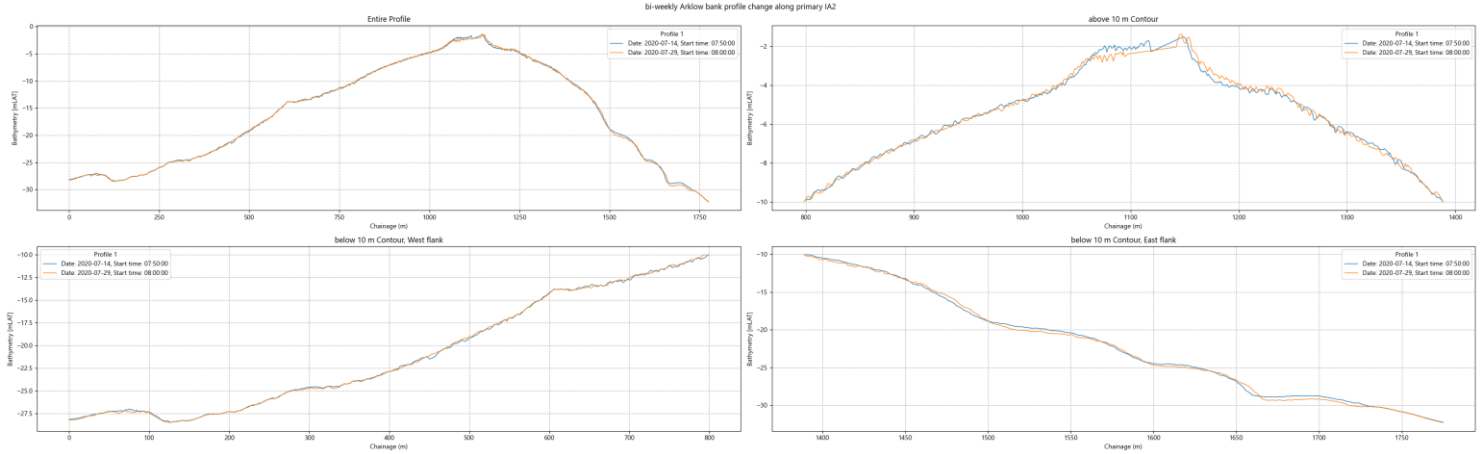


Figure 143. The profile extracted along the transect surveyed in IA2 over the period between 14.07.20 and 29.07.20. The full profile (top left panel), the zoomed in profile above the -10 m contour (top right panel), the west (bottom left panel) and east (bottom right panel) face of the bank in areas deeper than the -10 m contour are presented.

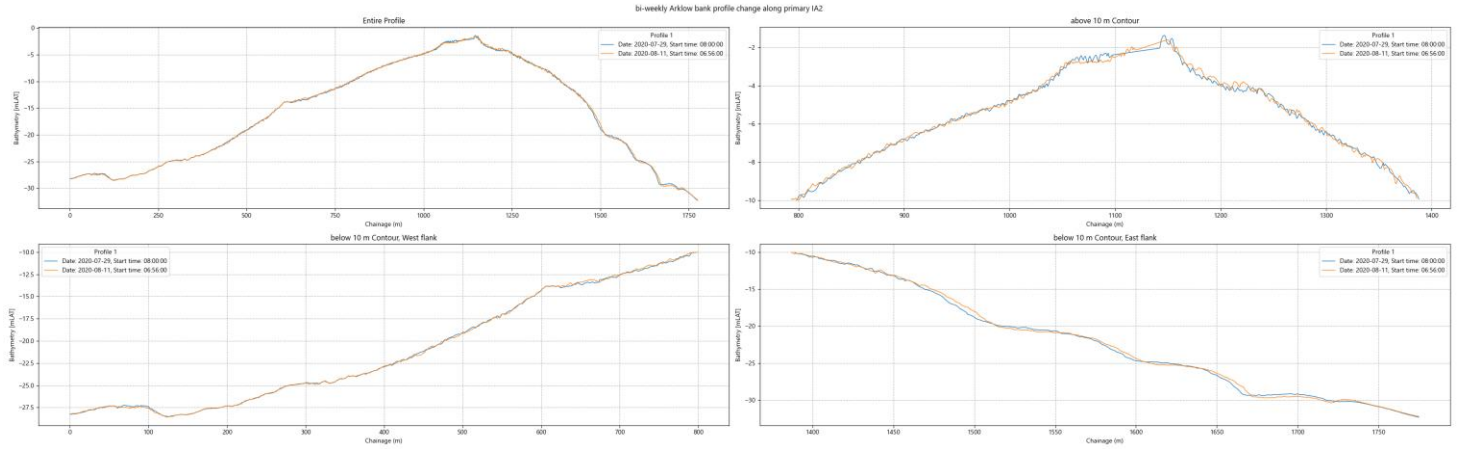


Figure 144. The profile extracted along the transect surveyed in IA2 over the period between 29.07.20 and 11.08.20. The full profile (top left panel), the zoomed in profile above the -10 m contour (top right panel), the west (bottom left panel) and east (bottom right panel) face of the bank in areas deeper than the -10 m contour are presented.

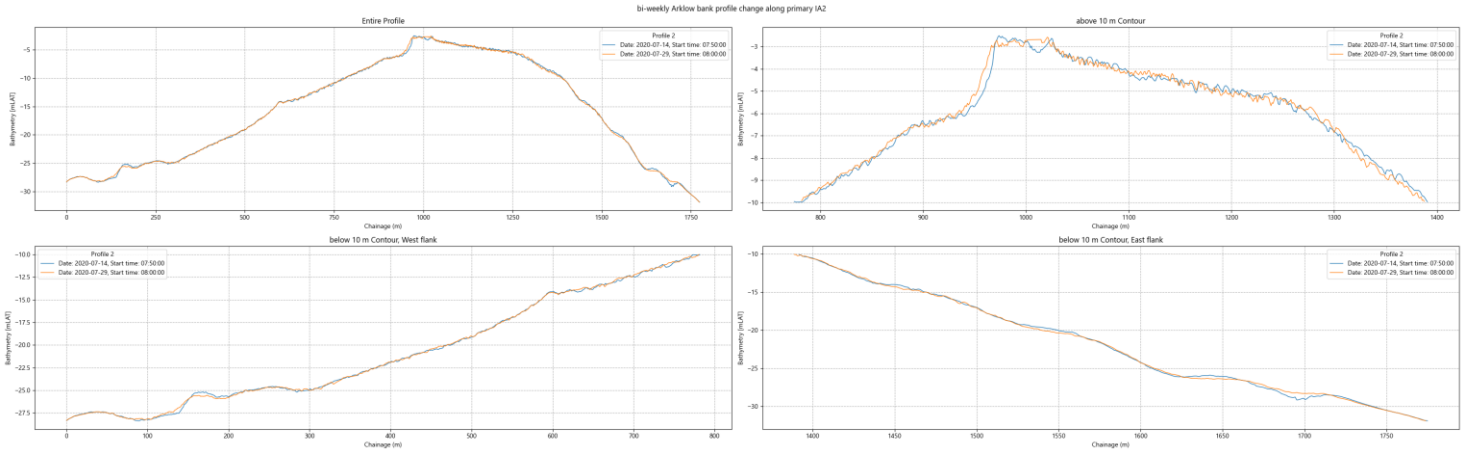


Figure 145. The profile extracted along the transect surveyed in IA2 over the period between 14.07.20 and 29.07.20. The full profile (top left panel), the zoomed in profile above the -10 m contour (top right panel), the west (bottom left panel) and east (bottom right panel) face of the bank in areas deeper than the -10 m contour are presented.

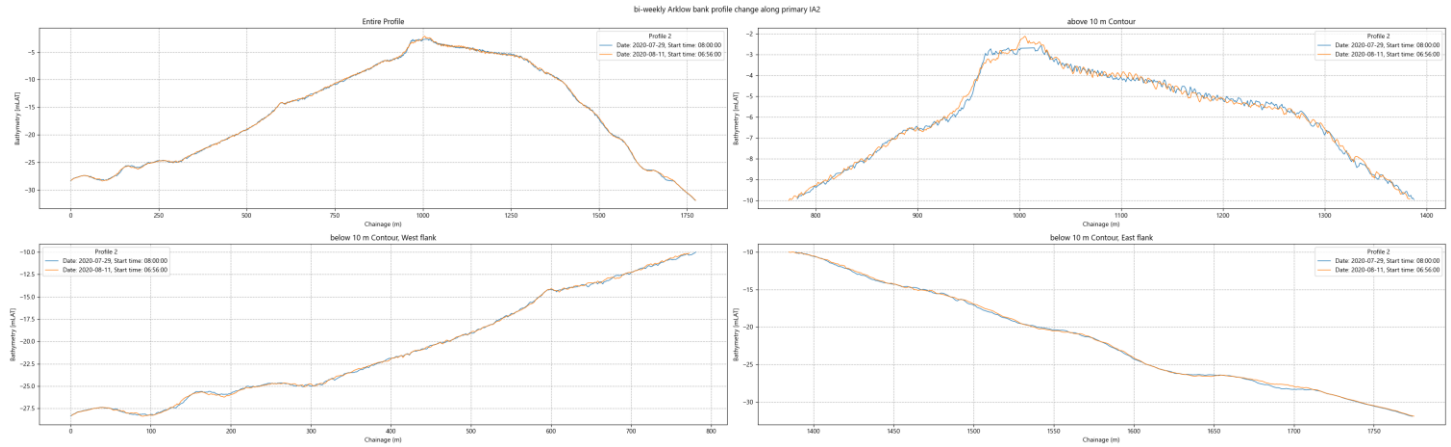


Figure 146. The profile extracted along the transect surveyed in IA2 over the period between 29.07.20 and 11.08.20. The full profile (top left panel), the zoomed in profile above the -10 m contour (top right panel), the west (bottom left panel) and east (bottom right panel) face of the bank in areas deeper than the -10 m contour are presented.

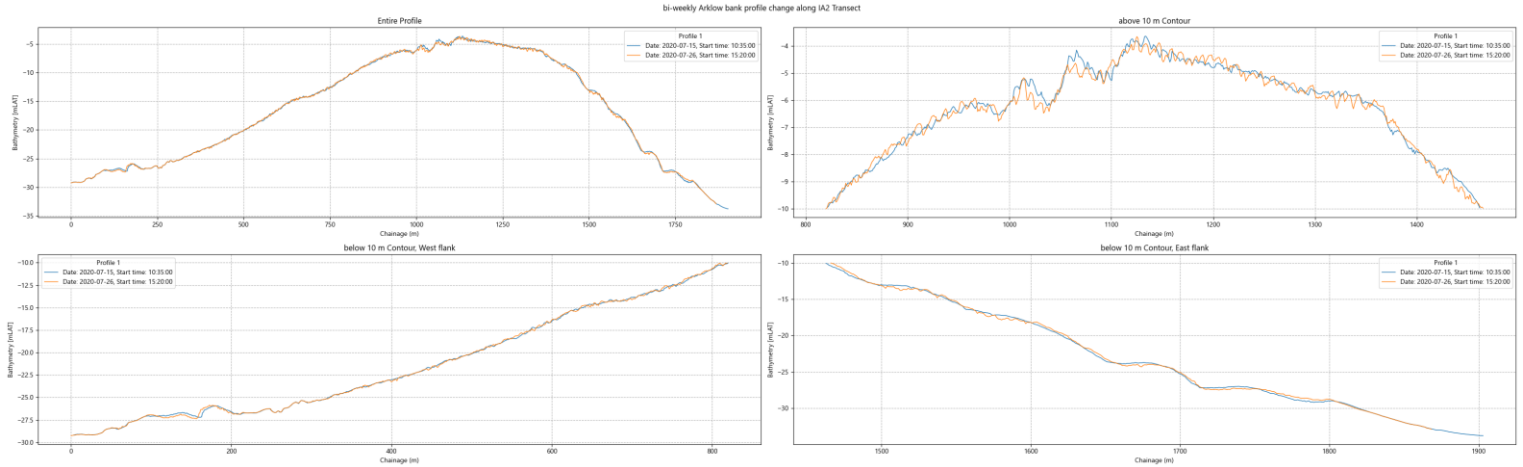


Figure 147. The profile extracted along the transect surveyed in IA2 over the period between 15.07.20 and 26.07.20. The full profile (top left panel), the zoomed in profile above the -10 m contour (top right panel), the west (bottom left panel) and east (bottom right panel) face of the bank in areas deeper than the -10 m contour are presented.

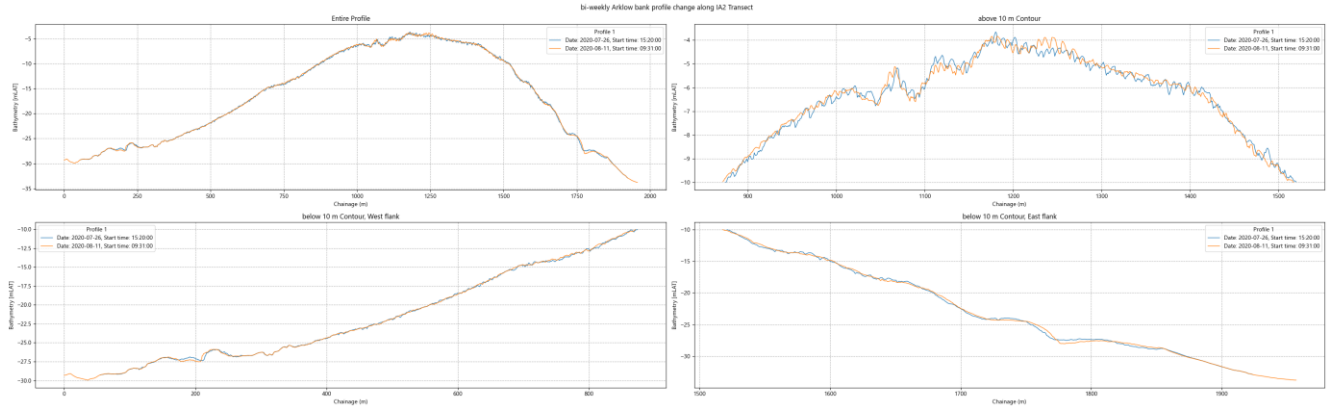


Figure 148. The profile extracted along the transect surveyed in IA2 over the period between 26.07.20 and 11.08.20. The full profile (top left panel), the zoomed in profile above the -10 m contour (top right panel), the west (bottom left panel) and east (bottom right panel) face of the bank in areas deeper than the -10 m contour are presented.

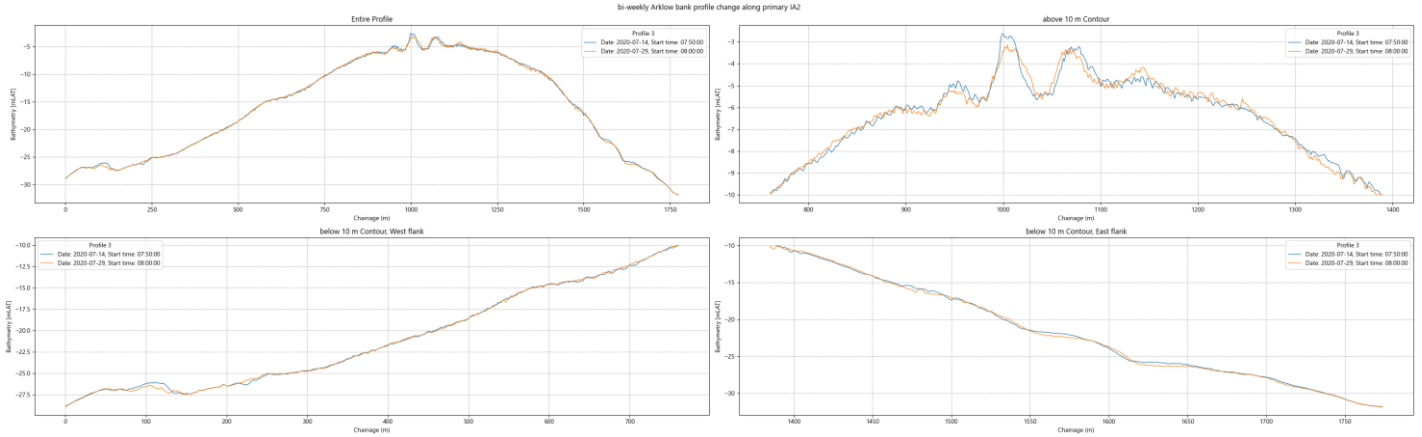


Figure 149. The profile extracted along the transect surveyed in IA2 over the period between 14.07.20 and 29.07.20. The full profile (top left panel), the zoomed in profile above the -10 m contour (top right panel), the west (bottom left panel) and east (bottom right panel) face of the bank in areas deeper than the -10 m contour are presented.

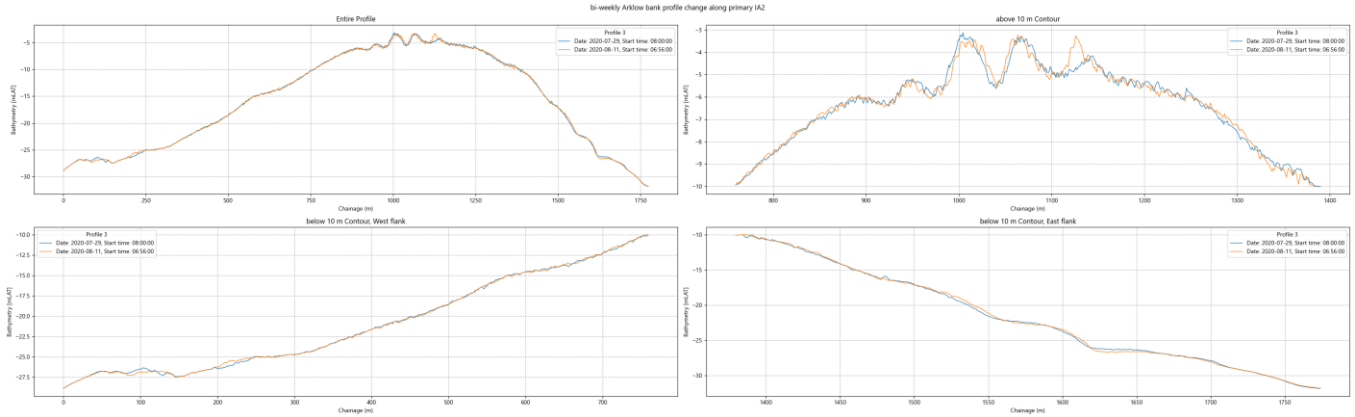


Figure 150. The profile extracted along the transect surveyed in IA2 over the period between 29.07.20 and 11.08.20. The full profile (top left panel), the zoomed in profile above the -10 m contour (top right panel), the west (bottom left panel) and east (bottom right panel) face of the bank in areas deeper than the -10 m contour are presented.

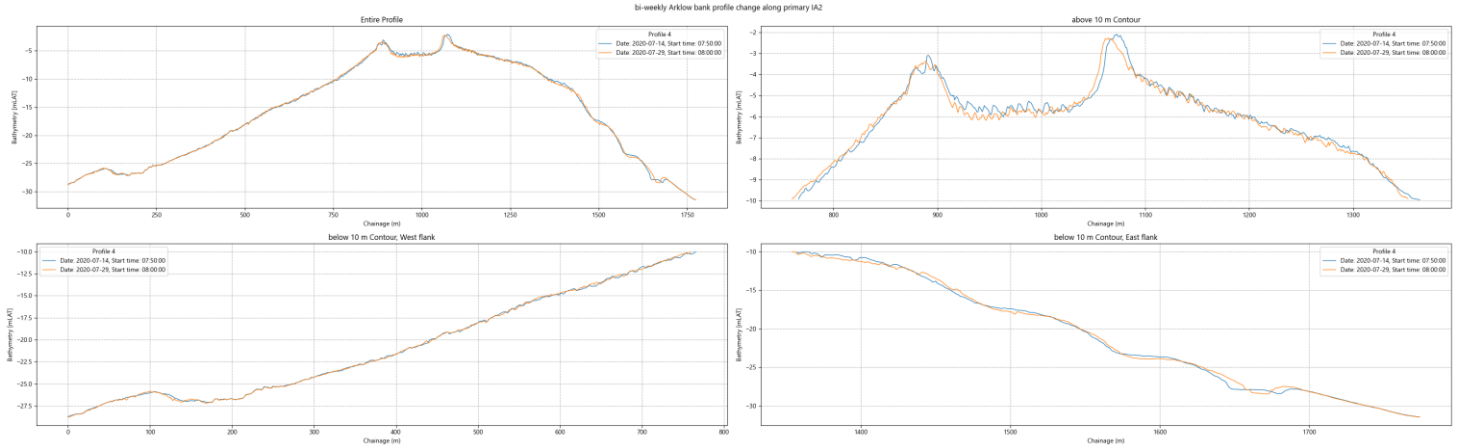


Figure 151. The profile extracted along the transect surveyed in IA2 over the period between 14.07.20 and 29.07.20. The full profile (top left panel), the zoomed in profile above the -10 m contour (top right panel), the west (bottom left panel) and east (bottom right panel) face of the bank in areas deeper than the -10 m contour are presented.

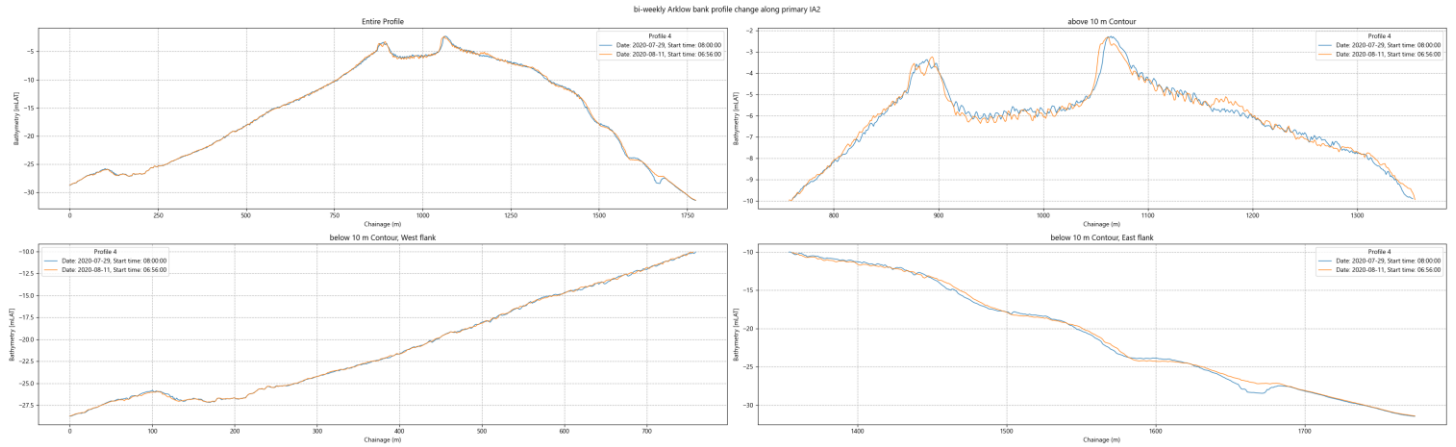


Figure 152. The profile extracted along the transect surveyed in IA2 over the period between 29.07.20 and 11.08.20. The full profile (top left panel), the zoomed in profile above the -10 m contour (top right panel), the west (bottom left panel) and east (bottom right panel) face of the bank in areas deeper than the -10 m contour are presented.

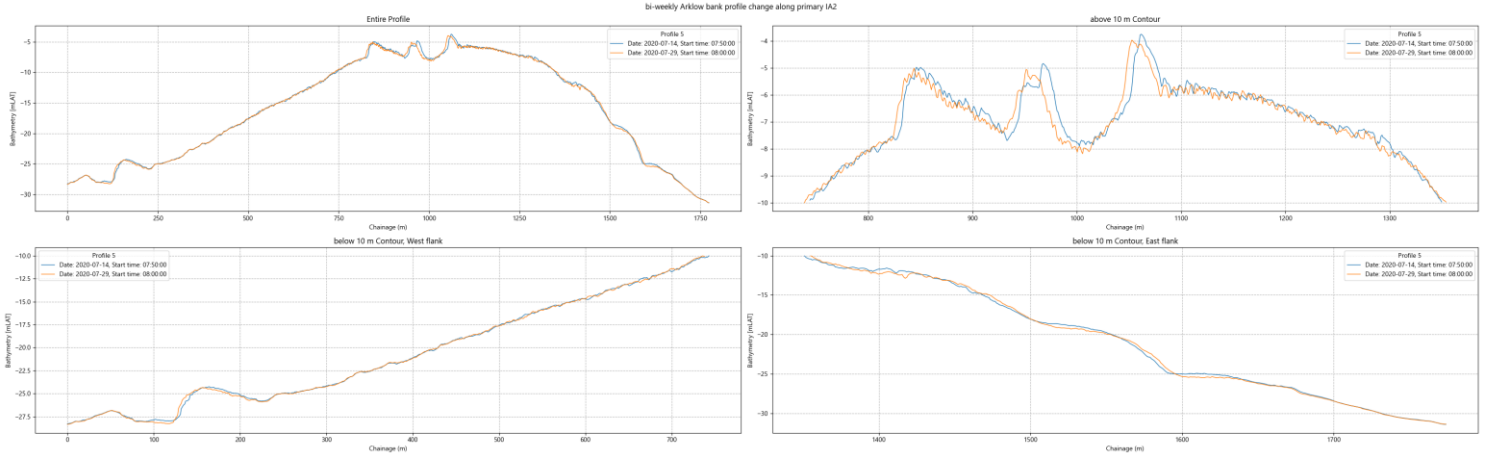


Figure 153. The profile extracted along the transect surveyed in IA2 over the period between 14.07.20 and 29.07.20. The full profile (top left panel), the zoomed in profile above the -10 m contour (top right panel), the west (bottom left panel) and east (bottom right panel) face of the bank in areas deeper than the -10 m contour are presented.

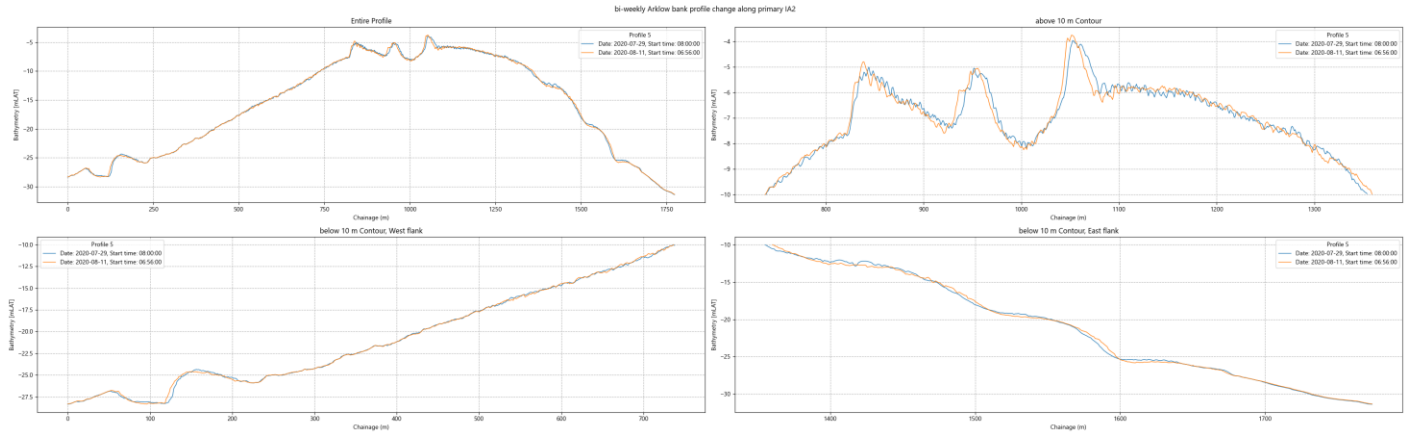


Figure 154. The profile extracted along the transect surveyed in IA2 over the period between 29.07.20 and 11.08.20. The full profile (top left panel), the zoomed in profile above the -10 m contour (top right panel), the west (bottom left panel) and east (bottom right panel) face of the bank in areas deeper than the -10 m contour are presented.

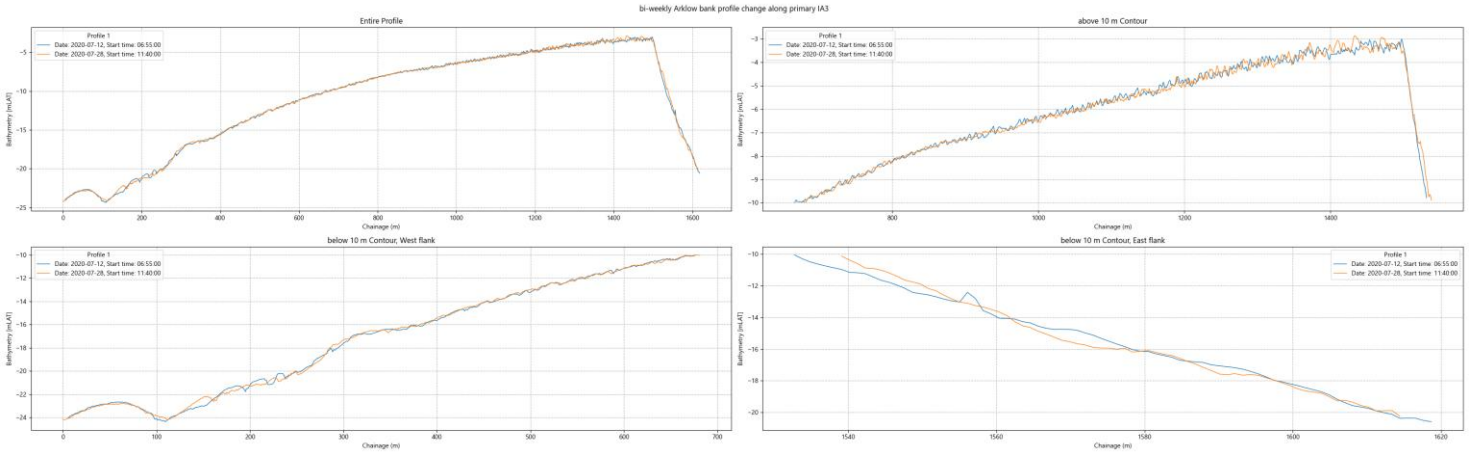


Figure 155. The profile extracted along the transect surveyed in IA3 over the period between 12.07.20 and 28.07.20. The full profile (top left panel), the zoomed in profile above the -10 m contour (top right panel), the west (bottom left panel) and east (bottom right panel) face of the bank in areas deeper than the -10 m contour are presented.

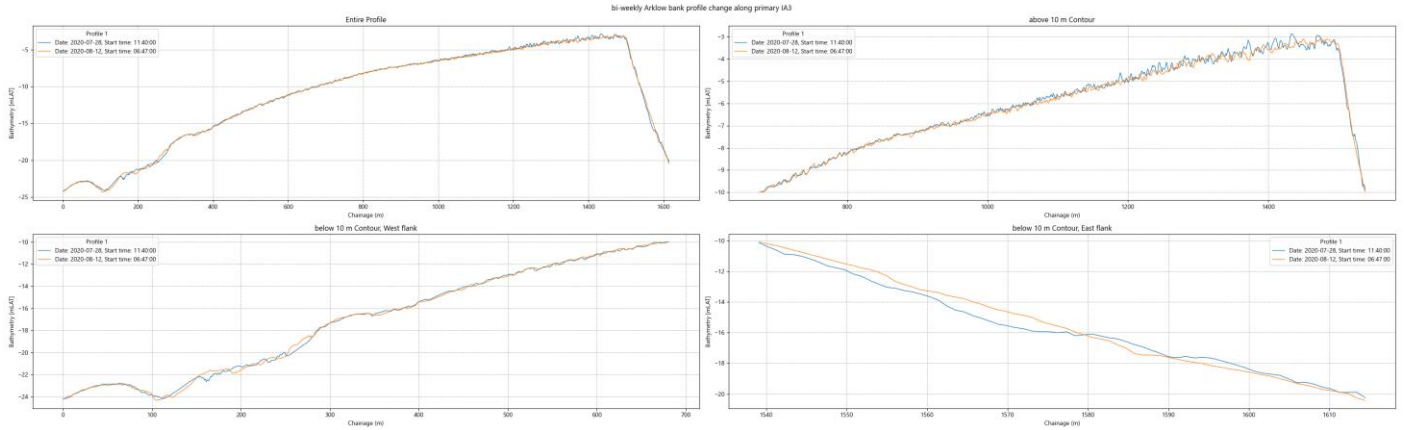


Figure 156. The profile extracted along the transect surveyed in IA3 over the period between 28.07.20 and 12.08.20. The full profile (top left panel), the zoomed in profile above the -10 m contour (top right panel), the west (bottom left panel) and east (bottom right panel) face of the bank in areas deeper than the -10 m contour are presented.

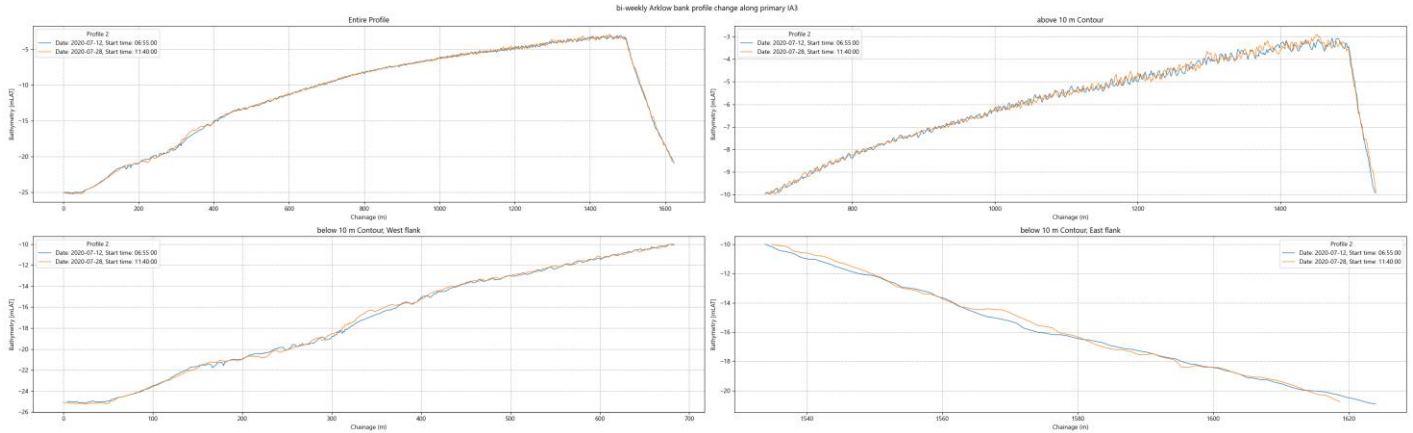


Figure 157. The profile extracted along the transect surveyed in IA3 over the period between 12.07.20 and 28.07.20. The full profile (top left panel), the zoomed in profile above the -10 m contour (top right panel), the west (bottom left panel) and east (bottom right panel) face of the bank in areas deeper than the -10 m contour are presented.

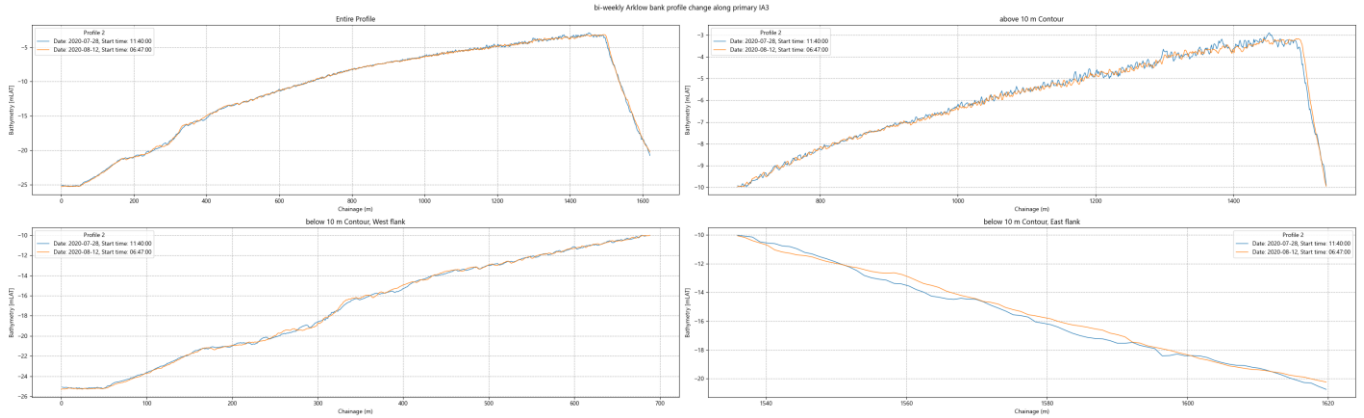


Figure 158. The profile extracted along the transect surveyed in IA3 over the period between 28.07.20 and 12.08.20. The full profile (top left panel), the zoomed in profile above the -10 m contour (top right panel), the west (bottom left panel) and east (bottom right panel) face of the bank in areas deeper than the -10 m contour are presented.

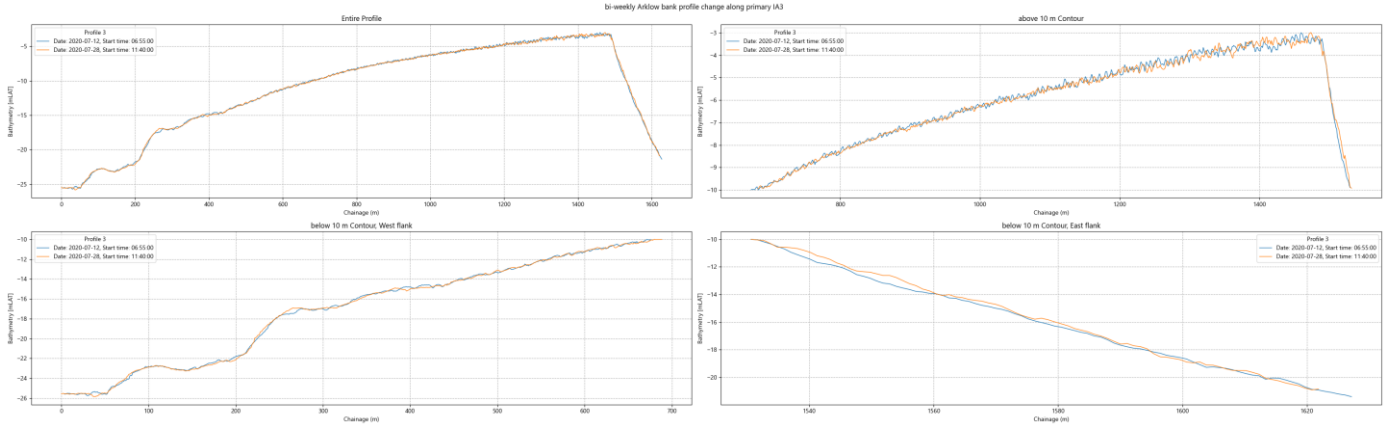


Figure 159. The profile extracted along the transect surveyed in IA3 over the period between 12.07.20 and 28.07.20. The full profile (top left panel), the zoomed in profile above the -10 m contour (top right panel), the west (bottom left panel) and east (bottom right panel) face of the bank in areas deeper than the -10 m contour are presented.

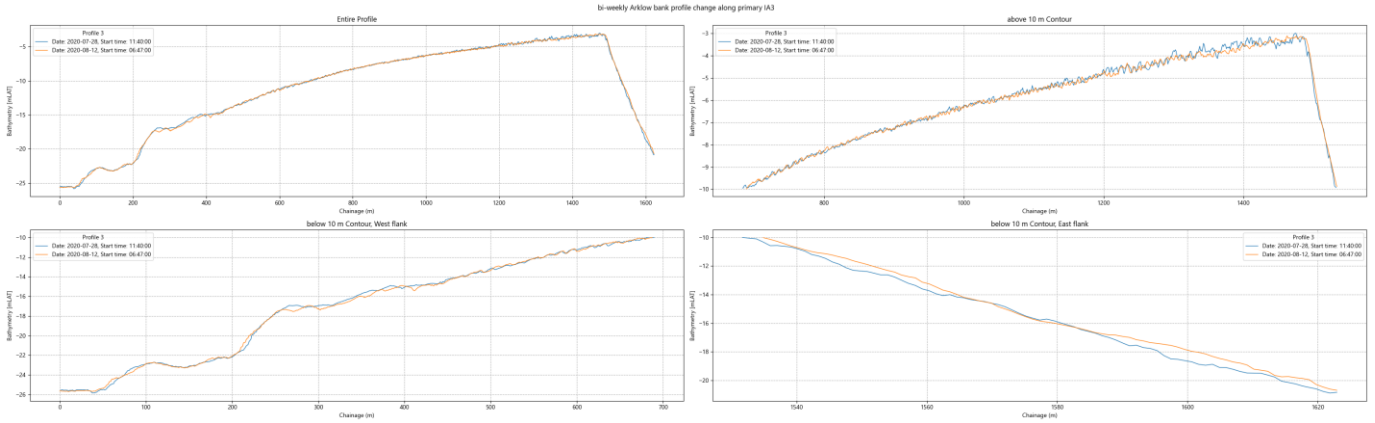


Figure 160. The profile extracted along the transect surveyed in IA3 over the period between 28.07.20 and 12.08.20. The full profile (top left panel), the zoomed in profile above the -10 m contour (top right panel), the west (bottom left panel) and east (bottom right panel) face of the bank in areas deeper than the -10 m contour are presented.

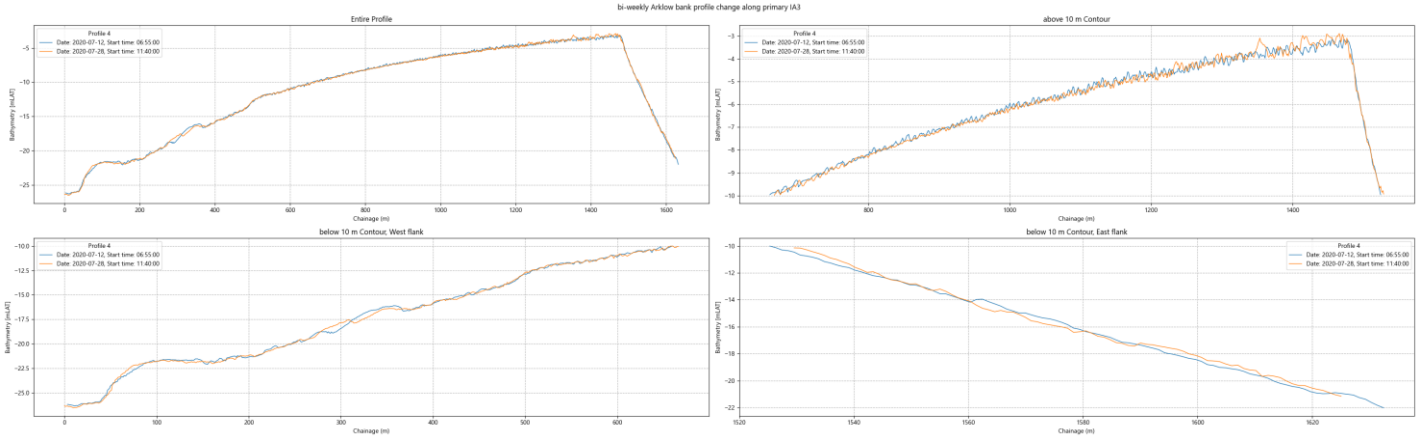


Figure 161. The profile extracted along the transect surveyed in IA3 over the period between 12.07.20 and 28.07.20. The full profile (top left panel), the zoomed in profile above the -10 m contour (top right panel), the west (bottom left panel) and east (bottom right panel) face of the bank in areas deeper than the -10 m contour are presented.

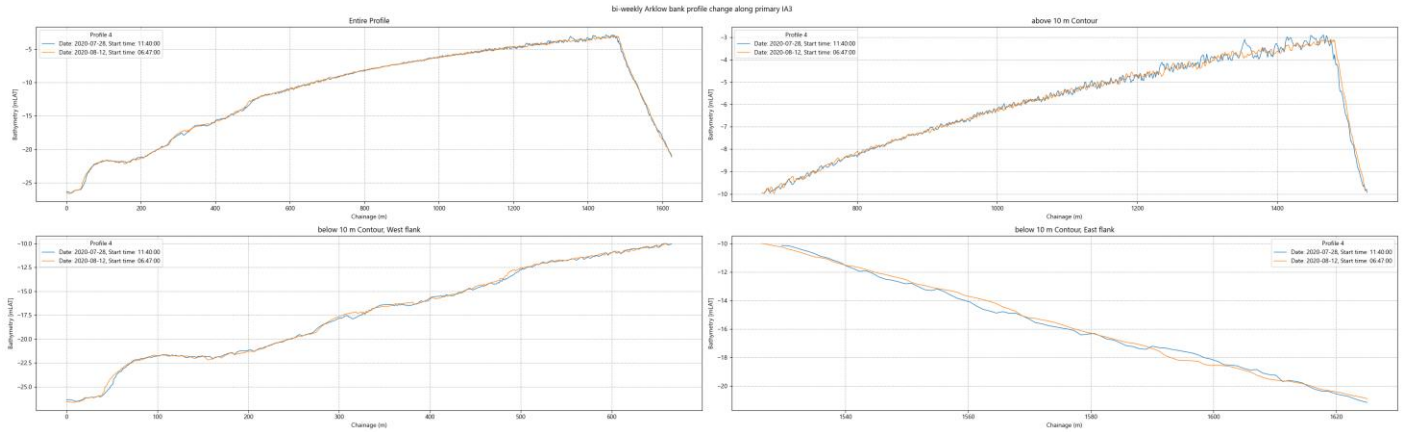


Figure 162. The profile extracted along the transect surveyed in IA3 over the period between 28.07.20 and 12.08.20. The full profile (top left panel), the zoomed in profile above the -10 m contour (top right panel), the west (bottom left panel) and east (bottom right panel) face of the bank in areas deeper than the -10 m contour are presented.

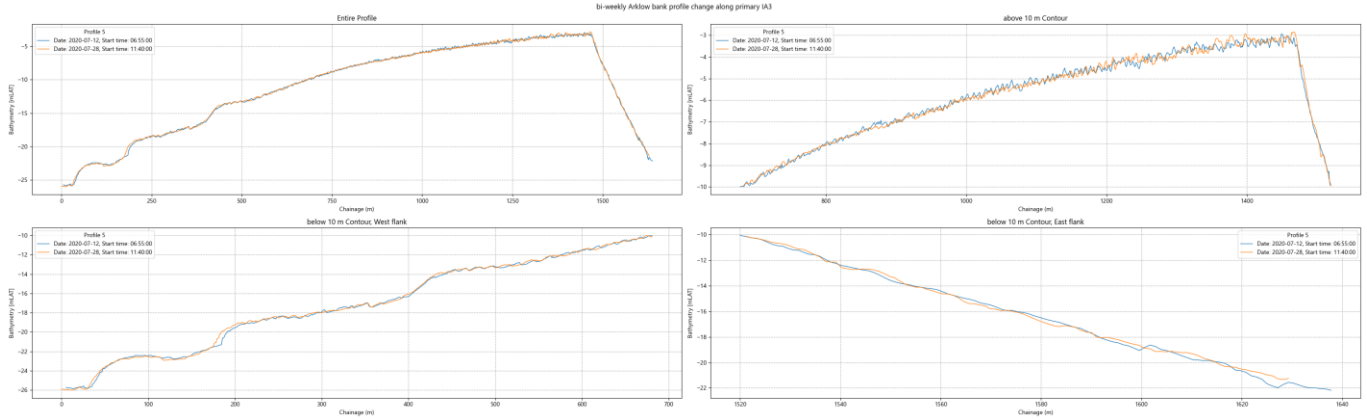


Figure 163. The profile extracted along the transect surveyed in IA3 over the period between 12.07.20 and 28.07.20. The full profile (top left panel), the zoomed in profile above the -10 m contour (top right panel), the west (bottom left panel) and east (bottom right panel) face of the bank in areas deeper than the -10 m contour are presented.

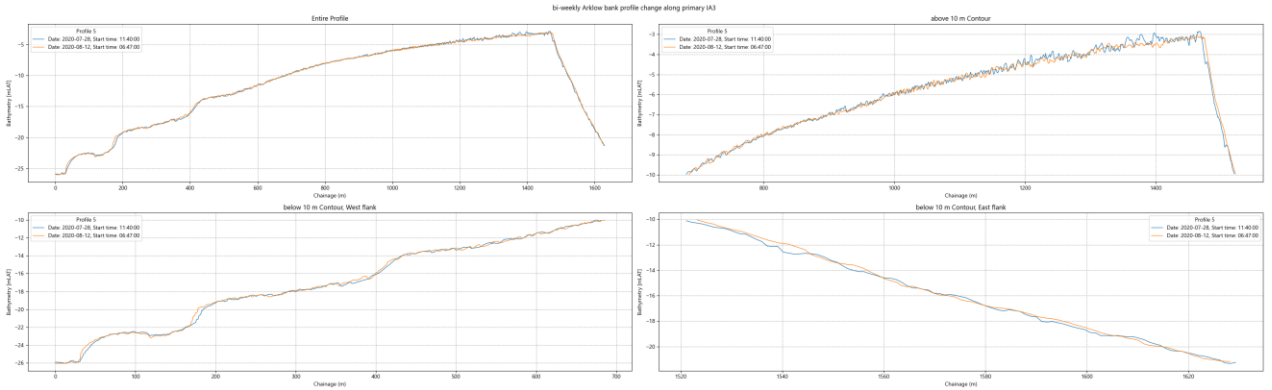


Figure 164. The profile extracted along the transect surveyed in IA5 over the period between 28.07.20 and 12.08.20. The full profile (top left panel), the zoomed in profile above the -10 m contour (top right panel), the west (bottom left panel) and east (bottom right panel) face of the bank in areas deeper than the -10 m contour are presented.

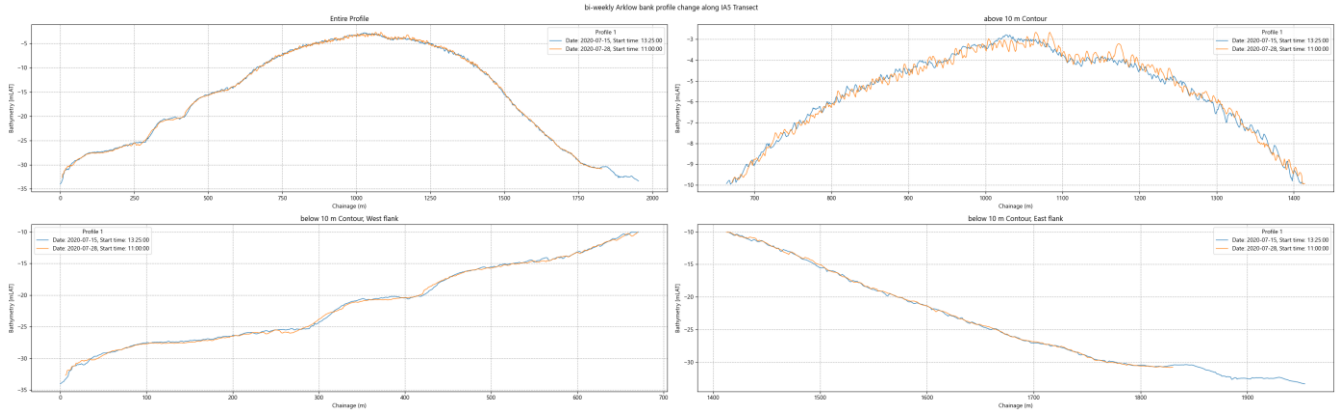


Figure 165. The profile extracted along the transect surveyed in IA5 over the period between 15.07.20 and 28.07.20. The full profile (top left panel), the zoomed in profile above the -10 m contour (top right panel), the west (bottom left panel) and east (bottom right panel) face of the bank in areas deeper than the -10 m contour are presented.

To assess the response of the bank over circa monthly timescales (periods of circa 3 – 4 weeks), a series of transects acquired from IA1, IA2, IA3, and IA5 were assessed. The bathymetry data available over this period are detailed in Table 16. The profiles are presented in Figure 166 to Figure 184.

Table 16. Bathymetry data available at monthly timescales.

IA	Sub-category	Filename	Survey Date	Start Time	End Time
IA1	Primary	IA1_P_PH01	11/07/2020	06:55	16:35
		IA1_P_PH03	09/08/2020	07:36	16:35
	Transect	IA1_TR_197_1	15/07/2020	09:17	09:50
		IA1_TR_220_1	07/08/2020	08:30	10:15
IA2	Primary	IA2_P_PH1	14/07/2020	07:50	16:15
		IA2_P_PH3	11/08/2020	06:56	09:23
	Transect	IA2_TR_197_1	15/07/2020	10:35	12:35
		IA2_TR_224_2	11/08/2020	16:00	16:15
IA3	Primary	IA3_P_PH1	12/07/2020	06:55	16:35
		IA3_P_PH3	12/08/2020	06:47	13:28
	Transect	IA3_TR_195_1	13/07/2020	17:25	17:35
		IA3_TR_220_2	07/08/2020	13:39	14:05
IA5	Transect	IA5_TR_197_1	15/07/2020	13:25	13:50
		IA5_TR_219_1	06/08/2020	12:30	12:55

Across the monthly timescale:

- Bedform movement observed at the crestline is significant, changing the seabed level significantly above the -10 mLAT contour, particularly in IA1 and IA3 where lateral movement in the region of metres was observed (Figure 166 to Figure 169 and Figure 178 to Figure 183). These profiles provide further corroborating evidence of the growth / decay of bedforms which persist above the -10 mLAT contour but also of potential wave influence within the shallowest regions of the bank where bedforms are removed from these regions of the bank, and then observed to re-form through time.
- Below the -10 mLAT contour, similar localised changes to the flanks of the bank are observed to those observed over bi-weekly timescales.

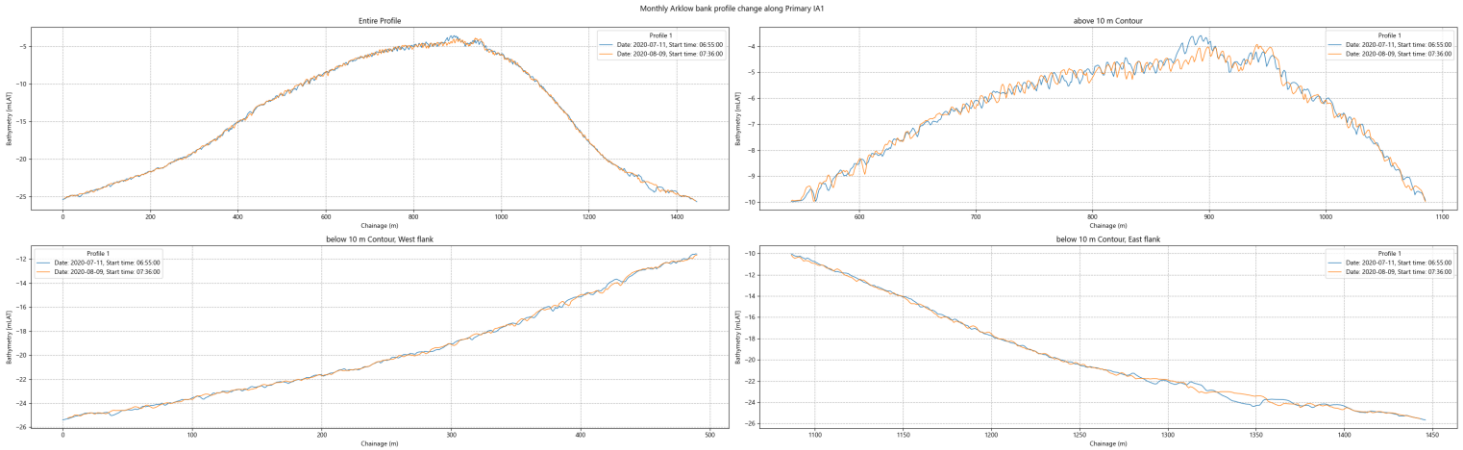


Figure 166. The profile extracted along the transect surveyed in IA1 over the period between 11.07.20 and 09.08.20. The full profile (top left panel), the zoomed in profile above the -10 m contour (top right panel), the west (bottom left panel) and east (bottom right panel) face of the bank in areas deeper than the -10 m contour are presented.

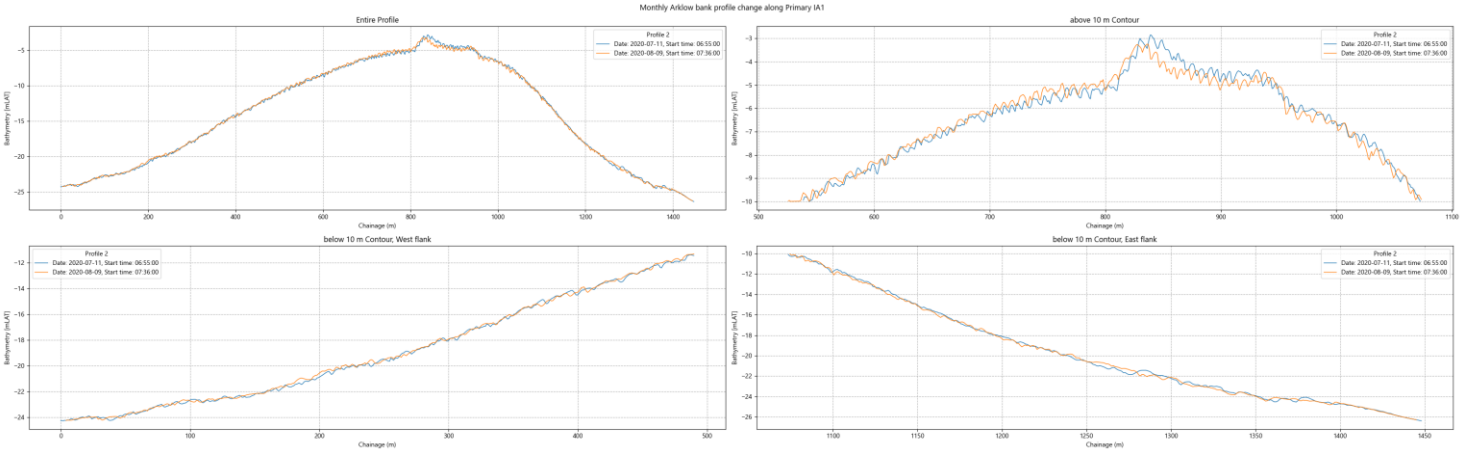


Figure 167. The profile extracted along the transect surveyed in IA1 over the period between 11.07.20 and 09.08.20. The full profile (top left panel), the zoomed in profile above the -10 m contour (top right panel), the west (bottom left panel) and east (bottom right panel) face of the bank in areas deeper than the -10 m contour are presented.

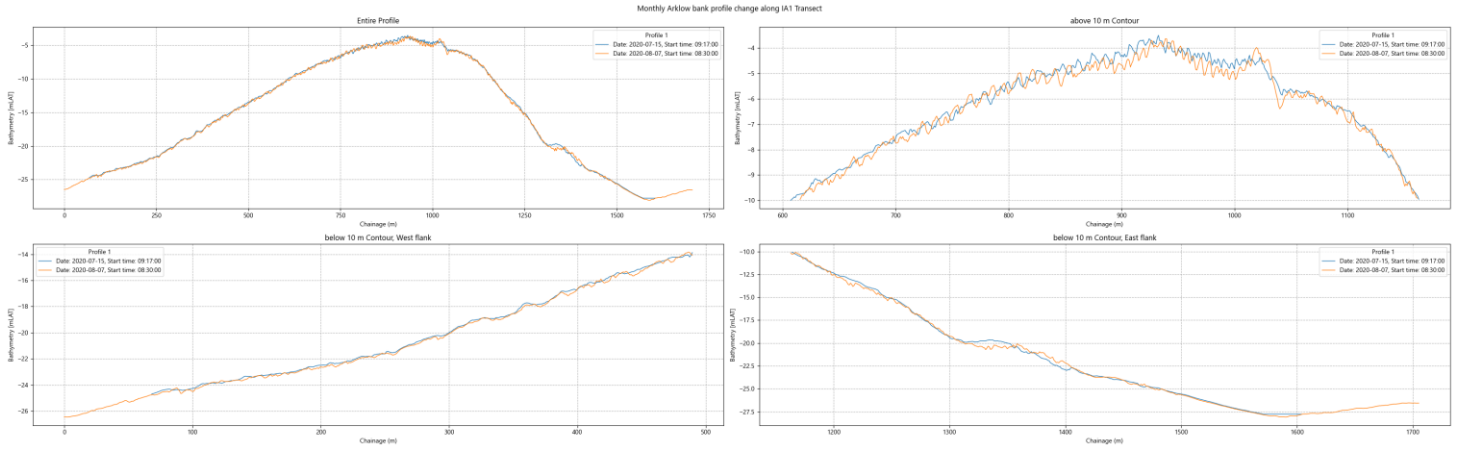


Figure 168. The profile extracted along the transect surveyed in IA1 over the period between 15.07.20 and 07.08.20. The full profile (top left panel), the zoomed in profile above the -10 m contour (top right panel), the west (bottom left panel) and east (bottom right panel) face of the bank in areas deeper than the -10 m contour are presented.

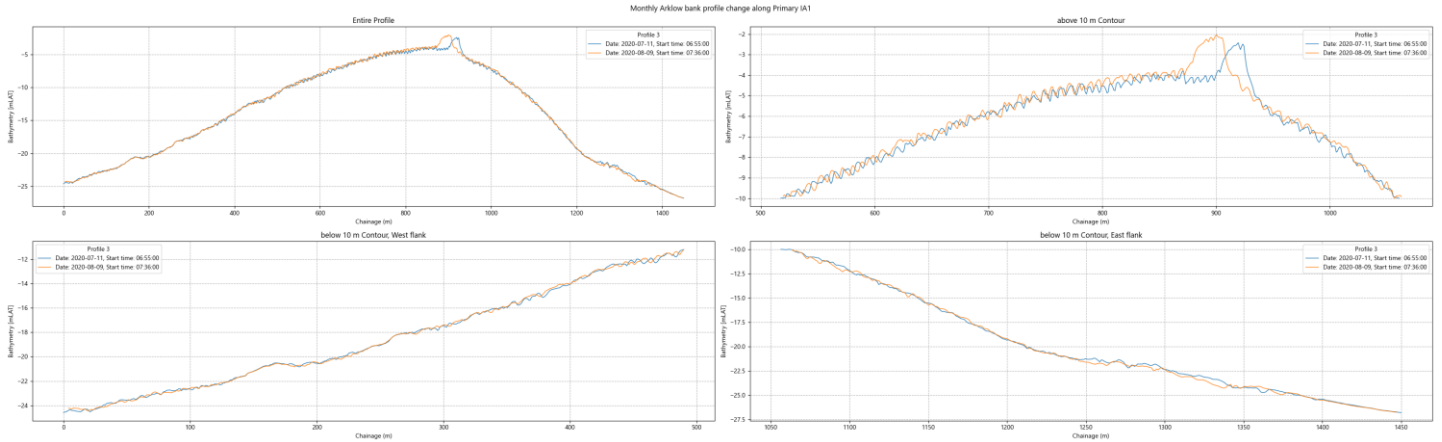


Figure 169. The profile extracted along the transect surveyed in IA1 over the period between 11.07.20 and 09.08.20. The full profile (top left panel), the zoomed in profile above the -10 m contour (top right panel), the west (bottom left panel) and east (bottom right panel) face of the bank in areas deeper than the -10 m contour are presented.

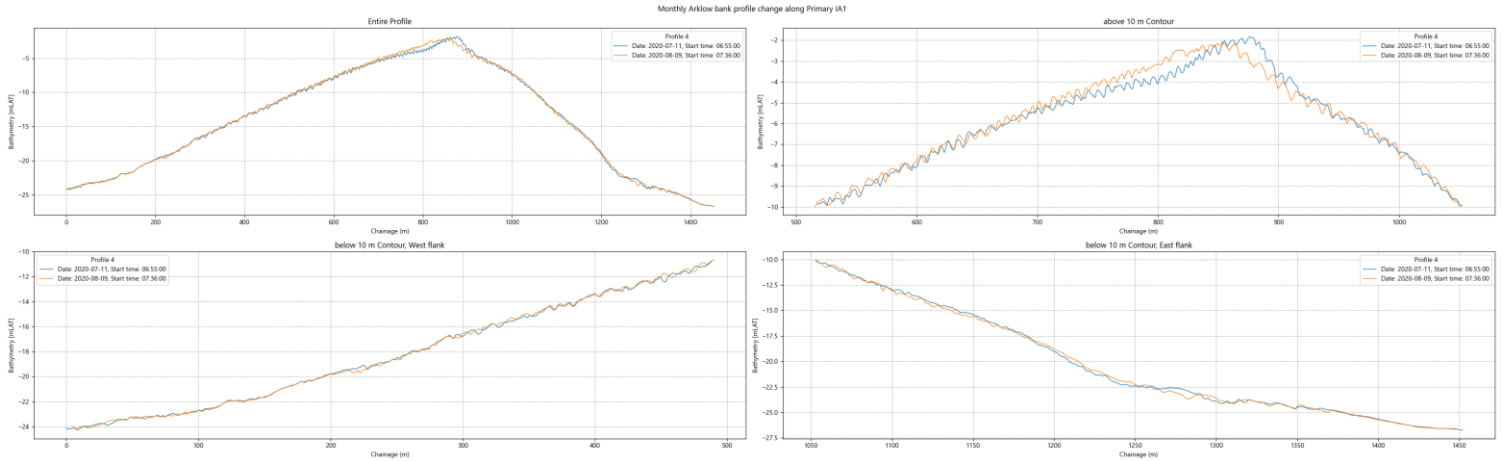


Figure 170. The profile extracted along the transect surveyed in IA5 over the period between 11.07.20 and 09.08.20. The full profile (top left panel), the zoomed in profile above the -10 m contour (top right panel), the west (bottom left panel) and east (bottom right panel) face of the bank in areas deeper than the -10 m contour are presented.

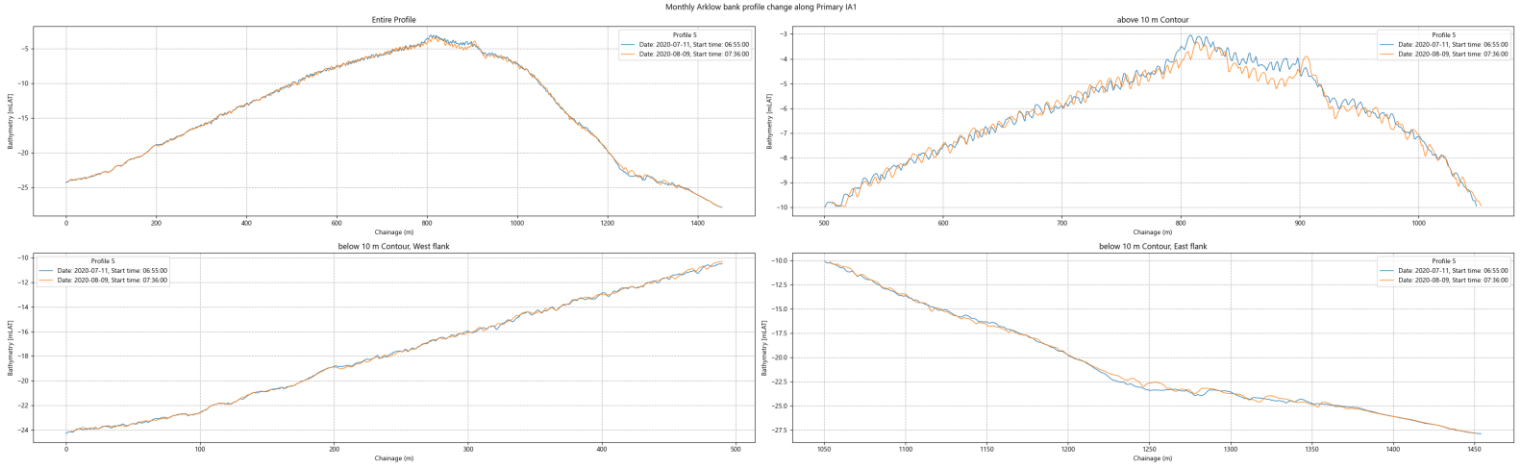


Figure 171. The profile extracted along the transect surveyed in IA5 over the period between 11.07.20 and 09.08.20. The full profile (top left panel), the zoomed in profile above the -10 m contour (top right panel), the west (bottom left panel) and east (bottom right panel) face of the bank in areas deeper than the -10 m contour are presented.

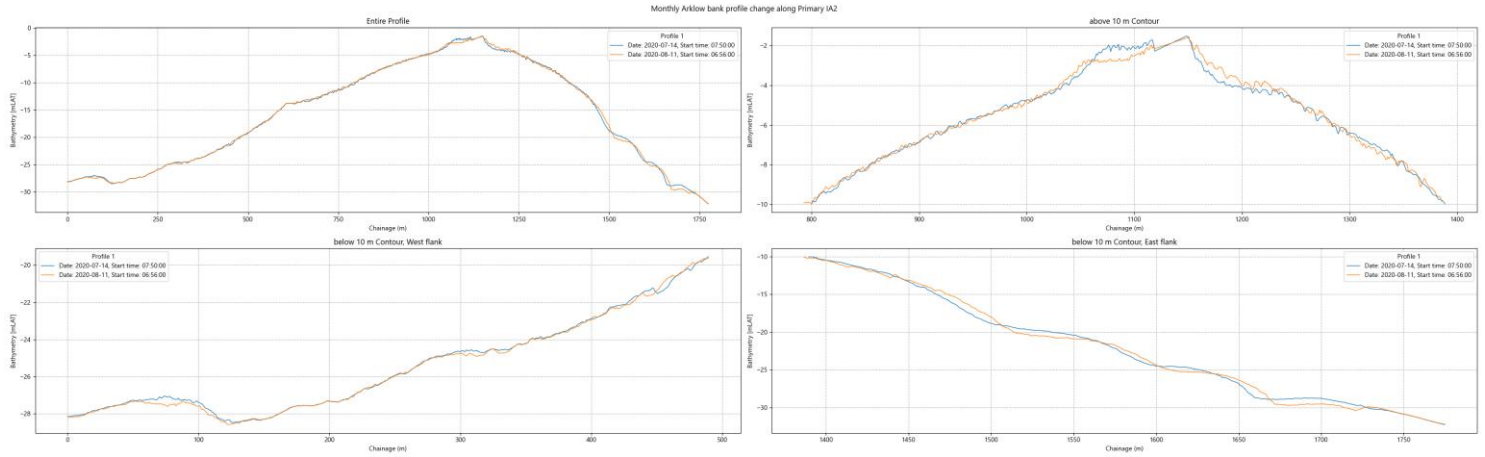


Figure 172. The profile extracted along the transect surveyed in IA2 over the period between 14.07.20 and 11.08.20. The full profile (top left panel), the zoomed in profile above the -10 m contour (top right panel), the west (bottom left panel) and east (bottom right panel) face of the bank in areas deeper than the -10 m contour are presented.

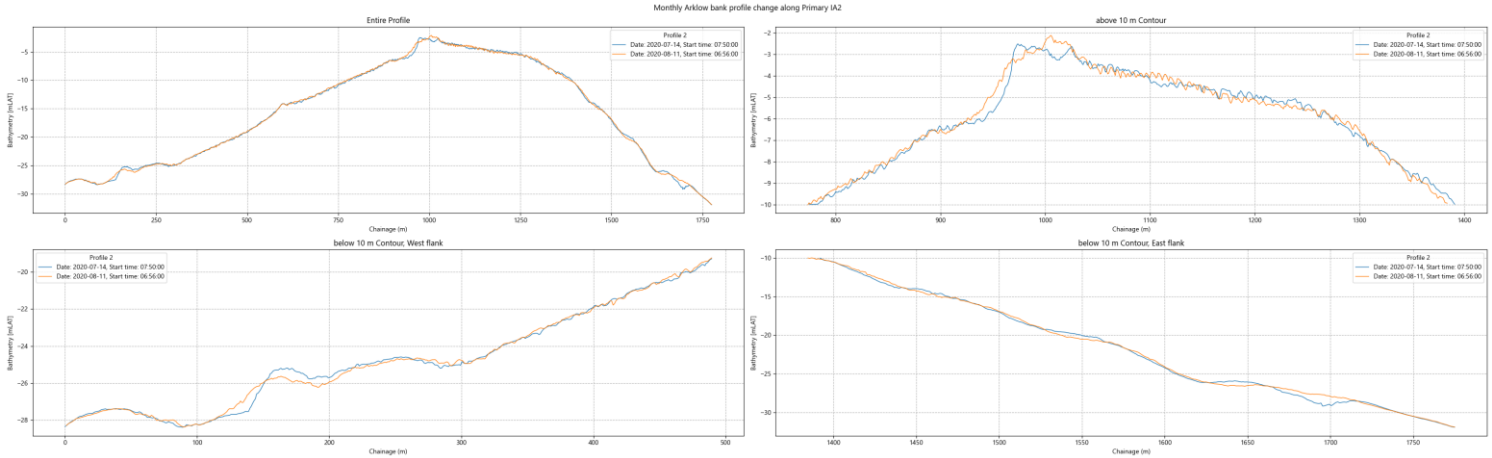


Figure 173. The profile extracted along the transect surveyed in IA2 over the period between 14.07.20 and 11.08.20. The full profile (top left panel), the zoomed in profile above the -10 m contour (top right panel), the west (bottom left panel) and east (bottom right panel) face of the bank in areas deeper than the -10 m contour are presented.

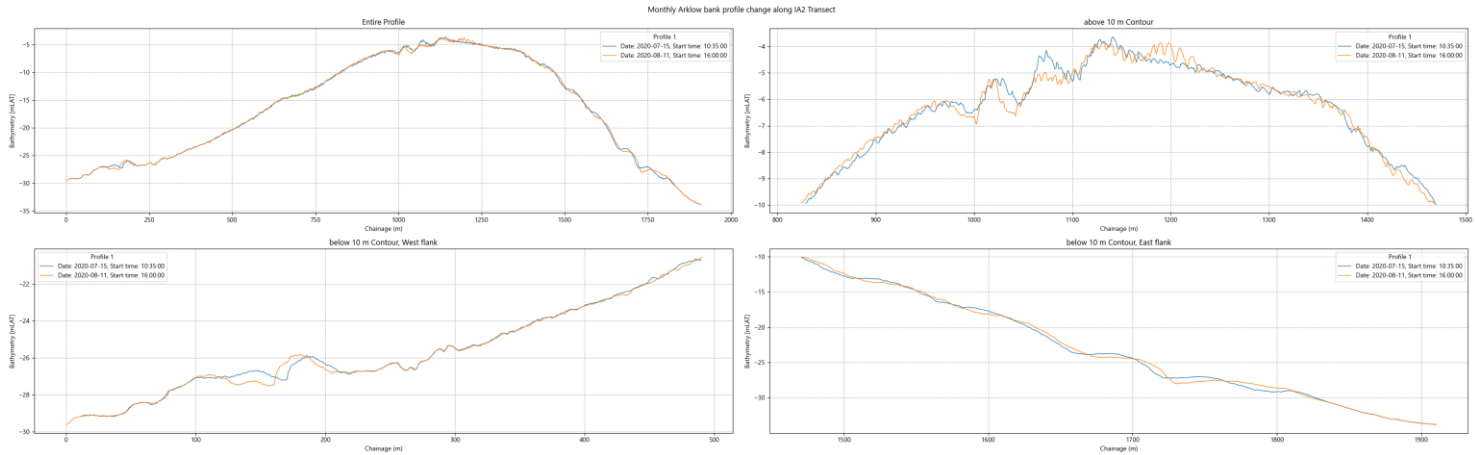


Figure 174. The profile extracted along the transect surveyed in IA2 over the period between 15.07.20 and 11.08.20. The full profile (top left panel), the zoomed in profile above the -10 m contour (top right panel), the west (bottom left panel) and east (bottom right panel) face of the bank in areas deeper than the -10 m contour are presented.

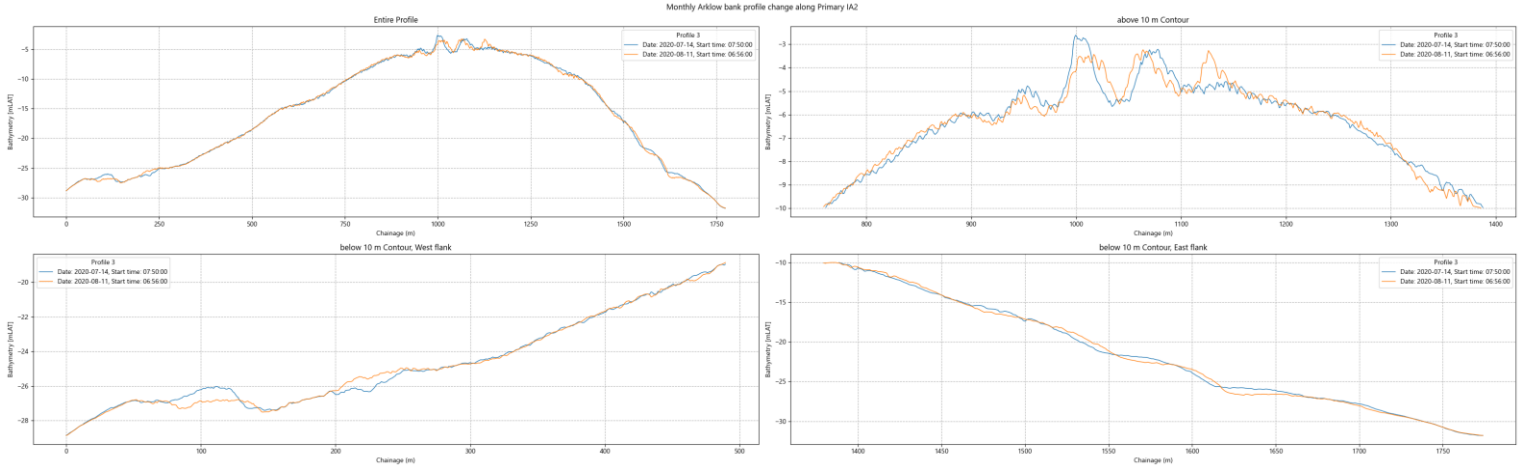


Figure 175. The profile extracted along the transect surveyed in IA2 over the period between 14.07.20 and 11.08.20. The full profile (top left panel), the zoomed in profile above the -10 m contour (top right panel), the west (bottom left panel) and east (bottom right panel) face of the bank in areas deeper than the -10 m contour are presented.

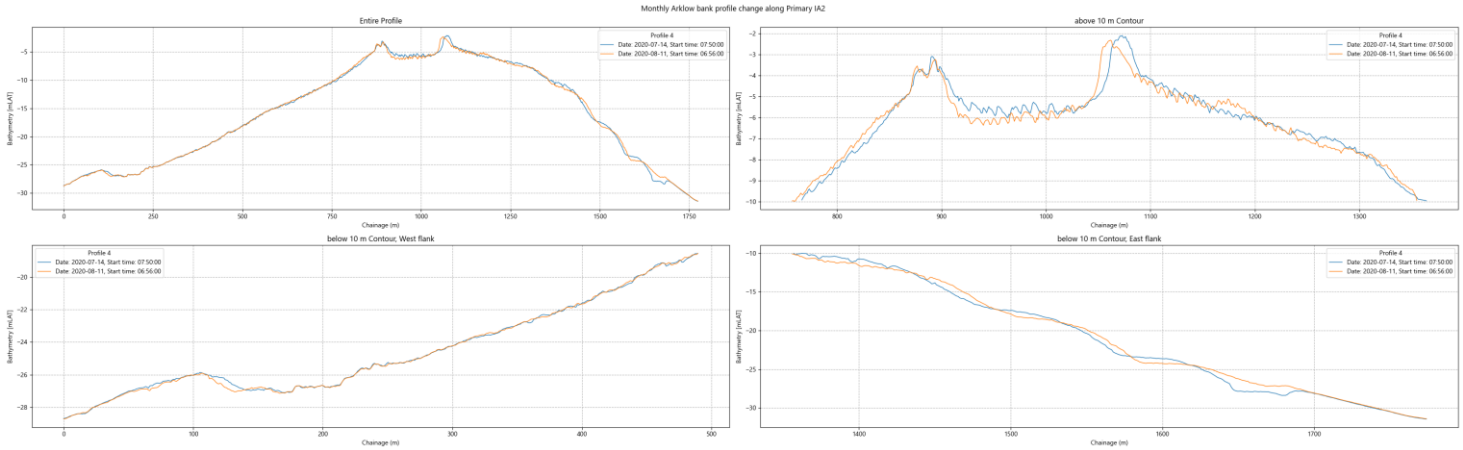


Figure 176. The profile extracted along the transect surveyed in IA2 over the period between 14.07.20 and 11.08.20. The full profile (top left panel), the zoomed in profile above the -10 m contour (top right panel), the west (bottom left panel) and east (bottom right panel) face of the bank in areas deeper than the -10 m contour are presented.

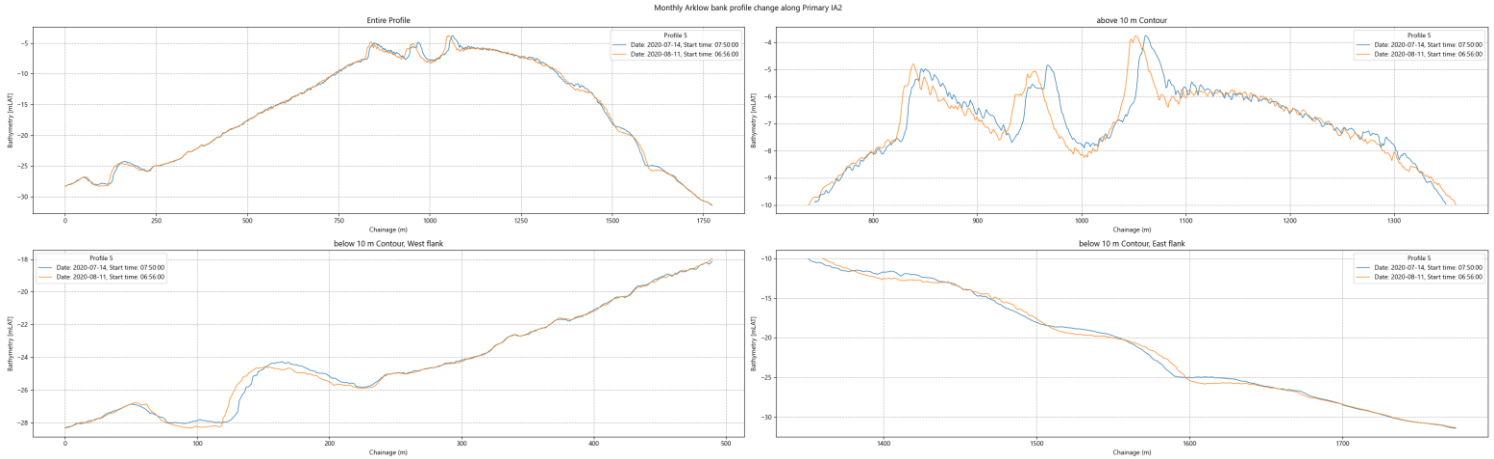


Figure 177. The profile extracted along the transect surveyed in IA2 over the period between 14.07.20 and 11.08.20. The full profile (top left panel), the zoomed in profile above the -10 m contour (top right panel), the west (bottom left panel) and east (bottom right panel) face of the bank in areas deeper than the -10 m contour are presented.

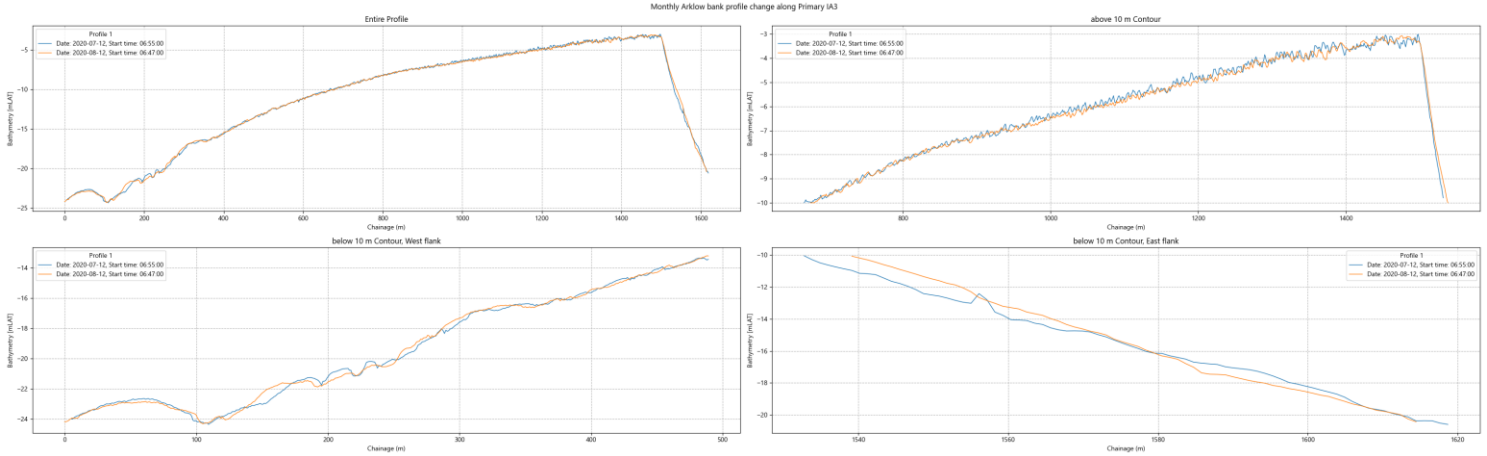


Figure 178. The profile extracted along the transect surveyed in IA3 over the period between 12.07.20 and 12.08.20. The full profile (top left panel), the zoomed in profile above the -10 m contour (top right panel), the west (bottom left panel) and east (bottom right panel) face of the bank in areas deeper than the -10 m contour are presented.

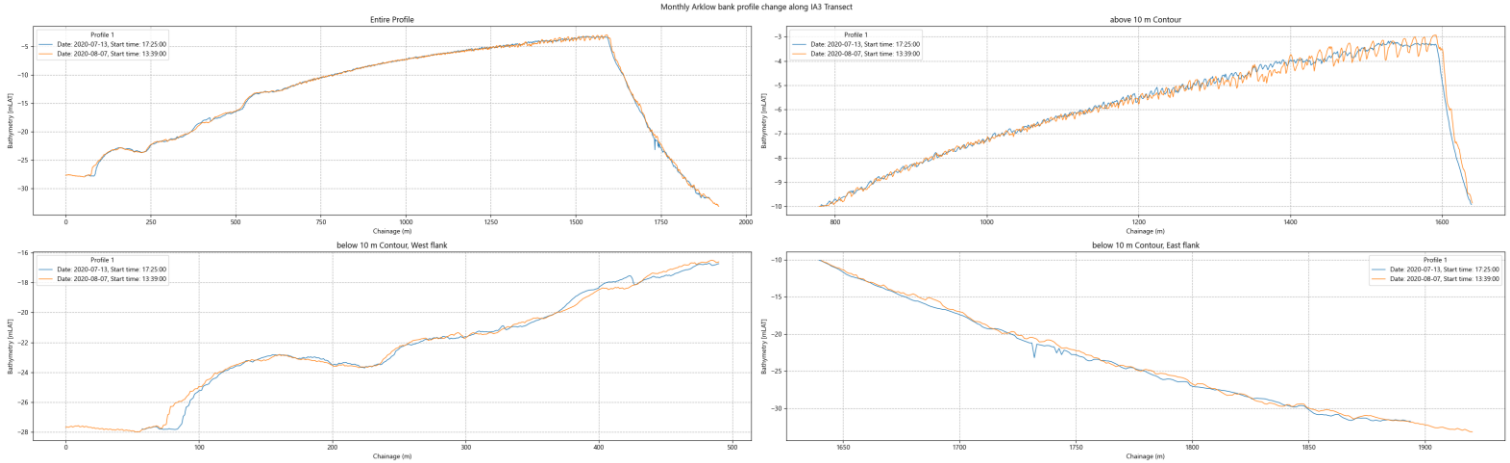


Figure 179. The profile extracted along the transect surveyed in IA3 over the period between 13.07.20 and 07.08.20. The full profile (top left panel), the zoomed in profile above the -10 m contour (top right panel), the west (bottom left panel) and east (bottom right panel) face of the bank in areas deeper than the -10 m contour are presented.

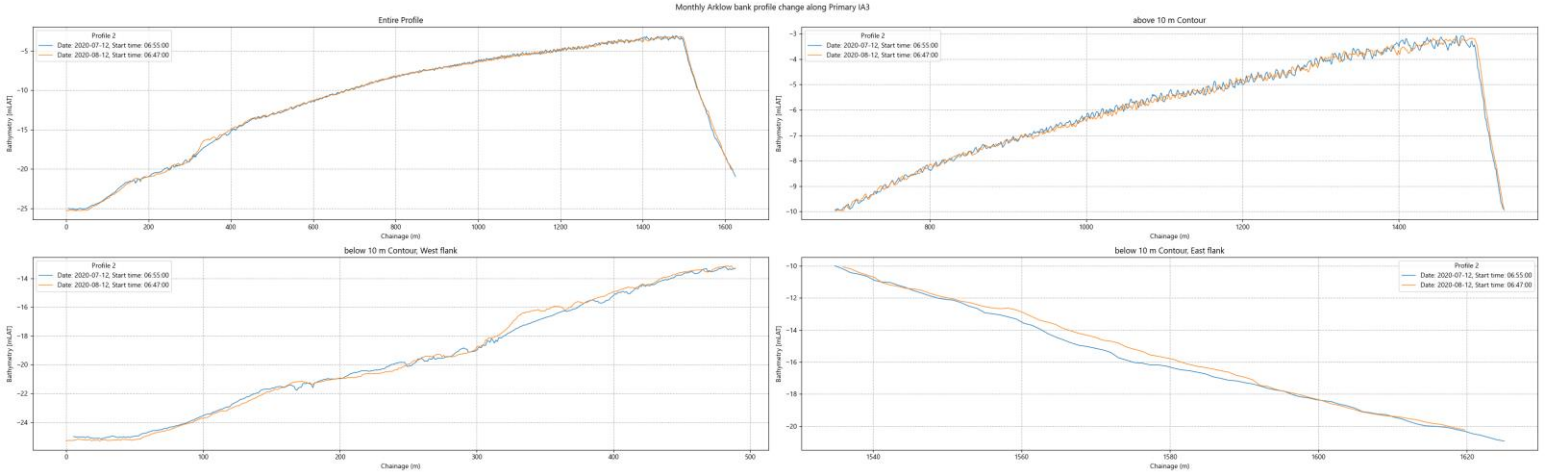


Figure 180. The profile extracted along the transect surveyed in IA3 over the period between 12.07.20 and 12.08.20. The full profile (top left panel), the zoomed in profile above the -10 m contour (top right panel), the west (bottom left panel) and east (bottom right panel) face of the bank in areas deeper than the -10 m contour are presented.

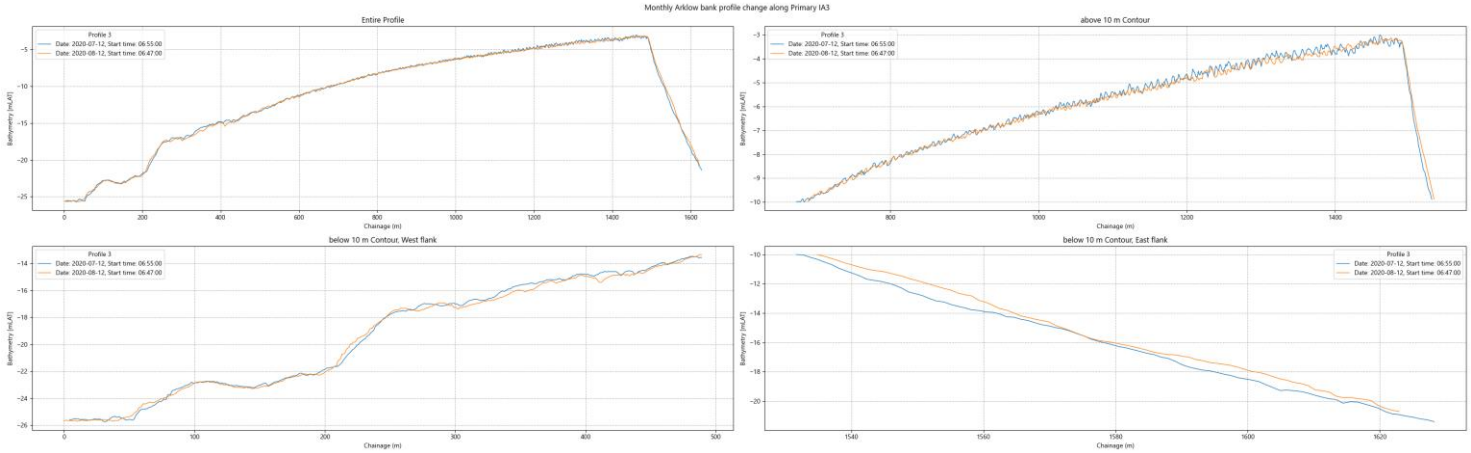


Figure 181. The profile extracted along the transect surveyed in IA3 over the period between 12.07.20 and 12.08.20. The full profile (top left panel), the zoomed in profile above the -10 m contour (top right panel), the west (bottom left panel) and east (bottom right panel) face of the bank in areas deeper than the -10 m contour are presented.

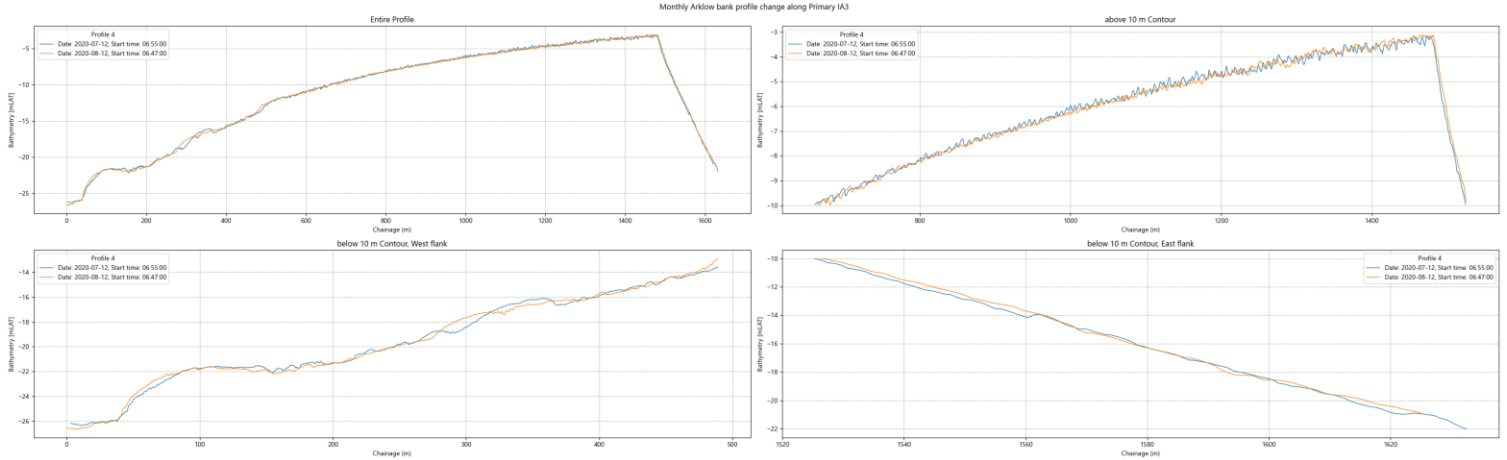


Figure 182. The profile extracted along the transect surveyed in IA3 over the period between 12.07.20 and 12.08.20. The full profile (top left panel), the zoomed in profile above the -10 m contour (top right panel), the west (bottom left panel) and east (bottom right panel) face of the bank in areas deeper than the -10 m contour are presented.

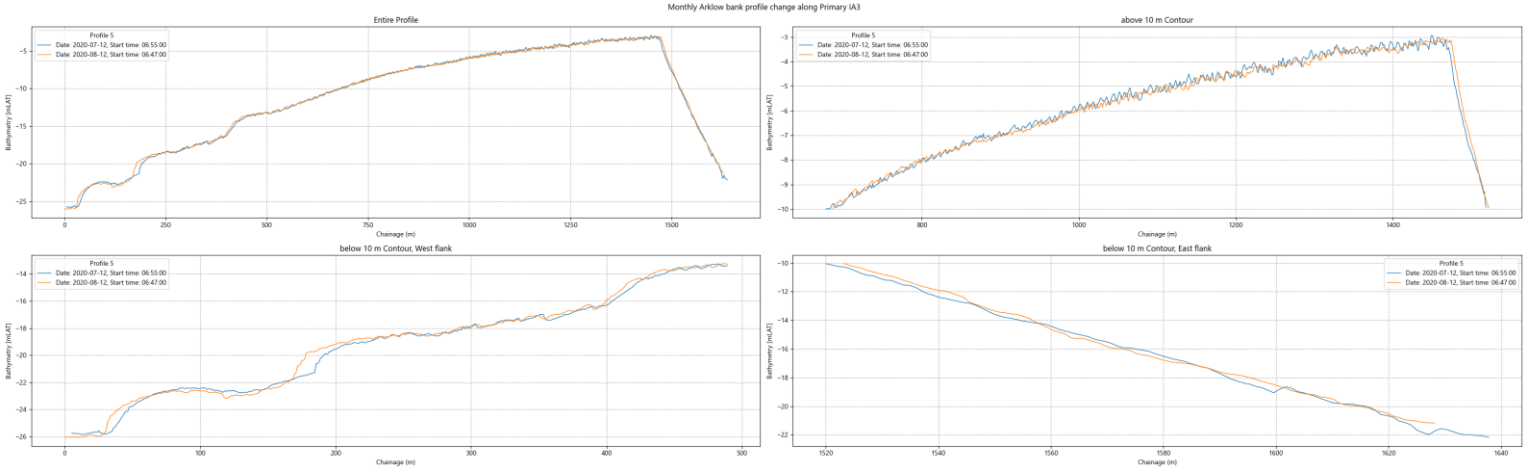


Figure 183. The profile extracted along the transect surveyed in IA3 over the period between 12.07.20 and 12.08.20. The full profile (top left panel), the zoomed in profile above the -10 m contour (top right panel), the west (bottom left panel) and east (bottom right panel) face of the bank in areas deeper than the -10 m contour are presented.

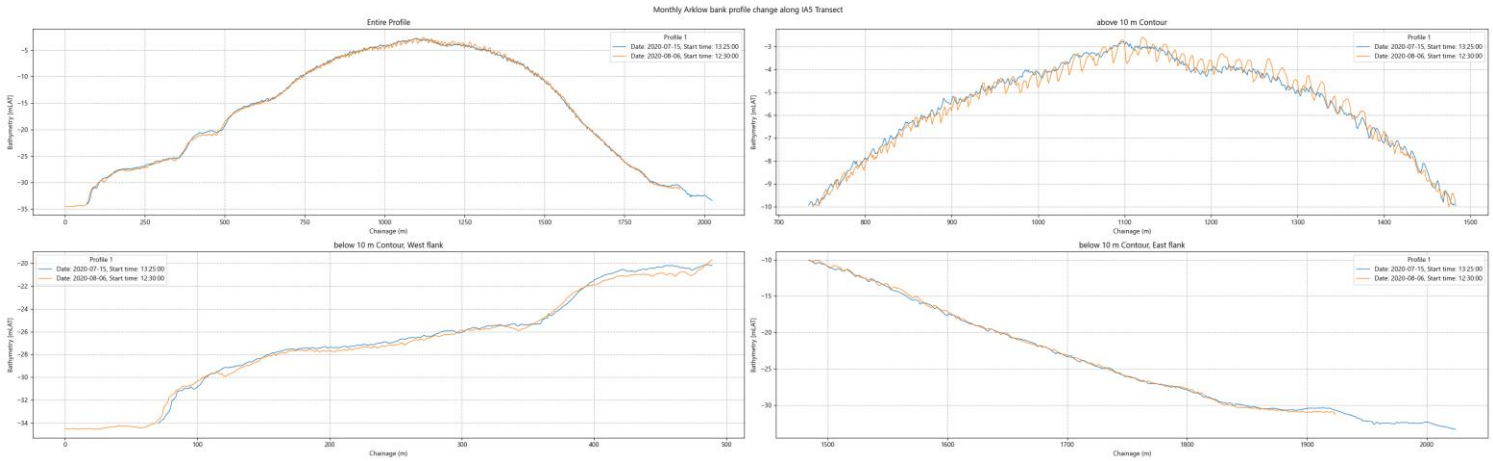


Figure 184. The profile extracted along the transect surveyed in IA5 over the period between 15.07.20 and 06.08.20. The full profile (top left panel), the zoomed in profile above the -10 m contour (top right panel), the west (bottom left panel) and east (bottom right panel) face of the bank in areas deeper than the -10 m contour are presented.

To assess the response of the bank over a yearly timescale, a series of transects acquired from inspection surveys of the Arklow Bank Phase 1 turbines were assessed. The bathymetry data available over this period are detailed in Table 17. In total, 12 profiles were extracted from these datasets and assessed. These profiles are presented on a spatial plot in Figure 185; these surveys are limited spatially with E – W transects covering circa 500 m of the bank profile. The profiles are presented in Figure 186 to Figure 192. Note: Figure 190 and Figure 191 present data over a period of 2 and 4 years due to gaps in the data record.

Table 17. Bathymetry data available at yearly timescales.

Filename	Survey Date
1_p_Oct05_CR_5000_04_1m	October \ 2005
2_p_June2006_GS_Cable_04	June \ 2006
3_p_April2007_Ch_04_1m	April \ 2007 *
4_p_May2008_CH_04	May \ 2008 *
5_p_apr09 CH_04	April \ 2009
6_p_jul11 Chart 04	July \ 2011
7_p_BANK April2015 FINAL	April \ 2015 *
8_p_ARKLOW BANK FINAL 4M GRID 2016	May \ 2016 *

*The data files did not include the date at which these surveys were conducted. It has been assumed that these surveys were conducted at the same as the individual phase 1 turbine surveys which were dated.

** Though these data are presented and considered as part of the assessment. At some locations near the bank crest and wind turbines, there is an absence of data due to safety restrictions placed on vessel movements in these areas. There is no consistency in the resolution and output definitions for the Phase 1 surveys. For example, the raw data in some years (e.g. 2015), are missing entirely. It should also be noted that the datums used in these surveys have been inconsistent historically (Cathie Associates Ltd, 2018) and thus these data carry a high uncertainty limiting their utility to the study.

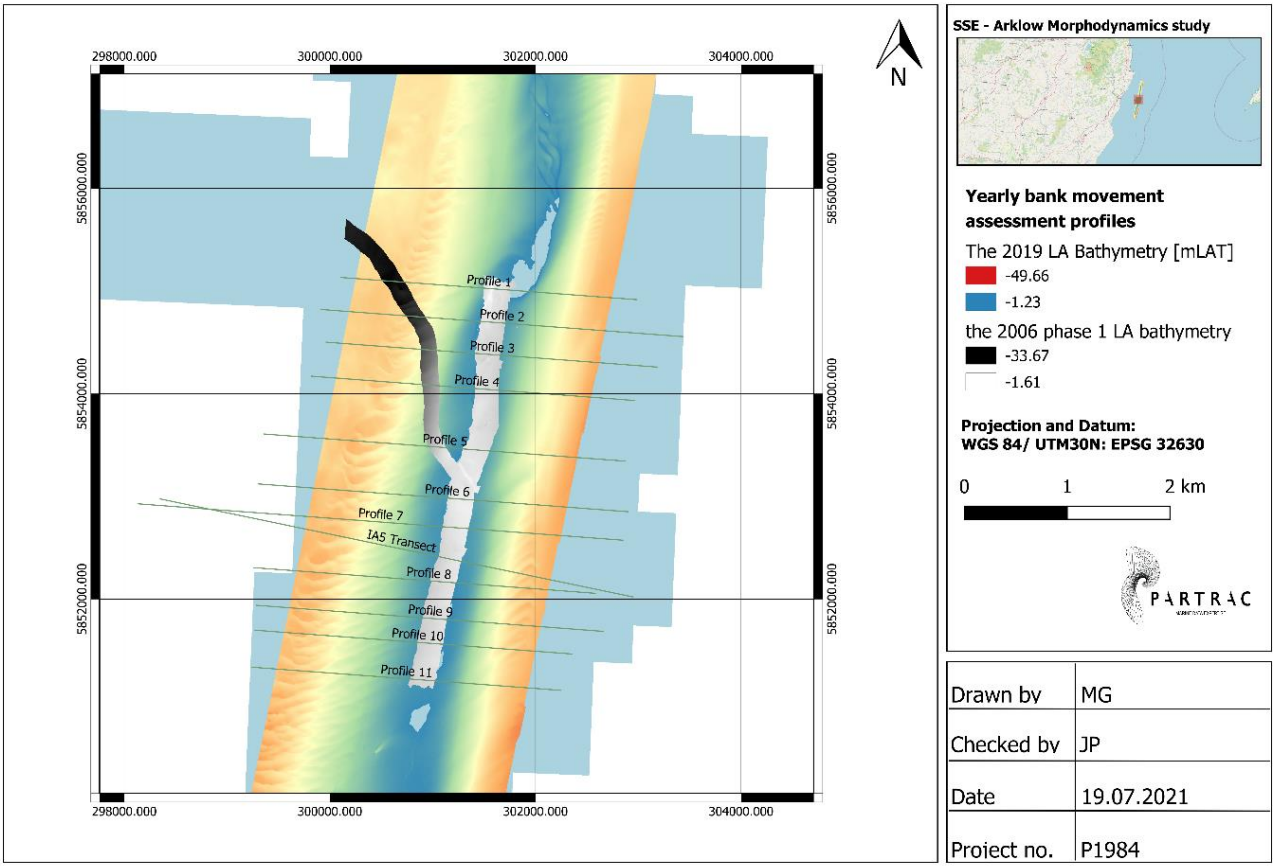


Figure 185. The profiles extracted from the survey data collected at the Phase 1 turbine locations between 2005 and 2016.

Assessment of bank movement on a yearly basis can be summarised as follows:

- Across periods of circa 1-year greater bed level change is observed, either as a result of bedform movement or local scour within the shallow regions of the area coincident with the Phase 1 turbines. In several profiles however it is clear bed level change is observed due to a repositioning of the crestline to the east or west driving a change to the slope of the east – west flank (though as these profiles are spatially limited conclusions regarding the changes to the bank profile below the shallowest regions of the bank are highly limited).
- Greater movement is observed to the north of the bank (profiles 1 to 6) when compared to profiles located to the south of the bank (profiles 7 to 12) (Figure 186 to Figure 192).

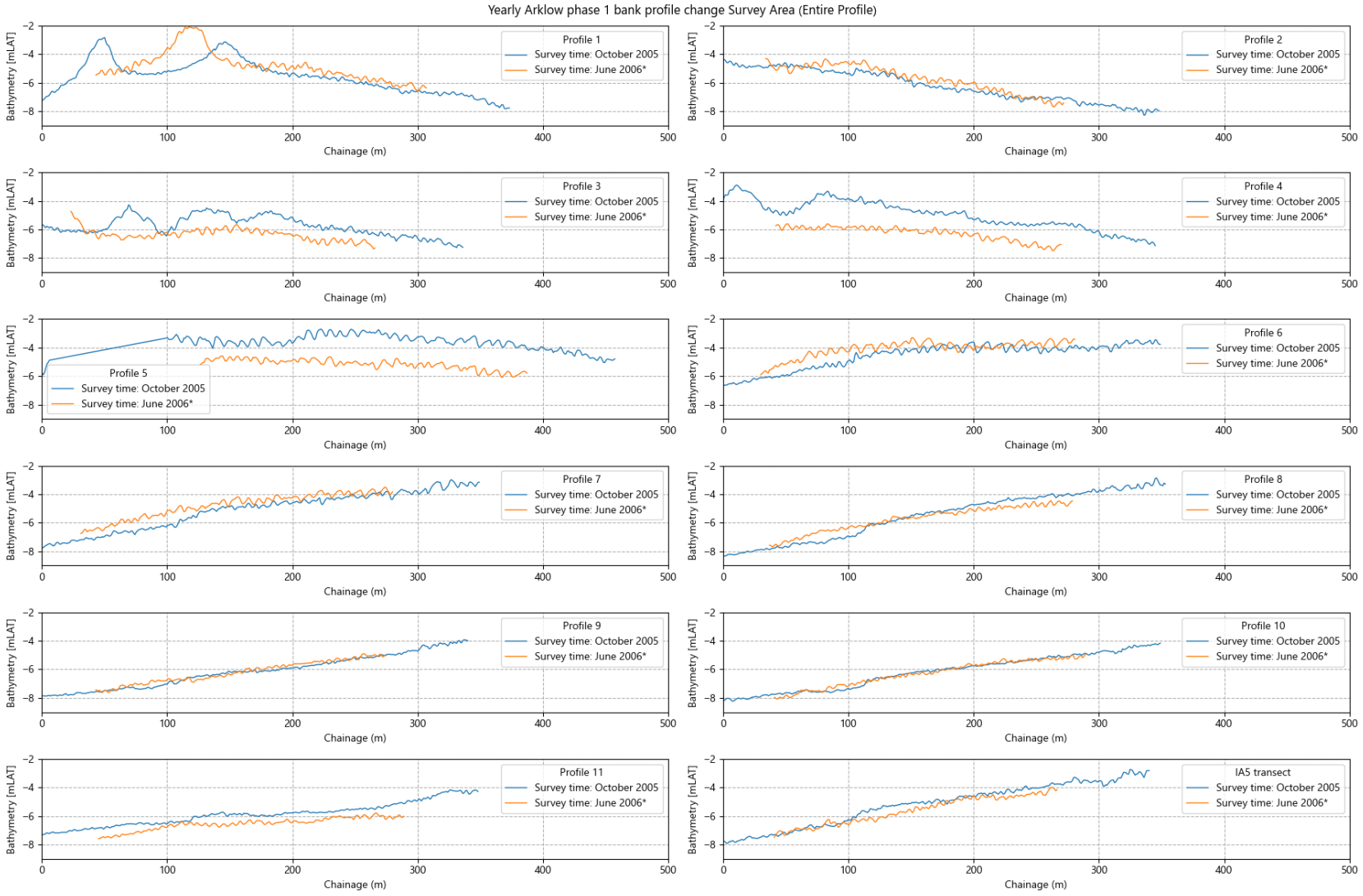


Figure 186. The 12 profiles extracted from the Phase 1 surveys over the period October 2005 and June 2006.

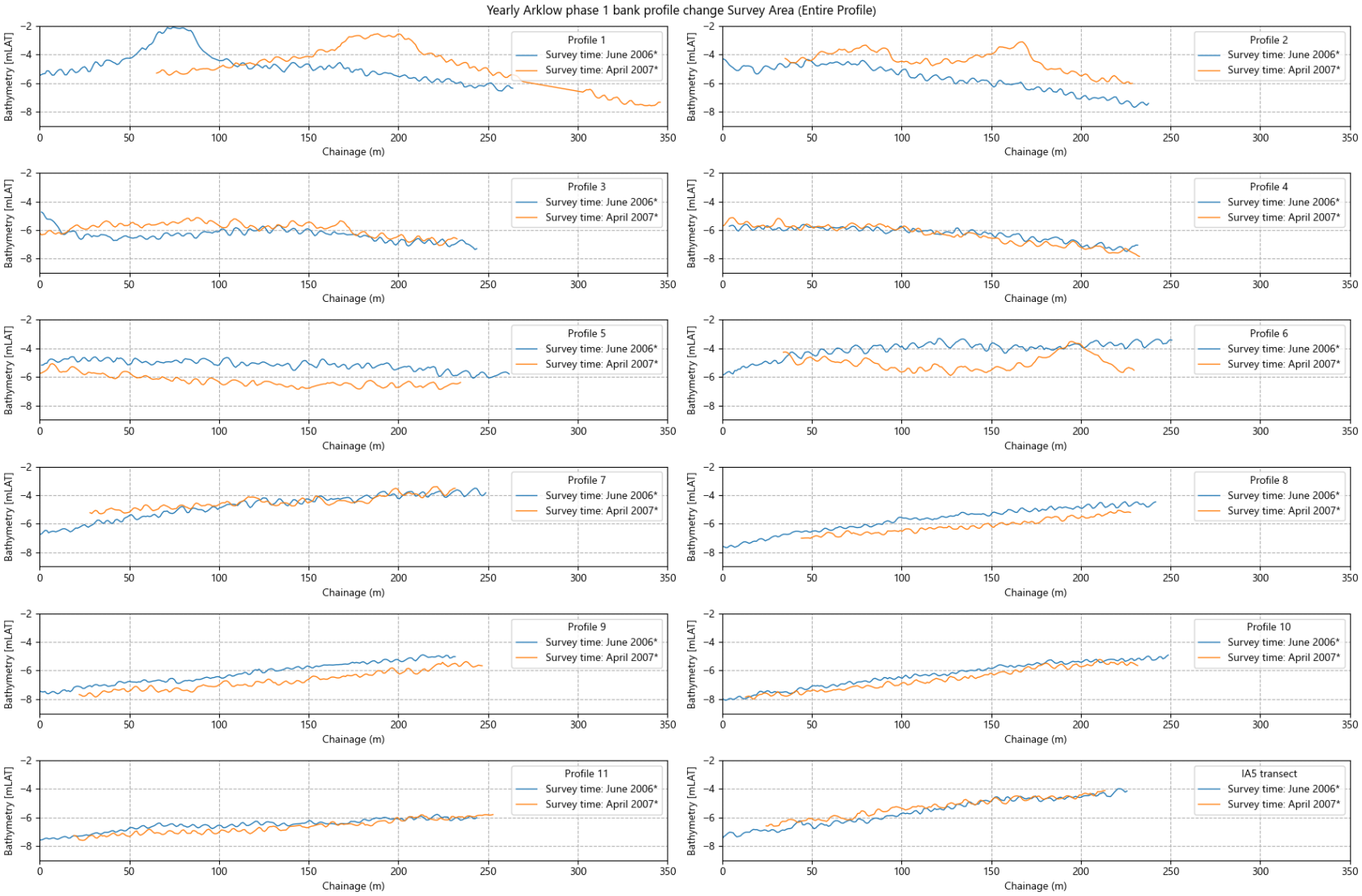


Figure 187. The 12 profiles extracted from the Phase 1 surveys over the period June 2006 to April 2007.

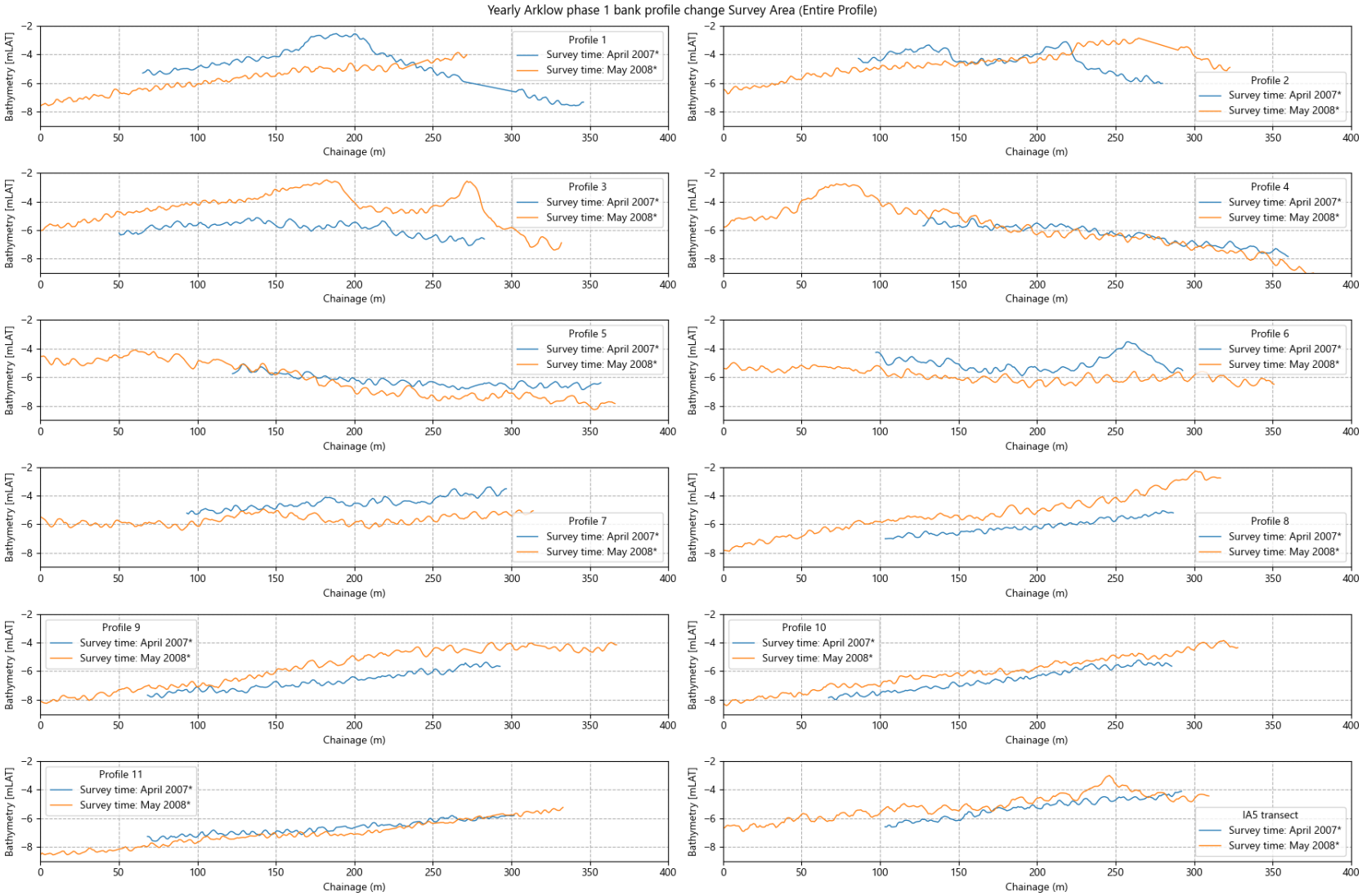


Figure 188. The 12 profiles extracted from the Phase 1 surveys over the period April 2007 to May 2008.

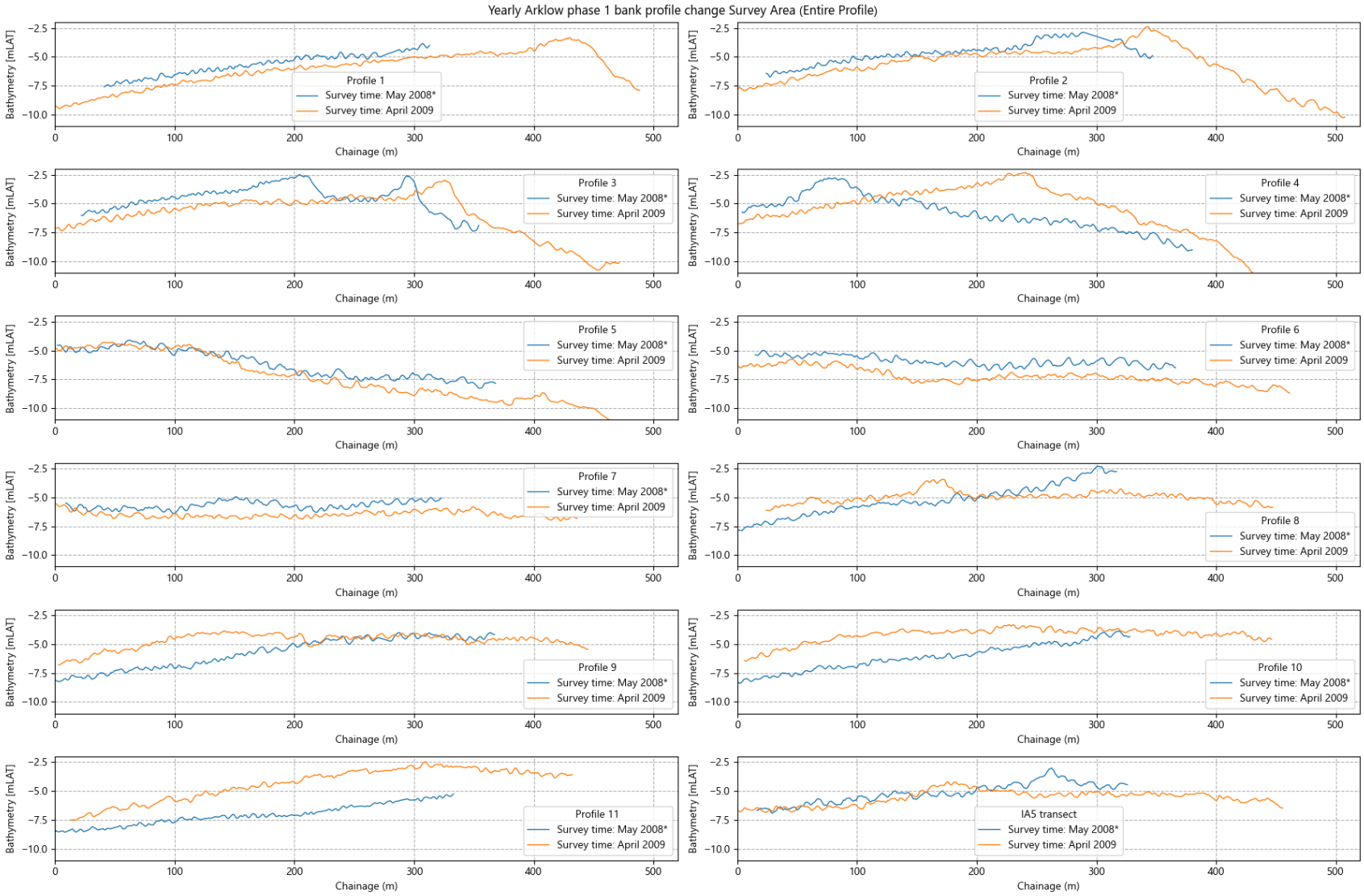


Figure 189. The 12 profiles extracted from the Phase 1 surveys over the period May 2008 to April 2009.

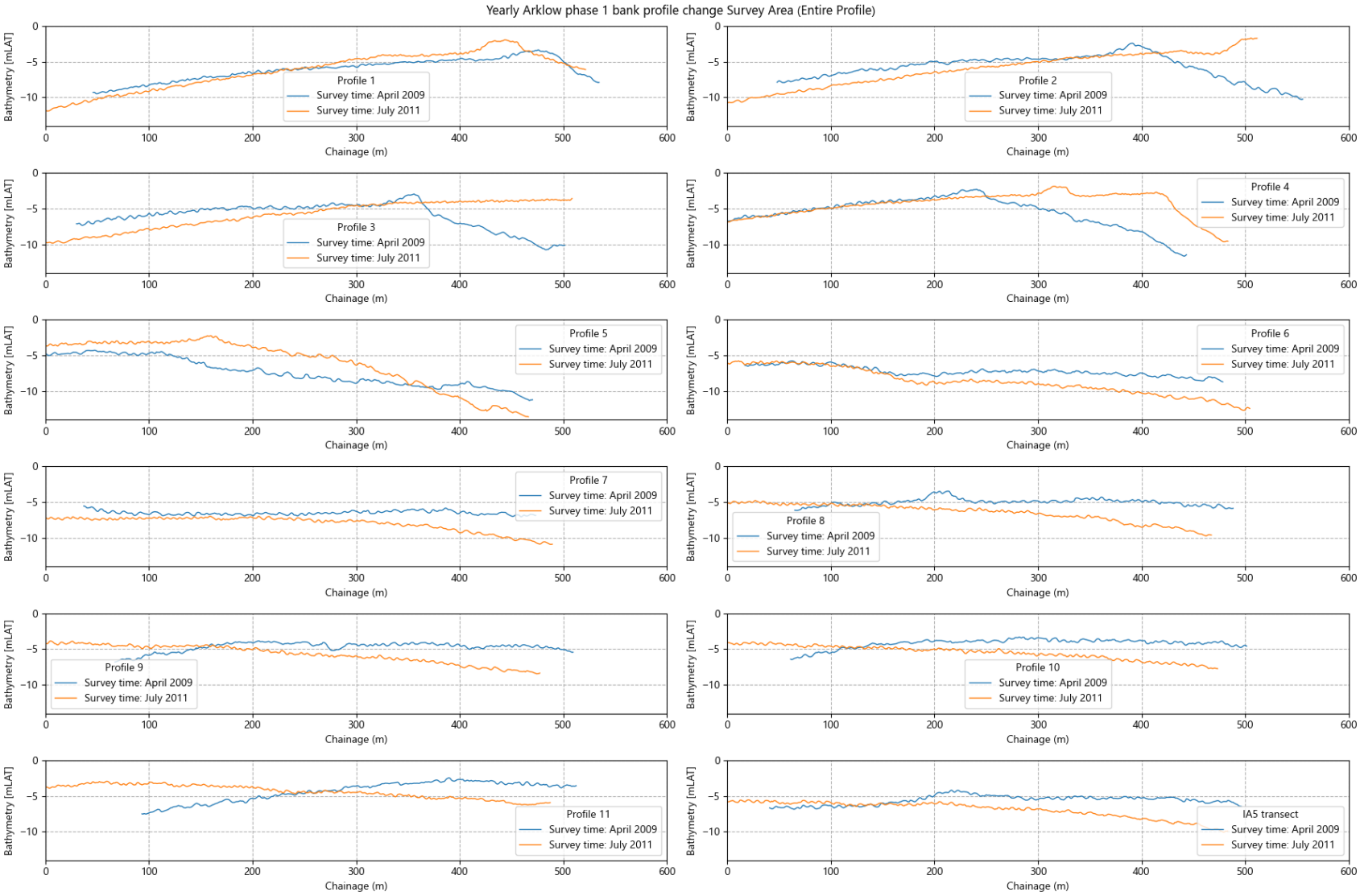


Figure 190. The 12 profiles extracted from the Phase 1 surveys over the period April 2009 and July 2011.

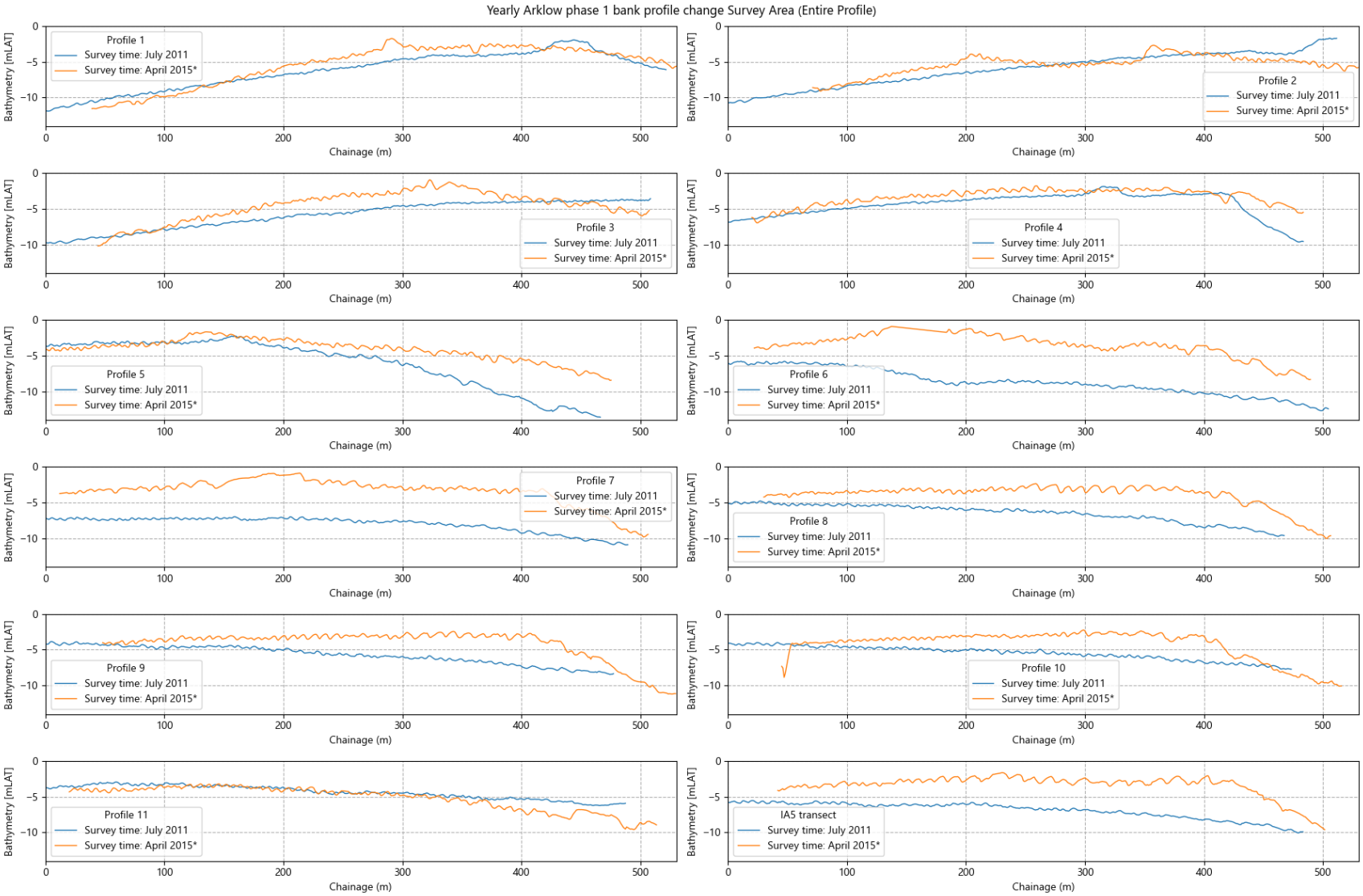


Figure 191. The 12 profiles extracted from the Phase 1 surveys over the period July 2011 and April 2015.

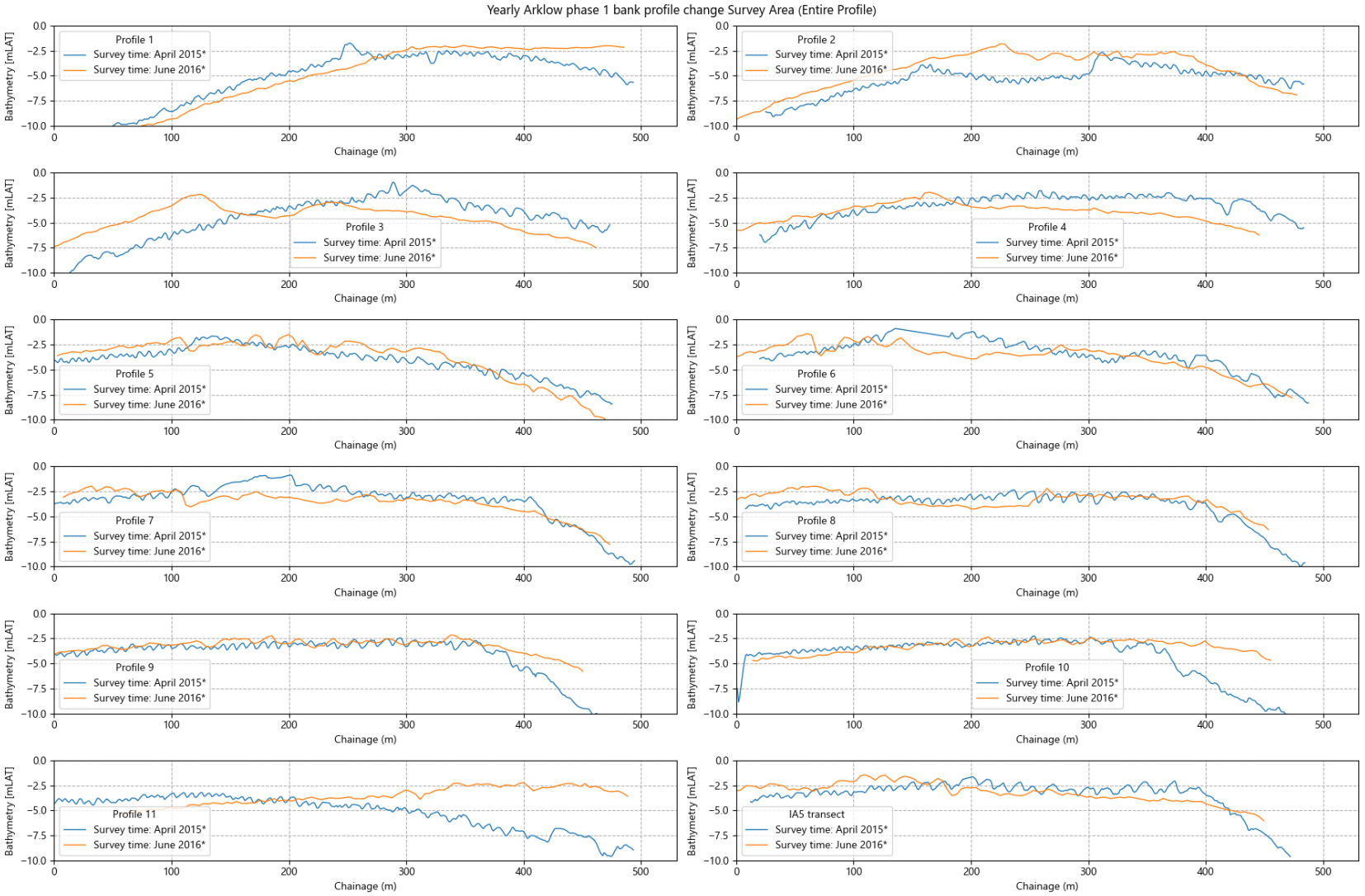


Figure 192. The 12 profiles extracted from the Phase 1 surveys over the period April 2015 and June 2016.

To assess the response of the bank over the long-term, the following datasets were inspected

- 2000 UKHO survey,
- 2016 Arklow bank survey,
- 2019 Arklow bank survey, and,
- 2020 repeat surveys (in IA1, IA2, and IA3).

* Considering the low resolution of the 2000 UKHO survey, profiles used for long-term assessment had to follow data points at which coverage from the 2000 survey exists and thus these profiles are not derived from a straight line.

The location of the profiles extracted coincident with IA1, IA2 and IA3 is presented on a map in Figure 193 to Figure 195, respectively. These data are presented in Figure 196 to Figure 198.

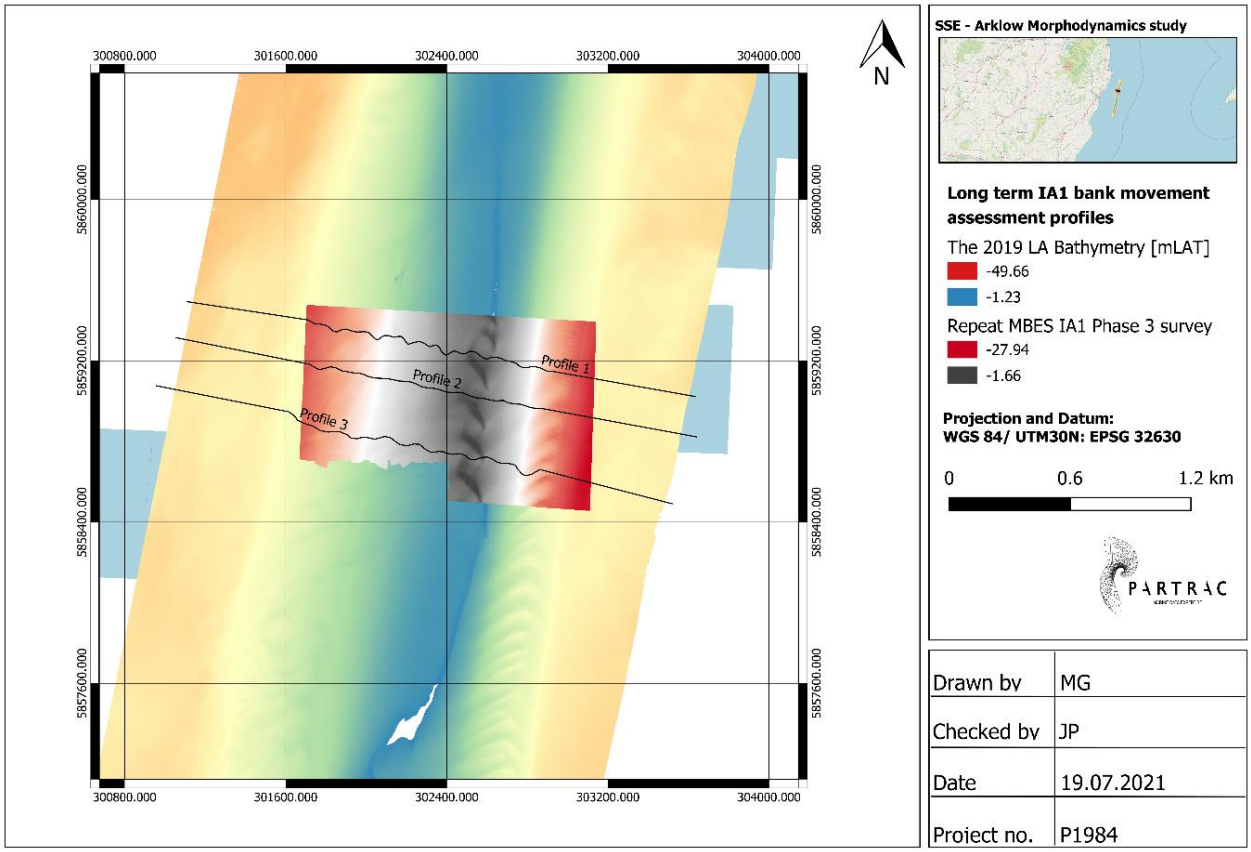


Figure 193. The profiles extracted coincident with IA1.

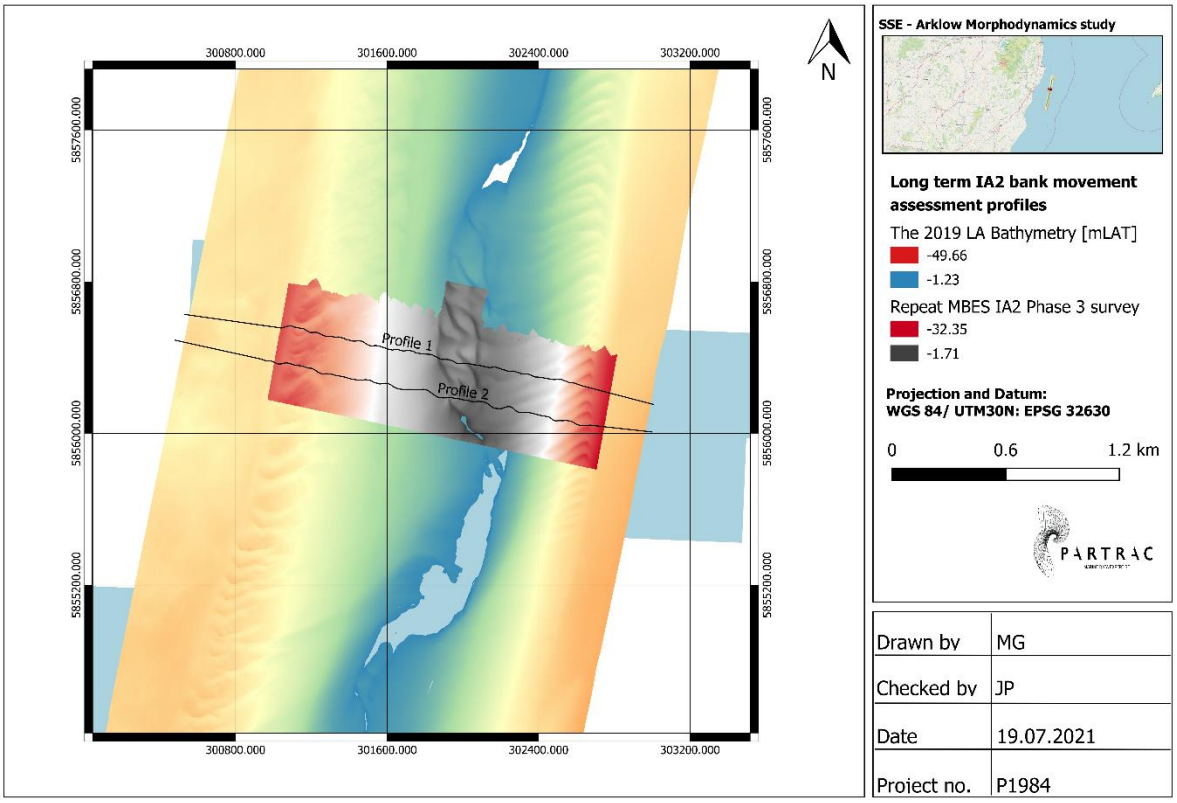


Figure 194. The profiles extracted coincident with IA2.

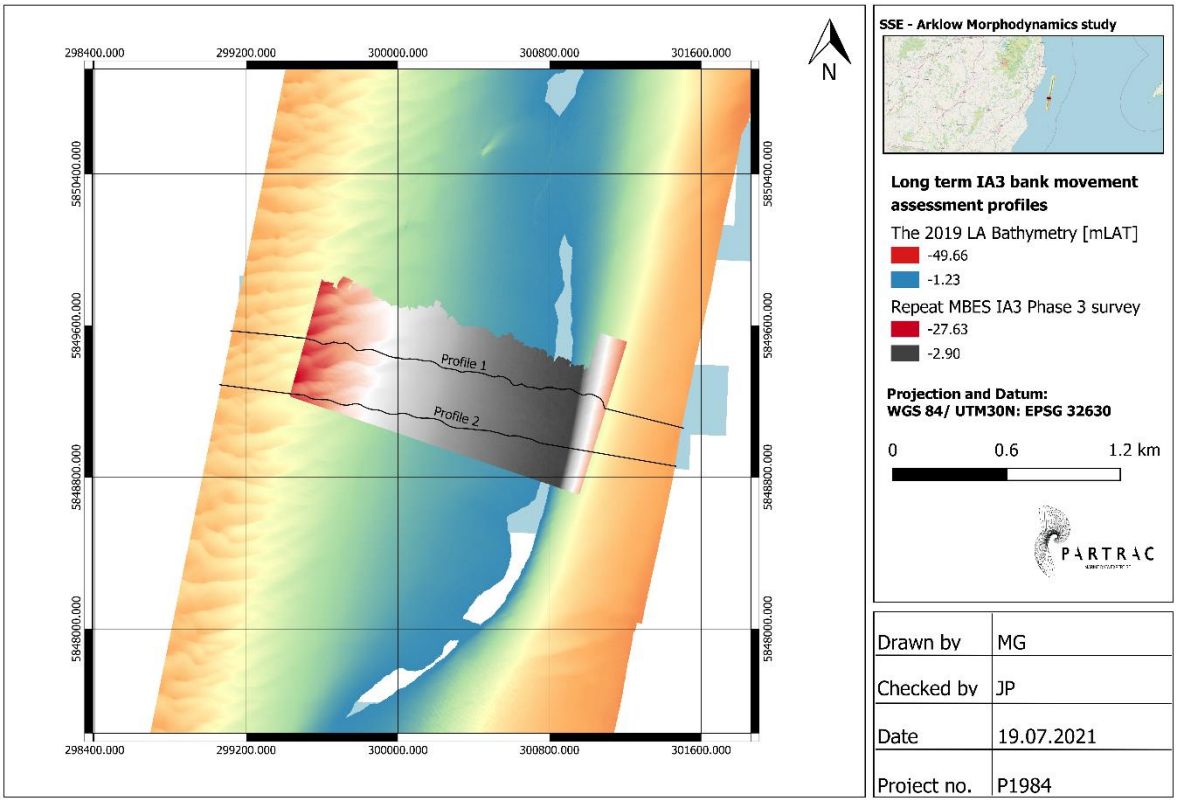


Figure 195. The profiles extracted coincident with IA3.

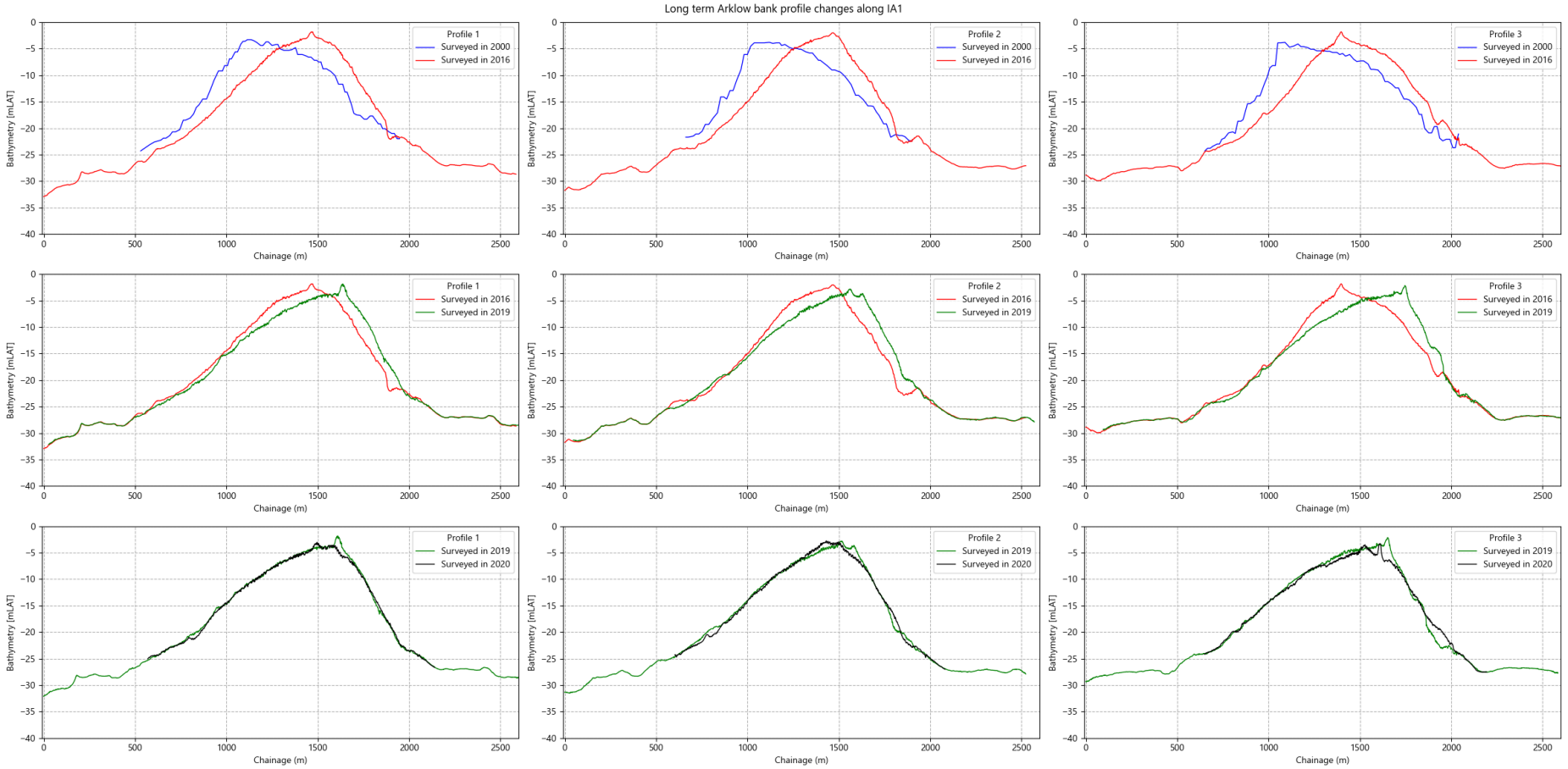


Figure 196. The three profiles extracted from areas of the bank coincident from IA1. The profiles compare data surveyed in 2000 and 2016 (top panel), 2016 and 2019 (centre panel) and 2019 and 2020 (bottom panel.

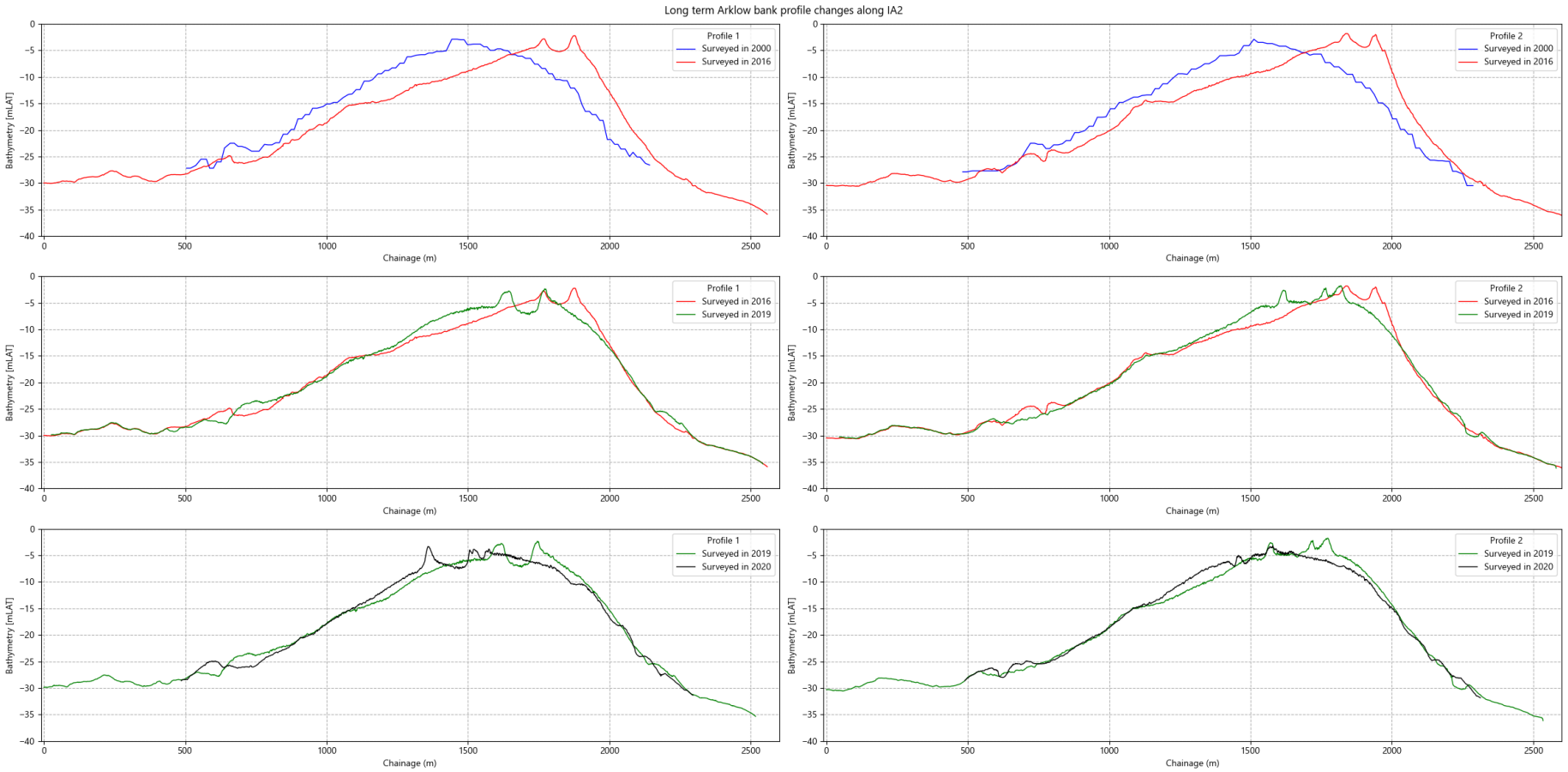


Figure 197. The two profiles extracted from areas of the bank coincident from IA2. The profiles compare data surveyed in 2000 and 2016 (top panel), 2016 and 2019 (centre panel) and 2019 and 2020 (bottom panel).

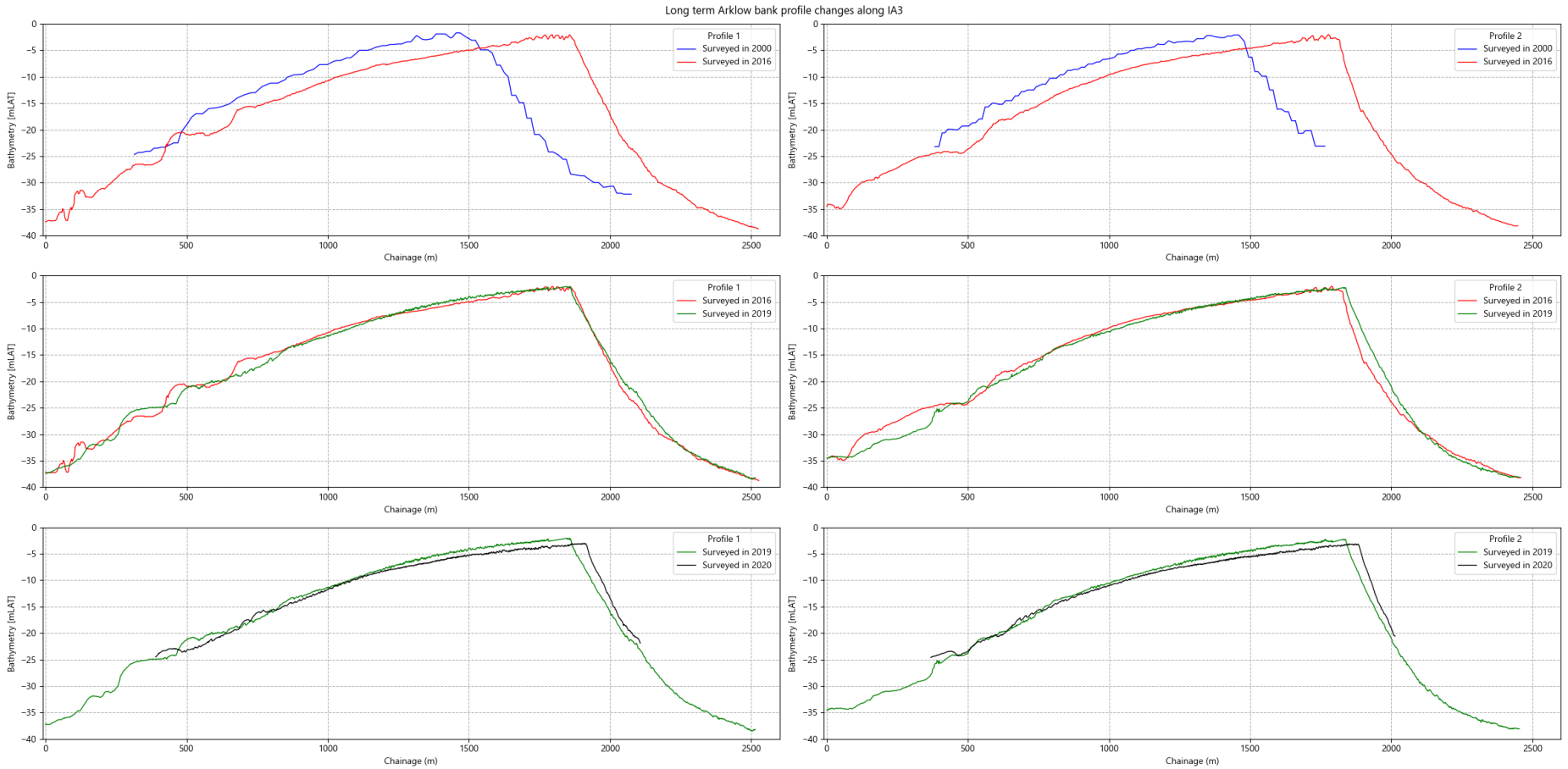


Figure 198. The two profiles extracted from areas of the bank coincident from IA2. The profiles compare data surveyed in 2000 and 2016 (top panel), 2016 and 2019 (centre panel) and 2019 and 2020 (bottom panel.

Away from the IA's surveyed in 2020, to assess long-term movement over the period 2000 to 2019, in total, 12 further profiles were assessed (Figure 199). These data are presented in Figure 200.

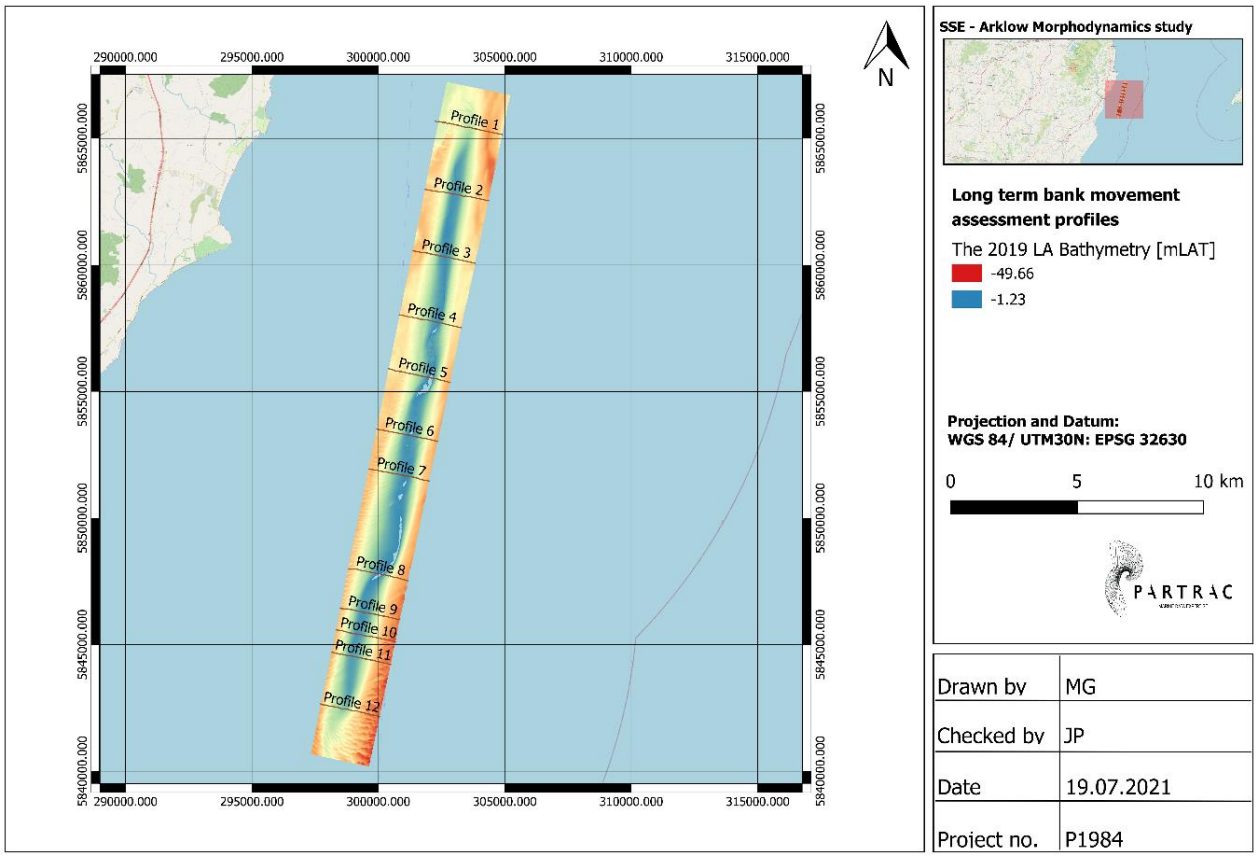


Figure 199. Profiles extracted along the length of Arklow Bank to consider movement of the bank over the period 2000 to 2019.

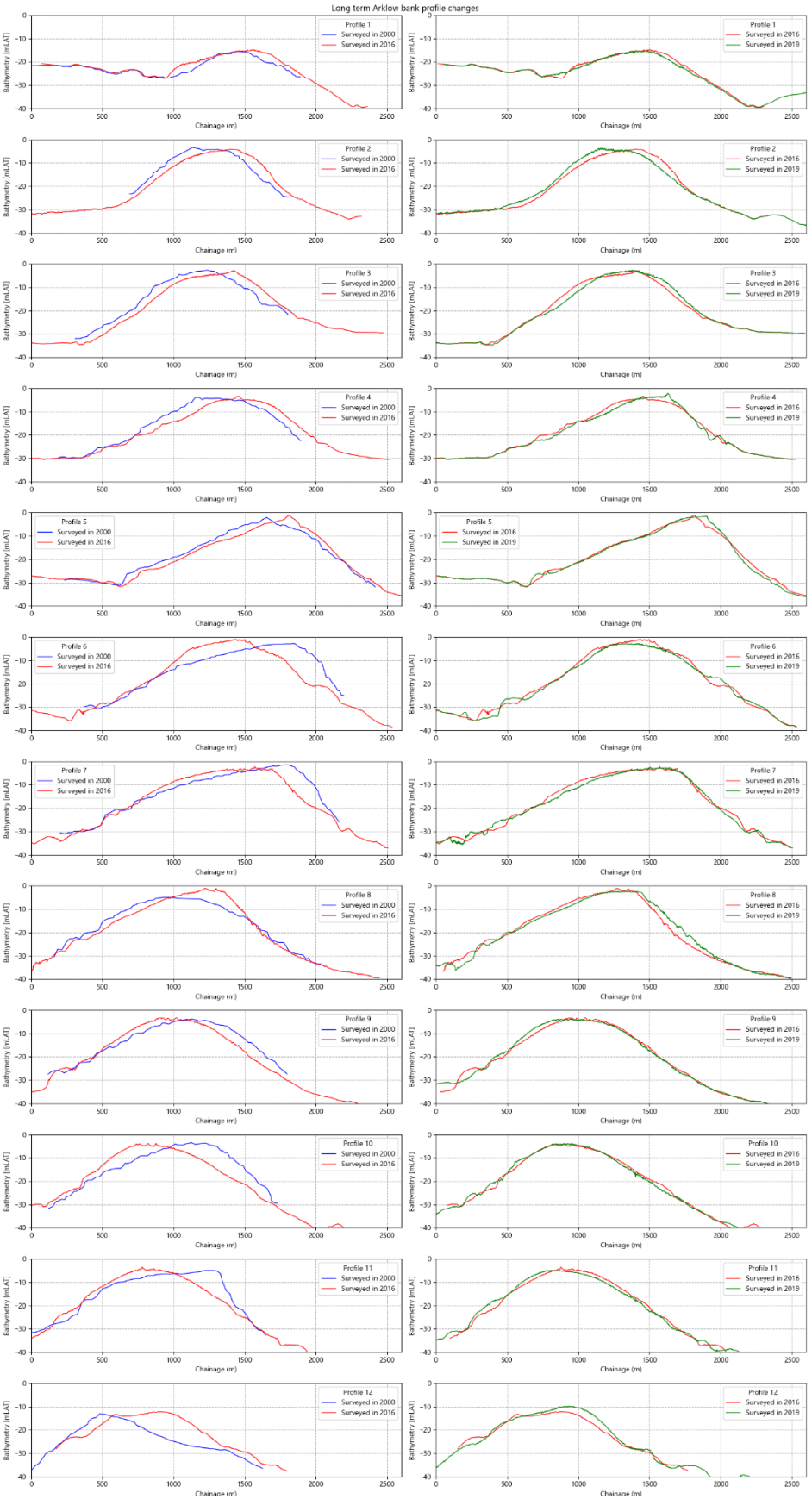


Figure 200. The profiles extracted along the length of the bank, comparing the data acquired in 2000 with those acquired in 2016 (left panel) and those acquired in 2016 and 2019 (right panel).

Longer term movement of the bank and resulting changes to the bank profile are summarised as follows:

- Between 2000 and 2016, within IA1 the crestline repositioned to the east across IA1 this resulted in lateral movement of the comparative position of the bank of up to ~70m below the -10 mLAT contour, and up to ~160 m above the -10 mLAT contour). The lateral movement of the bank eastwards continued between 2016 and 2019 with the bank above the -10 mLAT contour shifting by up to ~ 100 m, reducing to up to ~20 m below the - 10 mLAT contour (~20 m). A similar repositioning of the crestline and subsequent changes to the bank profile was observed in IA2 across this period.
- Although the bank's shape and profile changes through time in IA3, the magnitude of those vertical seabed changes is reduced when compared to those observed in IA1 and IA2, particularly between 2016 and 2019.
- Consideration of profiles outside the IA's showed that along profile 1 (to the north of the bank), the bank shows relatively negligible movement between 2000 to 2019.
- However, moving south along the bank, profiles 2, 3, 4 and 5 show greater movement in an eastward direction between 2000 and 2016, with the bank's - 10 mLAT contour line moving between approximately 70 m and 150 m during this period.
- The bank remained comparatively stable between 2000 and 2016 in profiles 6,7, and 8, whereas in profiles 9, 10, and 11 a repositioning of the crestline biased towards the west between the period from 2000 to 2019 was observed. The bank is observed to move east again along profile 12, but this movement of lower magnitude than that seen in the profiles extracted from locales to the north of the bank.

The foregoing data reveal the morphological response of the bank over the short, medium, and longer term and demonstrates how repositioning of the crestline through time has a potentially severe impact on local vertical bed level change. The greatest vertical change across the lease area occurs due to a repositioning of the crestline which alters the shape, and cross-sectional profile, of the bank. Second to this is the bed level change due to the movement of large-scale sandwave features along the flanks of the bank and at the head of the bank to the north and at the tail of the bank to the south. To the north of the bank, the E-W transects indicate that over the medium to the longer term, the relative position of the crestline, which on occasion comprises several crests likely associated with sandwaves in the shallowest regions of the bank, is biased towards the east, whereas the southern area is slightly more biased to the west. The results of processes occurring over the longer-term are not only the net effect of residual transport over the bank crest but also a function of the influence of waves (which is greater at the southern tail of the bank) and the opposing directions of tidal asymmetry driving circulation of sediments around the bank.

Changes to the bank shape through time can be further understood via a contour analysis. The relative position of the -10 m, -15 m and -20 m LAT contour within the data collected in the 2000, 2016 and 2019 datasets is plotted in Figure 201, Figure 202 and Figure 203, respectively. Variously, the -10 mLAT contour position extracted from the 2016 and

2019 dataset, at several locations along the bank moved to the east or west (but also extended to the south). This is further evidence corroborating the movement of the crestline and shallowest regions of the bank over the short, medium and long-term. This analysis shows that through time, the maximum change in the relative position of the -10 mLAT contour occurred in the southern section of the bank where the -10 mLAT contour moves position in an easterly direction by circa 300m between 2000-2016 increasing to circa 400m between 2000-2019 and in a southerly direction by ~960m between 2000-2016 increasing to ~1100 m between 2000-2019.

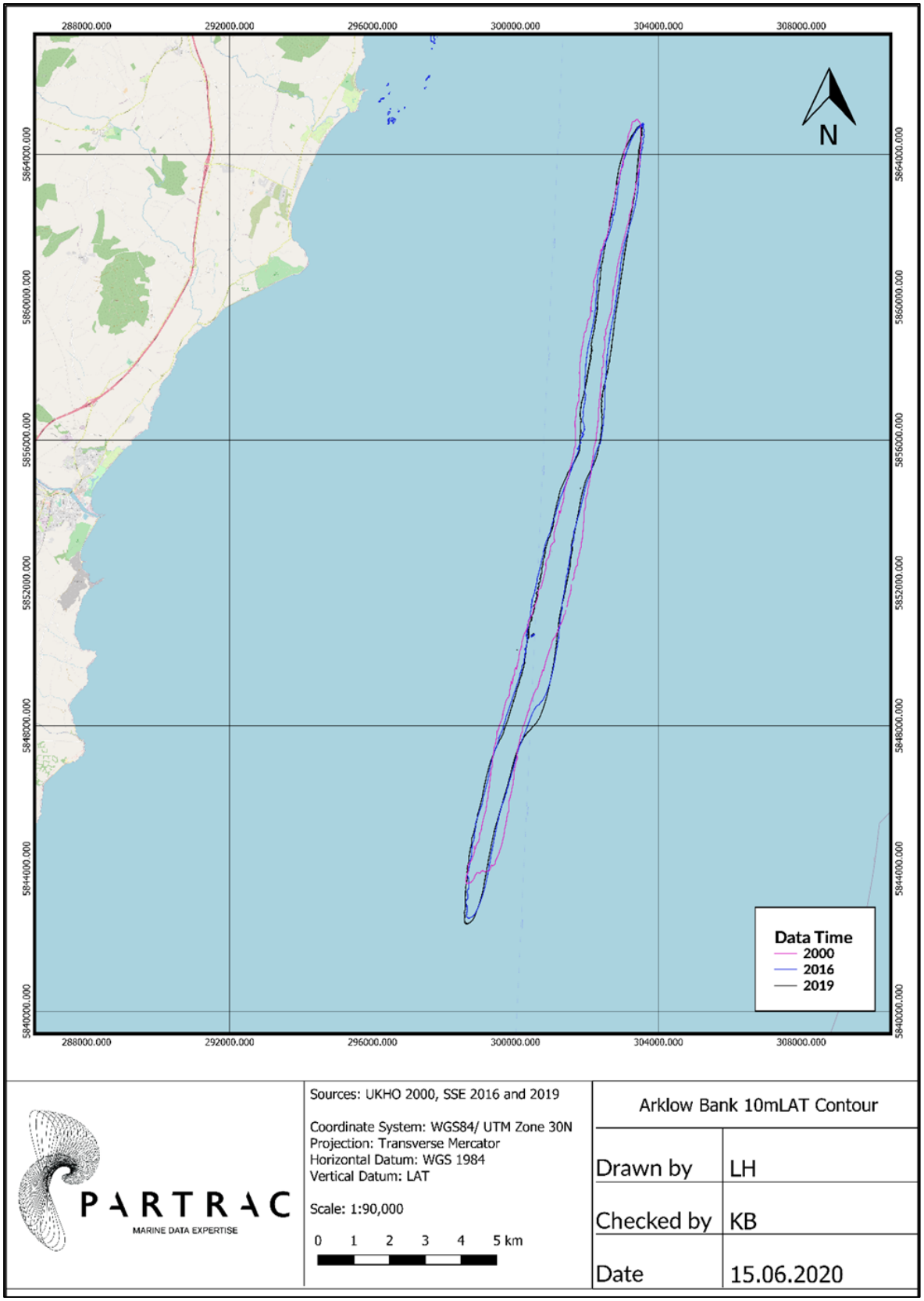


Figure 201. The -10 mLAT contour plotted from the 2000, 2016 and 2019 datasets.

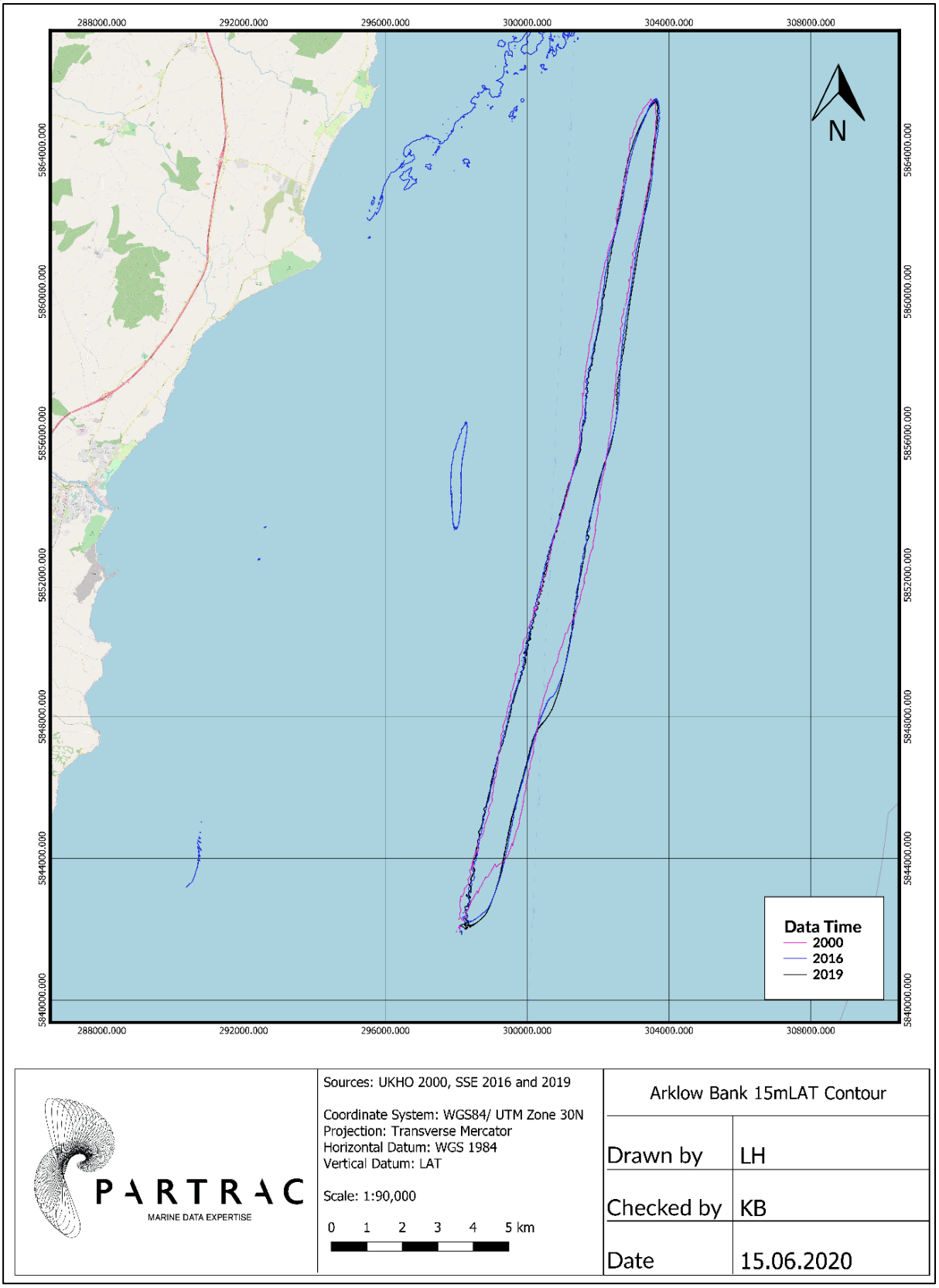


Figure 202. The – 15 mLAT contour plotted from the 2000, 2016 and 2019 datasets.

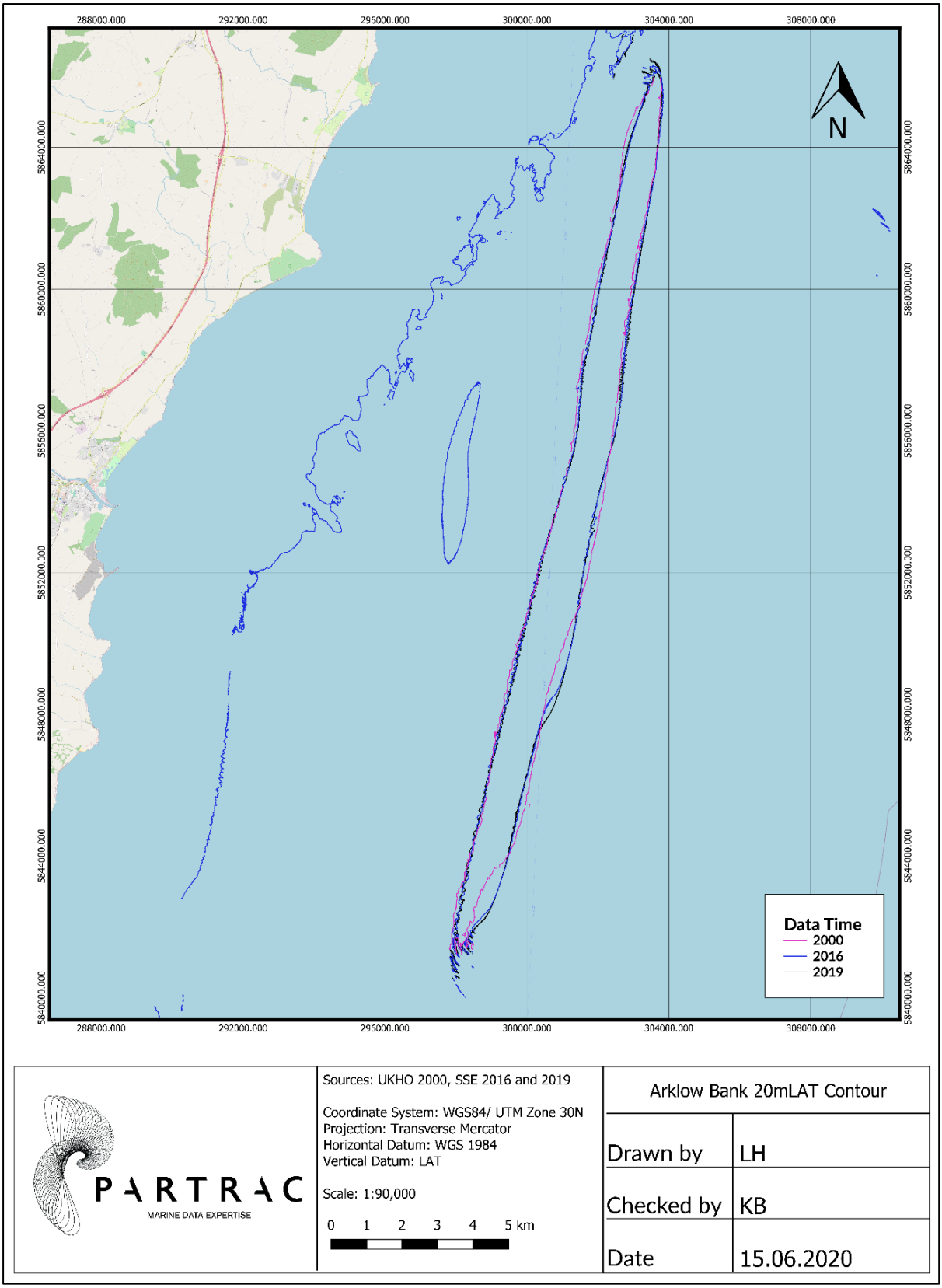


Figure 203. The -20 mLAT contour plotted on the 2000, 2016 and 2019 datasets.

To assess the movement of Seven Fathom Bank over the period 2011 to 2019, in total, 11 profiles were assessed (Figure 204). These data are presented in Figure 205 Note; available data is limited to the export cable routes.

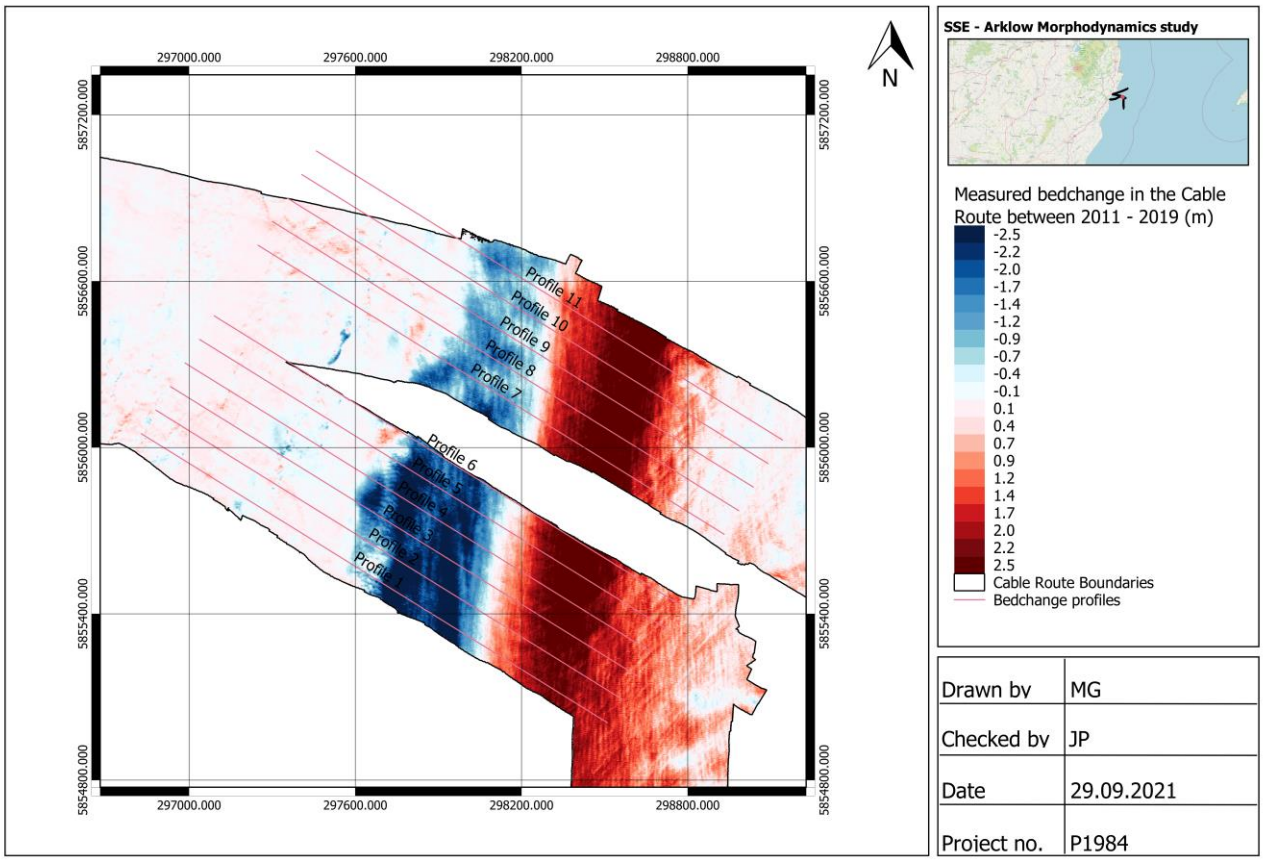


Figure 204. The observed bed level change over Seven Fathom Bank along the export cable route. The location of the profiles presented in Figure 205, is overlain.

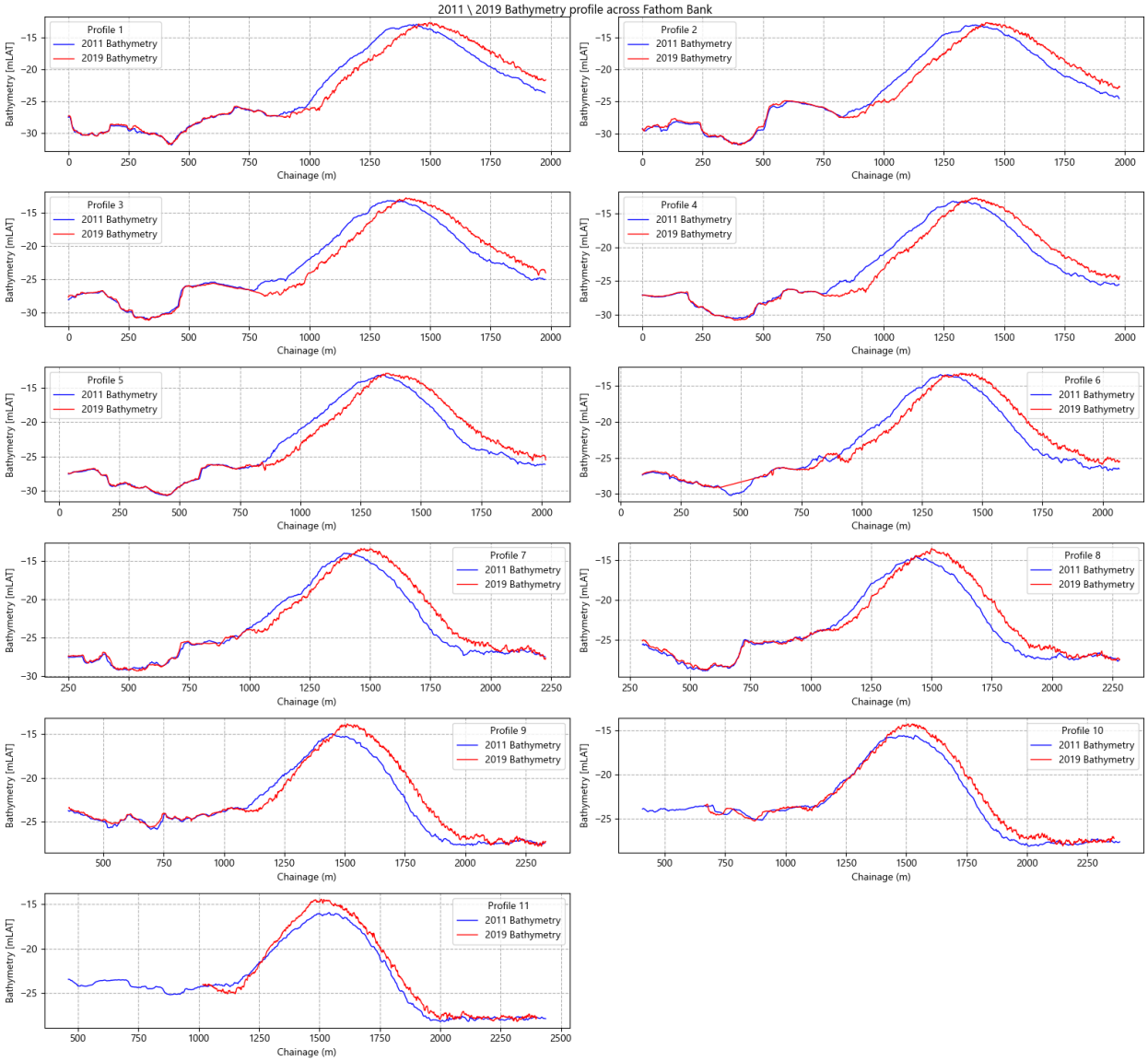


Figure 205. Data acquired in 2011 and 2019 along the export cable route in areas coincident with Seven Fathom Bank, presented in the form of cross section profiles.

Across the period 2011 to 2019, changes to the shape and profile of Seven Fathom Bank are summarised as follows:

- Between 2011 and 2019, in areas where coincident data is available (which is limited to the export cable route) the crestline repositioned to the east, and slightly shallowed (by circa 1 m).
- In the areas assessed, the eastward movement of the bank has had limited influence on the shape of the bank with the magnitude vertical seabed change between circa and 1 m to 3 m associated with the eastward movement of the bank.

The foregoing data reveal the morphological response of Seven Fathom bank between 2011 and 2019 is characterised by eastward movement. In an analogous fashion to Arklow Bank, the greatest vertical change across the lease area

occurs due to a repositioning of the crestline, driving change to the shape and profile of the bank flanks. Over this period, vertical bed level change is limited to circa 1 m to 3 m.

8.10 Conceptual Understanding of Processes Occurring at the Local Scale

Arklow Bank is maintained in dynamic equilibrium by the perpetual tidal processes, episodic wave processes, atmospheric (i.e. surge related) and Coriolis effects. These processes interact spatially (i.e. varying across the bank and with depth), and temporally (varying on timescales from a single tide through to decadal changes). The non-linear and complex processes that drives the evolution of such dynamic systems are typically characterized by multiple response pathways and subsequent system states. To estimate future seabed levels and determine the potential highest and lowest system states which may occur over the lifetime of the development, an integrated approach relying on a robust process understanding complemented by numerical modelling efforts, must be applied. This relies upon classifying, as accurately as possible, the response of the seabed and the bank features to the driving processes so as to establish a sufficiently detailed understanding to inform the application of numerical modelling to forecast potential changes to these features over the medium and long-term.

The knowledge derived from the assessment of the sedimentological, hydrodynamic and wave regimes at the local scale including for the detailed assessment of mobile bedforms and the response of the seabed through time, can be summarised as follows:

- Arklow Bank is classified as an Open Shelf Linear Bank. These bank types are characterised by a rotary circulation of sediments around the bank which is a function of the topography and orientation of the bank, differing residual tidal flow directions on either side of the bank (i.e. an ebb and flood dominance on the west and east side of the bank, respectively) and the Coriolis effect which drives sediment along the bank and onto the bank flank. The sandbank is 26 km in length, aligned north - north-east to south - south-west (at a bearing of 196^0 relative to true north). The width of the bank (as defined at the -20 m isobath) ranges from between 1.2 to 1.5 km.
- Arklow Bank is a broadly asymmetrical feature, in its present state with a slightly wider and more symmetrical profile in the north (1.5 km at the -30 m depth contour), and a narrower, and more asymmetrical, profile in the south (1.3 km at the -30 m contour). Steeper slopes are presently observed on the eastern (i.e. offshore) flank, compared to those on the western (i.e. inshore) flank (although the potential exists for this scenario to reverse over the lifetime of the development). The orientation of the bank is positioned at oblique angles to the peak tidal principal flow axis (Panigrahi *et al*, 2009). The bank is also offset by approximately 5^0 to 16^0 (in the anticlockwise direction) relative to the shoreline orientation. The bank itself divided into four sections, denoted 'northern region', 'central north', 'central south' and 'southern region'. These divisions broadly reflect

minor changes in the orientation of the bank. The defined regions across Arklow Bank (as observed in the 2019 bathymetric dataset) are described as follows:

- *Northern regions (bank head)*: In the northern regions Arklow Bank is characterized by a slightly wider, and more symmetrical profile. Sandwaves persist on both the east, and west, flanks. Sandwaves migrating around the head of the bank produce an elongated bank profile characterised by significant mobile features. The northern region of the bank is linked to the southern end of Wicklow Trough, which was influential during the formation of the bank, and in the modern era provides a transport pathway delivering sediment to the head of the bank.
- *Central north*: In the central north region, sandwaves persist on both the east, and west, flanks. In this region, the crestline, on occasion, shallows significantly and thus are susceptible to head difference effects. To the south of the region, the crestline is positioned to the west, beyond which the orientation of the bank shifts slightly in a clockwise direction where the crestline is re-positioned to the east. Where the crest is positioned to the west, sandwaves become more prominent along the east flank of the bank.
- *Central south*: In the central south region, in an analogous fashion to the central north region, sandwaves persist on both the east, and west, flanks. The crestline, on occasion, shallows significantly and thus are susceptible to head difference effects. To the south of the region, the crestline is positioned to the west, beyond which the orientation of the bank shifts slightly in a clockwise direction where the crestline is re-positioned to the east. Again, where the crest is positioned to the west, sandwaves are more prominent, along the east flank of the bank.
- *Southern regions (bank tail):* In the southern region of the bank, sandwaves persist on the both the east, and west, flanks but appear to be larger, and more prominent, on the east flank in this region. Sandwaves are migrating southward along the east flank forming a significant sandwave field to the south, and southeast, of the bank. At the southern tip of the bank (i.e. the tail of the bank) the orientation of these sandwaves changes from dominantly north to south along the east flank, towards a north-east to south-west axis at the southern tip of the bank. These features at the bank tail appear to dissipate into deeper water to the south of the bank. The tail of the bank is considered to be unconstrained in comparison to the north of the bank.

- Sediment transport from the north of Arklow Bank through Wicklow Trough is considered the primary source of sediment supply to the bank, although analysis of the sediment volume of the bank indicates that the bank is a semi-closed system. Despite the shoreline retreat observed between Arklow Harbour to Wicklow Head sediment inputs from the shoreline and from fluvial inputs (i.e. the Avoca river) are considered to be limited.
- Arklow Bank is in a location characterised by complex hydrodynamic processes (i.e. strong flow velocities despite a low tidal range, periods of double high water and wave exposure) due to its proximity to an amphidromic point, which, during spring tides is degenerate (i.e. located on land).

- The sediments across the lease area and export cable route are dominantly comprised of sand or gravelly or slightly gravelly sand. Along the export cable routes isolated areas of coarser sediment and glacial till exists.
- The orientation of the bank relative to the tidal flow axis, results in the east flank being more exposed to flow during the ebbing tide and the west flank being more exposed during the flooding tide. The tidal regime is also characterised by a flood and ebb dominance on either side of Arklow Bank driven by the tidal asymmetry, this drives net sediment transport (as evidenced by the net migration of sandwaves either side of the bank) southward on the east flank and northward on the west flank. The sediment transport regime is tidally dominated across all water depths. Across the lease area, these sediments are highly mobile. A mobile seabed often triggers a morphological response (i.e. an adjustment at the seabed) which can be manifested as a positive topographical change through time (via the formation of bedform features) or give rise to a general seabed lowering; each are dependent on the sediment supply to the area. Analysis indicates that surficial sediments are likely, even at water depths of circa -30 mLAT, to be mobilised on each tidal cycle i.e. Arklow Bank exists as a 'live bed' sediment transport regime. The mobility of sediments within the system is also evidenced by the formation of highly mobile, sandwaves and megaripples at the base of the bank, on the east and west flanks, at the northern head and southern tail of the bank, and on occasion, megaripples and small scale sandwaves occur within the shallowest regions on the crest of the bank (i.e. above the -10 mLAT contour).
- The bank is exposed to local sea waves and, infrequently, longer period swell waves. Swell waves, almost exclusively, approach the bank from the southern compass quadrants. Water depths at the bank crest shallow to 0.7 m relative to LAT, causing, on occasion, waves to break on the bank. Alongside breaking wave processes, processes akin to those occurring at the coastline likely occur across the shallowest regions of the bank. Wave orbital action is likely to suspend sediments, and in analogous fashion to the generation of longshore currents at the coastline, drive sediment along the bank crest. Furthermore, analogous processes to those observed in the swash zone (i.e. bed load, suspended load, sheet flow and single-phase flow) influences the sediment regime in the shallowest regions of the bank. These processes routinely act to sweep the shallowest regions of the bank of bedforms and as evidenced by the turbidity data, has the potential to sweep sediments off the bank crest. These episodic processes, in the shallowest regions of the bank, are a recurring feature within the sediment transport regime along the bank crest.
- Though waves have a significant influence on the sediment transport regime above the -10 mLAT contour, large waves, due to their infrequency, play a limited role in the wider sediment transport regime of the bank system and of the seabed between the bank and the coastline; this is evidenced by the turbidity data acquired during the metocean measurement campaign and complementary investigations conducted using the ABMS. The influence of waves on the sediment transport regime both in the lease area, and along the export cable routes, is limited both spatially and temporally, i.e. the influence of waves is limited to a short duration and only to the shallowest regions of Arklow Bank. Even during/following the largest storms the adjustment at the

seabed due to wave action (manifested within the shallowest regions of the bank by a lowering or flattening of the bank profile) is quickly re-established by the dominant tidal regime (i.e. smaller features superimposed on the crestline, once flattened or lowered, quickly re-build/re-form as mobile sediments are transported over the bank by the tide).

- Arklow Bank is a complex morphodynamic environment. It is comprised of different process environments, and across these environments different parts of the bank move at different rates (and directions) in response to different process influences and thus produce different individual effects which sum to produce an overall effect at the bank scale. Several authors have postulated about whether the full bank feature is migrating in position over the longer-term. A holistic view of all available data leads us to conclude that the bank (as a whole feature) is not migrating (i.e. there is no residual, long-term shift in location) *per se*. Residual flows over the crest, which are subject to changes in direction over time, drive a progressive shift of the bank in an easterly or westerly direction. However, this condition does not exist permanently, and any propensity for net bank movement is curtailed by the clockwise circulatory sediment transport around the base of the bank. In other words, whilst the bank itself displays changes in its profile, shape and elevation, the footprint of the sandbank on the seafloor remains ostensibly the same over extended timeframes due to a tidally modulated circulatory transport around the bank. This limiting position can be defined as the point at which the rate of accretion at the crestline is less than, or equal to, the (slope induced) rate of transport of sediment from the crestline to the base of the bank. If this condition is observed the crestline will not continue to move westward or eastward.
- The crest of Arklow Bank behaves in an analogous fashion to the crest of a large tidal sandwave. Predominantly, the upper part of the bank, including the crestline, moves both east and west, rather than migrating in a single direction. Cross-bank flows are caused by a head difference which occurs during the ebbing and flooding tide between the east and west of the bank (see Section 8.4) and arise as a result of the shallow nature of the crest region. The head difference creates a weir effect as water is held on one side of the bank, before 'flushing or surging' over the top. This effect is enhanced within the central regions of the bank, which is a function of the shape and profile of the bank. The water level head difference is a function of the direction of travel of the tidal wave (which is at an oblique angle to the orientation of the bank); atmospheric effects on water levels and local winds and the shallow topography of the bank itself. This transport pathway does not result in a progressive shift of the bank rather it results in movement of the upper regions of the bank and crestline from west to east or east to west. It is postulated that bank processes restrict how far the crestline can move either west or east. The net effects of residual transport at the crestline result in dominant transport over the crest of the bank in either east or west direction; where residual transport persists for an extended period, enhanced sediment supply to one side of the bank can contribute to the localised growth (and/or) decay of bedform which persist at the periphery of the bank to the east and west. Sandwaves are part of the overall bank forming process controlled by a set of distinctive process influences.

Where slope failure (temporarily) influence sandwaves at the base of the bank, the processes which drive transport in these regions rapidly transport sediments into another area of the bank system, resulting in the reformation of sandwave features.

- Above the -10 m contour, the shallowest regions of the bank and the crestline are characterised by the presence of ripple, megaripple and sandwave features. Seabed levels within the shallowest regions of the bank are maintained by persistent delivery of sediment from the flanks. Within the shallowest regions of the bank, the formation, migration, and growth of ripple, megaripple and small-scale sandwaves (which can lead to the development of multiple crestlines), results in persistent and transient, raising and lowering of seabed levels of between circa 1 m to 3 m. This is anticipated to continue over the lifetime of the development.
- Review of the 2000 data against the 2016 and 2019 data provides the best available data from which to consider the historic morphological response of the bank over the longer term. Review of these data show that, during this period, significant bed level change occurred due to the repositioning of parts of the bank with seabed levels lowering and rising by between 18 m and 25 m, respectively. The most severe vertical change was observed on the east flank (particularly the southeast flank) which is a function of the steep slopes on the east of the bank meaning a relatively small lateral shift of part of the bank results in significant vertical change down to, and beyond, the -20 mLAT contour. The slopes on the east flank resemble the lee slope of asymmetrical sandwaves which are often characterised by steep slope gradients which, only in isolated locations, exceed the angle of repose (i.e. suffer slope failure).
- Spatial plots of observed bed level change during the period 2016 to 2019, show significant, mobile, sandwaves persist on the western and eastern flanks and at the head of the bank to the north and the tail of the bank to the south. Asymmetry in tidal flows either side of the bank result in net migration of sandwaves to the north on the west flank and the south on the east flank driven by the flood / ebb dominance observed on the west and east flanks, respectively. During this period, the magnitude of bed level change across the bank is broadly consistent. Away from the large-scale features which surround the bank, and the highly mobile, shallow regions associated with the crestline, vertical change ranges from a lowering (i.e. erosion) of the seabed of circa. 1 - 3m and a rising seabed level (i.e. accretion) of circa. 1 – 2 m. In the areas characterised by large scale sandwaves up to 6 m vertical change is observed. At isolated points towards the central regions of the bank significant accretion is observed associated with the repositioning of the crestline, and local wave-tide influence. Comparing the high-resolution bathymetric datasets (i.e. data collected in 2016 and 2019) shows the crestline is mobile, repositioning parts of the top of the bank. The top of the bank, and the crestline, form the shallowest regions of the bank and are characterised by the presence of megaripple and sandwave features. The top of the bank and the crestline is postulated to be an area of sediment convergence; highly influenced by shallow water processes which continually act to modify the shape of the crestline and the profile of the shallowest regions of bank.

- The targeted, repeat bathymetry surveys conducted in 2020, provided study-critical data at strategic sections of the bank with which to calibrate the sediment transport model over the short-term, and further process understanding. Across this period (up to 6 weeks in the summer of 2020), in the areas on the bank surveyed, the net vertical change ranges between a lowering of the seabed (i.e. erosion) of up to 1.6 m and a rising of the seabed (i.e. accretion) of up to 3.5 m. These data also:
    - Provided further corroborating evidence of the scale of vertical change due to the movement of the large-scale sandwave features at the periphery of the bank. Note: the scale of vertical change reflects the amplitude (trough to crest) of these features.
    - Improved our understanding of the processes occurring in the most mobile shallowest regions of the bank providing tangible evidence of wave and tidal influence across the lease area (i.e. wave action flattens the bank profile, whereas tidal processes nourish the crestline and the shallowest regions of the bank).

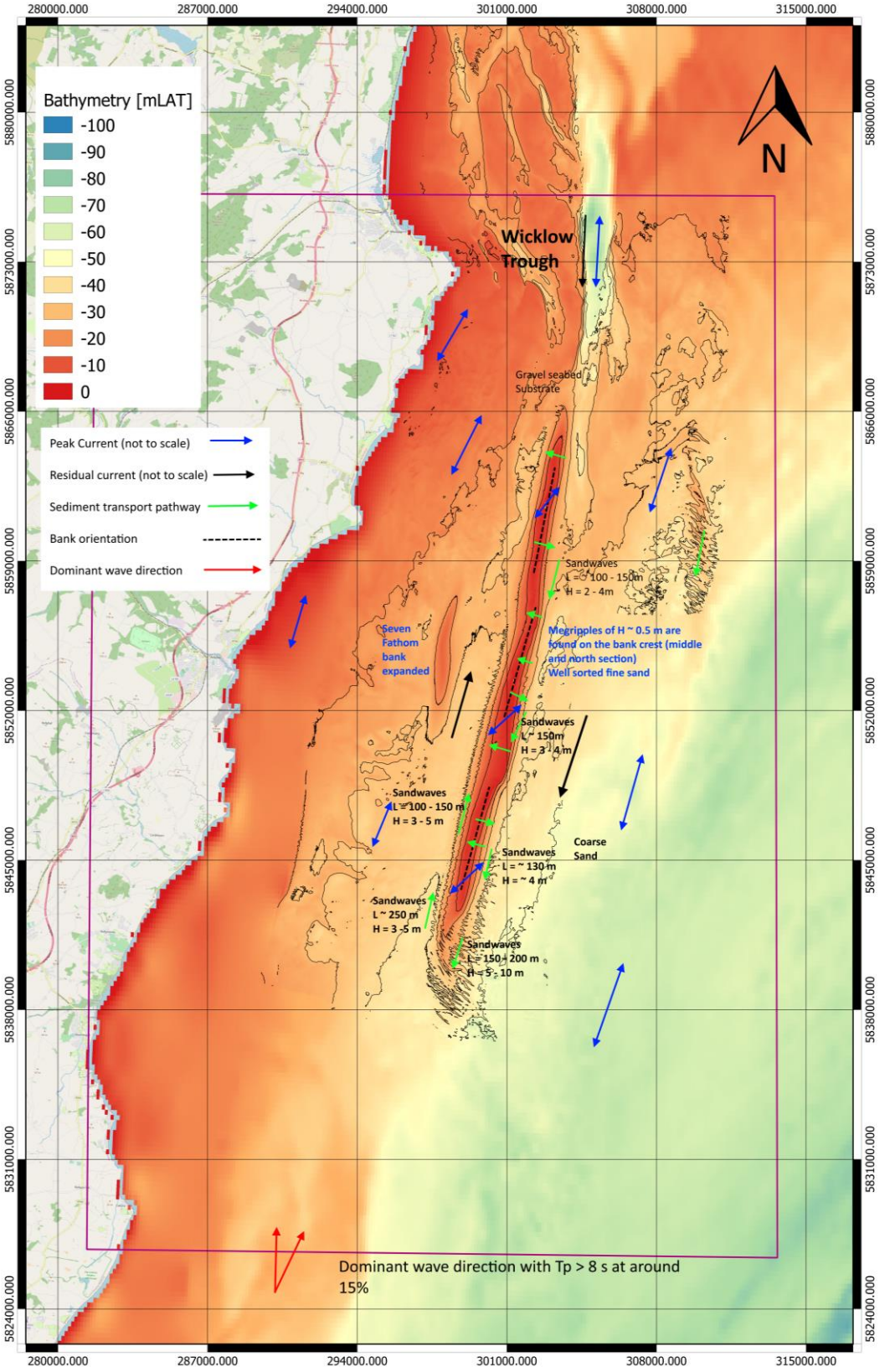


Figure 206. The conceptual site model at the local scale.

9 Predicting Future Seabed Levels

Seabed behaviour is the result of several processes which act, and interact, on a variety of space and time scales. Obtaining a detailed spatiotemporal understanding of potential seabed level variability relies upon the consideration of a range of information as well as a combination of suitable methods of analysis. Numerical modelling is a useful tool to aid and extend our understanding, particularly for forecasting change from observed conditions (e.g. Zanuttigh, 2007; and Brown and Davies, 2009). Coastal area morphodynamic models are used to predict short-term (days to months) bathymetric changes to address specific engineering challenges (Nicholson, *et al* 1997). Typically, numerical schemes focus on two-dimensional, depth-averaged approaches (e.g. Wang *et al*., 1992; Sato *et al*., 1995; Price *et al*., 1995), which provide a strong basis for performing detailed simulations of morphological evolution (i.e. to assess seabed level change through time) and have been proven to provide robust results during application over shorter time scales (e.g. Broker *et al*. 2007, Dronen and Deigaard, 2007). Approaches typically rely on commercially available modelling packages focused on the constituent physical processes (waves, currents, sediment transport), and rely on a feedback loop where the updated bed topography is applied into the hydrodynamic and sediment transport computations (this is a methodological necessity for more dynamic seabed environments). One of the key considerations in usefully applying such models for predictive purposes, is that good quality datasets are available. Within any analysis, numerical modelling tools perform poorly, when used with disparate or sparse datasets. Present data limitations have been discussed previously (see Section 3.3), and thus assumptions have been made to further the modelling exercise at this stage of the project (e.g. in regard to the grain size distribution of sediments which comprise the bank).

The best available evidence from which to assess the likely future response of the seabed is via the review and interrogation of the available bathymetric data, to understand the historic response of the seabed under the prevailing regimes. These data reveal that the greatest, and likely most persistent, observed changes to the seabed level across the lease area occur due to the east-west repositioning of the crestline driving changes to the bank profile. Second to this are the transient observed seabed level changes associated with mobile bedforms which form around most of the bank's perimeter. It is widely accepted that, at the bank scale, large scale bathymetric patterns will stay broadly similar over the longer-term (Hanna & Cooper (2002)., Schmitt. (2006)), and thus movement of the crestline does not result in migration of the bank over the longer term. This is evidenced by the fact that the bank, which is maintained in dynamic equilibrium with its surroundings, has maintained its overall position for at least a century according to historic Admiralty charts. Although the position of the bank is anticipated to broadly stay the same over the lifetime of the development, the dynamics of the sandbank are complex, and the sea region is unusual insofar as there is an (occasionally degenerate) amphidrome nearby, and yet tidal currents are comparatively strong, and the bank crest is exceptionally shallow. This results in the sediments which comprise the bank persisting in a 'live bed' regime. Investigations revealed that residual cross-bank flows drive the net movement of the bank (to the east and west), with

subtle imbalances in sediment transport over the crestline over the short, medium, and long-term, resulting in shifts of the crestline position to the east, and west, behaviour which appears to be analogous to that of a migrating large tidal sandwave, albeit occurring over longer periods of time.

Throughout the assessment, our understanding of the hydro-sedimentary processes which underpin the prevailing sediment transport regime across the lease area, and proposed export cable routes, has evolved. This understanding has informed the development, configuration, and application of the coupled hydrodynamic, wave and sediment transport model to provide outputs suitable to inform decision-making during design. This chapter describes the methodology for predicting future seabed levels. The morphological simulations performed, and the approach adopted, and the associated confidence limits with those predictions are detailed. By comparing the predicted bathymetries to the 2019 bathymetry the predicted magnitude of seabed level change is quantified.

To estimate the highest and lowest seabed levels which are likely to occur over the lifetime of the development a targeted modelling exercise was performed; following which the outputs were combined with those from the supporting data led analysis and moderated within the framework of the local scale CSM. At this stage, we have determined and provided the following estimated seabed levels as part of a complementary data package:

- The estimated Highest Seabed Level (HSBL); and,
- The estimated Lowest Seabed Level (LSBL).

The HSBL and LSBL demonstrate the potential envelope of seabed level variation we might expect to see over the lifetime of the development. These estimates are presented within the bounds of associated confidence limits. The schematic in Figure 207 shows the approach adopted to determine future seabed levels across the ABWP development area.

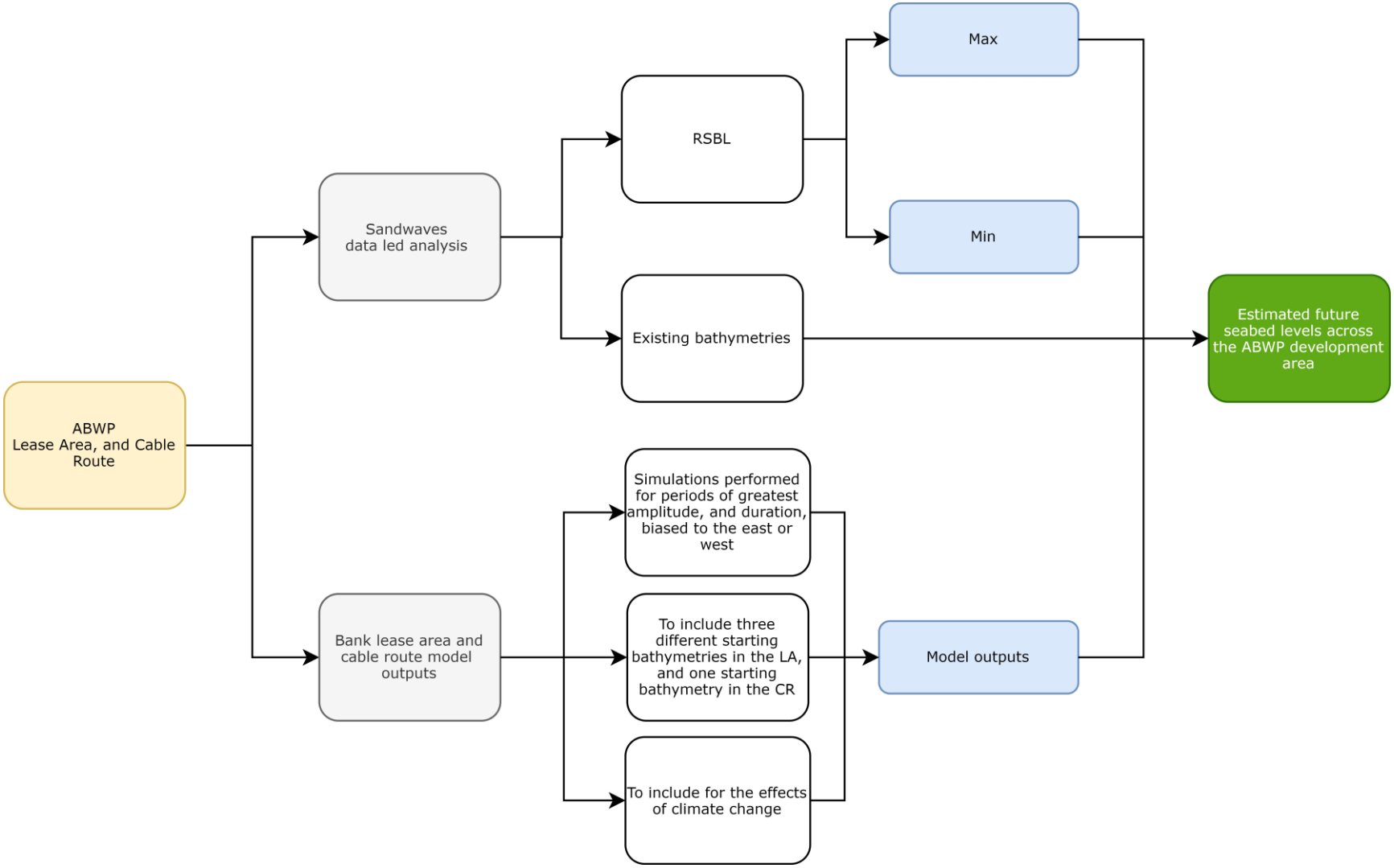


Figure 207. Flow chart showing approach adopted for determining future seabed levels for the different process environments across the development area.

9.1 Model Development

To support predictions of change at the seabed, a two-dimensional (and thus depth-averaged) coupled hydrodynamic / sediment transport (morphology) model of the seabed was developed utilising MIKE21 software (created by the Danish Hydraulic Institute [DHI]). The MIKE software is a proven commercial modelling package for use within coastal and marine engineering projects. The MIKE toolboxes '*Sediments*' and '*Morphology*', were utilised to assess sediment transport and morphological change across the site.

The development, setup and validation of the hydrodynamic and wave models and the sensitivity testing of the sediment transport model is described in detail in Appendix G, and MetOceanWorks Ltd (2021). The framework followed as part of the setup of the sediment transport model is detailed in Table 18.

Table 18. The framework for development of the sediment transport model.

Task	Notes
Implementation of Bathymetric Data	A composite bathymetry covering the ABWP lease area and export cable route was utilised across the model domain (described in detail in Appendix F). The three available bathymetry datasets across Arklow Bank, being data acquired in 2000, 2016 and 2019 were all individually merged and implemented within the model domain to enable simulations to be performed which utilised the available bathymetric data as the starting bathymetry for those model runs.
Grid-Size Generator	Different grid-sizes were tested for model convergence. The grid size forms a trade-off between the resolution of the model and the computing (and processing) time required. Based on these tests and the requirements of the study, the optimal configuration (grid size) is chosen and implemented within the model simulations (see Appendix G).
Model Tuning Parameters (Sensitivity Testing)	The influence on sediment transport of extremes of different sets of varied parameters, including the bed roughness, sediment grain size and driving conditions, were assessed through the process of validation. This key methodological step provides an initial check on how sensitive the output of the model is to each input (or tuning) parameter, enabling the configuration of the model to be optimised.
Determination of Simulation Blocks / Driving Conditions	Running long-term (i.e. several years to decades) simulations of sediment transport is not recommended due to the potential for 'compound errors' to occur, and the computational resources required to run such simulations. There are two available approaches to obviate the need for running long-term simulations: (i) inclusion of a speed up factor or (ii) dividing the period of interest into short-term blocks based on an analysis of the model hindcast record. In this study, we utilised a speed up factor because it allows the processes which form the primary drivers of morphological change across the development area to be assessed.
Model Verification (Performance Checking)	The ability of the model to predict the magnitude of vertical bed level change over various time periods across the ABWP development area were tested, and verified, against survey data. The performance of the model in terms of replicating the observed vertical bed level change over these periods is described in detail in Section 9.3.
Model Outputs:	Estimated future seabed levels and corresponding potential vertical bed level change which may occur across the lifetime of the development are presented in this report. The data is also provided separately as part of a data package in ASCII (.xyz) format. The predicted bed level is provided in the form of the lowest seabed level (LSBL) and the highest seabed level (HSBL).

Task	Notes
Further Analyses of Site Data	To support the morphodynamic analysis, the geological, geophysical, and hydrodynamic analyses are reviewed to ensure that all relevant physical processes and data not directly represented by the model are accounted or moderated for. In particular, the characteristics, and potential future evolution, of sub-grid scale bedforms.
Quantifying Confidence Limits for Predictions	Although MIKE21 is a powerful tool to assist in the study, and prediction of future site morphodynamics, the coefficients in the model rely on assumptions and simplify complex physical processes and interactions. The limitations of the model are discussed further in Section 9.3, where the confidence limits which should be applied to all predictions are detailed. Note: no additional tolerances for design purposes were applied to the data.

9.2 Model Setup: Morphological Reduction Technique

Due to the timescale constraints of a commercial project, simulating long periods of time using a high-resolution morphological model is not practicable. Therefore, a reduction technique has been employed, in combination with a morphological speed-up factor[30], to enable long periods of time (e.g., up to sixteen years) to be simulated, using shorter model runs (e.g. of between three and six months). To apply this technique, the long-term bias in sediment transport over the crest of the bank between the survey periods (2000 to 2016, and 2016 to 2019) was assessed. To obviate for short term effects in the bias, a running mean period was applied that was one third of the length of the period under consideration. For instance, for the 2000 to 2016 period, we apply a running mean period of 5.3 years (Figure 208). Subsequently six-month periods of sediment transport bias from the metocean hindcast were examined and plotted using a two-month running mean period (i.e., one third of the length of the period under consideration) (Figure 209). From this assessment the period that most closely resembled the observed behaviour in terms of sediment transport bias between 2000 and 2016, was selected[31].

As the results of model sensitivity testing presented in Figure 369 in Appendix G, and the foregoing analysis, shows waves, though capable of modifying the shallowest regions of the bank over the short-term (i.e. at the event scale), over the longer-term the system is tidally dominant, with tidal flows driving the long-term morphological response of the bank. Thus, it was concluded that the effects of storm waves did not need to be included in the long-term morphological simulations, as their influence on net sediment processes over these durations were limited. Finally, the model was run in morphological updating mode, meaning that the sediment transport model provides changes to the bed elevation at each time-step, and these are fed back to the hydrodynamic model, such that a feedback loop between morphodynamics and hydrodynamics was created.

30 A morphological speed-up factor is a simple multiplier used in the model setup, which multiplies the amount of bed level change in each timestep by a constant value. For instance, if a morphological speedup factor of 10 is selected, if each timestep of a one-month sediment transport simulation predicts a bed level increase of 1 mm, then the 'speeded up' model gives an increase of 10 mm at each timestep. This would allow a one-month period to be used to simulate an actual period of 10 months.

31 Applying this method for the validation run, the period selected to simulate the morphological change between 2000 and 2016 was 18 April to 18 October 2011, utilising a morphological speedup factor of 32.1. For the validation period 2016 to 2019, the period used to simulate the morphological change between 2016 and 2019 was 4 October to 7 December 1984, utilising a morphological speedup factor of 17.9.

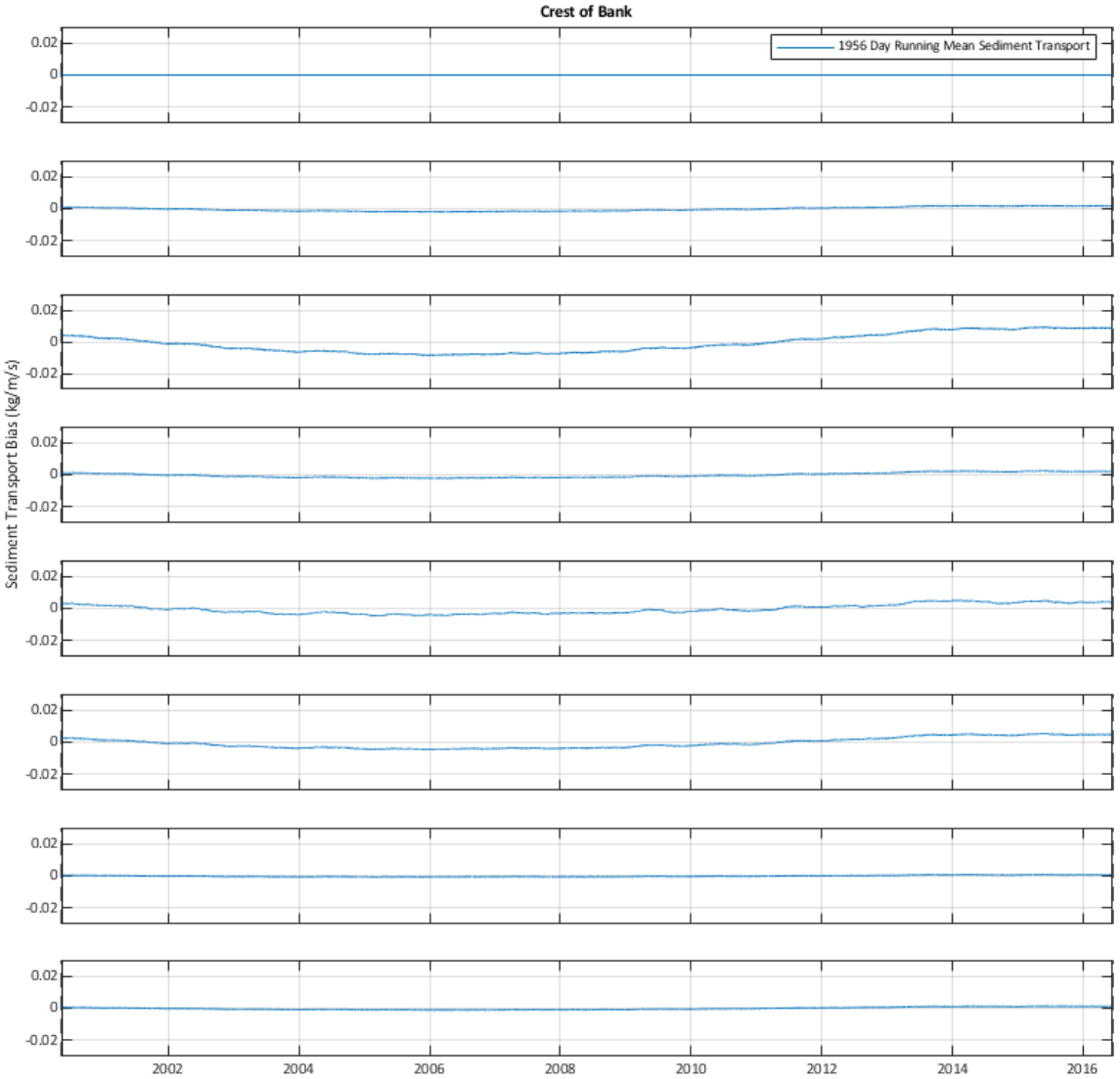


Figure 208. 5.3 year running mean sediment transport normal to the bank for eight positions along the bank crest (top to bottom, north to south).

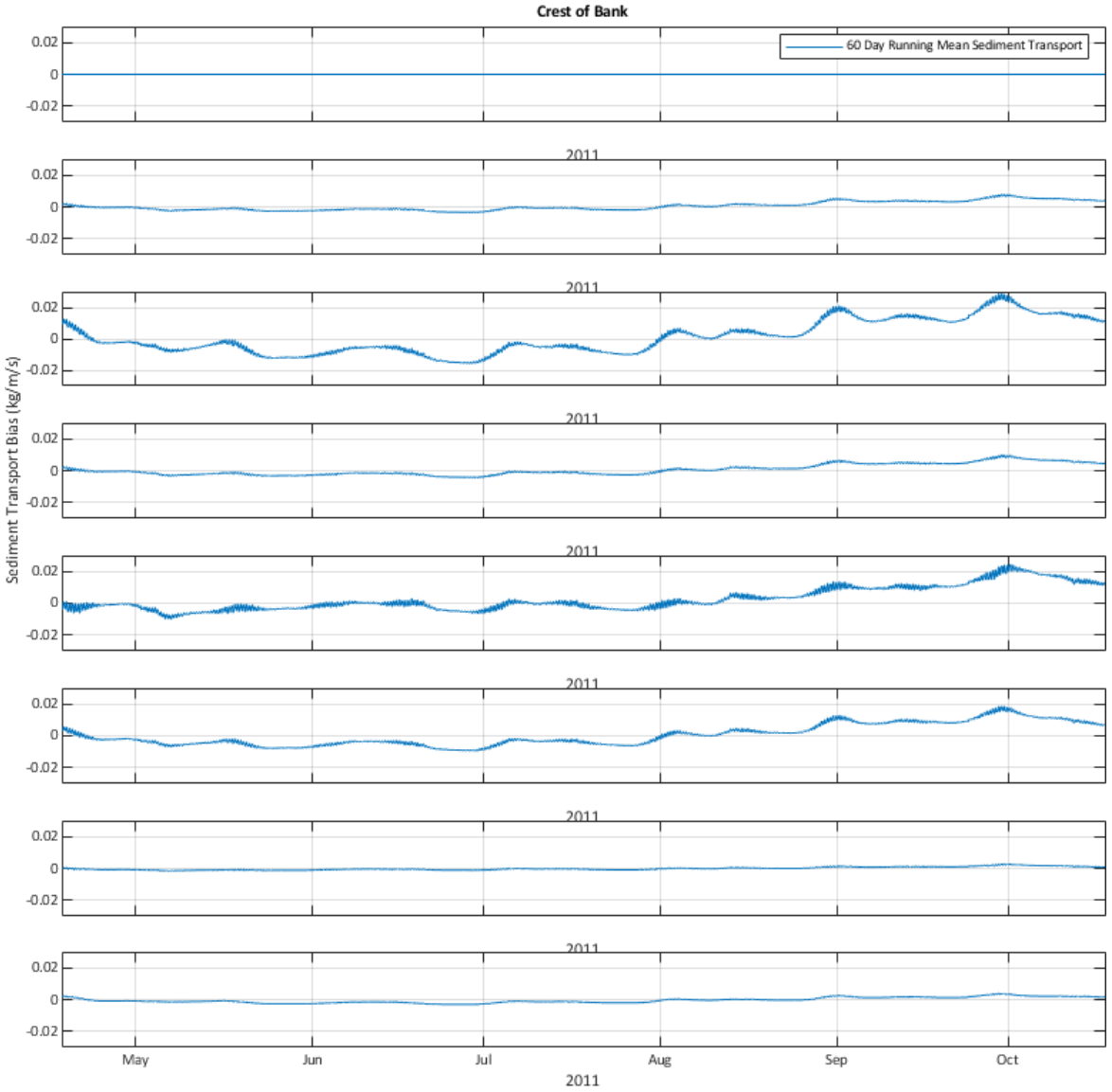


Figure 209. 60 day running mean sediment transport normal to the bank for eight positions along the bank crest (top to bottom, north to south).

9.3 Model Performance During Validation

Three pairs of bathymetric survey data exist which provide the best available information to determine observed historic vertical bed level change. Across the lease area and along the export cable routes determination of the bed level change between the datasets acquired in 2000 and 2016, and 2016 and 2019 and 2011 and 2019, respectively, were used to verify the predictive capability of the applied methodology. This step facilitates assessment of the confidence associated with model outputs.

One concept testing, and three validation scenarios, were tested using the available measured bathymetry data. These were:

- Concept testing using the 2020 repeat bathymetry surveys;

- Validation over the period 2000 to 2016 across the lease area;
- Validation over the period 2016 to 2019 across the lease area, and,
- Validation over the period 2011 to 2019 along the export cable route.

During validation, the sediment transport model was set-up using the driving models (i.e. the wave and hydrodynamic model) as input, along with all available information on sub-seabed and surficial sedimentological conditions within the model domain. Results of concept testing were compared against the existing geophysical and geotechnical evidence and repeat bathymetry data collected during the summer of 2020. This survey campaign was specifically designed to provide information on the short-term changes in bed level that occurred over discrete, defined areas of the bank (termed Investigation Areas, 'IA's'). To enable comparison, model predictions were generated over the period of the 2020 surveys[32]. To generate these data a hindcast record was developed for the coincident period, which was then applied as the driving conditions for the sediment transport simulation. The sediment transport model was then tuned to, as best as possible, correctly represent the short-term processes happening over the circa 4 – 6-week interval between the repeat bathymetry surveys. Model validation focused on the ability of the model to represent changes in bathymetry observed over the periods between the available surveys of the lease area, namely 2000 to 2016, 2016 to 2019 and for the cable route, namely 2011 to 2019. As these periods require longer run times, a reduction technique (described in Section 9.2) was applied to determine suitable driving conditions for each simulation. These conditions were then used as the driving input in conjunction with a morphological speed-up factor.

Through the process of concept testing and validation, tuning parameters that were applied included:

- Assessment of different driving conditions (including simulations with and without waves) and varying morphological speed-up factors;
- A spatially varying sediment grain size; and,
- Tuning of the bed roughness coefficient.

At the culmination of the validation exercise, estimated seabed levels produced were then interrogated to assess the capability of the model, and the approach adopted, to replicate the observed (measured) changes to the seabed during the elapsed time. The performance of the morphological model can be judged by assessing its' accuracy, and skill (Sutherland *et al*., 2004):

- *Model Accuracy*: A measure of the average size of the difference between a set of predictions and the corresponding observations (i.e. the Root Mean Square Error [RMSE]).

32 As these simulations were run over a relatively short period the use of a morphological speed-up factor was not required. It was not possible to implement the first available survey dataset from the 2020 campaign as the starting bathymetries for each model run, since vertical differences that may have occurred across the bank in the period between the 2019 survey and the start of the 2020 campaign, would result in vertical discontinuities at the edges of each of the areas surveyed. As such, the simulations were run using the 2019 bathymetry dataset.

- *Model skill*: A non-dimensional measure of the accuracy of a prediction relative to the accuracy of a baseline prediction (e.g. consideration of the accuracy of a prediction relative to the uncertainty of the bathymetric survey data).

Both spatially and temporally (considering the different elapsed time periods over which model performance has been assessed), direct statistical comparison of predicted and observed seabed levels has been performed to support robust assessment of model performance. These data are presented for the lease area and export cable route separately. Figure 210 and Figure 211 present spatial and cross-section profiles showing the predicted (modelled) bed level change across the lease area between 2016 and 2019. Figure 213 and Figure 214 present spatial and cross-section profiles showing the predicted (modelled) bed level change across the lease area between 2000 and 2016. Figure 216 and Figure 218 show these plots for the cable route between 2011 and 2019. Figure 212, Figure 215, and Figure 217 present Quantile Quantile, and scatter plots, showing the predicted vs observed bed level change within the lease area and export cable routes between 2016 and 2019, 2000 and 2016 and 2011 and 2019, respectively. Furthermore, to assess how model performance varies spatially, plots are presented with data for different areas of the bank and water depths. Finally, Table 19 presents the key statistics related to this analysis. The Root Mean Square Error (RMSE) between the predicted and observed bed level change ranges between 1.2 m and 1.8 m across the different regions of the lease area for the validation run between 2016 and 2019, increasing to between 2.0 m and 4.1 m for the validation run between 2000 and 2016. Along the export cable route, the RMSE ranges between 0.5 m and 0.6 m. It should be noted that in isolated locations, the absolute error (i.e. the discrepancy between observations and predictions) was significantly enhanced in comparison to the RMSE.

The purpose of the validation exercise was to demonstrate that our approach offers a viable method to predict future seabed levels, producing, broadly, correct patterns (i.e. qualitative similarities rather than quantitative correspondences) of bed level change across the lease area and export cable routes and replicating key driving processes and morphological trends across the short term, and longer term. Though model performance during validation, across the lease area, indicates the model was replicating key driving processes and producing broadly, correct patterns of change, significant discrepancies existed between the predicted and observed values of seabed level change over the period of assessment. As such, it was concluded that an approach which moderated the application of the model, focusing modelling efforts solely on supporting the assessment of the lateral (east-west) movement of the crestline and the subsequent effects on the shape and profile of the bank, was required.

The recognised shortcomings of the model during validation can be summarised as follows:

- Model predictions underestimate the magnitude of bed level change observed across the lease area over the period 2016 to 2019 and 2000 to 2016; underestimation is particularly evident in the more dynamic southern

portion of the bank. This is likely a function of several limiting factors of the model (discussed below) acting individually, or in combination.

- The model persistently lowers the crestline; this does not reflect reality where the seabed level at the crestline is broadly maintained through time.
- Though broadly the patterns of change within the model reflect observed patterns, on occasion, in isolated locations the model does not accurately represent the direction of movement of the crestline.
- On occasion, in isolated locations the discrepancy between the model predictions and observations is very large, but this is limited to areas where very large observed seabed level changes are observed (e.g. in the south-central region of the bank and the area anecdotally referred to as the 'hook').

The following reasons are offered to explain the potential sources of this discrepancy, which influence the results individually and cumulatively:

- The representation of Coriolis within the modelling software which is captured as a parameter in the solving of the underlying Navier Stokes equations and thus, likely has an almost negligible effect over the local scale model domain. Though, it is true that shallow bathymetric influences dominate the directional influences on flows, Coriolis is known to act to maintain the crest level of open shelf linear sandbanks such as Arklow Bank (Kenyon and Cooper 2005) and to a lesser degree, Seven Fathom Bank. Maintaining the crest level remains a significant challenge associated with the application of the model to assess the movement of the crestline and the subsequent effects on the shape and profile of the bank.
- Due to the model resolution, the physics which drive bedform formation migration are not captured within the model simulations. It is recognised that the migration of ripples, megaripples and small sandwaves form a key process delivering sediment to the crestline, and thus maintaining the level of the crestline through time.
- As detailed in Section 9.2, the approach adopted does not include for waves as it has been demonstrated, within the model, waves have limited effects on sand transport over the longer-term across the lease area as transport is tidally dominated. However, the data-led analysis revealed that waves play a role in the sediment transport regime above the -10 mLAT contour over the short-term. Above the -10 mLAT contour, and in areas of the bank most exposed to significant wave action (i.e. the southern tail and the south east flank of the bank), wave action is postulated (and potentially observed) to sweep the surface of bedforms, reducing over the short-term (i.e. the days that follow the wave event) the seabed level and smoothing the bank profile, until dominant tidal processes, once again drive the formation, and migration of bedforms in those areas. In the shallowest regions of the bank (i.e., at the crestline) wave action is postulated to be more severe with breaking waves occurring, and potentially, wave induced currents driving processes akin to longshore transport or swash zone processes observed at the shoreline[33]; such processes are not captured within the model.

33 Such processes are postulated to have triggered a resuspension event captured in the data record at Location E, where, at the crestline, wave action washed a plume of sediment from the crestline down to the flanks of the bank (see Section 8.6.3).

- As detailed in Section 9.2, the use of a reduction technique in combination with a morphological speed-up factor is a methodological necessity to assess the net effects of short-term processes over the longer term. However, this results in driving conditions being used for validation that were *representative* of the conditions which occurred over this period, not the conditions which *occurred* over these periods.
- The single beam bathymetry acquired in 2000 at approximately 100 m resolution is spatially limited (i.e. it does not cover the full extent of the lease area) and thus, to be integrated into the model domain and form the starting bathymetry for the 2000 – 2016 validation simulation, these data must be merged with data from surveys conducted in 2016. This results in a highly undesirable situation where, in some locations of the lease area, for practical necessity, the target system state exists as the starting bathymetry in the model and thus any changes to seabed level through the simulation will inevitably act to increase the discrepancy between the prediction of bed level change and observations of bed level change.
- It is postulated that all available bathymetry data may not accurately represent bank morphology as a single time step. This is a function of the size of the lease area and the practicalities of offshore operations. As such, data were obtained over periods of > 1 month, with variously data acquired on the flooding and ebbing tide. Due to the process understanding garnered from this study, it is now recognised that the composite bathymetry surface collated during post-processing of these data likely represent changes to bank morphology which occur over the lunar cycle (and beyond). This issue is exacerbated where you then compare two composite bathymetries. This could potentially result in a misleading picture of the magnitude of movement over this period as well as the transport patterns observed.
- In a 'live bed' sediment regime, the effects of porosity may have a significant influence on the relative mobility of seabed sediments where frequently moving sediments would likely have a higher porosity compared to more stable deposits which have had a chance to compact and de-water (Román-Sierra *et al.*, 2014). Porosity has not been applied as a tuning parameter as no data exists to ensure assumptions remain grounded in reality.
- The limited data available regarding the variability of sediment grain sizes, and the depth of the mobile layer, across the lease area, and export cable route, provides a limitation on what we can achieve at present. There exists both a limitation in the sediment grain size data being incomplete to achieve a definitive sediment grain size map, but also a limitation in the modelling software to account for spatiotemporal changes where sediments which are moved within the model cannot vary the implemented grain size map.

Performance of the model is improved in areas of the seabed coincident with the proposed export cable routes, however challenges also persist, particularly associated with Seven Fathom Bank, which is influenced by similar processes to those observed at Arklow Bank (but is far less dynamic) (see Section 8.2). Away from Seven Fathom Bank, at present, the risk to export cables associated with morphological change is low; with only limited seabed variability anticipated to occur. Where model predictions indicate greater propensity for change this highlights a potential risk to cabling in those areas of the seabed (e.g. in an area of enhanced flows close to Arklow Bank), which can support, for

example, downstream work packages such as the Cable Burial Risk Assessment (CBRA). It is noteworthy however, at this stage, limited quantitative information exists regarding the sedimentological conditions along the export cable route and thus the model predictions should be treated with caution until these data are available to the commission.

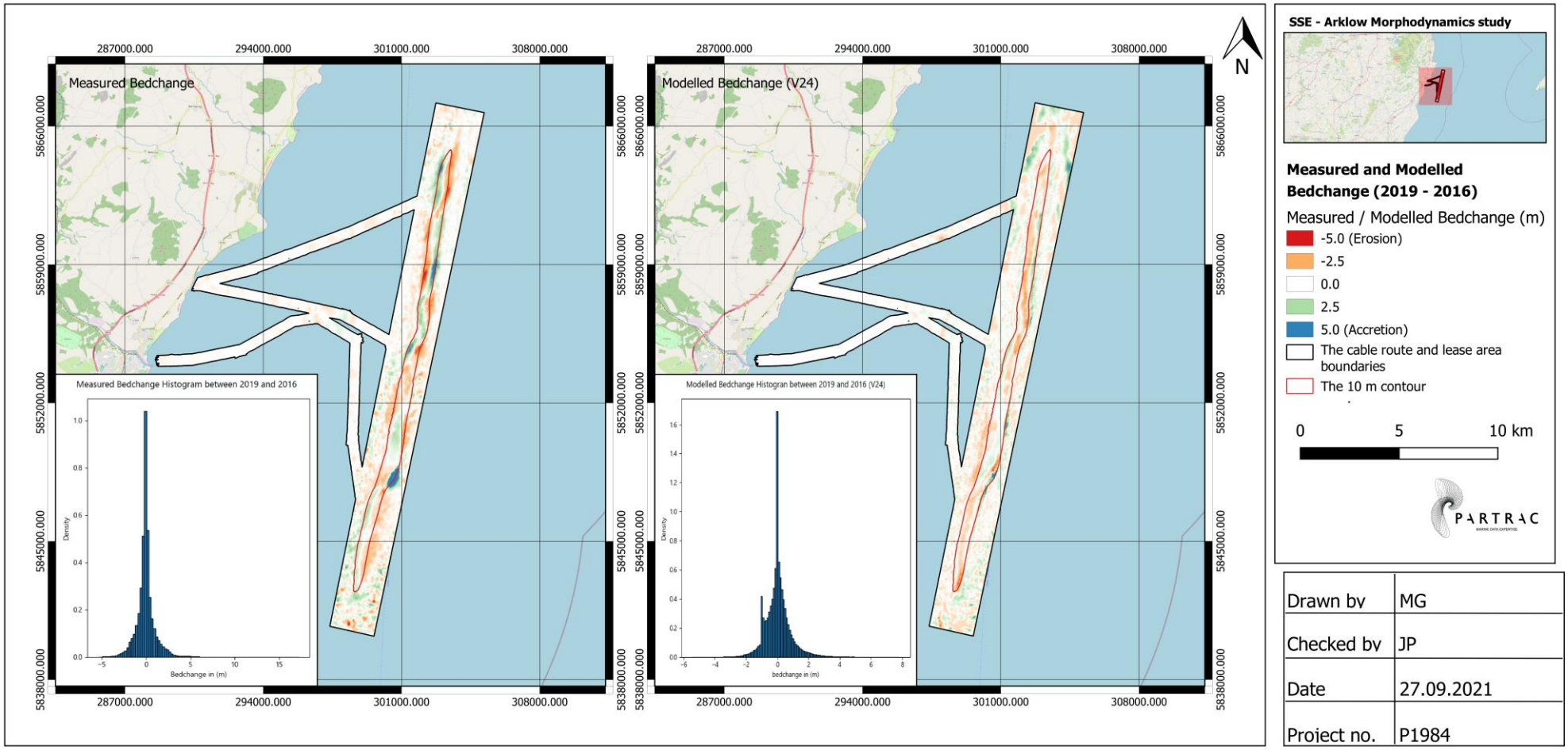


Figure 210. The observed (measured) and predicted (modelled) bed level change across the lease area and export cable routes over the validation period 2016 to 2019.

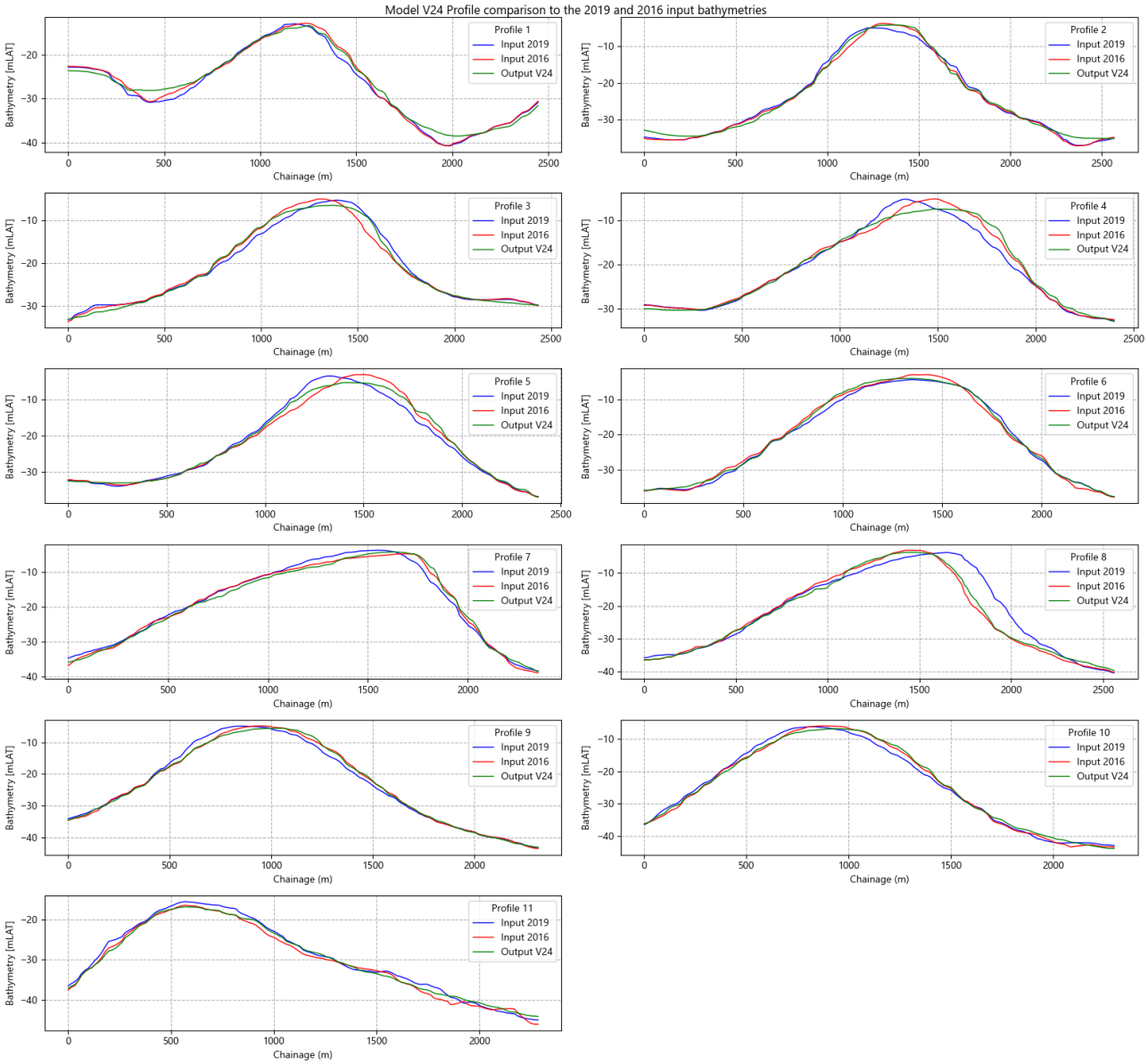


Figure 211 Cross section, west to east profiles of Arklow Bank. The profiles present the data from the 2016 and 2019 model input bathymetry and the model output following the 2016 to 2019 validation run.

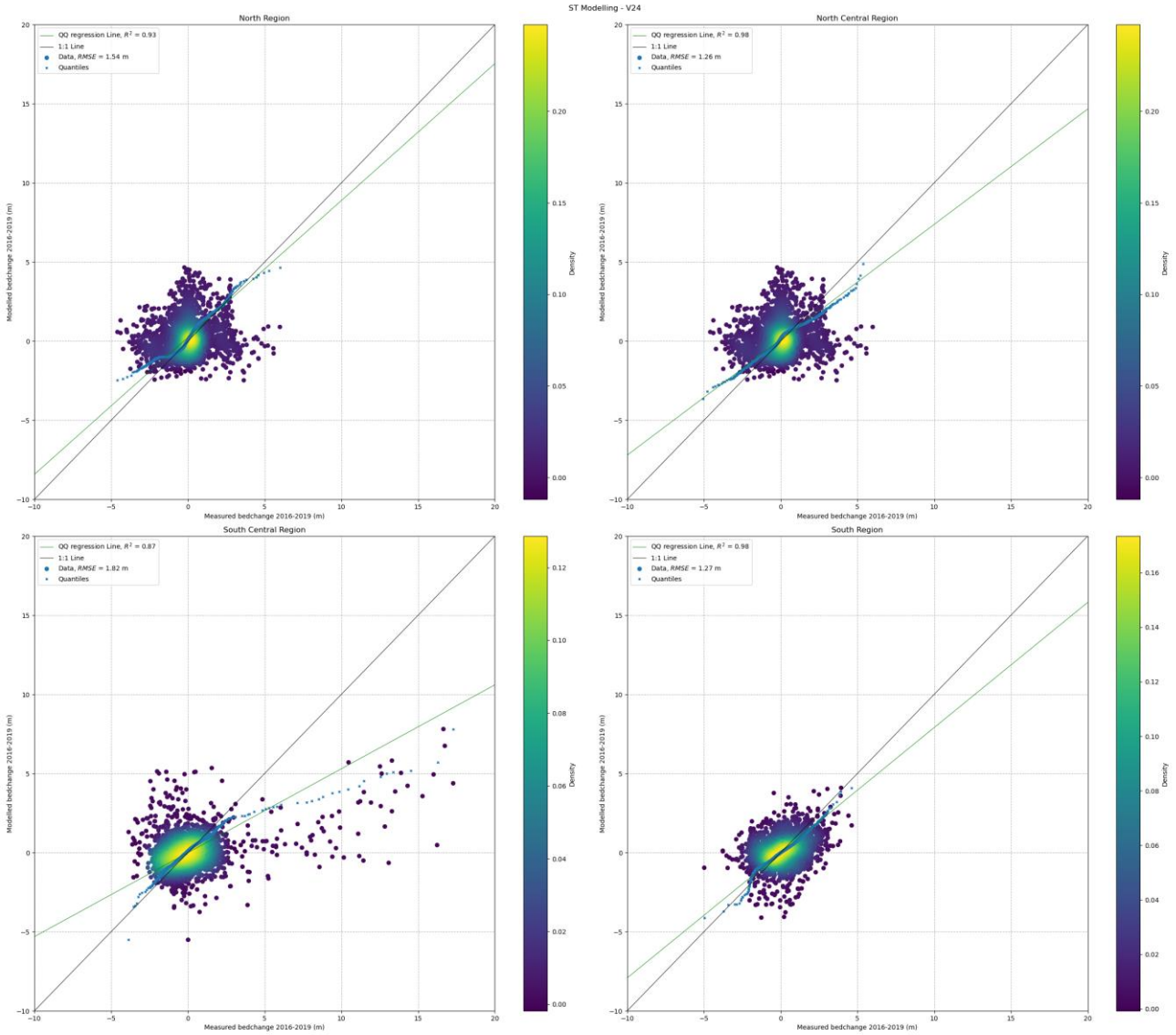


Figure 212. A scatter plot showing the discrepancy between observations (measured) and predictions (modelled) of vertical bed level change from 2016 to 2019 split by bank region. The quantiles and a regression line are also presented, along with a 1:1 reference line.

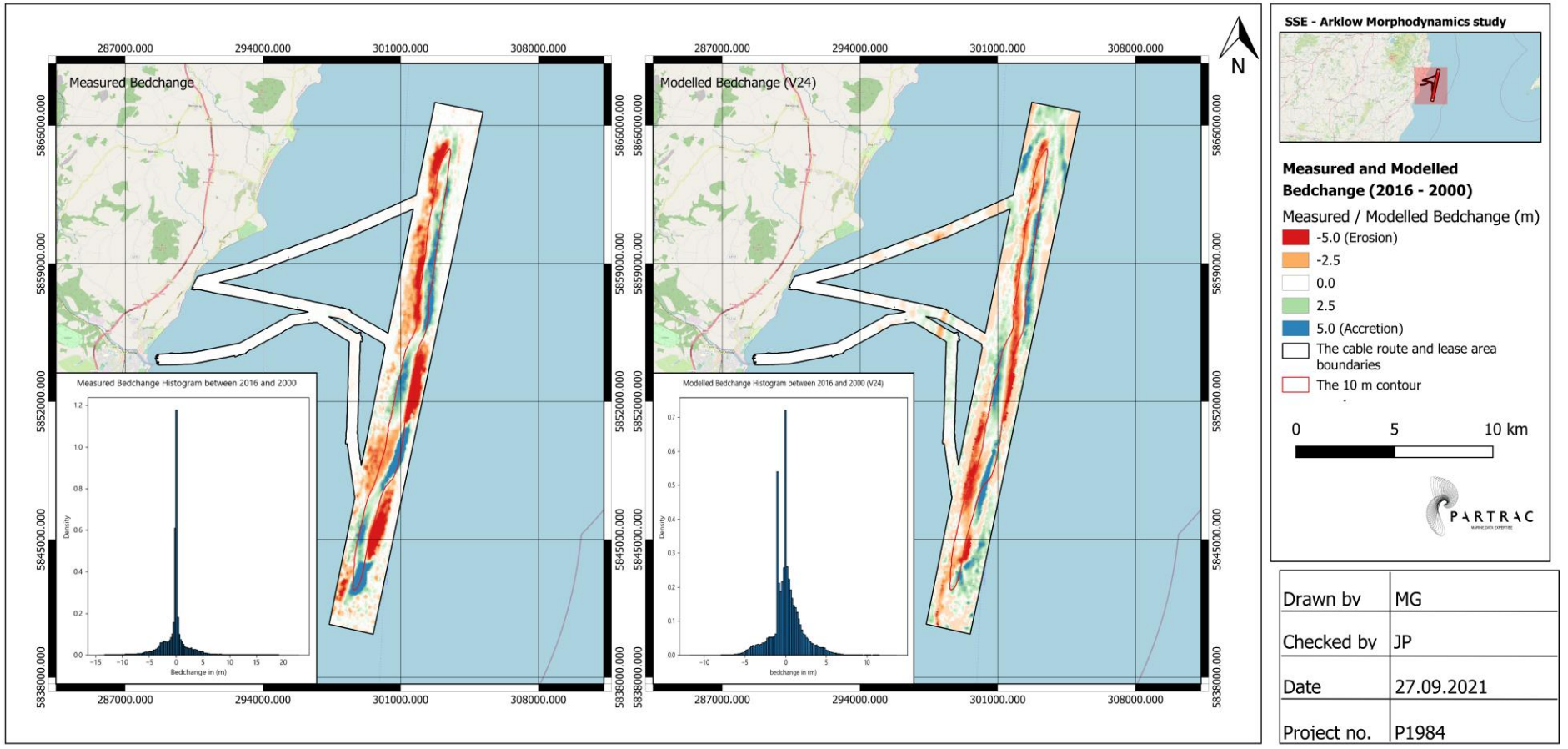


Figure 213. The observed (measured) and predicted (modelled) bed level change across the lease area and export cable routes over the validation period 2000 to 2016

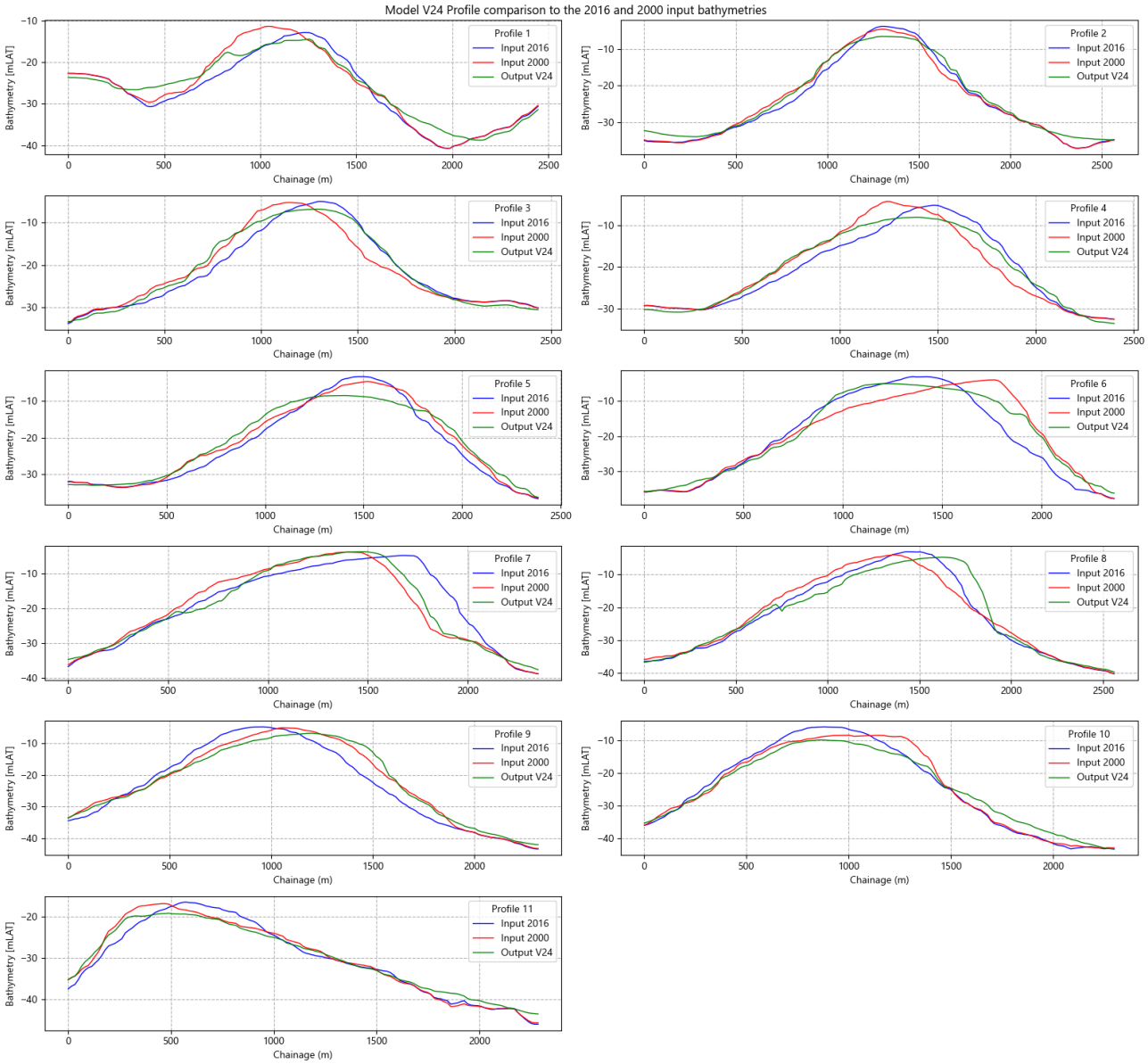


Figure 214. Cross section, west to east profiles of Arklow Bank. The profiles present the data from the 2016 and 2019 model input bathymetry and the model output following the 2016 to 2019 validation run.

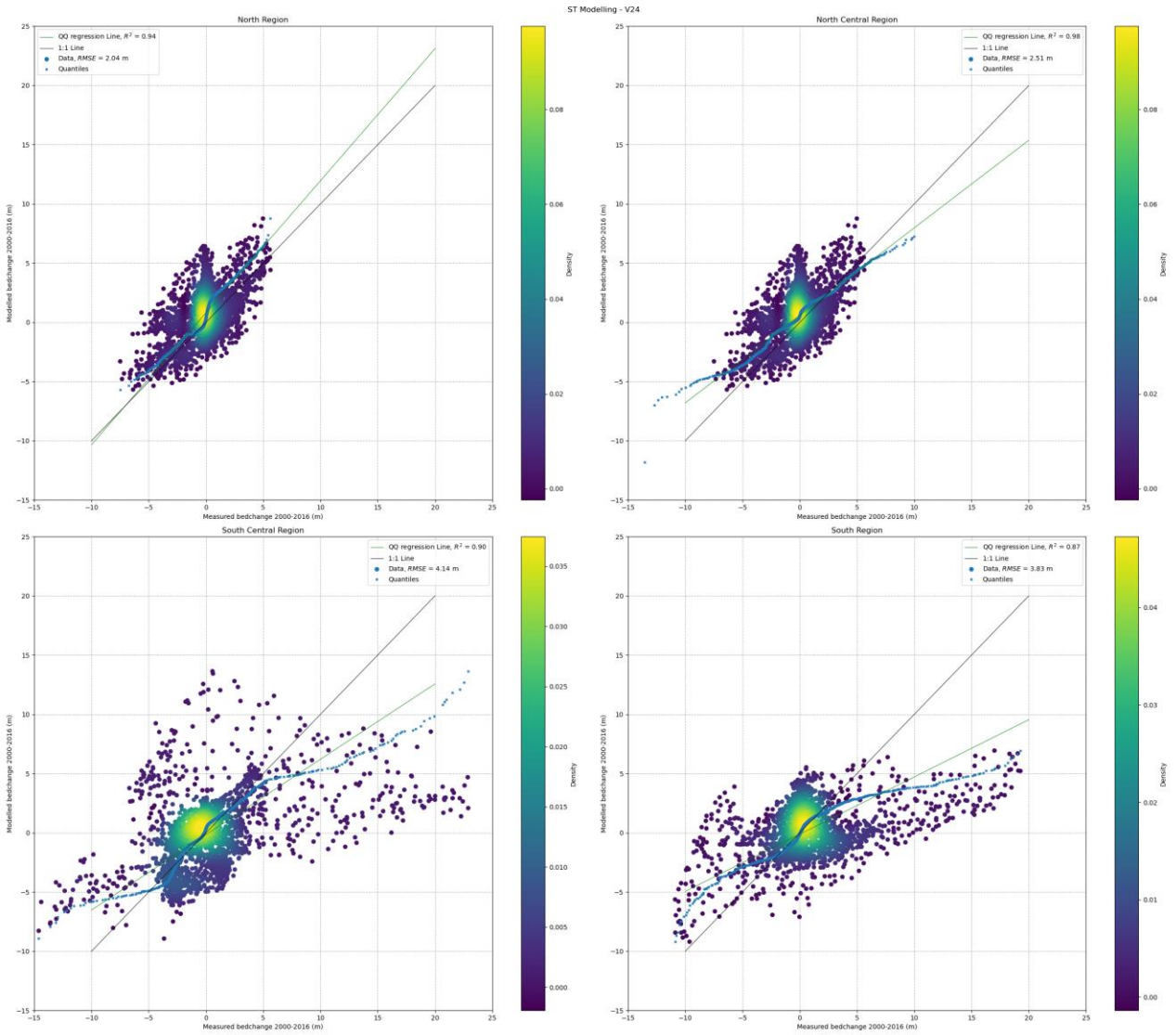


Figure 215. A scatter plot showing the discrepancy between observations (measured) and predictions (modelled) of vertical bed level change from 2000 to 2016 split by bank region. The quantiles and a regression line are also presented, along with a 1:1 reference line.

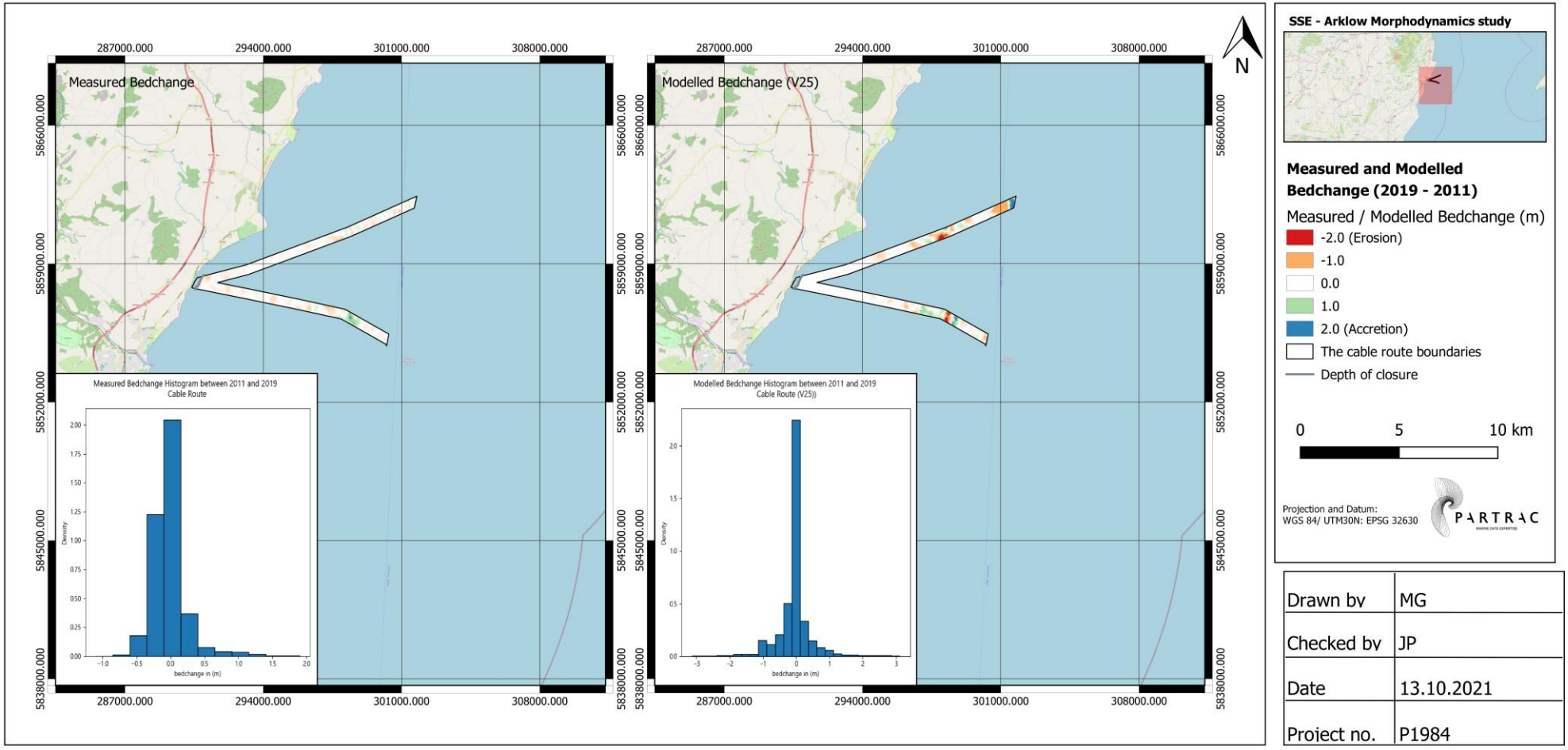


Figure 216. The observed (measured) and predicted (modelled) bed level change along the export cable routes over the validation period 2011 to 2019.

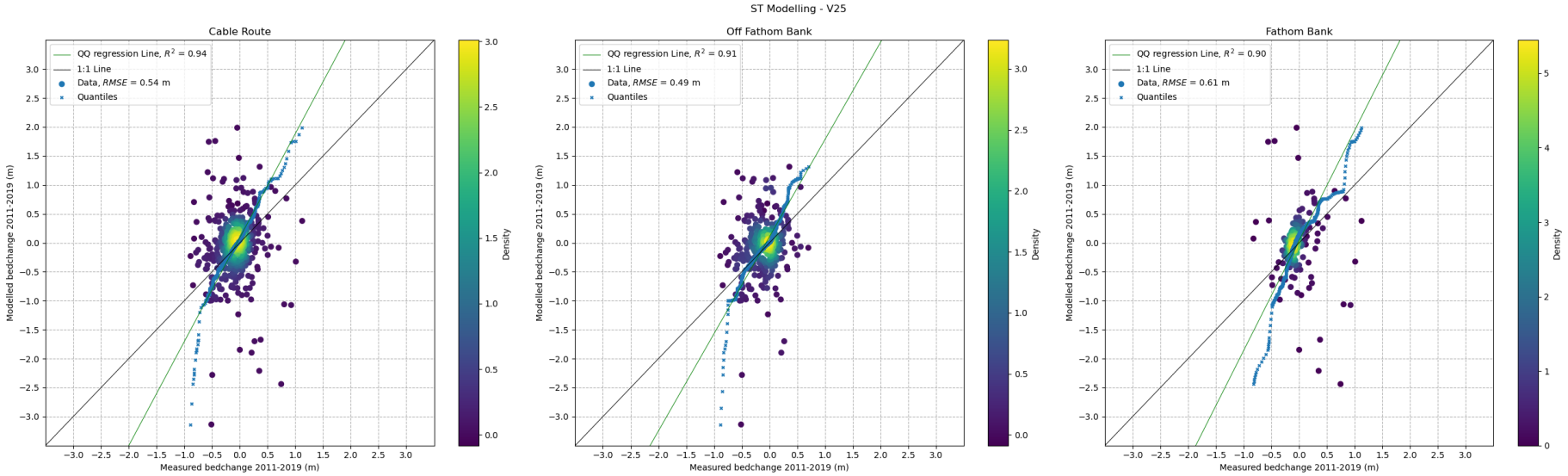


Figure 217. A scatter plot showing the discrepancy between observations (measured) and predictions (modelled) of vertical bed level change from 2011 to 2019 along the export cable route. The route is split by bank region. The quantiles and a regression line are also presented, along with a 1:1 reference line.

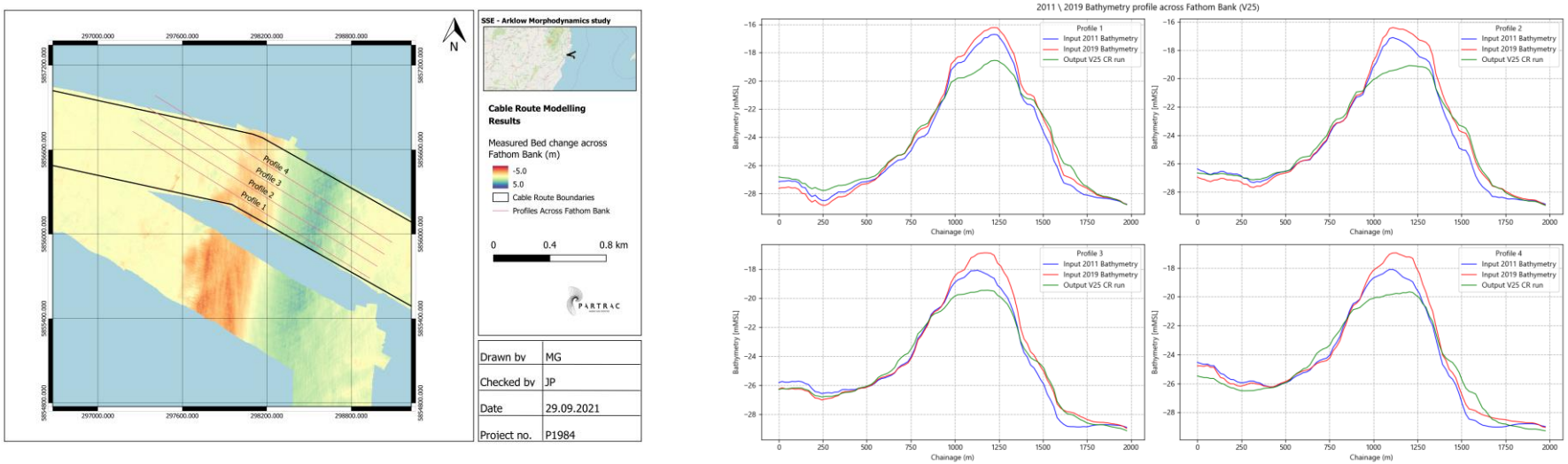


Figure 218. Four east – west cross section profiles of Seven Fathom Bank. The image to the left shows where the profiles were extracted from and the image to the right shows the bathymetry data as implemented in the model.

Table 19. The key statistics derived from the direct comparison of predicted vs measured bed level change across the validation periods 2000, 2016 and 2016 and 2019 across the development area.

Region	RMSE (2019 – 2016), expressed in m	Discrepancy range expressed in m	RMSE (2000 – 2016), expressed in m	Discrepancy range expressed in m	RMSE (2011 – 2019), expressed in m	Discrepancy range expressed in m
North Region	1.54	-6.35 – 5.70	2.04	-4.38 – 6.74	-	
North Central Region	1.26	-4.50 – 6.10	2.51	-7.30 – 11.73	-	
South Central Region	1.82	-15.75 – 7.13	4.14	-20.88 – 13.60	-	
South Region	1.27	-4.28 – 4.47	3.83	-14.85 – 9.99	-	
Cable Route	-		-		0.54	-4.19 – 0.56
Cable route 'off Seven Fathom Bank'	-		-		0.49	-2.95 – 0.31
Cable route 'on Seven Fathom Bank'	-		-		0.61	-4.19 – 0.56

9.4 Application of the Model

It is essential within the methodology that the limitations of numerical modelling, and the model(s) developed for the purposes of this study, are recognised, and where applicable, the use of the model is duly moderated. It is important to note the limitations of numerical modelling, which though a useful tool, ultimately provides best estimates of reality based on various assumptions and approximations. Inherently, they rely on simplifying processes occurring in the real world; where processes and process interactions are complex, this can lead to a discrepancy between model predictions and observations (a problem commonly referred to as 'compound error').

The performance of the model during validation confirmed that it was technically inadvisable to apply the model directly to forecast morphological change into the future. Despite this limitation, as the driving models effectively capture the key tidal processes responsible for sediment transport across the site, which includes the cross-bank flows driven by the tidal head difference and tidal asymmetry either side of the bank, application of the model is justified as it enables system states, beyond those observed in the available bathymetric datasets, to be estimated. This is critical where Arklow Bank (and to a lesser degree Seven Fathom Bank) displays multiple response pathways and thus has the potential to display multiple distinct system states across the lifetime of the development. It is also demonstrated that the model can reposition the crestline through time which poses the greatest threat to site infrastructure due to the magnitude of change which could occur, and the persistence of that change.

Considering this, a pragmatic approach which focused solely on assessing the influence of cross bank flows was developed. This approach recognises the primary challenge of modelling this environment being that distinct system states may occur at any point in time over the lifetime of the development due to the semi-random nature (due to the influence of atmospheric effects) of the processes which drive significant changes to the shape and profile of the bank itself. As such, we developed an approach which moderated the use of the model and in doing so targets the application of the model to support solely the assessment of the net migration of the crest line and the subsequent effects on the cross-section profile of the bank.

The highest and lowest potential system states are therefore determined from a composite of seabed levels derived from outputs from targeted model simulations relying on the three available starting bathymetries, existing bathymetric datasets and the minimum and maximum RSBL derived from the 2016 and 2019 bathymetry datasets. This will result in the highest and lowest system state being derived from 31 surfaces which have been either estimated, measured, or developed from complementary analyses.

The approach offers a pragmatic solution to a complex problem, benefits include:

- The approach adopted utilises or relies upon all available data, supporting analysis and our conceptual understanding of the site;
- The approach enables multiple system states to be assessed from the three different starting bathymetries providing greater confidence that the more extreme system states are being captured, or are being accounted for, within the outputs. This adds confidence that the approach adopted captures the (realistic), envelope of potential seabed level variation over the lifetime of the wind farm; and,
- Due to the use of the RSBLs, bedforms are accounted for which were observed on the flanks and above the -10 mLAT contour in the 2016 and 2019 datasets.

9.5 Model Simulations Performed

This section details the simulations performed to support the prediction of future seabed levels across the development area. To determine a suite of system states to support assessment of the envelope of the potential seabed level variation which may occur across the lifetime of the development, targeted simulations were performed. To ascertain the potential extreme positions of the bank, it is necessary to make recourse to the conditions driving morphological change of the bank. This assumes that the most extreme amplitude, or longest persisting positive or negative sediment transport bias over the crest of the bank leads to the most extreme position of the bank accessible to us (within the 39 year hindcast record available; thus, these estimates of the most extreme driving processes sit within the bounds of the 1 in 39-year return period). These were then combined with the three different available bathymetry datasets to

provide a suite of runs with a range of different driving conditions, over different periods, and different starting bathymetries, thus providing a comprehensive suite of model simulations from which to derive the required outputs. Figure 219 shows several large amplitude positive and negative events. The most extreme of these (biased eastwards and westwards) were selected for the simulations. There is also a longer-term signal repeating on approximately a 19-year cycle, and so two periods (again biased to the east or west) of 9.3 years were also selected. These four different driving conditions formed the basis of the environmental conditions used in the simulations. The periods selected are shown in Figure 219. The details of the simulation periods are provided in Table 20.

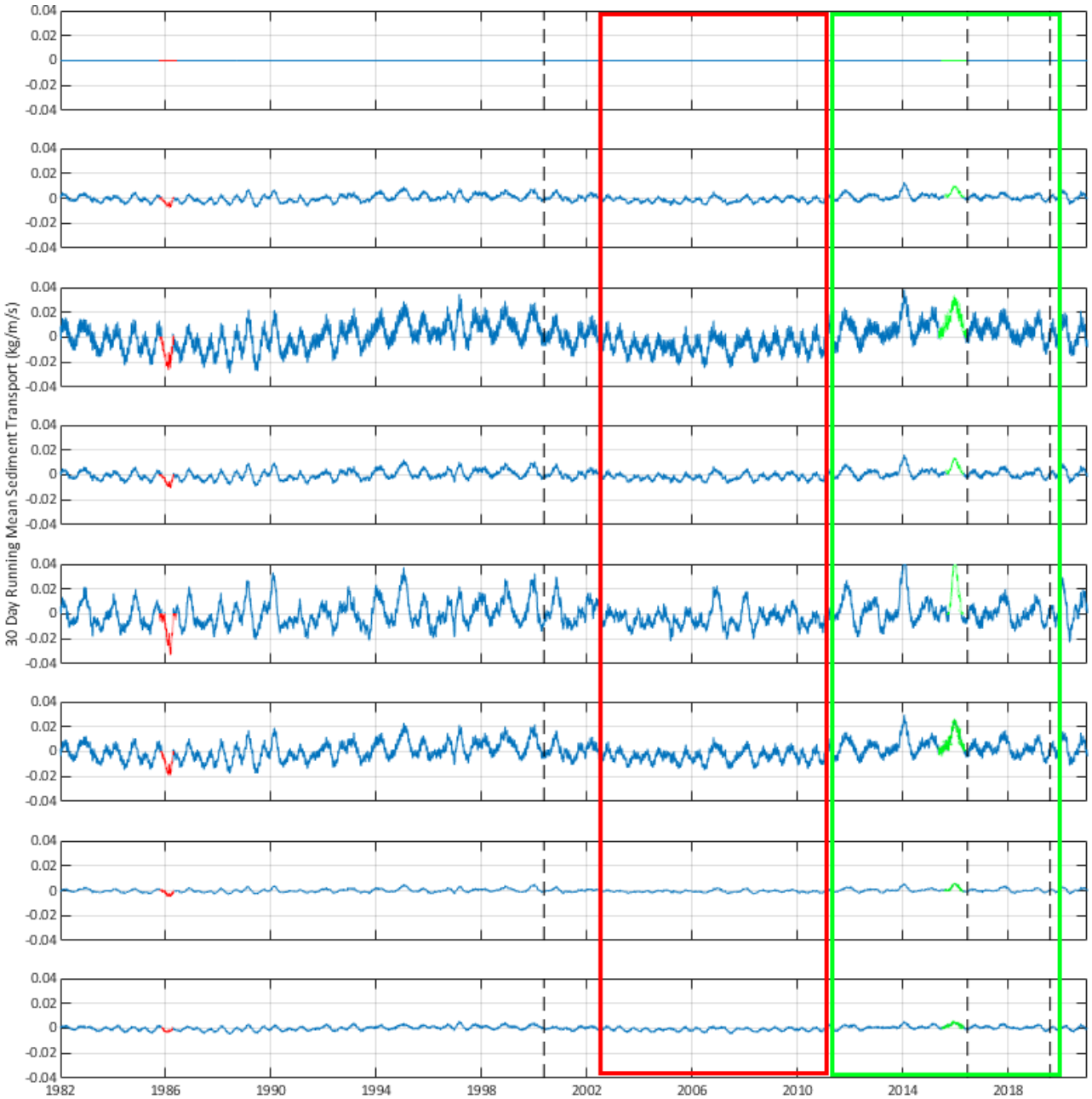


Figure 219. Periods selected for the simulations. Maximum durations indicated by coloured boxes, and maximum amplitudes indicated by coloured sections of the time series. Sediment transport biased westward is shown in red, and sediment transport biased eastwards shown in green.

Table 20. Details of morphological simulations performed.

Description	Dates selected	Dates Simulated	Morphological Speedup Factor
Maximum Positive Magnitude	29 October 2013 to 10 April 2014	29 October 2013 to 10 April 2014	1
Maximum Negative Magnitude	4 November 1985 to 11 April 1986	4 November 1985 to 11 April 1986	1
Maximum Positive Duration	9 May 2011 to 20 November 2019	7 November 2017 to 11 February 2018	32.47
Maximum Negative Duration	11 July 2002 to 9 May 2011	5 May 2019 to 21 Jul 2019	41.87

To support the delivery of primary study outputs, twenty-four targeted model simulations were conducted. The simulations performed were as follows:

Simulation 1: The 2000 bathymetry implemented in the model; conditions coincident with the greatest magnitude sediment transport at the crestline derived from the 1D sediment transport model (see Section 8.6.4 for details) predicted to dominantly drive sediment transport at the crestline eastward.

Simulation 2: The 2000 bathymetry implemented in the model; conditions coincident with the greatest magnitude sediment transport at the crestline derived from the 1D sediment transport model predicted to dominantly drive sediment transport at the crestline westward.

Simulation 3: The 2016 bathymetry implemented in the model; conditions coincident with the greatest magnitude sediment transport at the crestline derived from the 1D sediment transport model predicted to dominantly drive sediment transport at the crestline eastward.

Simulation 4: The 2016 bathymetry implemented in the model; conditions coincident with the greatest magnitude sediment transport at the crestline derived from the 1D sediment transport model predicted to dominantly drive sediment transport at the crestline westward.

Simulation 5: The 2019 bathymetry implemented in the model; conditions coincident with the greatest magnitude sediment transport at the crestline derived from the 1D sediment transport model predicted to dominantly drive sediment transport at the crestline eastward.

Simulation 6: The 2019 bathymetry implemented in the model; conditions coincident with the greatest magnitude sediment transport at the crestline derived from the 1D sediment transport model predicted to dominantly drive sediment transport at the crestline westward.

Simulation 7: The 2000 bathymetry implemented in the model; conditions coincident with the greatest duration sediment transport at the crestline derived from the 1D sediment transport model predicted to dominantly drive sediment transport at the crestline eastward.

Simulation 8: The 2000 bathymetry implemented in the model; conditions coincident with the greatest duration sediment transport at the crestline derived from the 1D sediment transport model predicted to dominantly drive sediment transport at the crestline westward.

Simulation 9: The 2016 bathymetry implemented in the model; conditions coincident with the greatest duration sediment transport at the crestline derived from the 1D sediment transport model predicted to dominantly drive sediment transport at the crestline eastward.

Simulation 10: The 2016 bathymetry implemented in the model; conditions coincident with the greatest duration sediment transport at the crestline derived from the 1D sediment transport model predicted to dominantly drive sediment transport at the crestline westward.

Simulation 11: The 2019 bathymetry implemented in the model; conditions coincident with the greatest duration sediment transport at the crestline derived from the 1D sediment transport model predicted to dominantly drive sediment transport at the crestline eastward.

Simulation 12: The 2019 bathymetry implemented in the model; conditions coincident with the greatest duration sediment transport at the crestline derived from the 1D sediment transport model predicted to dominantly drive sediment transport at the crestline westward.

Simulation 1 to simulation 12 were repeated to include for climate change effects following the approach described in Section 5.5.

9.6 Confidence Limits Applied to Future Seabed Levels

The results are presented in this report to two decimal places (i.e. to nearest 0.01 m) to be able to identify morphological trends and inform decision making within design. It should be considered however that morphological predictions over the longer term should always be treated with caution; they simply cannot be predicted with total accuracy. As such, morphological predictions should always be interpreted in tandem with consideration of their associated *confidence limits*.

The prediction of future seabed levels relies on both measured and modelled datasets and thus the assessment of confidence limits associated with this analysis comprises three separate contributions:

- Survey data precision limits;
- Confidence limits associated with the model predictions (i.e. model performance during the process of validation termed the *methodological uncertainty*); and,
- Evolution (i.e. temporal changes to the trough to crest height of mobile bedforms).

The quantification of the confidence limits associated with survey data precision limits, outputs from the model across the development area and bedform evolution is detailed in Section 9.6.1 to Section 9.6.3.

9.6.1 Survey Data Precision Limits

When performing bathymetric survey, the precision of the data acquired, is described in terms of the Total Vertical Uncertainty (TVU). These uncertainties are typically quantified by surveying a fixed structure on the seabed. Pre and post-processing methods (i.e. tidal reduction methods and corrections for ship movement) of the raw data can also contribute to survey data uncertainty. The bathymetry datasets collected in 2016, 2019 and 2020 were acquired to the International Hydrographic Organisation (IHO) order 1 A. Where known, these standards define confidence limits for the acquired data. The confidence limits associated with the bathymetric survey data was applied as a constant to all seabed levels, as follows:

- 2000 single beam bathymetry dataset (the accuracy of which was considered in detail by Cooper Marine Advisors Ltd, 2020); ± 1.00 m
- 2016, 2019 and 2020 MBES dataset acquired to IHO Special Order, ± 0.25 m.

The available bathymetric datasets formed a primary input into the sand transport model and is the principal dataset for assessment of bed level change ($\mathbf{t_x - t_0}$). Where bed level change is assessed from two available bathymetric datasets the associated confidence limits on the observed bed level change values are additive (i.e. comparing data acquired in 2000 and 2016; value is ± 1.25 m).

9.6.2 Methodological Uncertainty

The discrepancy between observations and predictions has been collated from the three validation runs (presented in Section 9.2) to produce a spatial plot of model confidence (i.e. where low discrepancy between predictions and observations is found the confidence in the model is greater and vice versa)[34].

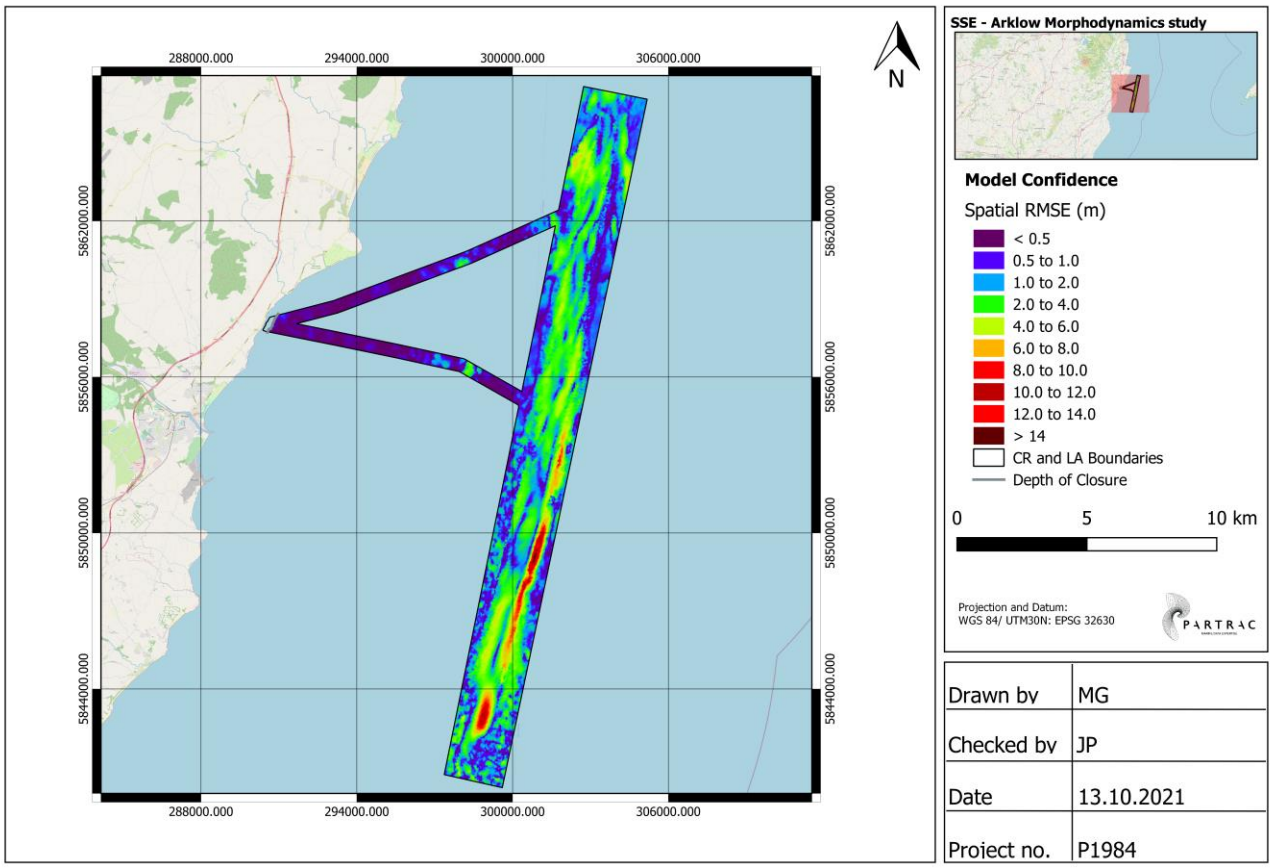


Figure 220. A map showing the spatial variation in error derived from the comparison of predictions vs observations of seabed level change over the period, 2000 to 2016, 2016 to 2019 and 2011 to 2019. It should be noted this is an error derived solely from the model output over the period assessed during validations.

Due to the shortcomings of the model, its application has been moderated. Thus, the map of error was not applied directly as part of the uncertainty band. Rather the map of error has been moderated to reflect the limited application of the model in the development of future seabed levels, to ensure that the consideration of uncertainty does not become overly (or unnecessarily) conservative and that study outputs are grounded in the bounds of reality. To do

34 To produce this map the difference between the measured and modelled bed change for the 2000 to 2016, 2016 to 2019, and on the cable route the 2011 to 2019 validation run at each point was obtained. For each data point the difference between predicted and observed were squared and summed (and within the lease area divided by two). The square root of this value was then determined and plotted spatially.

this, the spatially varying error was calculated as a percentage of the water depth[35] (LAT). Figure 221 shows the moderated error map in the form of a spatial plot. Figure 222 presents the unmoderated, and moderated, error data in the form of cross section profiles for reference.

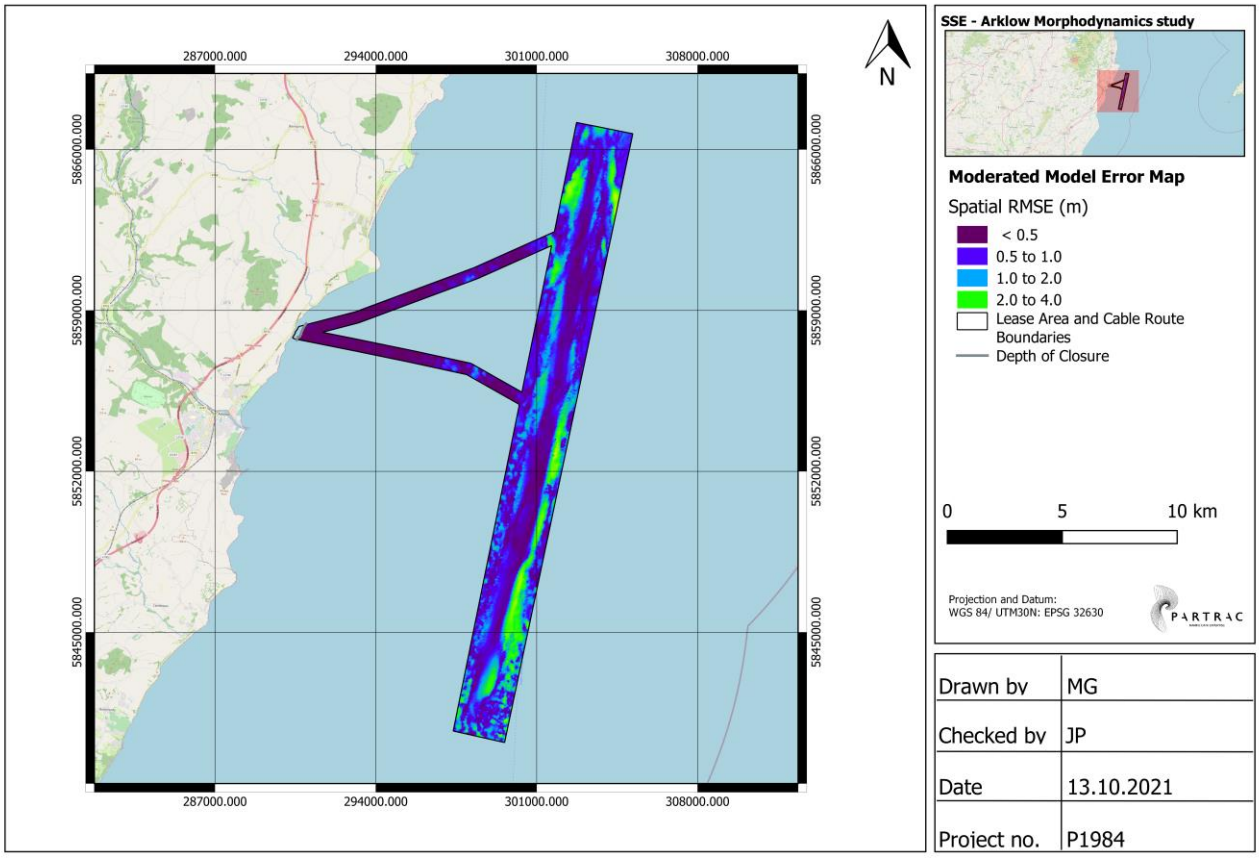


Figure 221. A map showing the spatial variation in error which has been moderated.

35 Water depth in this context, is the total absolute depth which is the vertical distance between the seabed where the bank does not exist (determined in GIS by removing the bank from the bathymetry and using a Triangulated Integrated Network (TIN) interpolation to determine seabed levels across the area) and the water surface (LAT).

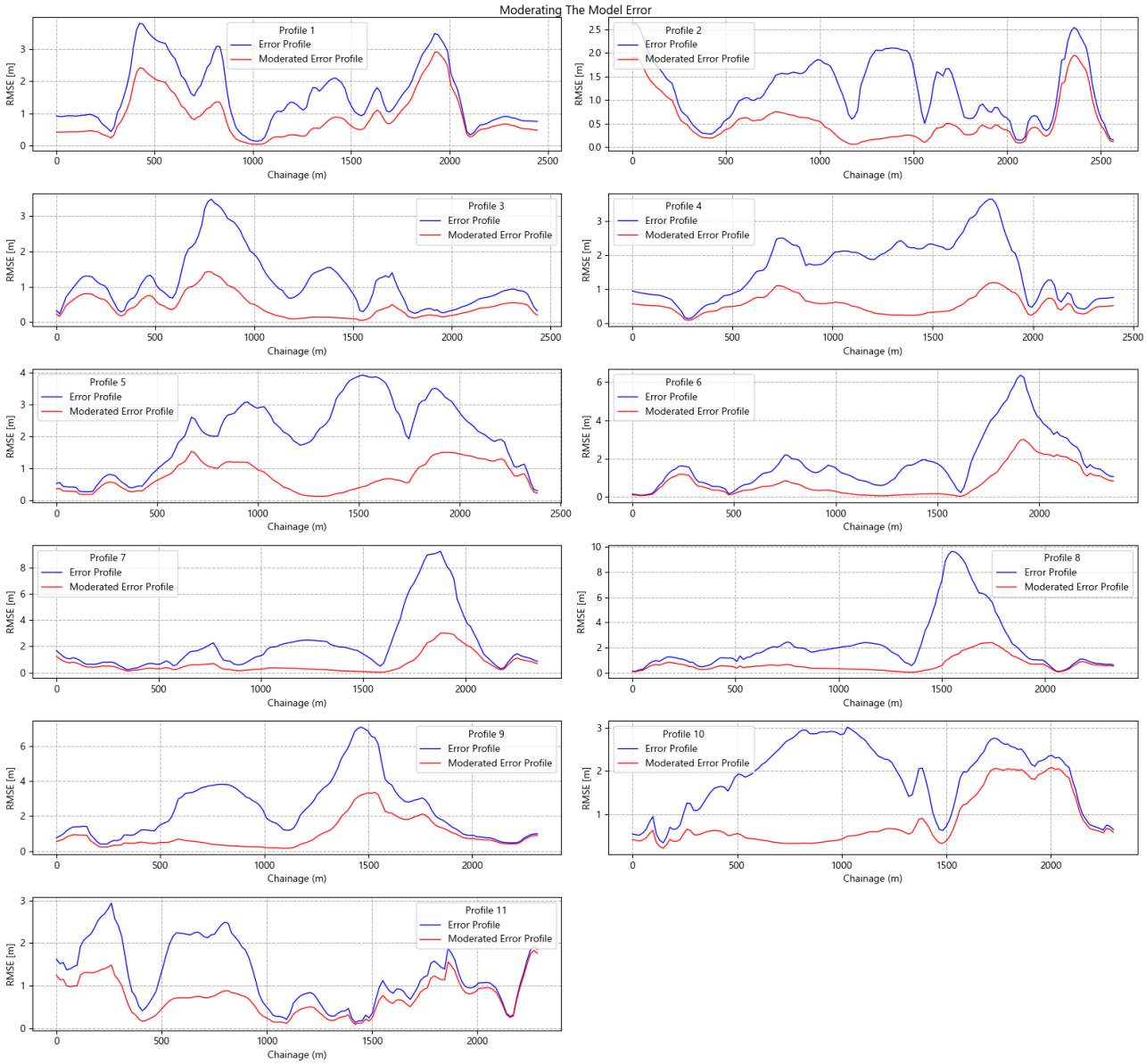


Figure 222. Cross section profiles showing the spatially varying average error (blue line) and the moderated error.

9.6.3 The Evolution of Mobile Bedforms

The analysis of mobile bedforms provides quantitative data on their characteristics (their height from trough to crest, wavelength, shape), their position within the lease area and their relative mobility (i.e. migration rates). Across the lifetime of the development, where sediment supply is maintained and the local hydrodynamic regime broadly remains the same, there is no evidence to suggest that these bedforms will cease to exist or that their characteristics will alter significantly (beyond those alterations observed between the survey datasets). As detailed in Section 8.8, A large body of scientific work exists regarding the potential growth (increase in sandwave height), decay (decrease in sandwave height) and evolution (i.e. changes to the shape, wavelength) of these features over time. Figure 223 shows an assessment of the growth potential of mobile bedforms which exist within the bathymetry datasets acquired in 2016

and 2019[36]. The spatially varying, maximum potential growth increase was added to the 'maximum' RSBL determined from the bathymetry data acquired in 2016 and 2019 to account for the potential growth of sandwaves through time (i.e. on the west flank, the determined 'maximum' RSBL, was raised [shallowed] by 6%). Note: no additional tolerance was included to the determined 'minimum' RSBL as the migration of sandwaves does not act to lower the seabed level across which they migrate.

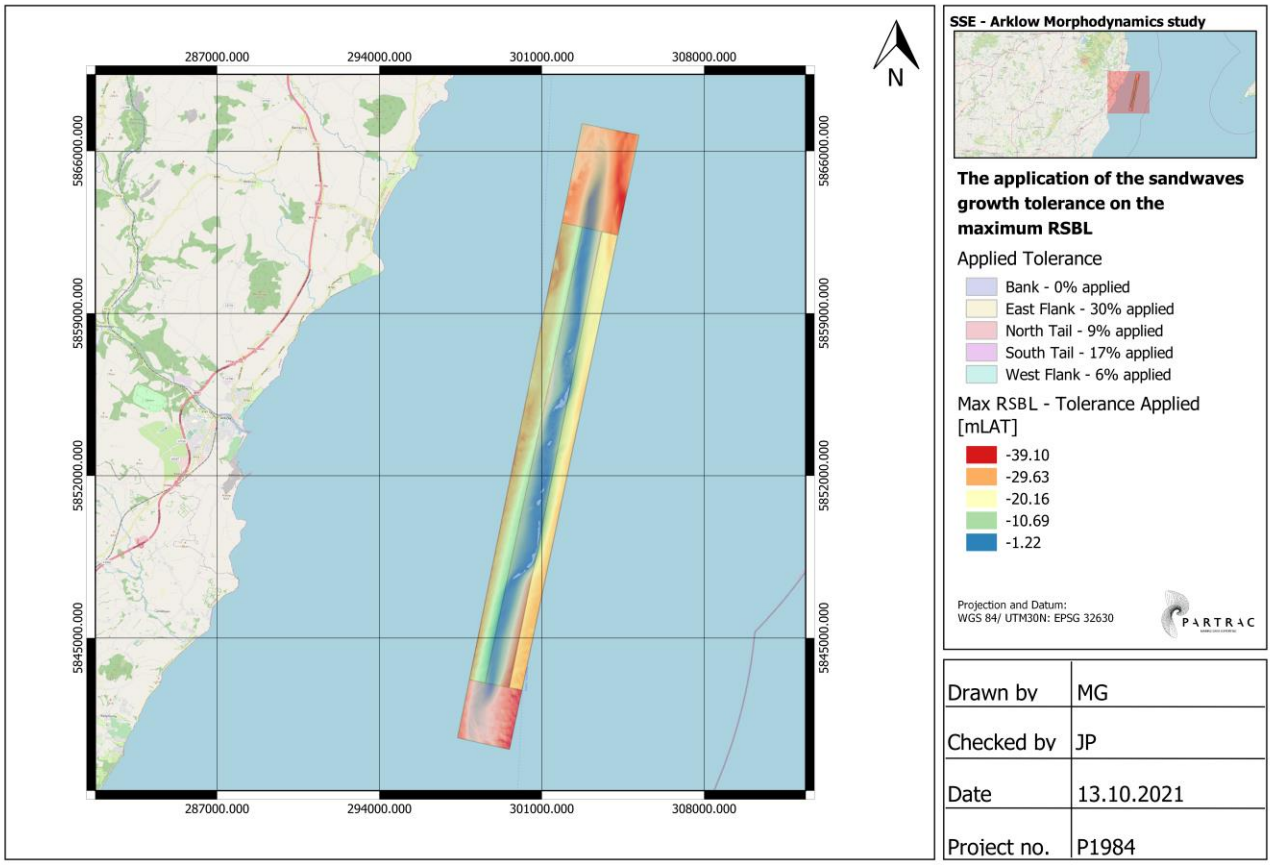


Figure 223. Growth potential of sandwaves to the east, west, north, and south of the bank.

Figure 224 illustrates how these statistics have been applied to the 'maximum' RSBL derived from analysis of the 2016 and 2019 data (described in Section 8.8). This approach provides an upward bound which captures the growth potential of sandwaves in different areas of the bank; the maximum and minimum[37] seabed levels were applied as part of the determination of future seabed levels to ensure mobile bedforms were accounted for as part of this process.

36 The map presents the maximum percentage difference between the sandwave statistics derived from the Fourier analysis (see Section 8.8) at the head of the bank, the east and west flanks, and the south of the lease area. Though determination of the minimum and maximum reference seabed level does account for megaripples, assessment of the growth potential is limited to sandwaves due to the prevalence of megaripples across the site and the limited risk posed by such features to seabed infrastructure.

37 A lower bound to these estimates has not been included as the available geophysical evidence indicates that around the periphery of the bank where large scale sand waves exist evidence exists that the underlying sedimentology (as observed in the troughs of such features) comprises a coarser deposit and thus it is not anticipated that significant seabed lowering beyond the determined 'minimum' RSBL is anticipated to occur.

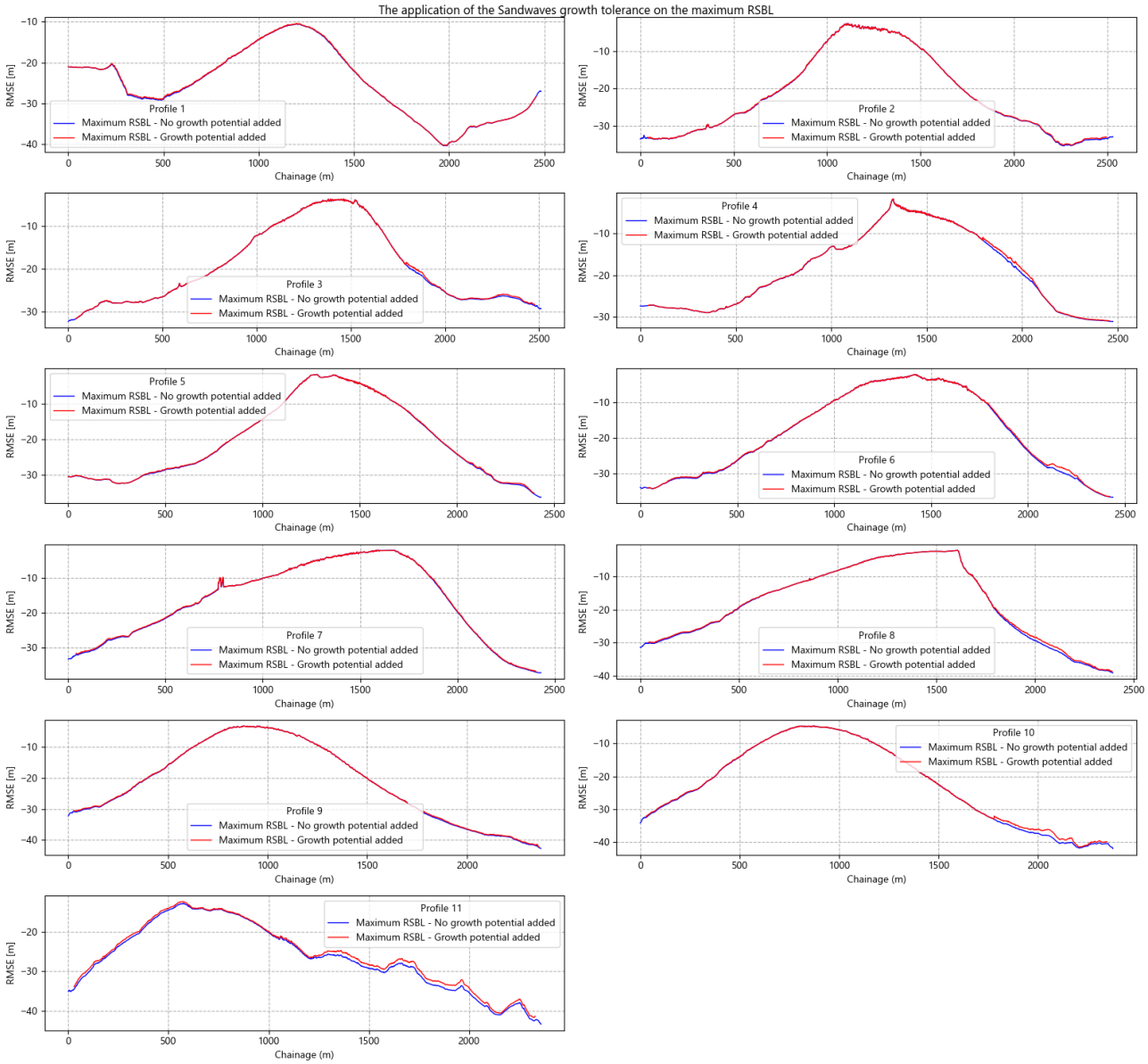


Figure 224. Cross section profiles along the length of Arklow Bank demonstrating how the 'maximum' RSBL has been raised to account for the growth potential of sandwaves in this area.

9.7 Combining Data Driven Analysis, Numerical Modelling Outputs and Confidence Limits

Two primary analytical tools exist, each with inherent strengths and weaknesses, to support prediction of future seabed levels; numerical modelling and data led analysis. Thus, the prediction of the highest/lowest seabed levels estimated to occur over the design life of the wind farm, relies upon the integration of both measured and modelled data coupled with observational findings and determined confidence limits[38]. Sediment transport models developed on the areal

38 Merging these data, and the derived surfaces, on occasion, results in sharp transitions between different process environments across the lease area.

scale of Arklow Bank cannot predict the evolution (or influence on seabed level changes) of smaller scale (i.e. sub-grid) morphological bedform features, such as sandwaves. As such, the findings of the independent, quantitative assessment of mobile sandwave features (facilitated by the determination of the RSBL) must support and be integrated with the model outputs. Principally, the analysis of bedform features relies on the interrogation of the available MBES datasets as described in Section 3.1. The aim of this interrogation is to quantify the characteristics of these features. At a site which is dominated by large-scale, persistent features, the aim of this process is to classify areas of the bank (which can be delimited spatially or by depth, or both) in terms of the impact of the migration of such features on the vertical bed level change predicted within these areas. For example, within an area of the seabed where features persist, and are mobile, transiently, seabed levels will change. The magnitude of this change, across space, and through time, is not a linear process but can be characterised broadly via determination of the mean and maximum observed height (trough to crest) of the features observed within the area, as a sandwave exists under conditions which allow that feature to attain an equilibrium crest height. For long-term morphological predictions, it is not possible to predict the evolution of these features (in terms of their shape, height, and rate of migration) with confidence. Thus, to account for the potential migration of these features, the growth potential is determined within each region of the bank and included as part of confidence limits for predicted seabed levels[39]. The predicted seabed levels are then derived by the union of the model predictions, minimum and maximum RSBL and existing bathymetries and bounded by applied confidence limits. Utilising this systems-based approach ensures that all complementary forms of analysis are considered and thus, beneficially, the approach is not wholly dependent upon numerical modelling. The final check on the seabed level predictions is performed via comparison of the predicted LSBL against the interpreted thickness of the sand deposit (or the potentially erodible layer) as derived from the existing geophysical interpretation. If the predicted seabed level exceeds the predicted thickness of the sand deposit this indicates the perceived limit on the magnitude of erosion at that location[40] (these analyses are presented in Section 10.1).

39 This approach supports the project goal of classifying zones of the seabed based on the likely magnitude of bed level change which may occur across the lifetime of the development, across the Bank (and the export cable routes).

40 No amendments to the data have been implemented as this assumes that directly beneath the sand deposit a non-erodible (or less erodible) strata persists. The existence and the potential erodibility of such strata has not been investigated as part of this study.

10 Predicted Seabed Levels

The primary output from the study is the estimated future seabed levels which may occur across the lifetime of the development (through to 2065, see Section 5.4). In predicting future seabed levels, we have relied on an evidence-led process which combines a range of model outputs with various measured datasets, and specific detailed analysis of a range of technical topics (e.g. sandwave analysis and the determination of the RSBL). These data and analyses were then considered, and where required moderated, within an overall framework of professional judgement. The HSBL and LSBL detail the predicted higher and lower states of the system during the lifetime of the development and thus demonstrate the potential envelope of potential variation we might expect to see at any time over this period. Prescribed confidence limits derived from the various contributing factors, were quantified, and integrated with the estimated seabed levels.

Figure 225 and Figure 227 presents cross-section profiles showing predicted seabed levels (i.e. estimated highest and lowest system states) derived from the model simulations, respectively. Figure 226 and Figure 228 shows the integration of all available surfaces, including all applied confidence limits, to derive the HSBL and LSBL, respectively.

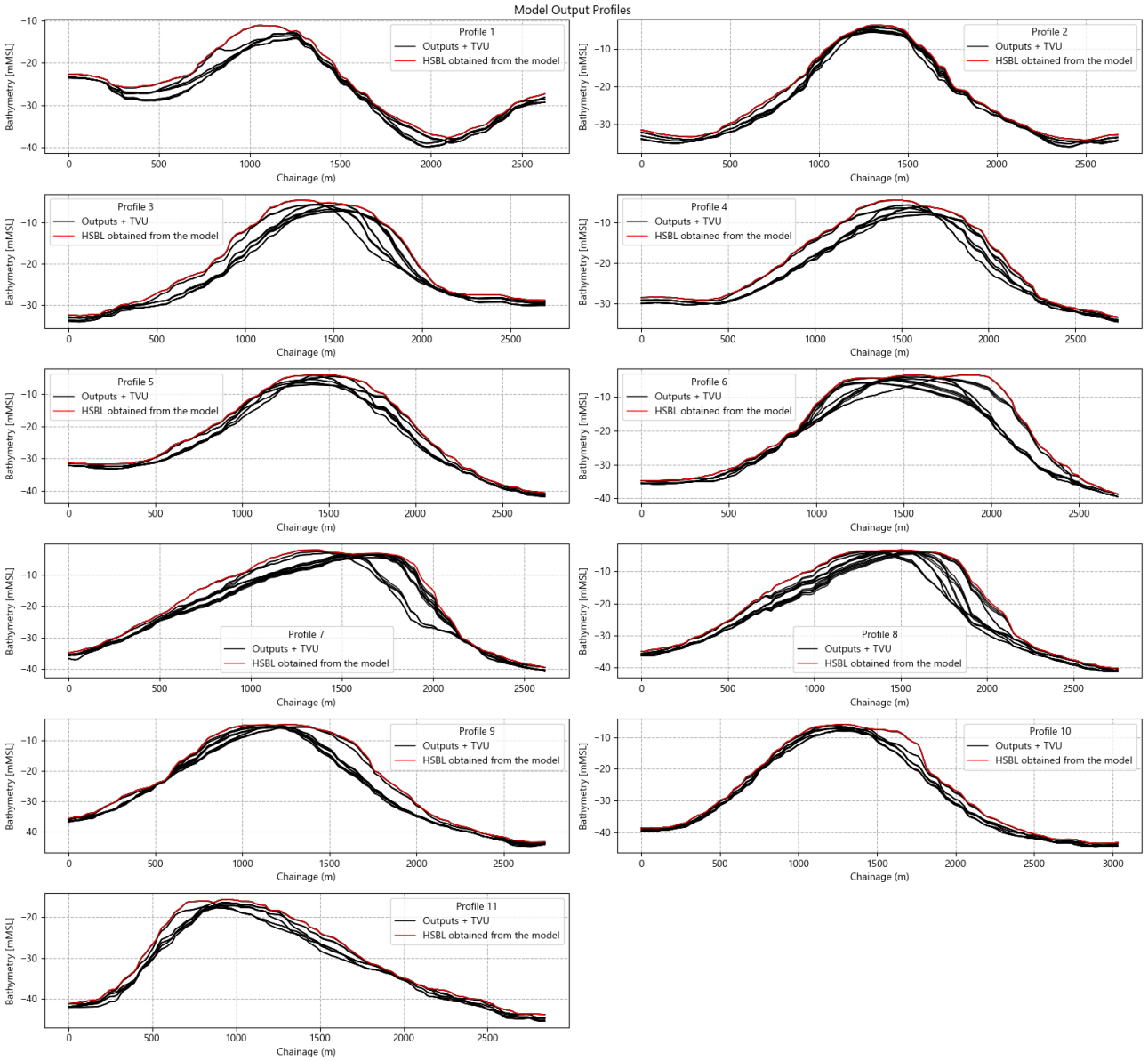


Figure 225. Predicted highest system state for Arklow Bank. The data are extracted from the 24 model simulations for locations along the length of Arklow Bank, presented in the form of cross-section profiles. The HSBL is traced and highlighted in red.

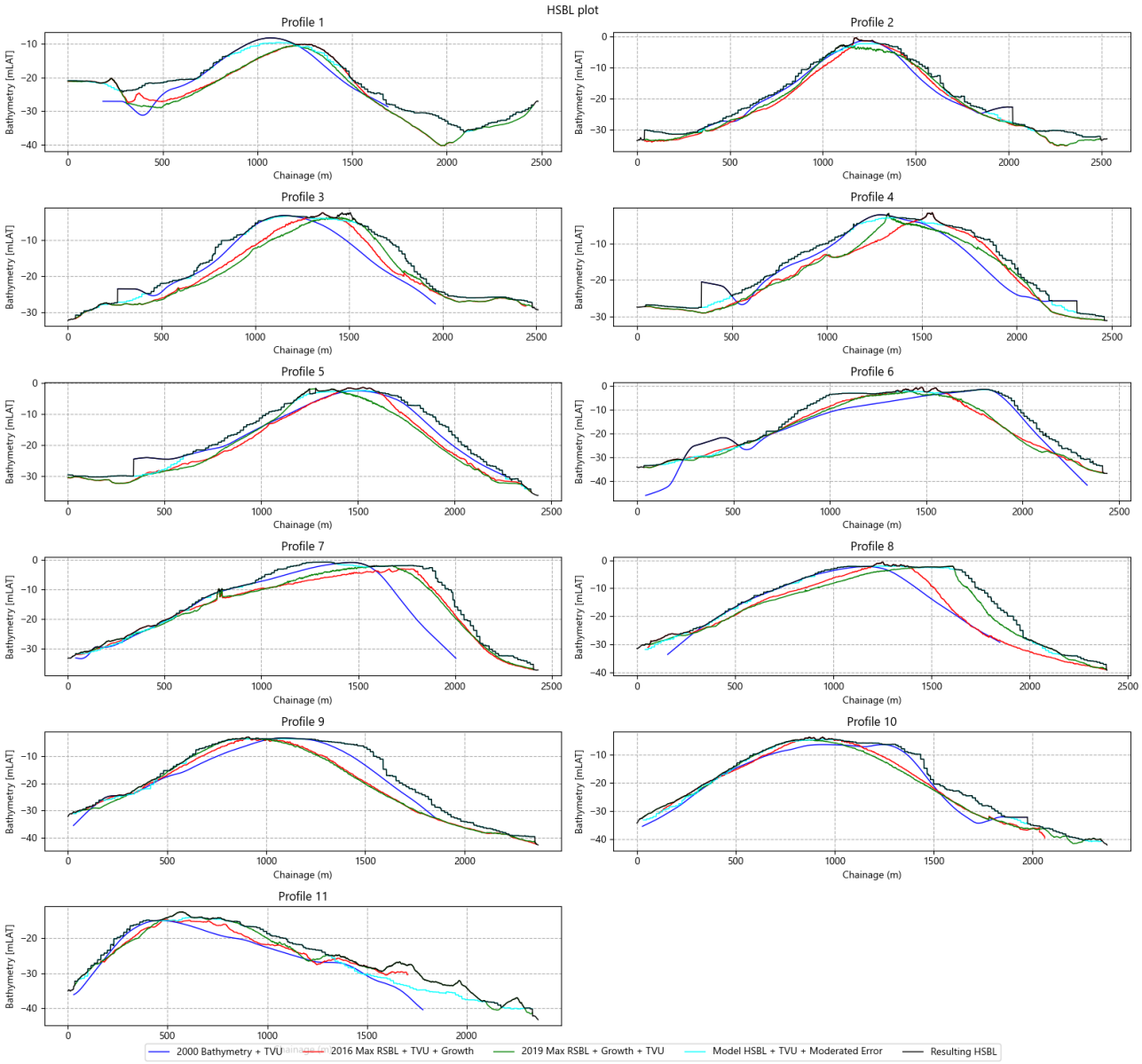


Figure 226. Surfaces derived from model outputs, complementary analysis (i.e. derived RSBL's), and existing bathymetries including for relevant contribution to applied confidence limits presented in the form of cross-section profiles along the length of Arklow Bank. The resulting, composite, HSBL is traced.

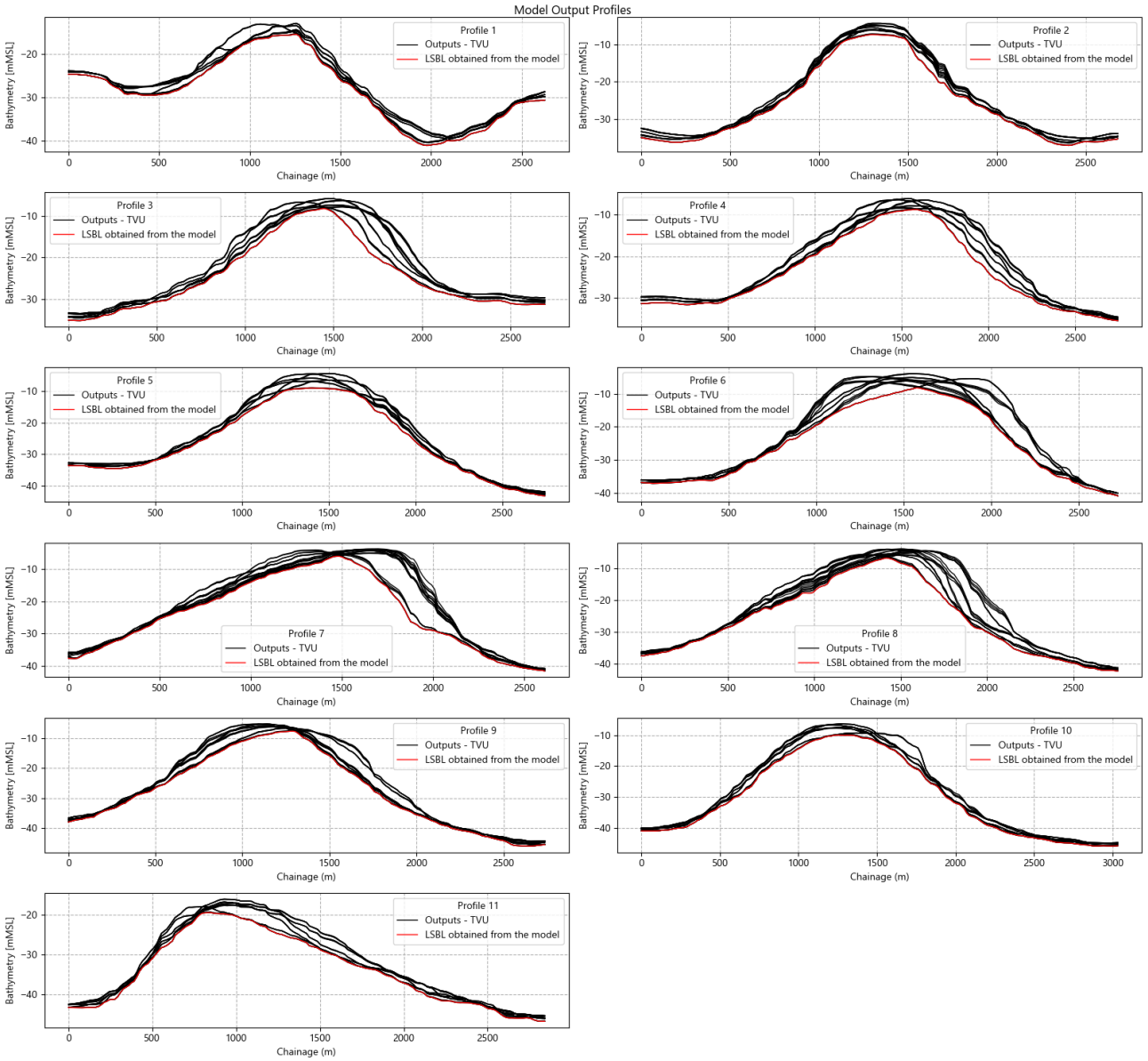


Figure 227. Predicted lowest system state for Arklow Bank. The data are extracted from the 24 model simulations for locations along the length of Arklow Bank, presented in the form of cross-section profiles. The LSBL is traced and highlighted in red.

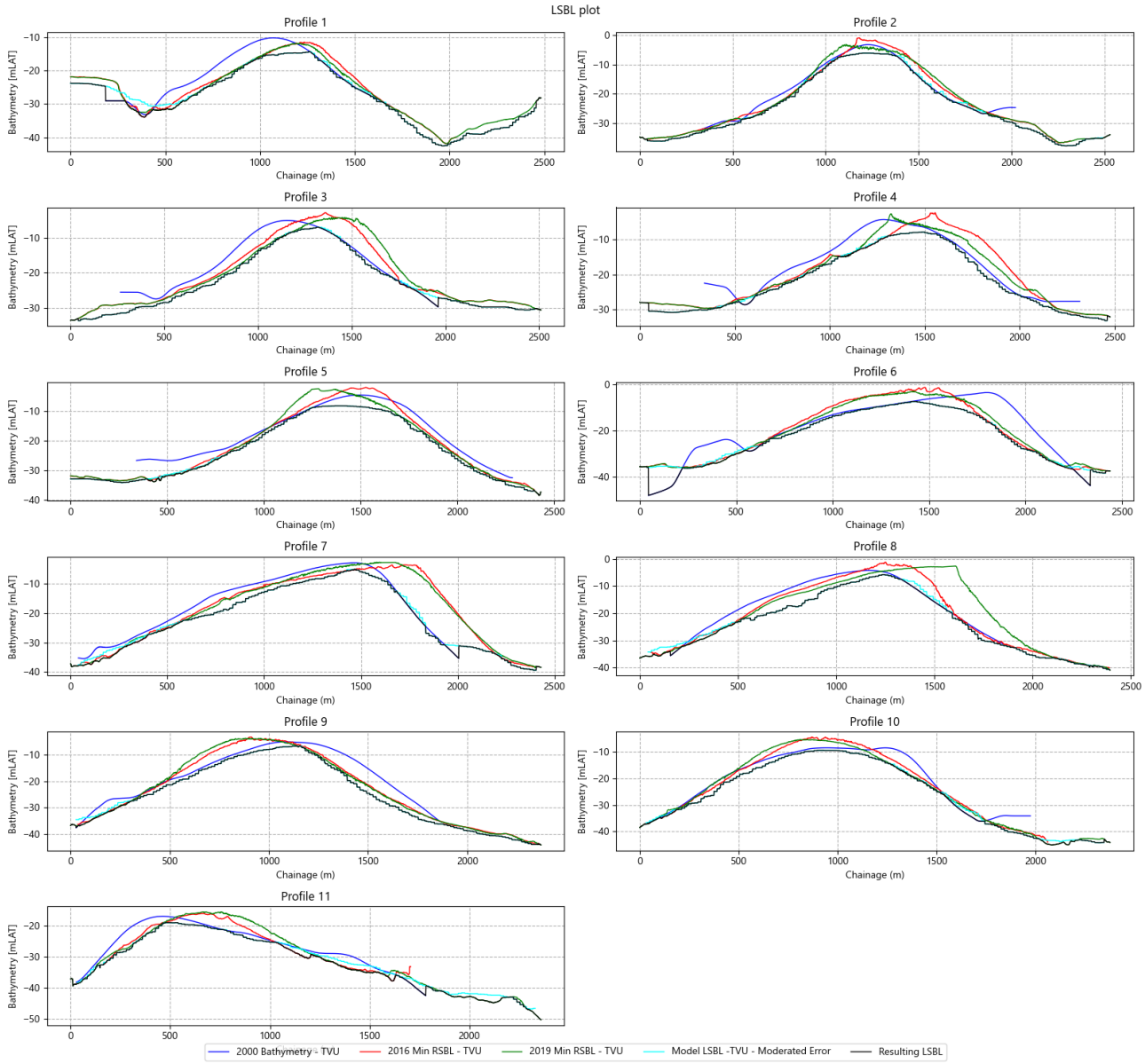


Figure 228. Surfaces derived from model outputs, complementary analysis (i.e. derived RSBL's), and existing bathymetries including for relevant contribution to applied confidence limits presented in the form of cross-section profiles along the length of Arklow Bank. The resulting, composite, LSBL is traced.

By comparing the estimated highest and lowest system state to the 2019 bathymetry, the predicted magnitude of bed level change which may potentially occur was determined. Figure 229 and Figure 230 shows the predicted magnitude of bed level change across the development area for the HSBL and LSBL, respectively. Cross- section profiles, showing the estimated potential envelope of seabed level variation along the length of Arklow Bank are presented in Figure 231. The magnitude of potential seabed level change within the different regions of the bank is summarised in Table 21.

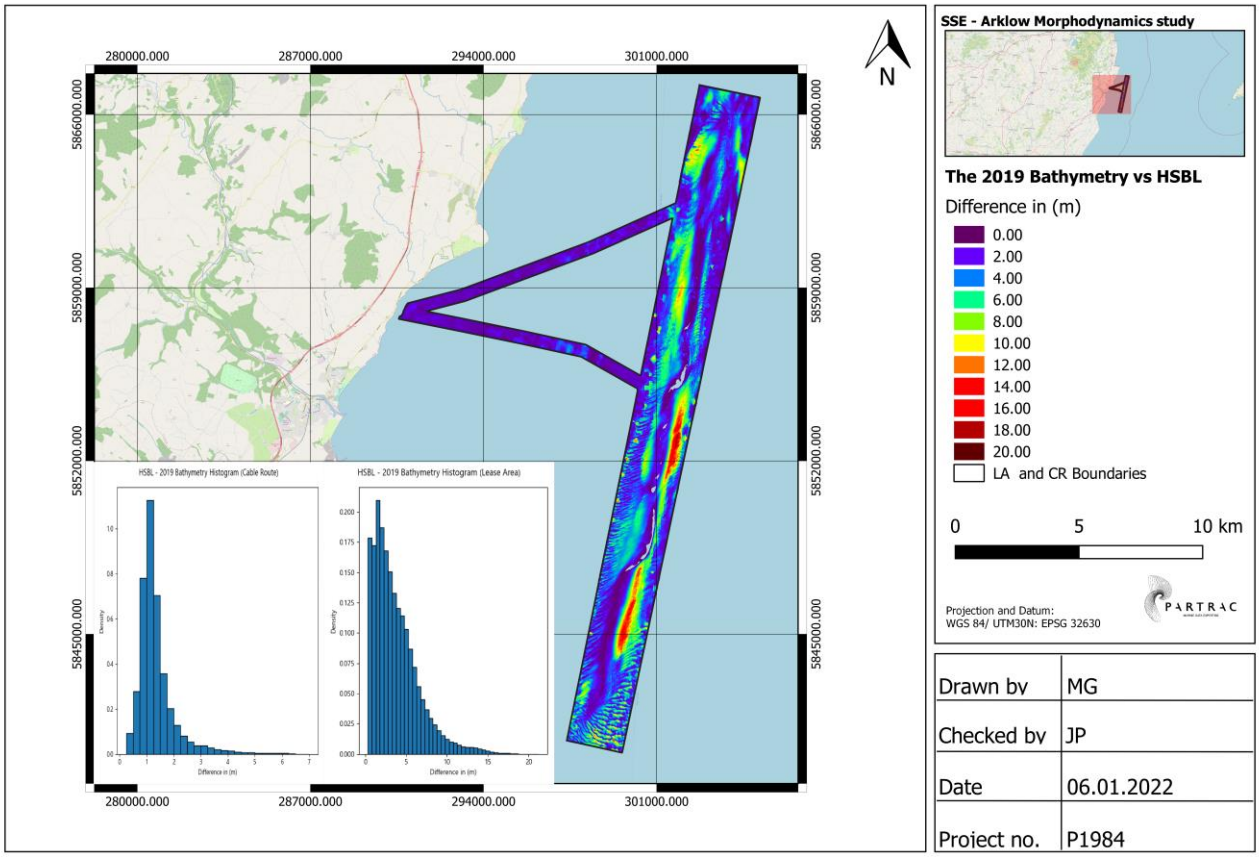


Figure 229. HSBL compared to the 2019 bathymetry showing the potential magnitude of raising of the seabed level predicted to occur across the lifetime of the development. The absolute difference between the two datasets is presented, however as this is the LSBL these differences reflect potential raising of the seabed level.

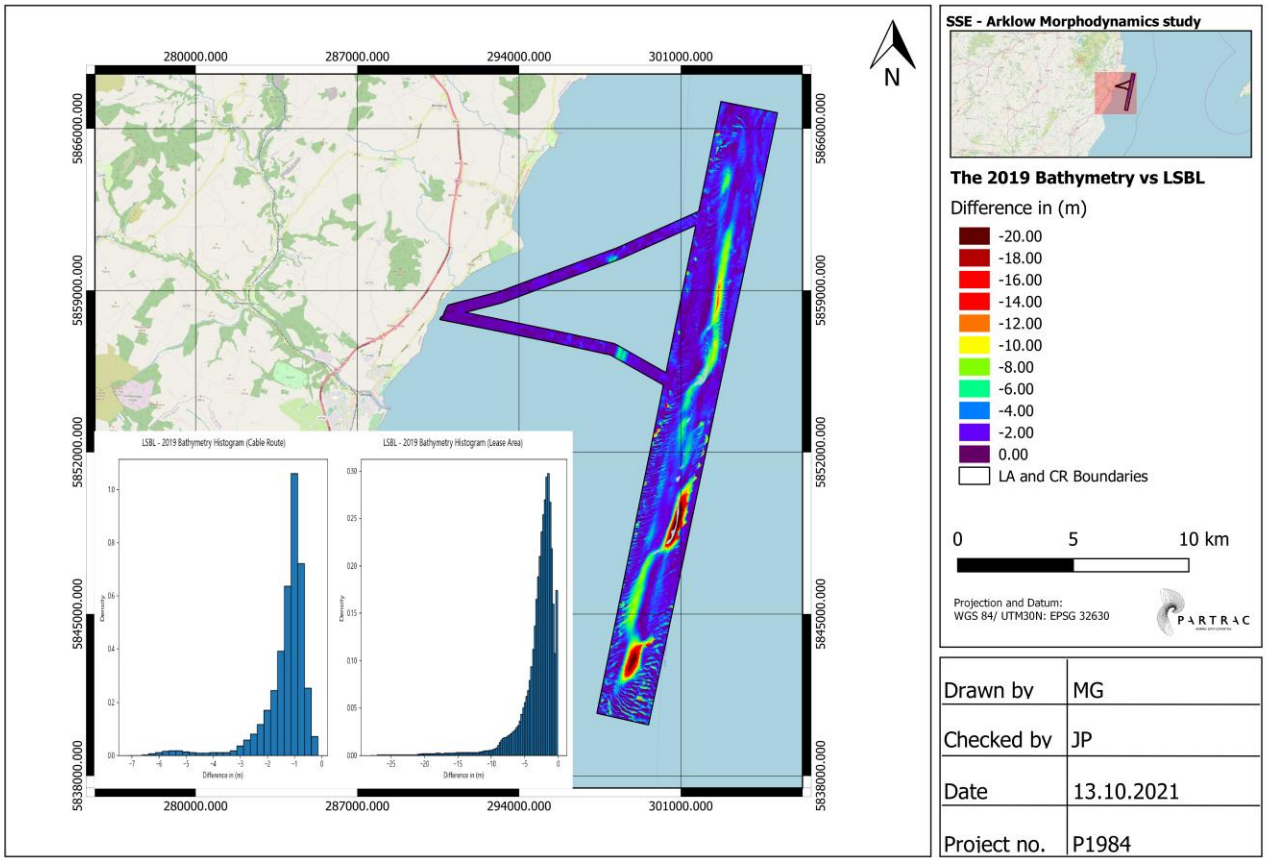


Figure 230. LSBL compared to the 2019 bathymetry showing the potential magnitude of lowering of the seabed level predicted to occur across the lifetime of the development. The absolute difference between the two datasets is presented, however as this is the LSBL these differences reflect potential lowering of the seabed level.

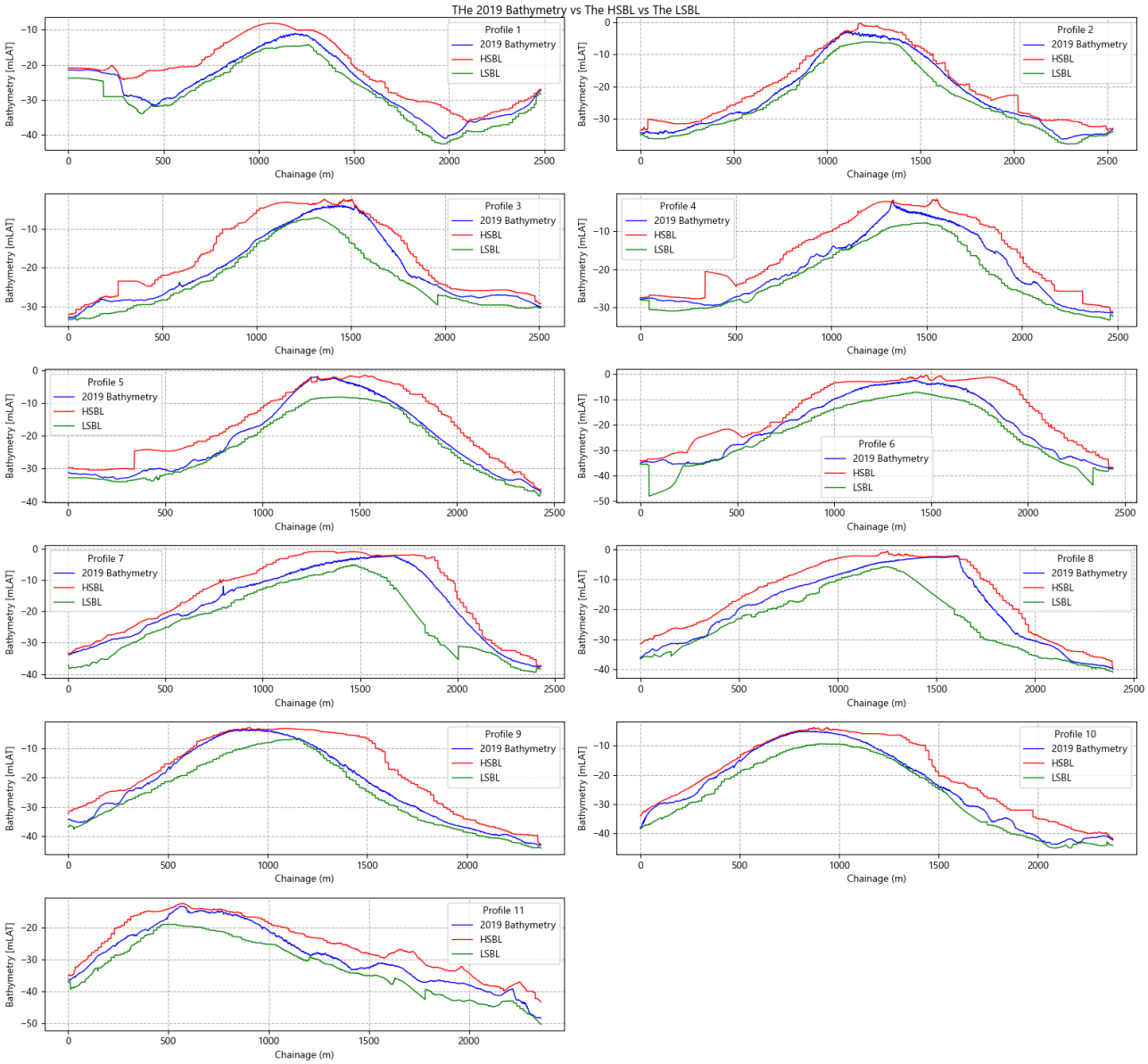
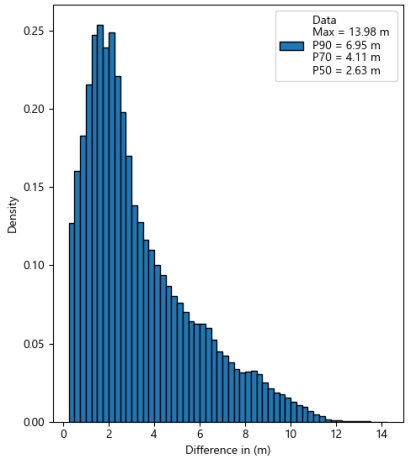
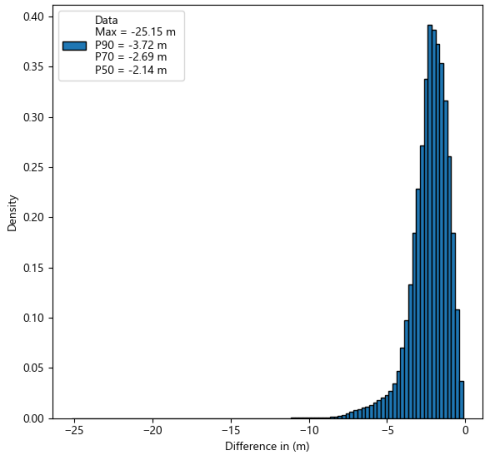
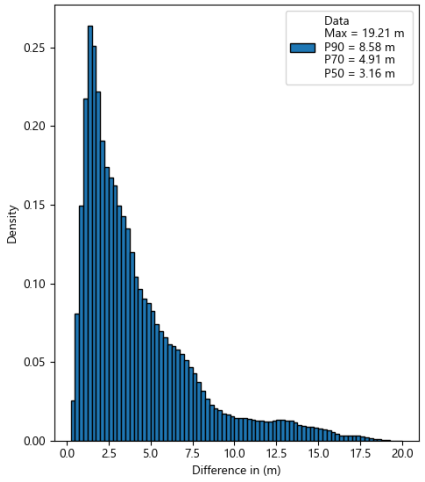
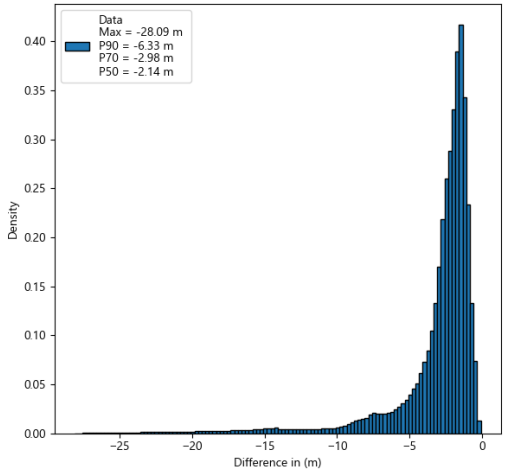
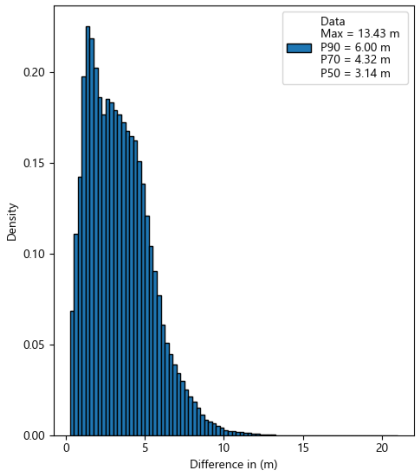
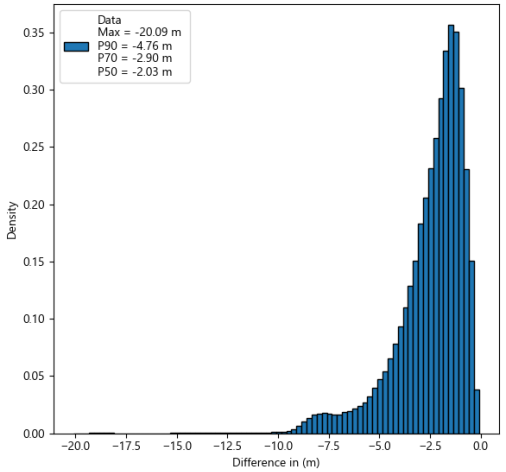
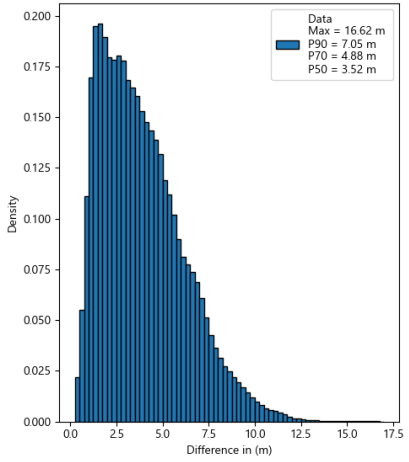
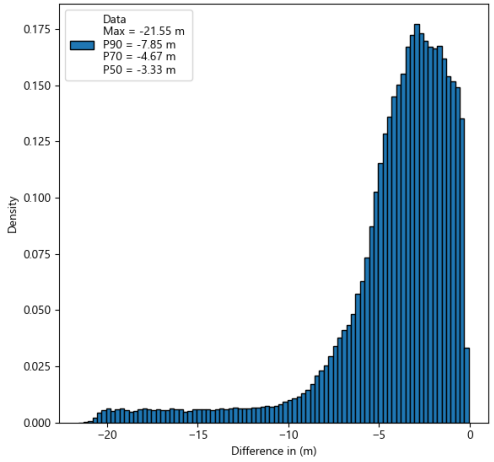
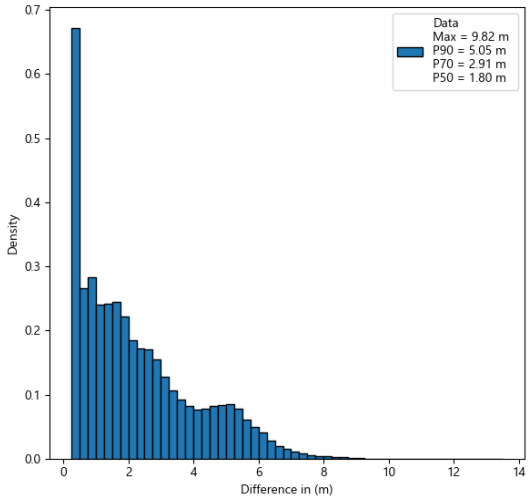
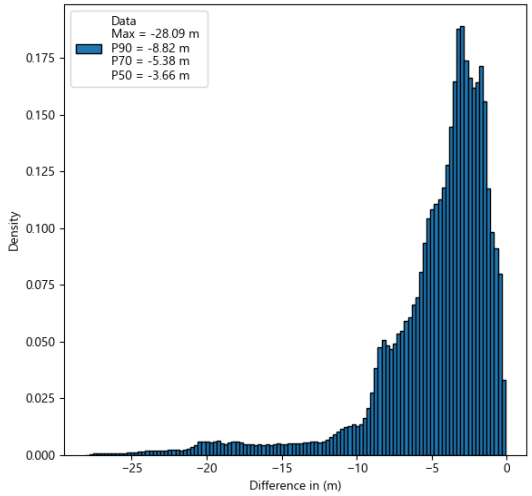
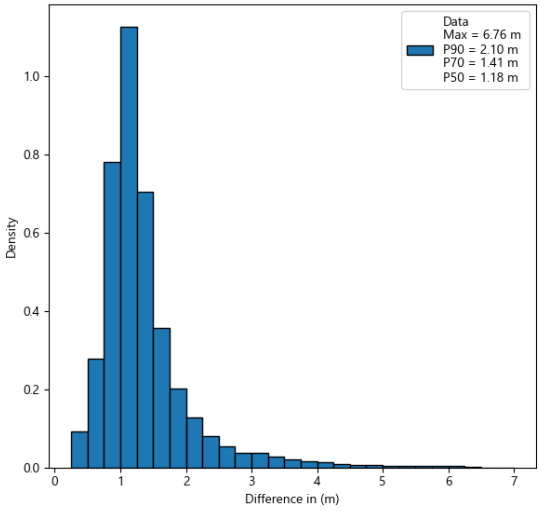
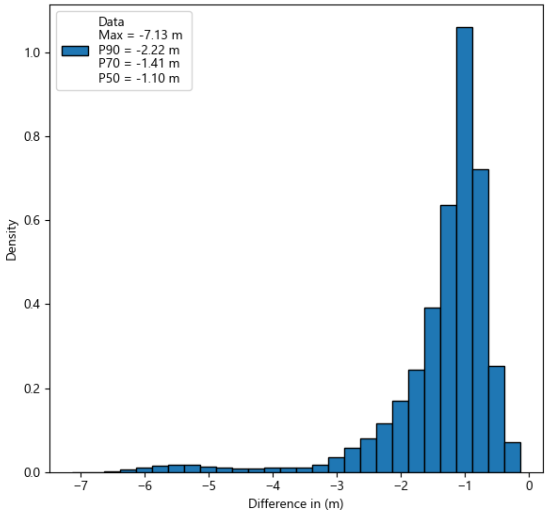


Figure 231. Cross-section profiles showing the potential envelope of seabed level variation which may occur across the lifetime of the development. The 2019 bathymetry is shown for reference.

Table 21. A summary of the predicted magnitude of lowering or raising of the seabed level which may occur across the lifetime of the development, split by region.

Region	Potential magnitude of seabed level change	Potential raising (m)	Potential lowering (m)
Head of the bank (to the north)	Towards the head of the bank the maximum potential for seabed raising is circa. 14 m (p90 = 6.95 m), but typical values range between 2 to 4 m (p50 = 2.63 m). The maximum potential for seabed lowering in this region is estimated to be circa. 25 m (p90 = 3.72 m), though typical values for predicted lowering are between 2 to 4 m (p50 =2.14 m).		
East Flank	On the east flank of the bank the maximum potential for seabed raising is circa. 19 m (p90 = 8.58 m), but typical values range between circa. 3 to 5 m (p50 = 3.16 m). The maximum potential for seabed lowering in this region is estimated to be circa. 28 m (p90 = 6.33 m), though typical values for predicted lowering are between 2 to 4 m (p50 =2.14 m).		

Region	Potential magnitude of seabed level change	Potential raising (m)	Potential lowering (m)
West Flank	On the west flank of the bank the maximum potential for seabed raising is circa. 13 m (p90 = 6.00 m), but typical values range between circa. 3 to 4 m (p50 = 3.14 m). The maximum potential for seabed lowering in this region is estimated to be circa. 20 m (p90 = 4.60 m), though typical values for predicted lowering are between 1 to 4 m (p50 =2.03 m).		
Tail of the bank (to the south):	At the tail of the bank the maximum potential for seabed raising is circa. 16 m (p90 = 7.05 m), but typical values range between circa. 3 to 5 m (p50 = 3.5 m). The maximum potential for seabed lowering in this region is estimated to be circa. 22 m (p90 = 7.85 m), though typical values for predicted lowering are between 1 to 6 m (p50 =3.33 m).		

Region	Potential magnitude of seabed level change	Potential raising (m)	Potential lowering (m)
Shallowest regions of the bank (i.e above the -10m contour as observed in the 2019 bathymetry)	Across the shallowest regions of the bank the maximum potential for seabed raising is circa. 10 m (p90 = 5.05 m), but typical values range between circa. 1 to 3 m (p50 = 1.80 m). The maximum potential for seabed lowering in this region is estimated to be circa. 28.09 m (p90 = 8.82 m), though typical values for predicted lowering are between 1 to 6 m (p50 =3.66 m).		
Export cable routes	Along the export cable routes the maximum potential for seabed raising is circa. 7 m (p90 = 2.10 m), but typical values range between circa. < 1 to 2 m (p50 = 1.18 m). The maximum potential for seabed lowering in this region is estimated to be circa. 7 m (p90 = 2.22 m), though typical values for predicted lowering are between < 1 to 2 m (p50 =1.10 m).		

10.1 LSBL vs. the Depth of the Mobile Layer

Comparing the predicted LSBL with the interpreted thickness of the potentially mobile sediment layer (i.e. the depth below seafloor of Unit 2 (See Section 8.6.2) indicated that in isolated locations along the export cable route, the predicted LSBL exceeds the interpreted thickness of the (potentially) mobile sand/gravel deposit. Figure 232 presents these analyses and reveals along the proposed cable routes, in isolated locations moving towards shore, the LSBL is predicted to exceed the depth of the non-erodible layer by up to circa. 1.5 m. Across the lease area, typically, the LSBL is not predicted to lower beyond the level of the interpreted non-erodible layer. However, on occasion, in highly isolated locations located near to the southern cable route junction, and towards the southwest of the bank, the predicted LSBL exceeds the interpreted depth of the mobile layer by up to circa. 1 m.

Note, within the context of this study, where the predicted erosion exceeds the interpreted thickness of the sand/gravel deposit the predicted seabed levels have ***not*** *been amended to reflect this. It is recommended that these data should be reviewed and updated when the geophysical data have been adequately ground-truthed following completion of the GI campaign, and greater confidence exists that the underlying deposit is likely to be non-erodible (or less erodible) than the overlying sand / gravel deposit.*

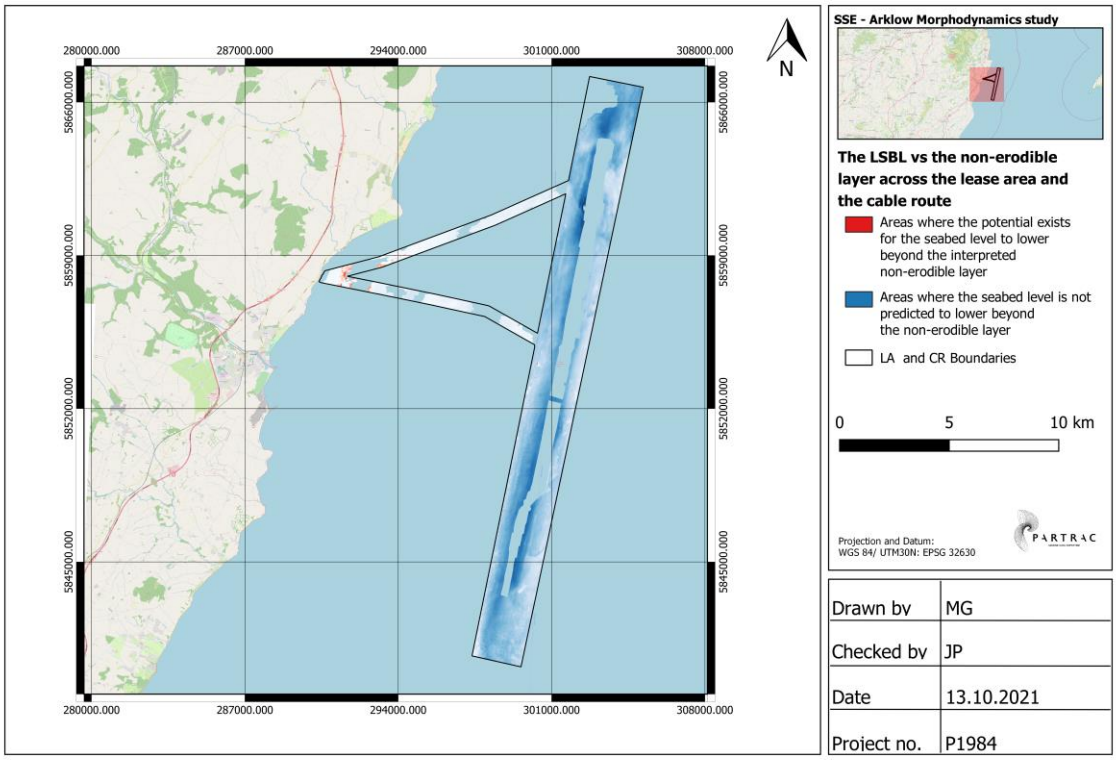


Figure 232. Comparison of the predicted LSBL against the depth of the interpreted non-mobile layer (seabed unit 2, GDG 2020). The regions coloured in red, shows where the seabed was predicted to lower beyond the level coincident with the interpreted non-erodible layer.

11 Implications for Foundations and Cabling

The foregoing analysis highlights the complex, highly dynamic, sediment transport and morphodynamic regimes which prevail across Arklow Bank and the wider lease area. Contrastingly, the foregoing analysis also shows the two proposed export cable routes, extending from the lease area to the coast, appear to be relatively stable in terms of sediment mobility through time. The following section summarises the consortium's view on the implications of the findings of the study of site morphodynamics for foundations and cabling. This draws upon our understanding developed over the course of the study and is provided to support dissemination of the study findings to downstream users of the study outputs. The greatest risk to seabed assets across the lease area and along the export cable route (principally in the area coincident with Seven Fathom Bank) is from the migration of mobile bedforms and changes to bank shape, and profile. Risk is considered via an assessment of the magnitude of vertical change and the duration of the effects. For example, regarding duration, sandwaves are predicted to be a transient, high-frequency migration and of relatively low amplitude (noting here very large sandwaves exist within the lease area). In comparison, repositioning of parts of the sandbank is characterised by low frequency migration and high magnitude, and potentially permanent or semi-permanent changes to seabed levels over the lifetime of the development.

11.1 Layout Optimisation and Seabed / Structure Interaction

Morphodynamic risks are related to large-scale (in the order of metres) seabed variations which occur due to natural processes unrelated to the presence of wind farm infrastructure. The risks associated with site morphodynamics are typically mitigated via careful selection of foundation locations and/or routing of inter-array cables with respect to the anticipated magnitude of vertical seabed level change. Alternatively, appropriate mitigation measures may be adopted. Often at complex sites, design relies on a combination of both options.

Across the lease area, the potential exists for significant bed level change to occur (i.e. on the order of metres), in almost all locations. Areas which show enhanced potential to display greater magnitude of change also persist (e.g. in areas where large scale sandwaves persist in the southern tail and areas along the east and west flanks of Arklow Bank). When assessing such a dynamic, and complex site, it is judicious to not only consider areas where the greatest potential magnitude of vertical seabed level change is predicted to occur, but also the confidence associated with those predictions, the likelihood of occurrence, and the duration/persistence of such change. Such assessment must consider the short-term processes which drive long-term changes to bank morphology. Consideration of such issues leads us to postulate the following:

- At the bank scale, it has been concluded that large scale bathymetric patterns are unlikely to change significantly over the lifetime of the development[41]. Greater confidence exists in determining the magnitude, and time scales, of vertical seabed level change associated with sandwave migration, rather than those changes associated with movement of the bank, driven by repositioning of the crestline. Furthermore, interpretation of the available evidence from the geophysical survey appears to indicate that sandwave areas on the west flank (thinly) overlie a coarser grained deposit, suggesting for these areas, that the determined ('minimum') RSBL broadly represents a seabed level beyond which the seabed is not likely to lower.
- Somewhat counterintuitively, the findings of the study indicate that the most dynamic region of the bank (i.e. areas of the bank exposed to wave action and thus broadly shallower than the -10 mLAT contour), typically does not display the greatest magnitude of vertical bed level change. This is primarily a function of the processes which act to deliver sediment to, and thus maintain, the level of the crestline. In this region sediments are dynamic, with short-term vertical seabed level change occurring on tidal time scales associated with the formation and migration of smaller scale mobile bedforms (i.e. ripples, megaripples and smaller sandwaves). Through time, the net result of processes occurring over tidal timescales (ebb and flood), the neap-spring and lunar phases, repositions the crestline to the east and west. A persistent asymmetry in terms of magnitude and/or duration of sediment transport between flood and ebb tides at the crestline results in a net movement over years and decades, which is analogous to a tidal sandwave (albeit at a slower rate), changes the shape and profile of the bank. These changes have the potential to drive significant, and more persistent, changes to seabed levels on the east and west flanks of the bank.
- Activities performed as part of the construction, operation and decommissioning of the proposed development have the potential to bring about changes to the local, and far field, hydrodynamic, metocean and sedimentary regimes. This report does not consider such effects. However, it is recognised, that there may be a requirement to design structures to be built in more dynamic areas of the seabed (i.e. areas of the seabed influenced by, or close to, mobile sandwave features). If this were the case, the interaction of sandwave features with structures becomes an important issue for engineering design, as does dredging requirements related to seabed levelling to prepare for foundation and cable installation. The resulting (transient) bed level change (i.e. the maximum amplitude trough to crest of the local features) provides a useful metric for assessing the likely bed level change over the longer term, however the interaction of sandwave features and structures is complex and a function of the sandwave characteristics, the seabed profile, structure design and local scour.
- Typically, when siting foundations, sites are considered preferrable where minimal seabed level variation is predicted to occur over the lifetime of the development. Accretion at the seabed, is generally considered to be less significant in terms of the risk to foundations, as local scour effects counteract (i.e. erode) accreting

41 This is to say, that it is not anticipated that any wholesale shift of the bank from its base area will occur, or that observed sandwave areas will significantly alter over the lifetime of the development.

sediment. The addition of scour protection may also aid in 'fixing' the seabed level around a monopile, though the performance of scour protection can be significantly compromised by a mobile seabed and undermined if the wider seabed lowers. Thus, dredging to remove the mobile layer, to reach a less erodible layer and then placement of scour protection at this level may be required. The preliminary assessment of local scour presented in Appendix H indicates scouring around monopiles is likely to be significant and thus scour protection would be an engineering necessity for the development (as was the case for turbines installed in Phase 1 of the development). Additionally, local scour and turbulence effects, requires consideration. Thus, within the context of wider site constraints, it is recommended that suitable distances between wreck sites and structures should be maintained and, where possible, structures should not be installed in direct series (i.e. one after another) along the prevailing flow axis.

Based on the scope of the current commission it is evident that a pro-active approach to considering site morphodynamics in design is being adopted at the ABWP. Ideally, turbine locations are to be sited in areas of the seabed where a lower magnitude of vertical change is predicted to occur or targeted to bedform fields where greater confidence exists in terms of the response of the seabed through time. Within bedform fields, foundations may be installed at the crest, or within the trough, of a sandwave. However, installation within sand wave troughs will minimise risks associated with lowering seabed levels and the likelihood of free spanning cables.

11.2 Cable Exposure, Burial or Re-burial

The mobility of sandwaves, and changes to the shape and profile of the bank, pose a potential risk to inter-array cabling across the lease area, and to a lesser degree, the export cables (especially where the southern cable route traverses Seven Fathom Bank).

As cables laid on the seabed are prone to damage, cables are buried beneath the seabed (Carbon Trust, 2015). Depending on the achieved burial depth, cables may still experience periods of further burial as well as periods of exposure across the lifetime of the development as the seabed level changes. The predicted magnitude of vertical change (raising or lowering of the seabed) across the lease area, indicates that the potential exists for cables to become exposed, or over buried. Excessive lowering of the seabed level leads to cable free spanning. Accretion at the seabed can also be a significant problem for buried electricity cables due to fatigue, or due to a greater thermal insulation effect, leading to potential issues within the cable associated with overheating. Furthermore, over-burial of cables, poses issues in terms of accessing and lifting the cable for maintenance and repair. Highly mobile sediments across the shallowest regions of the bank, due to porosity and effects associated with wave influence, may also enhance risks associated with reduced burial depths.

Assuming the cable is to be buried, and the burial depth of the cable in areas where mobile bedforms persist is to be determined relative to a RSBL (or the LSBL predicted), the risk associated with the migration of sandwave features relates to the accretion of sediment across the cable location. These effects would be transient and could potentially be factored into cable design. Of greater concern would be the encroachment of the sandbank onto buried cables, detrimentally impacting the cable and creating a potentially significant risk to the operability of the wind farm over the longer term. To understand this further, time series of seabed level change (Figure 234) have been extracted from the model at pertinent locations across the lease area and export cable route (Figure 233). These data indicate, that over the period simulated, changes to the seabed level at each of these locations is almost negligible, which corroborates one of the primary conclusions of the study, that across the lease area, this is not an erosional environment, rather it is a dynamic environment.



Figure 233. The points across the lease area and export cable from which time series data of bed level change have been extracted. These data are presented in the form of time series in Figure 234.

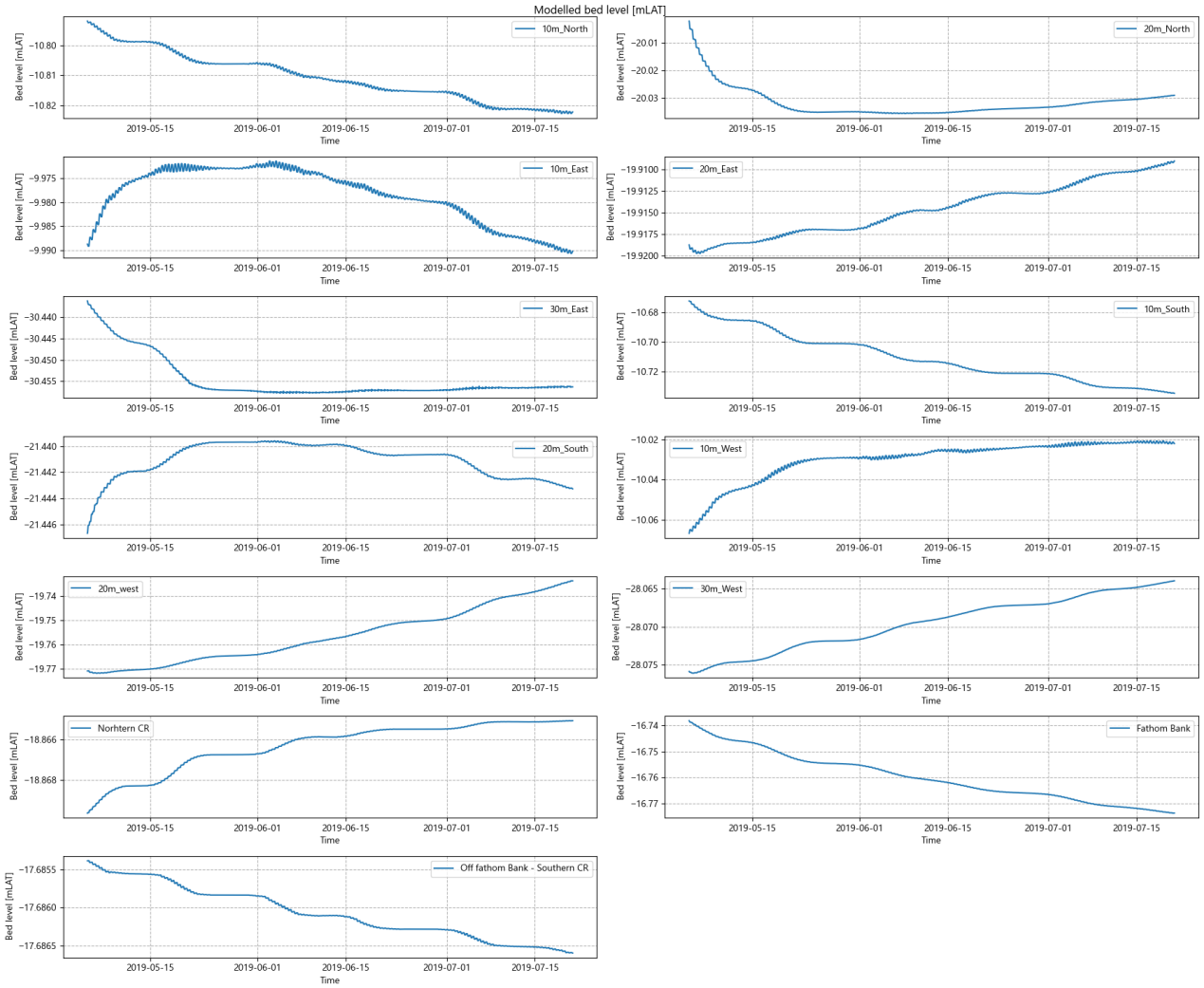


Figure 234. Predictions of seabed level change over a period of months, derived from a pertinent model simulation.

As discussed in Section 8.8, sandwave migration rates vary across the lease area, ranging from very low rates of migration (i.e., a few metres per year) up to 40 to 70 m per year. Though it varies spatially, typical wavelengths are between 150 m to 250 m and thus, in areas of the bank system characterised by high rates of migration, cable sections are likely to be influenced by rising and lowering seabed levels on multiple occasions across the lifetime of the development.

Across the bank system, the influence of seabed level variability regarding the likelihood and rate of cable exposure, burial and subsequent re-burial can be summarised as follows:

> *Sandwave areas around the flanks of the bank*: Cabling installed in sandwave areas around the flanks of the bank will be exposed to raising and lowering seabed levels over the lifetime of the development. Consideration of typical wavelengths and observed migration rates, indicate that over the 40-year design life, migrating sandwaves will raise or lower the seabed level, several times. For example, a cable buried in the trough

between sandwave crests, which display a wavelength of 250 m and a migration rate of 50 m per year, though would unlikely become exposed, would likely experience enhanced burial depths on a repeating 5 yearly cycle.

The east and west flanks: On the east and west flanks of the bank, shallowing towards the crestline, cables buried to below the established RSBL (or predicted LSBL) of the observed system state (i.e. against pre-construction survey bathymetry data)[42], over the short-term would experience slightly enhanced burial depths due to the migration of ripples and megaripples, though such effects would be transient and of low magnitude (typically < 1 m). Over the longer term (years to decades), the potential exists for a system state to occur which significantly lowers, or raises, the seabed level on the east and west flanks of the bank. Though these distinct system states occur gradually over the longer term, the resulting state of either free-spanning (or unprotected) cabling or potentially deeply buried cabling, will persist for longer periods (unless mitigation measures are taken). The frequency of occurrence and persistence of such events is difficult to predict with certainty but based on our process understanding, and assessment of historic changes to the bathymetry within the lease area, it is considered that the net response of the bank is the result of processes occurring on multiyear, or decadal, timescales (a finding corroborated by the modelling, with simulations targeting the maximum magnitude of sediment transport at the crestline showing lower magnitude changes to seabed level in comparison to those simulations targeting the maximum duration of sediment transport at the crestline).

Shallowest regions of the bank (i.e. above the -10 m LAT contour): Seabed levels within the shallowest regions of the bank are maintained by delivery of sediment to the crestline via bedload transport influenced by Coriolis. Three key processes occur in this region:

1. Persistent delivery of sediment to this shallowest region of the bank (and over the crestline);
2. The formation, migration, and growth of ripple, megaripple and small-scale sandwaves which can lead to multiple crestlines; and,
3. Periods of wave influence which sweeps these areas free of bedforms and smooths the bank profile (note; the tidally dominant, highly mobile sediment regime results in bedform reformation occurring quickly after such an event). Furthermore, wave influence can drive significant localised changes to the seabed level as evidenced in the period 2016 to 2019 in the area of the bank commonly referred to as *'the hook'*.

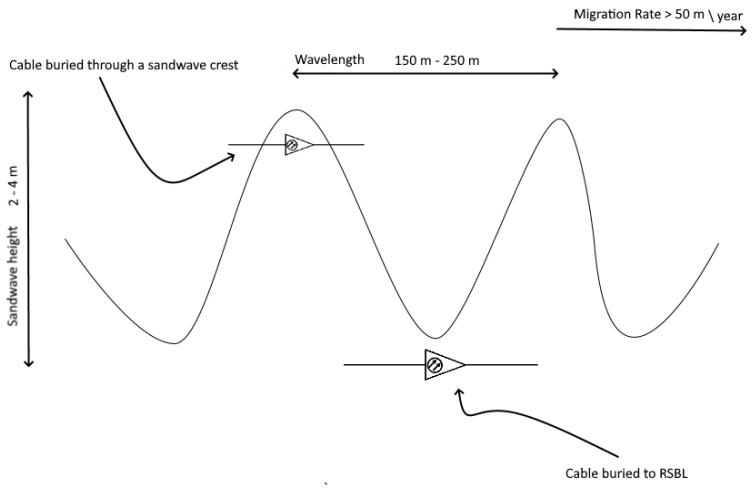
These processes result in both persistent and transient, raising and lowering seabed levels (of between circa 1 m to 3 m) over the lifetime of the development associated with the formation and migration of mobile

42 As the RSBL is derived from bathymetry data. At Arklow Bank, which is anticipated to display multiple distinct system states across the lifetime of the development, the RSBL should be estimated using the latest available bathymetry data.

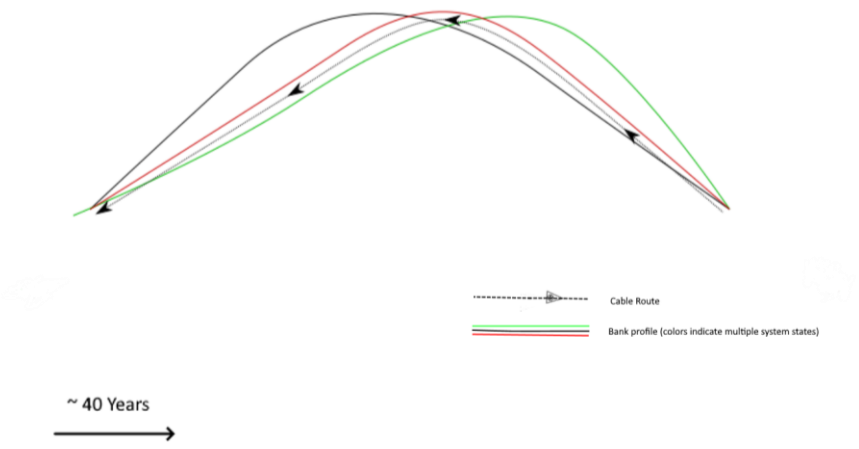
bedforms and wave influence. As these bedforms are dominantly comprised of ripples and megaripples (characterised by wavelengths of circa 5 to 20 m, and small-scale sandwaves, (characterised by wavelengths of circa 50 m to 100 m), a cable buried below the RSBL (of the observed system state i.e. against pre-construction survey bathymetry data), would likely experience enhanced burial depths repeatedly across the lifetime of the development. If, due to shallow water wave effects, buried cables became exposed, it is hypothesised that cabling in this region would potentially be re-buried relatively quickly (i.e. over periods of a few weeks or months) due to the reformation and migration of mobile bedforms (noting here that local scouring around a free-spanning cable may negate re-burial). As described previously, the net effect, over the period of years and decades, of the processes described above, reposition the crestline with significant effects on seabed levels on the east and west flank. These processes typically have limited influence on seabed levels in the shallowest regions of the bank. This is due to east – west movement at the crestline driving changes to the shape and profile of the bank, rather than directly lowering the level of the crestline.

Export Cable Routes: Comparatively, along the proposed export cable routes, the observed and predicted, vertical change is typically low. From a sediment mobility perspective, the northernmost cable route (which avoids Seven Fathom Bank) would be the preferable route to shore. This is because Seven Fathom Bank (though the analysis is significantly data limited), though far less dynamic than Arklow Bank, is exposed to those processes which drive changes to the bank shape and profile on Arklow Bank. Though the export cable routes appear to be broadly stable in terms of the observed seabed level, as water depths shallow towards the nearshore boundary of the study area, the risk associated with seabed mobility increases. Due consideration should be given to this issue at which time the data from the GI campaign becomes available to the study.

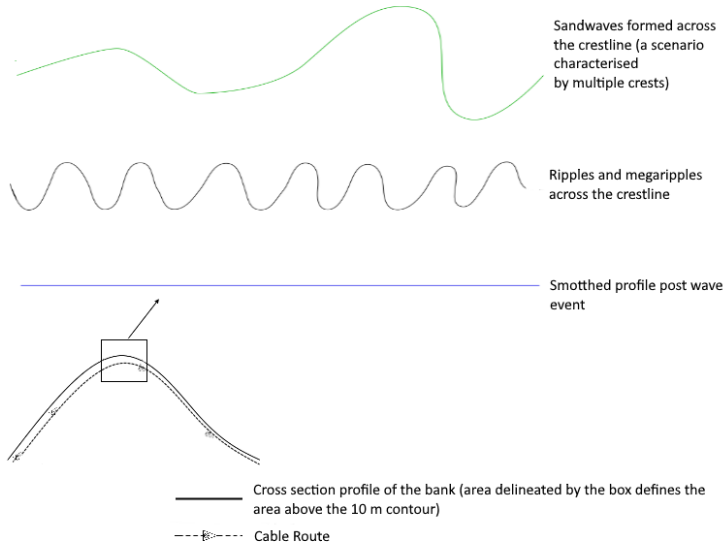
Figure 235 presents a schematic diagram detailing the implications for cabling in different process environments across the bank system.



1. *Sandwave areas around the flanks of the bank*



2. *The east and west flanks*



3. *Shallowest regions of the bank (i.e. above the -10 m contour)*

Figure 235. Schematic diagram presenting the implications for cabling across different process environments across the ABWP.

12 Concluding Remarks

This study was developed and undertaken to assess site morphodynamics within the ABWP lease area and along the two export cable routes. Seabed mobility issues have the potential to detrimentally impact upon infrastructure placed on, or under, the seabed and thus the subject requires careful consideration during the design stage of any offshore development. Morphodynamic risks are related to large-scale seabed variations (due to natural processes unrelated to the presence of structures). This study has strived to improve the overall understanding of the regional and local sediment regime in order to, as best as possible and within the limitations of the available data, predict the likely future morphological response of the seabed over the lifetime of the development and thus estimate future seabed levels to support design.

A total of 31 seabed levels derived from measured datasets, complementary analysis, and model predictions, were utilised to quantify the potential range of seabed level variability which is expected to occur across the lifetime of the development. These predictions include confidence limits which comprise the precision of the survey data, the confidence limits associated with the model predictions and the evolution of mobile bedforms. The seabed exists as a *live bed* sediment regime, and thus it is highly likely that significant morphological adjustment of seabed levels will occur over the lifetime of the development, a conclusion supported by analyses of the bed level change observed within consectutive bathymetric surveys. Comparison of the estimated LSBL, and HSBL, with the most recent bathymetry from 2019 shows a predicted (albeit highly localised) maximum estimated local seabed level lowering and raising of > 15 to 20 m. This scale of bed level variation serves to demonstrate, where avoidance and / or mitigation measures are not implemented, the significant risk to foundations and cabling associated with seabed dynamics across the lease area. Three distinct environments exist across the development area:

- Arklow Bank (coincident with the lease area)
- Seven Fathom Bank (the smaller satellite bank of Arklow Bank; across which the southernmost proposed export cable routes crosses); and,
- Export cable routes (which persist across areas of the seabed between the bank and the nearshore).

The following concluding remarks represent the principal findings of the study for Arklow Bank:

- Arklow Bank is maintained in dynamic equilibrium by the perpetual tidal processes, episodic wave activity, atmospheric (i.e. surge related) effects and Coriolis. These processes interact spatially (i.e. varying across the bank and with depth), and temporally (varying on timescales from a single tide [asymmetry between flood and ebb tides] through to decadal changes). The non-linear, and complex, processes that drives the evolution of such dynamic systems are typically characterised by multiple potential response pathways and thus have the potential to display multiple distinct system states.
- The contemporary form of Arklow Bank is classified as an Open Shelf Linear Bank. These bank types are

characterised by a clockwise circulation of sediments around the bank which is a function of the topography and orientation of the bank, tidal asymmetry (i.e. an ebb and flood dominance on the west and east side of the bank, respectively) and Coriolis which promotes transport along the bank and onto the bank flanks, towards the crest.

- Sediment transport from the north of Arklow Bank through Wicklow Trough is considered the primary, contemporary, source of sediment supply to the bank. Though potential connectivity between the coast and the bank has been demonstrated via targeted particle tracking simulations. In comparison, sediment pathways from the shoreline and from fluvial sources (i.e. the Avoca river) are considered to be limited. The foregoing analysis leads to the conclusion that the bank acts as a semi-closed system (i.e. the net sediment volume retained across the bank remains largely consistent over time).
- Arklow Bank is in a location characterised by complex hydrodynamic processes (i.e. strong flow velocities despite a low tidal range, periods of double high water) due to its proximity to an amphidromic point, which, during spring tides is degenerate (i.e. located on land). The tidal regime is characterised by a flood and ebb dominance on either side of Arklow Bank driven by the tidal asymmetry, this drives net sediment transport (as evidenced by the net migration of sandwaves either side of the bank) southward on the east flank and northward on the west flank. The sediment transport regime is tidally dominated across all water depths. Across the lease area, regardless of depth, sediments are highly mobile, with mobility enhanced in shallow water regions exposed to waves.
- As the general sediment transport regime is tidally dominant it is concluded that wave action plays a potentially limited role in the sediment transport regime occurring across the bank system. The evidence indicates that only the largest waves impacting the site, possess sufficient energy to mobilise seabed sediments at water depths greater than the –10 mLAT contour. However, in the shallowest regions of the bank, waves have a significant influence on local sediment transport, enhancing the relative mobility as waves impact the bank and storms track over the site. Such influence is dominantly observed at the crestline, where, on occasion, wave action sweeps the crestline free of bedforms. These effects are short-lived however and during a few tides, via bedload transport processes, bedforms reform and sediment delivery to the crestline is re-established.
- Cross-bank flows are caused by a tidal head difference which occurs during the ebbing and flooding tide between the east and west of the bank and arise because of the shallow nature of the crest region. The head difference creates a weir effect as water is held on one side of the bank, before 'flushing or surging' over the top. This effect is enhanced within the central regions of the bank, which is a function of the shape and profile of the bank in this area.
- The crest of Arklow Bank behaves in an analogous fashion to the crest of a large tidal sandwave, albeit over longer time scales. Predominantly, through time, the upper part of the bank, including the crestline, moves both east and west, rather than migrating in a single direction. A review of the historic bathymetry data

showed significant bed level change occurred due to the repositioning of the flanks of the bank profile with seabed levels lowering and rising by between 18 and 25 m, respectively.

- Several authors have postulated about whether the full bank feature is migrating in position over the longer-term. A holistic view of all available data leads to the conclusion that the bank (as a whole feature) is not likely to display a net shift in its relative location on the seabed, over the lifetime of the development (i.e. there is no residual, long-term shift in location). The bank has remained, broadly in its present location (relative to the coastline), over at least the last century or so. Asymmetry in cross bank flows, drives a progressive shift of the crestline in an easterly or westerly direction. However, this condition does not exist permanently, and any propensity for net bank movement is curtailed by the clockwise circulatory sediment transport around the base of the bank. In other words, whilst the bank itself displays changes in its profile, shape and elevation, the footprint of the sandbank on the seafloor remains ostensibly the same over extended timeframes due to a tidally driven circulatory transport around the bank. This limiting position can be defined as the point at which the rate of accretion at the crestline is less than, or equal to, the (slope induced) rate of sediment transport from the crestline to the base of the bank. If this condition occurs, the crestline will not continue to move westward or eastward.
- Spatial plots of observed bed level change during the period 2016 to 2019, also show large-scale, mobile, sandwaves persist on the western and eastern flanks and at the head of the bank to the north and the tail of the bank to the south. In these areas up to circa. 6 m vertical change was observed over this period associated with bedform migration (noting here sandwaves of greater than 10 to 15 m in height are observed in the sandwave field to the south of the bank).
- A coupled hydrodynamic / wave / sediment transport model was developed. Validation of the hydrodynamic and wave models, termed the 'driving models' of sediment transport simulations is described by MetOceanWorks Ltd (2021). Validation of the sediment transport model focused on the ability of the model to represent changes in bathymetry observed over the periods between the available surveys of the lease area, namely 2000 to 2016, 2016 to 2019 and for the cable routes, namely 2011 to 2019. To estimate future seabed levels and determine the potential highest and lowest system states which may occur over the lifetime of the development, an integrated approach was applied relying on a robust process understanding complemented by numerical modelling efforts. This relied upon classifying, as accurately as possible, the response of the seabed, and the bank feature, to the driving processes of sediment transport. This was designed to establish a sufficiently detailed understanding to inform the application of numerical modelling to support determination of the potential envelope of seabed level change likely to occur across the development area, over the lifetime of the development
- Across the lease area, model performance during validation, indicated that the model was replicating key driving processes and producing broadly, correct patterns of change, however significant discrepancies existed between the predicted and observed values of seabed level change over the period of assessment

(2000 to 2019). This was a function of the complexity of the site, the scale of seabed level variability, gaps in critical baseline data, and the intrinsic limitations of any modelling approach (and presently available software). As such, an approach which moderated the application of the model, focusing modelling efforts solely on supporting the assessment of the lateral (east-west) movement of the crestline and the subsequent effects on the shape and profile of the bank, was established. These outputs were subsequently integrated with measured bathymetry datasets and complementary analyses (i.e. derived RSBL's), and appropriate confidence limits applied.

- Morphological model simulations, informed by the foregoing analyses, were performed to assess the potential response of the seabed to various driving conditions. Predicted seabed levels which were determined from a composite of 31 surfaces, provide the estimated highest and lowest system states likely to occur over the lifetime of the development. The performance of the model during validation confirmed that it was technically inadvisable to apply the model directly to forecast morphological change into the future (even over the relative short-term to the point of installation in Q3 in 2025).
- Due to the scale of potential seabed level variability observed over the past two decades and which are predicted to continue to occur over the lifetime of the development, it is strongly recommended that additional study, data collection and targeted further monitoring (particularly in the period up to installation) is considered.

The following concluding remarks represent the principal findings of the study for Seven Fathom Bank:

- Seven Fathom Bank forms a satellite bank to Arklow Bank which is located approximately 1.5 km to the west of Arklow bank. Seven Fathom Bank has a similar orientation to that of Arklow Bank but is smaller being circa 5.5 km in length along the north – south axis. The magnitude of sediment transport observed on Seven Fathom Bank is reduced in comparison to Arklow Bank, which is a function of the deeper water depths across the bank crestline and sheltering from Arklow Bank.
- Across Seven Fathom Bank limited data is available to support the assessment of historic seabed level change, and the influence on seabed levels of mobile bedforms. Where the proposed southern export cable route traverses Seven Fathom Bank, comparison of the two available bathymetric datasets indicated an area of the bank migrated westward resulting in the seabed rising / lowering by up to circa. 5 m. Over the summer of 2020, only limited vertical change (circa +/- 1 m), over this limited temporal period, occurred. It is postulated that sandwaves are less prominent than observed on Arklow Bank.

The following concluding remarks represent the principal findings of the study for areas along the export cable routes (excepting Seven Fathom Bank):

- The seabed along the proposed cable routes can be considered, in terms of sediment dynamics, to be relatively stable when compared to the lease area. Along the routes, less erodible soils are observed and limited evidence of mobile bedforms exists. Seabed mobility potential is enhanced in close vicinity to Arklow

Bank (i.e. the lease area) and in nearshore regions where water depths shallow.

- Along the export cable route, typical values for predicted seabed level variation ranges between circa. 1 m to 1.5 m. These values indicate that the risk profile along the export cable route is generally low. The available data, and supporting analyses, leads us to conclude that due to potential seabed level change across Seven Fathom Bank, from a seabed mobility perspective, the northernmost export cable route, which avoids Seven Fathom Bank entirely, would be preferable.

A complementary data package including predicted future seabed levels (HSBL and LSBL) have been provided with this interpretative report. No additional tolerances beyond those described within this report have been included. Additional remarks regarding the implications of site morphodynamics for foundations and cabling were provided to support dissemination of the study findings to downstream users of these data.

12.1 Possible Next Steps

At the conclusion of the current stage of the morphodynamic study for the Arklow Bank Offshore Wind Farm it is judicious to identify, and briefly describe possible next steps which would potentially improve confidence in the predictions made regarding the estimated variation in future seabed levels across the lease area, to support the subsequent design process. Two options exist:

3. Further, data collection, specified, reviewed, and interpreted within the framework of conceptual understanding developed to date; and
4. Research and development type studies to explore potential further numerical modelling options or remote sensing opportunities for long term monitoring of the form, and profile, of the shallowest regions of the bank.

The foregoing analyses relied on a data led; systems-based approach complemented by numerical modelling efforts. Delivering outputs with suitable levels of confidence so that these can be applied to inform, support, and optimise, engineering design relies entirely on the availability of suitable, high quality, primary data (i.e. geotechnical and geophysical data, metocean and hydrodynamic datasets etc.). Where the potential exists for existing datasets to be bolstered by additional data/analyses to provide further lines of evidence from which to draw conclusions, these opportunities should be explored.

It is duly recognised that primary data from the GI campaign remains outstanding. Notwithstanding these data, to further bolster process understanding, support prediction of future seabed levels (including improving confidence in the determination of likely seabed levels at date of installation) the acquisition of further high-resolution bathymetry data across the lease area is recommended. Several options exist:

1. Acquisition of data across the entire lease area. This option would provide the best available information to the project supporting assessment of spatiotemporal changes to the bank profile and bedforms and

prediction of future seabed levels (via the provision of an additional surface which can be incorporated into the applied methodology used to derive of the estimated highest and lowest seabed levels).

2. Acquisition of data from targeted locations. The primary focus of targeted surveys should be the bank shape and relative position of the crestline, assessed via the acquisition of data along several east – west profiles. Note: such surveys could be optimised to support further data acquisition at the phase 1 turbine locations were this of benefit to the wider project.

In addition to further data collection, it has been postulated that research and development type projects may also benefit the study and wider project. Two options have been discussed to date:

1. Further numerical modelling focussed on the lease area.
2. Review of the potential application and value that satellite imagery could bring to present efforts by reviewing historic imagery.

To investigate these concepts further, small-scale R & D type pilot studies would be proposed, the overarching aim of which would be to assess the potential application and value of these options.

13 References

A.D, Weiss. (2001) Topographic position and landforms analysis Poster Presentation. ESRI Users Conference, San Diego, CA,

Aquatic Services Unit (2011). Benthic Ecology Monitoring Report: Arklow Bank Wind farm (Technical Report No. MS110101). Aquatic Services Unit.

ARUP, (2018). Irish Water: Arklow Wastewater Treatment Plant Project: Coastal Processes Assessment (EIA Report No. 247825– 00). ARUP.

Ashley, G. M. (1990), Classification of large-scale subaqueous bedforms: A new look on an old problem, J. Sediment. Petrol., 60(1), 160–172.

Bakare, A.-M., Simons, R., Morley, J., Guillas, S. (2011). Morphological evolution of the Great Yarmouth Sandbank & Channel System. Coastal Engineering Proceedings 1, 72.

Barabasi, A.L., Albert, R. and Schiffer, P. (1999). The physics of sandcastles; maximum angle of stability in wet and dry granular materials. Physica A, 266, 366-371.

Battjes, J.A., Janssen, J.P.F.M. (1978). Energy loss and set-up due to breaking random waves. Proceedings of 16th Conference on Coastal Engineering, Hamburg, Germany, 1978.

Battjes, J.A., Stive, M.J.F. (1984). Calibration and verification of a dissipation model for random breaking waves. Coastal Engineering 44, 649–660.

Belderson, R.H., Johnson, M.A., Kenyon, N.H., Stride, A.H. (1982). Offshore Tidal Sands, in: Sand Transport. Chapman & Hall, London.

Berge, C.W. (1995). Sedimentation of Arklow Bank, Irish Sea. University of Wisconsin--Madison. BGS publications online. http://pubs.bgs.ac.uk/publications.html?pubID=B01847# (accessed 8.1.19).

Blondeaux, P., Vittori, G. (2010). Formation of tidal sandwaves: Effects of the spring-neap cycle. J. Geophys. Res. 115, C10017.

Borsje, B., Kranenburg, W., Roos, P., Matthieu, J., and Hulscher, S. (2014) The role of suspended load transport in the occurrence of tidal sand waves. Journal of Geophysical Research: Earth Surface, 119(4), pp. 701-716.

BOTT, M. (1964) Gravity measurements in the north-eastern part of the Irish Sea. Quarterly Journal of the Geological Society, 120(1-4), pp. 369-394.

Brøker, Ida & Zyserman, Julio & Madsen, Erik & Mangor, Karsten & Jensen, John. (2007). Morphological Modelling: A Tool for Optimisation of Coastal Structures. Journal of Coastal Research - J COASTAL RES. 23. 1148-1158. 10.2112/04-0380.1.

Buchanan, J.B., Kain, J.M. (1984). Measurement of physical and chemical environment, in: Methods for the Study of Marine Benthos. Blackwell Scientific Publications, Oxford, UK, pp. 30–50.

Buijsman, M. and Ridderinkhof, H. (2008a) Long-term evolution of sand waves in the Marsdiep inlet. I: High-resolution observations. Continental Shelf Research, 28(9), pp. 1190-1201.

Buijsman, M. and Ridderinkhof, H. (2008b) Variability of secondary currents in a weakly stratified tidal inlet with low curvature. Continental Shelf Research, 28(14), pp. 1711-1723.

Carbon Trust. (2015). Cable Burial Risk Assessment Methodology. Guidance for the Preparation of Cable Burial Depth of Lowering Specification. CTC835.

Carter, D.J. (1993). Estimating extreme wave heights in the NE Atlantic from Geosat data (No. OTH 93 396), Health and Safety Executive - Offshore Technology Report. HMSO, London.

Cathie Associates Ltd. (2018). Arklow Bank Phase 2 OWF: Geological and Geotechnical Desk Top Study (Technical Report No. C928R01).

Clark, D. C., Hughes, A. L., Greenwood, S. L., Jordan, C., & Sejrup, H. P. (2012). Pattern and timing of retreat of the last British Irish Ice Sheet. Quaternary Science Reviews, 44, 112-146.

Cole, G. and Hallissy, T. (1924) Handbook of the geology of Ireland. London: Murby.

Cooper Marine Advisors Ltd (2020). Fugro 2000 MBES Data Quality Review. Document no: P1894.05. D07v01.FINAL01 - Fugro 2000 Data Quality Review.

Cooper, B., Rees, J., Coates, T. (2008). Review of Round 1 sediment process monitoring data - lessons learned (Technical Report No. Final Report). Department of Energy and Climate Change, Department for Environment Food and Rural Affairs.

Coughlan, M. (2018). Arklow Bank MBES Interpretation (Technical Note No. 18125). Gavin & Doherty Geosolutions.

Coughlan, M., Wheeler, A.J., Dorschel, B., Lordan, C., Boer, W., Gaever, P. van, Haas, H. de, Mörz, T. (2015). Record of anthropogenic impact on the Western Irish Sea mud belt. Anthropocene 9, 56–69.

Coughlan, M; Guerrini, M; Creane, S; O'Shea, M; Ward, S. L; Van Landeghem, K. J. J; Murphy, J; Doherty, P. (2021). A new seabed mobility index for the Irish Sea: Modelling seabed shear stress and classifying sediment mobilisation to help predict erosion, deposition, and sediment distribution. *Continental Shelf Research*. 229.

Cowell, P.J., Thom, B.G. (1994). Morphodynamics of coastal evolution. In: Carter, R.W.G., Woodroffe, C.D. (Eds.), Coastal Evolution: Late Quaternary Shoreline Morphodynamics. Cambridge University Press, Cambridge, United Kingdom and New York, NY, USA, pp. 83–86.

Cronin, K.M., Devoy, R.J.N., Gault, J. (2007). Modelling Estuarine Morphodynamics on the South Coast of Ireland. Journal of Coastal Research 7.

Dobson, M.R., Evans, W.E., James, K.H. (1971). The sediment on the floor of the Southern Irish Sea. Marine Geology 19, 183–204.

Dorst, L.L., Roos, P.C., Hulscher, S.J.M.H., Lindenbergh, R.C. (2009). The estimation of sea floor dynamics from bathymetric surveys of a sand wave area. J. Appl.Geodesy 3 (2), 97–120.

Draper. S., Harris, J. M., Cheng, L., White, D. J (2018). Seabed Processes: Sediment Transport, Scour, and Sedimentation. Encyclopedia of Maritime and Offshore Engineering.

Drønen, N. and R. Deigaard. (2007). Quasi-three-dimensional modelling of the morphology of longshore bars, Coastal Engineering, Vol. 54, Elsevier, 197-215.

Dyer, K. R., & Huntley, D. A. (1999). The origin, classifcation and modelling of sand banks and ridges. Continental Shelf Research, 19(1999), 1285-1330.

Dyer, K.R., Huntley, D.A. (1999). The origin, classification and modelling of sandbanks and ridges. Continental Shelf Research 19, 1285–1330.

Engelund, F. & Hansen, E. (1967) A Monograph on Sediment Transport in Alluvial Stream, 1-63. Teknisk Forlag, Copenhagen V, Denmark.

Engelund, Frank & Fredsøe, Jorgen. (1976). A Sediment Transport Model for Straight Alluvial Channels. Nord Hydrol. 7. 10.2166/nh.1976.0019.

Exner, F. M. (1925). Über die Wechselwirkung zwischen Wasser und Geschiebe in Flüssen. Sitzungsberichte. Abt. 2a, Mathematik, Astronomie, Physik Und Meteorologie (akademie Der Wissenschaften in Wien, Mathematisch-Naturwissenschaftliche Klasse).

Fahy, E., O'Toole, M., Stokes, D., Gallagher, M. (2002). Appraisal of the whelk (Buccinum undatum) fishery on a part of the Codling Bank following aggregate extraction for beach restoration at Bray, Co Wicklow (Technical Report No. Fisheries Leaflet No. 182). Marine Institute, Marine Fisheries Services Division, Abbotstown, Dublin 15.

Fairley, I., Masters, I., Karunarathna, H. (2016). Numerical modelling of storm and surge events on offshore sandbanks. Marine Geology 371, 106–119.

Flather, R.A. (1987). Estimates of extreme conditions of tide and surge using a numerical model of the north- west European continental shelf. Estuarine, Coastal and Shelf Science 24, 69–93.

Folk, R.L. (1954). The distinction between grain size and material composition in sedimentary rock nomenclature. Journal of Geology 62, 344–359.

Fredsøe, J. (1984). The turbulent boundary layer in combined wave-current motion. Journal of Hydraulic Engineering, 110, 1103–1120.

Fredsøe, J., Andersen, O. H., & Silberg, S. (1985). Distribution of suspended sediment in large waves. Journal of Waterway, Port, Coastal, and Ocean Engineering, 111(6), 1041-1059.

Friedrichs, C. T (2011). Tidal Flat Morphodynamics: A Synthesis. Treatise on Estuarine and Coastal Science, Academic Press, Pages 137-170.

Fugro Ltd (2020). Metocean and Hydrodynamic Data retrieved from the measurement campaign Arklow Bank Offshore Wind Park. 6 months of data provided.

Fugro Ltd (2020a). Arklow Offshore Wind Farm Metocean Survey. Data Report – Deployment 1. Document no: 181399-R-01(01).

Fugro Ltd (2021) Final Data Report. Arklow Offshore Wind Farm Metocean Survey. Hampshire: Fugro.

Fugro Ltd. (2000). Offshore Wind farm Development: Arklow Bank, Irish Sea Geotechnical Site Investigation Laboratory and In-situ Report (Technical Report No. 04520–2).

G. J. Komen, L. Cavaleri, M. Donelan, K. Hasselmann, S. Hasselmann and P. A. E. M. Janssen (1994). Dynamics and Modelling of Ocean Waves, Cambridge, UK: Cambridge University Press.

Gao, S., Collins, M.B. (2014). Holocene sedimentary systems on continental shelves. Marine Geology, 50th Anniversary Special Issue 352, 268–294.

Gavin & Doherty Geosolutions / Ramboll. (2020). Arklow Bank Wind Park WTG Substructure Concept - Design Report Stage 1. Design report: LF100034-MIP-FN-RPT-0001.

Gavin and Doherty Geosolutions (GDG) Ltd (2020). Arklow Bank Offshore Wind Park – Ground Model Report. Document reference: 19158-002-02.

Grant, W.D. and Madsen, O.S. (1979). Combined wave and current interaction with a rough bottom. Journal of Geophysical Research: Oceans and Atmospheres, 84(C1), 1797–1808.

Guedes Soares, C. (1984). Representation of double-peaked sea wave spectra. OceanEng. 11, 185–207.

Haeseler, J. (2004) Extreme waves in the Celtic Sea and the English Channel on 14-15 February 2014. Deutscher Wieterdienst, 5pp.

Hallermeier, R. J. (1983). Sand Transport Limits in Coastal Structure Design, Proceedings, Coastal Structures '83, American Society of Civil Engineers, pp. 703-716.

Hallermeier, R.J. (1981c). Seaward limit of significant sand transport by waves: an annual zonation for seasonal profiles. Vicksburg: U.S. Army Engineer Waterways Experiment Station, Coastal Engineering Research Centre. Coastal Engineering Technical Aide CETA 81-2.

Hanna, J. E., Cooper J. A. G. (2002). Mesoscale Morphological Changes on Linear, Nearshore Sandbanks, Co. Wexford, SE Ireland. *Journal of Coastal Research*. Special Issue 36 (36), 356-364.

Harris, J.M., Whitehouse, R.J.S., Sutherland, J. (2011). Marine Scour and Offshore Wind: Lessons Learnt and Future Challenges, in: Volume 5: Ocean Space Utilization; Ocean Renewable Energy. Presented at the ASME 2011 30th International Conference on Ocean, Offshore and Arctic Engineering, ASME, Rotterdam, The Netherlands, pp. 849–858.

Harris, P., Pattiaratchi, C. B., Collins, M. B., & Dalrymple, R. W. (1995). What is bedload parting? In B. W. Flemming, & A. Bartholoma¨ (Eds.), Tidal signatures in modern and ancient sediments Vol. 24 (pp. 3–18). Oxford: Blackwell, International Association of Sedimentologists Special Publications.

Hasselmann, S., Hasselmann, K., Allender, J.H., Barnett, T.P. (1985). Computations and Parameterizations of the Nonlinear Energy Transfer in a Gravity-Wave Specturm. Part II: Parameterizations of the Nonlinear Energy Transfer for Application in Wave Models. J. Phys. Oceanogr. 15, 1378–1391.

Holmes, R., Tappin, D.R. (2005). DTI Strategic Environmental Assessment Area 6, Irish Sea, seabed and surficial geology and processes (No. Commissioned Report CR/05/057), British Geological Survey. Natural Environmental Research Council, Edinburgh.

Houthuys, R., Trentesaux, A., & De Wolf, P. (1994). Storm influences on a tidal sandbank's surface (Middelkerke Bank, southern North Sea). Marine Geology, 121, 23–41.

Howarth, M.J. (2005). Hydrography of the Irish Sea (SEA6 Technical Report No. POL Internal Document 174). UK Department of Trade and Industry.

Hulscher, S.J.M.H., Brink, G.M. van den. (2001). Comparison between predicted and observed sandwaves and sandbanks in the North Sea. Journal of Geophysical Research: Oceans 106, 9327–9338.

Hulscher, S.J.M.H., de Swart, H.E., de Vriend, H.J. (1993). The generation of offshore tidal sandbanks and sandwaves. Continental Shelf Research 13, 1183–1204.

Huthnance, J.M. (1982). On one mechanism forming linear sandbanks. Estuarine, Coastal and Shelf Science 14, 79–99.

Huthnance, J.M., Humphery, J.D., Knight, P.J., Chatwin, P.G., Thomsen, L., White, M. (2002). Near-bed turbulence measurements, stress estimates and sediment mobility at the continental shelf edge. Progress in Oceanography, Benthic processes and dynamics at the NW Iberian Margin: results of the OMEX II Program 52, 171–194.

Jackson, D.I., Jackson, A.A., Evans, D., Wingfield, R.T.R., Barnes, R.P., Arthur, M.J. (1995). United Kingdom offshore regional report: The geology of the Irish Sea. HMSO for the British Geological Survey, London.

Jones, L.A., Coyle, M.D., Gilliland, P.M., Larwood, J.G., Murray, A.R. (2004). The Irish Sea Marine Natural Area: A contribution to regional planning and management of the seas around England. English Nature.

Kenyon, N. H., Belderson, R. H., Stride, A. H., & Johnson, M. A. (1981). Offshore Tidal Sandbanks as Indicators of Net Sand Transport and as Potential Deposits. In S. D. Nio, R. T. Shüttenhelm, & T. C. Van Weering (Eds.), Holocene marine sedimentation in the North Sea Basin (Vol. 5, pp. 257-268). International Association of Sedimentologisits Special Publication.

Kenyon, N.H., Cooper, B. (2005). Sandbanks, sand transport and offshore wind farms (Technical Report). ABP Marine Environmental Research Ltd (ABPmer).

Knaapen, M.A.F., Hulscher, S.J.M.H. (2002). Regeneration of sand waves after dredging. Coast. Eng. 46 (4), 277–289. doi:10.1016/S0378-3839(02)00090-X.

Komen, G.J., Hasselmann, K., Hasselmann, K. (1984). On the Existence of a Fully Developed Wind-Sea Spectrum. J. Phys. Oceanogr. 14, 1271–1285.

Kraus, N.C., and Harikai, S. (1983). Numerical model of the shoreline change at Oarai Beach. Coastal Engineering, 7: 1–28.

Lambeck, K., & Purcell, A. P. (2001). Sea-level change in the Irish Sea since the Last Glacial Maximum: Constraints from isostatic modelling. Journal of Quaternary Science, 16(5), 497-506. doi:10.1002/ jqs.63B.

Lambkin, D.O., Harris, J.M., Cooper, W.S., Coates, T. (2009). Coastal Process Modelling for Offshore Wind Farm Environmental Impact Assessment: Best Practice Guide 104.

Larsen, S., Roulund, A., Brooks, A., Chaffey, A. (2016). Sandwaves and mega ripples at race bank (UK) offshore wind farm, in: Scour and Erosion. Presented at the 8th International Conference on Scour and Erosion, CRC Press, Oxford, UK, pp. 237–245.

Lyard, C. L (2017). "FES2014, a new finite elements tidal model for global ocean," in Ocean Dynamics.

Masselink, G., Short, A.D. (1993). The Effect of Tide Range on Beach Morphodynamics and Morphology: A Conceptual Beach Model. Journal of Coastal Research 9, 785–800.

Massey, J., Gaughran, A., Oliviera, E., RPS Group, Ecofys (2017). Environmental baseline study for the development of renewable energy sources, energy storages and a meshed electricity grid in the Irish and North seas (No. WP3 Final Baseline Environmental Report).

McCarron, C.J., Van Landeghem, K.J.J., Baas, J.H., Amoudry, L.O., Malarkey, J. (2019). The hiding-exposure effect revisited: A method to calculate the mobility of bimodal sediment mixtures. Marine Geology 410, 22– 31.

Mellett, C.L., Long, D., Cartar, G. (2015). Geology of the seabed and shallow subsurface: The Irish Sea (Energy and Marine Geoscience Programme No. Commissioned Report CR/15/057). British Geological Survey.

Met Office UK. United Kingdom Climate Projections (2018). Available online: https://www.metoffice.gov.uk/research/approach/collaboration/ukcp/index.

MetOceanWorks (2021). Metocean Data Overview – Arklow Bank Offshore Wind Farm. Report SSE_C00002_R02_Metocean_Data_Overview, for Sure Partners Limited. 13 August 2021.

Nicholson, J. & Brøker, Ida & Roelvink, Dano J.A. & Price, D. & Tanguy, Jean-Michel & Moreno, L. (1997). Intercomparison of coastal area morphodynamic models. Coastal Engineering - COAST ENG. 31. 97-123. 10.1016/S0378-3839(96)00054-3.

ORDTEK, (2018). Unexploded Ordnance (UXO) Hazard and Risk Assessment with Risk Mitigation Strategy (Technical Report No. JM5473), Arklow Bank Offshore Wind Farm.

Panigrahi, J.K., Ananth, P.N., Umesh, P.A. (2009). Coastal morphological modelling to assess the dynamics of Arklow Bank, Ireland. International Journal of Sediment Research 24, 299–314.

Pantin, H.M., Evans, C.D.R. (1984). The Quaternary history of the central and southwestern Celtic Sea. Marine Geology 57, 259–293.

Partrac Ltd (2019). Arklow Bank Wind Park Sediment Dynamics Study - Stage 1 Report. Document Reference: P1894.05.D01v02 - Stage 1 report_PARTRAC_MASTER_20-12-2019 (2).

Partrac Ltd (2020a). Proposed Sediment Transport Model Simulations. Document ref: P1894.05.D04.v01 - Proposed model simulations.

Partrac Ltd (2020b). Approach to Stage 2 and Program. Document ref: P1894.05.D04.v01 - Stage 2 Approach and Program.

Passchier, Sandra & Kleinhans, Maarten. (2005). Observations of sand waves, megaripples, and hummocks in the Dutch coastal area and their relation to currents and combined flow conditions. J. Geophys. Res. 110. 10.1029/2004JF000215.

Petersen, T., Sumer, B., Fredsøe, J. (2014). Edge scour at scour protections around offshore wind turbine foundations, in: Cheng, L., Draper, S., An, H. (Eds.), Scour and Erosion. CRC Press, pp. 587–592.

Pierson,W.J. and Moskowitz,L., (1964).A proposed spectral form for fully developed wind sea based on the similarity theory of S. A. Kitaigorodskii. J. Geophys. Res. 69,5181–5190.

Pingree, R.D., Griffiths, D.K. (1978). Tidal fronts on the shelf seas around the British Isles. Journal of Geophysical Research 83, 4615–4622.

Price, D. M., Chester, T. J., Southgate, H. N (1995). PISCES. A morphodynamic coastal area model. Final Report. Report SR411, Hydraulics Research Waliingford, 14 pp.

Pugh., D. T (1981). Tidal amphidrome movement and energy dissipation in the Irish Sea. Geophys. J. R. a m. SOC. (1981) 67,515-527.

Ramboll Environ (2016). Arklow Bank: Dumping at sea permit application supporting information. Ramboll Environ.

Reynaud, J.-Y., Dalrymple, R.W. (2012). Shallow-Marine Tidal Deposits, in: Davis Jr., R.A., Dalrymple, R.W. (Eds.), Principles of Tidal Sedimentology. Springer Netherlands, Dordrecht, pp. 335–369.

Robins, P.E., Neill, S.P., Lewis, M.J., Ward, S.L. (2015). Characterising the spatial and temporal variability of the tidal-Stream Energy resource over the northwest European shelf seas. Applied Energy 147, 510–522.

Robinson, K., Darbyshire, T., Van Landeghem, K., Lindenbaum, C., McBreen, F., Creaven, S., Ramsay, K., Mackie, A.S.Y., Mitchell, N., Wheeler, A., Wilson, J., Rees, E.I.S., O'Beirn, F. (2008). HABMAP Volume 1: Southern Irish Sea seabed habitat surveys. Studies in Marine Biodiversity and Systematics from the National Museum of Wales. (No. 5), BIOMOR.

Robinson, K.A., Mackie, A.S.Y., Lindenbaum, C., Darbyshire, T., van Landeghem, K.J.J., Sanderson, W.G. (2012). Seabed Habitats of the Southern Irish Sea, in: Seafloor Geomorphology as Benthic Habitat. Elsevier, pp. 523– 537.

Roche, C., O. Lyons, D., Farinas Franco, J., O'Connor, B. (2007). Benthic surveys of sandbanks in the Irish Sea (No. Irish Wildlife Manuals No.29). Department of the Environment, Heritage and Local Government, Dublin, Ireland.

Roetert, T., Raaijmakers, T., Borsje, B (2017). Cable route optimization for offshore wind farms in morphodynamic areas. *The 27th International Ocean and Polar Engineering Conference*. San Francisco.

Román-Sierra, J; Muñoz-Perez, J.J; Navarro-Pons, M (2014). Beach nourishment effects on sand porosity variability. *Coastal Engineering*. 83, 221-232.

Roos, P.C., Hulscher, S.J.M.H. (2002). Formation of offshore tidal sandbanks triggered by a gasmined bed subsidence. Continental Shelf Research 22, 2807–2818.

Roos, P.C., Hulscher, S.J.M.H. (2003). Large-scale seabed dynamics in offshore morphology: Modelling human intervention. REV GEOPHYS 41, 1010.

RPS Group, OPW (2010a). Irish Coastal Protection Strategy Study - Phase 2 - Southeast Coast (Work Packages 2, 3, 4A - Technical Report No. IBE0104), Strategic Assessments of Coastal Flooding and Erosion Extents. Dalkey Island to Carnsore Point Pilot Area.

Saorgus Energy Limited, (2013). Dublin Array: An Offshore Wind Farm on the Kish and Bray Banks (Environmental Impact Statement No. Volume 1-5). Addendum.

Sato, K., Shuto, N., Tanaka, H. (1995). Numerical simulations of the sand spit flushing at a river mouth. In: Chinese Hydraulic Engineering Society and International Research and Training Center on Erosion and Sedimentation (Editors), Advances in Hydro-Science and Engineering, Vol II, Part B, Tsinghua University Press, Beijing, pp 1399-1406.

Schmitt, T. G. (2006). Morphology and dynamics of headland connected sandbanks from high resolution bathymetric surveys: Helwick and Nash Sands, Bristol Channel, U.K.. *PhD Thesis*.

Seacore (2002). Arklow Bank Wind Park, Phase 1 (Interim Report No. 33–122).

Smith, D.B. (1988). Morphological development of the Sandettie South Falls Gap: a degeneration ebb dominated tidal passage in the southern North Sea, in: Tide-Influenced Sedimentary Environments and Facies, Sedimentology and Petroleum Geology. D. Reidel Publishing Company, Dordrecht, Holland, pp. 51–64.

Soulsby, R.L. (1997). Dynamics of marine sands, 1st ed. Thomas Telford.

Soulsby, R. L., Davies, A. G., Wilkinson, R. H (1983). The Detailed Processes of Sediment Transport by Tidal Currents and by Surface Waves. Institute of Oceanographic Sciences Report No 152, 80pp.

Soulsby, R.L. and Whitehouse, R.J.S.W. (1997). Threshold of sediment motion in coastal environment. Proceedings of Pacific Coasts and Ports 1997 Conference, 1, 149-154, New Zealand.

Sterlini, F., Hulscher, S.J.M.H., Hanes, D.M. (2009). Simulating and understanding sand wave variation: a case study of the Golden Gate sand waves. J. Geophys. Res. 114 (F02007). doi:10.1029/2008JF000999.

Sterlini, Fenneke & Hulscher, Suzanne & Hanes, Daniel. (2009). Simulating and understanding sand wave variation: A case study of the Golden Gate sand waves. Journal of Geophysical Research. 114. 10.1029/2008JF000999.

Stride, A.H. (1982). Offshore Tidal Sands: Processes and deposits. Springer Netherlands.

Sturt, F., Garrow, D., & Bradley, S. (2013). New models of Northwest European Holocene palaeogeography and inundation. Journal of Archaeological Science, 40, 3963-3976.

Sumer, B. and Fredsøe, J. (2002) The Mechanics of Scour in the Marine Environment. World Scientific, Advanced Series on Ocean Engineering, Volume 17.

Sumer, B. and Fredsøe, J. (2006) Hydrodynamics around cylindrical structures. London: World Scientific Pub.

Tobias CJ (1989) Morphology of sand waves in relation to current, sediment and wave data along the Eurogeul, North Sea; Report GEOPRO 1989.01; Department of Physical Geography, University of Utrecht, The Netherlands.

Tooley, M.J. (1985). Sea levels. Progress in Physical Geography: Earth and Environment 9, 113–120.

Van Dijk, Thaiënne & Kleinhans, Maarten. (2005). Processes controlling the dynamics of compound sand waves in the North Sea, Netherlands. Journal of Geophysical Research. 110. 10.1029/2004JF000173.

Van Landeghem, K.J.J., Baas, J.H., Mitchell, N.C., Wilcockson, D., Wheeler, A.J. (2012). Reversed sediment wave migration in the Irish Sea, NW Europe: A reappraisal of the validity of geometry-based predictive modelling and assumptions. Marine Geology 295–298, 95–112.

Van Landeghem, K.J.J., Uehara, K., Wheeler, A.J., Mitchell, N.C., Scourse, J.D. (2009). Post-glacial sediment dynamics in the Irish Sea and sediment wave morphology: Data–model comparisons. Continental Shelf Research 29, 1723–1736.

van Maanen, B., Nicholls, R., French, J., Barkwith, A., Bonaldo, D., Burningham, H., Brad Murray, A., Payo, A., Sutherland, J., Thornhill, G., Townend, I., van der Wegen, M., and Walkden, M. (2016) Simulating mesoscale coastal evolution for decadal coastal management: A new framework integrating multiple, complementary modelling approaches. Geomorphology, 256, pp. 68-80.

Van Oyen, T., Blondeaux, P. (2009). Grain sorting effects on the formation of tidal sandwaves. J. Fluid Mech. 629, 311–342.

Van Rijn, (2015). Principles of Sedimentation and Erosion Engineering in Rivers, Estuaries and Coastal Seas, update 2015. Published by Mrs P. Boon.

van Rijn, L.C. (2018). Channel Slopes of Mud, Silt and Sand. Available: https://www.leovanrijn-sediment.com/papers/Channelslopesbrief2018.pdf. Last accessed 04/08/2020.

van Rijn, L.C. (1993). Principles of Sediment Transport in Rivers, Estuaries and Coastal Seas. Aqua Publications, Amsterdam, The Netherlands.

van Rijn, L.C. (2012). Principles of sedimentation and erosion engineering in rivers, estuaries and coastal seas. Aqua Publications, Amsterdam.

van Santen, R., de Swart, H., and van Dijk, T. (2011) Sensitivity of tidal sand wavelength to environmental parameters: A combined data analysis and modelling approach. Continental Shelf Research, 31(9), pp. 966-978.

Wang, Z. B.; Karssen, B.; Roelfzema, A. and Winterwerp, J.C. (1992). A morphodynamic modeling system. Proceedings of the 2nd International Conference on Hydraulic and Environmental Modelling of Coastal, Estuarine and River Waters, ed. R.A. Falconer, S.N. Chandler-Wilde, S.Q. Liu Vol 1, pp 301-312.

Ward, S.L., Neill, S.P., Van Landeghem, K.J.J., Scourse, J.D. (2015). Classifying seabed sediment type using simulated tidal-induced bed shear stress. Marine Geology 367, 94–104.

Warren, K.P., Keary, R. (1989). The sand and gravel resources of the Irish Sea Basin, in: The Irish Sea Basin: A Resource at Risk. Geographical Society of Ireland, Dublin, pp. 65–79.

Wheeler, A.J., Walshe, J., Sutton, G.D. (2001). Seabed mapping and seafloor processes in the Kish, Burford, Bray and Fraser Banks area, South-Western Irish Sea. Irish Geography 34, 194–211.

Whitehouse, R., Beech, N., Hulscher, S., Huntley, D. (1997). Understanding the behaviour and engineering significance of offshore and coastal sandbanks. HR Wallingford Technical Report 697.

Whitehouse, R. J. S., Chesher, T. J. (1994). Seabed roughness in tidal flows. A review of existing measurements. HR Wallingford. Report SR360.

Whitehouse, R., Harris, J., Rees, J. (2008). Dynamics of scour pits and scour protection - Synthesis report and recommendations (Milestones 2 and 3) (Research Advisory Group No. Final Report). Department of Energy and Climate Change, Department for Environment Food and Rural Affairs.

Whitehouse, R.J.S., Harris, J.M., Sutherland, J., Rees, J. (2011). The nature of scour development and scour protection at offshore wind farm foundations. Marine Pollution Bulletin 62, 73–88.

Whomersley, P., Wilson, C., Clements, A., Brown, C., Long, D., Leslie, A., Limpenny, D. (2010). Understanding the marine environment – seabed habitat investigations of submarine structures in the mid Irish Sea and Solan Bank Area of Search (AoS) 138.

Wilson, J.G., Mackie, A.S.Y., O'Connor, B.D.S., Rees, E.I.S., Darbyshire, T. (2001). Benthic biodiversity in the Southern Irish Sea. 2, 2,. National Museums & Galleries of Wales, Cardiff.

Woodroffe, C.D. (2002). Coasts: Form, Process and Evolution. Cambridge University Press, Cambridge (623 pp.).

Woodroffe, C.D., Murray-Wallace, C.V. (2012). Sea-level rise and coastal change: the past as a guide to the future. Quat. Sci. Rev. 54, 4–11.

Young. I (1999). "Wind generated ocean waves," in Ocean Engineering, Elsevier.

Zanuttigh, B. (2007). Numerical modelling of the morphological response induced by low-crested structures in Lido di Dante, Italy. Coastal Engineering, 54, 31-47.

Ziegler, P.A. (1982). Geological atlas of western and central Europe (Technical Report). Shell Internationale Petroluem, Maatschappij B.V.

14 Appendix A: Data Available to the Commission

Table 22 and Table 23 summarises the data sources utilised as part of the study of site morphodynamics.

Table 22. The bathymetry data available to the assessment of site morphodynamics. The utility of these data to the study of site morphodynamics and the assessment of processes occurring at various spatio-temporal scales is described.

Filename	Survey Date	Res	Area covered	Notes	Max	Min	Mean	Range	Std_Dev	Folder
2000_2006-359018_Arklow_Bank	Surveyed in 2000 (month?)	120 * 120	The majority of Arklow Phase 2 LA	Survey obtained from UKHO	-0.60	-30.40	-13.77	7.83	37.80	UKHO
AUTUMN\XYZ\Sep04_T_001_G	Surveyed in Sept 2004	1 * 1	Turbine 1		-4.31	-6.23	-5.51	0.25	1.92	2004 \ Autumn
AUTUMN\XYZ\Sep04_T_002_G	Surveyed in Sept 2004	1 * 1	Turbine 2		-4.96	-6.74	-6.13	0.23	1.78	
AUTUMN\XYZ\Sep04_T_003_G	Surveyed in Sept 2004	1 * 1	Turbine 3		-4.53	-6.70	-5.73	0.47	2.17	
AUTUMN\XYZ\Sep04_T_004_G	Surveyed in Sept 2004	1 * 1	Turbine 4		-3.83	-7.41	-5.11	0.45	3.58	
AUTUMN\XYZ\Sep04_T_005_G	Surveyed in Sept 2004	1 * 1	Turbine 5		-1.18	-6.64	-2.44	0.62	5.46	
AUTUMN\XYZ\Sep04_T_006_G	Surveyed in Sept 2004	1 * 1	Turbine 6		-2.10	-5.77	-3.82	0.64	3.67	
AUTUMN\XYZ\Sep04_T_007_G	Surveyed in Sept 2004	1 * 1	Turbine 7		-4.09	-7.34	-5.78	0.79	3.25	
AUTUMN\XYZ\Sep04-May04_T_004_G (6)	bed change between Sept 2004 and May 2004	1 * 1	Turbine 4	bedchange	0.86	-1.89	-0.36	0.36	2.75	
AUTUMN\XYZ\Sep04-May04_T_004_G	bed change between Sept 2004 and May 2004	1 * 1	Turbine 4	bedchange - duplicate	0.86	-1.89	-0.36	0.36	2.75	
CR_Cht_01_1m	Surveyed in Spring 2004 (specifc month not available)	1 * 1	Cable Route		-3.25	-20.87	-14.74	3.38	17.62	2004 \ Spring
CR_Cht_02_1m	Surveyed in Spring 2004 (specifc month not available)	1 * 1	Cable Route		-16.84	-26.84	-20.79	2.49	10.00	

Filename	Survey Date	Res	Area covered	Notes	Max	Min	Mean	Range	Std_Dev	Folder
CR_Cht_03_1m	Surveyed in Spring 2004 (specifc month not available)	1 * 1	Cable Route		-16.68	-33.43	-27.85	3.51	16.75	
CR_Cht_04_1m	Surveyed in Spring 2004 (specifc month not available)	1 * 1	Cable Route		-3.18	-34.86	-23.13	9.25	31.68	
May04_T_001_G	Surveyed in May 2004	1 * 1	Turbine 1		-4.36	-6.24	-5.27	0.29	1.88	
May04_T_002_G	Surveyed in May 2004	1 * 1	Turbine 2		-4.74	-6.67	-5.82	0.28	1.93	
May04_T_003_G	Surveyed in May 2004	1 * 1	Turbine 3		-3.62	-6.51	-5.18	0.53	2.89	
May04_T_004_G	Surveyed in May 2004	1 * 1	Turbine 4		-2.57	-7.02	-4.76	0.39	4.45	
May04_T_005_G	Surveyed in May 2004	1 * 1	Turbine 5		-1.33	-6.52	-2.30	0.74	5.19	
May04_T_006_G	Surveyed in May 2004	1 * 1	Turbine 6		-2.23	-7.17	-4.14	0.75	4.94	
May04_T_007_G	Surveyed in May 2004	1 * 1	Turbine 7		-4.53	-7.75	-6.17	0.80	3.22	
Turb_01_1m	Surveyed in Spring 2004 (specifc month not available)	1 * 1	Turbine 1		-4.92	-8.20	-6.37	0.52	3.28	
Turb_02_1m	Surveyed in Spring 2004 (specifc month not available)	1 * 1	Turbine 2		-5.51	-8.64	-6.96	0.51	3.13	
Turb_03_1m	Surveyed in Spring 2004 (specifc month not available)	1 * 1	Turbine 3		-3.78	-8.70	-6.35	0.87	4.92	
Turb_04_1m	Surveyed in Spring 2004 (specifc month not available)	1 * 1	Turbine 4		-3.82	-8.27	-5.77	0.55	4.45	
Turb_05_1m	Surveyed in Spring 2004 (specifc month not available)	1 * 1	Turbine 5		-2.39	-8.25	-3.44	0.60	5.86	
Turb_06_1m	Surveyed in Spring 2004 (specifc month not available)	1 * 1	Turbine 6		-2.63	-8.50	-5.55	0.92	5.87	
Turb_07_1m	Surveyed in Spring 2004 (specifc month not available)	1 * 1	Turbine 7		-4.17	-8.95	-6.86	0.80	4.78	

Filename	Survey Date	Res	Area covered	Notes	Max	Min	Mean	Range	Std_Dev	Folder
Oct05_CR_5000_01_1m	Surveyed in October 2005	1 * 1	Cable Route		-0.46	-17.95	-14.06	3.51	17.49	2005 \ Autumn
Oct05_CR_5000_02_1m	Surveyed in October 2005	1 * 1	Cable Route		-15.63	-26.16	-20.32	2.71	10.53	
Oct05_CR_5000_03_1m	Surveyed in October 2005	1 * 1	Cable Route		-15.63	-33.30	-27.22	3.66	17.67	
Oct05_CR_5000_04_1m	Surveyed in October 2005	1 * 1	Cable Route	The survey covers phase 1 Turbine 1 through 7 as well	-1.95	-33.68	-9.65	8.59	31.73	
Oct05_T_01	Surveyed in October 2005	1 * 1	Turbine 1		-4.03	-7.34	-5.84	0.55	3.31	
Oct05_T_02	Surveyed in October 2005	1 * 1	Turbine 2		-4.57	-7.74	-6.07	0.69	3.17	
Oct05_T_03	Surveyed in October 2005	1 * 1	Turbine 3		-3.17	-6.92	-5.02	0.82	3.75	
Oct05_T_04	Surveyed in October 2005	1 * 1	Turbine 4		-2.58	-7.34	-4.34	0.59	4.76	
Oct05_T_05	Surveyed in October 2005	1 * 1	Turbine 5		-2.76	-9.28	-4.62	0.73	6.52	
Oct05_T_06	Surveyed in October 2005	1 * 1	Turbine 6		-3.23	-6.96	-5.49	0.63	3.73	
Oct05_T_07	Surveyed in October 2005	1 * 1	Turbine 7		-2.78	-7.00	-5.16	0.80	4.22	
Diff_Jun06-Oct05_T_01	bed change between June 2006 and Oct 2005	1 * 1	Turbine 1	bedchange	1.27	-1.81	-0.52	0.52	3.08	2006
Diff_Jun06-Oct05_T_02	bed change between June 2006 and Oct 2005	1 * 1	Turbine 2	bedchange	0.87	-0.96	-0.18	0.26	1.83	
Diff_Jun06-Oct05_T_03	bed change between June 2006 and Oct 2005	1 * 1	Turbine 3	bedchange	0.57	-1.21	-0.32	0.31	1.78	
Diff_Jun06-Oct05_T_04	bed change between June 2006 and Oct 2005	1 * 1	Turbine 4	bedchange	1.24	-1.85	-0.31	0.45	3.09	
Diff_Jun06-Oct05_T_05	bed change between June 2006 and Oct 2005	1 * 1	Turbine 5	bedchange	1.66	-3.49	-1.49	0.60	5.15	
Diff_Jun06-Oct05_T_06	bed change between June 2006 and Oct 2005	1 * 1	Turbine 6	bedchange	0.84	-3.21	-0.89	0.57	4.05	
Diff_Jun06-Oct05_T_07	bed change between June 2006 and Oct 2005	1 * 1	Turbine 7	bedchange	1.01	-1.87	-0.11	0.40	2.88	

Filename	Survey Date	Res	Area covered	Notes	Max	Min	Mean	Range	Std_Dev	Folder
GS_Cable_01	Surveyed in 2006 (month not specified)	1 * 1	Cable Route		-1.75	-17.53	-13.79	3.53	15.78	
GS_Cable_02	Surveyed in 2006 (month not specified)	1 * 1	Cable Route		-15.68	-26.34	-20.27	2.77	10.66	
GS_Cable_03	Surveyed in 2006 (month not specified)	1 * 1	Cable Route		-15.77	-33.56	-27.12	3.67	17.79	
GS_Cable_04	Surveyed in 2006 (month not specified)	1 * 1	Cable Route	The survey covers phase 1 Turbine 1 through 7 as well	-1.50	-33.90	-10.53	9.05	32.40	
Jun06_T_01_1m	Surveyed in June 2006	1 * 1	Turbine 1		-4.12	-7.59	-6.30	0.52	3.47	
Jun06_T_02_1m	Surveyed in June 2006	1 * 1	Turbine 2		-4.47	-7.70	-6.10	0.64	3.23	
Jun06_T_03_1m	Surveyed in June 2006	1 * 1	Turbine 3		-3.55	-7.01	-5.32	0.69	3.46	
Jun06_T_04_1m	Surveyed in June 2006	1 * 1	Turbine 4		-2.29	-7.19	-4.34	0.60	4.90	
Jun06_T_05_1m	Surveyed in June 2006	1 * 1	Turbine 5		-4.21	-9.26	-6.13	0.64	5.05	
Jun06_T_06_1m	Surveyed in June 2006	1 * 1	Turbine 6		-4.22	-8.07	-6.34	0.47	3.85	
Jun06_T_07_1m	Surveyed in June 2006	1 * 1	Turbine 7		-1.58	-7.22	-4.93	1.16	5.64	
Apr07_T_04_1m	Surveyed in April 2007	1 * 1	Turbine 4		-23.33	-28.98	-25.70	1.18	5.65	2007
Apr07_Area_01	Surveyed in April 2007	1 * 1	Area west of Turbine 06		-1.87	-4.68	-3.36	0.43	2.81	
Apr07_Arklow_River	Surveyed in April 2007	1 * 1	Arklow river mouth		-4.45	-8.82	-6.64	0.60	4.37	
Apr07_T_01_1m	Surveyed in April 2007	1 * 1	Turbine 1		-4.98	-8.01	-6.70	0.54	3.03	
Apr07_T_02_1m	Surveyed in April 2007	1 * 1	Turbine 2		-3.02	-7.09	-5.10	0.67	4.07	
Apr07_T_03_1m	Surveyed in April 2007	1 * 1	Turbine 3		-2.51	-9.13	-5.42	0.87	6.62	
Apr07_T_05_1m	Surveyed in April 2007	1 * 1	Turbine 4		-4.86	-9.13	-6.92	0.76	4.27	
Apr07_T_06_1m	Surveyed in April 2007	1 * 1	Turbine 5		-4.21	-7.78	-6.18	0.63	3.57	
Apr07_T_07_1m	Surveyed in April 2007	1 * 1	Turbine 6		-2.13	-6.58	-4.43	0.81	4.45	
Ch_01_1m	Surveyed in 2007 (month not specified)	1 * 1	Cable route		-2.33	-17.58	-14.15	3.23	15.25	

Filename	Survey Date	Res	Area covered	Notes	Max	Min	Mean	Range	Std_Dev	Folder
Ch_02_1m	Surveyed in 2007 (month not specified)	1 * 1	Cable route		-15.73	-26.21	-20.30	2.78	10.48	
Ch_03_1m	Surveyed in 2007 (month not specified)	1 * 1	Cable route		-15.66	-33.57	-27.15	3.80	17.91	
Ch_04_1m	Surveyed in 2007 (month not specified)	1 * 1	Cable route	The survey covers phase 1 Turbine 1 through 7 as well	-2.19	-33.71	-11.79	9.63	31.52	
Diff_April07-June06_T04	bed change between April 2007 and June 2006	1 * 1	Turbine 4	bedchange	0.34	-1.45	-0.64	0.23	1.79	
Diff_April07-June06_T05	bed change between April 2007 and June 2006	1 * 1	Turbine 5	bedchange	1.38	-0.71	0.17	0.28	2.09	
Diff_April07-June06_T06	bed change between April 2007 and June 2006	1 * 1	Turbine 6	bedchange	2.04	-4.81	-0.82	1.29	6.85	
Diff_April07-June06_T07	bed change between April 2007 and June 2006	1 * 1	Turbine 7	bedchange	0.93	-2.54	-0.94	0.53	3.47	
Diff_Area 01_Apr07 - Jun06	bed change between April 2007 and June 2006	1 * 1	Area west of Turbine 06	bedchange	2.50	-2.87	0.02	0.78	5.37	
Diff_April07-June06_T02	bed change between April 2007 and June 2006	1 * 1	Turbine 2	bedchange	3.42	-0.82	0.89	0.70	4.24	
Diff_April07-June06_T03	bed change between April 2007 and June 2006	1 * 1	Turbine 3	bedchange	1.75	-2.54	-0.19	1.05	4.29	
Ch_02_xs - Ch_02_lines	Files failed to process, to be investigated further									
Ch_03_xs - Ch_03_lines	Files failed to process, to be investigated further									
Ch_04_bank xs - Ch_04_bank lines	Files failed to process, to be investigated further									
Ch_04_xs - Ch_04_lines	Files failed to process, to be investigated further									

Filename	Survey Date	Res	Area covered	Notes	Max	Min	Mean	Range	Std_Dev	Folder
Diff_April07-June06_T01	Files failed to process, to be investigated further									
Ch_01_xs - Ch_01_lines	Files failed to process, to be investigated further									
Diff_T_05_May08-Apr07	bed change between May 2008 and April 2007	1 * 1	Turbine 5	bedchange	4.06	0.42	2.17	0.48	3.64	2008
CH_01	Surveyed in 2008 (month not specified)	1 * 1	Cable route		-2.56	-17.45	-14.04	3.17	14.89	
CH_02	Surveyed in 2008 (month not specified)	1 * 1	Cable route		-15.64	-26.01	-20.17	2.75	10.37	
CH_03	Surveyed in 2008 (month not specified)	1 * 1	Cable route		-15.45	-33.21	-27.02	3.8	17.76	
CH_04	Surveyed in 2008 (month not specified)	1 * 1	Cable route	The survey covers phase 1 Turbine 1 through 7 as well	-1.54	-33.21	-10.17	8.73	31.67	
Diff_Area_01_May08-Apr07	bed change between May 2008 and April 2007	1 * 1	Turbine 1	bedchange	3.92	-1.23	1.2	1.12	5.15	
Diff_T_01_May08-Apr07	bed change between May 2008 and April 2007	1 * 1	Turbine 2	bedchange	2.33	0.14	1.24	0.29	2.19	
Diff_T_02_May08-Apr07	bed change between May 2008 and April 2007	1 * 1	Turbine 3	bedchange	1.42	-1.13	0.28	0.37	2.55	
Diff_T_03_May08-Apr07	bed change between May 2008 and April 2007	1 * 1	Turbine 4	bedchange	2.69	-1.35	0.63	0.69	4.04	
Diff_T_04_May08-Apr07	bed change between May 2008 and April 2007	1 * 1	Turbine 6	bedchange	4.97	-0.45	2.48	1.08	5.42	
Diff_T_06_May08-Apr07	bed change between May 2008 and April 2007	1 * 1	Turbine 7	bedchange	1.27	-3.42	-1.22	0.98	4.69	
Diff_T_07_May08-Apr07	bed change between May 2008 and April 2007	1 * 1	Area west of turbine 06	bedchange	4.19	0.48	1.93	0.57	3.71	
May08_Area 01_1m	Surveyed in May 2008	1 * 1	Turbine 1		-23.1	-28.96	-25.86	1.28	5.86	

Filename	Survey Date	Res	Area covered	Notes	Max	Min	Mean	Range	Std_Dev	Folder
May08_T_01_1m	Surveyed in May 2008	1 * 1	Turbine 2		-4.04	-9.04	-6.95	0.65	5	
May08_T_02_1m	Surveyed in May 2008	1 * 1	Turbine 3		-3.4	-7.83	-5.8	0.88	4.43	
May08_T_03_1m	Surveyed in May 2008	1 * 1	Turbine 4		-2.68	-7.19	-4.72	0.74	4.51	
May08_T_04_1m	Surveyed in May 2008	1 * 1	Turbine 5		-5.13	-9.18	-6.74	0.48	4.05	
May08_T_05_1m	Surveyed in May 2008	1 * 1	Turbine 6		-5.3	-10.99	-8.06	1.02	5.69	
May08_T_06_1m	Surveyed in May 2008	1 * 1	Turbine 7		-1.78	-7.47	-4.46	0.97	5.69	
May08_T_07_1m	Surveyed in May 2008	1 * 1			-2.67	-7.04	-5.17	0.68	4.37	
CH_03 xes - CH_03 lines	Files failed to process, to be investigated further, Update: small coverage area (lines) in the cable route									
CH_04 bank xes - CH_04 bank lines	Files failed to process, to be investigated further, Update: small coverage area (lines) in the cable route									
CH_01 xes - CH_01 lines	Files failed to process, to be investigated further, Update: small coverage area (lines) in the cable route									
CH_02 xes - CH_02 lines	Files failed to process, to be investigated further, Update: small coverage area (lines) in the cable route									
apr09 CH_01	Surveyed in April 2009	1 * 1	Cable route		-2.73	-17.62	-14.08	3.16	14.89	2009
apr09 CH_02	Surveyed in April 2009	1 * 1	Cable route		-15.61	-26.25	-20.22	2.77	10.64	
apr09 CH_03	Surveyed in April 2009	1 * 1	Cable route		-15.58	-33.46	-27.28	3.72	17.88	
apr09 CH_04	Surveyed in April 2009	1 * 1	Cable route	The survey covers phase 1	-1.97	-34.2	-9.18	7.88	32.23	

Filename	Survey Date	Res	Area covered	Notes	Max	Min	Mean	Range	Std_Dev	Folder
				Turbine 1 through 7 as well						
apr09_Area_1	Surveyed in April 2009	1 * 1	Area west of Turbine 6		-24.04	-28.4	-25.95	0.89	4.36	
apr09_T_01	Surveyed in April 2009	1 * 1	Turbine 1		-2.69	-6.8	-4.78	0.93	4.11	
apr09_T_02	Surveyed in April 2009	1 * 1	Turbine 2		-3.01	-6.5	-4.39	0.48	3.49	
apr09_T_03	Surveyed in April 2009	1 * 1	Turbine 3		-3.94	-7.02	-5.45	0.52	3.08	
apr09_T_04	Surveyed in April 2009	1 * 1	Turbine 4		-5.86	-16.4	-8.56	1.72	10.54	
apr09_T_05	Surveyed in April 2009	1 * 1	Turbine 5		-4.7	-16.13	-9.4	1.75	11.43	
apr09_T_06	Surveyed in April 2009	1 * 1	Turbine 6		-1.97	-6.65	-4.89	0.79	4.68	
apr09_T_07	Surveyed in April 2009	1 * 1	Turbine 7		-4.22	-7.95	-5.81	0.7	3.73	
T 01 June 2010	Surveyed in June 2010	1 * 1	Turbine 1		-2.75	-5.44	-3.94	0.33	2.69	2010
T 02 June 2010	Surveyed in June 2010	1 * 1	Turbine 2		-3.63	-6.44	-4.78	0.36	2.81	
T 03 June 2010	Surveyed in June 2010	1 * 1	Turbine 3		-5.12	-7.94	-6.45	0.37	2.82	
T 04 June 2010	Surveyed in June 2010	1 * 1	Turbine 4		-6.5	-15.65	-9.5	1.35	9.15	
T 05 June 2010	Surveyed in June 2010	1 * 1	Turbine 5		-3.28	-12.06	-7.1	2.23	8.78	
T 06 June 2010	Surveyed in June 2010	1 * 1	Turbine 6		-3.59	-6.59	-4.98	0.44	3	
T 07 June 2010	Surveyed in June 2010	1 * 1	Turbine 7		-4.73	-10.33	-6.92	0.8	5.6	
diff T_01 jun2010 - apr2009	bed change between June 2010 and April 2009	1 * 1	Turbine 1		2.82	-0.67	1.02	0.71	3.49	
diff T_02 jun2010 - apr2009	bed change between June 2010 and April 2009	1 * 1	Turbine 2		0.88	-1.87	-0.58	0.48	2.75	
diff T_03 jun2010 - apr2009	bed change between June 2010 and April 2009	1 * 1	Turbine 3		0.51	-2.48	-1.13	0.41	2.99	
diff T_04 jun2010 - apr2009	bed change between June 2010 and April 2009	1 * 1	Turbine 4		4.08	-2.89	-0.39	1.15	6.97	
diff T_05 jun2010 - apr2009	bed change between June 2010 and April 2009	1 * 1	Turbine 5		8.36	-2.89	3.34	1.81	11.25	
diff T_06 jun2010 - apr2009	bed change between June 2010 and April 2009	1 * 1	Turbine 6		1.31	-0.83	0.22	0.28	2.14	
diff T_07 jun2010 - apr2009	bed change between June 2010 and April 2009	1 * 1	Turbine 7		0.55	-3.79	-1.21	0.58	4.34	

Filename	Survey Date	Res	Area covered	Notes	Max	Min	Mean	Range	Std_Dev	Folder
jul11 Chart 01	Surveyed in July 2011	1 * 1	Cable route		-1.99	-17.46	-13.94	3.2	15.47	2011
jul11 Chart 02	Surveyed in July 2011	1 * 1	Cable route		-15.83	-26.18	-20.19	2.74	10.35	
jul11 Chart 03	Surveyed in July 2011	1 * 1	Cable route		-15.16	-33.32	-26.89	3.87	18.16	
jul11 Chart 04	Surveyed in July 2011	1 * 1	Cable route	The survey covers phase 1 Turbine 1 through 7 as well	-1.46	-34.23	-9.16	7.74	32.77	
jul11 Met Mast 100m	Surveyed in July 2011	1 * 1	Area south of Tubrine 1		-2.33	-6.62	-3.69	0.47	4.29	
jul11 T_01 200m	Surveyed in July 2011	1 * 1	Phase 1Turbine 1		-3.24	-6.54	-4.55	0.42	3.3	
jul11 T_02 200m	Surveyed in July 2011	1 * 1	Phase 1 Turbine 2		-4.24	-7.28	-5.65	0.52	3.04	
jul11 T_03 200m	Surveyed in July 2011	1 * 1	Phase 1 Turbine 3		-4.9	-8.4	-7.03	0.48	3.5	
jul11 T_04 200m	Surveyed in July 2011	1 * 1	Phase 1 Turbine 4		-2.54	-17.14	-8.4	2.44	14.6	
jul11 T_05 200m	Surveyed in July 2011	1 * 1	Phase 1 Turbine 5		-2.13	-12.83	-6.05	2.22	10.7	
jul11 T_06 200m	Surveyed in July 2011	1 * 1	Phase 1 Turbine 6		-4.16	-7.86	-5.63	0.7	3.7	
jul11 T_07 200m	Surveyed in July 2011	1 * 1	Phase 1 Turbine 7		-3.84	-8.26	-5.81	1.01	4.42	
Vol Met Mast 2011-2010	bed change between 2011 and 2010 (month not specified)	1 * 1	Area south of Tubrine 1		5.69	1.56	4.07	0.53	4.13	
Vol T_01 2011-2010	bed change between 2011 and 2010 (month not specified)	1 * 1	Phase 1 Turbine 1		0.33	-2.46	-0.82	0.38	2.79	

Filename	Survey Date	Res	Area covered	Notes	Max	Min	Mean	Range	Std_Dev	Folder
Vol T_02 2011-2010	bed change between 2011 and 2010 (month not specified)	1 * 1	Phase 1 Turbine 2		0.72	-1.85	-0.94	0.34	2.57	
Vol T_03 2011-2010	bed change between 2011 and 2010 (month not specified)	1 * 1	Phase 1 Turbine 3		0.78	-1.71	-0.53	0.31	2.49	
Vol T_04 2011-2010	bed change between 2011 and 2010 (month not specified)	1 * 1	Phase 1 Turbine 4		3.75	-4.47	0.32	1.49	8.22	
Vol T_05 2011-2010	bed change between 2011 and 2010 (month not specified)	1 * 1	Phase 1 Turbine 5		2.88	-2.97	0.53	1.12	5.85	
Vol T_06 2011-2010	bed change between 2011 and 2010 (month not specified)	1 * 1	Phase 1 Turbine 6		0.72	-2.3	-0.61	0.38	3.02	
Vol T_07 2011-2010	bed change between 2011 and 2010 (month not specified)	1 * 1	Phase 1 Turbine 7		3.66	-0.73	1.32	0.67	4.39	
Vol Met Mast 2012-2011	bed change between 2012 and 2011 (month not specified)	1 * 1	Area south of Tubrine 1		0.66	-1.85	-0.41	0.37	2.51	2012
Vol_diff 2012-2011 T_01	bed change between 2012 and 2011 (month not specified)	1 * 1	Phase 1 Turbine 1		1.57	-2.88	-1.07	0.62	4.45	
Vol_diff 2012-2011 T_02	bed change between 2012 and 2011 (month not specified)	1 * 1	Phase 1 Turbine 2		0.5	-1.83	-0.71	0.28	2.33	
Vol_diff 2012-2011 T_03	bed change between 2012 and 2011 (month not specified)	1 * 1	Phase 1 Turbine 3		0.4	-1.59	-0.51	0.33	1.99	
Vol_diff 2012-2011 T_04	bed change between 2012 and 2011 (month not specified)	1 * 1	Phase 1 Turbine 4		9.26	-1.64	4.64	2.1	10.9	

Filename	Survey Date	Res	Area covered	Notes	Max	Min	Mean	Range	Std_Dev	Folder
Vol_diff 2012-2011 T_05	bed change between 2012 and 2011 (month not specified)	1 * 1	Phase 1 Turbine 5		8.66	-2.03	2.66	1.92	10.69	
Vol_diff 2012-2011 T_06	bed change between 2012 and 2011 (month not specified)	1 * 1	Phase 1 Turbine 6		2.12	-0.68	0.28	0.33	2.8	
Vol_diff 2012-2011 T_07	bed change between 2012 and 2011 (month not specified)	1 * 1	Phase 1 Turbine 7		1.92	-0.82	0.52	0.32	2.74	
Apr13 Met Mast	Surveyed in April 2013	1 * 1	Area south of Turbine 1		-2.74	-7.78	-4.52	0.92	5.04	2013
Apr13 T_01	Surveyed in April 2013	1 * 1	Phase 1 Turbine 1		-4.16	-8.74	-6.35	0.59	4.58	
Apr13 T_02	Surveyed in April 2013	1 * 1	Phase 1 Turbine 2		-4.91	-9.3	-6.87	0.71	4.39	
Apr13 T_03	Surveyed in April 2013	1 * 1	Phase 1 Turbine 3		-3.09	-10.44	-7	1.31	7.35	
Apr13 T_04	Surveyed in April 2013	1 * 1	Phase 1 Turbine 4		-0.29	-6.93	-3.02	1.12	6.64	
Apr13 T_05	Surveyed in April 2013	1 * 1	Phase 1 Turbine 5		-1.25	-4.67	-3.02	0.62	3.42	
Apr13 T_06	Surveyed in April 2013	1 * 1	Phase 1 Turbine 6		-2.13	-6.32	-4.43	0.84	4.19	
Apr13 T_07	Surveyed in April 2013	1 * 1	Phase 1 Turbine 7		-2.68	-8.16	-5.35	1.14	5.48	
xyz Data from 2014 is missing (while images exist), will attempt to find it in the Arklow sharepoint										
BANK 2015 FINAL	Surveyed in 2015 (month not mentioned)	1 * 1	Phase 1 Cable route end (bank area)	The survey covers phase 1 Turbine 1 through 7 as well	-0.22	-33.49	-8.5	9.13	33.27	2015
Chart_01 2015 FINAL (edit)	Surveyed in 2015 (month not mentioned)	1 * 1	Phase 1 Cable route		-3.91	-17.79	-14.36	2.96	13.88	

Filename	Survey Date	Res	Area covered	Notes	Max	Min	Mean	Range	Std_Dev	Folder
Chart_02 2015 FINAL (edit)	Surveyed in 2015 (month not mentioned)	1 * 1	Phase 1 Cable route		-15.81	-26.34	-20.47	2.73	10.53	
Chart_03 2015 FINAL (edit)	Surveyed in 2015 (month not mentioned)	1 * 1	Phase 1 Cable route		-14.44	-33.49	-27.25	3.96	19.05	
diff 2015 - 2014 Met Mast	bed change between 2015 and 2014 (month not specified)	1 * 1	Area south of Turbine 1		2.31	-2.34	-0.26	1.03	4.65	
diff 2015 - 2014 T_01	bed change between 2015 and 2014 (month not specified)	1 * 1	Phase 1 Turbine 1		7.22	-1.11	3.64	1.34	8.33	
diff 2015 - 2014 T_02	bed change between 2015 and 2014 (month not specified)	1 * 1	Phase 1 Turbine 2		7.54	-0.28	3.1	1.31	7.82	
diff 2015 - 2014 T_03	bed change between 2015 and 2014 (month not specified)	1 * 1	Phase 1 Turbine 3		2.44	-2.07	0.44	0.65	4.51	
diff 2015 - 2014 T_04	bed change between 2015 and 2014 (month not specified)	1 * 1	Phase 1 Turbine 4		4.64	-1.31	1.31	1.06	5.95	
diff 2015 - 2014 T_05	bed change between 2015 and 2014 (month not specified)	1 * 1	Phase 1 Turbine 5		0.51	-3.28	-1.04	0.6	3.79	
diff 2015 - 2014 T_06	bed change between 2015 and 2014 (month not specified)	1 * 1	Phase 1 Turbine 6		1.82	-1.8	0.06	0.54	3.62	
diff 2015 - 2014 T_07	bed change between 2015 and 2014 (month not specified)	1 * 1	Phase 1 Turbine 7		4.99	-0.62	2.17	0.7	5.61	
Met Mast FINAL	Surveyed in 2015 (month not mentioned)	1 * 1	Area south of Turbine 1		-3.28	-6.71	-4.23	0.35	3.43	
T_01 FINAL	Surveyed in 2015 (month not mentioned)	1 * 1	Phase 1 Turbine 1		-3.06	-6.62	-4.17	0.52	3.56	
T_02 FINAL	Surveyed in 2015 (month not mentioned)	1 * 1	Phase 1 Turbine 2		-1.91	-6.61	-3.09	0.39	4.7	

Filename	Survey Date	Res	Area covered	Notes	Max	Min	Mean	Range	Std_Dev	Folder
T_03 FINAL	Surveyed in 2015 (month not mentioned)	1 * 1	Phase 1 Turbine 3		-0.57	-6.71	-2.53	0.72	6.14	
T_04 FINAL	Surveyed in 2015 (month not mentioned)	1 * 1	Phase 1 Turbine 4		-0.39	-6.46	-2.55	0.62	6.07	
T_05 FINAL	Surveyed in 2015 (month not mentioned)	1 * 1	Phase 1 Turbine 5		-2.46	-7.54	-4.45	0.87	5.08	
T_06 FINAL	Surveyed in 2015 (month not mentioned)	1 * 1	Phase 1 Turbine 6		-0.7	-6.84	-3.38	1.08	6.14	
T_07 FINAL	Surveyed in 2015 (month not mentioned)	1 * 1	Phase 1 Turbine 7		-1.08	-8.92	-4.37	1.47	7.84	
ARKLOW BANK FINAL 4M GRID 2015	Survyed in 2015 (according to file name)	4 * 4	Phase 1 bank	The survey covers phase 1 Turbine 1 through 7 as well	-0.33	-12.44	-3.89	1.62	12.11	2016
CABLE ROUTE 4M GRID	Not specified	4 * 4	Entire Phase 1 cable route		-0.19	-33.65	-21.22	6.53	33.46	
diff 2016 - 2015 Met Mast	bed change between 2016 and 2015 (month not specified)	1 * 1	Area south of Turbine 1		3.29	0.48	1.89	0.39	2.81	
Met	Not specified	1 * 1	Area south of Turbine 1		-4.51	-9.11	-6.03	0.51	4.6	
T1	Not specified	1 * 1	Phase 1 Turbine 1		-0.88	-6.72	-3.89	0.73	5.84	
T2	Not specified	1 * 1	Phase 1 Turbine 2		-1.14	-7.66	-3.82	1.16	6.52	
T3	Not specified	1 * 1	Phase 1 Turbine 3		-0.74	-6.5	-3.17	0.78	5.76	
T4	Not specified	1 * 1	Phase 1 Turbine 4		-1.87	-6.58	-3.46	0.5	4.71	
T5	Not specified	1 * 1	Phase 1 Turbine 5		-1.24	-6.91	-2.79	0.66	5.67	

Filename	Survey Date	Res	Area covered	Notes	Max	Min	Mean	Range	Std_Dev	Folder
T6	Not specified	1 * 1	Phase 1 Turbine 6		-1.87	-5.58	-3.74	0.68	3.71	
T7	Not specified	1 * 1	Phase 1 Turbine 7		-3.11	-7.11	-4.77	0.78	4	
Diff 2017 - 2016 Met Mast	bed change between 2017 and 2016 (month not specified)	1 * 1	Area south of Turbine 1	bedchange	2.24	-0.94	0.72	0.37	3.18	2017
Diff 2017 - 2016 T_01	bed change between 2017 and 2016 (month not specified)	1 * 1	Phase 1 Turbine 1	bedchange	3.12	-2.26	0	0.54	5.38	
Diff 2017 - 2016 T_02	bed change between 2017 and 2016 (month not specified)	1 * 1	Phase 1 Turbine 2	bedchange	1.83	-3.9	-0.47	0.81	5.73	
Diff 2017 - 2016 T_03	bed change between 2017 and 2016 (month not specified)	1 * 1	Phase 1 Turbine 3	bedchange	2.61	-1.92	-0.02	0.59	4.53	
Diff 2017 - 2016 T_04	bed change between 2017 and 2016 (month not specified)	1 * 1	Phase 1 Turbine 4	bedchange	4.59	-2.79	-0.37	1.21	7.38	
Diff 2017 - 2016 T_05	bed change between 2017 and 2016 (month not specified)	1 * 1	Phase 1 Turbine 5	bedchange	4.53	-0.54	1.64	0.59	5.07	
Diff 2017 - 2016 T_06	bed change between 2017 and 2016 (month not specified)	1 * 1	Phase 1 Turbine 6	bedchange	0.56	-3.84	-1.43	0.7	4.4	
Diff 2017 - 2016 T_07	bed change between 2017 and 2016 (month not specified)	1 * 1	Phase 1 Turbine 7	bedchange	0.86	-3.3	-1.15	0.69	4.16	
Diff 2018 - 2017 Met Mast	bed change between 2018 and 2017 (month not specified)	1 * 1	Area south of Turbine 1	bedchange	0.77	-1.8	-0.32	0.36	2.57	2018
Diff 2018 - 2017 T_01	bed change between 2018 and 2017 (month not specified)	1 * 1	Phase 1 Turbine 1	bedchange	3	-1.48	0.2	0.57	4.48	

Filename	Survey Date	Res	Area covered	Notes	Max	Min	Mean	Range	Std_Dev	Folder
Diff 2018 - 2017 T_02	bed change between 2018 and 2017 (month not specified)	1 * 1	Phase 1 Turbine 2	bedchange	2.76	-0.93	0.92	0.59	3.69	
Diff 2018 - 2017 T_03	bed change between 2018 and 2017 (month not specified)	1 * 1	Phase 1 Turbine 3	bedchange	2.55	-0.71	0.58	0.5	3.26	
Diff 2018 - 2017 T_04	bed change between 2018 and 2017 (month not specified)	1 * 1	Phase 1 Turbine 4	bedchange	3.01	-2.31	0.81	0.99	5.32	
Diff 2018 - 2017 T_05	bed change between 2018 and 2017 (month not specified)	1 * 1	Phase 1 Turbine 5	bedchange	2.7	-0.46	0.97	0.42	3.16	
Diff 2018 - 2017 T_06	bed change between 2018 and 2017 (month not specified)	1 * 1	Phase 1 Turbine 6	bedchange	2.83	-0.71	1.09	0.64	3.54	
Diff 2018 - 2017 T_07	bed change between 2018 and 2017 (month not specified)	1 * 1	Phase 1 Turbine 7	bedchange	2.13	-3.51	-0.32	1.1	5.64	
Arklow_Bathy_2016	2016	2 * 2	Phase 2 Bank		-0.56	-49.528	-23.15	50.21	11.69	2016
GDG_19158_UTM30N_LA_2019_1M_MBES_Bathymetry	2019	1 * 1	Phase 2 Bank		-0.88	-51.48	-22.47	50.59	11.12	2019
GDG_19158_CR_UTM30N_MBES_Bathymetry	2019	1 * 1	Phase 2 cable route options		-1.9	-39.88	-22.1	37.9	7.26	
2011 data - Merged INFOMAR surveys covering regions coincident with the proposed export cable routes (these were later merged with surveys of Arklow Bank performed in 2016).	2011 / 2016	3 * 3	Phase 2 cable route and Lease area		-0.38	-119.79	-28.06	119.40	11.33	
IA1_P_PH01	11/07/2020	0.25 * 0.25	IA1 Primary		-0.4	-28.19	-13.8516	27.79	7.42	2020 Repeat MBES survey
IA1_P_PH02	25/07/2020	0.25 * 0.25	IA1 Primary		0.3	-28.15	-14.5325	28.45	7.52	
IA1_P_PH03	09/08/2020	0.25 * 0.25	IA1 Primary		-0.17	-28.14	-14.2436	27.97	7.49	
IA1_S_PH01	15/07/2020	0.25 * 0.25	IA1 Secondary		-4.78	-28.1	-18.5946	23.32	7.10	

Filename	Survey Date	Res	Area covered	Notes	Max	Min	Mean	Range	Std_Dev	Folder
IA1_S_PH03	25/07/2020	0.25 * 0.25	IA1 Secondary		-1.67	-28.13	-16.1663	26.46	8.08	
IA1_TR_197_1	15/07/2020	0.25 * 0.25	IA1 Transect		-3.14	-27.9	-14.6164	24.76	7.34	
IA1_TR_202_1	20/07/2020	0.25 * 0.25	IA1 Transect		-3.16	-28.14	-16.1602	24.98	7.99	
IA1_TR_203_1	21/07/2020	0.25 * 0.25	IA1 Transect	Post Slack Water	-2.78	-28.09	-15.5121	25.31	7.77	
IA1_TR_203_2	21/07/2020	0.25 * 0.25	IA1 Transect	Pre-Slack Water	-3.14	-28.15	-15.1376	25.01	7.70	
IA1_TR_219_1	06/08/2020	0.25 * 0.25	IA1 Transect		-3.26	-28.15	-17.7039	24.89	7.72	
IA1_TR_220_1	07/08/2020	0.25 * 0.25	IA1 Transect		-2.76	-28.12	-18.1378	25.36	7.52	
IA2_P_PH01	14/07/2020	0.25 * 0.25	IA2 Primary		-0.61	-32.43	-15.6656	31.82	8.63	
IA2_P_PH02	29/07/2020	0.25 * 0.25	IA2 Primary		-0.57	-32.49	-15.7703	31.92	8.59	
IA2_P_PH03	11/08/2020	0.25 * 0.25	IA2 Primary		-0.48	-32.46	-15.6475	31.98	8.66	
IA2_S_PH01	14/07/2020	0.25 * 0.25	IA2 Secondary		-2.37	-29.01	-18.3864	26.64	7.14	
IA2_S_PH02	15/07/2020	0.25 * 0.25	IA2 Secondary		-0.12	-29.08	-18.5362	28.96	7.10	
IA2_S_PH03	10/08/2020	0.25 * 0.25	IA2 Secondary	Weather conditions not good	-2.29	-31.65	-17.7338	29.36	7.77	
IA2_TR_197_1	15/07/2020	0.25 * 0.25	IA2 Transect		-0.94	-33.81	-17.3286	32.87	9.05	
IA2_TR_202_1	20/07/2020	0.25 * 0.25	IA2 Transect		-3.48	-33.81	-17.0636	30.33	8.87	
IA2_TR_203_1	21/07/2020	0.25 * 0.25	IA2 Transect	Pre-Slack Water	-3.31	-34.02	-17.7254	30.71	9.22	
IA2_TR_203_2	21/07/2020	0.25 * 0.25	IA2 Transect	Post Slack Water	-3.3	-33.91	-17.6674	30.61	8.95	
IA2_TR_207_1	25/07/2020	0.25 * 0.25	IA2 Transect	Low Slack Water	-3.26	-33.78	-16.6499	30.52	8.90	
IA2_TR_208_1	26/07/2020	0.25 * 0.25	IA2 Transect	High Slack Water	-3.36	-32.93	-16.8559	29.57	8.63	
IA2_TR_219_1	06/08/2020	0.25 * 0.25	IA2 Transect		-3.35	-34.78	-18.5273	31.43	9.15	

Filename	Survey Date	Res	Area covered	Notes	Max	Min	Mean	Range	Std_Dev	Folder
IA2_TR_220_1	07/08/2020	0.25 * 0.25	IA2 Transect		-3.38	-33.85	-19.1105	30.47	9.08	
IA2_TR_224_1	11/08/2020	0.25 * 0.25	IA2 Transect		-2.94	-33.81	-19.0404	30.87	9.03	
IA2_TR_224_2	11/08/2020	0.25 * 0.25	IA2 Transect		-3.29	-34.53	-18.7302	31.24	8.96	
IA3_P_PH1	12/07/2020	0.25 * 0.25	IA3 Primary		-0.75	-27.98	-10.6349	27.23	6.50	
IA3_P_PH2	28/07/2020	0.25 * 0.25	IA3 Primary		-0.62	-28.33	-11.0813	27.71	6.53	
IA3_P_PH3	12/08/2020	0.25 * 0.25	IA3 Primary		-1.18	-28.27	-11.3279	27.09	6.50	
IA3_S_PH2	26/07/2020	0.25 * 0.25	IA3 Secondary		-2.88	-26.82	-13.5512	23.94	5.85	
IA3_TR_195_1	13/07/2020	0.25 * 0.25	IA3 Transect		-3.06	-40.12	-14.8053	37.06	7.96	
IA3_TR_197_1	15/07/2020	0.25 * 0.25	IA3 Transect		-3.04	-33.65	-15.5437	30.61	9.02	
IA3_TR_219_1	06/08/2020	0.25 * 0.25	IA3 Transect		-2.69	-33.04	-14.4038	30.35	8.04	
IA3_TR_220_1	07/08/2020	0.25 * 0.25	IA3 Transect		-0.99	-33.45	-15.4689	32.46	8.36	
IA3_TR_220_2	07/08/2020	0.25 * 0.25	IA3 Transect		-2.45	-34.15	-15.1225	31.7	8.47	
IA4_P_PH1	10/07/2020	0.25 * 0.25	IA4 Primary		-12.06	-30.11	-20.2497	18.05	4.53	
IA4_P_PH2	24/07/2020	0.25 * 0.25	IA4 Primary		-12.39	-28.86	-20.142	16.47	4.50	
IA4_P_S_PH3	08/08/2020	0.25 * 0.25	IA4 Primary		-12.47	-28.8	-20.1285	16.33	4.50	
IA4_S_PH1	10/07/2020	0.25 * 0.25	IA4 Secondary		-21.67	-30.11	-25.2409	8.44	1.47	
IA4_TR_197_1	15/07/2020	0.25 * 0.25	IA4 Transect		-13.03	-27.91	-21.3388	14.88	4.57	
IA4_TR_219_1	06/08/2020	0.25 * 0.25	IA4 Transect		-13	-27.8	-20.8921	14.8	4.58	

Filename	Survey Date	Res	Area covered	Notes	Max	Min	Mean	Range	Std_Dev	Folder
IA4_TR_220_1	07/08/2020	0.25 * 0.25	IA4 Transect		-0.36	-32.04	-21.7552	31.68	4.52	
IA5_TR_197_1	15/07/2020	0.25 * 0.25	IA5 Transect		-2.73	-35.59	-16.5783	32.86	10.09	
IA5_TR_198_2	16/07/2020	0.25 * 0.25	IA5 Transect	Low Slack Water	-2.7	-57.71	-15.6148	55.01	9.62	
IA5_TR_202_1	20/07/2020	0.25 * 0.25	IA5 Transect	High Slack Water	-2.64	-35.82	-16.9775	33.18	10.22	
IA5_TR_203_1	21/07/2020	0.25 * 0.25	IA5 Transect	Slack Water	-2.62	-35.3	-16.5359	32.68	9.57	
IA5_TR_203_2	21/07/2020	0.25 * 0.25	IA5 Transect	Slack Water	-2.65	-35.7	-15.0962	33.05	9.26	
IA5_TR_210_1	28/07/2020	0.25 * 0.25	IA5 Transect	10 mins past low slack water	-2.57	-34.44	-16.4619	31.87	9.41	
IA5_TR_210_2	28/07/2020	0.25 * 0.25	IA5 Transect	10 mins before high slack water	-2.49	-35.6	-16.8195	33.11	9.94	
IA5_TR_211_1	29/07/2020	0.25 * 0.25	IA5 Transect		-2.72	-34.41	-16.2811	31.69	9.31	
IA5_TR_219_1	06/08/2020	0.25 * 0.25	IA5 Transect		-2.43	-34.76	-17.3404	32.33	9.88	
IA5_TR_220_1	07/08/2020	0.25 * 0.25	IA5 Transect		-2.41	-34.75	-17.9312	32.34	9.55	
IA5_TR_220_2	07/08/2020	0.25 * 0.25	IA5 Transect		-2.37	-35.61	-16.9885	33.24	9.81	

Table 23. The data sources utilised as part of the study of site morphodynamics.

	Document/file name	Document/Data type	Issue Date	Data Info	Author	Source	Spatial cover	Application / Utility
Hydrographic and Metocean Conditions	Hydrographic and Underwater Inspections – Post construction Phase 1	Reports	2004 to 2017		Various	SSE	Arklow Bank Phase 1	Literature review
	Hydrography of the Irish Sea	SEA6 Technical Report	2005		Howarth M. J.	UK DTI	Regional	Literature review
	M2, M5 Wave Buoy	.CSV data	1984 to 2017	Wave and wind data of hourly-mean		Marine Data Centre, Marine Institute, Ireland	Regional	Input and validation data
	Arklow Harbour Tidal Gauge	.CSV data	1984 to 2017	Hourly- mean tidal level and period		Marine Data Centre, Marine Institute, Ireland	Regional	Input and validation data
	Fugro Metocean Data	.CSV data and report	2020	Half hourly data, for temperature, conductivity, salinity, density, turbidity waves, water level, currents,in five locations in the bank	Various	Fugro	Local	Model validation and data-led analysis

	Document/file name	Document/Data type	Issue Date	Data Info	Author	Source	Spatial cover	Application / Utility
Geophysical Survey	Fugro Phase 1 Interpretative Report 04504-1	Report and PDF charts No data available	2000	Irish National Grid Chart Datum	Fugro/ Hydrographic Surveys	SSE	Arklow Bank	Literature Review
	Seacore Geophysical Interim Report 221002	Report and PDF charts No data available	2002		Seacore	SSE	Arklow Bank, Phase 1	Literature Review
Bathymetry	ARK_Bathymetry140by230_EMODnet	.GeoTIFF		WGS84/UTM29 140m x 230m resolution	EMODnet	SSE	Regional	Regional GIS analysis
	INFOMAR_2016_2011	.GeoTIFF	2011 and 2016	WGS84/UTM29 2-10m resolution	INFOMAR	SSE	Meso-scale	Highest level of confidence data in bathymetry
	Arklow_Rambol_Bathymetry	Report and PDF charts	2000		Ramboll	SSE	Arklow Bank	Literature Review
	Arklow Bathy	Report and PDF charts	2002	Irish National Grid/ Ordnance Survey of Ireland's approximate MSL	Seacore	SSE	Arklow Bank phase 1	Literature review

	Document/file name	Document/Data type	Issue Date	Data Info	Author	Source	Spatial cover	Application / Utility
	OCB Chart 1787 A1, A7, B1, B24, C1 and C14	GeoTIFF charts	1847 to 2005	Bathymetry contour lines (require georeferencing)	Various	UKHO	Meso-scale	GIS volume assessment
	Post-construction bathymetric surveys	.GeoTIFF and .Surfer data	2004 to 2018	WGS84/UTM29 2-5m resolution		SSE	Arklow Bank, Phase 1 Turbines T1 to T7 and part of cable route	Assess bedforms near turbines and cables.
	Arklow Bank MBES Interpretation	Technical Reports and PDF charts of 2016 and 2011 Survey	2018	WGS84/UTM29	Coughlan, M.	GDG	Arklow Bank	Literature review
	2019 Bathymetry Survey	Technical reports, and Raster files	2019	WGS84/UTM29	Various	GDG	Arklow bank – Phase 2	Bathymetry used in model set-up and for data led assessment of the lease area\cable route

	Document/file name	Document/Data type	Issue Date	Data Info	Author	Source	Spatial cover	Application / Utility
	2020 Repeat MBES surveys	Technical report, and raster data,	2019	WGS84/UTM29 0.25 * 0.25 m res, mLAT	Various	Alpha Marine	4 investigation areas in the bank and one along the cable route	Model cal-val, and data led analysis of the lease area and the cable route
Seabed Features/ Surficial Sediment	Benthic surveys of sandbanks in the Irish Sea	Technical Reports	2007		Roche et al.	Department of the Environment, Heritage and Local Government	Regional	Literature review
	Benthic biodiversity in the Southern Irish Sea	Book	2001		Wilson J. G.		Regional	Literature review
	Seabed Substrate	1:250k shapefile		WGS84	EMODnet Geology	EMODnet	Regional	GIS
Seabed/Sub-	DTI Strategic Environmental Assessment Area 6, Irish Sea, seabed and surficial geology and processes	Technical Report	2005		Holmes, R. and Tappin, D. R.	BGS	Regional	Literature review

	Document/file name	Document/Data type	Issue Date	Data Info	Author	Source	Spatial cover	Application / Utility
	Geology of the seabed and shallow subsurface: The Irish Sea	Technical Report	2015		Mellett et al.	BGS	Regional	Literature review
	Cardigan bay/ St. George's Channel Geology map	1:250k chart	1990/2009	WGS84	BGS	BGS	Regional	GIS
	Offshore Wind farm Development Arklow Bank, Irish Sea. Geotechnical Site Investigation and In-situ Report 04520-2	Report and Lab results in Appendices	2000	Irish National Grid	Fugro	SSE	Arklow Bank	Literature review
	Arklow Bank Phase 2 OWF: Geological and Geotechnical Desk Top Study	Technical Report	2018		Cathie Associates	SSE	Regional and Arklow Bank	Literature review
	Arklow Bank: Dumping at Sea Permit Application Supporting Information	Technical Report	2016		Ramboll Eviron	Ramboll	Meso-scale	Literature review
	Arklow Bank Geophysical Survey, Ground Model report and Interpreted Data	Report, and raster files	2019	WGS84/UTM30N Varying resolution	Various	GDG	Arklow Bank, Phase 2	Interpretation of the non-erodible layer, and detailed geophysical and geotechnical understanding of the

	Document/file name	Document/Data type	Issue Date	Data Info	Author	Source	Spatial cover	Application / Utility
								local region
Sediment Dynamics	Coastal Morphological modelling to assess the dynamics of Arklow Bank, Ireland	Journal Article	2009		Panigrahi et al.		Meso- scale	Literature review
	Arklow Bank 18125_Bathymetric_Change	PDF chart of bed change between 2016 and 2000 Survey	2018	WGS84/UTM29	Coughlan, M.	Gavin & Doherty Geosolutions	Meso- scale	Literature review
	Arklow Bank Survey 2000	.CSV dataset	2000	WGS84/UTM29 30m resolution	Unknown	UKHO	Arklow Bank	GIS analysis
	INFOMAR_2016_2011	.GeoTIFF	2011 and 2016	WGS84/UTM29 2-10m resolution		INFOMAR	Local to Meso- scale	GIS analysis of sandwaves features
	DTI Strategic Environmental Assessment Area 6, Irish Sea, seabed and surficial geology and processes	Technical Report	2005		Holmes, R. and Tappin, D. R.	BGS	Regional	Literature review on BPZ
	Post-glacial sediment dynamics in the Irish Sea and sediment wave morphology: Data–model	Journal Articles	2009		Van Landeghem et al.	Continental Shelf Research, 29(14),	Regional	

	Document/file name	Document/Data type	Issue Date	Data Info	Author	Source	Spatial cover	Application / Utility
	Comparisons					1723–1736		
	Reversed sediment wave migration in the Irish Sea, NW Europe: A reappraisal of the validity of geometry-based predictive modelling and assumptions	Journal Articles	2012		Van Landeghem et al.	Marine Geology, 295–298, 95–112	Regional	

Appendix B: Determining the Depth of Closure

Hallermeier (1981, 1983) defined three profile zones, i.e. the littoral zone, shoal or buffer zone and the offshore zone. This partition defined two closure depths, namely:

- an "inner" (closer to shore) closure depth h_{in} at the seaward limit of the littoral zone, and;
- an "outer" or "lower" (further from shore) closure depth h_{out} at the seaward limit of the shoal/buffer zone.

The following calculations presented by Hallermeier (1981) were used to determine h_{in} and h_{out}

$$h_{in} = 2.28H - 68.5\left(\frac{H^2}{gT^2}\right) \quad (1)$$

where $H = H_{12h/y}$ is the effective wave height just seaward of the breaker zone that is exceeded for 12 hours per year, i.e. the significant wave height with a probability of yearly exceedance of 0.137%, T is the wave period associated with H, and g is the acceleration of gravity.

From Hallermeier (1983):

$$h_{out} = 0.018 H_m T_m \sqrt{\frac{g}{D_{50}(s-1)}} \quad (2)$$

where H_m and T_m are the median wave height and period respectively, D_{50} is the median sediment diameter and s is the ratio of specific gravity of sand to that of fluid (about 2.65). As we can see h_{in} is solely related to the wave parameters, irrespective of typical sediment diameters, ranging between 0.16 and 0.42 mm, as validated and described by Hallermeier (1978, 1981), whereas h_{out} requires both hydrodynamic and sedimentological parameters. They are relevant for MLW (mean low water) conditions.

Appendix C: The Formation of Sand Banks on the Eastern Irish Seaboard

Pleistocene glaciation

Towards the end of the Pleistocene (around 23,000 BP) sea levels were much lower than the present day with most of Scotland, Wales and Ireland covered in an ice sheet (Figure 236). This ice sheet included a large glacier slowly flowing through the Irish Sea (Irish Sea Glacier).



Figure 236. Maximum extent of ice sheet, circa 23 ka BP, after Clark, Hughes, Greenwood, Jordan, & Sejrup (2012). Blue arrows indicate glacial movement.

The action of the glacier (as well as previous periods of glaciation) shaped the main basin of the Irish Sea and gouged deep features into the land mass, including Celtic Deep, St. George's Channel and North Channel. The glaciation process also created smaller, discrete tunnel (submarine) valleys (e.g. Wicklow Trough), as well as leaving large amounts of glacial moraine across the bed of the Irish Sea. This coarse substrate is unlikely

to be susceptible to erosion under present metocean conditions. The distribution of glacial moraine is expected to largely mimic the distribution of the overlying glacier, thus there would have been a well-defined boundary at the edge of the glacier, which may also have caused cliffing against higher and more geologically resistant land in some locations. The location now occupied by Arklow Bank would have been covered by the Irish Sea Glacier at this time. Since this area is also immediately downstream of Wicklow Trough, then outflows (e.g. sub-glacial deposits of basal till) produced during the generation of this tunnel valley feature would also be expected to have spread across the local area.

Key developments:

- shaping of the Irish Sea basin
- creation of Wicklow Trough
- production of glacial moraine deposits

Pleistocene to Holocene transition

Warmer climates marked the end of the Pleistocene, leading to the retreat of the ice sheet and melting of glaciers. This caused sea levels to rise rapidly, initiating the commencement (circa 11,700 BP) of marine transgression through the Holocene period.Marine transgression caused progressive inundation of low-lying coastal land, resulting in the coastline in these locations moving landward. The inundated areas then became susceptible to wave and tidal processes, with erodible areas releasing (Holocene) sediments for transport and deposition in more quiescent locations, including infilling of some paleovalleys. In comparison, seaward areas covered with glacial moraine, or areas with harder geology, would have been less susceptible to erosion at this time, leaving discrete coastal promontories and seabed ridges.

Key developments

- rising sea levels
- commencement of marine transgression

Early Holocene, circa 11,000 BP

At the beginning of the Holocene (circa 11,000 BP) mean sea level (based on values determined from Wicklow) is estimated to have been around 45 m below present day mean sea level (Figure 237).

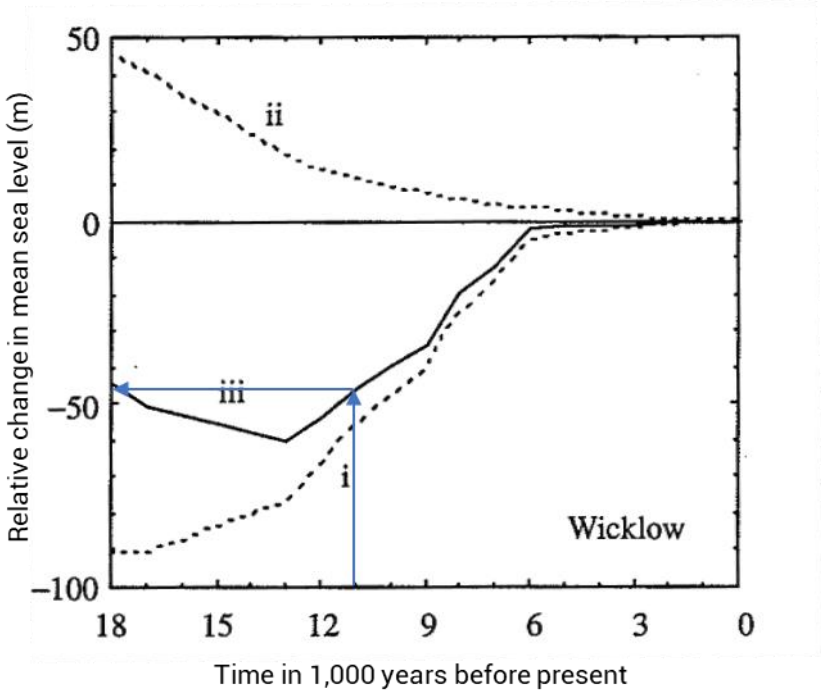


Figure 237. Predicted components of sea level change (i. contribution from distant ice sheets, ii. contribution from local ice sheet, iii. net predicted sea level change) (adapted from Lambeck & Purcell, 2001) with indication of mean sea level at 11,000 BP.

Figure 238 shows an indicative alignment of the former coastline based on the contemporary 45 m mean sea level isobath derived from EMODnet 2018 bathymetry. This reconstruction is generally consistent with independent work presented in Sturt, Garrow, & Bradley (2013). The general orientation of the former coastline was to the north-north-east, terminating in a headland promontory where the coastline orientation changed to the north-north-west. This area was backed by a relatively flat coastal plain. The alignment of the 45 m contour correlates with a distinct cliff edge at the headland which is likely to have been formed by the Irish Sea Glacier. Wicklow Trough cuts across the coastal plain in a north-south orientation but is unlikely to have been connected to the sea at this time. In addition, the trough may have been more expansive and has subsequently been subjected to erosion of the southern extent (evidenced by a contemporary deepened area running parallel along the northern end of Arklow Bank) with some deposition and infilling within the trough (evidenced by the contemporary northern extent of India Bank). The location now occupied by Arklow Bank remained part of mainland Ireland at this time, with glacial moraine present across areas previously covered by the Irish Sea Glacier.

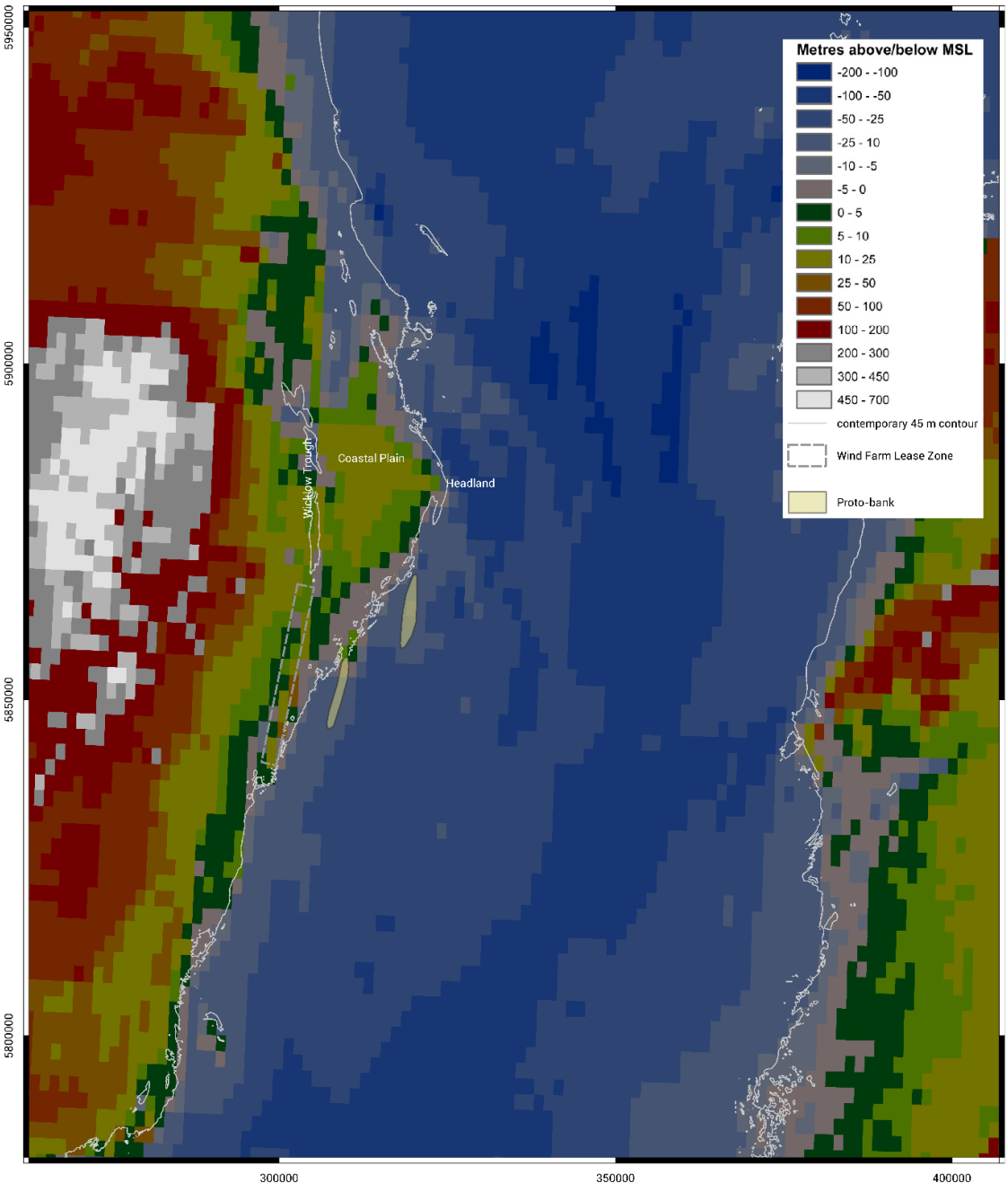
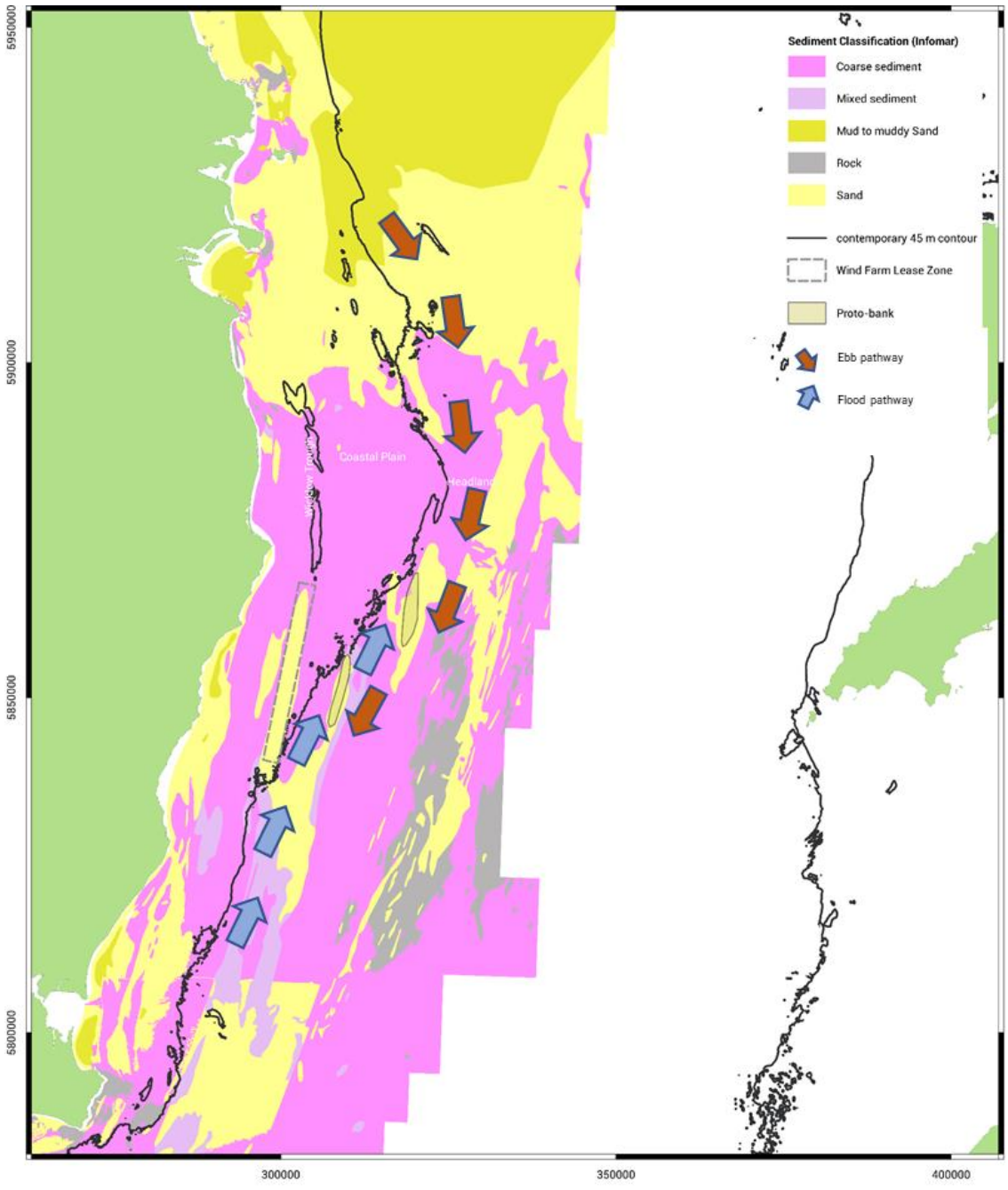


Figure 238. Indicative alignment of the former coastline at commencement of Holocene (circa 11,000 BP).

Areas experiencing substantial erosion and deposition in the period to the present day would account for some local adjustments to the position of the isobath. Examining contemporary distributions of surficial sediment provides a basis to infer those areas with a cover a coarse sediments or rock have mainly been erosional surfaces, whereas areas with sands and muds have mainly been depositional (Figure 239). Based on

this informed premise, this area can be inferred to have been an erosional surface at the time of coastal plain submergence and now comprises of coarse sediments. This is also generally the case for areas south of the coastal plain due to marine transgression stripping away mobile sediments. Against this surface of coarse sediment there are discrete regions where there is a cover of surficial sand. The likelihood is the majority of this sediment was originally eroded by marine transgression to create a sediment supply which then became subject to sediment transport and deposition in local areas. Contemporary bathymetry shows two clusters of (now) moribund sandwaves to the east of Arklow Bank, coincident with contemporary areas described as sandy. These areas are expected to have been active for sediment transport circa 11,000 BP and more substantial (in volume) at this time, initially formed as headland associated Type 3(B) banks on a recessional coastline (Dyer & Huntley, 1999). [Type 3(B) – formed by retreating coastline and/or headland which gives rise to formation and abandonment of banks. Once isolated from their source of material these type of banks become modified by tidal currents and operate like Type 1 Open Shelf Linear Sand Banks]. The sediment supply for these features would have come from the process of marine transgression. During the flood tide a sediment pathway is expected to have moved sediments (tidally and wave driven) in a north-north-easterly direction along the coast and eventually into deeper water where weaker flows would have encouraged deposition (Figure 239). Conversely, the ebb tide would have driven a southerly sediment pathway around the headland. The convergence of these pathways led to the development of the sandbank features (sediment stores). The bank feature furthest to the east is likely to have formed first, but as sea levels continued to rise and the coastline receded, conditions may have then favoured the subsequent formation of the second bank. The first bank would then have become moribund with sediment supply reducing, leading to the decline in sandy sediment retained in this area.



COOPER MARINE ADVISORS	0 10 20 30 km Licences: Contains Irish Public Sector Data (Geological Survey) licensed under a Creative Commons Attribution 4.0 International (CC BY 4.0) licence	Arklow Bank Wind Park Sediment Dynamics Study
		Date: 25-Sep-2020
		Projection: EPSG:32630
		Drawn by: WSC

Figure 239. Variation of contemporary surficial sediment types along with inferred sediment transport pathways circa 11,000 BP.

Key developments

- Rapid rates of sea level rise
- Marine transgression leading to sediment supply
- Net movement of sediments along the coast in a north-north-easterly direction driven by flood tide and southerly waves
- Development of sandbanks at convergence of sediment pathways
- Area now occupied by Arklow Bank remaining part of mainland Ireland
- Wicklow Trough land-locked

Holocene, circa 8,500 BP

Sea levels continued to rise at a rapid rate and by 8,500 BP approached around 35 m below present day mean sea level (Figure 240), an increase of around 15 m from the beginning of the Holocene, an equivalent rate of sea level rise of 6 mm/year up to this period.

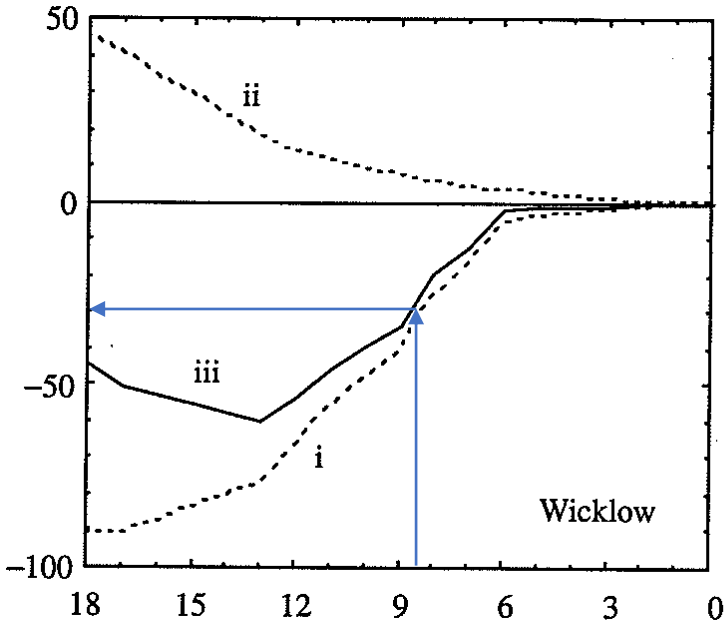
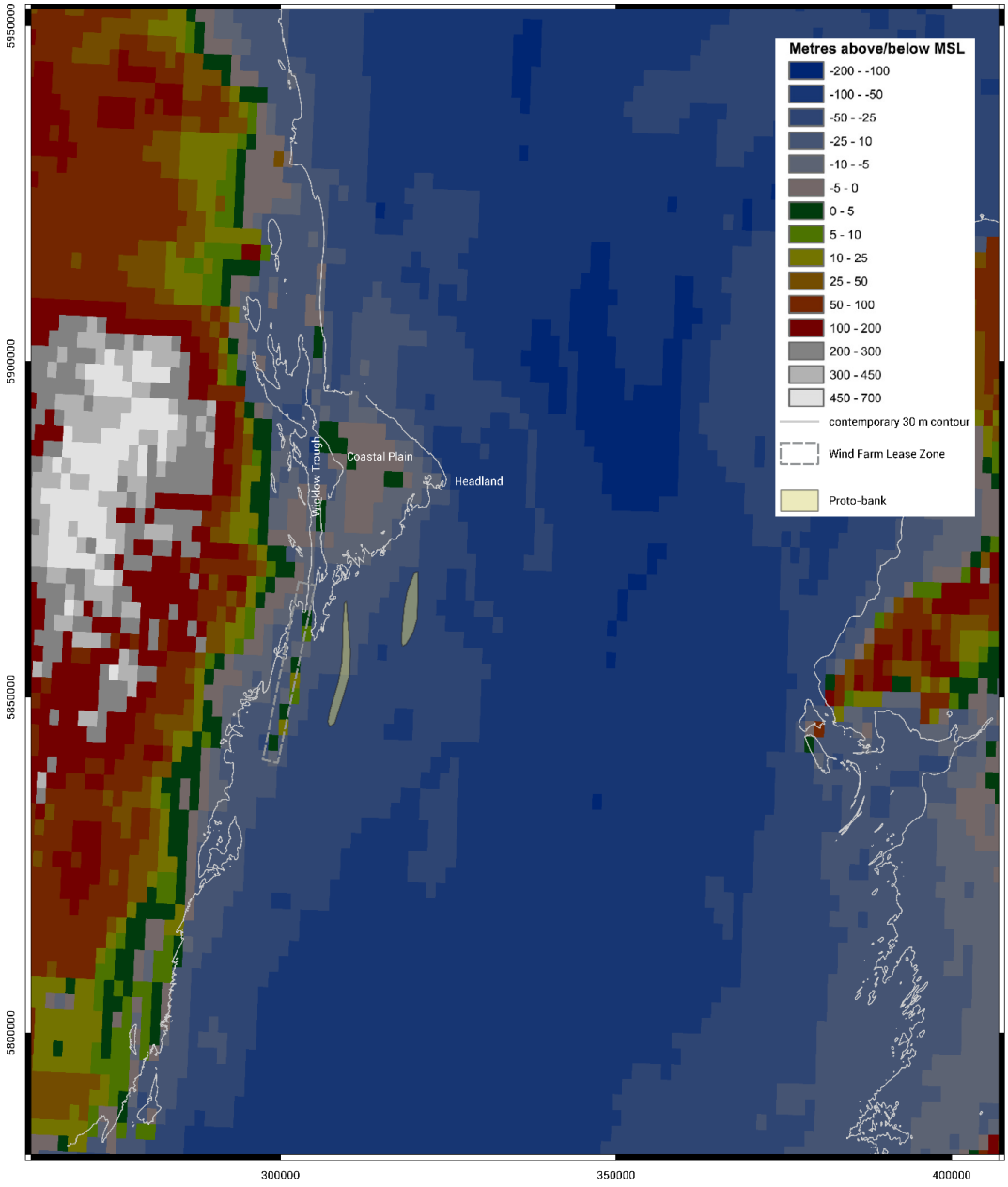


Figure 240. Predicted components of sea level change (i. contribution from distant ice sheets, ii. contribution from local ice sheet, iii. net predicted sea level change) (adapted from Lambeck & Purcell, 2001) with indication of mean sea level at 8,500 BP.

The indicative alignment of the former coastline at this time is shown in Figure 241.



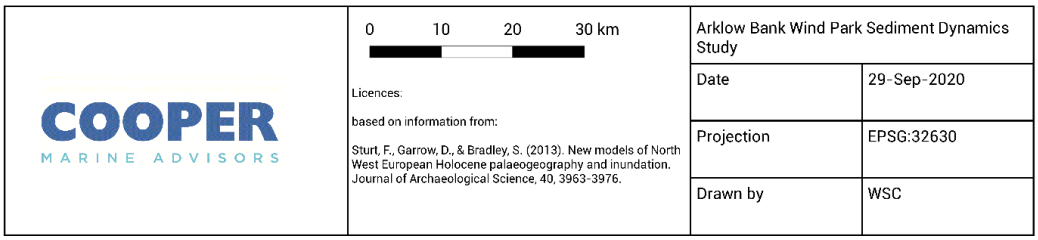


Figure 241. Indicative alignment of the former coastline on reconstructed landscape and seascape during Holocene (circa 8,500 BP)

The continuing marine transgression saw the coastline retreat further to the west and north with the newly inundated areas offering additional sediment supply. The area now occupied by Arklow Bank became submerged along tidal exchange commenced through Wicklow Trough. During the ebb tide strong "channelled" flows would have purged the trough of any mobile sediments in the direction of Arklow Bank.

This is likely to have provided both the mechanism and the additional sediment supply necessary to commence bank development at this location (n.b. becoming the third sandbank in the sequence). The area now occupied by Seven Fathom Bank is likely to have remained part of the mainland at this time. The two banks to the east of Arklow Bank are likely to have undergone some changes during this period. The most easterly bank became detached from the receding coastline, and the increased water depths (by around 15 m) caused this feature to become moribund. The bank closer to Arklow Bank, and in shallower water, remained active and extended in length to the north as the coastline receded. There was a notable change in orientation for this new northern section of the bank, mimicking a more northerly change in orientation of the immediate coastline. From this period onwards, the opening of Wicklow Trough to tidal exchange diverted previous sediment pathways to the east, which sustained this bank, to move in a southerly direction to instead initiate the development of Arklow Bank. This adjacent bank then became moribund.

Key developments

- Continuation of rapid rates of sea level rise submerging the area now occupied by Arklow Bank
- Continuation of marine transgression leading to further sediment supply
- Net movement of sediments along the coast in a north-easterly direction driven by flood tide and waves
- Wicklow Trough opens to tidal exchange, modifying sediment pathways reaching this point and moving sediments to the south with strong "channelled" ebb flows
- Commencement of processes suited to initial phase of development of Arklow Bank
- Easterly banks become deeper with reduced sediment supply leading to moribund conditions

Holocene, circa 7,500 BP

Sea levels continued to rise at a rapid rate and by 7,500 BP approached around 15 m below present day mean sea level (Figure 242), an increase of around 30 m from the beginning of the Holocene. The period from 8,500 to 7,500 BP appears to represent the highest rate of sea level rise, estimated to be 15 mm/year.

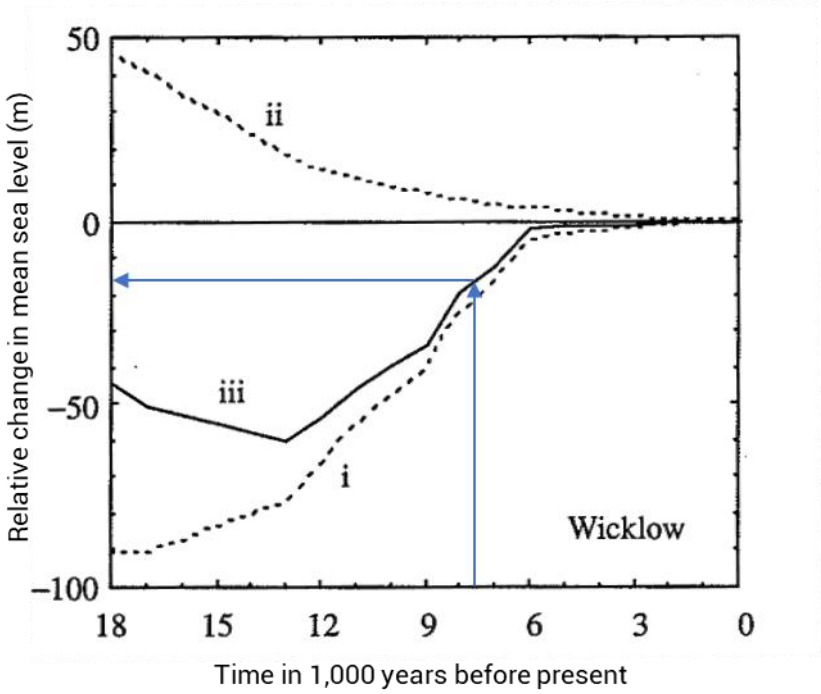
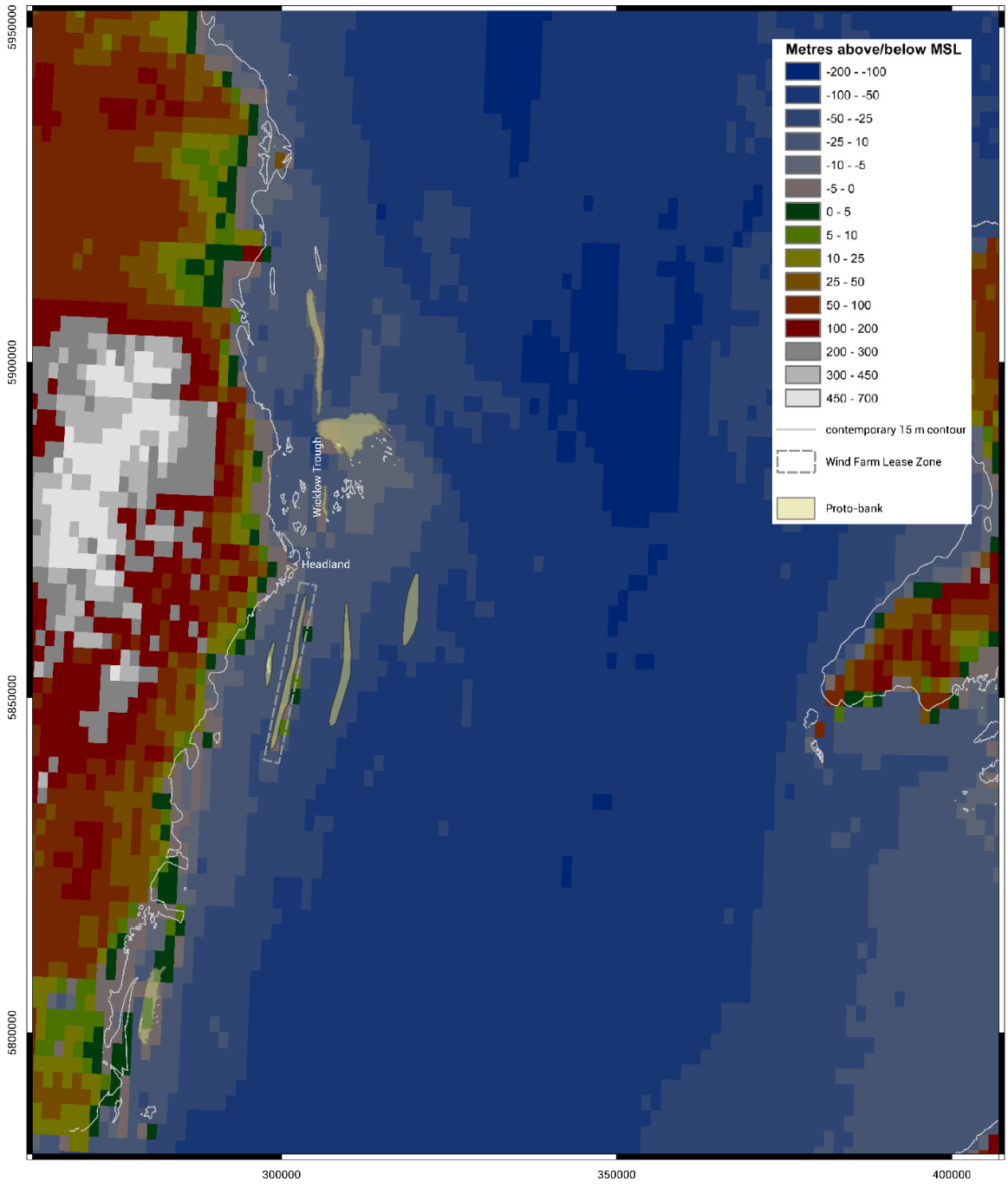


Figure 242. Predicted components of sea level change (i. contribution from distant ice sheets, ii. contribution from local ice sheet, iii. net predicted sea level change) (adapted from Lambeck & Purcell, 2001) with indication of mean sea level at 7,500 BP.

The indicative alignment of the former coastline at this time is shown in Figure 243. By 7,500 BP, increased sea levels submerged the coastal plain and easterly headland area. However, the seabed topography associated with these features still provided a major influence on the direction of local tidal flows, along with strong channelled flows running through Wicklow Trough. A bank formed in the area now occupied by the northern part of Arklow Bank (as a Type 3B recessional headland bank), with flood-tide sediment pathways to the north-north-east and strong ebb flows from Wicklow Trough moving sediment to the south. Both banks to the east of Arklow Bank remained moribund by the deeper water, combined with further recession of the coastline and submergence of the coastal plain. The reduction of sediment supply further to the east (in favour of supplying proto-Arklow Bank) also caused these two banks to diminish in profile.



COOPER MARINE ADVISORS	0 10 20 30 km Licences: based on information from: Sturt, F., Garrow, D., & Bradley, S. (2013). New models of North West European Holocene palaeogeography and inundation. Journal of Archaeological Science, 40, 3963-3976.	Arklow Bank Wind Park Sediment Dynamics Study Date: 29-Sep-2020 Projection: EPSG:32630 Drawn by: WSC

Figure 243. Indicative alignment of the former coastline on reconstructed landscape and seascape during Holocene (circa 7,500 BP)

Between 8,500 to 7,500 BP the coastline also receded past the area now occupied by Severn Fathom Bank, with this smaller bank in shallower water also initially formed as a Type 3B recessional headland bank. The

size of the bank is likely to reflect the relatively short period when this sandbank forming process occurred, combined with a later slowdown of marine transgression. Further to the north, other banks began to form, including India and Codling on the submerged coastal plain as well as Kish and Bray Banks at the northern end of Wicklow Trough. To the south, Blackwater Bank now also began to form.

Key developments

- Continuation of rapid rates of sea level rise submerging the coastal plain to the north
- Continuation of marine transgression leading to further sediment supply
- Net movement of sediments along the coast in a north-easterly direction driven by flood tide and waves
- Wicklow Trough provides an important tidal exchange to help modify sediment pathways reaching this point and moving sediments to the south with strong ebb flows
- Development and growth of proto-Arklow Bank as a Type 3B sandbank, associated with a receding headland to the north
- Banks to the east of Arklow Bank remained moribund, progressively diminishing in stature

Holocene, circa 6,000 BP

From 7,500 to 6,000 BP mean sea levels increased by around 14 m (Figure 244) with a rate of sea level rise estimated to be around 9 mm/year. Mean sea level at this time was around 1 m below present levels with the rate of sea level rise from 6,000 BP to present day slowing down, estimated to be a rate of <0.2 mm/year.

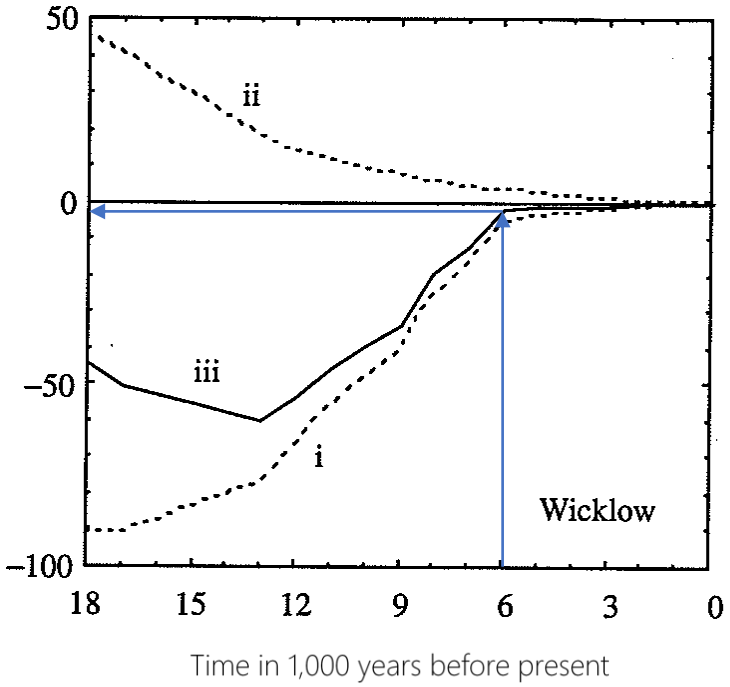
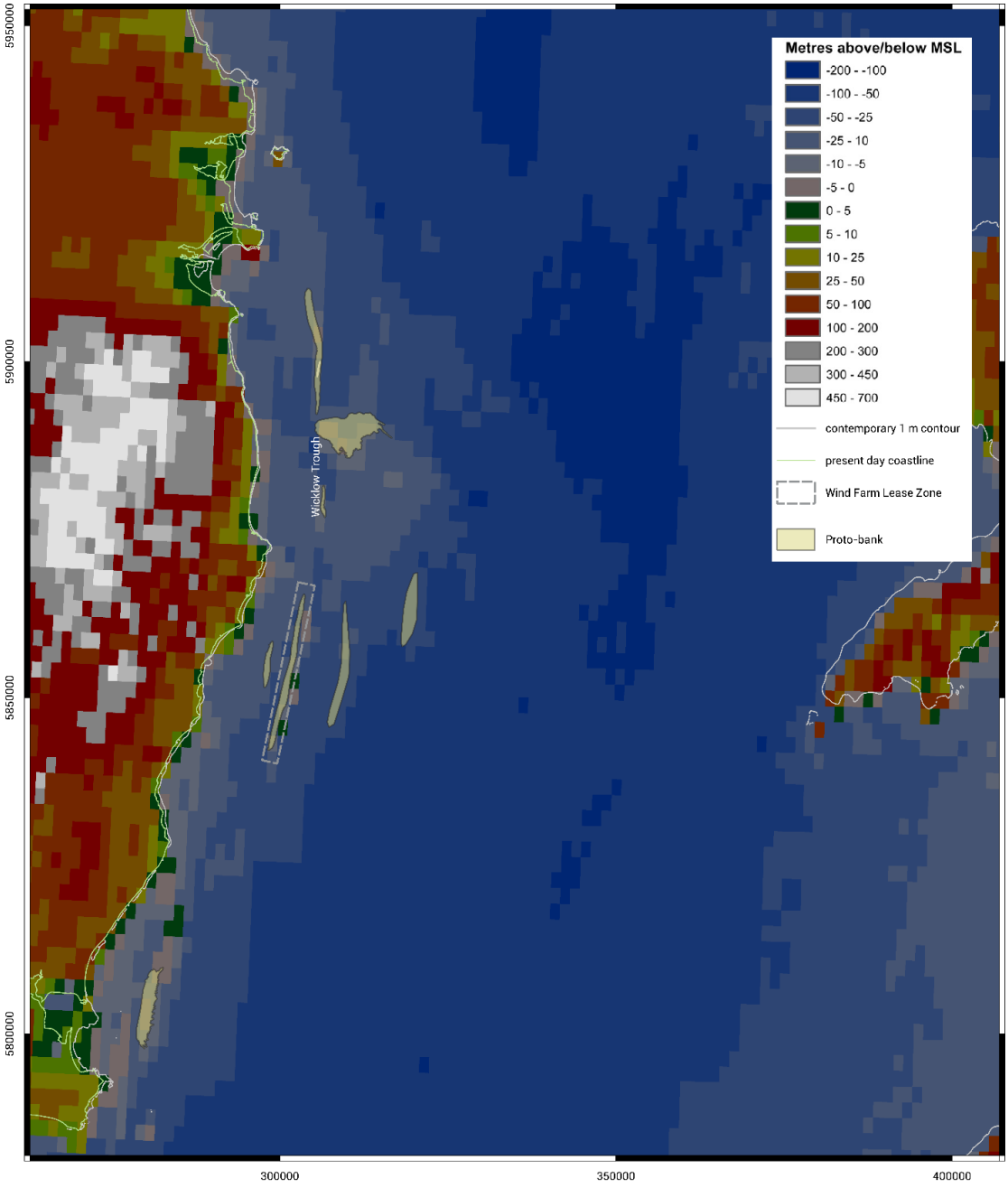


Figure 244. Predicted components of sea level change (i. contribution from distant ice sheets, ii. contribution from local ice sheet, iii. net predicted sea level change) (adapted from Lambeck & Purcell, 2001) with indication of mean sea level at 6,000 BP.

The indicative alignment of the former coastline at this time is shown in Figure 245, with the coastline close to the present-day position in many areas.



COOPER MARINE ADVISORS	0 10 20 30 km Licences: based on information from: Sturt, F., Garrow, D., & Bradley, S. (2013). New models of North West European Holocene palaeogeography and inundation. Journal of Archaeological Science, 40, 3963-3976.	Arklow Bank Wind Park Sediment Dynamics Study Date: 29-Sep-2020 Projection: EPSG:32630 Drawn by: WSC

Figure 245. Indicative alignment of the former coastline on reconstructed landscape and seascape during Holocene (circa 6,000 BP)

The increased slope of the land around much of the coastline, combined with substantially reduced rates of sea level rise, slowed down marine transgression, and reduced further sediment supply for this later period of the Holocene.

The northern end of Arklow Bank remained linked to the southern end of Wicklow Trough, with the flow regime over the wider area becoming less influenced by the submerged coastal plain, and more rectilinear overall (flood tide to the north and ebb tide to the south). The typology of the Arklow Bank switched to Type 1: Open shelf linear ridge (Dyer & Huntley, 1999) as the main process to sustain the bank. Combined with strong rectilinear flows, the bank is likely to have narrowed and elongated to the south at this time, but largely using the existing bank volume rather than from any additional sediment material, due to cessation of the marine transgression.

Key developments

- Slowed sea level rise halted marine transgression reducing further sediment supply
- Flow environment changed to mainly rectilinear flows north to south
- Receded coastline removing headland influence
- Wicklow Trough provides an important tidal exchange to help enhance local sediment pathways
- Future evolution of Arklow Bank as a Type 1 sandbank
- Easterly banks further diminished in stature

The development of Arklow Bank is part of a sequence of marine transgression driven by a rapid rate of sea level rise through the early part of the Holocene, creating a recessional coastline and high levels of sediment supply from newly inundated areas of land. The change in orientation of the coastline to the north against a flat coastal plain created a tidal circulation which helped spawn a series of headland associated recessional sandbanks (Type 3(B)) on a seabed formed of glacial moraine. As sea levels continued to rise, the coastline further receded and the combination of coastal process then favoured new banks forming further to the west and in shallower water, leaving former banks to the east in deeper water with a much-reduced sediment supply. These easterly banks eventually became moribund due to loss of sediment supply and weaker near-bed flows. By around 8,500 BP sea level rise opened Wicklow Trough to tidal exchange, providing the conditions to form a new bank at the southern confluence of this feature. By 7,500 BP the coastal plain became submerged altering the local flow regime leaving a headland to influence the formation of Arklow Bank as a Type 3(B) sandbank. By 6,000 BP sea levels submerged the coastal plain to such an extent that the former headland was submerged and that flows became more rectilinear. At this time, Arklow became a Type 1: Open shelf linear sandbank. The association of the northern end of the bank with Wicklow Trough supported bank development by offering enhanced ebb flows and additional sediment supply from the coastal plain to

the north (a location which is now associated with a bedload parting area). The slowing of sea level rise from this time against a generally steeper coastline has reduced sediment supply which then slowed down further bank development to form a present-day equilibrium condition. The future long-term development of Arklow Bank remains linked to changes in mean sea level, coastal recession, sediment supply and flow interactions with Wicklow Trough.

Appendix D: Threshold Current Speed (U_{cr})

The threshold current speed U_{cr} was determined using the coefficients presented by Soulsby (1997). These are valid for non-cohesive sediments and for sediment diameters of > 0.1 mm:

$$U_{cr} = 7\left(\frac{h}{d_{50}}\right)^{1/7} \left[g(s-1)d_{50}\, f(D_*)\right]^{1/2} \quad (3)$$

With:

$$f(D_*) = \frac{0.30}{1 + 1\,2D + 0.055\,[1 - \exp(-0.020\,D_*)]} \quad (4)$$

$$D_* = \left[\frac{g\,(s-1)}{v^2}\right]^{1/3} d_{50}$$

Where:

s = ratio of densities of grain and water.

v -= kinematic viscosity of water.

Appendix E: Flow Through the Water Column

In shallow coastal waters the flow, and thus sediment transport, are largely controlled by seabed friction. A current flowing over the seabed experiences friction with the bed; this forms a turbulent boundary layer which in shallow waters may occupy the entire water depth. Comparatively, in deeper waters the boundary layer occupies the lower part of the water column, above which water flows are unaffected by friction (the so-called 'free-stream'). To understand this aspect further, vertical current profiles measured at each frame location (in the absence of surface waves) were assessed (Figure 246). Table 24 presents key statistics regarding the bed shear stress impacting the seabed during the period of assessment.

The vertical current profiles reveal, in all cases examined, a depth-limited boundary layer, indicating currents through the water column are influenced by the proximity of the seabed, and the near bed hydrodynamics which govern sediment transport across the 5 monitoring sites, are broadly similar. Tidal (relative) variations in water level (typically < 2 m) do not change this situation. The bed shear stress varies temporally (across the tidal cycle) and spatially (at each frame location) coincident with variations in local current speeds, indicating differences in the magnitude, and rate, of sediment transport may be anticipated at the 5 measurement sites. Differences in flow magnitudes observed between the sites, and thus, bed shear stress impacting the seabed, is a function of broad scale variation in the tidal regime, and local influences on the flow regime.

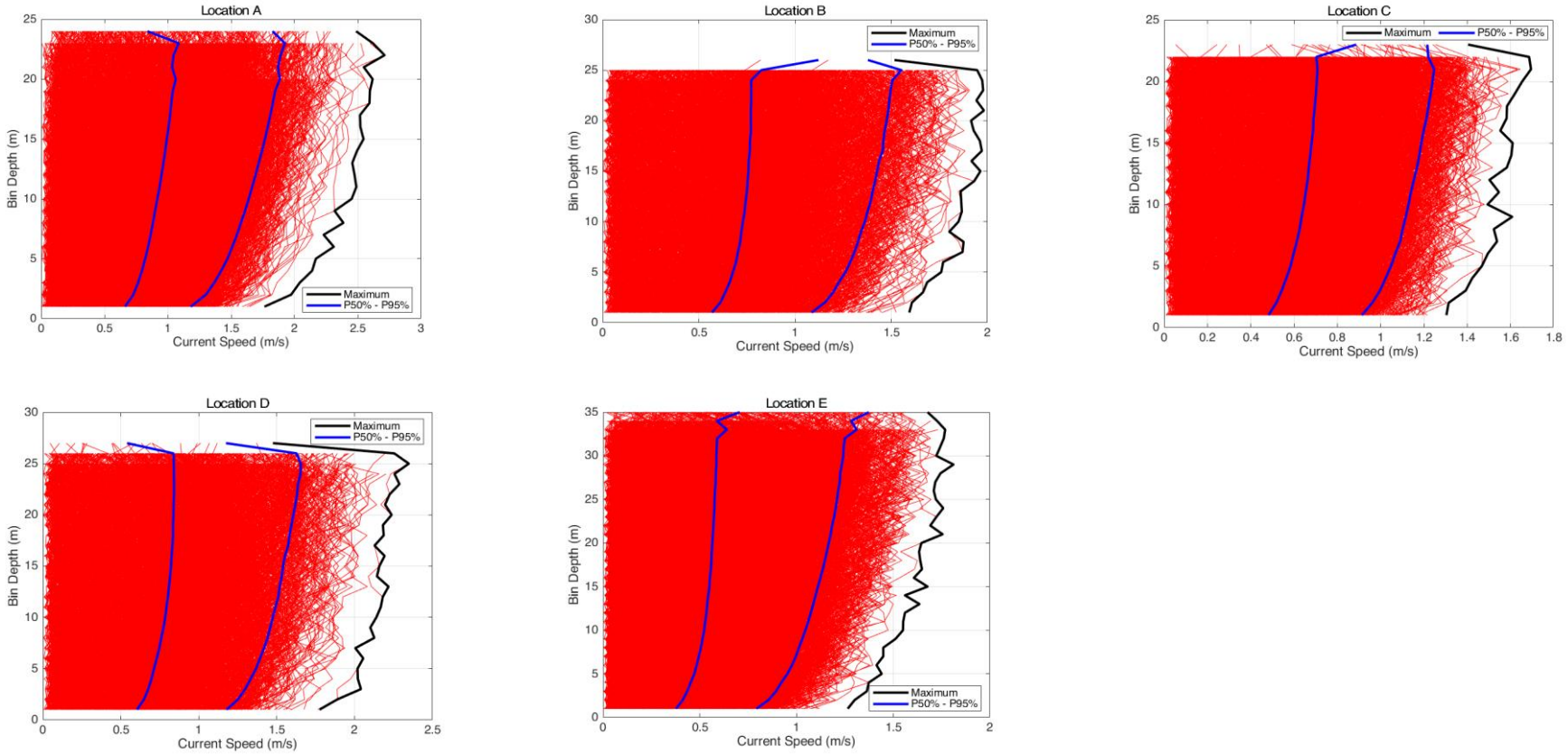


Figure 246. Vertical profiles showing current speed through the water column measured at frame location 'A' to 'E' across a representative ebb / flood phase during a period of negligible wave action.

Table 24. The bed shear stress impacting the seabed due to tidal currents at each frame location during the ebb / flood phase during a period of negligible wave action.

Frame Location	Approximate Water Depth (m)	Shear Stress at the seabed (N/m^2)				
		Maximum	Mean	P50%	P90%	P95%
Location A	28	13.983	2.579	2.169	5.643	6.750
Location B	27	8.339	1.681	1.351	3.890	4.760
Location C	26	5.439	1.233	1.039	2.729	3.180
Location D	28	11.452	1.988	1.563	4.650	5.651
Location E	38	5.704	1.013	0.728	2.461	3.089

Appendix F: Sandwave Analysis

The following plots show the profiles extracted from the Fourier transform analysis to support assessment of sandwave migration rates across the lease area. The results of this analysis are presented in Figure 109 and discussed in Section 8.8. Figure 247 shows the location of each profile extracted, and Figure 248 to Figure 349 presents those data from each profile location.

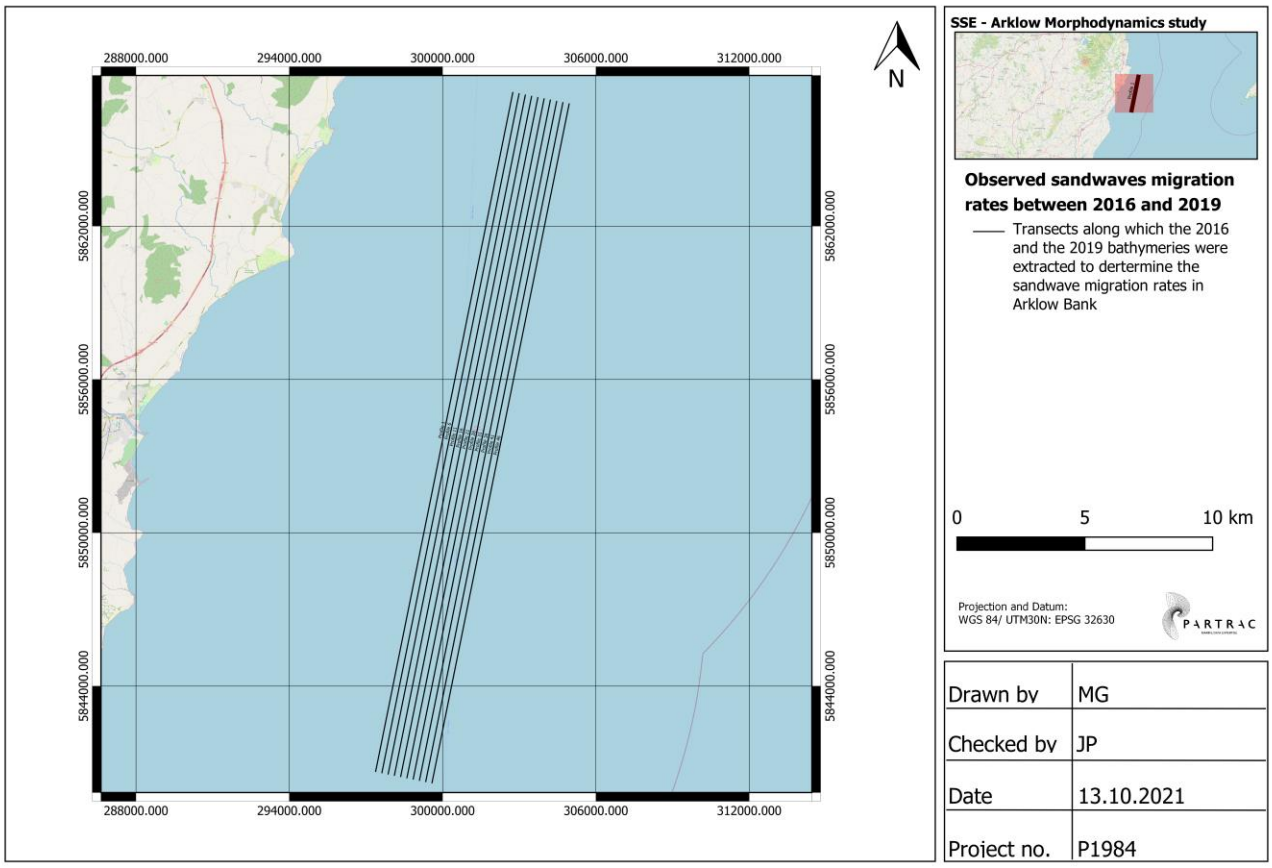


Figure 247. Transects from which profiles were extracted to assess sandwave migration rates.

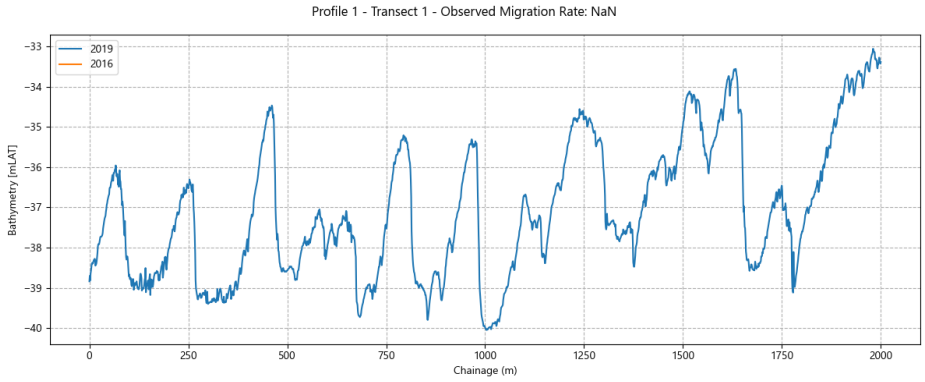


Figure 248. Observed sandwave migration between 2016 and 2019 on profile 1, transect 1. The maximum observed sandwave migration rate, and direction of migration, is detailed at the top of the plot.

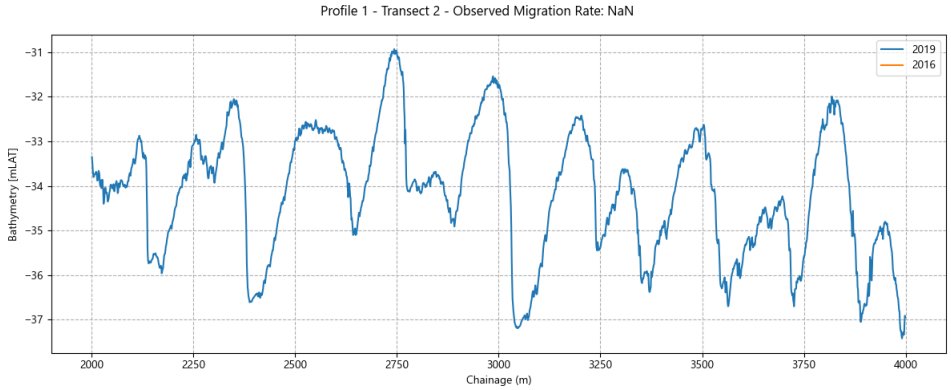


Figure 249. Observed sandwave migration between 2016 and 2019 on profile 1, transect 2. The maximum observed sandwave migration rate, and direction of migration, is detailed at the top of the plot.

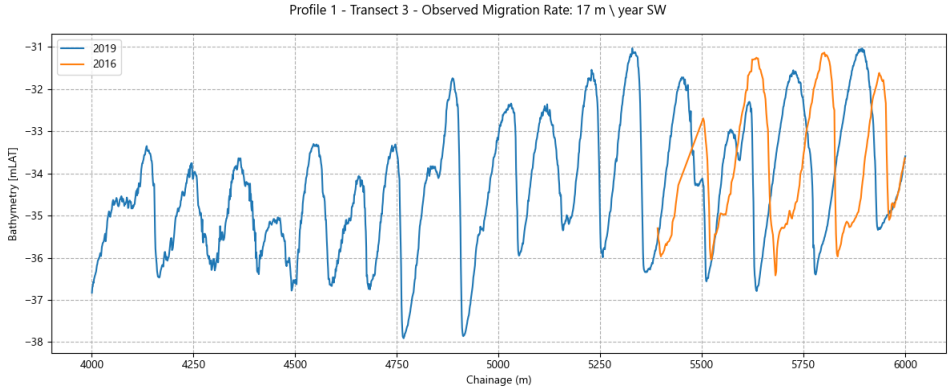


Figure 250. Observed sandwave migration between 2016 and 2019 on profile 1, transect 3. The maximum observed sandwave migration rate, and direction of migration, is detailed at the top of the plot.

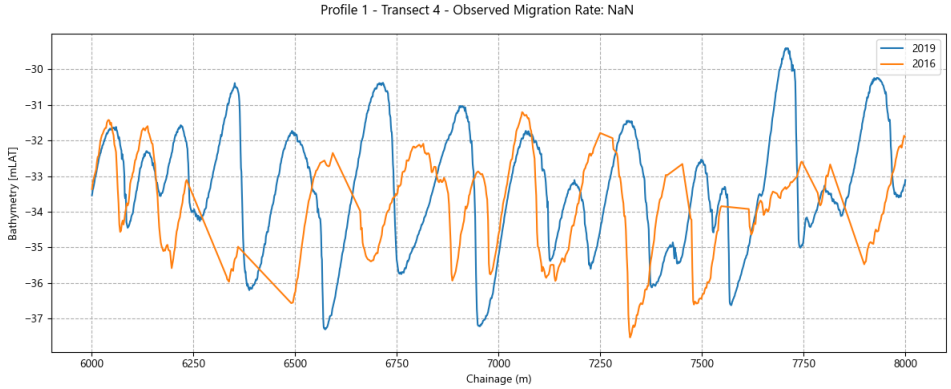


Figure 251. Observed sandwave migration between 2016 and 2019 on profile 1, transect 4. The maximum observed sandwave migration rate, and direction of migration, is detailed at the top of the plot.

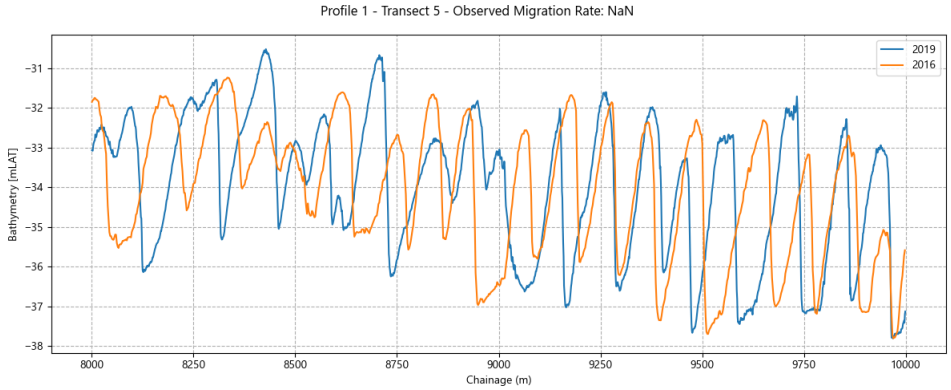


Figure 252. Observed sandwave migration between 2016 and 2019 on profile 1, transect 5. The maximum observed sandwave migration rate, and direction of migration, is detailed at the top of the plot.

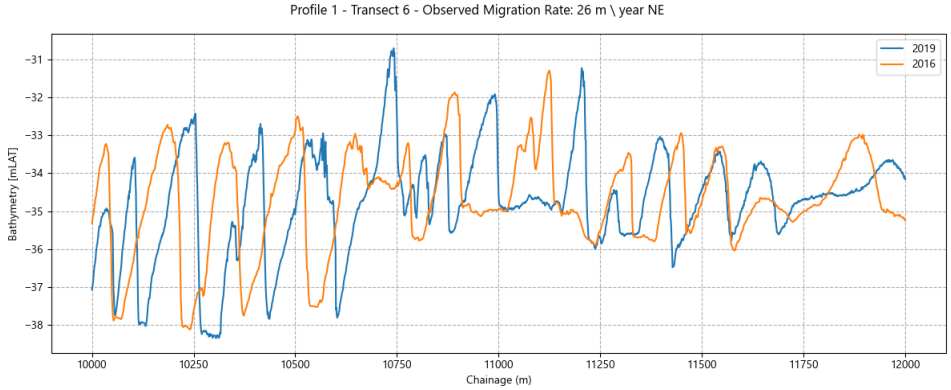


Figure 253. Observed sandwave migration between 2016 and 2019 on profile 1, transect 6. The maximum observed sandwave migration rate, and direction of migration, is detailed at the top of the plot.

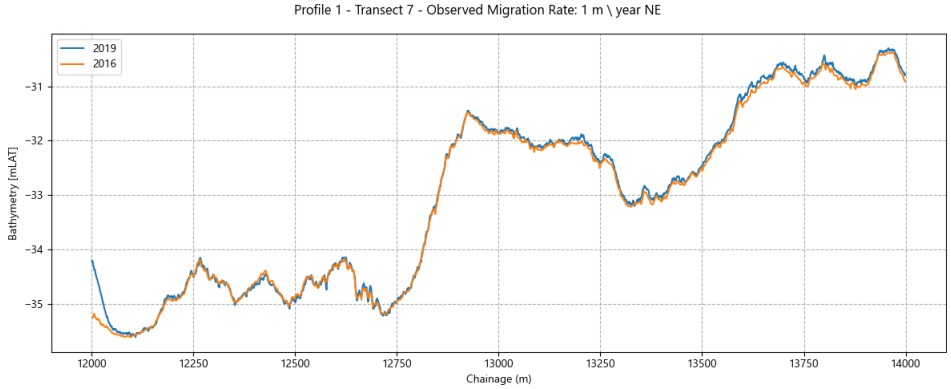


Figure 254. Observed sandwave migration between 2016 and 2019 on profile 1, transect 7. The maximum observed sandwave migration rate, and direction of migration, is detailed at the top of the plot.

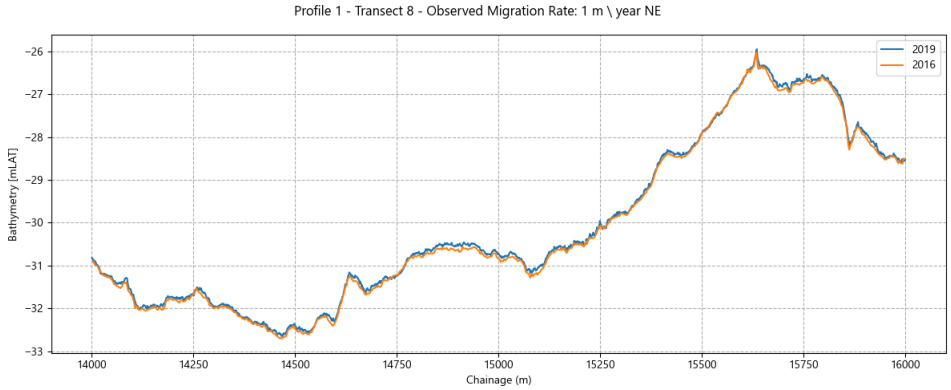


Figure 255. Observed sandwave migration between 2016 and 2019 on profile 1, transect 8. The maximum observed sandwave migration rate, and direction of migration, is detailed at the top of the plot.

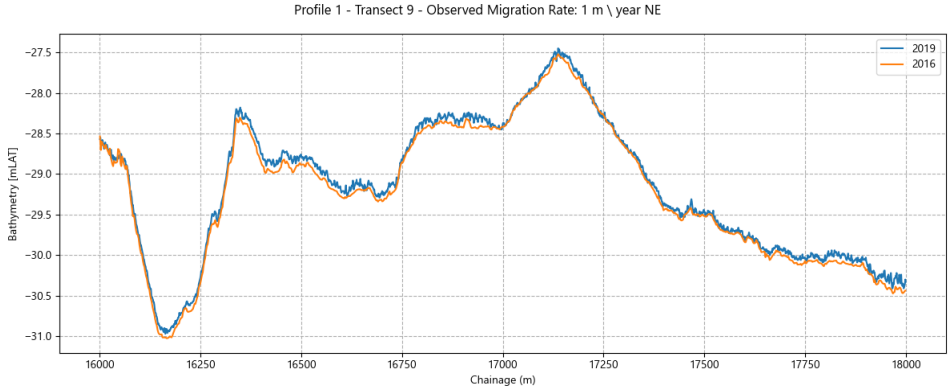


Figure 256. Observed sandwave migration between 2016 and 2019 on profile 1, transect 9. The maximum observed sandwave migration rate, and direction of migration, is detailed at the top of the plot.

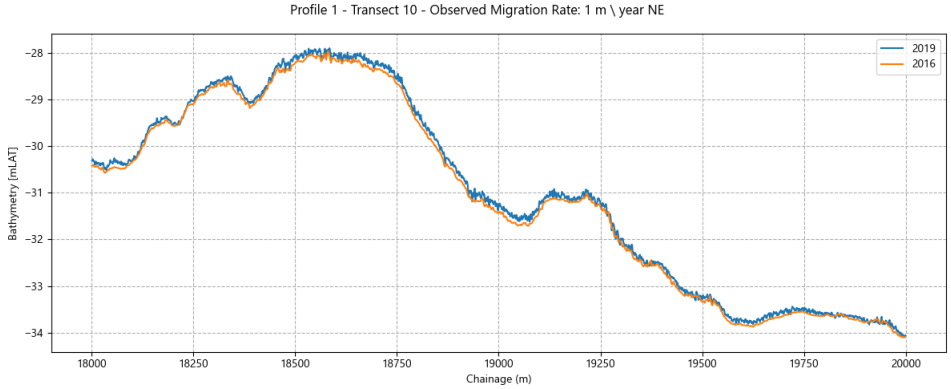


Figure 257. Observed sandwave migration between 2016 and 2019 on profile 1, transect 10. The maximum observed sandwave migration rate, and direction of migration, is detailed at the top of the plot.

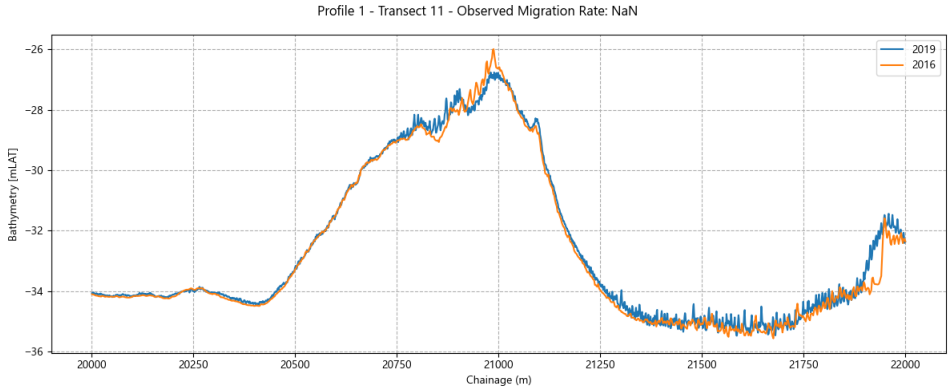


Figure 258. Observed sandwave migration between 2016 and 2019 on profile 1, transect 11. The maximum observed sandwave migration rate, and direction of migration, is detailed at the top of the plot.

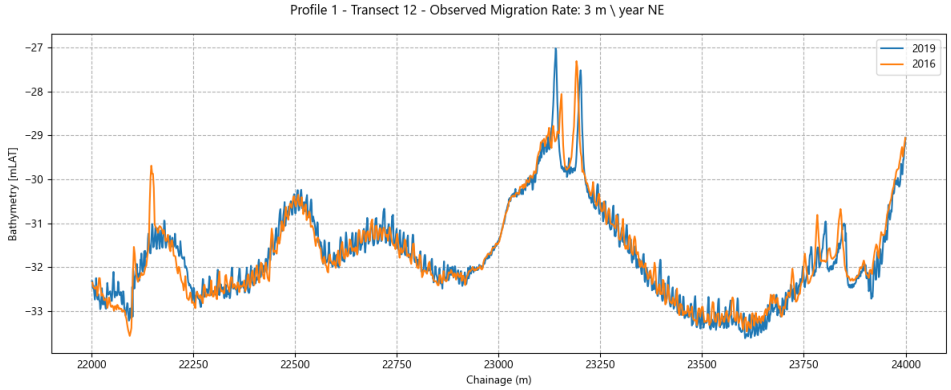


Figure 259. Observed sandwave migration between 2016 and 2019 on profile 1, transect 12. The maximum observed sandwave migration rate, and direction of migration, is detailed at the top of the plot.

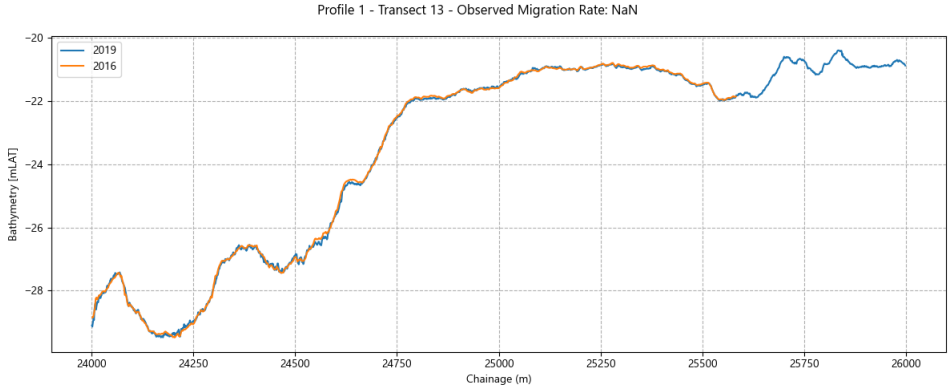


Figure 260. Observed sandwave migration between 2016 and 2019 on profile 1, transect 13. The maximum observed sandwave migration rate, and direction of migration, is detailed at the top of the plot.

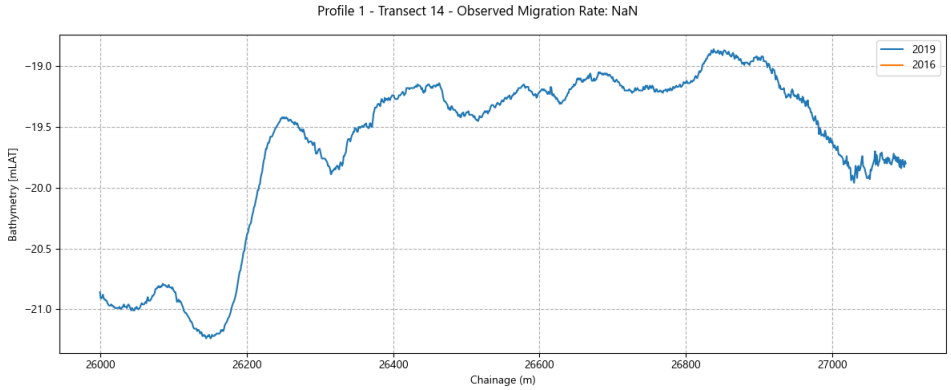


Figure 261. Observed sandwave migration between 2016 and 2019 on profile 1, transect 14. The maximum observed sandwave migration rate, and direction of migration, is detailed at the top of the plot.

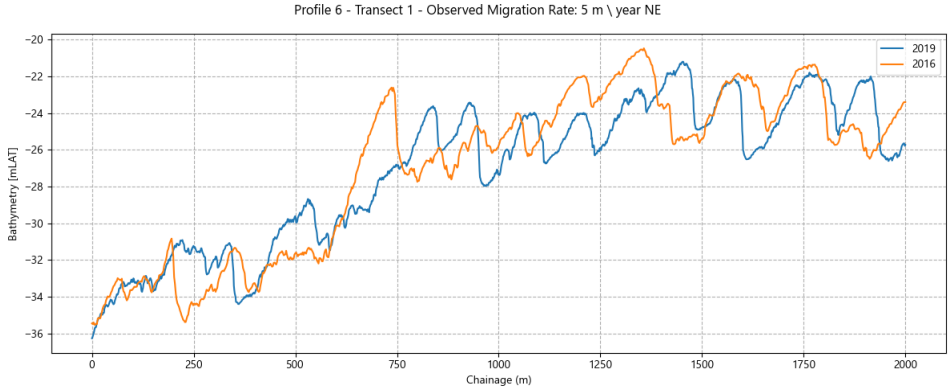


Figure 262. Observed sandwave migration between 2016 and 2019 on profile 6, transect 1. The maximum observed sandwave migration rate, and direction of migration, is detailed at the top of the plot.

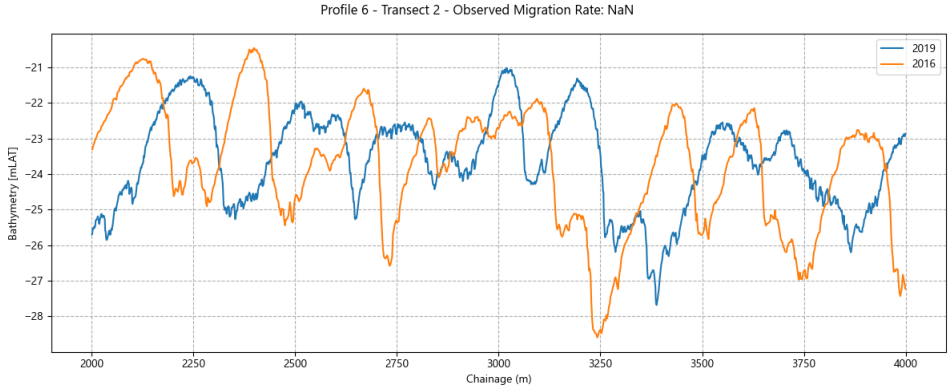


Figure 263. Observed sandwave migration between 2016 and 2019 on profile 6, transect 2. The maximum observed sandwave migration rate, and direction of migration, is detailed at the top of the plot.

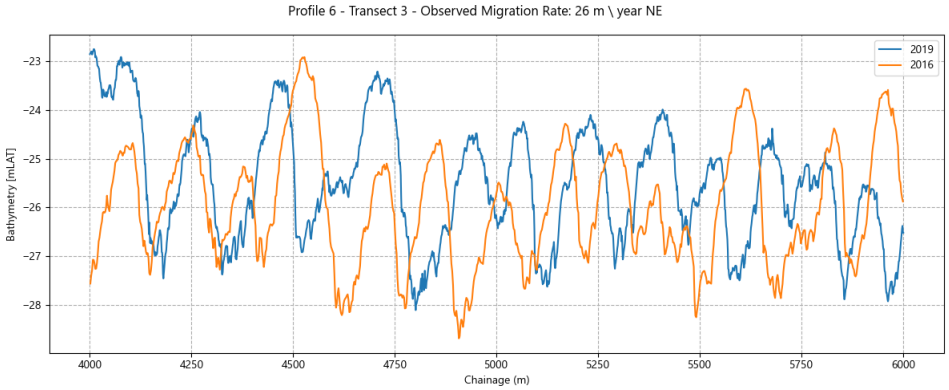


Figure 264. Observed sandwave migration between 2016 and 2019 on profile 6, transect 3. The maximum observed sandwave migration rate, and direction of migration, is detailed at the top of the plot.

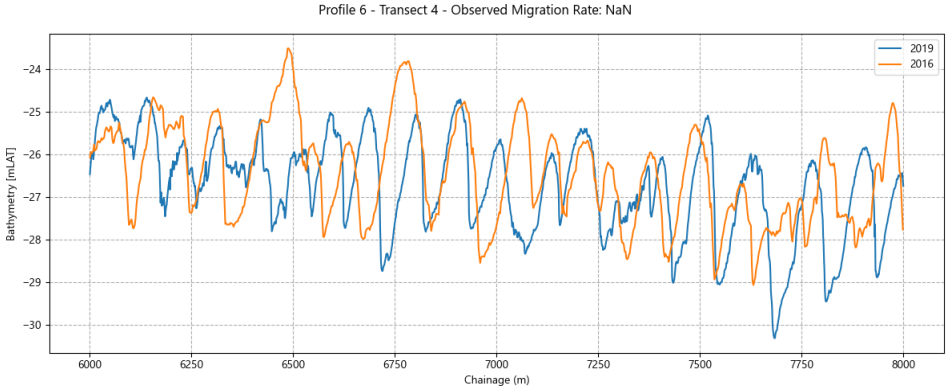


Figure 265. Observed sandwave migration between 2016 and 2019 on profile 6, transect 4. The maximum observed sandwave migration rate, and direction of migration, is detailed at the top of the plot.

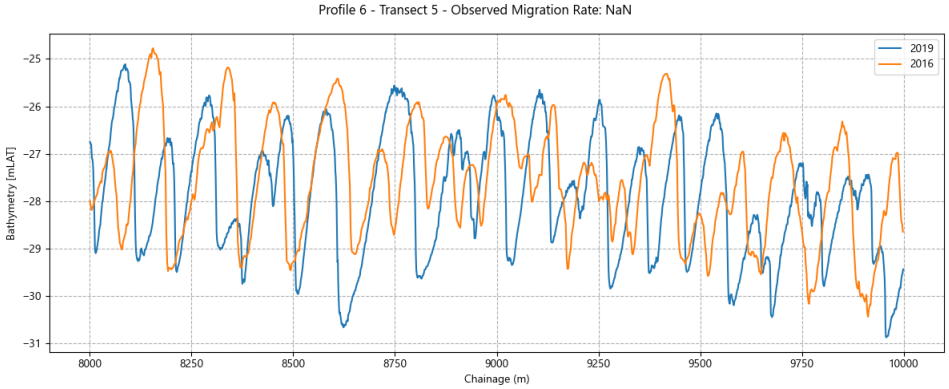


Figure 266. Observed sandwave migration between 2016 and 2019 on profile 6, transect 5. The maximum observed sandwave migration rate, and direction of migration, is detailed at the top of the plot.

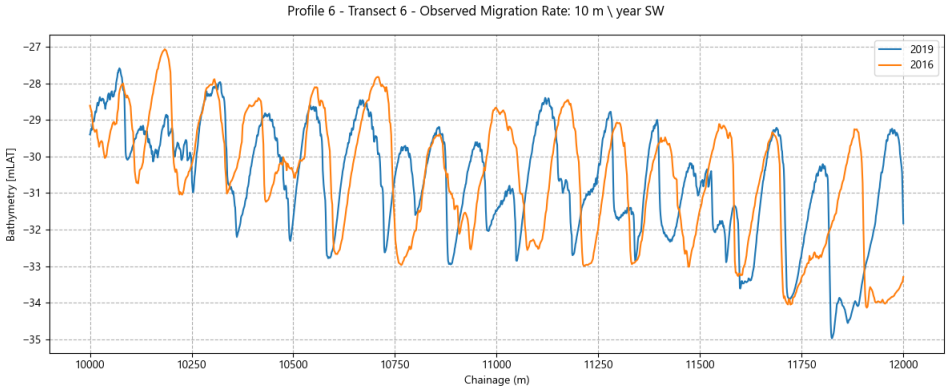


Figure 267. Observed sandwave migration between 2016 and 2019 on profile 6, transect 6. The maximum observed sandwave migration rate, and direction of migration, is detailed at the top of the plot.

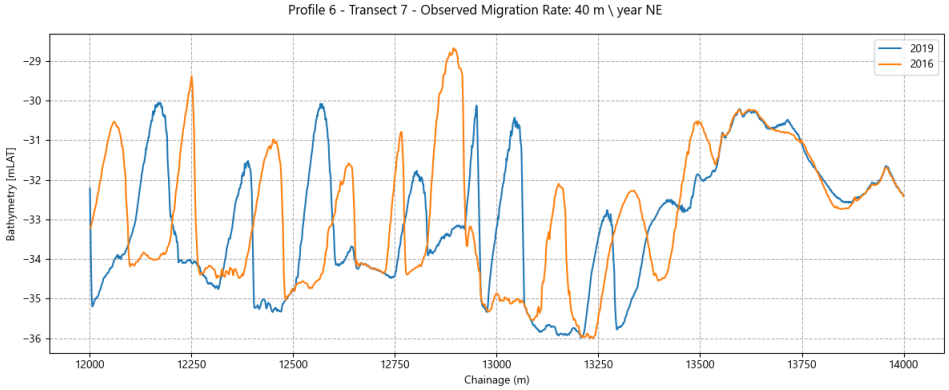


Figure 268. Observed sandwave migration between 2016 and 2019 on profile 6, transect 7. The maximum observed sandwave migration rate, and direction of migration, is detailed at the top of the plot.

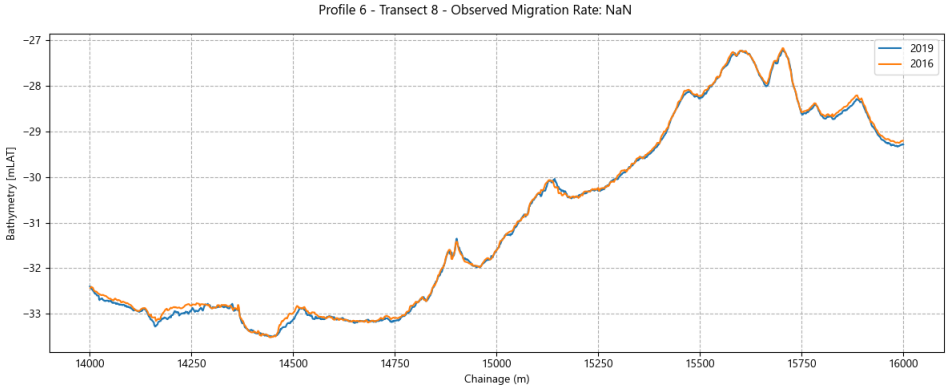


Figure 269. Observed sandwave migration between 2016 and 2019 on profile 6, transect 8. The maximum observed sandwave migration rate, and direction of migration, is detailed at the top of the plot.

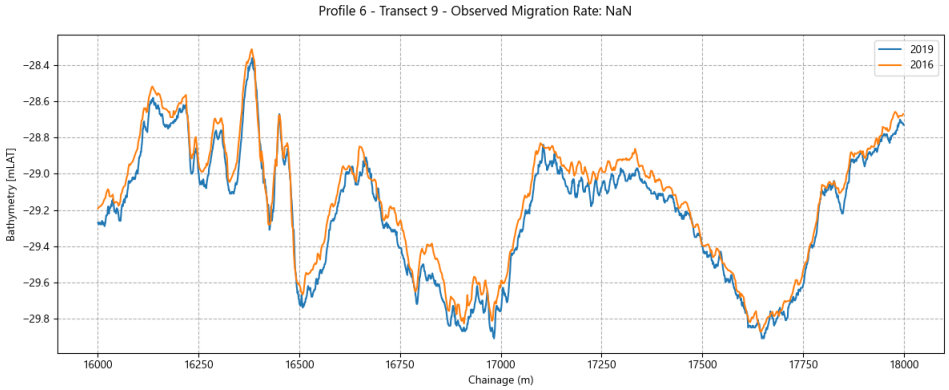


Figure 270. Observed sandwave migration between 2016 and 2019 on profile 6, transect 9. The maximum observed sandwave migration rate, and direction of migration, is detailed at the top of the plot.

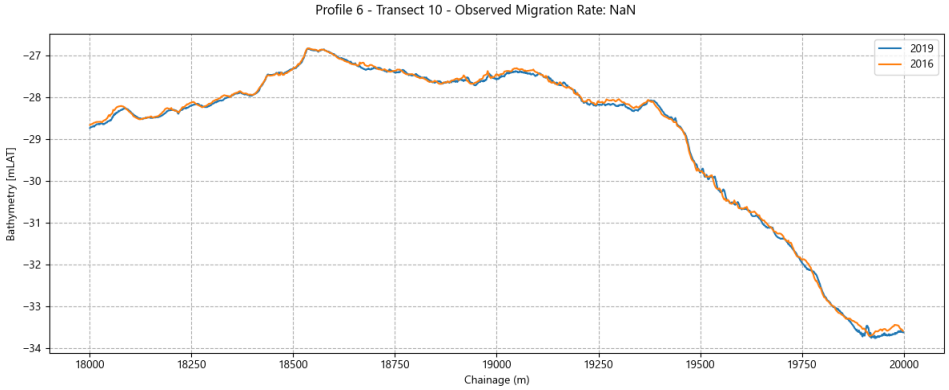


Figure 271. Observed sandwave migration between 2016 and 2019 on profile 6, transect 10. The maximum observed sandwave migration rate, and direction of migration, is detailed at the top of the plot.

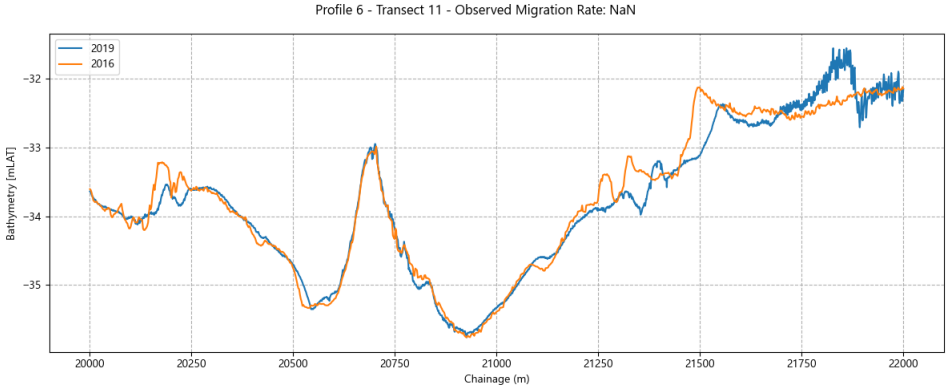


Figure 272. Observed sandwave migration between 2016 and 2019 on profile 6, transect 11. The maximum observed sandwave migration rate, and direction of migration, is detailed at the top of the plot.

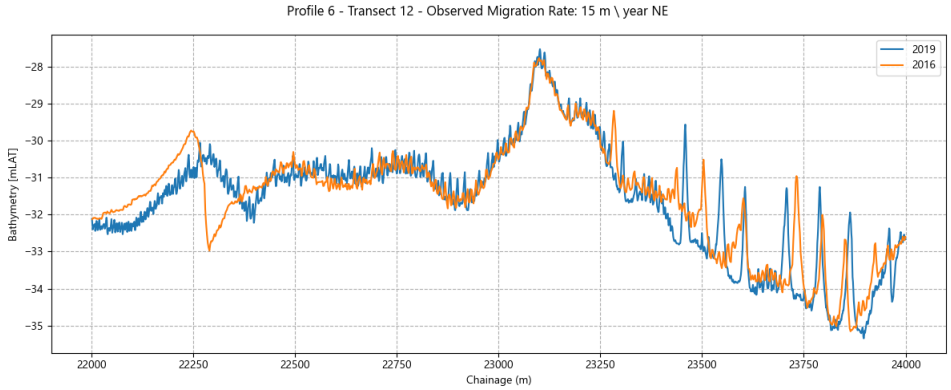


Figure 273. Observed sandwave migration between 2016 and 2019 on profile 6, transect 12. The maximum observed sandwave migration rate, and direction of migration, is detailed at the top of the plot.

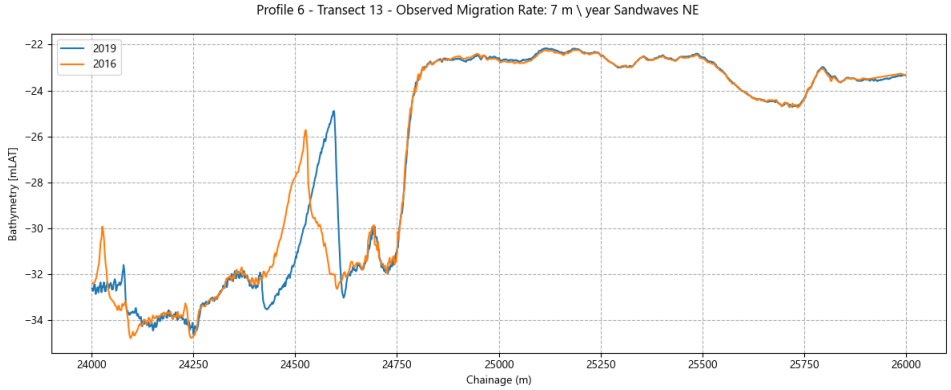


Figure 274. Observed sandwave migration between 2016 and 2019 on profile 6, transect 13. The maximum observed sandwave migration rate, and direction of migration, is detailed at the top of the plot.

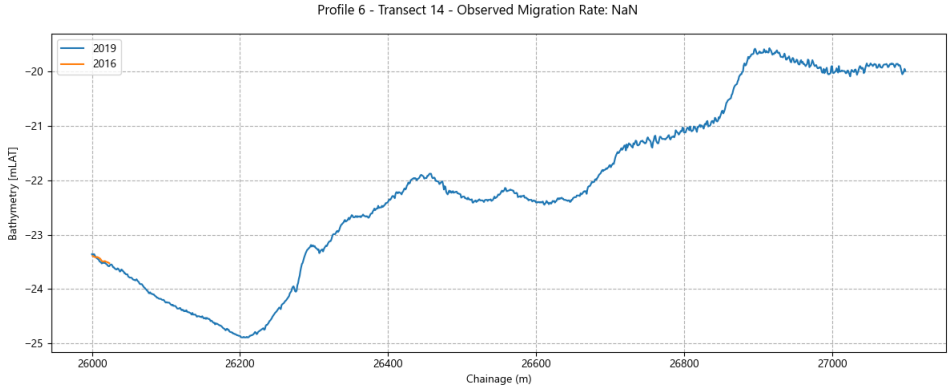


Figure 275. Observed sandwave migration between 2016 and 2019 on profile 6, transect 14. The maximum observed sandwave migration rate, and direction of migration, is detailed at the top of the plot.

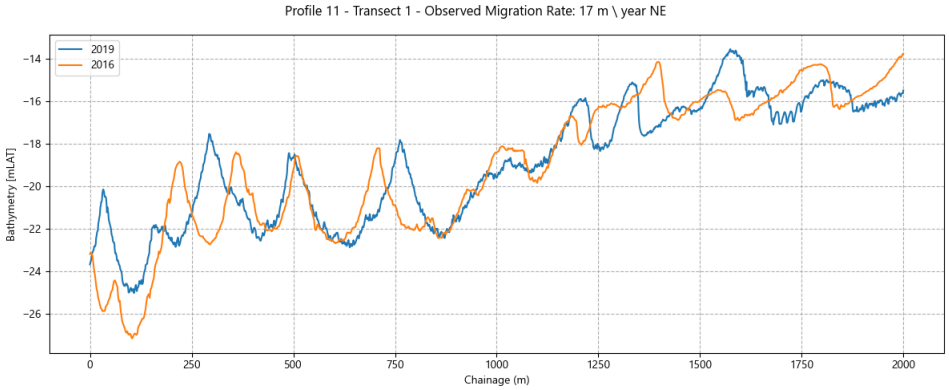


Figure 276. Observed sandwave migration between 2016 and 2019 on profile 11, transect 1. The maximum observed sandwave migration rate, and direction of migration, is detailed at the top of the plot.

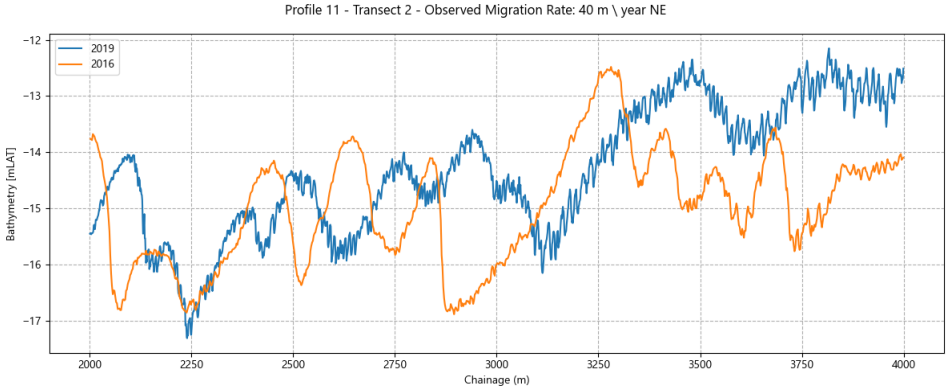


Figure 277. Observed sandwave migration between 2016 and 2019 on profile 11, transect 2. The maximum observed sandwave migration rate, and direction of migration, is detailed at the top of the plot.

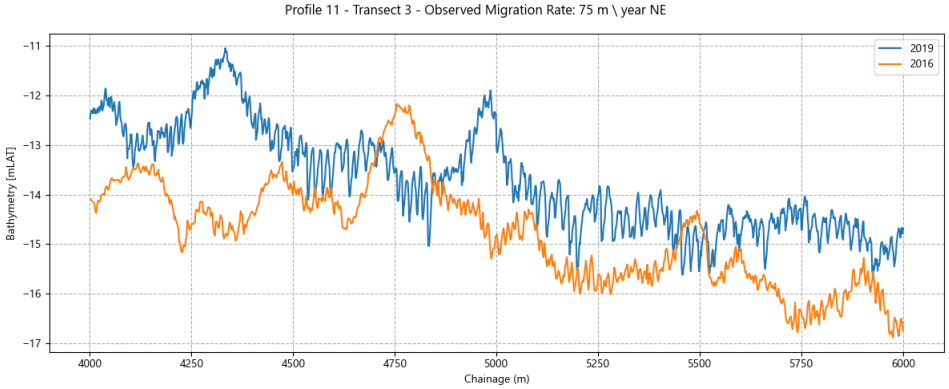


Figure 278. Observed sandwave migration between 2016 and 2019 on profile 11, transect 3. The maximum observed sandwave migration rate, and direction of migration, is detailed at the top of the plot.

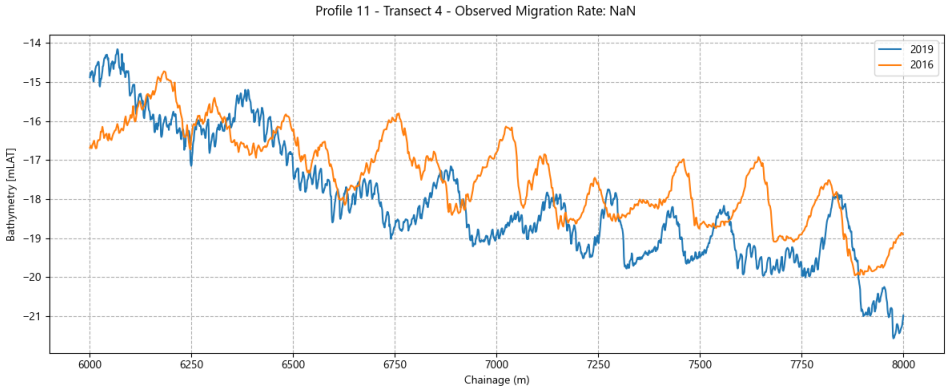


Figure 279. Observed sandwave migration between 2016 and 2019 on profile 11, transect 4. The maximum observed sandwave migration rate, and direction of migration, is detailed at the top of the plot.

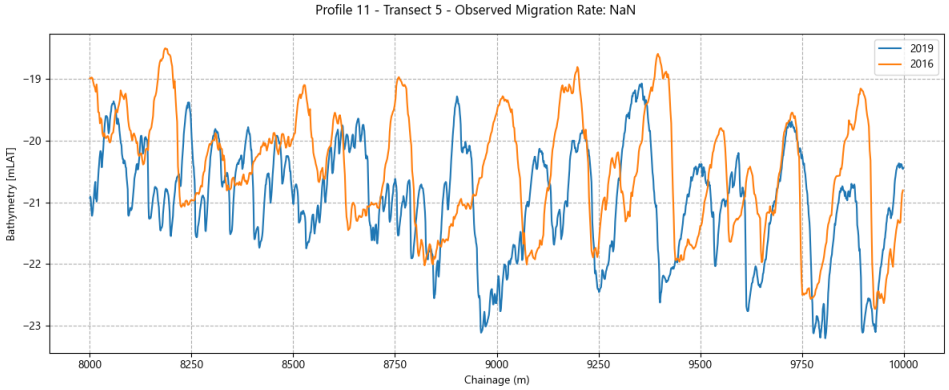


Figure 280. Observed sandwave migration between 2016 and 2019 on profile 11, transect 5. The maximum observed sandwave migration rate, and direction of migration, is detailed at the top of the plot.

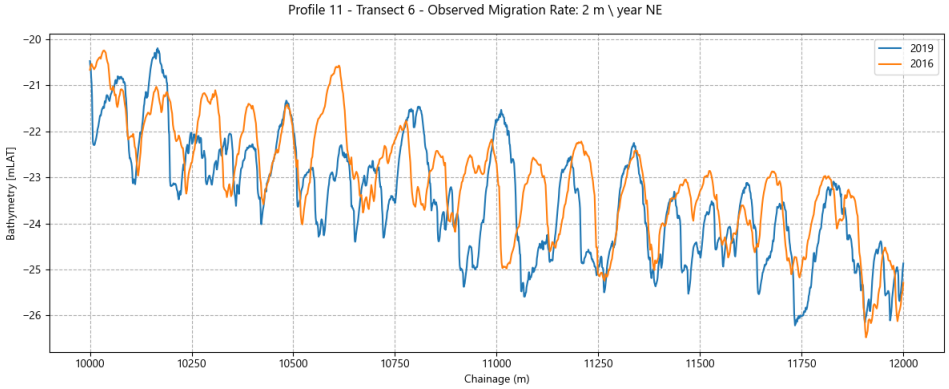


Figure 281. Observed sandwave migration between 2016 and 2019 on profile 11, transect 6. The maximum observed sandwave migration rate, and direction of migration, is detailed at the top of the plot.

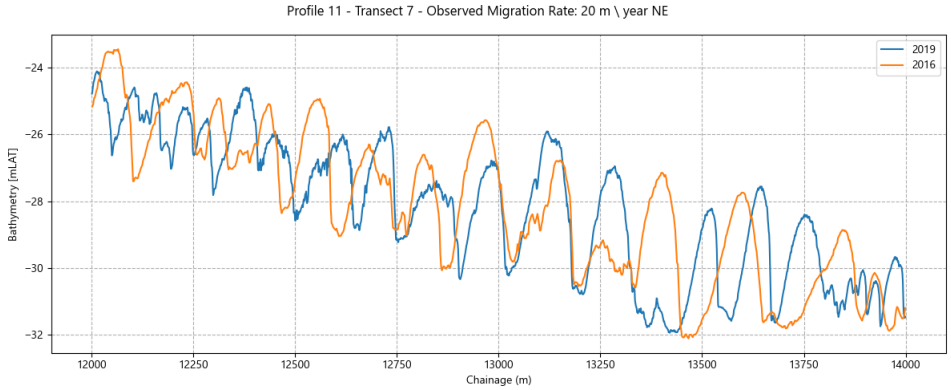


Figure 282. Observed sandwave migration between 2016 and 2019 on profile 11, transect 7. The maximum observed sandwave migration rate, and direction of migration, is detailed at the top of the plot.

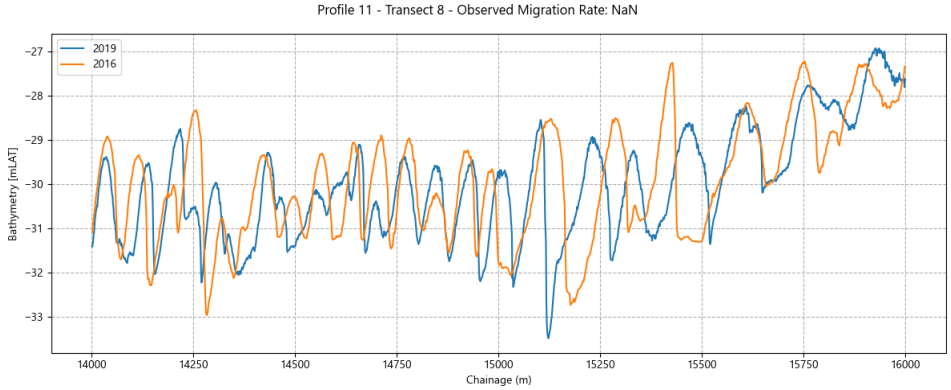


Figure 283. Observed sandwave migration between 2016 and 2019 on profile 11, transect 8. The maximum observed sandwave migration rate, and direction of migration, is detailed at the top of the plot.

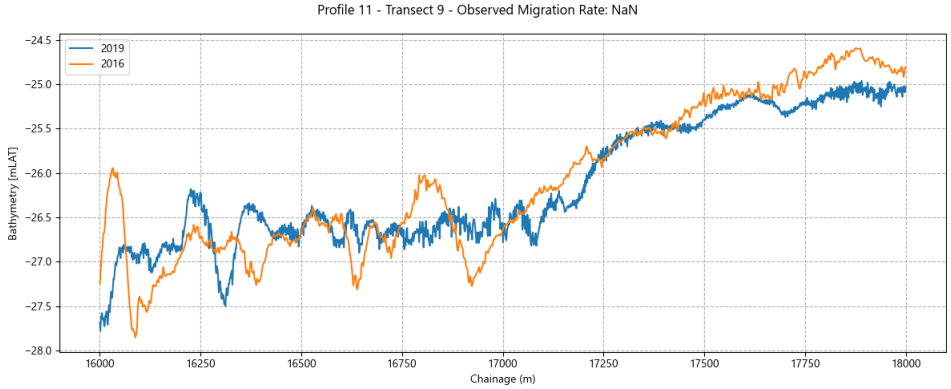


Figure 284. Observed sandwave migration between 2016 and 2019 on profile 11, transect 9. The maximum observed sandwave migration rate, and direction of migration, is detailed at the top of the plot.

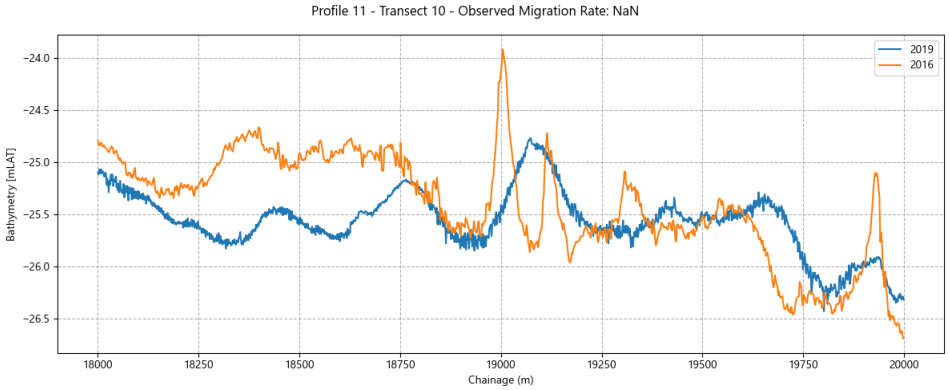


Figure 285. Observed sandwave migration between 2016 and 2019 on profile 11, transect 10. The maximum observed sandwave migration rate, and direction of migration, is detailed at the top of the plot.

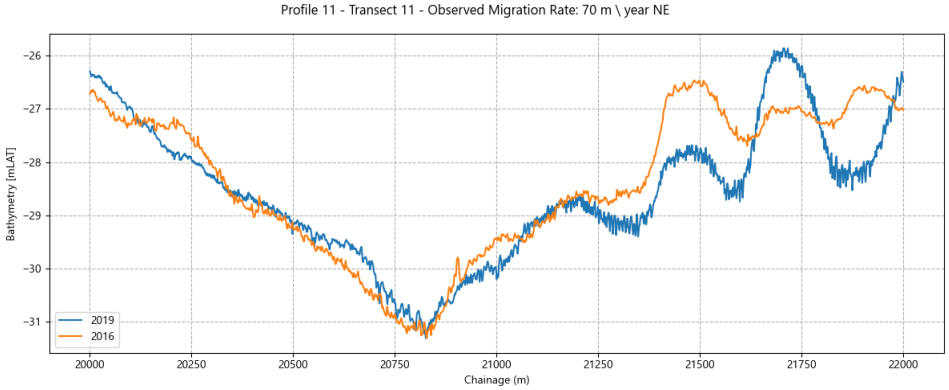


Figure 286. Observed sandwave migration between 2016 and 2019 on profile 11, transect 11. The maximum observed sandwave migration rate, and direction of migration, is detailed at the top of the plot.

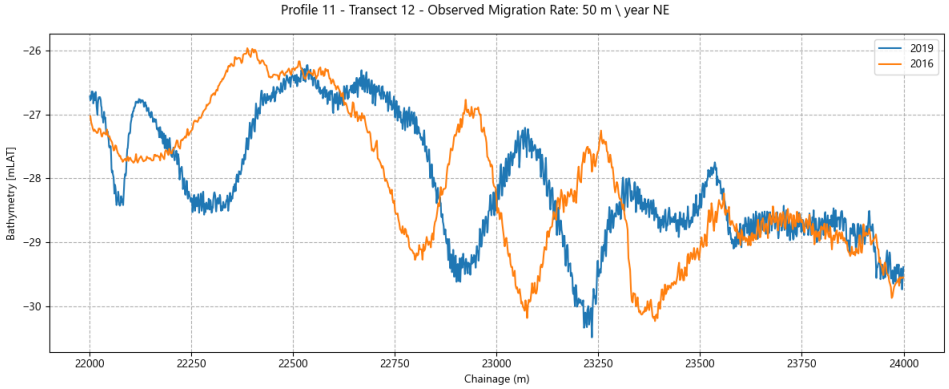


Figure 287. Observed sandwave migration between 2016 and 2019 on profile 11, transect 12. The maximum observed sandwave migration rate, and direction of migration, is detailed at the top of the plot.

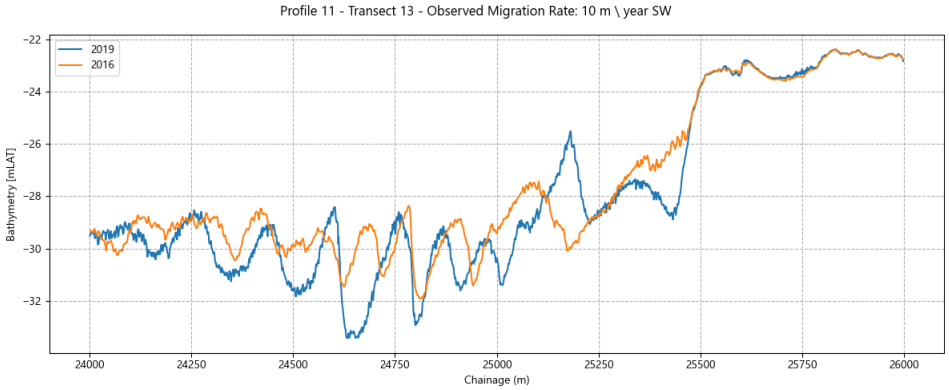


Figure 288. Observed sandwave migration between 2016 and 2019 on profile 11, transect 13. The maximum observed sandwave migration rate, and direction of migration, is detailed at the top of the plot.

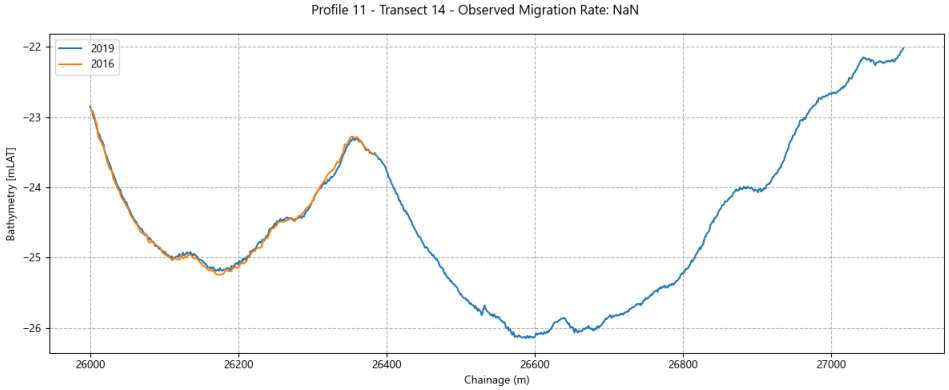


Figure 289. Observed sandwave migration between 2016 and 2019 on profile 11, transect 14. The maximum observed sandwave migration rate, and direction of migration, is detailed at the top of the plot.

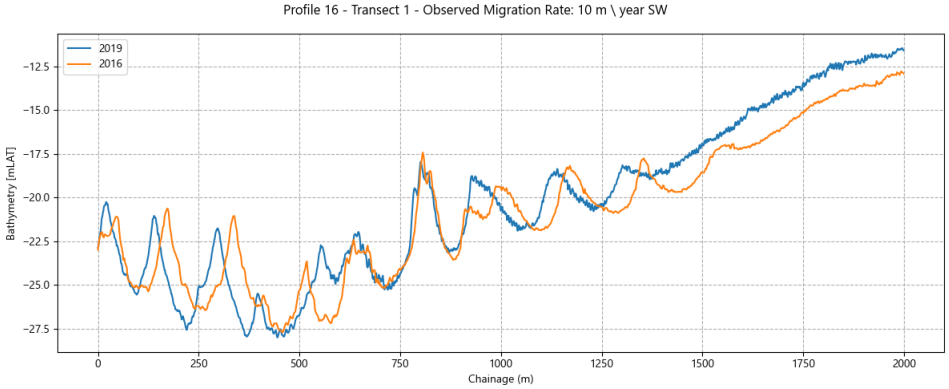


Figure 290. Observed sandwave migration between 2016 and 2019 on profile 16, transect 1. The maximum observed sandwave migration rate, and direction of migration, is detailed at the top of the plot.

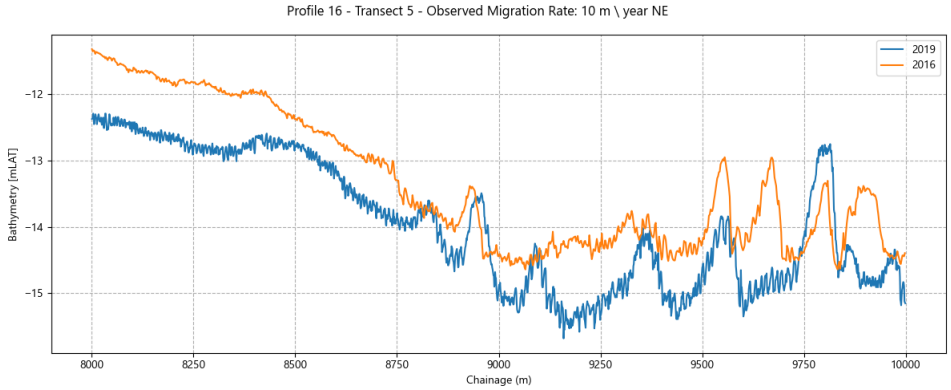


Figure 291. Observed sandwave migration between 2016 and 2019 on profile 16, transect 5. The maximum observed sandwave migration rate, and direction of migration, is detailed at the top of the plot.

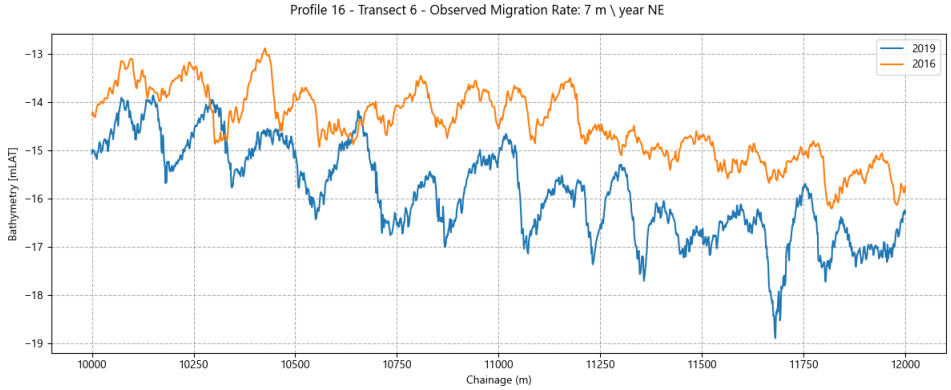


Figure 292. Observed sandwave migration between 2016 and 2019 on profile 16, transect 6. The maximum observed sandwave migration rate, and direction of migration, is detailed at the top of the plot.

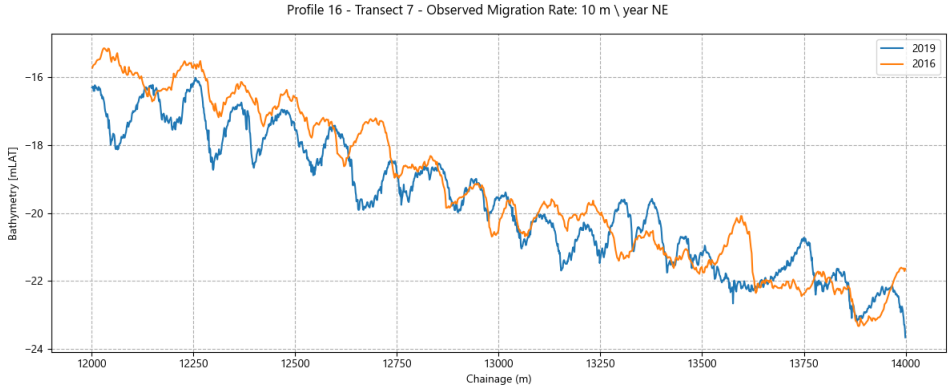


Figure 293. Observed sandwave migration between 2016 and 2019 on profile 16, transect 7. The maximum observed sandwave migration rate, and direction of migration, is detailed at the top of the plot.

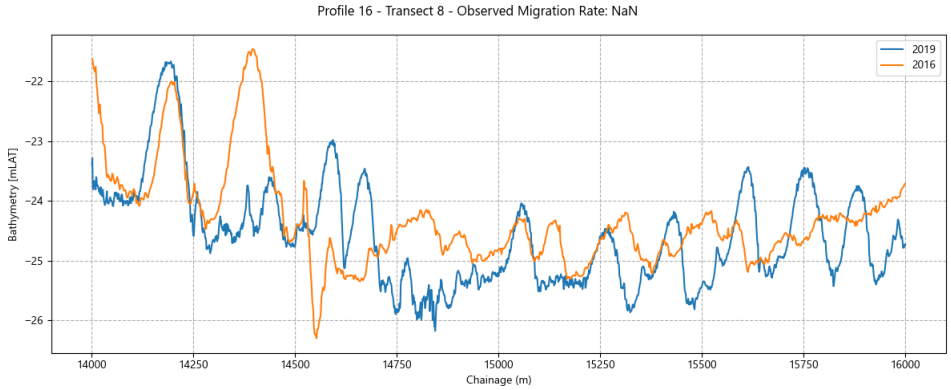


Figure 294. Observed sandwave migration between 2016 and 2019 on profile 16, transect 8. The maximum observed sandwave migration rate, and direction of migration, is detailed at the top of the plot.

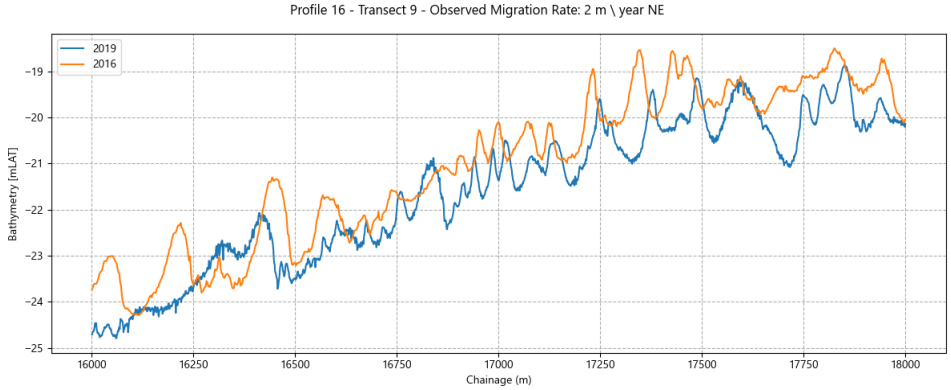


Figure 295. Observed sandwave migration between 2016 and 2019 on profile 16, transect 9. The maximum observed sandwave migration rate, and direction of migration, is detailed at the top of the plot.

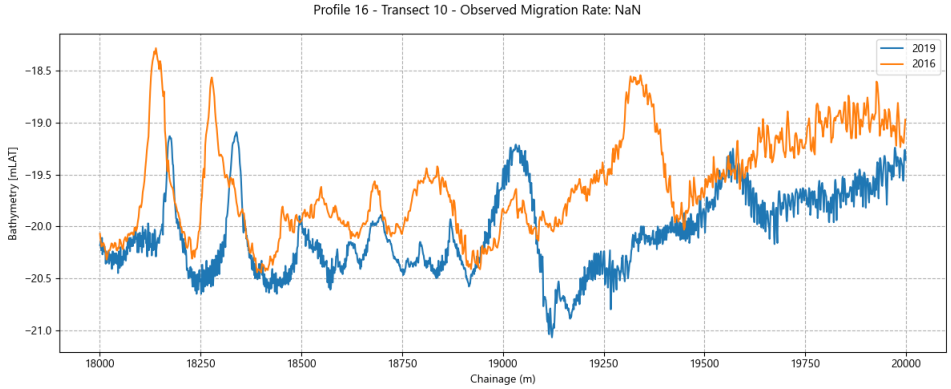


Figure 296. Observed sandwave migration between 2016 and 2019 on profile 16, transect 10. The maximum observed sandwave migration rate, and direction of migration, is detailed at the top of the plot.

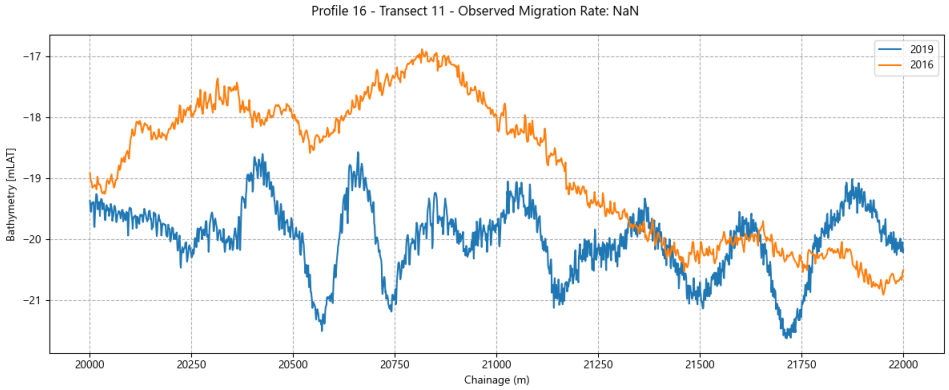


Figure 297. Observed sandwave migration between 2016 and 2019 on profile 16, transect 11. The maximum observed sandwave migration rate, and direction of migration, is detailed at the top of the plot.

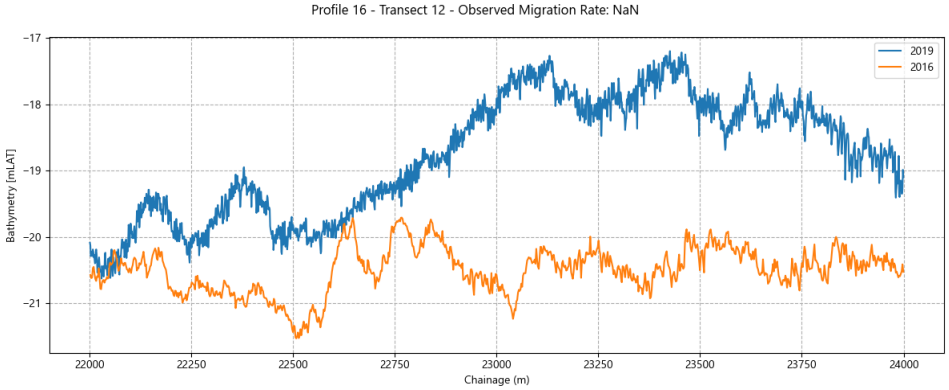


Figure 298. Observed sandwave migration between 2016 and 2019 on profile 16, transect 12. The maximum observed sandwave migration rate, and direction of migration, is detailed at the top of the plot.

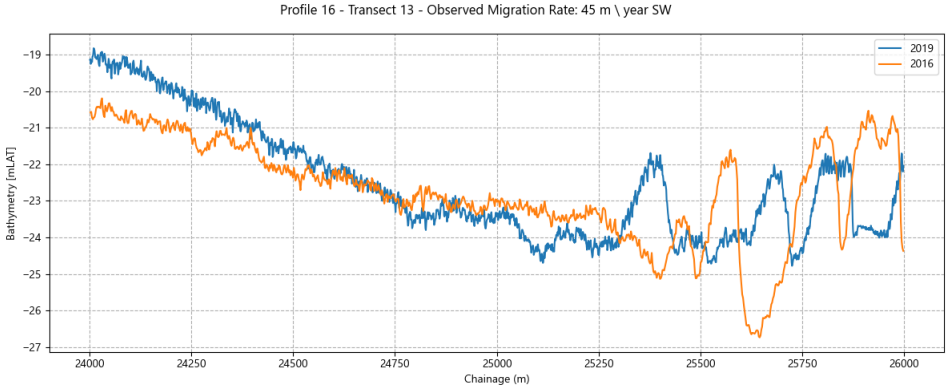


Figure 299. Observed sandwave migration between 2016 and 2019 on profile 16, transect 13. The maximum observed sandwave migration rate, and direction of migration, is detailed at the top of the plot.

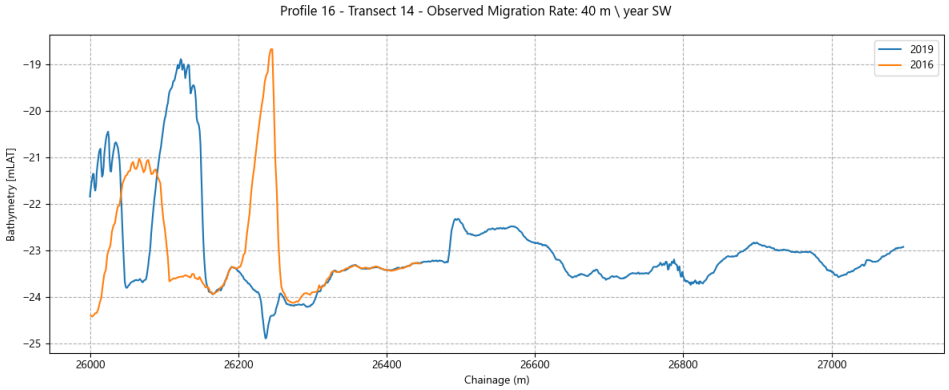


Figure 300. Observed sandwave migration between 2016 and 2019 on profile 16, transect 14. The maximum observed sandwave migration rate, and direction of migration, is detailed at the top of the plot.

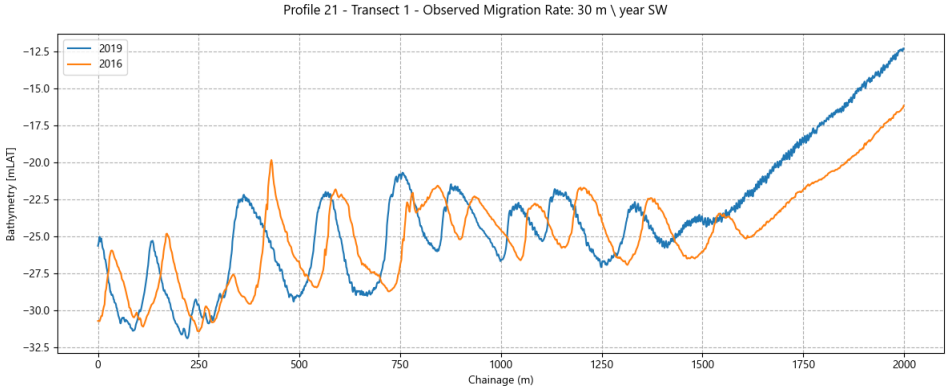


Figure 301. Observed sandwave migration between 2016 and 2019 on profile 21, transect 1. The maximum observed sandwave migration rate, and direction of migration, is detailed at the top of the plot.

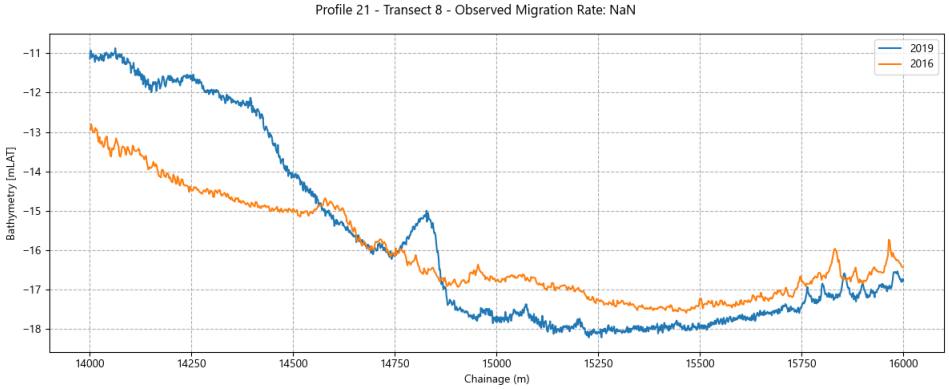


Figure 302. Observed sandwave migration between 2016 and 2019 on profile 21, transect 8. The maximum observed sandwave migration rate, and direction of migration, is detailed at the top of the plot.

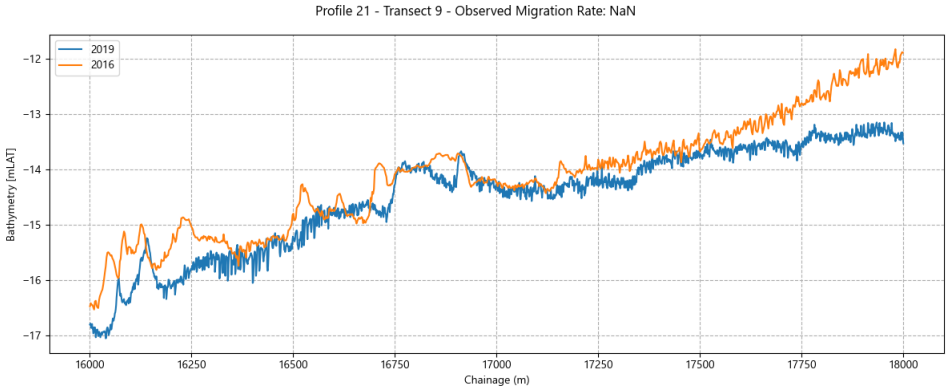


Figure 303. Observed sandwave migration between 2016 and 2019 on profile 21, transect 9. The maximum observed sandwave migration rate, and direction of migration, is detailed at the top of the plot.

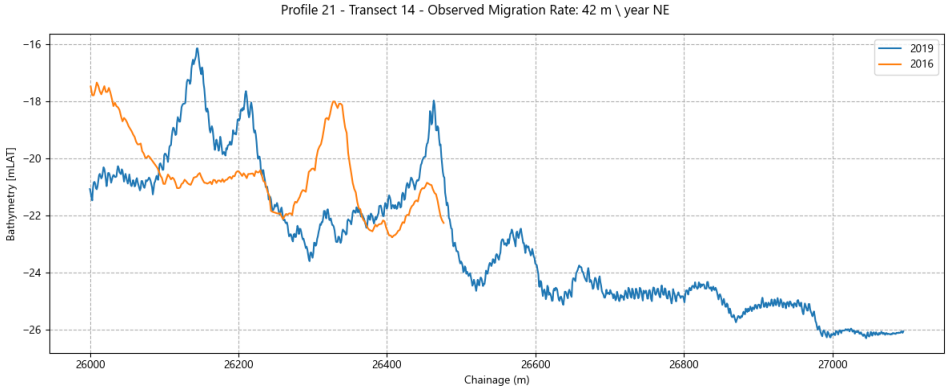


Figure 304. Observed sandwave migration between 2016 and 2019 on profile 21, transect 14. The maximum observed sandwave migration rate, and direction of migration, is detailed at the top of the plot.

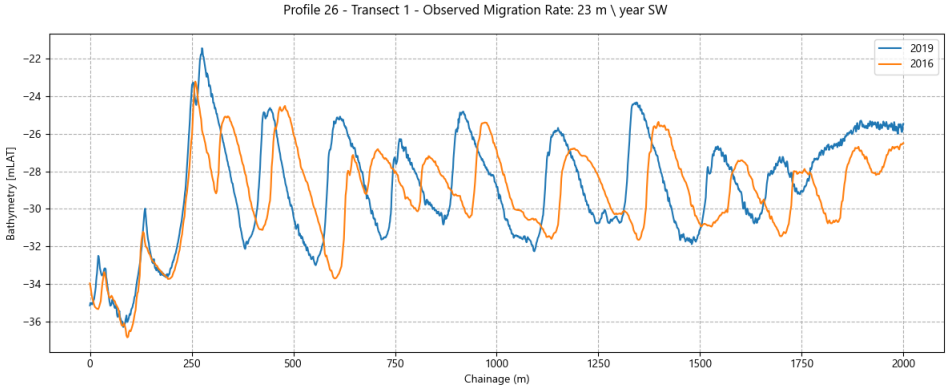


Figure 305. Observed sandwave migration between 2016 and 2019 on profile 26, transect 1. The maximum observed sandwave migration rate, and direction of migration, is detailed at the top of the plot.

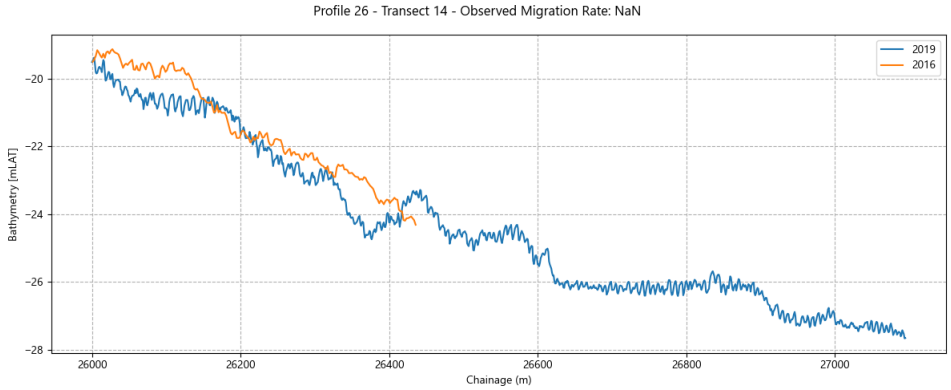


Figure 306. Observed sandwave migration between 2016 and 2019 on profile 26, transect 14. The maximum observed sandwave migration rate, and direction of migration, is detailed at the top of the plot.

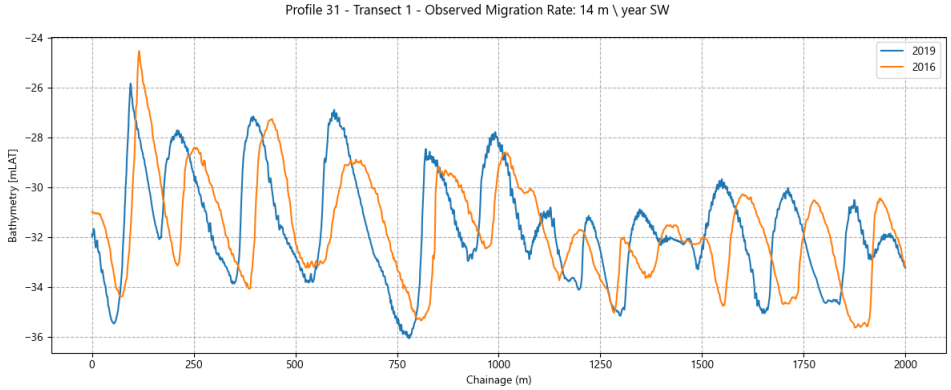


Figure 307. Observed sandwave migration between 2016 and 2019 on profile 31, transect 1. The maximum observed sandwave migration rate, and direction of migration, is detailed at the top of the plot.

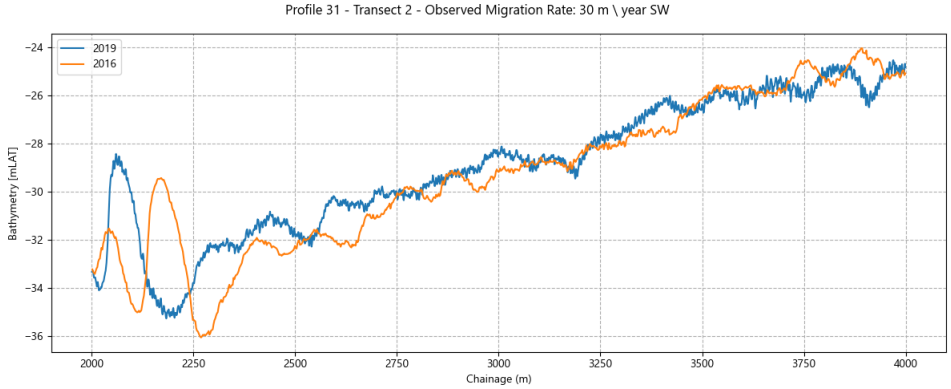


Figure 308. Observed sandwave migration between 2016 and 2019 on profile 31, transect 2. The maximum observed sandwave migration rate, and direction of migration, is detailed at the top of the plot.

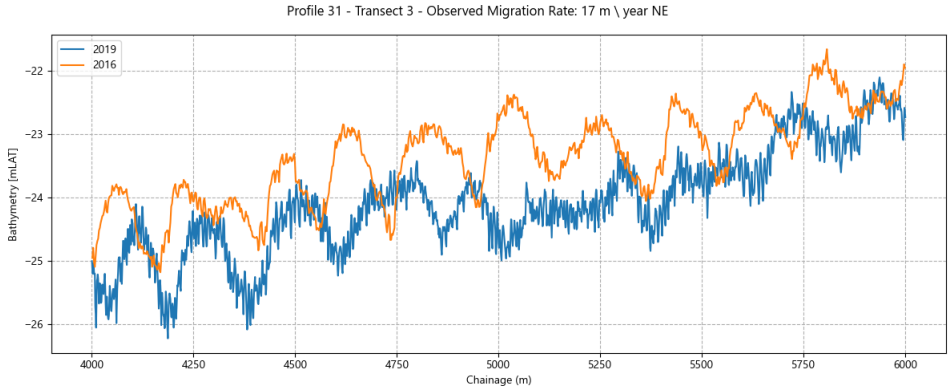


Figure 309. Observed sandwave migration between 2016 and 2019 on profile 31, transect 3. The maximum observed sandwave migration rate, and direction of migration, is detailed at the top of the plot.

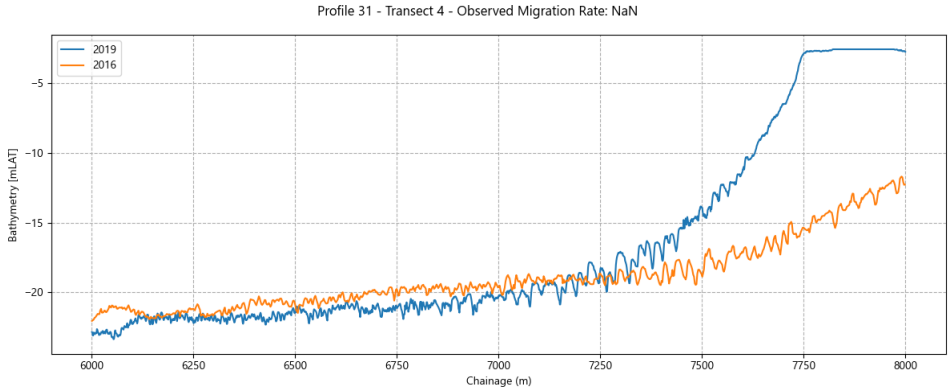


Figure 310. Observed sandwave migration between 2016 and 2019 on profile 31, transect 4. The maximum observed sandwave migration rate, and direction of migration, is detailed at the top of the plot.

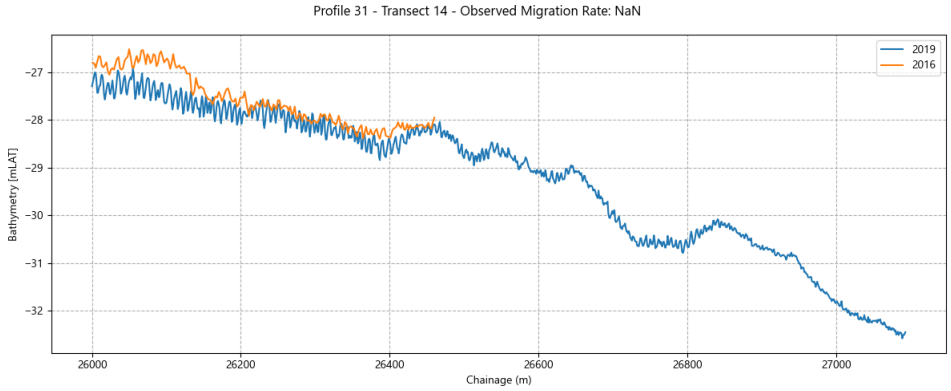


Figure 311. Observed sandwave migration between 2016 and 2019 on profile 31, transect 14. The maximum observed sandwave migration rate, and direction of migration, is detailed at the top of the plot.

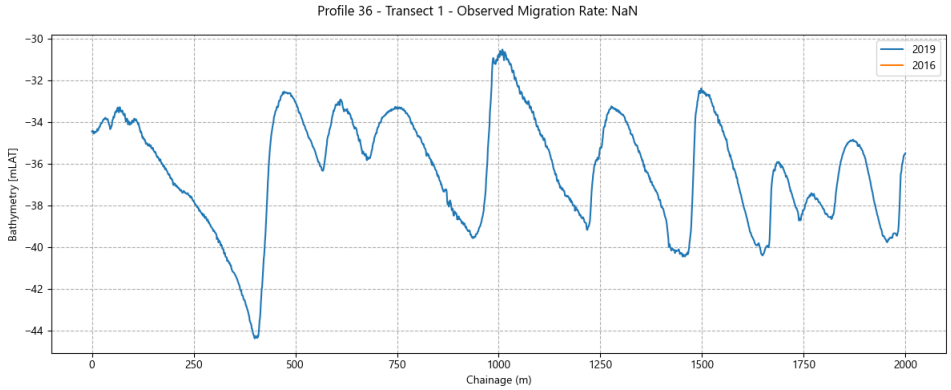


Figure 312. Observed sandwave migration between 2016 and 2019 on profile 36, transect 1. The maximum observed sandwave migration rate, and direction of migration, is detailed at the top of the plot.

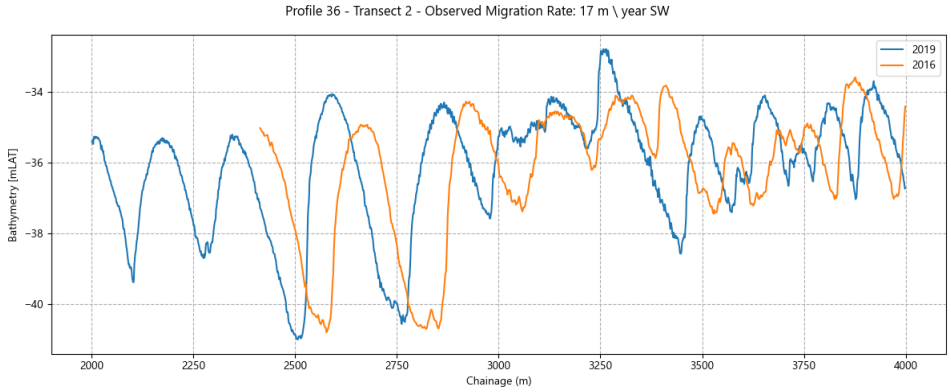


Figure 313. Observed sandwave migration between 2016 and 2019 on profile 36, transect 2. The maximum observed sandwave migration rate, and direction of migration, is detailed at the top of the plot.

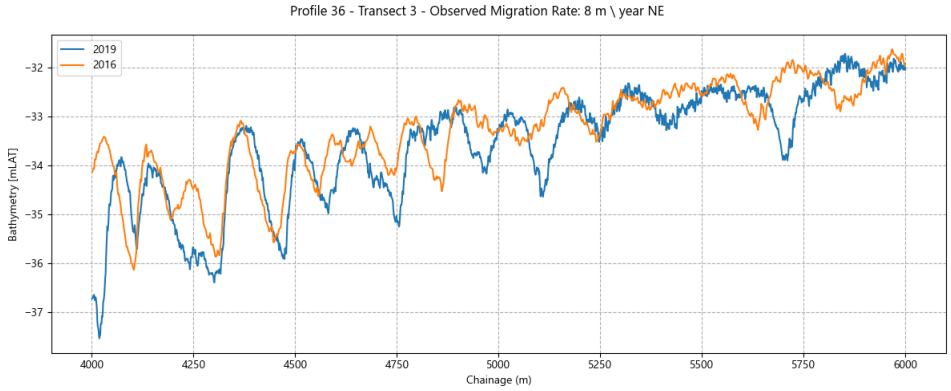


Figure 314. Observed sandwave migration between 2016 and 2019 on profile 36, transect 3. The maximum observed sandwave migration rate, and direction of migration, is detailed at the top of the plot.

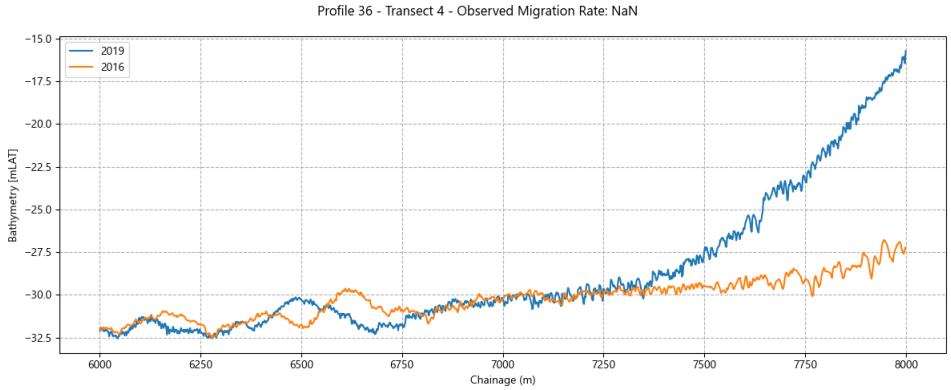


Figure 315. Observed sandwave migration between 2016 and 2019 on profile 36, transect 4. The maximum observed sandwave migration rate, and direction of migration, is detailed at the top of the plot.

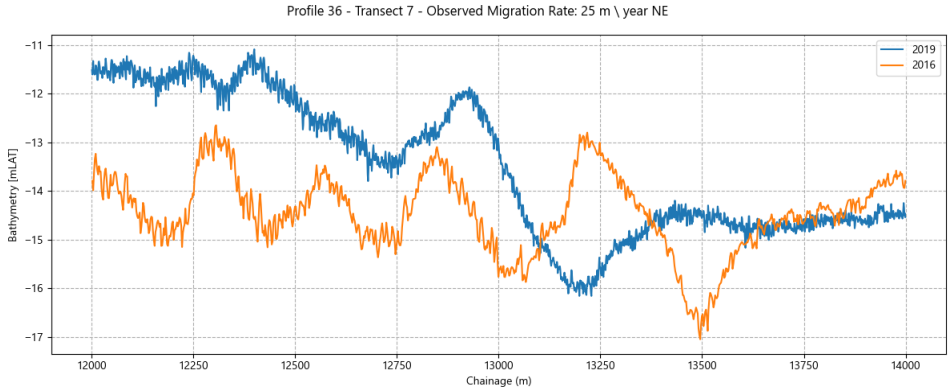


Figure 316. Observed sandwave migration between 2016 and 2019 on profile 36, transect 7. The maximum observed sandwave migration rate, and direction of migration, is detailed at the top of the plot.

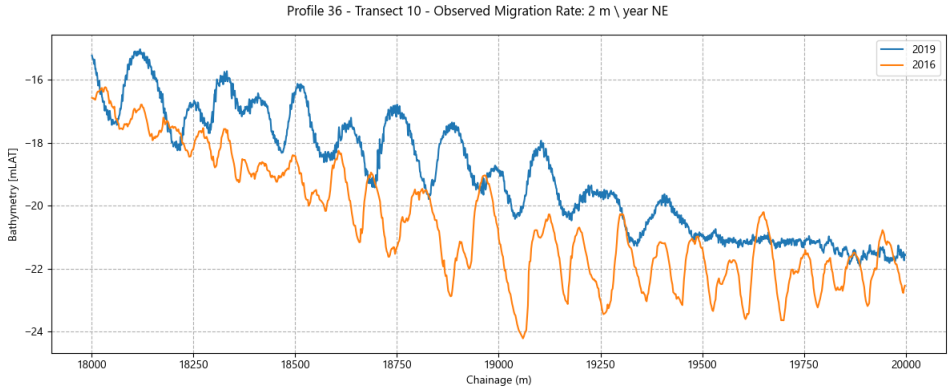


Figure 317. Observed sandwave migration between 2016 and 2019 on profile 36, transect 10. The maximum observed sandwave migration rate, and direction of migration, is detailed at the top of the plot.

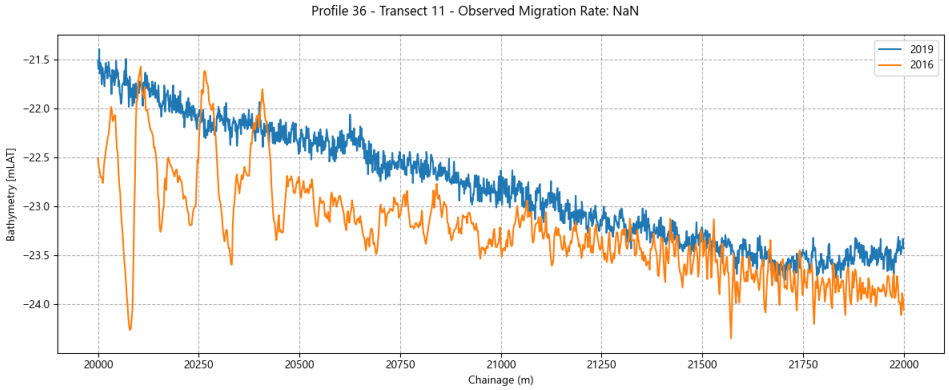


Figure 318. Observed sandwave migration between 2016 and 2019 on profile 36, transect 11. The maximum observed sandwave migration rate, and direction of migration, is detailed at the top of the plot.

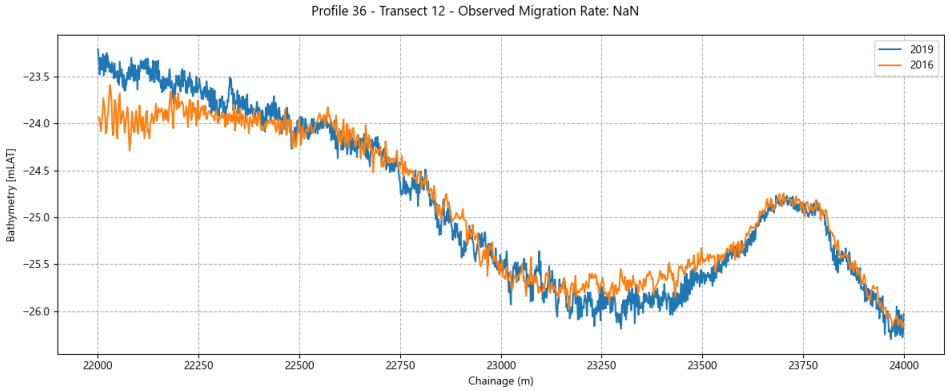


Figure 319. Observed sandwave migration between 2016 and 2019 on profile 36, transect 12. The maximum observed sandwave migration rate, and direction of migration, is detailed at the top of the plot.

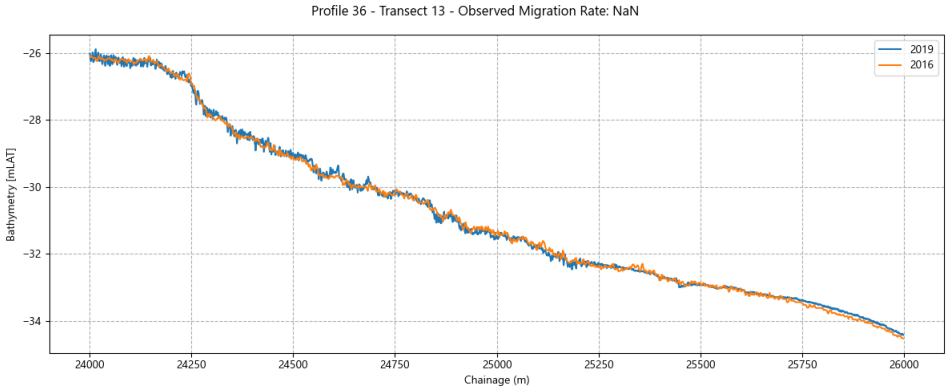


Figure 320. Observed sandwave migration between 2016 and 2019 on profile 36, transect 13. The maximum observed sandwave migration rate, and direction of migration, is detailed at the top of the plot.

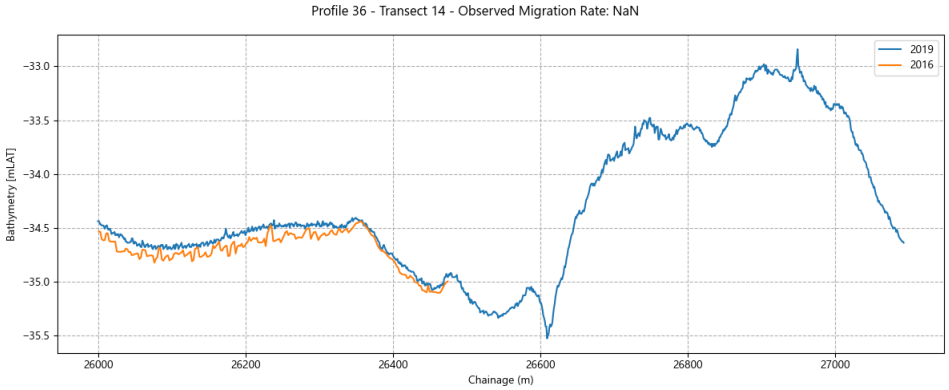


Figure 321. Observed sandwave migration between 2016 and 2019 on profile 36, transect 14. The maximum observed sandwave migration rate, and direction of migration, is detailed at the top of the plot.

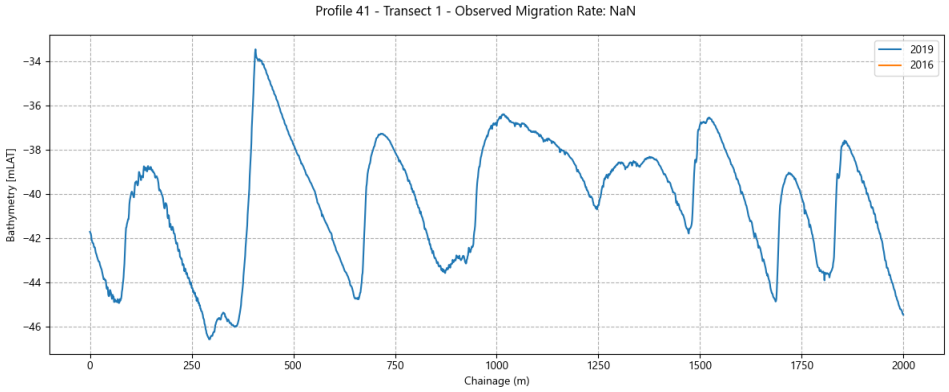


Figure 322. Observed sandwave migration between 2016 and 2019 on profile 41, transect 1. The maximum observed sandwave migration rate, and direction of migration, is detailed at the top of the plot.

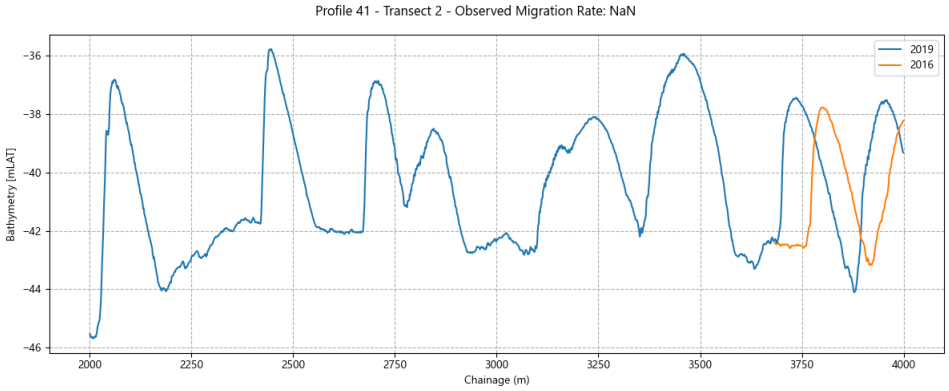


Figure 323. Observed sandwave migration between 2016 and 2019 on profile 41, transect 2. The maximum observed sandwave migration rate, and direction of migration, is detailed at the top of the plot.

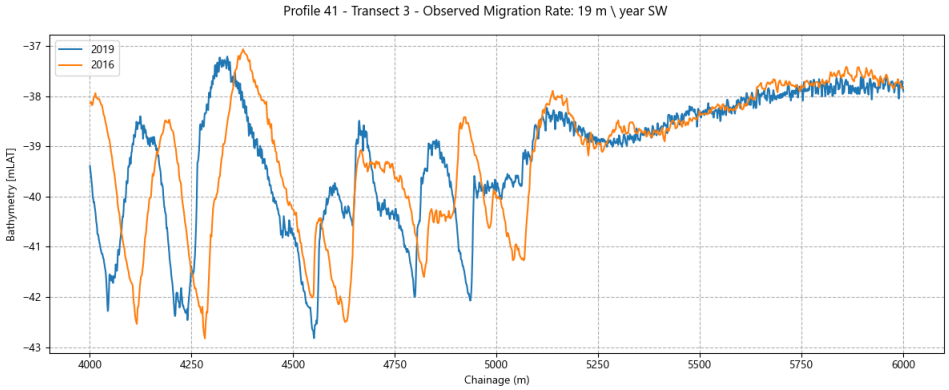


Figure 324. Observed sandwave migration between 2016 and 2019 on profile 41, transect 3. The maximum observed sandwave migration rate, and direction of migration, is detailed at the top of the plot.

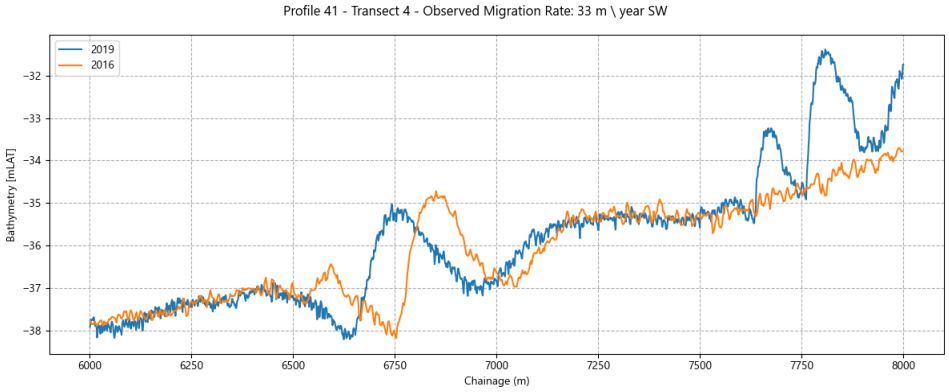


Figure 325. Observed sandwave migration between 2016 and 2019 on profile 41, transect 4. The maximum observed sandwave migration rate, and direction of migration, is detailed at the top of the plot.

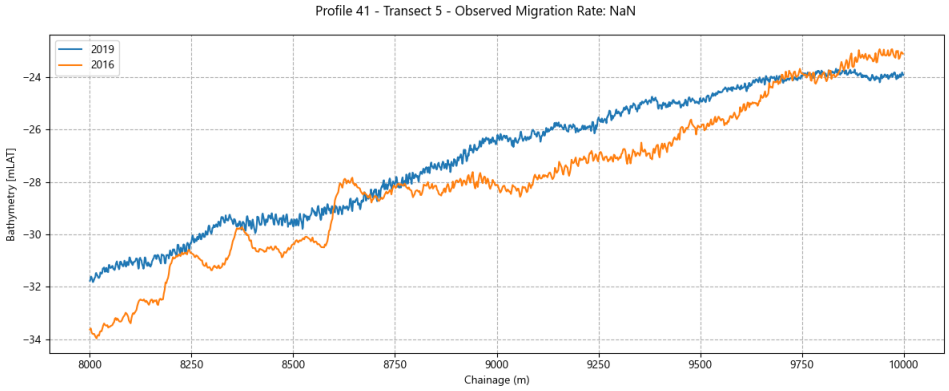


Figure 326. Observed sandwave migration between 2016 and 2019 on profile 41, transect 5. The maximum observed sandwave migration rate, and direction of migration, is detailed at the top of the plot.

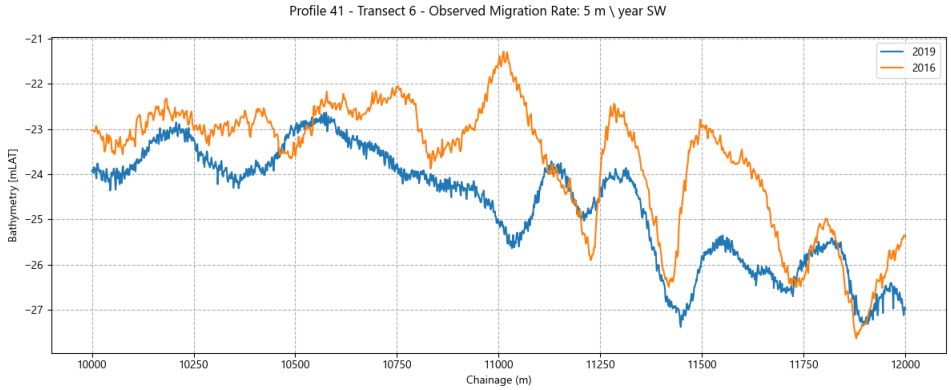


Figure 327. Observed sandwave migration between 2016 and 2019 on profile 41, transect 6. The maximum observed sandwave migration rate, and direction of migration, is detailed at the top of the plot.

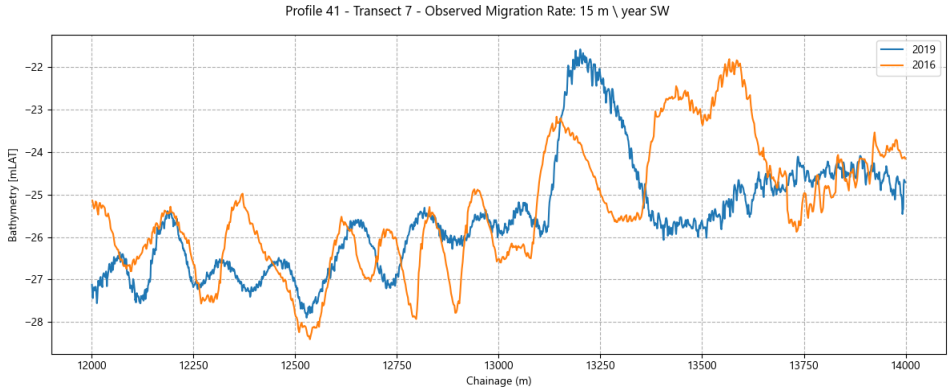


Figure 328. Observed sandwave migration between 2016 and 2019 on profile 41, transect 7. The maximum observed sandwave migration rate, and direction of migration, is detailed at the top of the plot.

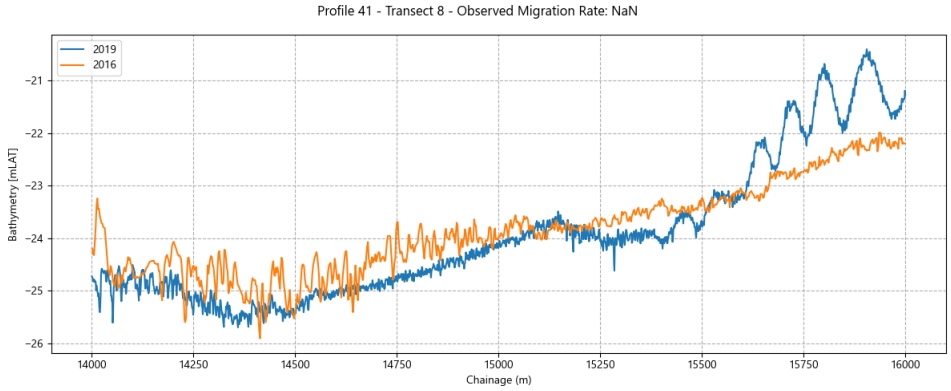


Figure 329. Observed sandwave migration between 2016 and 2019 on profile 41, transect 8. The maximum observed sandwave migration rate, and direction of migration, is detailed at the top of the plot.

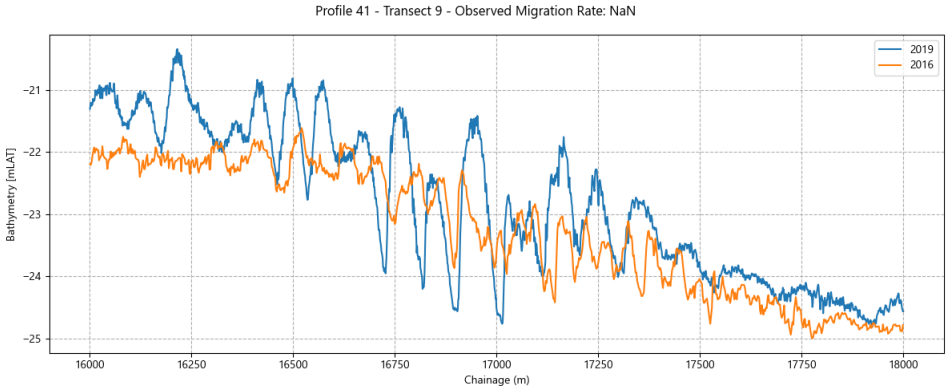


Figure 330. Observed sandwave migration between 2016 and 2019 on profile 41, transect 9. The maximum observed sandwave migration rate, and direction of migration, is detailed at the top of the plot.

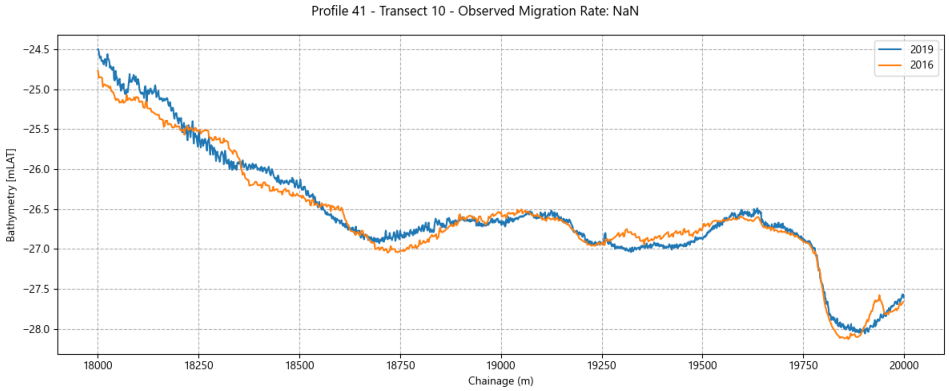


Figure 331. Observed sandwave migration between 2016 and 2019 on profile 41, transect 10. The maximum observed sandwave migration rate, and direction of migration, is detailed at the top of the plot.

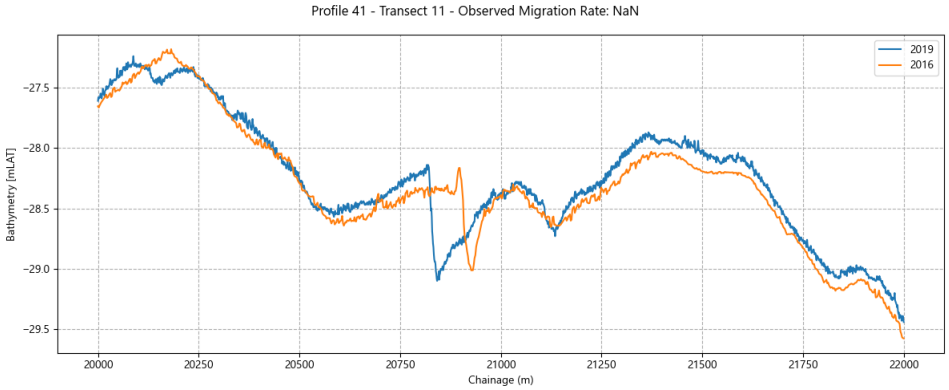


Figure 332. Observed sandwave migration between 2016 and 2019 on profile 41, transect 11. The maximum observed sandwave migration rate, and direction of migration, is detailed at the top of the plot.

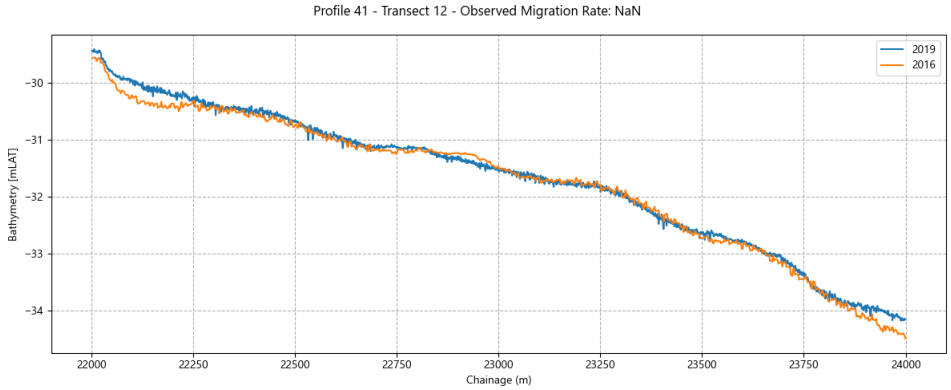


Figure 333. Observed sandwave migration between 2016 and 2019 on profile 41, transect 12. The maximum observed sandwave migration rate, and direction of migration, is detailed at the top of the plot.

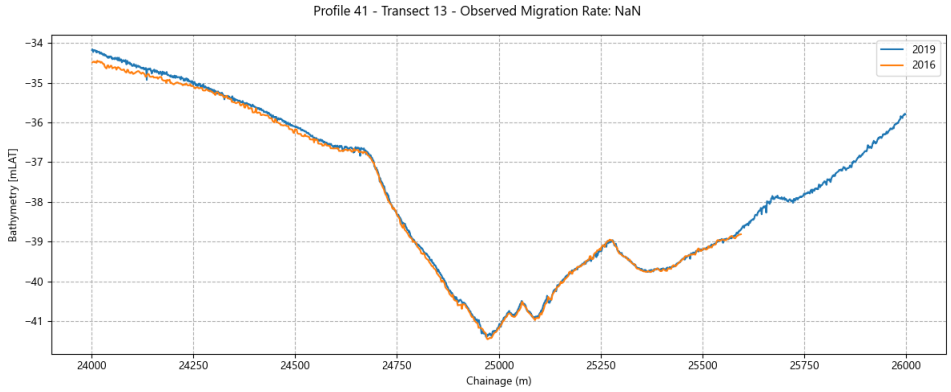


Figure 334. Observed sandwave migration between 2016 and 2019 on profile 41, transect 13. The maximum observed sandwave migration rate, and direction of migration, is detailed at the top of the plot.

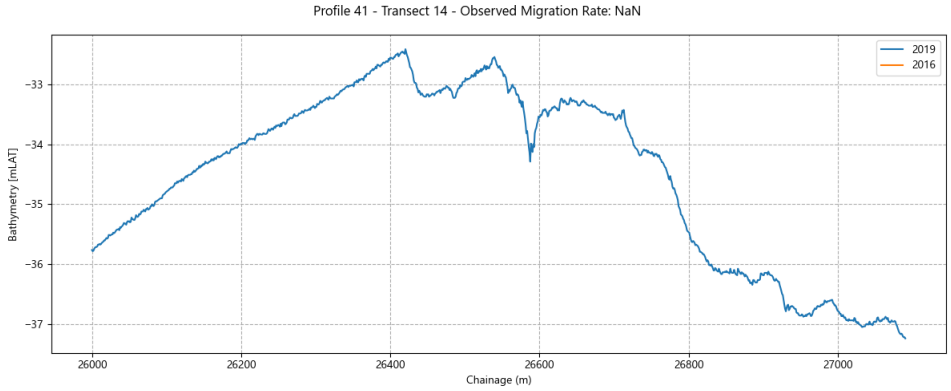


Figure 335. Observed sandwave migration between 2016 and 2019 on profile 41, transect 14. The maximum observed sandwave migration rate, and direction of migration, is detailed at the top of the plot.

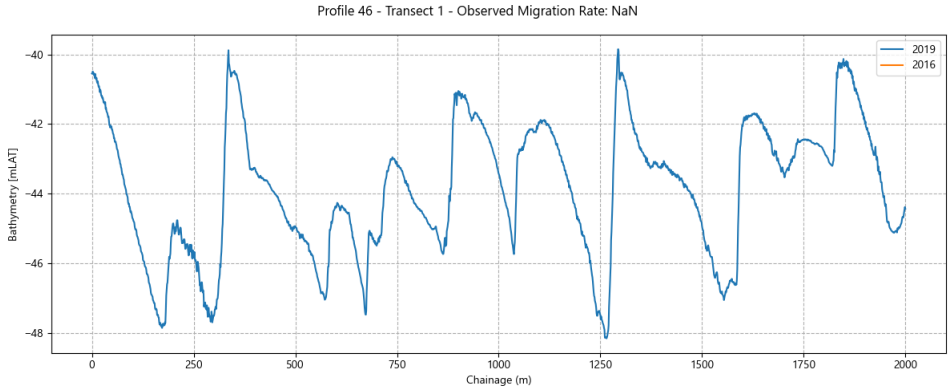


Figure 336. Observed sandwave migration between 2016 and 2019 on profile 46, transect 1. The maximum observed sandwave migration rate, and direction of migration, is detailed at the top of the plot.

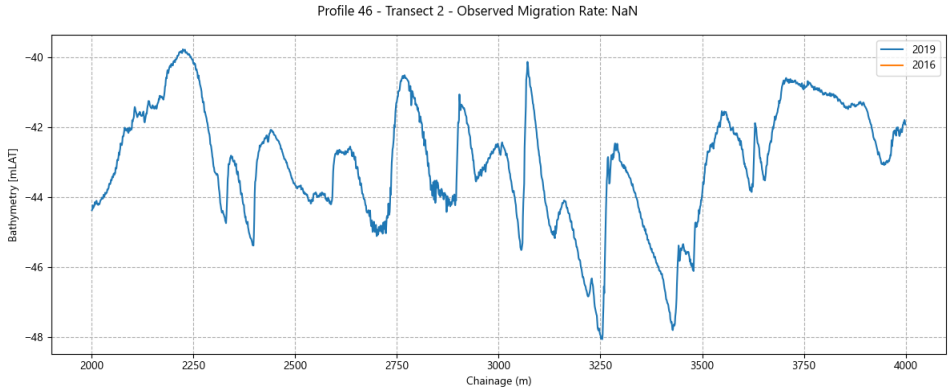


Figure 337. Observed sandwave migration between 2016 and 2019 on profile 46, transect 2. The maximum observed sandwave migration rate, and direction of migration, is detailed at the top of the plot.

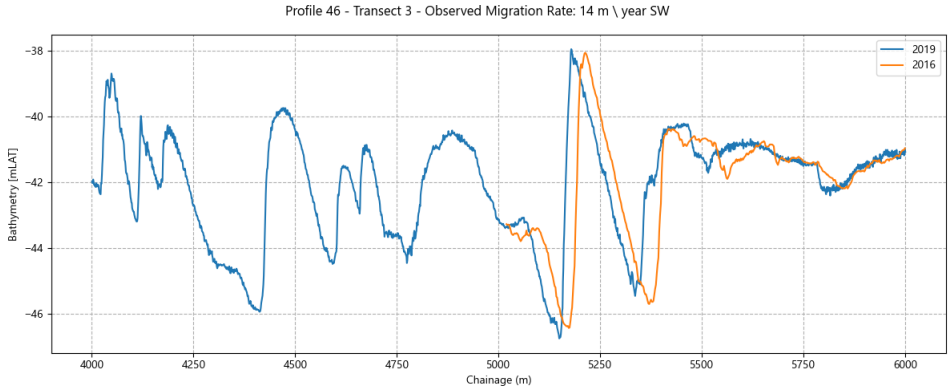


Figure 338. Observed sandwave migration between 2016 and 2019 on profile 46, transect 3. The maximum observed sandwave migration rate, and direction of migration, is detailed at the top of the plot.

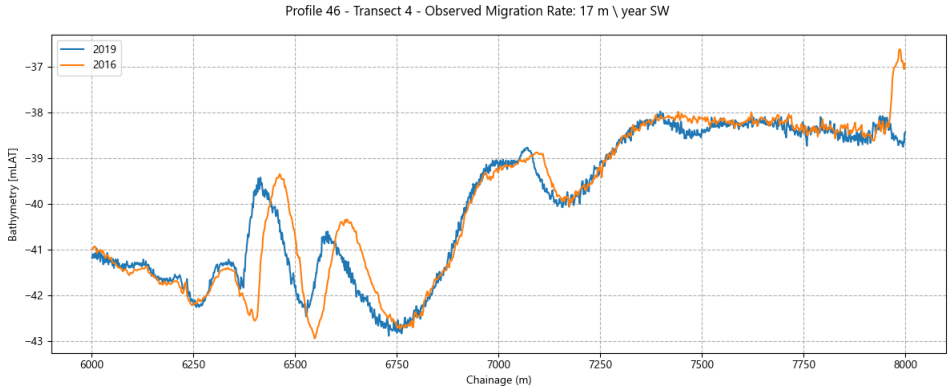


Figure 339. Observed sandwave migration between 2016 and 2019 on profile 46, transect 4. The maximum observed sandwave migration rate, and direction of migration, is detailed at the top of the plot.

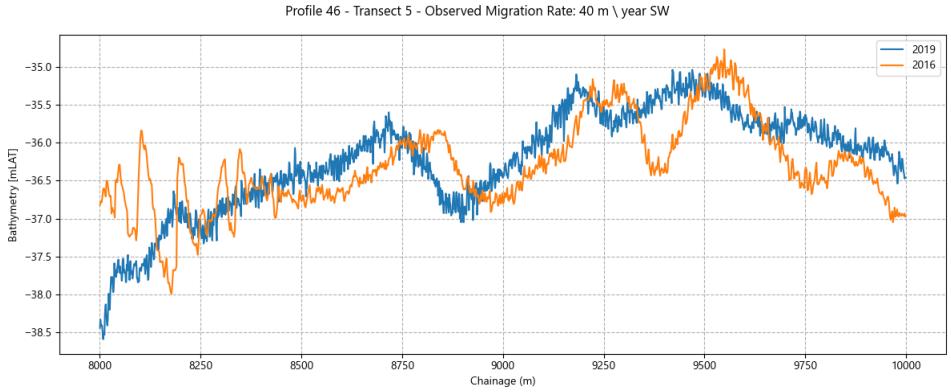


Figure 340. Observed sandwave migration between 2016 and 2019 on profile 46, transect 5. The maximum observed sandwave migration rate, and direction of migration, is detailed at the top of the plot.

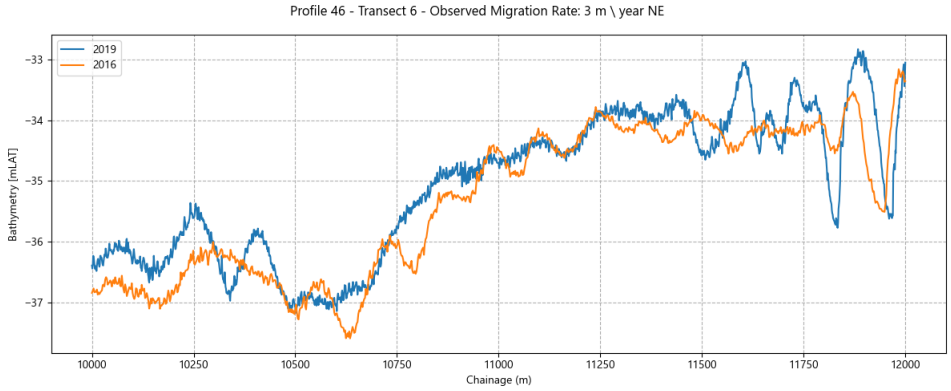


Figure 341. Observed sandwave migration between 2016 and 2019 on profile 46, transect 6. The maximum observed sandwave migration rate, and direction of migration, is detailed at the top of the plot.

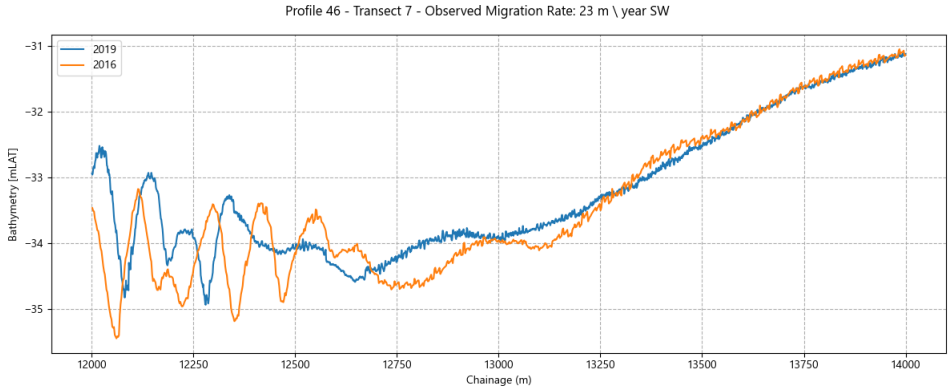


Figure 342. Observed sandwave migration between 2016 and 2019 on profile 46, transect 7. The maximum observed sandwave migration rate, and direction of migration, is detailed at the top of the plot.

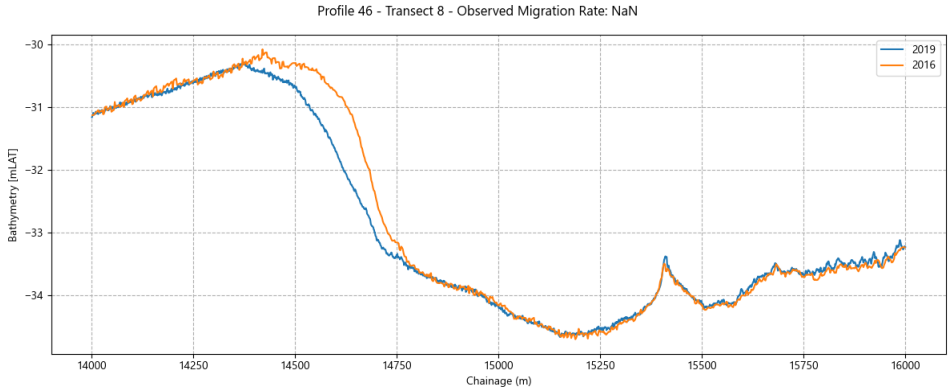


Figure 343. Observed sandwave migration between 2016 and 2019 on profile 46, transect 8. The maximum observed sandwave migration rate, and direction of migration, is detailed at the top of the plot.

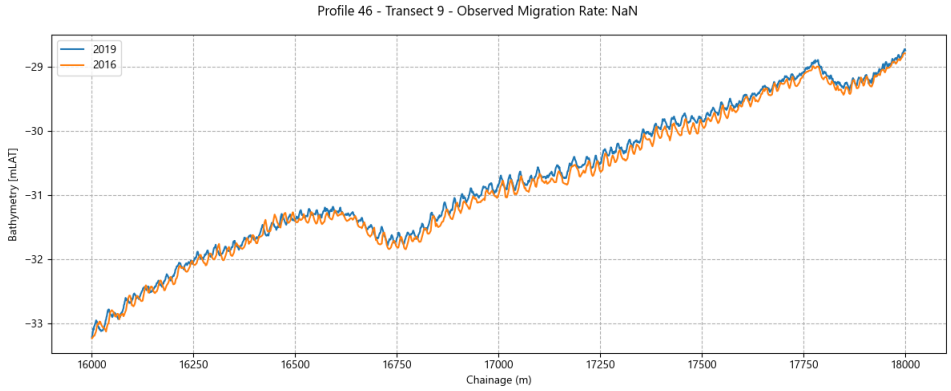


Figure 344. Observed sandwave migration between 2016 and 2019 on profile 46, transect 9. The maximum observed sandwave migration rate, and direction of migration, is detailed at the top of the plot.

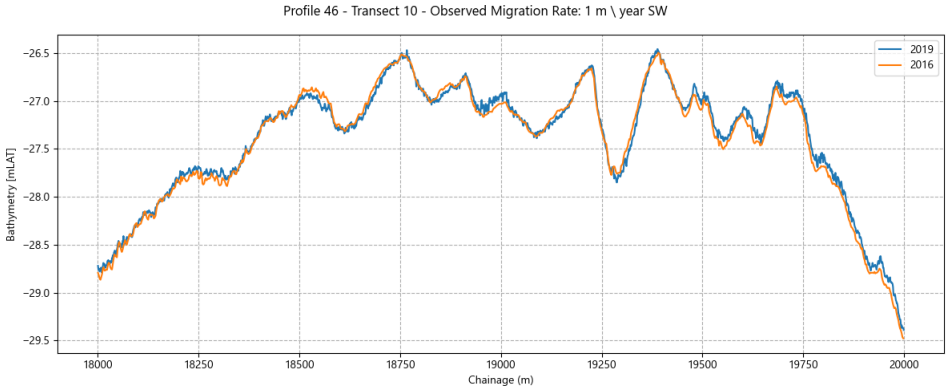


Figure 345. Observed sandwave migration between 2016 and 2019 on profile 46, transect 10. The maximum observed sandwave migration rate, and direction of migration, is detailed at the top of the plot.

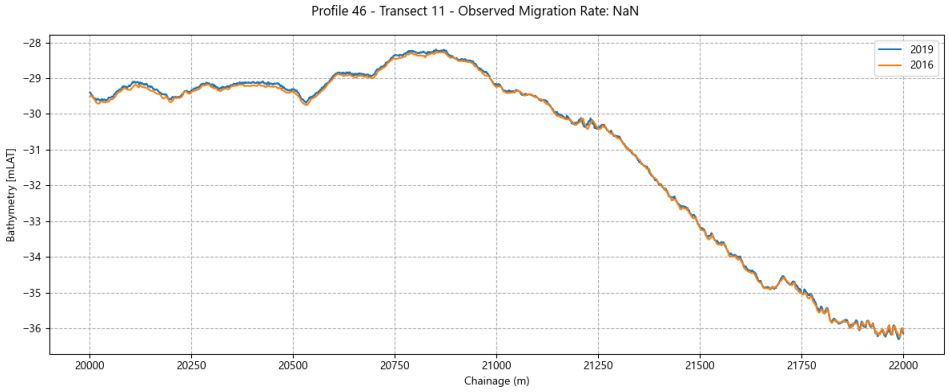


Figure 346. Observed sandwave migration between 2016 and 2019 on profile 46, transect 11. The maximum observed sandwave migration rate, and direction of migration, is detailed at the top of the plot.

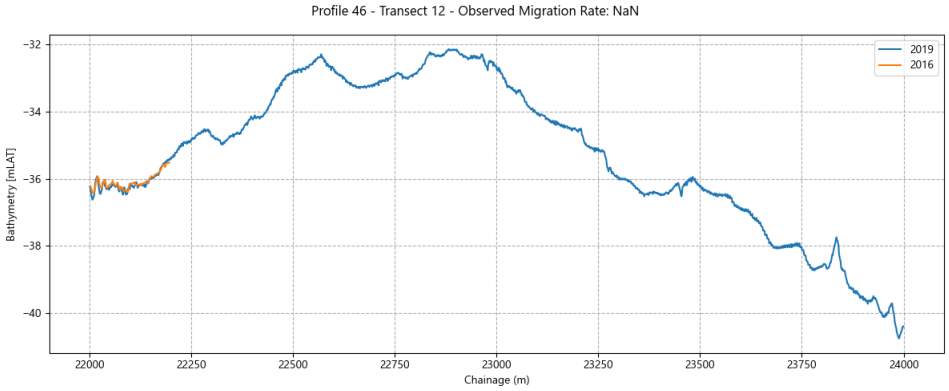


Figure 347. Observed sandwave migration between 2016 and 2019 on profile 46, transect 12. The maximum observed sandwave migration rate, and direction of migration, is detailed at the top of the plot.

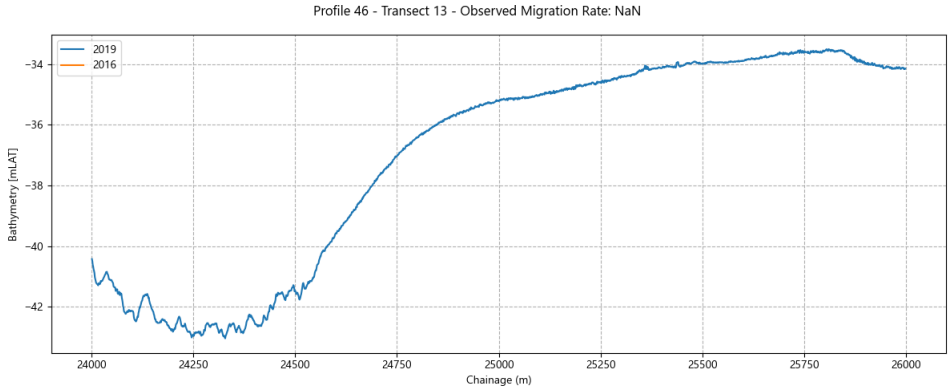


Figure 348. Observed sandwave migration between 2016 and 2019 on profile 46, transect 13. The maximum observed sandwave migration rate, and direction of migration, is detailed at the top of the plot.

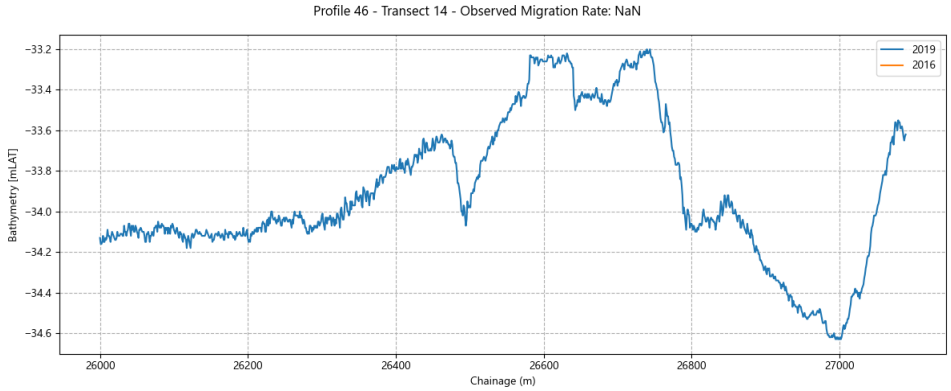


Figure 349. Observed sandwave migration between 2016 and 2019 on profile 46, transect 14. The maximum observed sandwave migration rate, and direction of migration, is detailed at the top of the plot.

Appendix G: Merging Bathymetry Datasets

When merging bathymetry from different sources, special care must be taken. This is particularly important for sediment transport applications where any sudden jumps or 'hard edges' in bathymetry could potentially result in large sediment transport in that area. This occurs because the model tries to move the bathymetry toward an equilibrium under the ambient hydrodynamic and wave forcings. Appendix F describes the process by which the bathymetry datasets were merged using a tapering method to avoid sudden vertical shifts at dataset edges. The available bathymetry datasets, and the spatial extent of the model are shown in Figure 350.

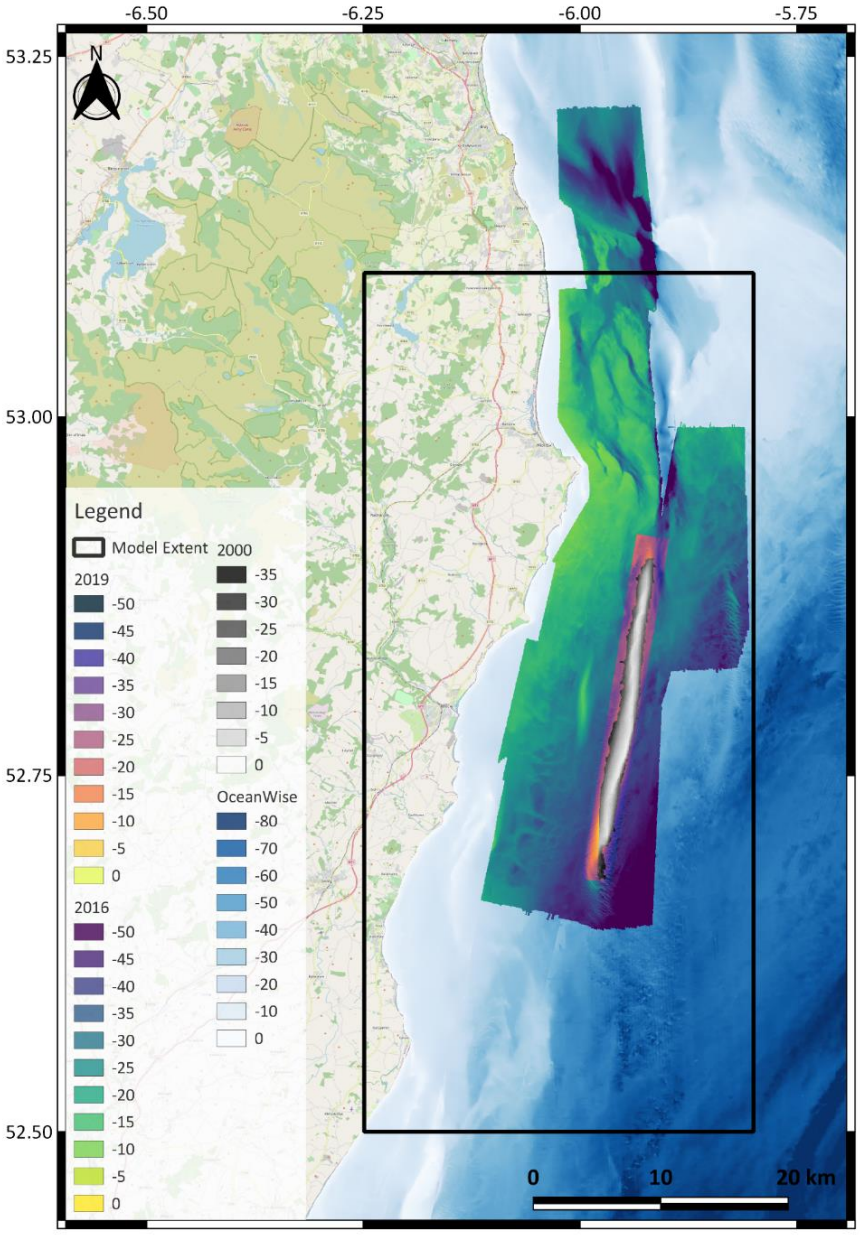


Figure 350. All available bathymetry data (relative to MSL).

To join the three datasets, two merges were required:

- 2016 bathymetry into Oceanwise, and
- 2019 bathymetry into 2016 bathy.

The 2016 bathymetry into Oceanwise merge used a defined internal buffer of the 2016 bathymetry. A 1 km buffer distance was chosen since this avoids the transition area overlapping the bank/lease area. Figure 351 shows the bathymetry differences for these datasets, with the buffer zone overlaid.

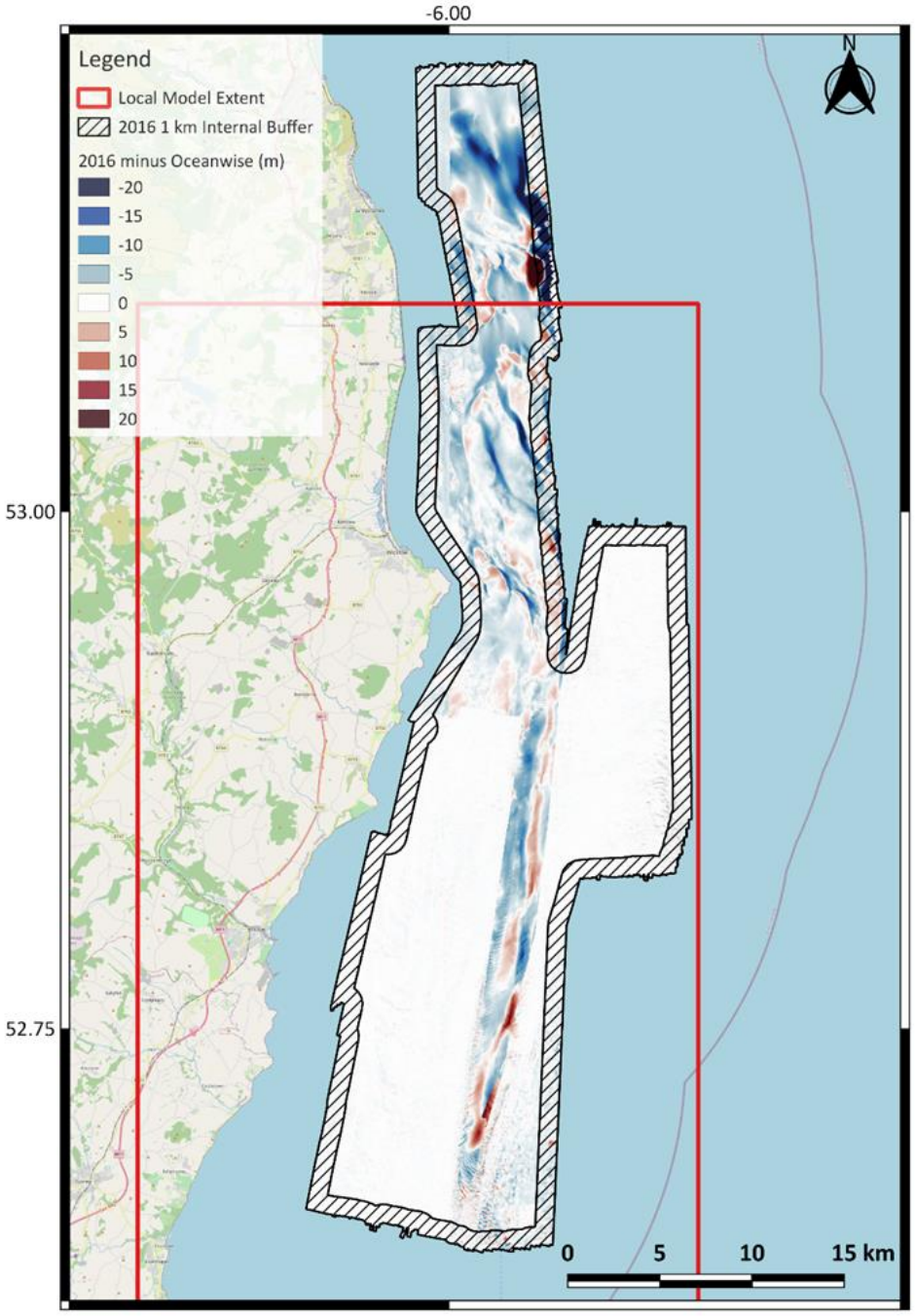


Figure 351. Difference between 2016 bathymetry survey data and Oceanwise data, with 1 km buffer zone overlaid.

The following method was employed to create the taper between the 2016 and Oceanwise data:

1) Linearly interpolate all Oceanwise grid points onto 2016 survey points.
2) For each point within the taper zone:
    a. Find the shortest distance to the inner boundary of the buffer zone.
    b. Find the shortest distance to the outer boundary of the buffer zone.
    c. Assign the point a normalised value based on these distances, given by:

$$f = \frac{Do}{Do+Di} \tag{6}$$

Where:

Do = Distance to Outer Boundary, and

Di = Distance to Inner Boundary.

This is effectively the fraction of the total distance along a line from the outer to inner boundaries of the buffer zone passing through the point. It is not necessarily a straight line, since outer and inner boundaries are rarely exactly perpendicular, but it represents the shortest route which passes through the point. Note that this is ascribed a value of zero for points on the outer boundary of the buffer zone, and a value of 1 for points on the inner boundary of the buffer zone.

    d. A cosine taper is then applied to *f*. This gives a 'weight', hereafter referred to as *w*, which smoothly transitions from 1 on the outer boundary to zero on the inside boundary.
    e. Calculate the merged value as:

$$m=(w \times MF)+[(1-w)\times S] \tag{7}$$

Where:

MF = Oceanwise data, and

S = 2016 Survey Data.

3) Review various diagnostic plots (a selection of which are presented in Figure 352 to Figure 356) to ensure no unwanted artefacts are introduced to the resulting bathymetry.

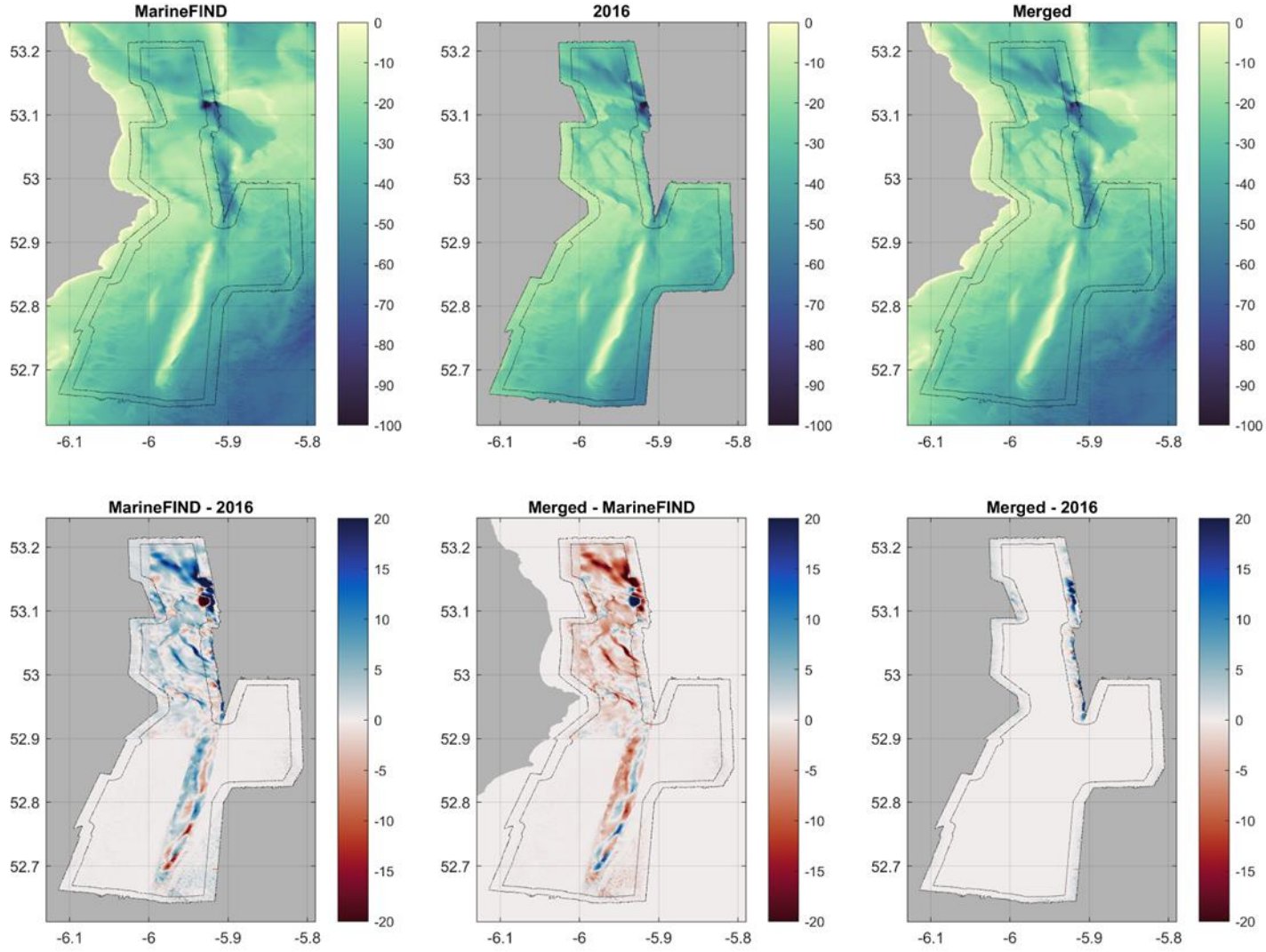


Figure 352. Bathymetry merge 2016 to Oceanwise – diagnostic plot – overview.

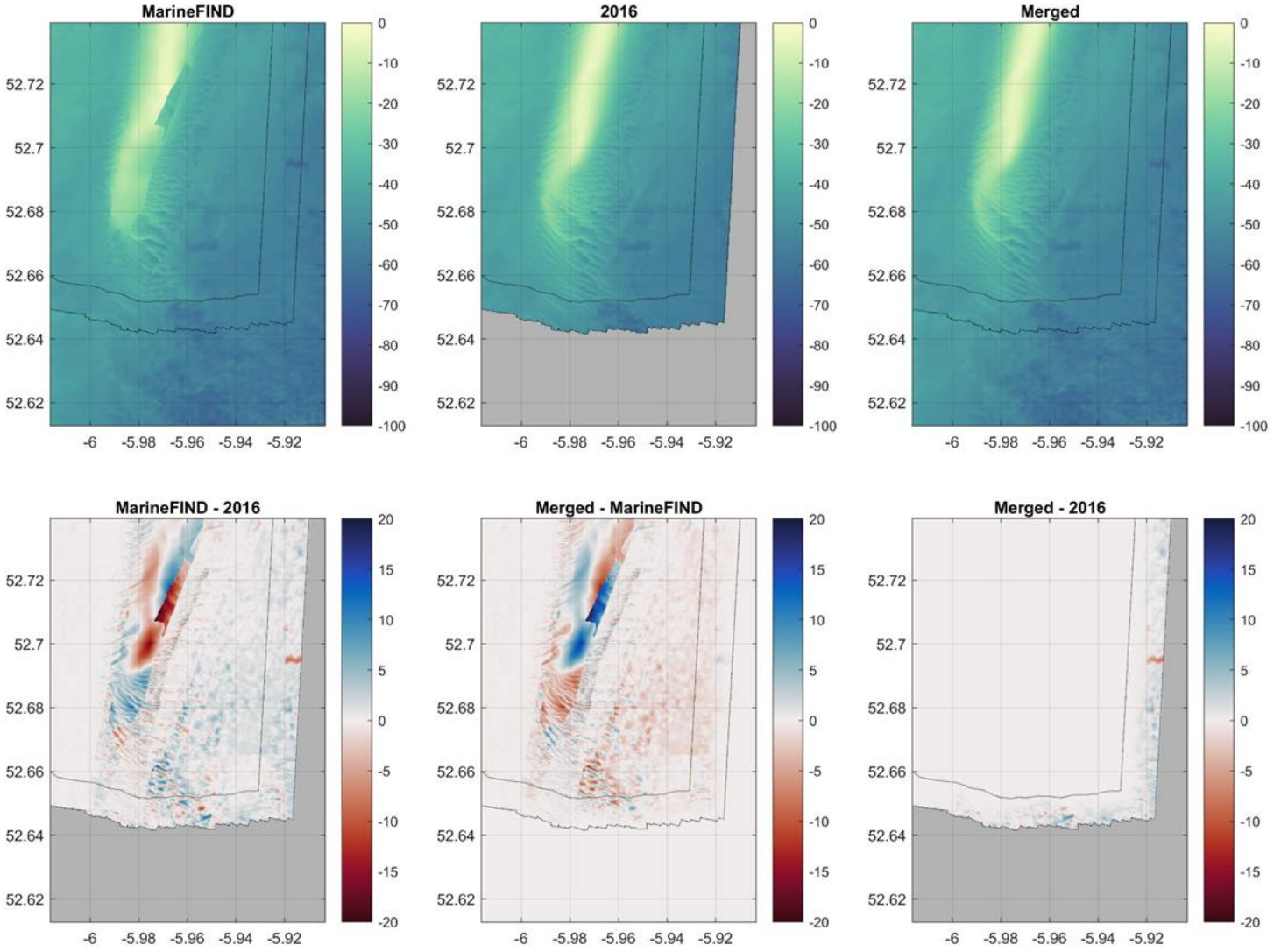


Figure 353. Bathymetry merge 2016 to Oceanwise – diagnostic plot – southeast corner.

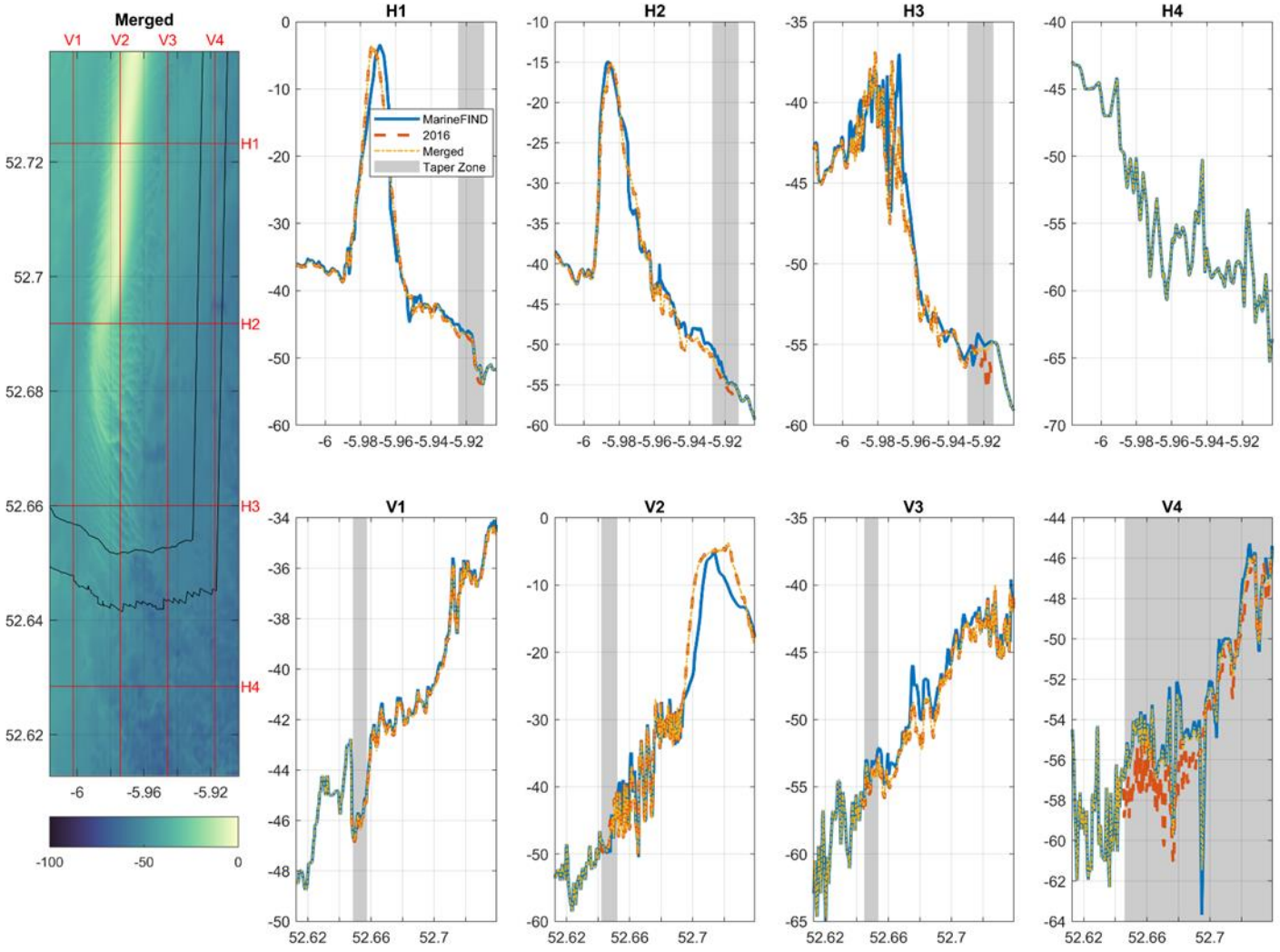


Figure 354. Bathymetry merge 2016 to Oceanwise – transect diagnostic plot – southeast corner.

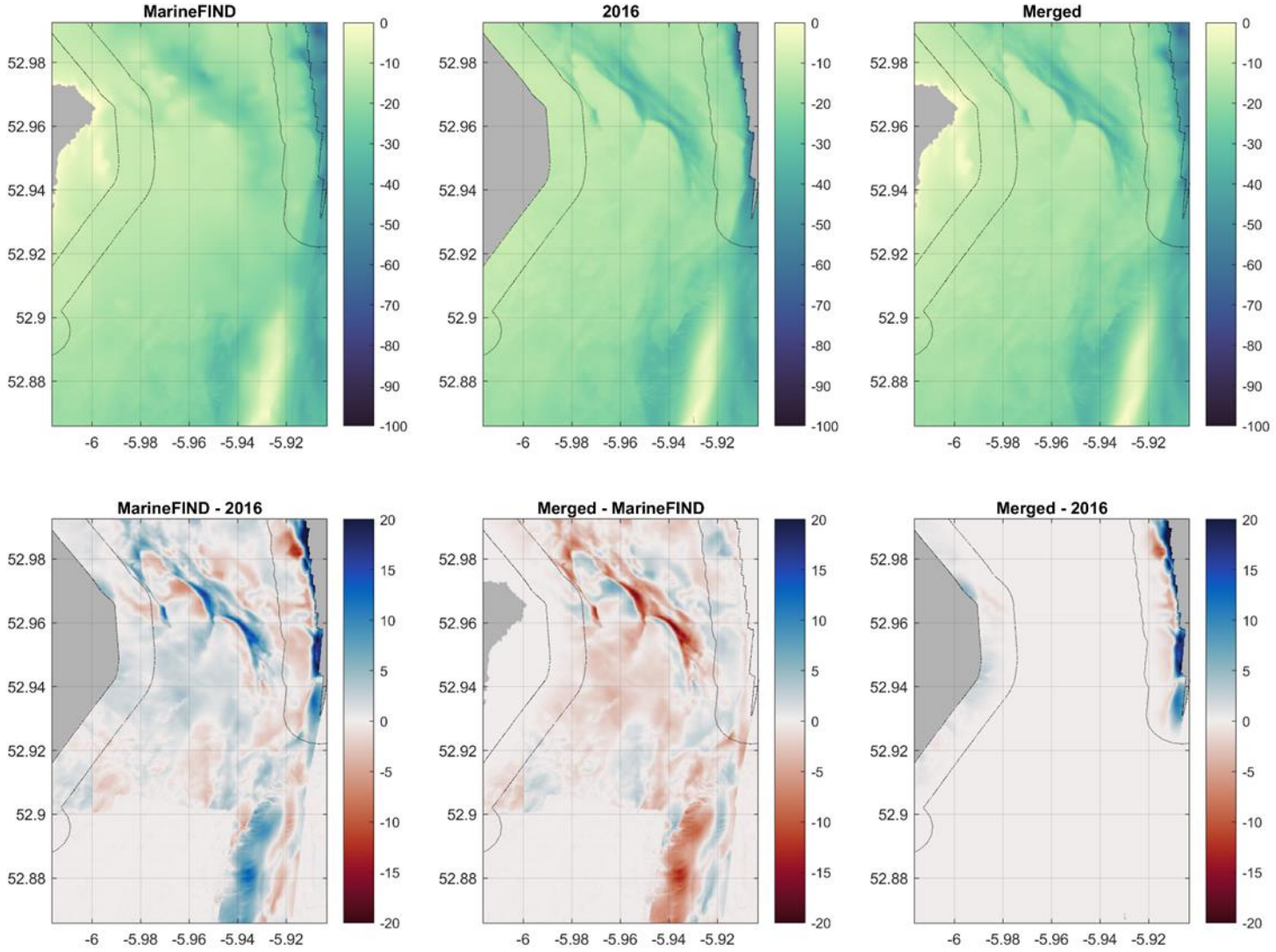


Figure 355. Bathymetry merge 2016 to Oceanwise – diagnostic plot – northwest of bank.

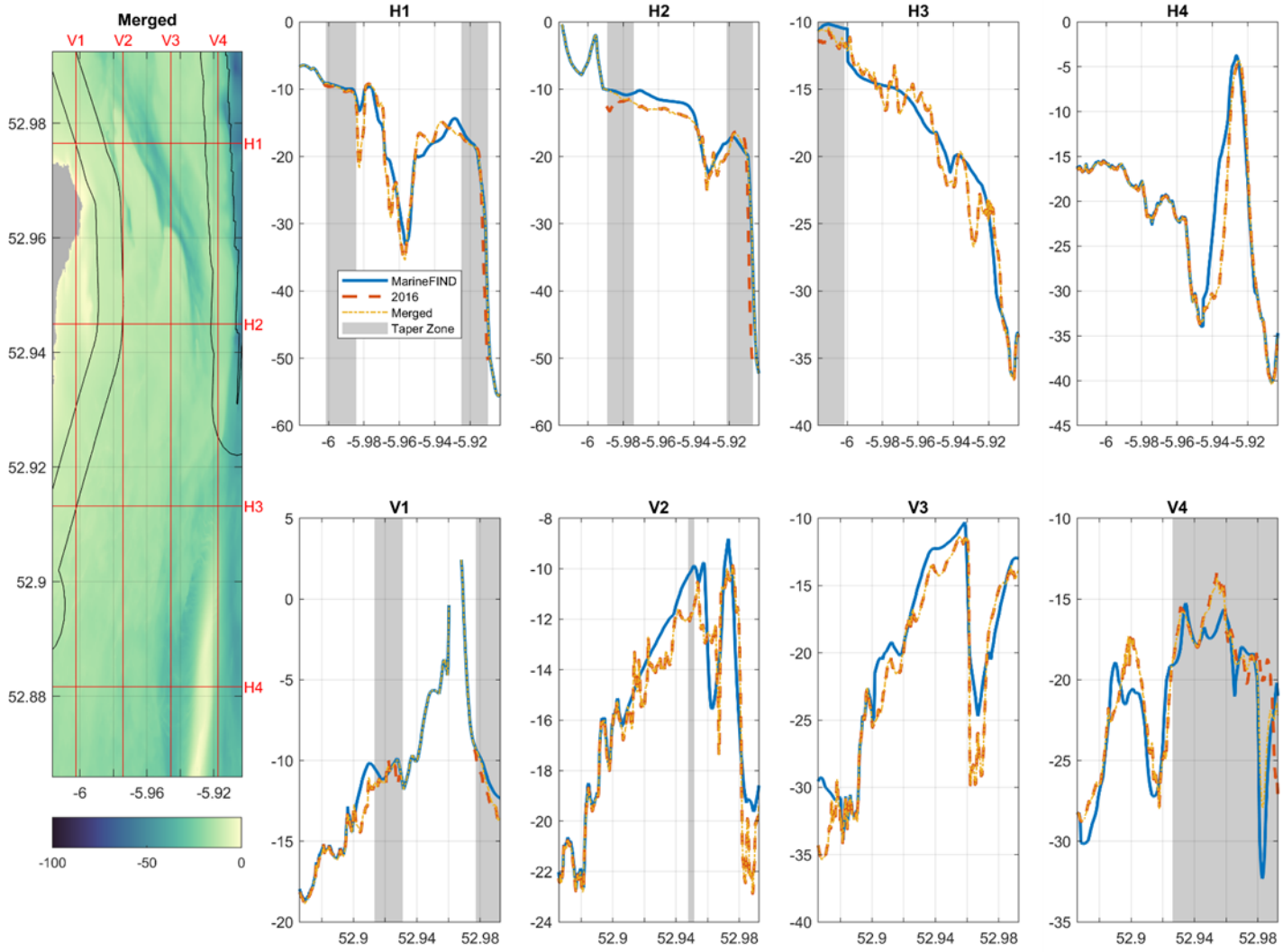


Figure 356. Bathymetry merge 2016 to Oceanwise – diagnostic plot – northwest of bank.

The 2019 into 2016 merge used a contour of difference between 2019 and 2016 around the bank to define the buffer zone. The area where the difference between the 2019 and 2016 bathymetry is < 0.2 m and > -0.2 m was selected and buffered by 250 m. Figure 357 shows the bathymetry differences for these datasets, and the buffer zone overlaid.



Figure 357. Difference between 2019 and 2016 bathymetry survey data, with 250 m buffer zone overlaid

Because the 2019 survey data is narrow on the longitudinal axis, a slightly different approach was employed for the merge of the 2016 to 2019 data, compared to the 2016 to Oceanwise merge. This was to avoid a taper zone where the two datasets overlap, as it would potentially influence the higher-priority 2019 data. To obviate for this, large areas of the taper zone are positioned entirely outside the 2019 data, but the inner boundary of the taper zone is always within, or on the edge of, the 2019 data. The following method was employed:

1. For each 2016 data point in the taper zone:
    a. Find the closest 2019 point inside the inner buffer zone boundary
    b. Find the closest 2016 point (anywhere, i.e. inside or outside the buffer zone) to this 2019 point. Review to make sure these are sufficiently close (the furthest is *circa* 2 m)
    c. Find the difference in elevation between these two points. This represents the 'target' bathymetry elevation change for this point at the inner boundary.
    d. Find the distance from this closest 2019 point
    e. Find the distance to the outer buffer zone boundary
    f. Assign the point a normalised value based on the distances, given by:

$$f = \frac{\mathrm{Do}}{\mathrm{Do}+\mathrm{Di}} \tag{8}$$

    This is 0 on the outer boundary, 1 at the closest 2019 point. This is not necessarily a straight line, since outer and inner boundaries are rarely exactly perpendicular, but the shortest route which passes through the point
    g. Apply a cosine taper, giving a weight, hereafter w, that smoothly transitions from 0 on the outer boundary to 1 on the inner boundary.
    h. Calculate the merged value as:

$$\mathrm{m} = \mathrm{s16} + \mathrm{w}\times\mathrm{T} \tag{9}$$

    Where:
    S16 = 2016 Survey Data.
    T = Target Elevation Change at Inner Boundary
2. Review various diagnostic plots (a selection is presented in Figure 358 to Figure 362) to ensure no unwanted artifacts are introduced to the resulting bathymetry.

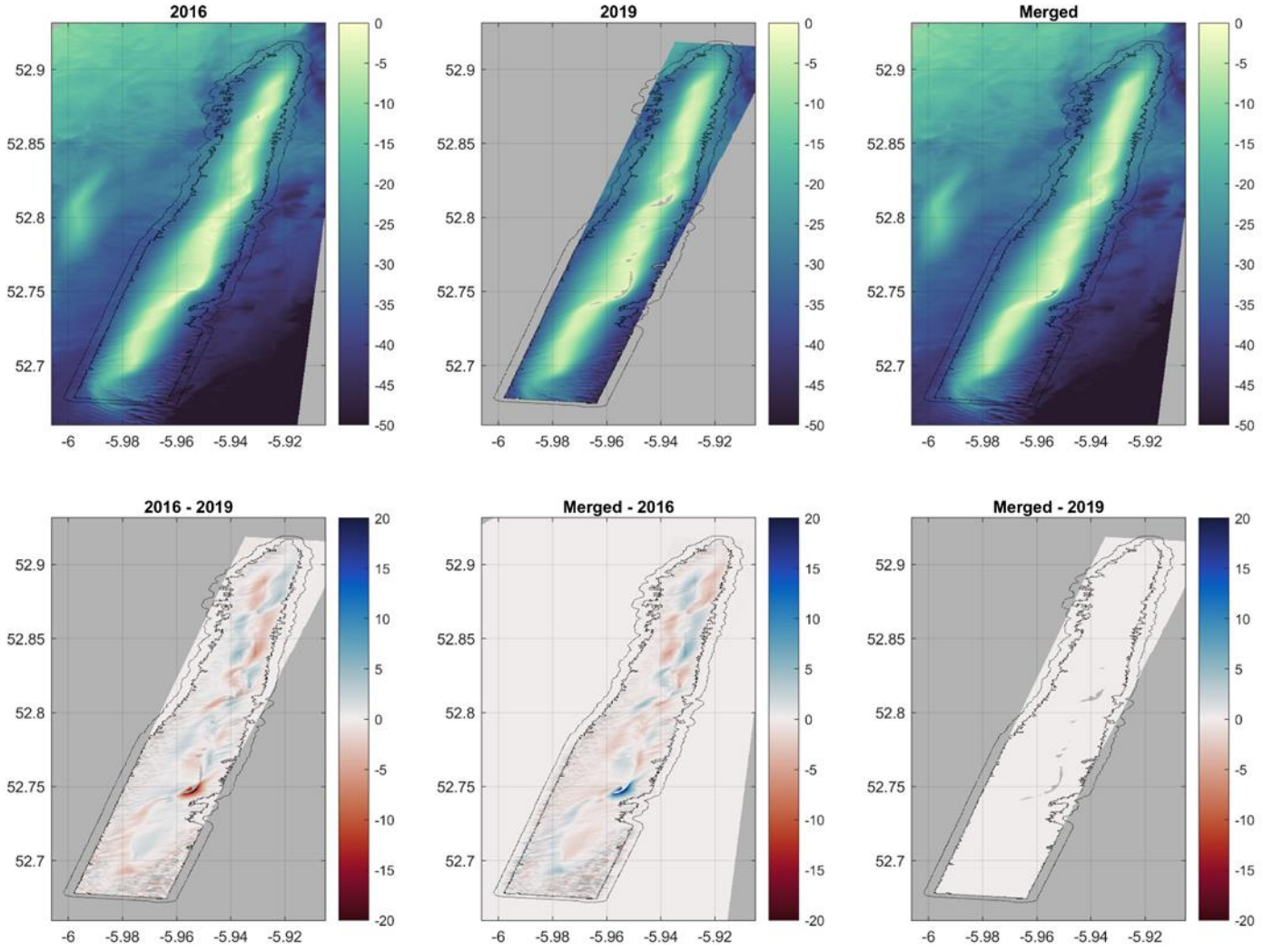


Figure 358. Bathymetry merge 2019 to 2016 – diagnostic plot – overview.

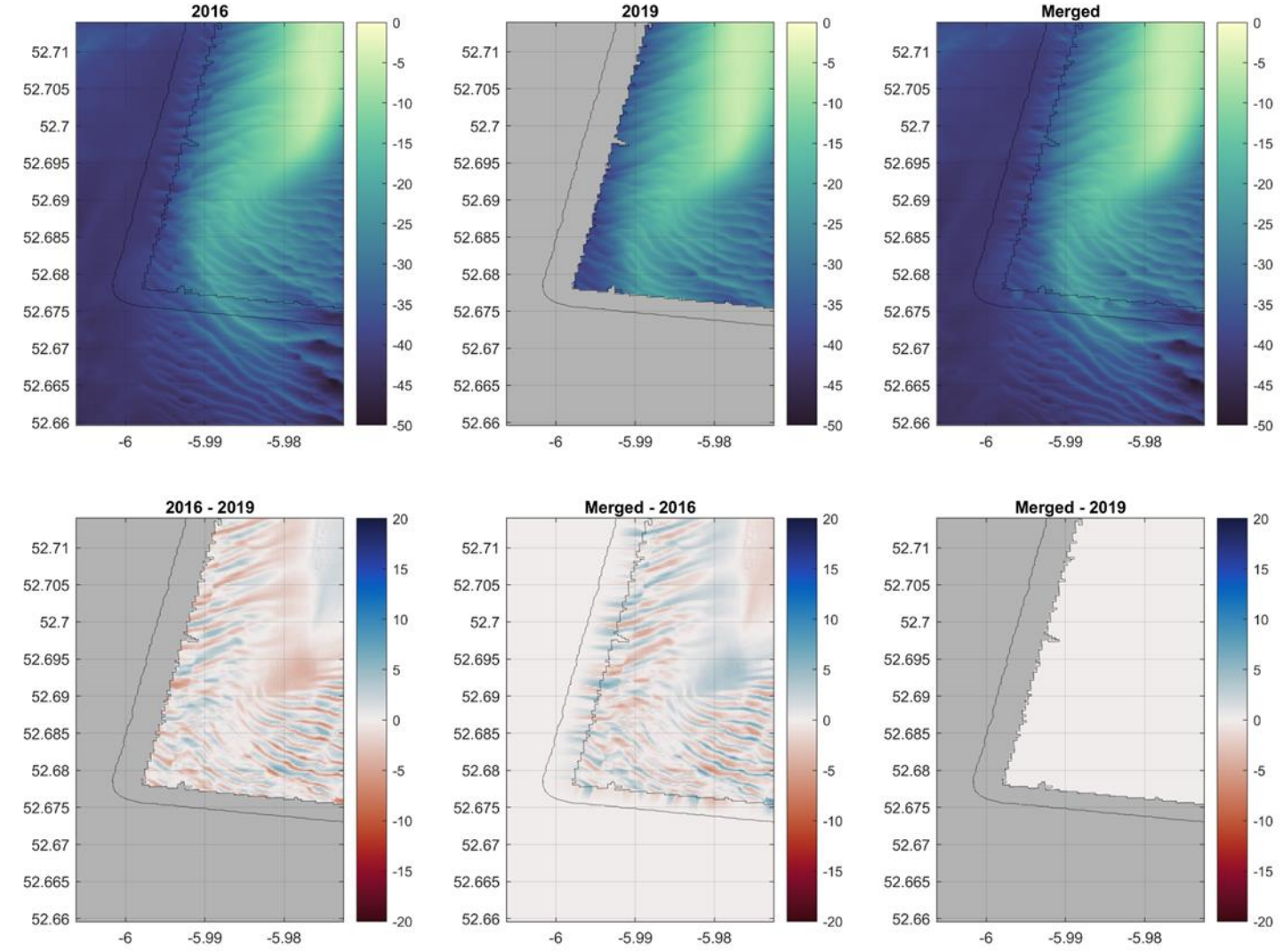


Figure 359. Bathymetry merge 2019 to 2016 – diagnostic plot – southwest corner.

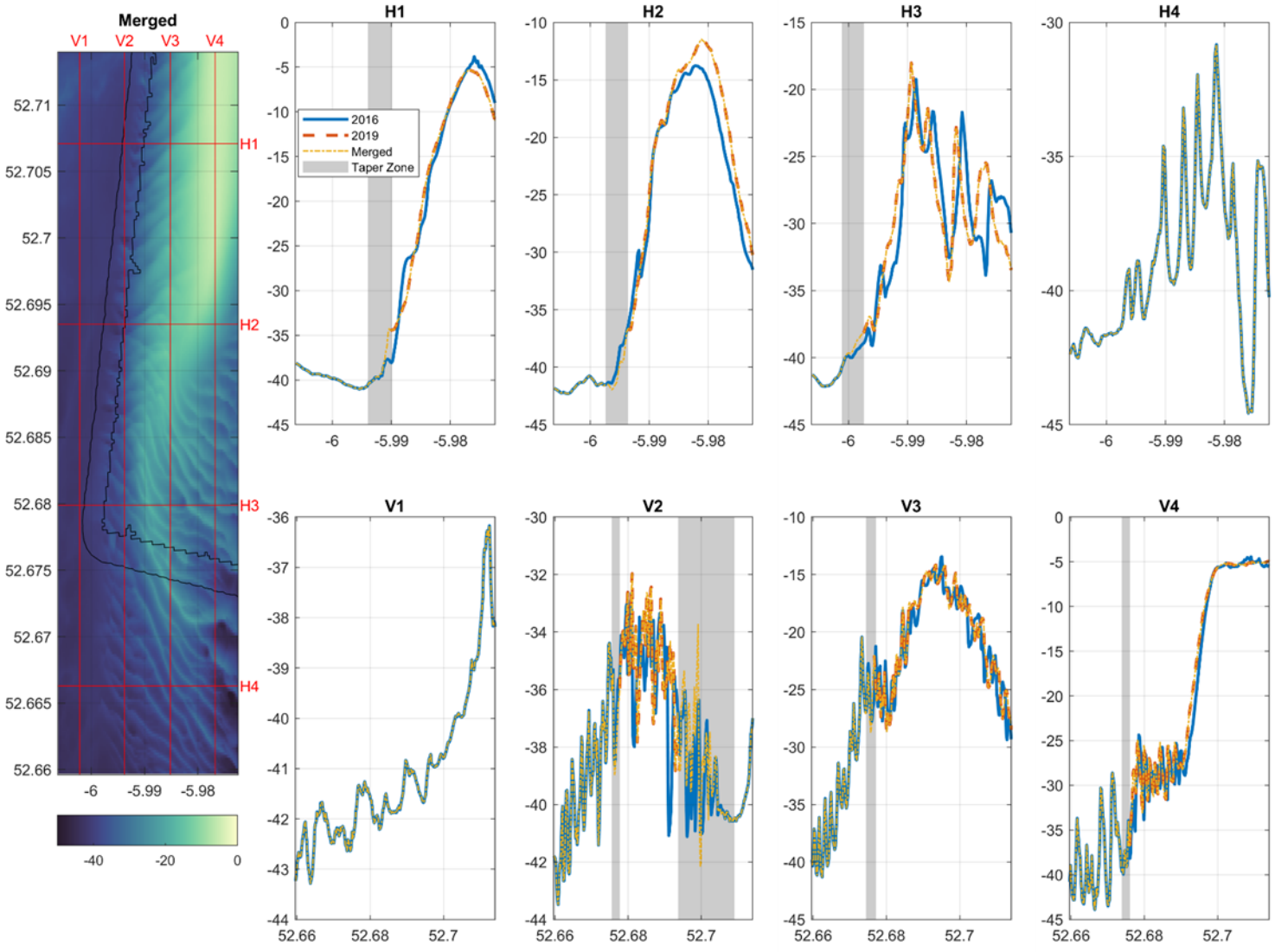


Figure 360. Bathymetry merge 2019 to 2016 – transect diagnostic plot – southwest corner.

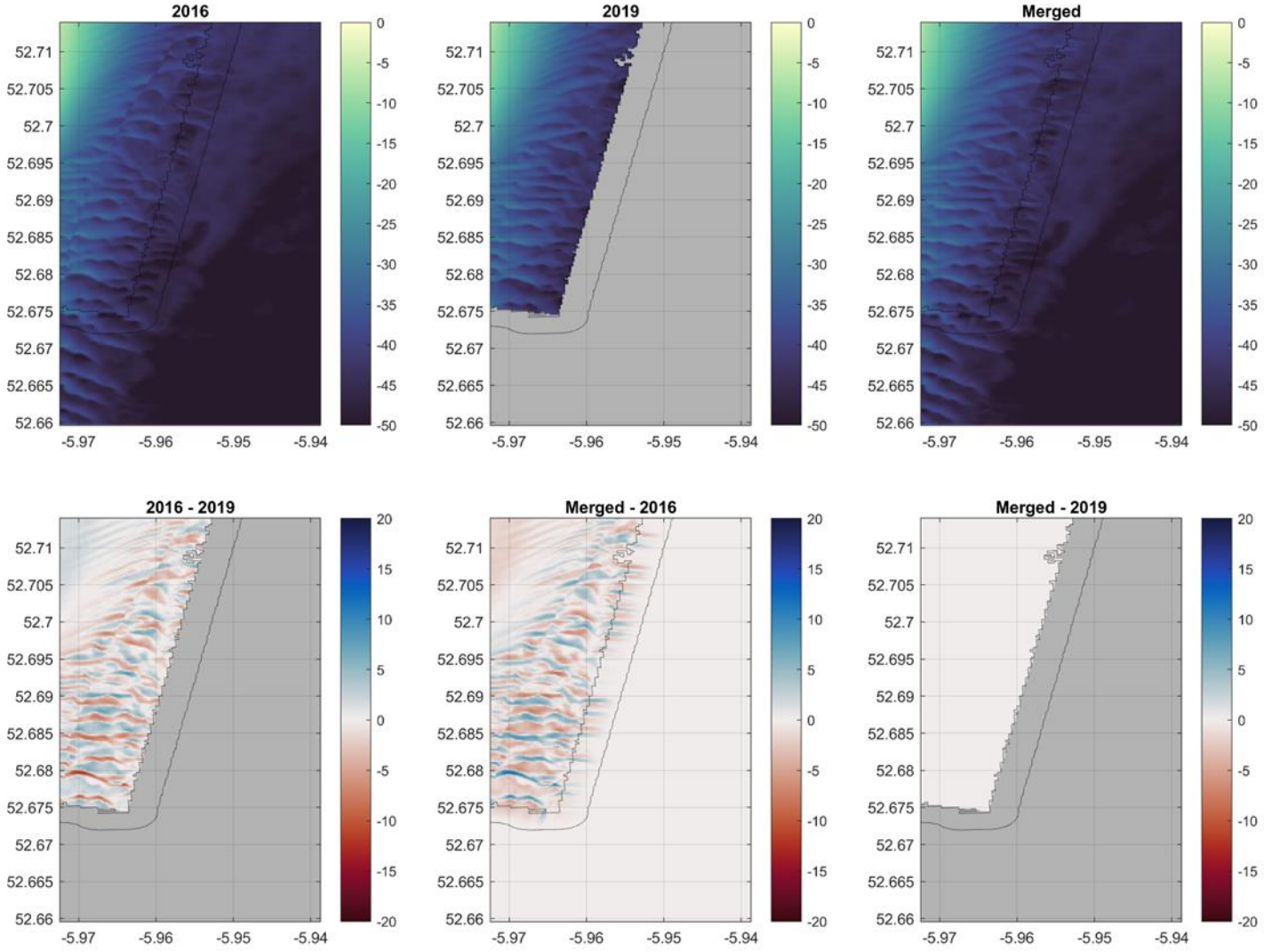


Figure 361. Bathymetry merge 2019 to 2016 – diagnostic plot – southeast corner.

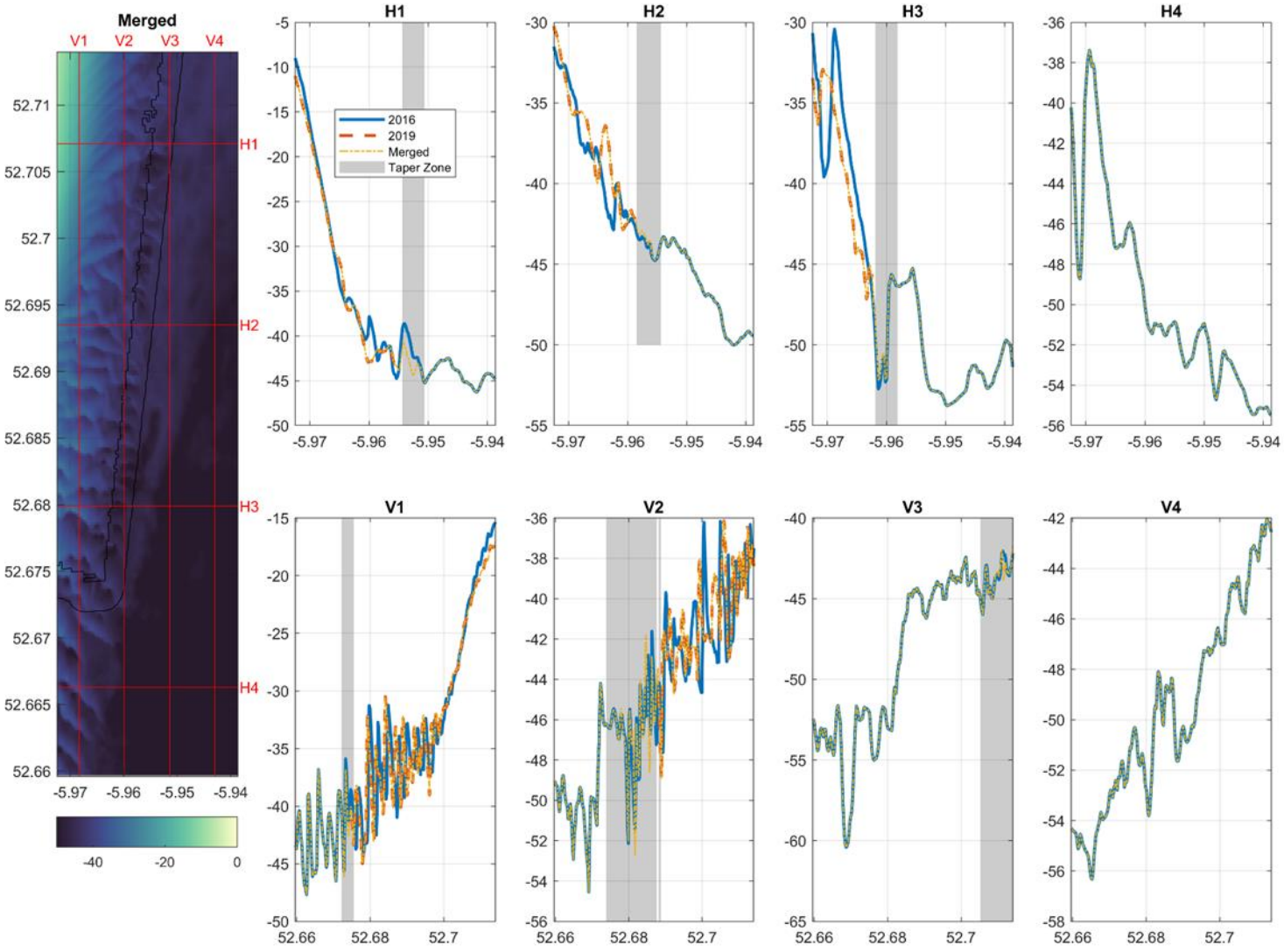


Figure 362. Bathymetry merge 2019 to 2016 – transect diagnostic plot – southeast corner

The coastline was discretised using the coastline layers from OpenStreetMap, which, when compared against satellite imagery, was found to have a better representation of coastal features than data available from the Ordnance Survey Ireland. Special attention was paid to the positioning of headlands along the south-eastern coastline of Ireland, to ensure proper representation of flow deflections and wave sheltering in the models. Small-scale features such as harbour breakwaters were excluded from the model.

All datasets were reduced to a mean sea level (MSL) datum before use, using the MSL to LAT values provided by the FES2014 dataset, and the combined datasets were visually inspected for any obvious depth discontinuities before being applied to the model. Whilst the bathymetry utilised in creating the model grid aims to provide the best possible representation of the profile of the seabed, there are several sources of possible uncertainty in the level of accuracy finally achieved by the model grid, for instance:

- Inaccuracies in the original surveys
- The gridding of the original survey data to produce a mean value for each grid node
- Vertical discontinuities between different survey datasets
- The merging of the various data sources, including reduction to a common vertical datum
- The interpolation of the bathymetry to the model grid
- The spatial resolution of the model grid, in relation to the scale of the features being represented (e.g. smoothing out small-scale features such as sandwaves to represent in a coarser scale grid).

Appendix H: Arklow Bank Modelling Suite (ABMS)

The SWAN (Simulating WAves Nearshore) Wave Model

Numerical modelling of waves in coastal areas is a useful means of understanding wave climatology and wave processes over broad areas and over longer periods. Wave hindcast models typically use long-term historical wind datasets to simulate the formation of waves over a water body. They generate historic wave conditions, which are validated at certain times, and points in space, using measured wave data. As the period over which *in situ* data are available is limited, and wave climates can display a high degree of intra-annual variability, modelling studies enable short-term monitoring campaigns to be extended to the long-term in order to derive representative long-term data for sediment transport description and estimation of extreme metocean conditions. SWAN is a third-generation wave model, developed at Delft University of Technology which accounts for the following physics relevant to the present study:

- Wave propagation in time and space, shoaling, refraction due to current and depth, frequency shifting due to currents and non-stationary depth
- Wave generation by wind
- Three- and four-wave interactions
- White-capping, bottom friction and depth-induced wave breaking
- Wave-induced set-up
- Diffraction

The SWAN model has been applied to describe wave influences on sediment transport across Arklow Bank, including the effects of storms. Spectral wave boundary conditions for the SWAN model originated from ECMWF-ERA interim data, to generate results over a 40-year period between 1979 to 2019 (the hindcast period). The SWAN model domain includes all of the southern Irish sea. The model grid size was nested, and varied from 5 km offshore, through 2 km, to a 600 m grid size extending across Arklow Bank.

The MIKE21FM 2D Hydrodynamic Model

An appreciation of tidal currents at the regional and local scale is available through the development of a hydrodynamic hindcast model developed using the MIKE21 modelling software. In a similar manner to the wave hindcast model, a validated hydrodynamic hindcast allows a greater understanding of the variations in the astronomical tidal water levels and currents, but also the impacts of higher energy conditions (for instance, surges) on currents in the area. Tidal boundary conditions originated from the Finite Element Solution FES2014 dataset on a 7 km grid. Atmospheric forcing originated from the ECMWF-ERA5 dataset. This comprised wind speed and direction and pressure fields to ensure that atmospheric surge effects were robustly represented in the model. The local model

has a spatial resolution varying between 225 and 150 m, and 75 m within the wind park lease boundary and a 1 km buffer surrounding the lease area.

The Sand Transport Module

The Sand Transport (ST) module of MIKE 21 Flow Model FM was used for the sediment transport modelling. This model describes erosion, transport, and deposition of sand (non-cohesive sediment) under the action of currents and waves or pure current. Bed load and suspended load transport modes are described by the model.

ST provides options to calculate sand transport using three different model types:

- Pure current
- Pure current - Multi fraction / multi-layer
- Waves and current

For this study, where waves were anticipated to be a contributing driver of sediment transport, the 'Waves and current' model type was used. In this model setup, the sand transport rates are found by interpolation in pre-calculated sediment transport tables. The sediment transport tables are calculated separately from the model runs, allowing greater efficiency when running multiple simulations. The sediment transport tables contain the total load (combined bed load and suspended load) sediment transport rates (in $m^3/s/m$) for a range of pre-defined cases. The calculation range used for this project is provided in Table 25:

Table 25. Scenarios of sediment transport calculated.

Parameter	Minimum value	Maximum value	Number of divisions
Current Speed	0.01	2.334	15
RMS Wave Height	0.01	4.67	15
Peak wave period	1	18.38	12
Wave height/Water depth	0.000125	44.4	9
Angle current/waves	0	360	9
Grain size	0.15	1.20	7
Sediment grading	1.63	6.83	6
Bed Slope, perpendicular to current	-0.08	0.08	9
Bed Slope, normal to current	-0.08	0.08	9

The above table results in over 744,000,000 predicted sediment transport rates for a wide range of scenarios expected to occur in the study area. In each case, a mean horizontal velocity-based shear stress is calculated, consisting of:

- the time-averaged shear stress associated with wave motion;
- the shear stress associated with wave breaking; and,
- the shear stress due to gradients in the water surface (and hence flow).

The horizontal shear stress is then used to calculate the total load transport dry volume by the method of Engelund and Fredsøe (1976), where the bedload transport is calculated by the instantaneous Shields parameter. The vertical profile of suspended sediment concentration is calculated using the vertical diffusion equation for suspended sediment after the method of Fredsøe *et al* (1985). The model then looks up the relevant transport rate for the given combination of conditions at each cell centre, at each timestep, and undertakes a transport calculation. The rate of bed level change is then calculated from the dry volume transport using the Exner equation (sediment continuity equation).

Model Inputs and Model Domain

Data used to create the coastline, bathymetry, boundaries, and any atmospheric forcing for the model is described in MetOceanWorks Ltd (2021).

For the sediment transport modelling, a local-scale hydrodynamic model was used. The domain of the local model and its relationship to the European domain model providing its boundaries is shown in Figure 363. The spatial resolution of the model was 75 m within the lease zone and surrounds.

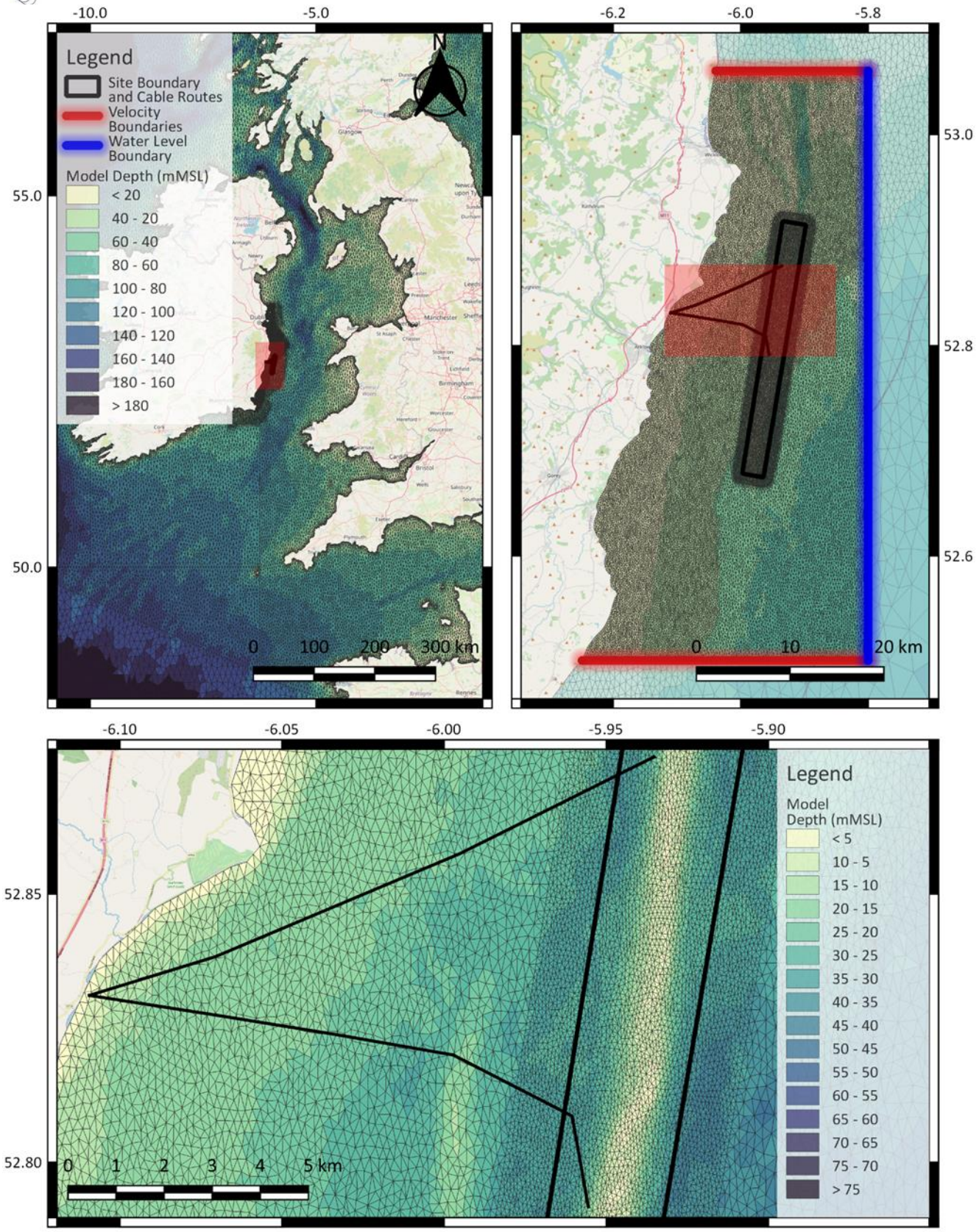


Figure 363. Domain of the local-scale model used in sediment transport modelling.

Validation of the Hydrodynamic and Wave Models (termed the *driving models*)

Validation of the driving models of sediment transport is detailed in the metocean overview document (MetOceanWorks Ltd, 2021). However, in addition to the validation of the model for water levels, current speeds, and current directions, of particular interest to this project is how well the difference in water level between the east and the west of the bank is represented by the model as this has been confirmed as one of the key process drivers influencing vertical seabed level change across the lease area (see Section 8.6.4). To assess this, simultaneous water level data from frame locations B1 and D1 (on the north-western and north-eastern flanks of the bank, respectively) were extracted. The instantaneous difference in water level was calculated by subtracting the water level at frame location D1 from the water level at frame location B1. These data were then compared against the same water level difference extracted from the model. The results are shown in the top panel of Figure 364.

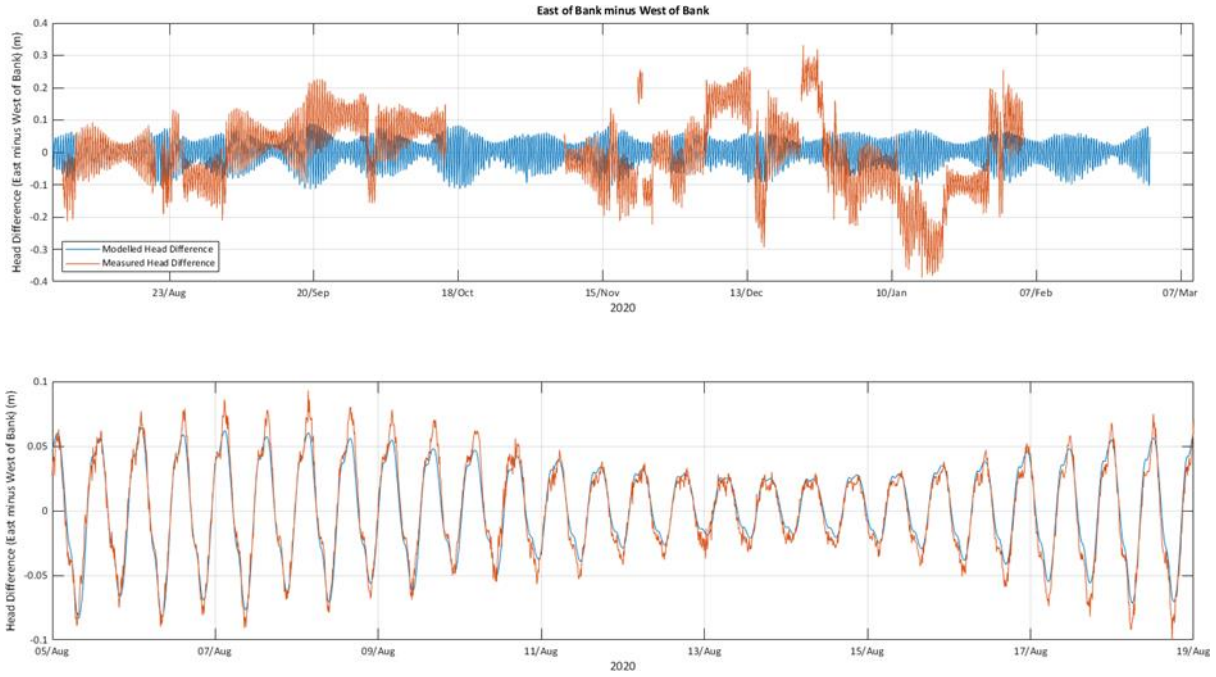


Figure 364. Time-series comparison of measured and modelled water level difference between east and west of the bank.

The measured signal appears to jump abruptly, suggesting issues in either instrument stability or data processing. However, there is a brief period of two weeks toward the beginning of the measurements where the data appear stable. This is shown in the bottom panel of Figure 364. For this period, the model skill appears to be excellent, with small-scale (millimetric) features, such as flood and ebb stands being well-represented. Figure 365 shows the validation plot using the data where the instrument was stable; the statistics suggest excellent model skill in representing the water level difference between east and west of the bank.

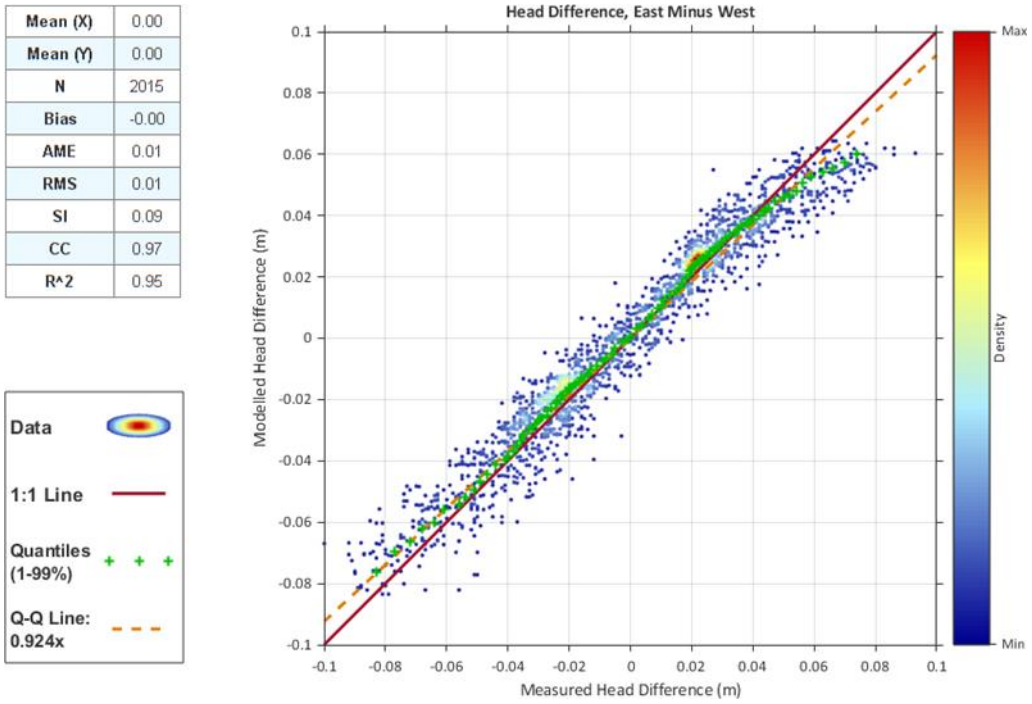


Figure 365. Validation scatter plot of difference in water level head difference between east and west of the bank, selected data.

Boundary Conditions

The models (i.e. the local-scale hydrodynamic model) were driven at its northern and southern boundaries using velocities, and at its eastern boundary by water levels, from the European basin-scale model described in detail in MetOceanWorks Ltd (2021).

Model Parameter Settings

The model was initially set up using the various sedimentological, geotechnical, and geophysical data available to the study at this stage. This included data on the variation in grading and composition of surficial sediments derived from INFOMAR and from historical borehole data supplied by SSE, and the spatial distribution of the erodible depth from a geophysical campaign. INFOMAR provides GIS layers showing the spatial distribution of different sediment types, classified using a five-point Folk scale. The distribution of sediments is shown in Figure 366 below. For reference the Folk scale is also provided.

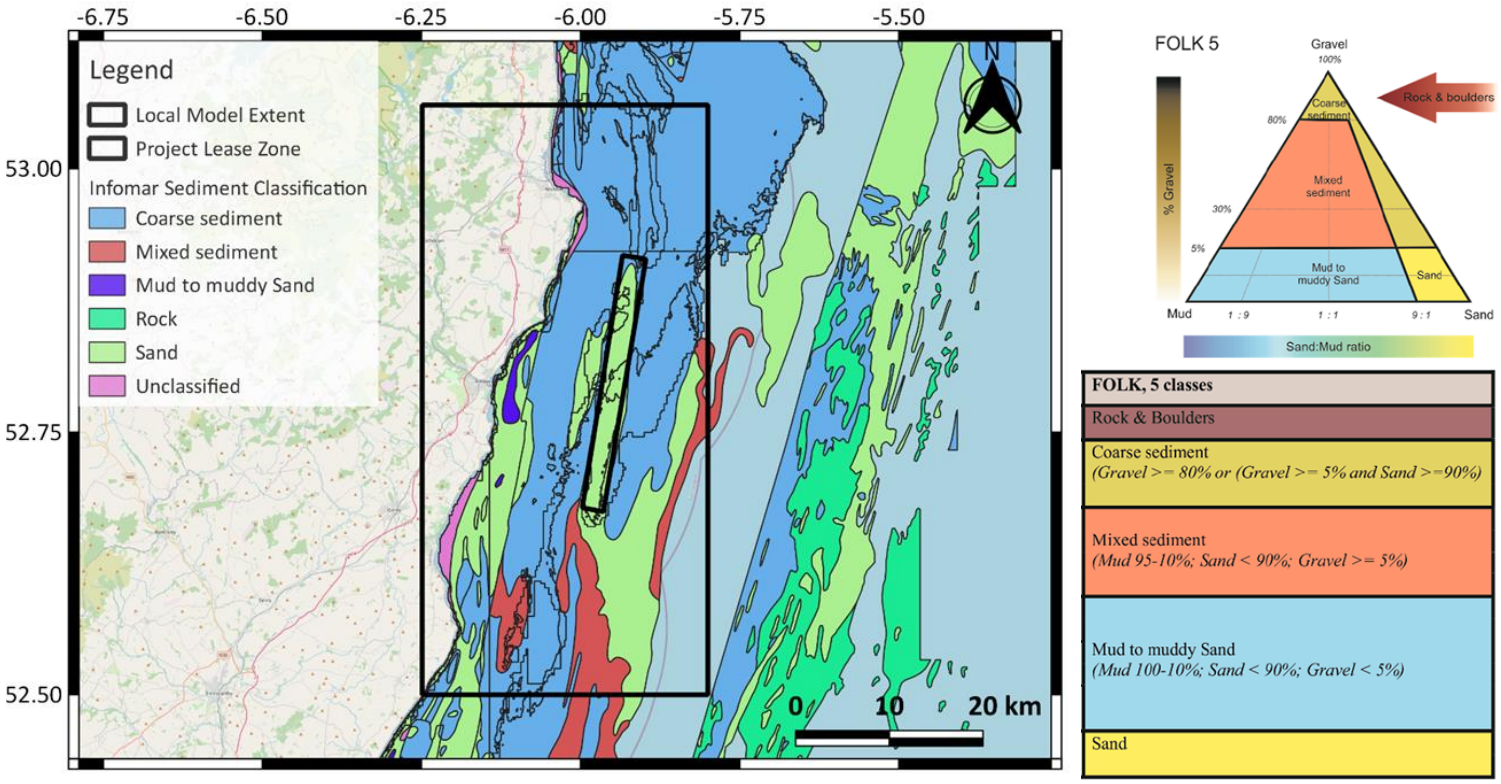


Figure 366. INFOMAR spatial distribution of sediments and the 5 class Folk classification applied.

Based on the information provided by INFOMAR and the Folk scale classification scheme, the sediment properties shown in Table 26 were assigned to the model. Figure 367 shows the spatial distribution of d_{50} sediment sizes used in the model, after concept testing.

Table 26. Sediment description and grain size assigned to the sediment transport map.

Sediment description	Grain size (µm)		
	d_{16}	d_{50}	d_{84}
Muddy Sand	50	150	300
Sand	150	250	400
Mixed Sediment	50	300	2,000
Coarse Sediment	300	1,000	2,500

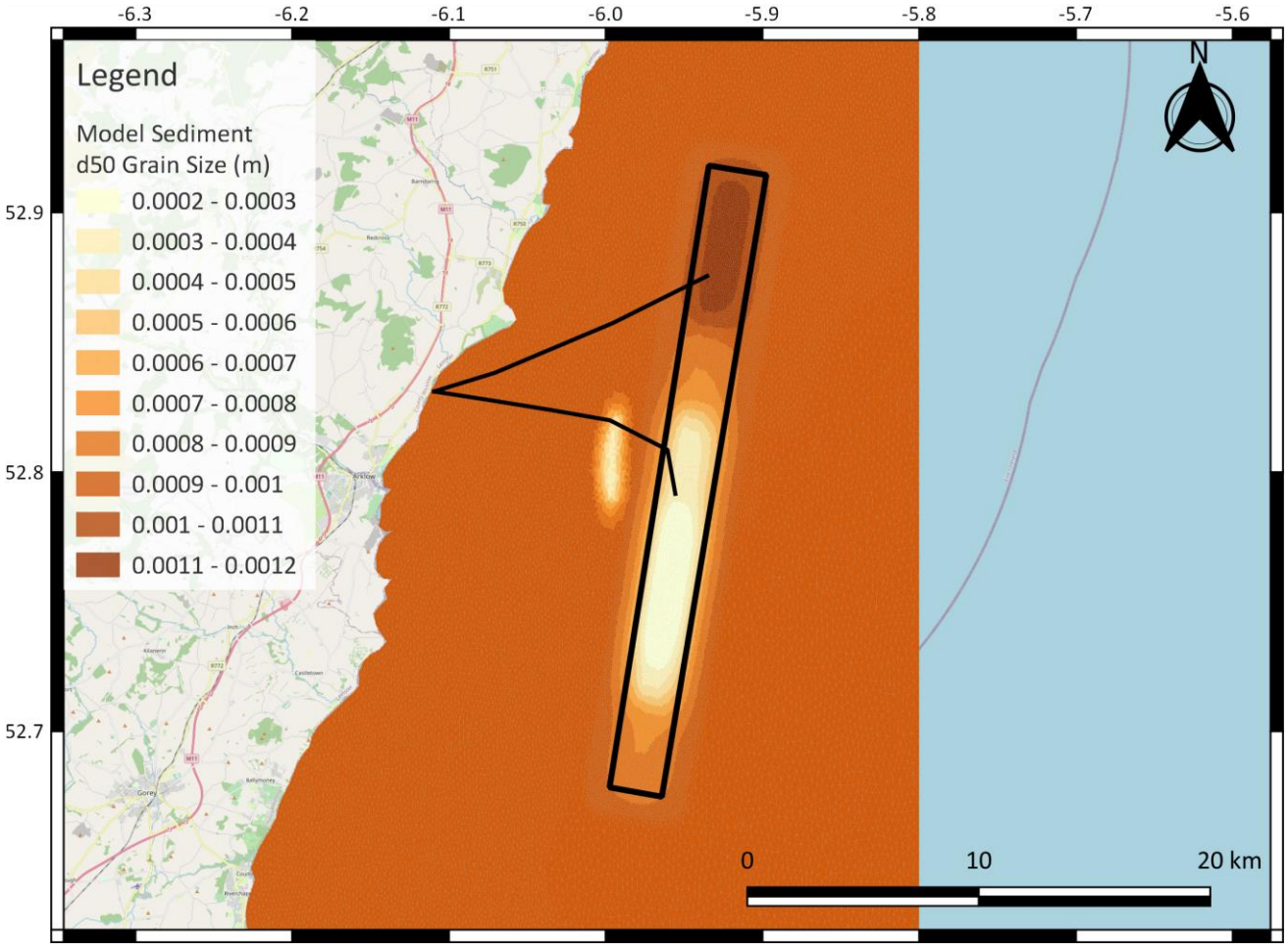


Figure 367. Map of sediment grain size used in sediment transport modelling.

MIKE ST uses a combination of the d_{50} (median) grain size, and a 'spreading coefficient' to define the seabed sediments. The spreading coefficient is defined:

$$\text{Spreading Coefficient} = \sqrt{\frac{d84}{d16}} \quad (10)$$

The spreading coefficient informs the model of how well sorted, or otherwise, the sediments to be modelled are, around the median grain size. A lower number denotes better sorted sediments. It is noteworthy that the d_{50} and grading coefficient maps, though spatially varying, remains fixed in time throughout the model run (i.e. sediment transport from one area of classification into another will change the sediment type according to the properties of the new area).

The project geophysical campaign has provided data on the estimated thickness of the mobile (erodible) layer across the lease area and along the proposed export cable routes. Owing to incomplete coverage of the data within the model extents (e.g. at areas along the central section of the bank), the data was interpreted qualitatively based on depth contours, to provide the sediment layer thickness map implemented in the model and presented in Figure 368.

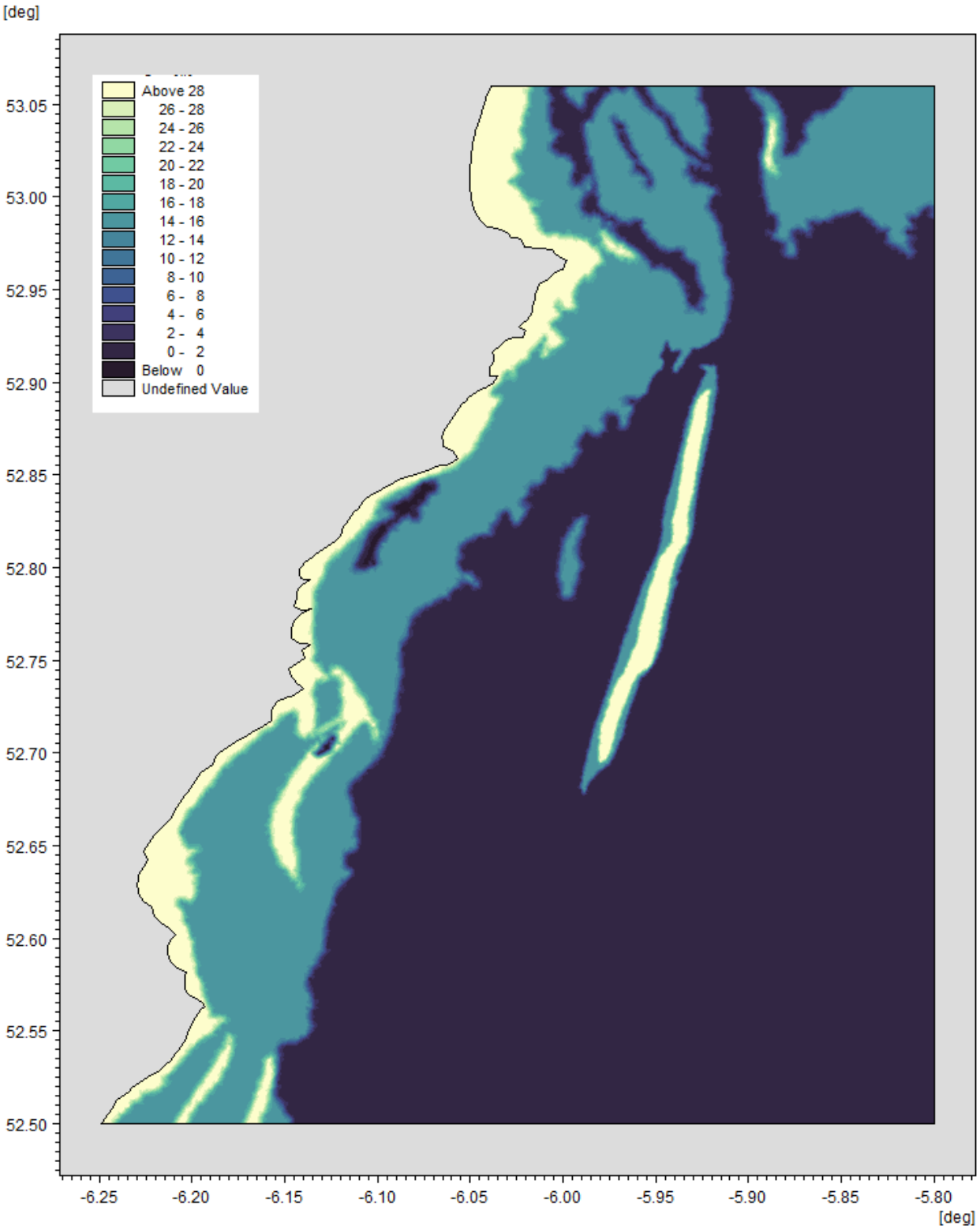


Figure 368. Map showing the depth of the mobile layer as implemented across the local model domain.

Model Sensitivity Testing

As part of the validation exercise described in Section 9 model sensitivity testing was performed, to:

- Aid understanding of the processes affecting the morphology of the bank; and,

- Provide evidence for focussing modelling efforts on the most important processes influencing seabed and bank morphology.

This exercise indicated that:

- The grain size and roughness coefficient tended to have a broadly linear effect on the magnitudes of transport, with the application of a smaller grain size promoting more sediment transport and a coarser grain size reducing the magnitude of transport. The final grain size and bed roughness configuration offered the best results during validation and were deemed sufficiently representative considering the limit on data presently available to the study at this stage.
- Sensitivity testing indicated that storm waves have a limited and short-term destructive influence on the morphology of the bank. We tested our standard model set up with constant, P50 (median) waves throughout an entire 65 day run. We then performed the same test with the same model set up but included a 48-hour period around day 33 where wave conditions start at P50 at hour 0 and increase linearly up to a 1 in 50-year event peak at hour 24, and then decrease linearly to P50 wave conditions at hour 48.
- Simulations were run without the inclusion of a speed-up factor for the validation period 2016 to 2019 with no significant improvement in the ability of the model to represent changes to the vertical seabed level change over this period. This is corroborating evidence that the use of a speed-up factor was justified within the methodology.

The results of sensitivity testing regarding storm events are shown in Figure 369 for the positions of six model extraction points (map at top of image), followed by a time-series showing the input wave conditions for the 1 in 50-year event run. The following six time-series plots then show bed levels at each of the six extraction points throughout the run, both for the 1 in 50-year event run, and for the P50 wave run. Figure 369 suggests that waves have an almost indiscernible effect on bed levels at the bank; due to these results it was concluded that the effects of storm waves did not need to be included in the long-term morphological simulations, as their influence on net sediment processes over these durations were limited.

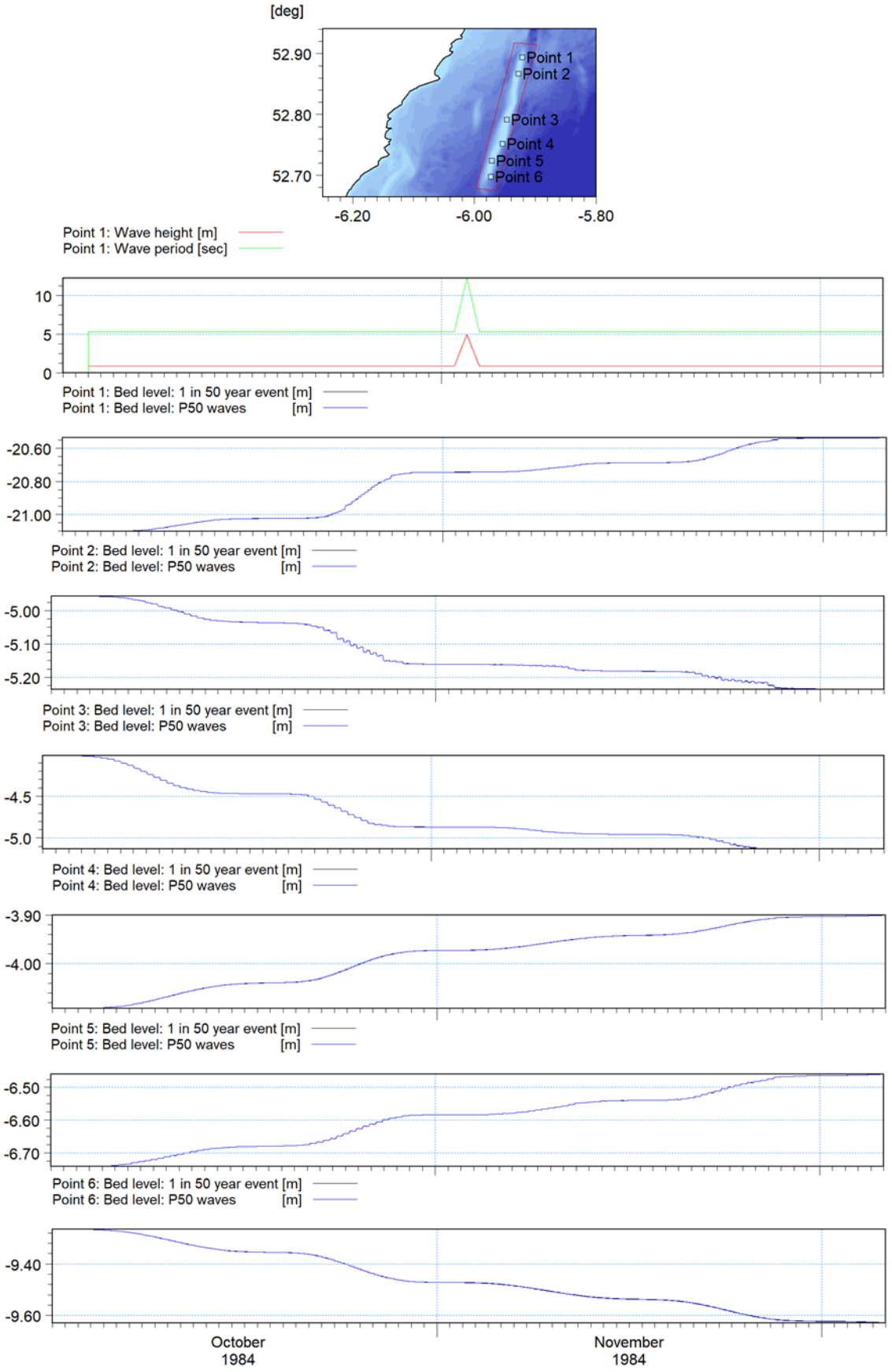


Figure 369. Effect of storm waves on bed levels as derived from sensitivity runs.

Appendix I: Local Scour Potential

The design engineer must consider the potential for scour development around the installed foundation. For piled foundations scour will lower the pile fixation level or, for structures put on the seabed (e.g. gravity bases), potentially cause undermining of the foundations. As such, foundations installed on the shallow continental shelf almost universally are now protected against scour via installation of rock protection that are of sufficient size, and cover a sufficient areal extent, to, as best as possible, fix the seabed level in the close vicinity of the foundation.

Scour is the phenomenon of seabed sediments being eroded around the base of the foundation. Scour induced transport which leads to, on occasion, significant erosion around the base of foundations, particularly when situated in non-cohesive sediments, it is driven by flow acceleration and increased turbulence in the local flow field which creates a horseshoe vortex around the foundation. Because of the increased flow velocities and turbulent vortices, the bed shear stresses increase around the foundation. Consequently, the sediment erosional capacity increases, and local erosion (scour) develops where the scour potential is greater than the local sediments resistance to motion. As a scour hole develops, the strength of the large-scale eddy structures is weakened, thereby reducing the transport rate from the local scour region. An equilibrium state is established (or re-established) at which stage, either the rate of sediment infill of the scour hole is equal to the rate of erosion, or where the critical shear stress required to mobilise sediments at the bottom of the scour hole is equal to, or greater than, the shear stress acting on the seabed. Seabed level changes can either enhance or reduce scour effects, i.e., if the scour hole occurs in an area of the seabed which is lowering scour will be enhanced whereas if the seabed level is rising scour effects may be reduced. The mechanics of scour is presented in greater detail in Sumer and Fredsoe (2002, 2006).

Scour development is a function of pile dimension, local seabed structure and composition and the nature of the local hydrodynamic and wave climate (for shallow water sites). It is evident that ABWP exists as a *live bed* sediment regime and thus the seabed sediment is also mobile outside the zone of influence of a structure. Closer to structures the critical threshold for mobility will be exceeded more regularly (or for a more sustained period), and thus the relative mobility of seabed sediments will be enhanced. Any foundation type on Arklow Bank will experience scour if left unprotected. At this stage the exact dimensions of the structures are not yet known, and, also, the foundation locations are yet to be confirmed. Due to the highly dynamic sediment regime observed across Arklow Bank and recognising that scour protection was installed for the Phase 1 turbine locations (and considered in detail at the time by Whitehouse *et al* [2011]), the scenario assessed as part of this study of *'free scour development'* where the foundation is installed into or on top of the unprotected seabed, is rather unrealistic. However, quantitative assessment of the shape, equilibrium scour depth and timescale for development of the scour holes provides useful supplementary information to support the design of scour protection during design.

To quantify the potential magnitude of local scour around the WTG monopile substructures, time series of current and wave conditions were extracted from hindcast data derived from the coupled hydrodynamic / wave model and used as incident conditions to drive the prediction of scour using the MIKE21 scour calculator toolbox. Scenarios were performed for scour around a single monopile (monopile dimensions as defined in the concept design phase). The model was driven by the maximum bed shear stress due to currents and waves, calculated by one of three methods: Fredsoe (1984), Grant and Madsen (1979) and Soulsby (1995). Scour development is calculated over a representative 1-year period (2017) at 30 s timesteps. The input parameters applied are detailed in Table 27. For input to the scour calculator, the still water depth at the location of the turbine was extracted from the 2019 bathymetry. The total water depth is obtained by adding surface elevation from the hydrodynamic hindcast. The representative results for WTG 74 are presented in Figure 370.

Table 27. Input parameters applied to the MIKE21 Scour Calculator Toolbox.

Parameters	Value	Unit
Pile Diameter	6.5	[m]
Initial Scour Depth	0.0	[m]
Scour Depth/Pile Diameter	1.3*	
Mean Sediment Diameter	0.25**	[mm]
Angle of repose	32	[°]

* *In tidally dominant environments, particularly live bed conditions, such as Arklow Bank, the scour depth of 1.3D, where D is monopile diameter, is applicable.*

** *Sensitivity testing was performed on a range of mean sediment diameters (ranging from 0.15 – 2.5 mm). These analyses show only minor difference between cases. Note: the lease area is dominantly comprised of sand; and the d_{50} of 0.25 mm was applied as part of the simulation. This analysis also assumes that the sediment type and composition does not vary through depth and thus scour can continue unabated until the equilibrium scour depth is reached.*

Based on a representative case, without scour protection, and assuming sediment properties remain consistent with depth, the scour depth under combined forcing of waves and currents reaches its equilibrium of 8.5 m at 14 days after its installation. The maximum scour width (radius) is circa. 22 m (limited by the angle of repose). The orientation of the long axis of scour reflects the tidal axis. Simulations conducted for other turbine locations across the lease area have shown highly similar results of circa. 13 days to 15 days to reach the equilibrium scour depth. It is strongly recommended that further, more detailed, site and structure-specific computations are performed by the designer to determine an appropriate scour mitigation strategy for each foundation.

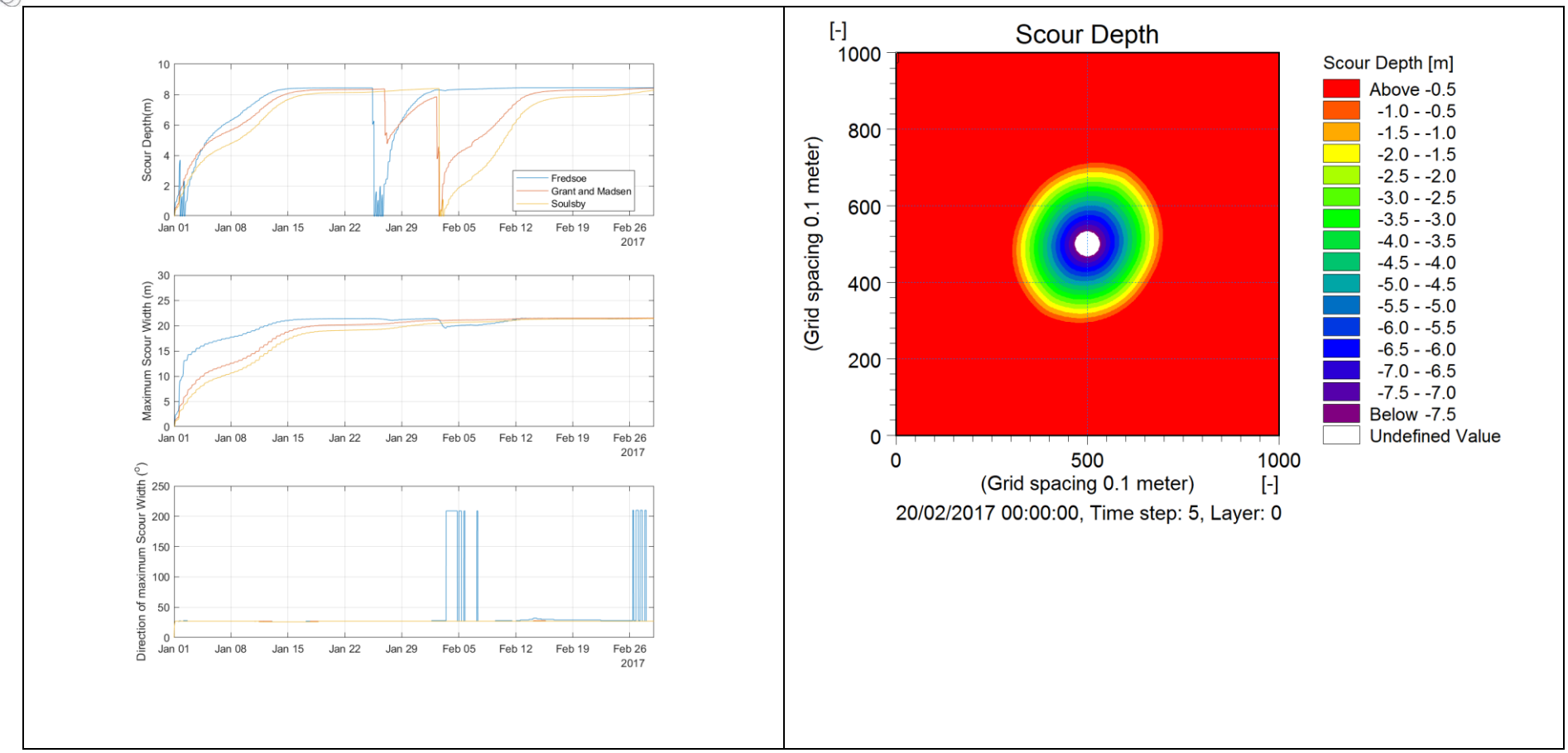


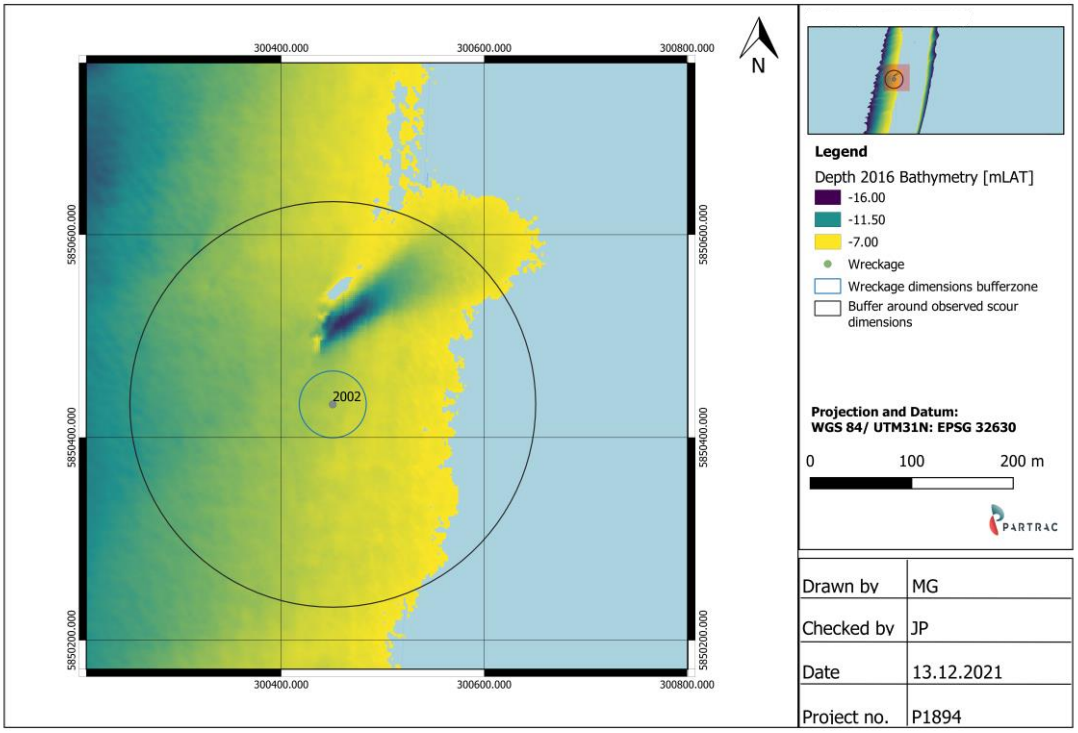
Figure 370. Time series of model outputs during the first 2 months of the simulation (left panel). The spatial plot of scour for WTG 74, calculated using the Fredsoe method, is also presented as an example (right panel).

Historic evidence from existing wind farms shows that separation between wind farm turbines of circa 8 to 10 blade diameters, and scales < 0.1 km, is sufficient to mitigate for the potential interaction of foundation induced turbulent flow wakes. Where this can be achieved, array scale morphological effects are likely to be negligible. Cumulative scour effects can also be enhanced where other seabed obstructions exist including wrecks. A total of 32 shipwrecks were identified within the lease area (GDG, 2020), with 7 of the 32 shipwrecks listed as "known wrecks", 6 listed as "possible wrecks", and 19 locations listed as anomalies that could be potential wrecks. Of particular relevance to local, and cumulative, scour effects across the ABWP lease area, are nine shipwrecks (which were either buried or observed). These wrecks were deemed relevant to the study due to their size, which has the potential to influence the local flow field Table 28. Though several potential wrecks appear along the proposed cable routes, negligible scouring was evident in the bathymetry data (due to a largely non-erodible seabed of gravelly sediments) and thus has not been considered further as part of this assessment.

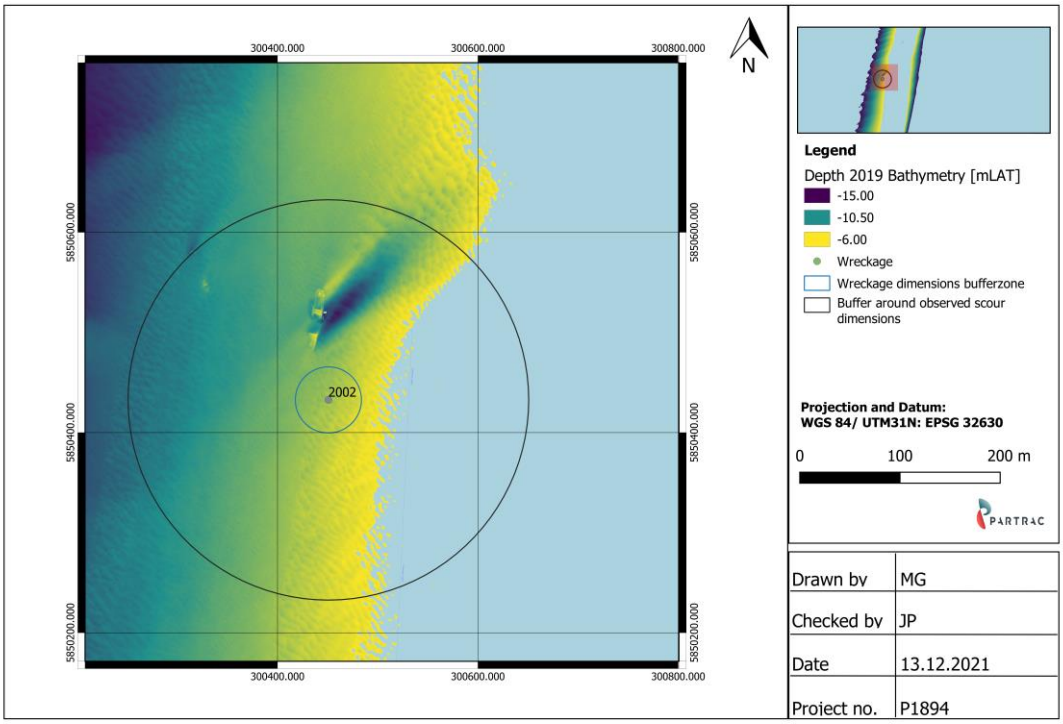
Table 28. Wrecks of significance within the ABWP lease area.

MAA ID as detailed in GDG (2020)	Name	Notes regarding current wreck condition	Dimensions (length,width and height m)
2001	Aremenian (SS)	No trace of wreck on bathymetry or SSS data. however, a magnetic anomaly is observed, the wreck is possibly buried.	57.8 x 15.3 x 4.3
2002	Hellenis	The wreck is observed on the bed, it appears the wreck migrated northwards.	66.9 * 8.8
2014	Unknown	The wreck is observed on the bed, appears to have migrated northwards.	8 x 5.8
2015	Unknown	The wreck is observed on the bed, appears to have migrated northwards.	23.0 x 10.0
2026	Unknown	Traces of wreck or a buried cable can be seen on the bathymetry.	Unknown
2027	Unknown	Traces of wreck can be seen on the bathymetry.	20.7 x 4.6
2031	Unknown	Traces of wreck can be seen on the bathymetry.	24.1 x 7.9 x 2.0
2037	Unknown	No trace of wreck on bathymetry or SSS data. however, a magnetic anomaly is observed, the wreck is possibly buried.	0.2 x 0.2 x 6.0
2039	Unknown	Traces of wreck can be seen on the bathymetry.	19.5 x 0.6

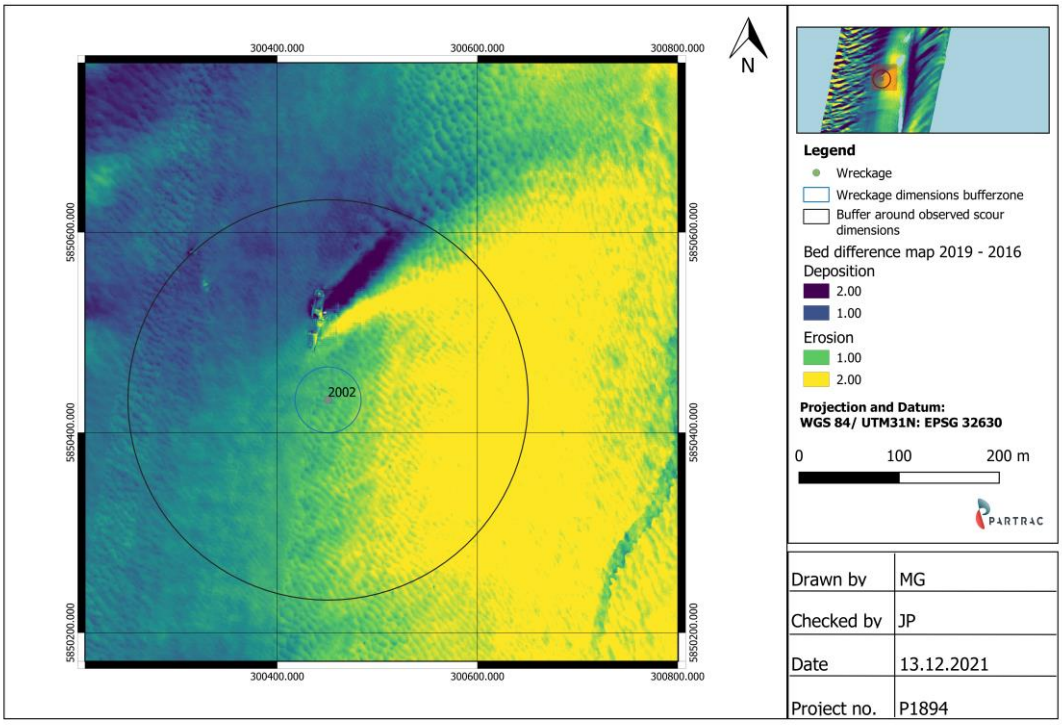
In the bathymetry data acquired in 2016 and 2019, scour holes were observed near wreck locations #2002 and #2039. Figure 371 and Figure 372 show the detailed bathymetry around these two locations. The maximum depth of the scour hole observed in the data was circa 3.6 m and 7.2 m for wreck id #2002 and #2039, respectively. The length of the scour pit, elongated along the axis NNE – SSW, at wreck #2002 had reduced from circa 190 m in 2016 to circa 86 m in 2019, the scour pit at wreck #2039 was circa 44 m long, elongated along the axis NE-SW, was not evident within the bathymetry data acquired in 2019. These data indicate that these scour pits may experience periods of infilling (note; from two surveys it is not possible to draw conclusions regarding infilling, particularly at a highly dynamic site where other processes may influence local seabed levels).



Wreck ID #2002 - 2016 Bathymetry

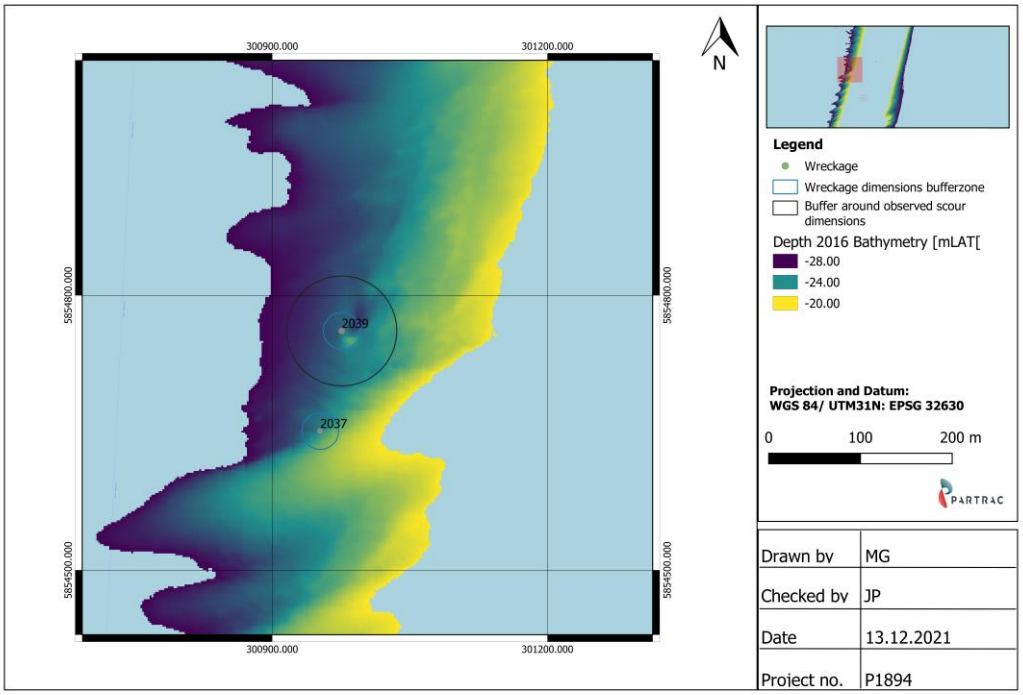


Wreck ID #2002 - 2019 Bathymetry

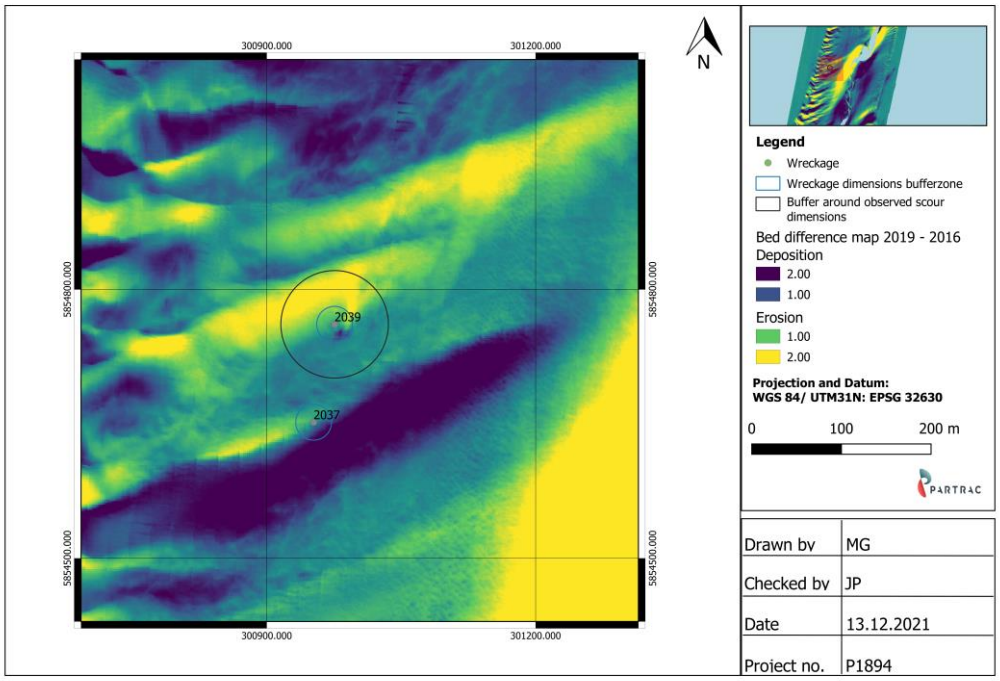


Wreck ID #2002 – Seabed level difference plot 2016 to 2019

Figure 371. Scour hole in close vicinity to wreck id 2002 observed in the bathymetry data acquired in 2016 (top panel) and 2019 (middle panel).



Wreck ID #2039 - 2016 Bathymetry



Wreck ID #2039 – Seabed level difference plot 2016 to 2019

Figure 372. Scour hole in close vicinity to wreck id 2039 observed in the bathymetry data acquired in 2016 (ltop panel). Note the scour hole was not evident at this location in the data acquired in 2019.

PAGE INTENTIONALLY LEFT BLANK